CLNS-12-2084
LBNL-6054E
CBP-910

The CESR Test Accelerator Electron Cloud Research Program Phase I Report

Editors: *M. A. Palmer, M. G. Billing, G. F. Dugan, M. A. Furman and D. L. Rubin*

January 11, 2013

Program Contributors:

N. Omcikus[1], K.C. Harkay[2], R. Dowd[3], W. Guo, S.Y. Zhang[4], R.L. Holtzapple[5], L. Fabrizio[5], M. Randazzo[5], D. Asner[6], M. Cunningham[6], D. Carmody[7], J. Chu[7], F. Antoniou[8], S. Calatroni[8], F. Caspers[8], M. Gasior[8], R. Jones[8], Y. Papaphilippou[8], J. Pfingstner[8], G. Rumolo[8], H. Schmickler[8], M. Taborelli[8], D. Gonnella[9], J. Jones[10], A. Wolski[10], D. Teytelman[11], J.P. Alexander[12], J. Barley[12], L. Bartnik[12], M.G. Billing[12], K.R. Butler[12], J.R. Calvey[12], S.S. Chapman[12], G.W. Codner[12], M. Comfort[12], C.C. Conolly[12], J.V. Conway[12], J.A. Crittenden[12], C.A. Dennett[12], J.A. Dobbins[12], G.F. Dugan[12], N. Eggert[12], M. Ehrlichman[12], E. Fontes[12], M.J. Forster[12], R.E. Gallagher[12], S.W. Gray[12], S. Greenwald[12], D.L. Hartill[12], W. Hartung[12], Y. He[12], R. Helms[12], L. Hirshman[12], W.H. Hopkins[12], J. Kaminsky[12], J. Kandaswamy[12], J-S. Kim[12], D.L. Kreinick[12], B. Kreis[12], J. Lanzoni[12], Z. Leong[12], Y. Li[12], H. Liu[12], X. Liu[12], J.A. Livezey[12], A. Lyndaker[12], J. Makita[12], M. McDonald[12], V. Medjidzade[12], R.E. Meller[12], T.P. Moore[12], T.I. O'Connell[12], M.A. Palmer[12], S.B. Peck[12], D.P. Peterson[12], G.A. Ramirez[12], M.C. Rendina[12], P. Revesz[12], D.H. Rice[12], N.T. Rider[12], D.L. Rubin[12], D.C. Sagan[12], S. Santos[12], J. Savino[12], R.M. Schwartz[12], R. Seeley[12], J. Sexton[12], J. Shanks[12], J.P. Sikora[12], E.N. Smith[12], K.W. Smolenski[12], K.G. Sonnad[12], M. Stedinger[12], C.R. Strohman[12], A.B. Temnykh[12], M. Tigner[12], J.T. Urban[12], S. Vishniakou[12], S. Wang[12], W. Whitney[12], T. Wilksen[12], H.A. Williams[12], Y. Yariv[12], M.C. Ross[13], C.Y. Tan[13], R. Zwaska[13], B. Carlson[14], K. Hammond[15], M. Lawson[16], C. Cude[17], T. Demma[18], J. Flanagan[19], H. Fukuma[19], T. Ishibashi[19], P. Jain[19], K. Kanazawa[19], S. Kato[19], K. Kubo[19], K. Ohmi[19], K. Oide[19], H. Sakai[19], K. Shibata[19], Y. Suetsugu[19], H. Tajima[19], M. Tobiyama[19], J. Urakawa[19], R.J. Macek[20], J. Byrd[21], C.M. Celata[21], J.N. Corlett[21], S. De Santis[21], M.A. Furman[21], A. Jackson[21], R. Kraft[21], D.V. Munson[21], G. Penn[21], D.W. Plate[21], A. Rawlins[21], M. Venturini[21], M. Zisman[21], E.L. Wilkinson[22], H. Jin[23], L. Boon[24], A.F. Garfinkel[24], D. Kharakh[25], J. Ng[25], M.T.F. Pivi[25], L. Wang[25], R.P. Badman[26], S. Veitzer[27], L. Schächter[28], P. Kehayias[29], and L. Hales[30]

[1]American River College, Sacramento, CA 95841, U.S.A.
[2]Argonne National Laboratory, Argonne, IL 60439, U.S.A.
[3]Australian Synchrotron, Clayton, 3168, Australia.
[4]Brookhaven National Laboratory, Upton, NY 11973, U.S.A.
[5]Physics Department, California Polytechnic State University, San Luis Obispo, CA 93407, U.S.A.
[6]Department of Physics, Carleton University, Ottawa, Ontario, K1S 5B6, Canada.
[7]Department of Physics, Carnegie Mellon University, Pittsburgh, PA, 15389, U.S.A.
[8]CERN, CH-1211 Genève 23, Switzerland.
[9]Department of Physics, Clarkson University, Potsdam, NY 13699, U.S.A.
[10]Cockroft Institute, Warrington, Cheshire, U.K.
[11]Dimtel, Inc., San Jose, CA 95124, U.S.A.
[12]Cornell Laboratory for Accelerator-based Sciences and Education, Cornell University, Ithaca, NY, 14850, U.S.A.
[13]Fermi National Accelerator Laboratory, Batavia, IL 60510, U.S.A.

[14]Physics Department, Grove City College, Grove City, PA 16127, U.S.A.
[15]Department of Physics, Harvard University, Cambridge, MA 02138, U.S.A.
[16]Department of Physics, Harvey Mudd College, Claremont, CA 91711, U.S.A.
[17]Department of Physics, Indiana University, Bloomington, IN 47405, U.S.A.
[18]Istituto Nazionale di Fisica Nucleare - Laboratori Nazionali di Frascati, 00044 Frascati, Italy.
[19]High Energy Accelerator Research Organization (KEK), Tsukuba, Ibaraki 305-0801, Japan.
[20]Los Alamos National Laboratory, Los Alamos, NM 87544, U.S.A.
[21]Lawrence Berkeley National Laboratory, Berkeley, CA 94270, U.S.A.
[22]Department of Physics, Loyola University, Chicago, IL, 60626, U.S.A.
[23]Department of Physics, Postech, Pohang, Gyeongbuk 790-784, R.O.K.
[24]Department of Physics, Purdue University, West Lafayette, IN 47907, U.S.A.
[25]SLAC National Accelerator Laboratory, Menlo Park, CA 90425, U.S.A.
[26]Department of Physics, Syracuse University, Syracuse, NY 13244, U.S.A.
[27]Tech-X Corporation, Boulder, CO, 80303, U.S.A.
[28]Department of Electrical Engineering, Technion-IIT, Haifa, 32000, Israel.
[29]Department of Physics and Astronomy, Tufts University, Medford, MA 02155, U.S.A.
[30]Department of Physics and Astronomy, University of Utah, Salt Lake City, UT 84112, U.S.A.

Contents

List of Figures

List of Tables

Chapter 1

Introduction

A new generation of particle accelerators is being designed and constructed to explore the frontiers of high energy physics. This endeavor requires machines that exceed the performance of any of those currently in operation. The challenges of these new machines come in many forms. Some issues require greater manufacturing and assembly precision, others require the development of new technologies, and still others require that we understand in greater detail the physical processes that can impact the performance of these machines. In this last category, a recurring issue for both hadron and lepton colliders is the development of electron plasma within the accelerator vacuum chambers. This plasma, commonly referred to as an "electron cloud," can interact with and destabilize the high intensity particle beams required for our exploration of both the intensity and energy frontiers.

1.1 The CesrTA Research Program

The build-up of the electron cloud (EC) in the positron damping ring (DR) of the International Linear Collider (ILC) is one of the principal risk factors for the overall physics performance of the accelerator. In positron storage and damping rings, electrons are produced in the accelerator vacuum chambers through photoemission and secondary emission. Interaction between the resulting EC and the beam can lead to single- and multi-bunch instabilities in the beam. The onset of a single-bunch head-tail instability, which cannot in general be controlled by a conventional feedback system, will lead to emittance growth in the beam. For the ILC DR, which targets a geometric vertical emittance of 2 pm-rad, we must ensure that the machine can be operated safely below this instability threshold. Below the threshold for the onset of single-bunch instabilities, sub-threshold emittance dilution may still occur through the interaction of the beam with the nonlinear fields of the EC. With the ultra low emittance target of the ILC DR, there is little margin for such emittance diluting effects. Hence this area was identified as one requiring further R&D in order to complete the ILC technical design.

The CesrTA research program was approved in late 2007 to carry out electron cloud R&D in support of the ILC technical design. The first dedicated experiments using the Cornell Electron-Positron Storage Ring (CESR) began in March 2008 after the conclusion of 28 years of colliding beam operations for the CLEO experiment [1, 2]. Two principal goals were specified for the program. The first was to characterize the build-up of the EC in each of the key magnetic field

regions of the accelerator, particularly in the dipoles and wigglers, and to study the most effective methods of suppressing it in each of these regions. This required the design and installation of detectors to study the local build-up of the cloud in each of these environments as well as a supporting simulation program to fully characterize and understand the results. A key element of the experimental approach was to create four dedicated electron cloud experimental regions to support flexible tests of any mitigation technique under consideration for use in the damping ring. This approach enabled a comprehensive set of comparisons of the relevant EC mitigation methods and has provided a solid foundation on which to base the design of future machines. The flexibility of the machine has enabled detailed probes of the surface parameters of the various mitigations within an operating accelerator, thus providing a unique physics reach. These studies have relied on the ability to:

- Operate with beam energies between 1.8 and 5.3 GeV;
- Operate with both electron and positron beams;
- Employ flexible bunch patterns within the beam, including variations in spacing and intensity;
- Operate over a wide range of beam, and bunch, intensities;
- Operate over a wide range of emittances, with and without damping wigglers.

The second principal goal was to study the impact of the EC on ultra low emittance beams. No positron ring has achieved the 2 pm-rad vertical emittance design target of the ILC DR. By benchmarking EC instability and emittance growth simulations in an emittance regime near to that specified for the DR, and by being able to systematically validate those simulations over a range of operating emittances, our confidence in the projections of the final DR performance has been significantly improved. These results have helped guide the R&D effort towards a damping ring design which we are confident can meet the specifications required by the ILC.

In order to carry out this broad experimental program to understand and mitigate the impact of the electron cloud in future high intensity accelerators, CESR was reconfigured as a damping ring in 2008. Over the course of the 3-year Phase I R&D program, the ring's beam instrumentation was upgraded to allow low emittance optics correction and for the characterization of ultra low emittance bunch trains. In parallel, a suite of local electron cloud detectors and diagnostics were deployed throughout the electron cloud experimental regions to characterize the environment of these beams and the surface physics of the vacuum system. The low emittance tuning techniques that were developed, along with the physics results obtained, represent one of the most comprehensive experimental studies of accelerator physics issues relevant to future high intensity and ultra low emittance machines.

1.2 CesrTA Parameters and Experimental Reach

The CESR storage ring, outfitted with independently powered quadrupoles and sextupoles and 18 meters of superconducting damping wigglers is enormously flexible. The linac and synchrotron provide full energy injection of electron and positron beams. The storage ring magnets allow operation over an energy range of 1.8 to 5.6 GeV. Multibunch feedback systems stabilize motion in all three planes of trains of bunches with bunch spacing of as few as 4 ns. The single cell 500 MHz superconducting RF system operates over a range of gradients that enables investigations of bunch

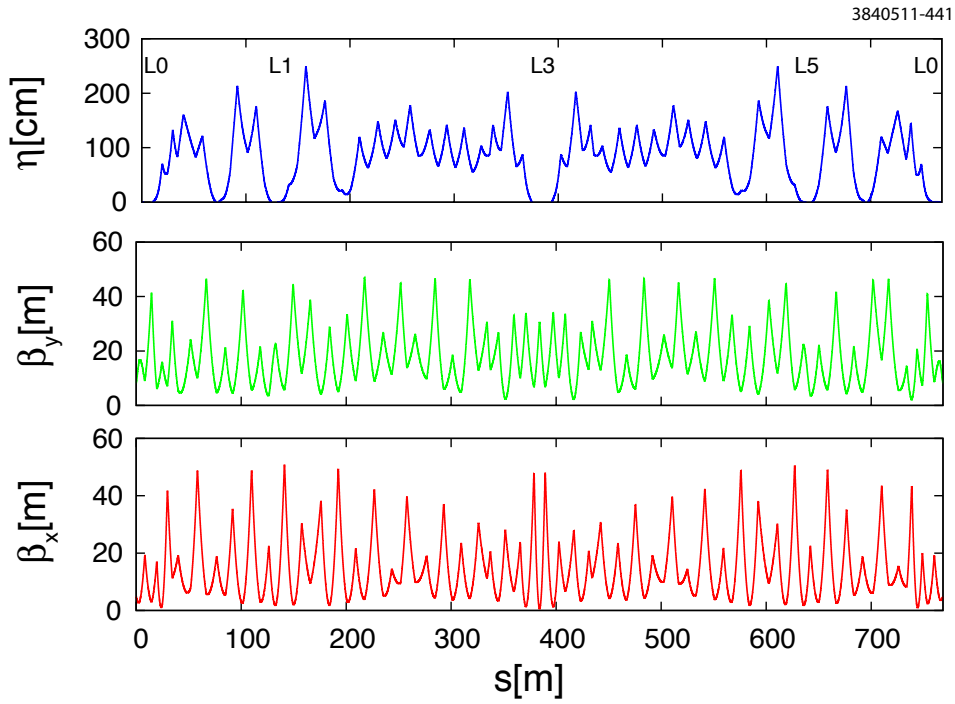

Figure 1.1: Design optics functions of low emittance ($\epsilon_x = 2.6$ nm-rad) lattice, with horizontal dispersion, η, at the top and the vertical and horizontal amplitude functions, β_y and β_x below. Regions of zero horizontal dispersion where damping wigglers are located are the L0 straight ($s = 0 \pm 10$ m where there are 6 wigglers) and L1 (126.7 m to 132.7 m, 3 wigglers) and L5 ($s = 635.8\ m$ to $s = 641.8\ m$, 3 wigglers). L3 (384.2 $\pm$ 9 m) is the experimental straight that includes the chicane for electron cloud studies and the in-situ SEY station. Retractable mirrors are used to reflect synchrotron radiation generated in the bends on either side of the L3 straight to the cave where optical instruments are located.

length dependencies. The complement of more than 100 steering correctors and 25 skew quad correctors is sufficient to eliminate relevant sources of vertical emittance dilution.

1.2.1 Low Emittance Optics

We achieve minimum emittance at about 2 GeV beam energy with the superconducting damping wigglers operating at 1.9 T field.The wigglers reduce the radiation damping time by an order of magnitude and the horizontal emittance by a factor of 5 with respect to the wiggler off condition. The lattice functions are arranged so that there is zero horizontal dispersion in the wiggler straights. The relatively strong focusing and high horizontal tune minimizes the dispersion in the bend magnets and the resulting horizontal emittance. The lattice functions for the minimum emittance 2.085 GeV optics are shown in Figure 1.1. The sextupoles are deployed to correct chromaticity in two families. Dynamic aperture is shown in Figure 1.2.

The damping wigglers are essential to achieving the low emittance in these optics. However it is worth noting that, in the limit of a wiggler dominated ring, the minimum emittance is determined by the horizontal emittance generated within the wigglers themselves. With 12 wigglers, that

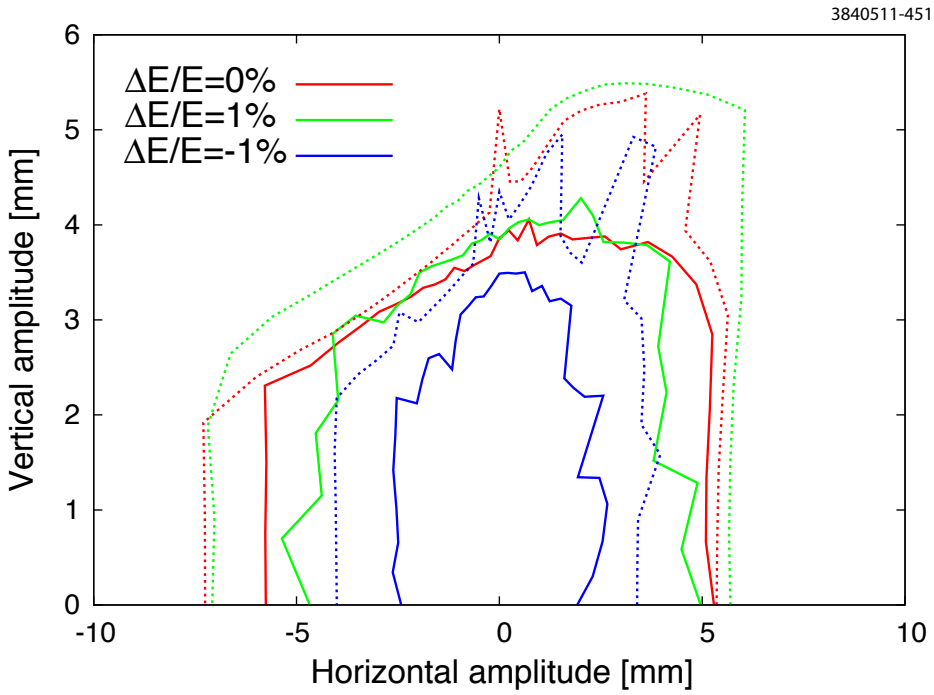

Figure 1.2: Simulation of the dynamic aperture for the low emittance lattice at 2.085GeV. The solid curves are the maximum initial amplitude that survives 1000 turns at betatron tunes $Q_h = 14.595$, $Q_v = 9.63$, and synchrotron tune $Q_z = 0.0645$. The red, green and blue correspond to initial energy offsets of $0, \pm 1\%$. The dashed lines are the maximum initial amplitude that survives for 20 turns and so approximate the physical aperture. Particles are lost at the real physical boundaries of the vacuum chamber.

minimum is indeed obtained with a 1.9 T wiggler field. Higher wiggler fields will further reduce the damping time, but will increase the emittance due to the wiggler dispersion. The only way to further reduce the emittance with wigglers would be to increase the total length of wigglers, rather than increasing the wiggler field.

1.2.2 Energy Reach

We have designed and commissioned optics at 1.8, 2.085, 2.3 and 2.8 GeV, with all wigglers at 1.9 T field. At beam energy greater than 3 GeV, wiggler operation is limited to the those in the L0 straight. The vacuum chambers adjacent to the arc wigglers cannot sustain the heat load generated at high energies. Table 1.1 lists some of the CesrTA lattice configurations that have been used for various measurements.

1.2.3 Knobs

The flexibility of the CESR control system allows the possibility of creating element groups for closed orbit, β, dispersion, and coupling bumps. We use orbit bumps to align the beam with the x-ray beam lines for the x-ray beam size monitor. In general, the beam size depends on emittance

Table 1.1: CesrTA Lattice configurations

Lattice Name	Energy [GeV]	Emittance [nm-rad]	Wigglers @ 1.9 T	β_v at xBSM e^+ source	Wiggler radiation [%]
CTA_2085MEV_xr20M_20091205	2.085	2.6	12	20	87
CTA_2085MEV_xr40M_20091205	2.085	2.6	12	40	87
CTA_1800MEV_xr40M_20110520	1.800	2.0	12	40	90
CTA_2085MEV_20090516	2.085	2.6	12	5.8	87
CTA_2300MEV_XR40M_20110531	2.3	3.2	12	40	84
CTA_3000MEV_Q0H_20090822	3.0	10.0	6	11.4	58
CTA_4000MEV_23NM_20090816	4.0	23	6	10.7	47
CTA_5000MEV_40NM_20090513	5.0	40	6	7.2	37
CTA_5000MEV_20090311	5.0	74	0	11.3	0

ϵ, amplitude function β, dispersion (η), and energy spread δ, according to $\sigma = \sqrt{\epsilon\beta + (\eta^2\delta^2)}$. It is often convenient to be able to independently vary β, ϵ and dispersion to explore beam size monitor systematics and properties of the lattice. β-bumps are used to manipulate the beta function at the x-ray and visible light beam size monitor source points. A closed dispersion bump at the source of the horizontal beam size monitor allows a measurement of the contribution of the energy spread to the beam size. Closed coupling/dispersion bumps are used to vary vertical dispersion (and therefore vertical emittance) in a controlled way. We have developed code to automatically compute coefficients and load into the control system data base, complete sets of orbit, and coupling/dispersion bumps for each new lattice configuration. An example of the effect of such a coupling/dispersion bump is shown in Figure 1.3.

1.3 Program Summary

The research encompassed in the CesrTA program will provide critical input to the design of low emittance positron damping rings, as regards tolerance to the electron cloud effect. A variety of mitigations have been characterized and compared using retarding field analyzers (RFAs) to measure growth of the electron cloud in dipoles, quadrupoles, and wigglers, as well as field free regions. RFAs measure local properties of the electron cloud and are therefore well suited to testing the effective of mitigations and how it depends on local magnetic fields. Physics parameters, including secondary emission yield and quantum efficiency have been extracted from the data. The time development and decay of the cloud has been measured using shielded pickups and time resolving RFAs, further constraining the model parameters.

In order to learn about the global properties of the cloud, and how the cloud density depends on location within a train of bunches, we measure the tune shift of each and every bunch. The tune shift depends on the density of the cloud witnessed by that particular bunch. Indeed the tune shift is a direct measure of the density of the cloud traversed by each and every bunch in the train.

Finally, a single pass, bunch by bunch beam size monitor provides a measure of the effect of the cloud on the vertical emittance. Combined with the tune shift measurement, we can identify precisely the threshold for emittance growth. From the beam spectra we learn about cloud induced instabilities.

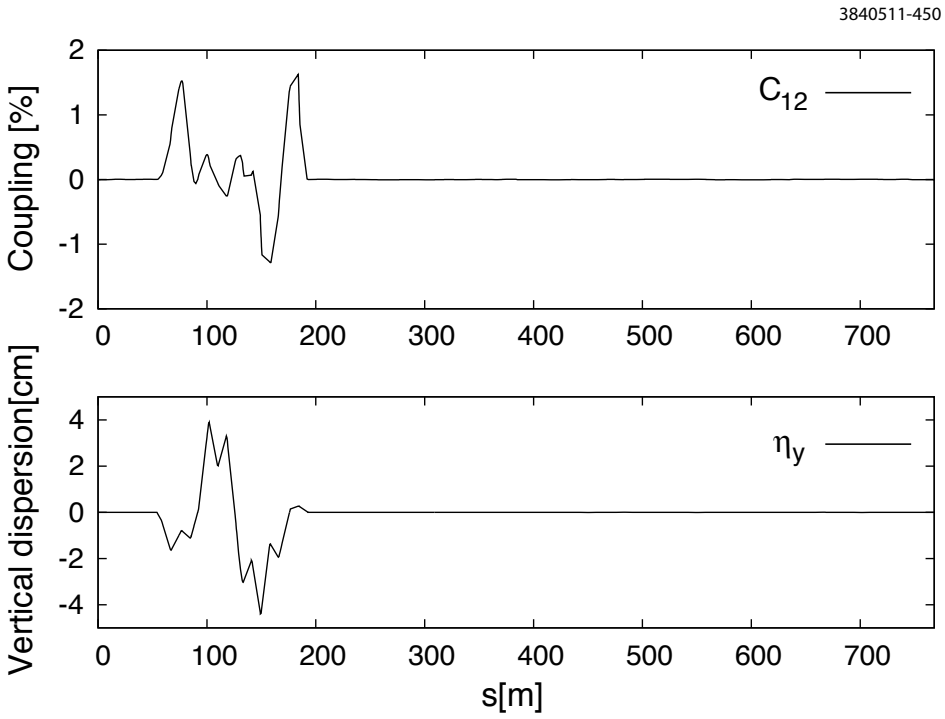

Figure 1.3: The closed coupling and vertical dispersion bump is generated with seven skew quads. The theoretical change to the vertical emittance (assuming that the unperturbed machine has zero coupling and zero vertical dispersion), is 25 pm-rad. The dispersion peak appears in the L1 region of the west arc wiggler straight. Bumps like this one are used to characterize the vertical beam size monitor and to vary emittance for investigation of IBS, ion, and electron cloud effect.

The combination of direct measurements and sophisticated modeling is the basis for the design of the ILC positron damping ring and specification of bunch configuration and beam current.

Along the way we have by necessity developed a variety of wiggler dominated storage ring lattice configurations, instrumentation and techniques for emittance tuning, and explored sensitivities to misalignments.

1.4 Content

Chapter II, "The CESR Conversion" describes the reconfiguration of the storage ring for low emittance operation, the vacuum chamber modifications, and instrumentation for measuring the properties of the electron cloud and its effect on the beam. In Chapter III we discuss emittance tuning techniques. Characterization of the electron cloud is to a large extent in terms of the physics parameters of the model. In chapter IV we introduce the model and the relevant physical processes. The observations of cloud growth, the comparison of model with the data, and the effectiveness of various mitigations is the subject of chapter V. Electron cloud beam dynamics are discussed in chapter VI, including electron cloud induced tune shifts, emittance growth, and single bunch instabilities.

In chapter VII we attempt to summarize the state of the electron cloud model in view of the

comparison with the CesrTA measurments. Recommendations for electron cloud mitigations the ILC damping ring are presented in chapter VIII. A brief discussion of outstanding questions, and plans for addressing them is the subject of chapter IX.

Chapter 2

The CESR Conversion to a Damping Ring Configuration

2.1 Overview of CESR Modifications

The conversion of CESR to permit the execution of the CesrTA program required several extensive modifications. These included significant reconfiguring of CESR's accelerator optics by removing the CLEO high energy physics detector and its interaction region, moving six superconducting wigglers and reconfiguring the L3 straight section. There were also major vacuum system modifications to accommodate the changes in layout of the storage ring guide-field elements, to add electron cloud diagnostics and to prepare regions of the storage ring to accept beam pipes for the direct study of the electron cloud. A large variety of instrumentation was also developed to support new electron cloud diagnostics, to increase the capabilities of the beam stabilizing feedback systems and the beam position monitoring system, to develop new X-ray beam size diagnostics and to increase the ability for studying beam instabilities. This conversion process and the instruments developed for the CesrTA program are described in the following sections.

2.2 Vacuum System Modifications

2.2.1 Overview

CESR vacuum system is an essential part of accelerator beam transport lines, capable of storing total beam currents up to 500 mA (or single beam up to 250 mA) at a beam energy of 5.3 GeV. As shown in Figure 2.1 the CESR vacuum system, with a total length of 768.44 m, consists of primarily bending chambers in the arcs, two long straight sections, namely L0 (18.01 m in length) and L3 (17.94 m in length), and four medium length straights (namely, $L1, L5$, both 8.39 m in length and $L2, L4$, both 7.29 m in length).

With exception of L0 and L3, CESR vacuum beam pipes are made from aluminum extrusions (Type 6063 alloy), with built-in pumping and cooling channels. The vacuum pumping in the arcs is dominated by the home-made distributed ion pumps (DIPs) inserted into the pumping channel of the extrusion, although ion pumps are installed periodically. The L0 straight section

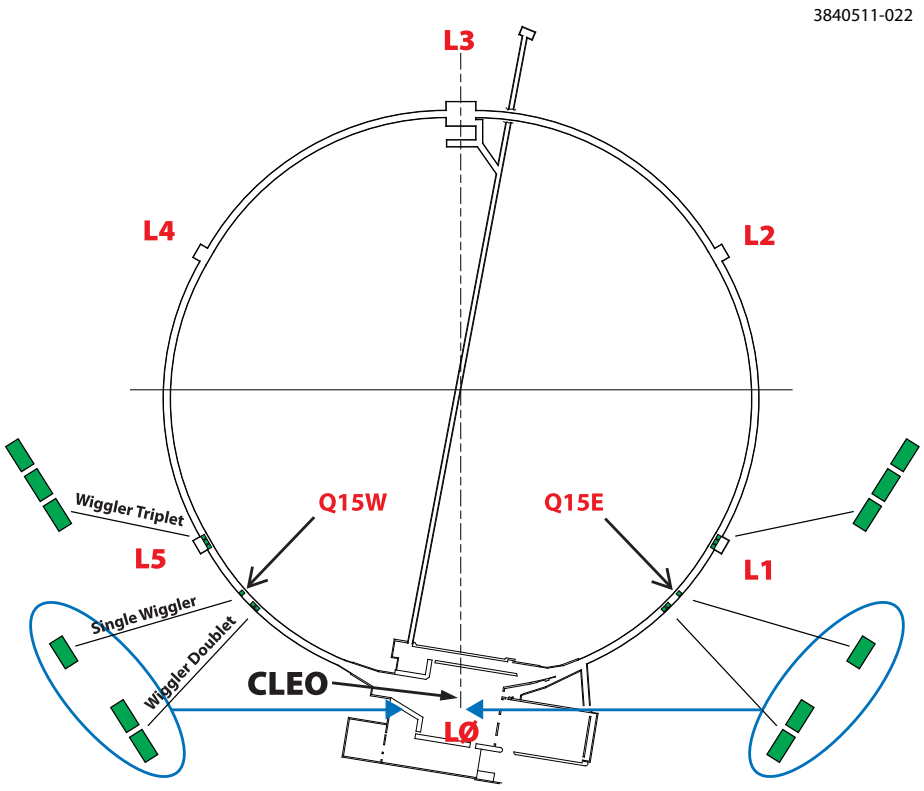

Figure 2.1: The reconfiguration of the CESR vacuum system provided space in two long regions in L0 and L3, and two flexible short regions at Q15W and Q15E. Hardware for electron cloud studies was installed in these regions.

was the interaction region for the CLEO High-Energy Physics (HEP) experiment, hosting the CLEO Detector at the center of L0. Massive titanium sublimation pumping (TiSP) [3] was implemented in L0 to achieve ultra-high vacuum (UHV) during the high current HEP operations for CLEO. In the CESR-c/CLEO-c era, 12 home-built superconducting wigglers (SCWs) were installed in CESR, with two triplets at $L1$ and $L5$, two doublets and two singlet SCWs in the arcs (see Figure 2.1). This complement of SCWs plays an important role in the CesrTA program. Over the nearly 29 year of operation prior to the CesrTA conversion the CESR vacuum system performed satisfactorily, with average dynamic pressure in the low 10^{-9} torr with more than 400 mA of stored beams of electrons and positrons.

At the conclusion of CLEO-c HEP program in March 2008, staged modifications were carried out to convert CESR into the test accelerator CesrTA. The motivation for the vacuum system modification is to support the physics programs of CesrTA, including: (1) Ultra-low emittance lattice design, tuning and associated beam instrumentations, and (2) electron cloud studies, suppression technique development and verification. During the design and implementation of the CesrTA vacuum system conversion, the following two important aspects were of pre-eminant consideration:

- To create environments where both local- and collaborator-provided test chambers and equipment can be easily installed and tested.
- To ensure the continuing successful operations of Cornell High Energy Synchrotron Source

(CHESS) at CESR.

The physical modification of CESR vacuum system started in May 2008 during a scheduled accelerator shutdown. But the bulk of the vacuum system reconfiguration was carried out in two long shutdowns, July 2008 and February 2009. The following list summarizes the scope of vacuum modifications during scheduled accelerator shutdowns.

1. May 27 – June 3, 2008:
   - Implemented a Cornell thin-style RFA on a CESR dipole chamber at B12W location.
   - Replaced two CESR-c SCWs with RFA-equipped drift chambers at Q14W location.
2. July 7 – October 23, 2008:
   - Replaced four more CESR-c SC wigglers from Q15W, Q14E/Q15E (see Figure 2.1) with new beam pipes equipped with EC diagnostics.
   - Created Q15W and Q15E short experimental sections.
   - Completed L0 reconfiguration, including removal of the central part of the CLEO HEP Detector and the IR vacuum chambers, installation of 6 SCWs (4 CESR-c and two RFA-equipped CesrTA SCWs) and many new chambers suited with EC diagnostics (such as RFAs and BPM/TE-wave buttons).
   - Partially reconfigured L3 region, including removal of a pair of (high beam impedance) electrostatic vertical separators.
3. February 23 – March 2, 2009:
   - Completed L3 central region reconfiguration, including installation of SLAC PEP EC beam pipes and chicane magnets.
   - Installed a photon-stop vacuum chamber, to replace a CLEO-c HEP-era fast-luminosity monitor chamber [4], at Q3W location. This new chamber, enabled storing up to 100 mA positron beam current in CESR at 5 GeV beam energy, with all 6 L0 SCWs in operation.
4. June 16 – July 23, 2009:
   - Installed first RFA-equipped quadrupole vacuum chamber, and in-situ SEY measurement stations in the L3 experimental region.
   - Installed test chambers at Q15W/E sectors.
   - Implemented three RFA-equipped SCWs in the L0 region.

The CesrTA vacuum system reconfiguration, as depicted in Figure 2.1, created four dedicated CesrTA experimental regions. The list below highlights the main features of these experimental sections.

- L0 EC Region: This region hosts a string of 6 superconducting wigglers, having 3 of them fitted with RFA-equipped beam pipes. The main function of this experimental section is to investigate EC dynamics and suppression techniques in the wiggler field.
- L3 EC Region: This region features EC studies in dipole and quadrupole fields and field-free drifts, as well as in-situ SEY measurement stations.

- Q15W & Q15E Test Sectors: These two short sectors each contain one CESR normal bend and a short straight and are intended for test new chambers with new EC diagnostics and EC suppression coatings.

During the reconfiguration and the first 3 years of the CesrTA program, over 40 new vacuum chambers and components were installed in or rotated through CESR vacuum system for the CesrTA program. Almost all of these new chambers were designed and constructed in-house. Many EC diagnostics and/or EC suppression features are successfully incorporated in these new chambers. The implemented EC diagnostics include RFAs at various types of magnets, shielded pickup buttons, and beam buttons for TE-wave measurement. The evaluated suppression techniques include many types of coatings (TiN, amorphous- and diamond-like carbon and non-evaporable getter), grooved walls and clearing electrode. A summary of the diagnostic chambers, evaluated for EC suppression, are shown in Table 8.1. Stringent QA/QC procedures were followed in the production of these new UHV components and chambers, including design reviews/approvals, UHV-compatible practices during assembly and installation, and pre-installation vacuum bakeouts. These efforts have resulted in very high degree of availability of the vacuum system for both CesrTA programs and CHESS operations.

2.2.2 Electron Cloud Experimental Regions

In this section, we provide details of the CesrTA EC experimental regions in terms of the vacuum system modification and performance.

2.2.2.1 L0 Wiggler Test Region

The CESR L0 long straight section (18.01 m in length), formerly the CLEO-c HEP Interaction Region (IR), was completely re-configured for the CesrTA research programs, through two major CESR Shutdowns. The modified L0 EC experimental region is shown in Figure 2.2. During a 4-month shutdown, starting July 7, 2008, the entire L0 straight section was modified. The modification included the following tasks:

- All L0 IR vacuum chambers, as well as the central portion of the CLEO detector assembly were removed.
- A new supporting rail system was designed and installed through the inner-bore of the remaining CLEO Outer detector.
- Six superconducting wigglers (SCWs) were moved to the new supporting rails and new cryogenic transfer lines were installed. The three SCWs toward the eastern-side of L0 are the original CESR-c style, while the three SCWs toward the western-side of L0 were fitted with RFA-equipped beam pipes (see detail in Section 2.2.3.3).
- Additionally 7 new vacuum beam pipes were also constructed, and installed in this region, in order to bridge between the SCWs. Many EC diagnostics were attached to these new chambers, including three insertable segmented RFAs, eight sets of beam buttons as BPMs and TE-Wave transmitters/receivers.
- A pair of RF-shielded expansion bellows assemblies (aka sliding joints) were included with the new chambers to allow thermal expansions during beam operations and to provide flexibility

for vacuum components exchange at various stages of the CesrTA program.

Most of the new vacuum chambers in L0 region are made of copper extrusions (the same kind used as CESR-c SCW beam pipe), having cooling channels welded on both sides of the beam pipes. Achieving an adequate level of ultra-high vacuum (UHV) during both the CesrTA and CHESS operations is essential in the vacuum system design for this experimental region. Figure 2.3 shows installed vacuum pumps and gauges. Two types of UHV pumps in use are sputter ion pumps (SIPs) and non-evaporable getter pumps (NEGs). At each SCW location one NEG and one small SIP are installed at a single pumping port. At the center of this region a large SIP was installed. The 6 NEGs provide the main vacuum pumping for the region, though periodic re-activations of these NEGs are required. The 7 SIPs provide primary pumping during the initial beam conditioning of the vacuum chambers (after a vacuum intervention of the region), as well as supplementary pumping of non-gettable gases (such as Ar and CH_4). The vacuum performance of the region is monitored by 5 cold-cathode ion gauges (CCGs) and one residual gas analyzer (RGA). During the CesrTA program the L0 region had been vented three times for installations of RFA-equipped SCWs with different EC suppression techniques. As expected, a period of beam conditioning is required to achieve acceptable vacuum level after each vacuum intervention. Typical beam conditioning behavior is displayed in Figure 2.4, where the beam-induced pressure rise (dP/dI in 10^{-9}torr/Amp) is plotted against accumulated beam dosage (in Amp · hr).

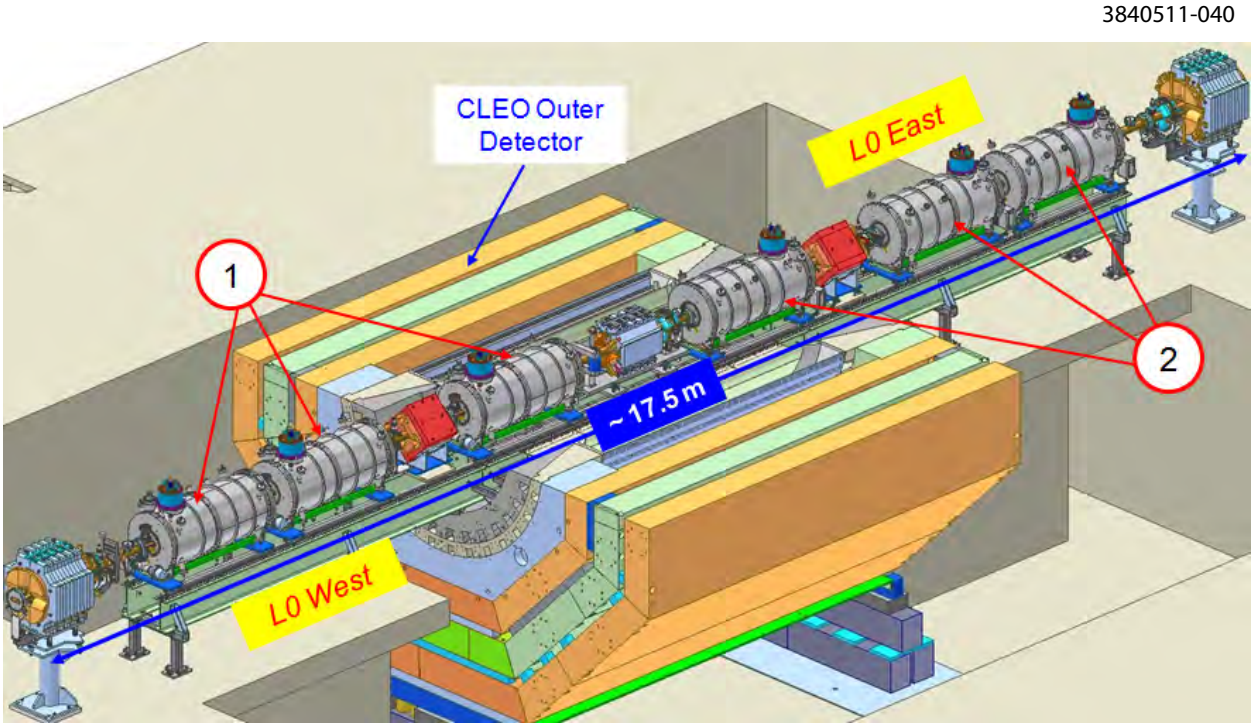

Figure 2.2: L0 center CesrTA EC experimental region, consists of (1)three RFA-equipped SCWs and (2) three CESR-c SCWs. Many other EC diagnostics, such as RFA in the drifts, BPMs and TE-Wave buttons, are also implemented. The six SCWs in the region are labelled, from west to east, SCW02WB, SCW02WA, SCW01W, SCW01E, SCW02EA and SCW02EB. Detailed engineering information of the L0 experimental region can be found in two CLASSE drawings with LEPP Drawing Numbers 6085-012 (Vacuum String + Magnets + Supports) and 6085-045 (Vacuum String only).

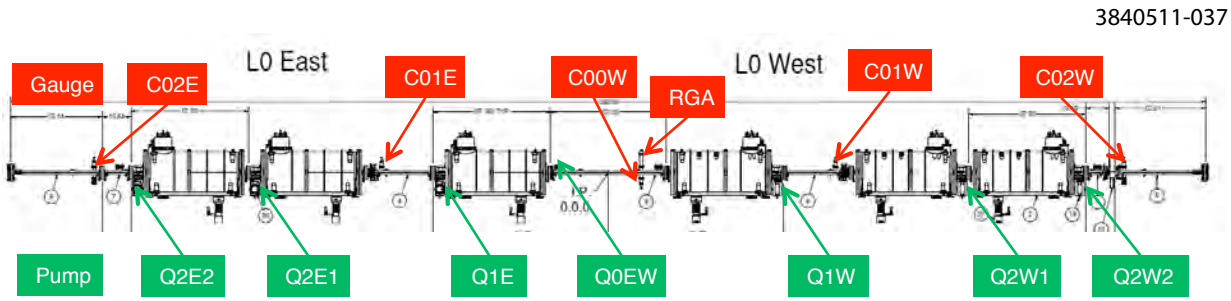

Figure 2.3: Vacuum Pumping and Instrumentation in the L0 Center CesrTA EC experimental region. At locations (labeled in *GREEN* as Q2E2, Q2E1, Q1E, Q1W, Q2W1 and Q2W2), a combination of a NEG and a small SIP is installed, while at the center of the region (labeled in *GREEN* as Q0EW), a large SIP is installed. Five cold-cathode ion gauges and a residual gas analyzer (as labeled in *RED*) are also installed in the region to monitor the vacuum system performance.

- Very high pressure rises were observed initially at each startup, due to high SR-induced desorption yield on exposed surfaces. The beam-induced pressure rise drops quickly with accumulated beam dosage (D), typically following $\frac{dP}{dI} \propto D^{-\alpha}$, with $\alpha = 0.6 \sim 1.0$.
- The vacuum level in the region usually becomes acceptable for beam operation after accumulating 30∼50 $Amp \cdot hr$ beam dose at each startup.
- The vacuum in the L0 West (as measured by C00W, C01W and C02W, see Figure 2.3) is always significantly worse than the symmetrical locations in the L0 East, during beam-operations, though the base pressures are comparable throughout the L0 region. L0 West hosts three RFA-equipped SCWs, while L0 East hosts three CESR-c SCWs. Higher SR-induced outgassing rate from TiN coated beam pipes at L0 Center and SCWs is a likely reason for worse vacuum in the L0 West.
- RGA data at L0 Center indicated desorption of nitrogen, most likely from TiN coated surfaces. As shown in Figure 2.5, the desorption of N_2 is even more evident with higher energy SR photons generated by the SCWs with 4-GeV positron beam.

It is critical to study EC buildup and suppression in the wiggler magnetic field for the ILC Positron Damping Ring conditions, that is with significant positron beam current at 4∼5 GeV. However, the string of six SCWs at the L0 region will generate up to 40-kW SR power with 100 mA positron beam at the beam energy of 5 GeV. To deal with this intense SR power, vacuum chambers on the west side of the L0 region (that is, down-stream of positron beam relative to the SCW-string) had to be modified. Figure 2.6 shows the layout of the area. Specifically, a CESR-c era aluminum vacuum chamber, that was a part of CLEO-c fast luminosity monitor (FLM), could not safely stop this high SR power from the SCW-string. A new photon-stop (PS) chamber was constructed to replace FLM chambers. The PS chamber, as shown in Figure 2.7, is made of OFHC copper, with a ∼2.85 m long water-cooled bar to intercept the main SR power from the SCW-string and with a large Ti-sublimation pump ante-chamber to deal with expected gas-load from SR-induced desorption. Thermal analysis (also shown in Figure 2.7) verified the design to have sufficient safety factor to handle the expected SR power. To ensure proper cooling, eight thermocouples (TCs) are attached to the PS chamber. The measured temperature rises by these TCs agreed reasonably well with the values as predicted by the ANSYS calculation.

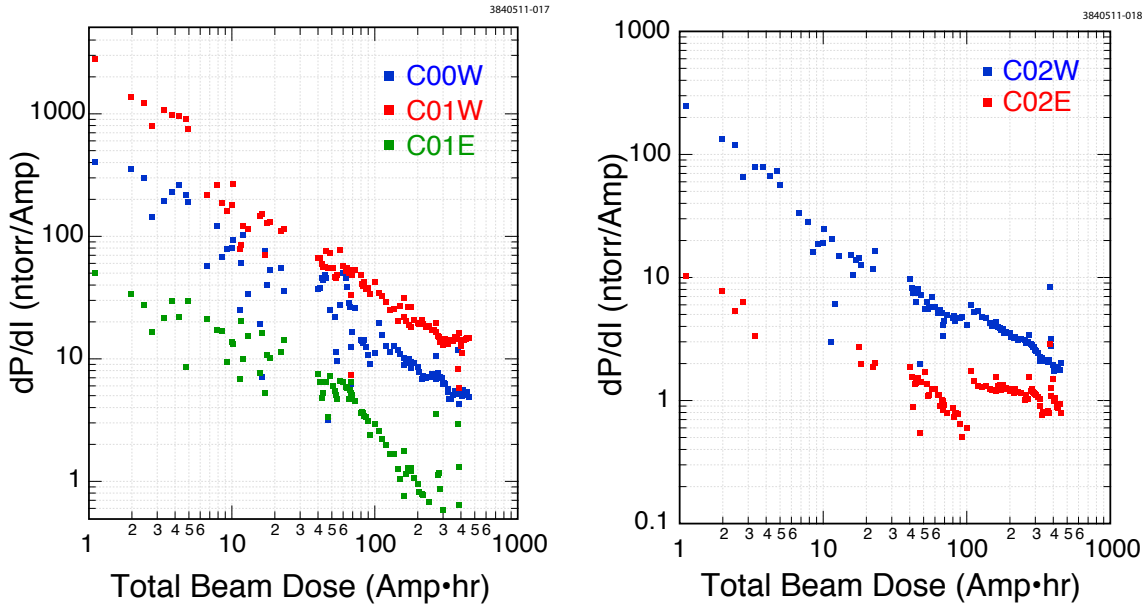

Figure 2.4: Beam induced pressure rise in the L0 EC experimental region during CHESS operations as a function beam dosage. The locations of the vacuum gauges are shown in Figure 2.3

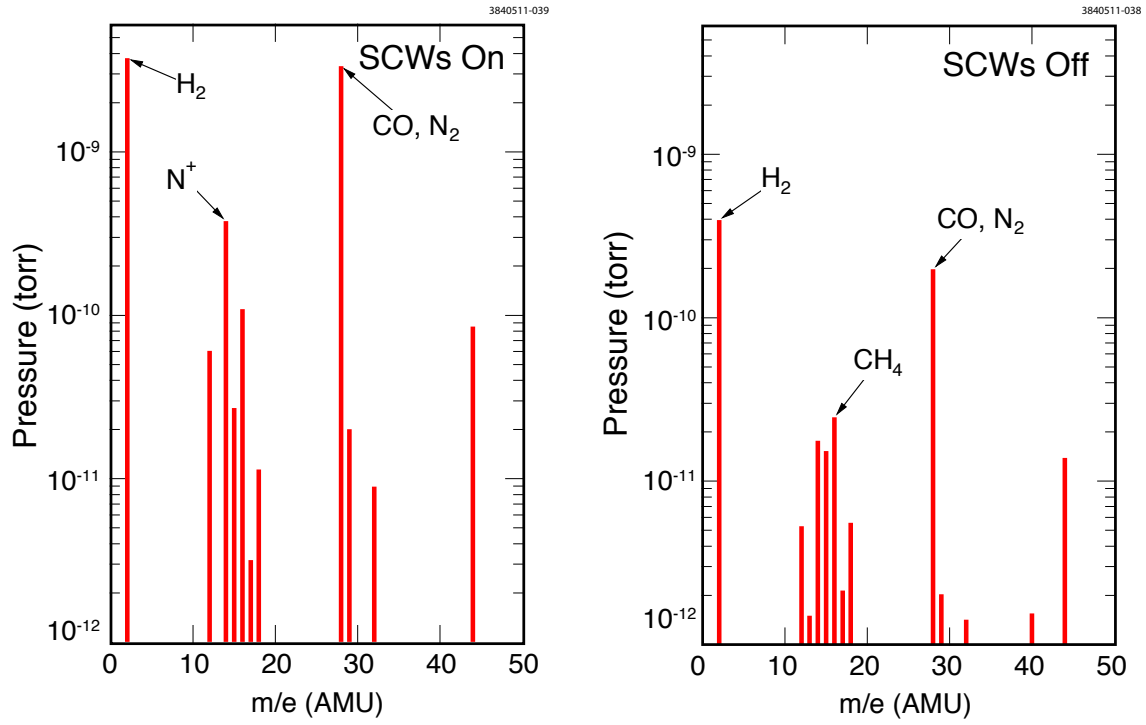

Figure 2.5: RGA spectra at L0 Center, with 120 mA positron at 4-GeV, with SCWs ON (left) and OFF (right). The relative peak heights of signals at $\frac{m}{e}$ =28 and 14 clearly indicated desorption of N_2 with SCWs on, due to higher energy SR photons.

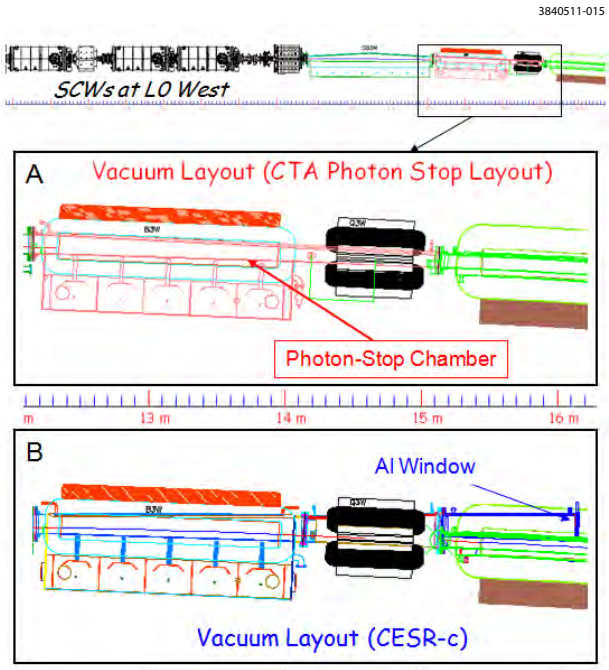

Figure 2.6: A specially designed photon-stop chamber (A) replaced CESR-c era FLM chambers (B), enabling operations of L0 SCWs with a positron beam at 5 GeV.

2.2.2.2 Arc Test Regions

Upon the removal of the CESR-c SCWs from CESR arcs, two EC experimental sections were created on both east and west sides of CESR (see Figure 2.1). At the former locations of CESR-c SCW-doublets, a pair of copper beam pipes were installed for each SCW-doublet, as shown in Figure 2.8. The longer copper beam pipe of the two was coated with TiN thin film for half of its length (while the other half remained bare copper). Two segmented RFAs were installed at each end of this EC test chamber to compare EC-intensity on TiN coated copper to the bare copper. Since these EC-test chambers reside in long vacuum sectors in CESR, they are not intended to be frequently replaced.

To allow frequent exchanges of EC test chambers, while the minimizing impact to the accelerator operations, two very short experimental regions were created in place of two CESR-c SCWs in the Q15W and Q15E locations in the arcs. Additional RF-shielded UHV gate valves were installed at these two regions, so that only a very small portions (approximately 8.2 m in length) of the CESR vacuum, which includes only one dipole bending chamber and a short straight, may be vented to N_2 in order to replace a test chamber in the short straight. Figure 2.9 shows photographs of the Q15 experimental regions, as they were created during the summer 2008 CESR shutdown. Many test chambers were rotated through the Q15 test regions during the CesrTA program, as described in Section 2.2.3.

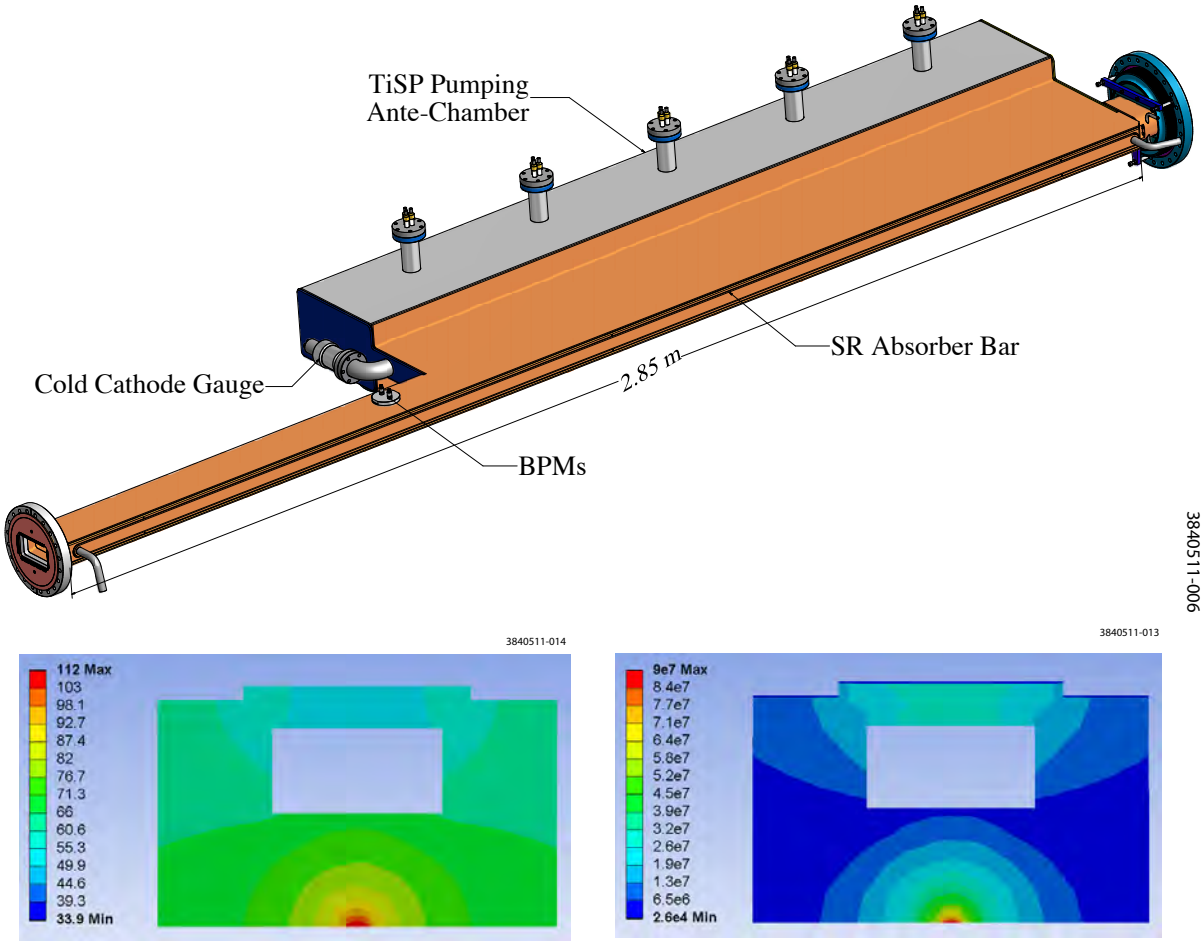

Figure 2.7: Drawing of the photon stop chamber (top); ANSYS calculation of temperature rise on the cooling bar in degrees Celsius (bottom left) and thermal stress in Pascals (bottom right).

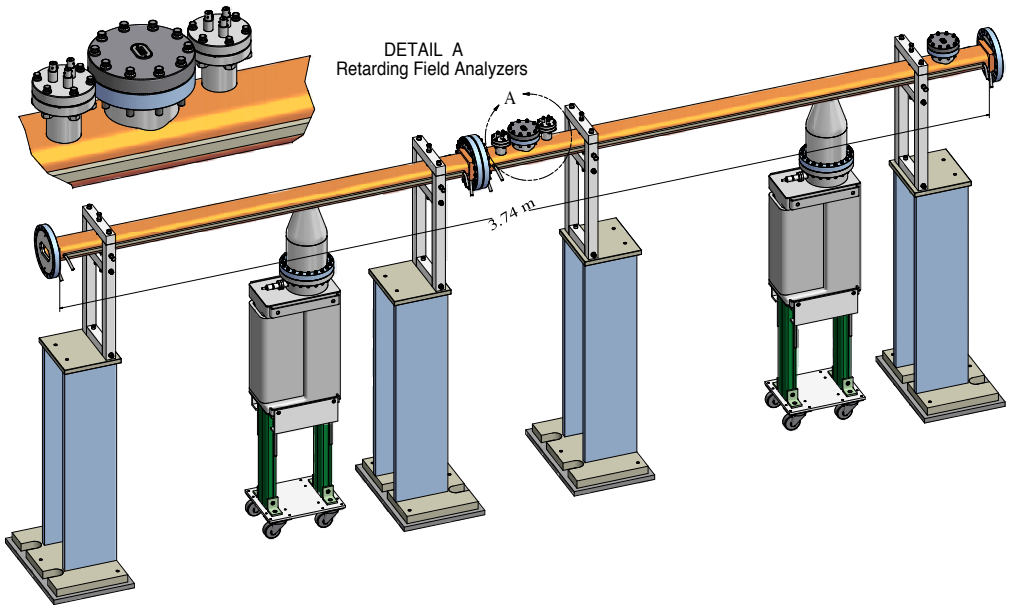

Figure 2.8: EC experiment section created by the removal of SCW-doublets in CESR.

2.2.2.3 L3 Test Region

The CESR L3 long straight section (see Figure 2.1) was another area of major modification of CESR vacuum system. To accommodate the design and fabrication of the vacuum components and to be compatible with the availability of the technical resources of the laboratory, this CesrTA EC experimental region (illustrated in Figure 2.10) was constructed through two major CESR shutdowns, as summarized below.

- During a 3-month shutdown in the summer 2008, a pair of electrostatic vertical separators were replaced with beam pipes originally used in the CLEO IR region. These CLEO IR region beam pipes had adequate cooling and vacuum pumping to handle SR from the hard bends. They also facilitated smooth transitions of beam aperture cross-section from the rectangular at the end of the soft bends to the required 90 mm diameter round pipe. A pair of RF-shielded all-metal gate valves were also installed, thus setting the stage for the final EC experimental region configuration.

- The L3 center EC experimental region (17.94 m in length) was installed during a 2-week long shutdown in the spring 2009. With gate valve isolation from the rest of CESR, it is sufficiently flexible to allow the venting of this experimental section for CesrTA EC studies. As its location is furthest away from CHESS area, the impact to the CHESS operations is minimal. Normally, approximately 10 Amp·hr of beam processing is sufficient after each venting of this region.

As shown in Figure 2.10 vacuum pumping in the L3 experimental region is normally by three sputter ion pumps (SIPs) and two Ti-sublimation pumps (TiSPs). Vacuum system performance in the region is monitored by three evenly spaced CCGs (see Figure 2.10) and a RGA at the center. A typical vacuum beam conditioning performance for the region after venting the L3 experimental region is displayed in Figure 2.11.

Figure 2.9: Two very short EC experimental sections were created in the CESR arcs. Top: photograph showing the chamber adjacent to Q15E, including the downstream bending magnet. Bottom: close-up photographs of the place-holder test chambers in Q15W (left) and Q15E (right).

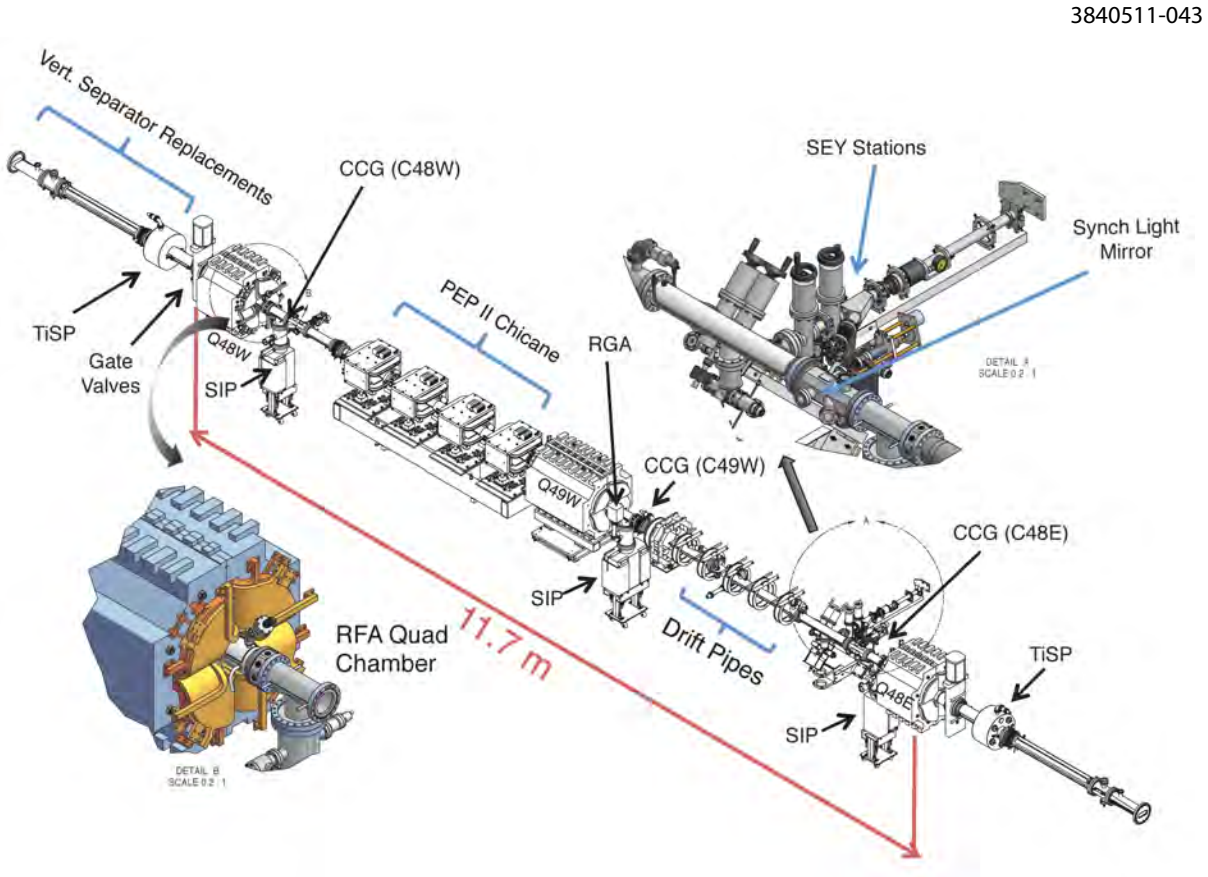

Figure 2.10: L3 CesrTA EC experimental region

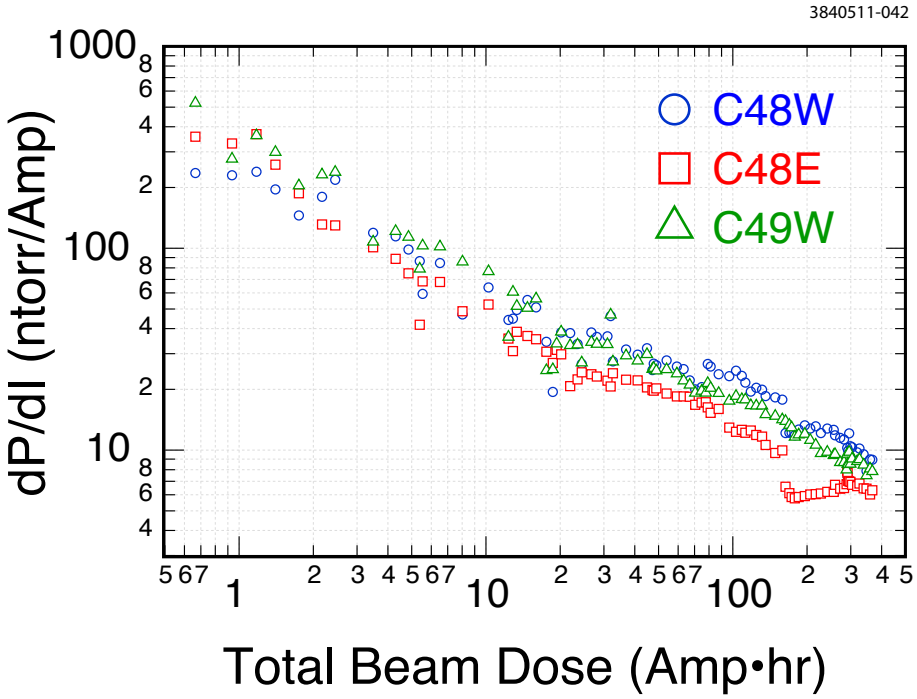

Figure 2.11: Typical vacuum beam conditioning performance for the L3 experimental region

Many EC studies have been conducted in the L3 EC experimental region with several types of beam- and EC-diagnostic instruments on test chambers in the presence of different configurations of magnetic fields, as listed below. The details of these test chambers and EC diagnostics are given in Section 2.2.3 and Section 2.3.

- Diagnostics chambers in dipole magnets (formerly the PEP-II Chicane). Tested chambers included extruded aluminum chamber with rectangular grooves, and TiN-coating.
- Drift test chambers, including aluminum chamber with rectangular grooves (PEP-II chambers) and stainless chambers with NEG coating.
- A quadrupole chamber fitted with thin-style RFA at Q48W, first with bare aluminum surface, and then with TiN-coated aluminum.
- Synchrotron light mirrors for electron/positron bunch length measurements. The highly polished beryllium mirrors are retractable to avoid damage from high SR power during the CHESS operations. Fully enclosed delivery systems guide the SR light to a Streak-camera.
- An in-situ SEY measurement system allows test samples to be exposed to SR during beam operations, primarily in CHESS operations, and then the SEY of the exposed samples are measured in scheduled accelerator accesses. The in-situ SEY measurement system consists of a PEP-II beam pipe assembly housing the SEY apparatus with two Cornell SEY measuring stations.
- Special beam-buttons assemblies (with 8 pickup buttons) served as a TE-wave measurement system for EC studies, as shown in Figure 2.12.
- An RF-Shielded pickup provided by the LBNL team.

2.2.3 Experimental Vacuum Chambers

During CesrTA vacuum system reconfiguration and throughout the CesrTA program, many new EC experimental vacuum chambers were rotated through CESR. Many EC diagnostics and EC suppression techniques were integrated into these experimental chambers. The EC diagnostics included RFAs, SPUs, beam-buttons (for both BPMs and TE-wave), while the tested EC suppression techniques included coatings, grooved surfaces and a clearing electrode. In this section, we will describe the design, construction and vacuum characterisitics for these experimental chambers. The functionality and the associated EC measurement performance of the EC diagnostics, and efficacy of the EC suppression techniques are presented elsewhere in this report (see Section 2.3 and Section 2.4 and Chapter 5).

In this section the EC experimental chambers are cataloged by the type of magnetic fields where the chambers resided: the field-free drifts, the dipole fields, the wiggler fields and the quadrupole field.

2.2.3.1 Drift Chambers

Many new CesrTA vacuum chambers were installed in field-free drifts to complete the beam transport beamlines during the CesrTA vacuum system conversion. To maximize the usage of available

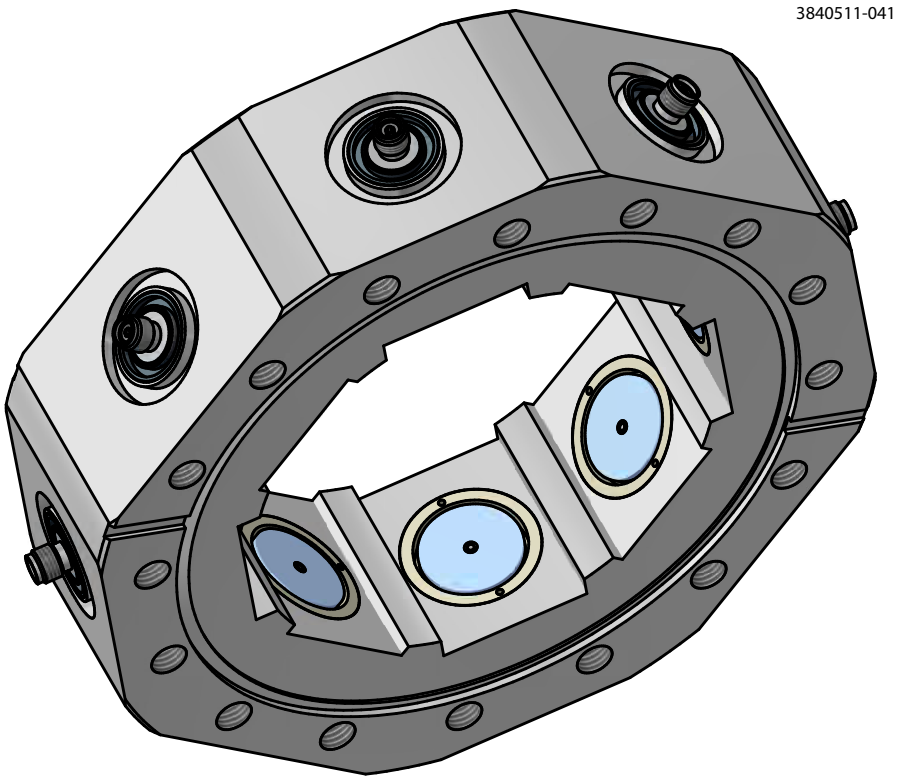

Figure 2.12: Special 8-button assemblies are used in L3 Experimental region. The vertical and horizontal buttons were used as TE-wave transmitters/receivers, while the other four are used as BPM pickups.

space in the drifts, many functional components were integrated into these new chambers, including vacuum pumps and gauges, beam instrumentation (BPMs), EC diagnostics (RFAs, SPUs, etc.) and EC-suppression coatings (TiN). In this sub-section, only the EC experimental chambers deployed in the dedicated test regions are described in detail. In most cases, other chambers were installed on a one-time basis in parts of CESR where there could be a major impact to CESR operations with vacuum interventions. However, a list of these experimental chambers is given here for completeness.

- Copper chambers at Q14W and Q14E locations in CESR, as shown in Figure 2.8, as replacement beam pipes for the CESR-c SCW-doublets. Insertable segmented RFAs (a Cornell thin-style design, using flexible printed circuits as electron detectors) were installed in these chambers in the early stage of the CesrTA program, to test and verify the thin-style RFA design.
- Almost all the copper chambers in the L0 experimental region (see Figure 2.2) are fitted with beam buttons (as BPMs and as TE-wave transmitters/receivers) and with the insertable RFAs.

Q15 Region Test Chambers These regions have been used extensively for the study of various passive coatings, including TiN, amorphous carbon (a-C) and diamond-like carbon (DL-C), in order to evaluate their EC-suppression effectiveness, as well as their vacuum performance in an intense SR environment. These studies are in collaborations with the CLIC/CERN and the KEK groups.

To fulfill the above research goals, an experimental chamber design was developed to allow the characterization of the EC growth and decay and its transverse distribution within the vacuum chamber for different wall surfaces and with progressive beam-processed conditions. The design of this EC experimental chamber is illustrated in Figure 2.13. The beam pipe is machined from a standard CESR aluminum (Type 6063-T6 alloys) extrusion. For EC measurements an RFA port and a set of 4 SPUs are added to the chamber. The two sets of SPUs are directly welded to the top of the beam pipe, using explosion-bonded aluminum-to-stainless steel blocks. Arrays of small holes (0.75 mm in diameter) that connect the SPUs to the beam space are directly drilled vertically through the beam pipe top wall ($\sim$2.5 mm in thickness), as shown. Backing plates made of similar materials were used in drilling these tiny holes to reduce the incidence of burrs. The RFA housing is machined from a separate block of explosion-bonded aluminum-to-stainless steel material, and is welded to the cutout on top of the beam pipe. The lower face of the RFA housing matches curvature of the beam pipe aperture. Small holes are drilled through the three milled flat sufaces, connecting the RFA port to the beam space. These RFA holes have similar geometrical dimensions as the SPU holes, 0.75 mm in diameter and $\sim$2.5 mm in thickness, and are grouped into three 'segments' on each flat, with each segment containing 44 holes (thus a total of $9\times44 = 396$ holes). The segmented hole pattern allows the sampling of the transverse distribution of the EC in the beam pipe. The dimensions of the RFA and SPU holes are chosen to ensure no significant leakage of the beam's RF fields into the SPU and RFA, while allowing as much transmission of cloud electrons from the beam pipe into the SPU and RFA as possible.

Over the past 3-year CesrTA program, five Q15 experimental chambers were fabricated and tested in the Q15W and Q15E regions. Among these experimental chambers, four types of interior surfaces and two types of RFA designs were tested. The four types of tested surfaces are: bare aluminum (as it was originally extruded), amorphous carbon coatings (coated by CERN/CLIC), TiN coating (by

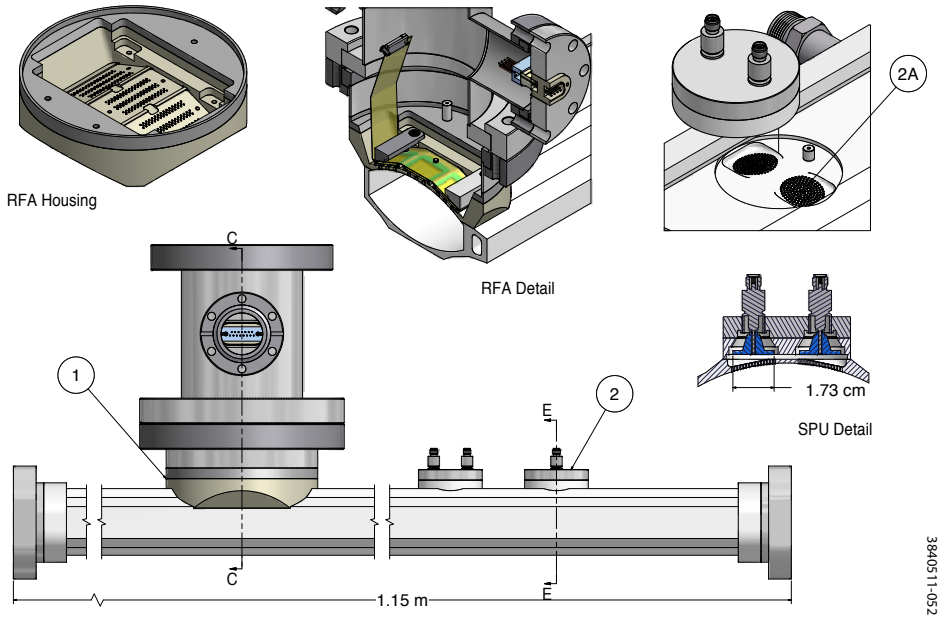

Figure 2.13: Q15 EC Test Chamber, equipped with a RFA (1) and 4 SPUs (2)

Cornell) and diamond-like carbon coating (by KEK). Table 2.1 summarizes these test chambers. Figure 2.14 shows a typical installation of these experimental chambers. The vacuum pumping of the test chamber is by a 110-l/s noble-diode ion pump, and the two adjacent distributed ion pumps at B13W/E and B15W/E. Since the gas conductance between the beam space and the RFA port is very limited, a small ion pump (8-l/s) was installed for the RFA port. The vacuum performance of each test chamber is monitored by a cold-cathode ion gauge (CCG) and an RGA during the beam runs. SR-induced gas desorption from the chamber surfaces dominates the gas load. As for all newly installed vacuum chambers, very high SR-induced pressure rises were measured from these experimental chambers, but the SR-induced desorption decreases rapidly with the accumulated beam dose. In Figure 2.15, the beam conditioning characteristics of the four surfaces are compared. To make the SR-induced desorption measurements from the four types of surfaces, all the data points shown were taken during CHESS operations, when there are roughly equal stored electron and positron beam currents, making the total SR flux similar at both the Q15W and Q15E locations. The data in Figure 2.15 indicates:

- All coatings, except the DL-C, have similar beam conditioning characteristics, as compared to the bare aluminum surfaces. By contrast the DL-C coating indicates significantly higher outgassing rates.
- However, the RGA data in Figure 2.16 show that DL-C coating has a much 'cleaner' desorbed gas composition, i.e. it is dominated by hydrogen.

Two generations of RFA designs were used on the Q15 experimental chambers. The first generation was adapted from the thin RFA design used for a CESR dipole chamber (see Section 2.2.3.2 and Figure 2.32). As listed in Table 2.1, this thin-style design was used in the first four test chambers, including a bare aluminum chamber, two amorphorous carbon coated chambers, and a TiN coated chamber (in Runs #1 and #2).

Photos of a thin-style RFA are shown in Figure 2.17. In the thin-style design, UHV-compatible

Table 2.1: Summary of Q15W and Q15E Experimental Vacuum Chambers (VCs)

VC#	Surface	RFA Style	Test Period	Location	Note
1	Aluminum	Thin	2010.04∼2011.01	Q15W	Reference surface
2	TiN Run#1	Thin	2009.12∼2010.01	Q15E	TiN coating via DC sputtering at Cornell
	TiN Run#2	Thin	2010.08∼2011.01	Q15W	Same chamber as above
	TiN Run#3	Insertable	2011.02∼2011.07	Q15W	Cross-comparison of two RFA designs
3	a-C#1	Thin	2009.12∼2010.04	Q15W	a-C coating via DC sputtering at CERN[a]
4	a-C#2 Run#1	Thin	2010.04∼2011.01	Q15E	a-C coating via DC sputtering at CERN[b]
	a-C#2 Run#2	Insertable	2011.07∼present	Q15W	Cross-comparison of two RFA designs
5	DL-C	Insertable	2011.02∼present	Q15E	DL-C coating via pulsed DC plasma-CVD, supplied by KEK

[a] A 150°C pre-installation bakeout was performed, as a standard CESR practice, after installation of the thin RFA. An a-C coated coupon went through the bakeout, and was sent back to CERN for analysis. The peak SEY value $\delta \sim 1.5$ was measured on the coupon, much higher than the other coupons ($\delta \leq 1.1$) at CERN. It was suspected the sub-monolayer trace of silicon on the a-C coating was responsible for the higher SEY. One possible source of silicon was the silicone adhesive on the UHV-Kapton tape used on the thin RFA assembly.

[b] In this round of RFA installation, efforts were made to reduce adhesive Kapton tape by at least 90%, and the preinstallation bakeout temperature was reduced to 120°C. However, higher δ and higher trace levels of Si were still observed in the witness coupon!

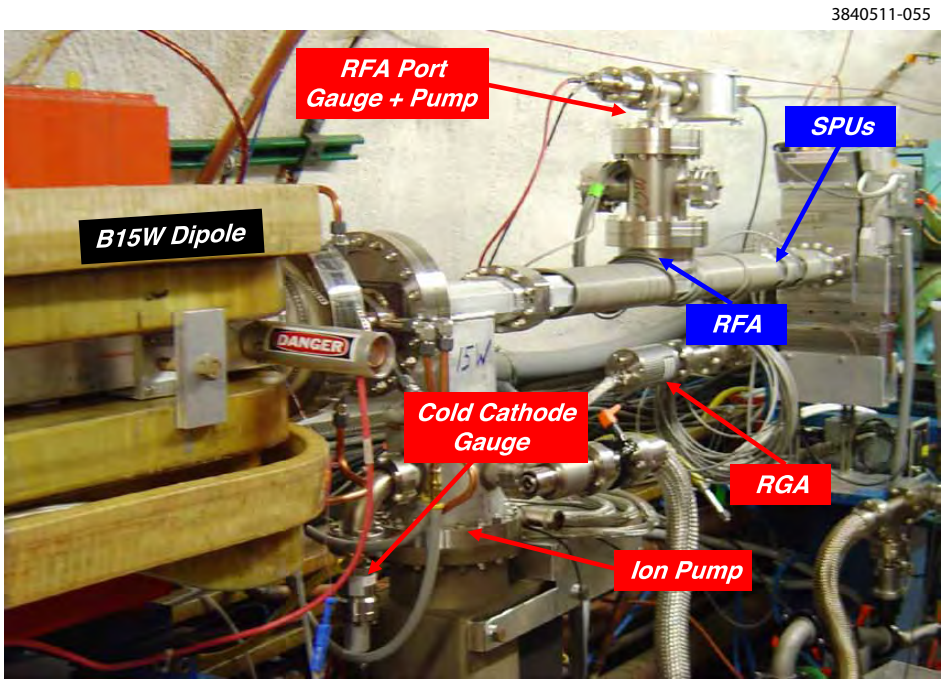

Figure 2.14: A Q15 EC experimental chamber installed at Q15W in CESR.

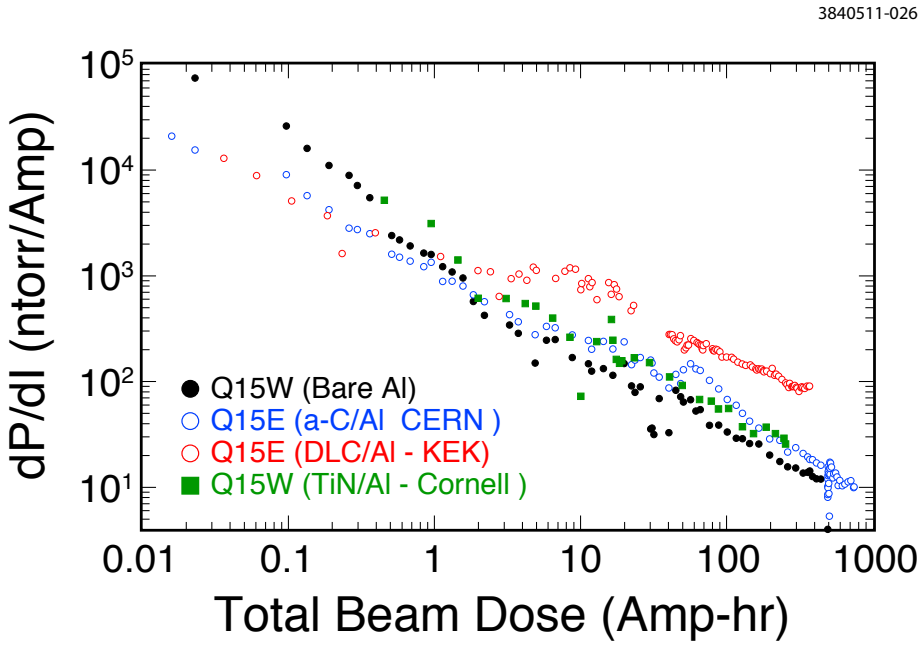

Figure 2.15: History of beam-induced vacuum conditioning of four Q15 EC test chambers with different surfaces.

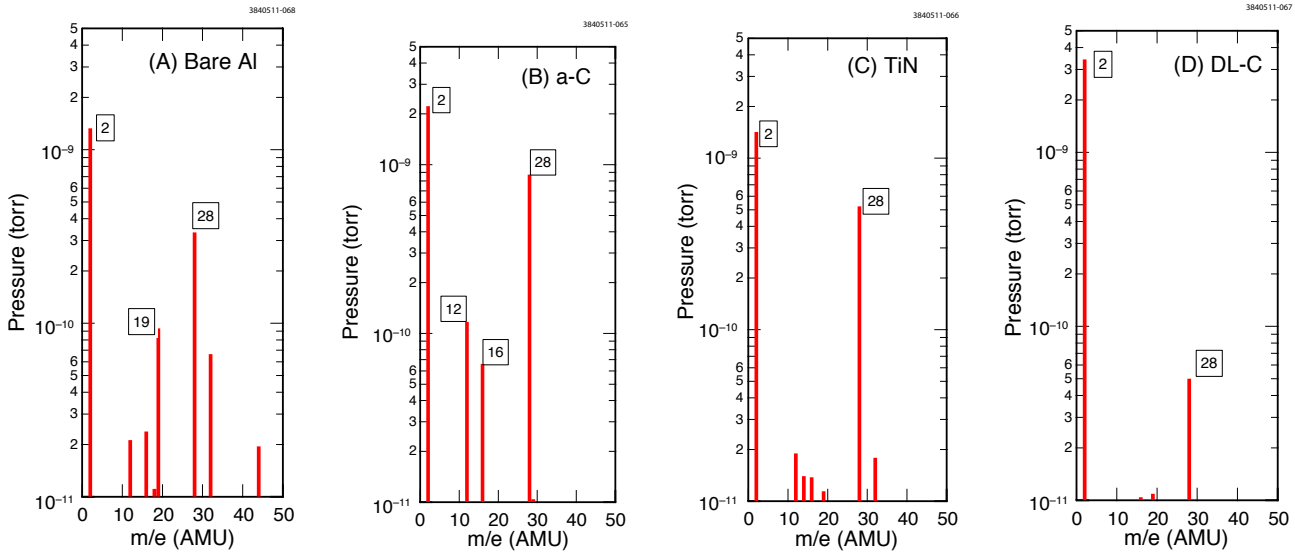

Figure 2.16: Typical RGA spectra for four Q15 EC test chambers with different surfaces, as labeled. All RGA spectra were recorded during CHESS operations, with ∼400 mA stored beam current in CESR, after significant beam processing (with the beam dose over 400 Amp·Hr).

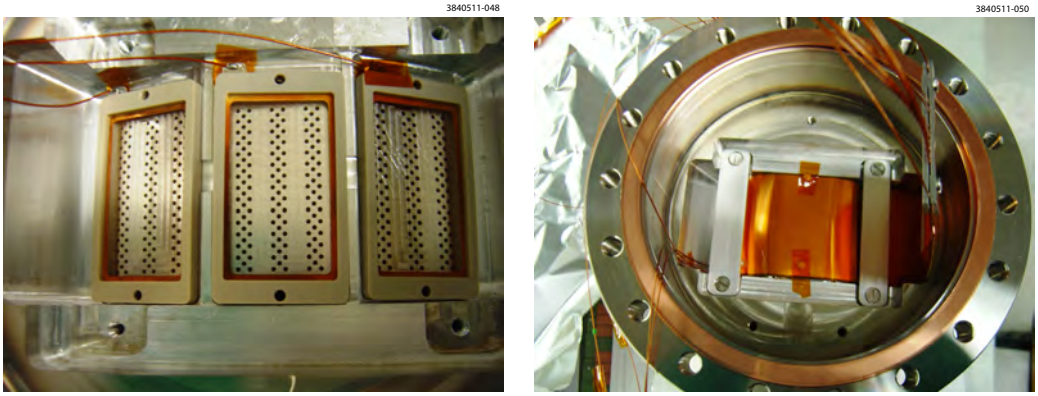

Figure 2.17: Photos of the Cornell Dipole thin-style RFA taken while it was being installed into the Q15 experimental chamber. Left: the three high-transparency retarding grids after installation onto the beam pipe. The beam pipe holes are clearly visible through the fine meshes of the grids. Right: installation of the collector circuit, which is clamped down with aluminum bars.

Kapton tape with Silicone adhesive (Model # KAP-TP-36-2S from Accu-Glass Products, Inc.) was used to electrically isolate the flexible RFA collector circuit. We performed independent vacuum evaluation of the Kapton tape, by measuring vacuum total pressure as well as the RGA spectrum of the tape at 230°C. The vacuum tests indicated no unusual outgassing from the tape, thus qualifying their applications in CESR vacuum system. However, traces (∼6% mono-layer) of silicon were measured on the a-C coated samples that were present during the 150°C bakeout of the first a-C coated RFA chamber. This trace of silicon contamination may have contributed to a much higher measured SEY than was observed on the witness sample. In the second a-C coated chamber, although the amount of Kapton tape was reduced by more than 90%, an even higher level of silicon contamination and higher SEY was still measured on the witness a-C coated coupons!

Thus a second generation of the Q15 RFA design was developed, to be completely adhesive-free. This fully insertable RFA assembly is illustrated in Figure 2.18. The insertable RFA consists of three high-transparency copper meshes, with the bottom mesh grounded and second and third meshes permitted to be individually biased. These meshes are nested in frames made of PEEK, and connected through Kapton-coated wires. The flexible circuit RFA collector was replaced with copper bars. The insertable RFA was installed in the fifth Q15 test chamber, with diamond-like carbon coating. To provide cross calibration between the two RFA designs, the thin-style RFA in the TiN coated test chamber was replaced with the insertable one. (Refer to Table 2.1)

L3 Chambers In the east side of the L3 experimental region (see Figure 2.10), a field-free section (of ∼2-m in length) is allocated for EC studies. Three types of beam pipes were tested in this section, as listed below.

- Aluminum beam pipe with smooth interior wall, provided by PEP-II
- Aluminum beam pipe with rectangular fins (grooves) provided by PEP-II
- NEG-coated beam pipes

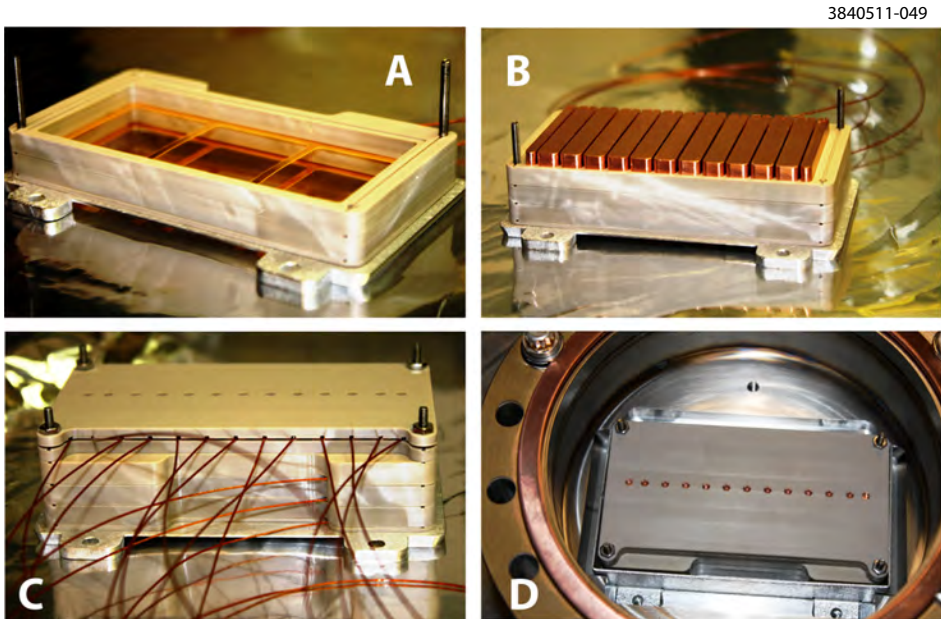

Figure 2.18: Photographs of insertable RFA used in Q15 experimental chambers. (A) High-transparency gold-coated copper meshes after mounting in PEEK frames. (B) Copper bar collectors mounted above the meshes. (C) RFA assembly with PEEK top cap, after soldering all connections (including 2 grids and 13 collectors). (D) Insertable RFA in the vacuum port of a test chamber (for clarity, wires are not shown).

PEP-II Chambers Direct measurements and previous simulation work on rectangular groove samples have shown an SEY well below unity, as low as δ_{max} ~0.6 [5–8]. Following the successful tests on several groove samples with different materials and coatings, four aluminum (type 6063-T6 alloy) test chambers were manufactured. Two of the chambers had smooth interior surfaces, as shown in Figure 2.19. The other two chambers were constructed with rectangular grooves, having two different groove depths, as detailed in Figure 2.20 and 2.21. All these aluminum extrusions have effective inner diameters of 89 mm, identical to both the stainless steel chambers located in the PEP-II straight section, and the nominal CESR L3 beam pipes.

All four test chambers include two vacuum ports (one with 100 mm diameter and one with 38 mm diameter) on the bottom for insertion of electron collectors. In the larger port, 500 1.6 mm diameter holes (in a 20 x 25 pattern) connect the beam space to the collector, as shown in Figure 2.22. Similarly, 50 holes with 1.6 mm diameters (in a 5 x 10 pattern) connect the beam space to the collector in the smaller port. The diameter of these holes are chosen to meet requirement of diameter-to-wall-thickness ratio of 1:3 in order to limit the penetration of EM field, generated by the passing bunch, into the electron collector ports. The electron collector, used in the large port, is shown in Figure 2.23. The beam pipe assembly is illustrated in Figure 2.24, which includes a re-entrant SR mask on one end of the chamber. All four EC chambers were then coated with a TiN thin film.

These four EC chambers were originally tested in the PEP-II LER (see Figure 2.25). Following the tests in the PEP-II, these chambers were re-deployed in the CESR L3 EC drift section for continuation of the EC mitigation studies.

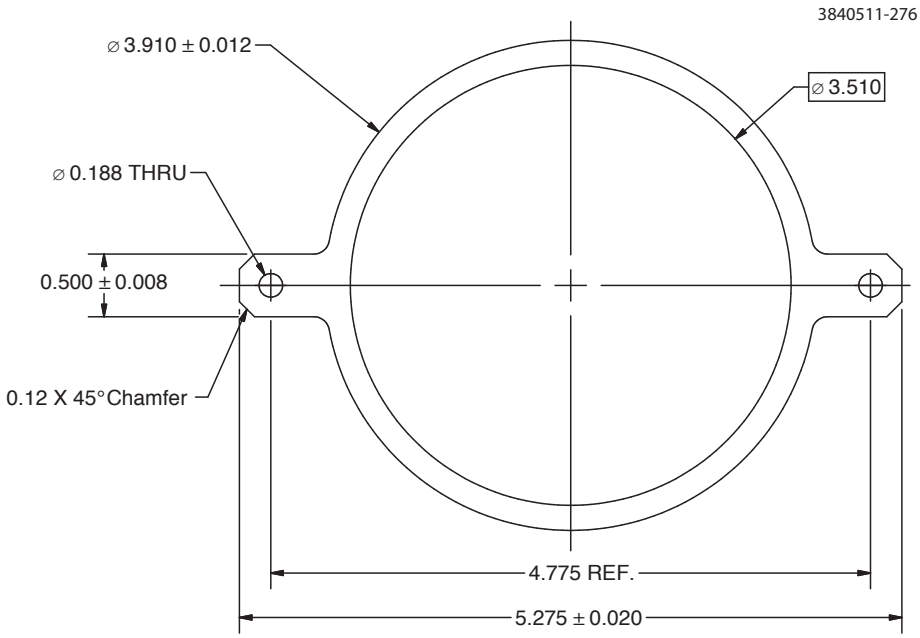

Figure 2.19: Cross section of PEP-II aluminum beam pipe with a smooth interior wall. The beam pipe was extruded with type 6063-T6 aluminum alloy.

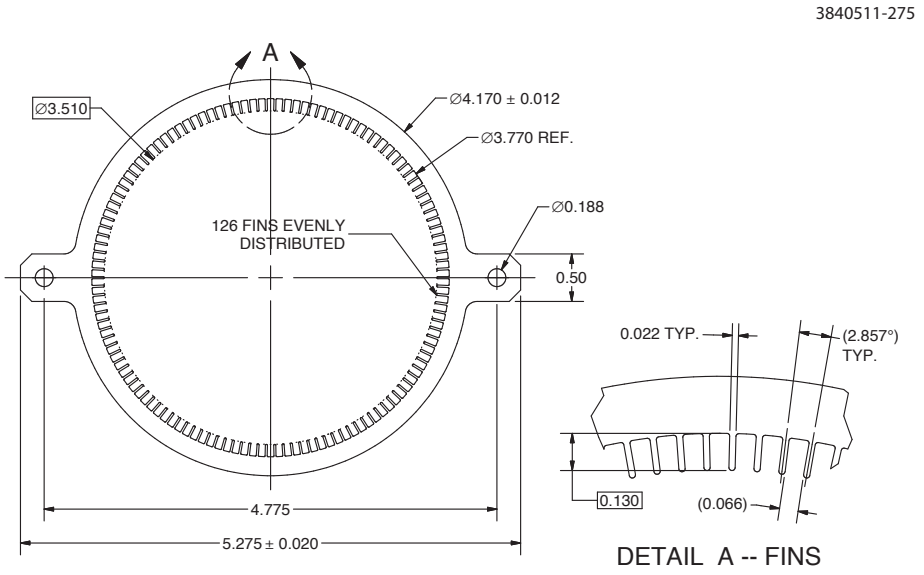

Figure 2.20: Cross section of PEP-II aluminum beam pipe with a 3.3 mm deep rectangular grooves. The beam pipe was extruded with type 6063-T6 aluminum alloy.

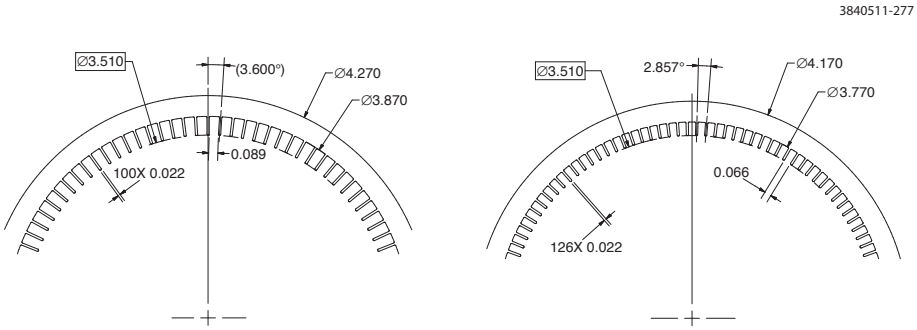

Figure 2.21: Details of rectangular grooves of two different groove depths on PEP-II aluminum beam pipes. The left shows grooves with depth of 4.5 mm, and right with depth of 3.3 mm. The beam pipes were extruded with type 6063-T6 aluminum alloy.

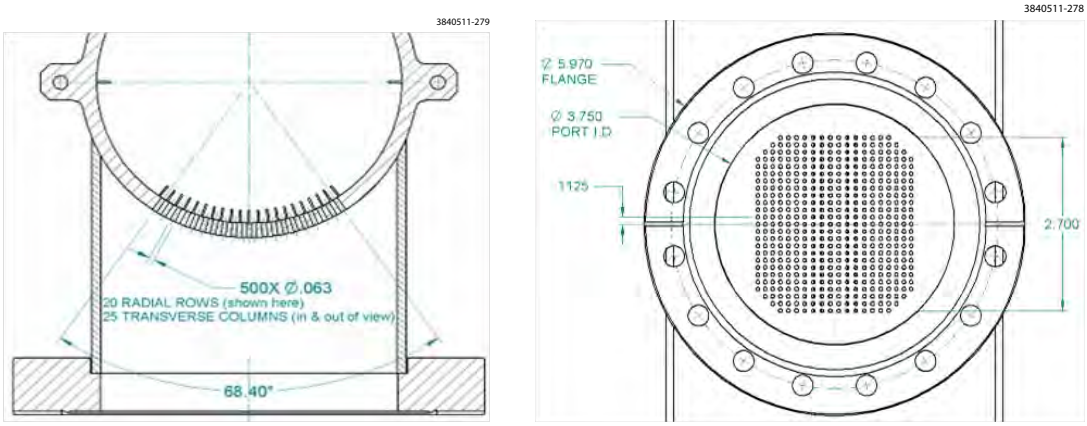

Figure 2.22: Beam pipe holes for the large electron detector ports built into each of the four test chambers. Left: front sectional view. Right: bottom view.

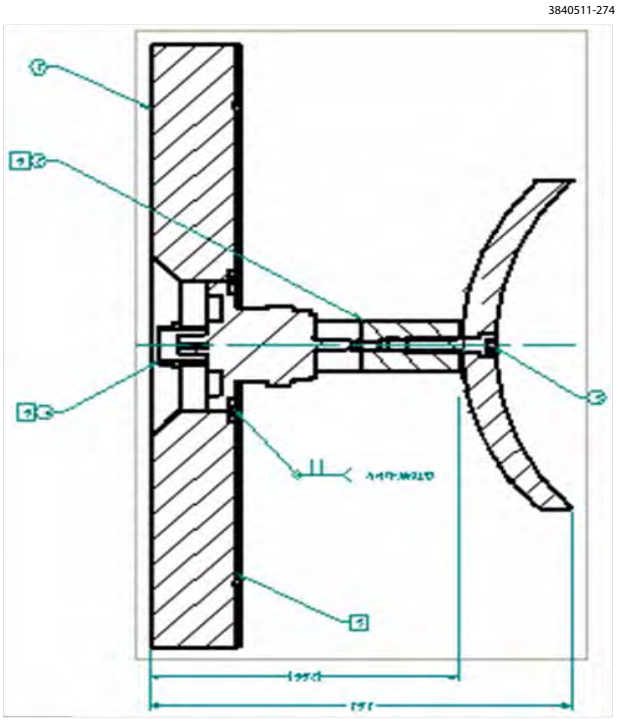

Figure 2.23: Electron collector plate in the larger port of PEP-II EC chambers.

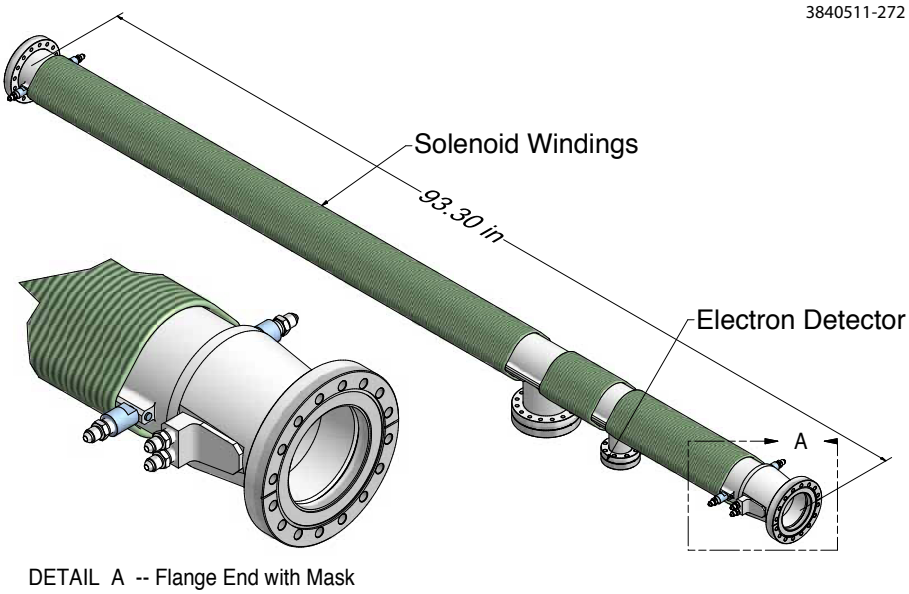

Figure 2.24: PEP-II EC vacuum chambers tested in the L3 experimental region.

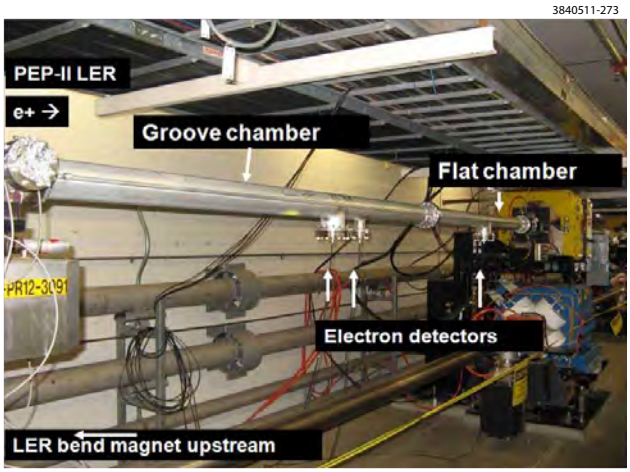

Figure 2.25: The four PEP-II drift EC chambers were tested in PEP-II LER, prior to deployment in CesrTA L3 EC Region.

NEG Test Section A Ti/Zr/V non-evaporable getter (NEG) thin film [9, 10] has been shown to have a low SEY, after its activation at elevated temperatures under vacuum. The activated NEG coating also has the benefit of providing vacuum pumping. A NEG-coated test chamber, equipped with EC diagnostics, was built and tested in the drift section of the L3 experimental region. To prevent rapid saturation of the activated NEG thin film in the test chamber from residual gases in the surrounding beam pipes, the test chamber was sandwiched between two 1-m long NEG coated beam pipes, as shown in Figure 2.26. The EC test chamber was equipped with three APS-style RFAs at three angles and an RF-shielded pickup on the top (see Figure 2.27). All three chambers were made of stainless steel (Type 304L).

The NEG thin film deposition was done by SAES Getter Inc., via a DC magnetron sputtering method, using twisted wires of Ti, Zr and V as the sputtering cathode. The thickness of the NEG thin film is $\sim$2 μm. During the coating process, all diagnostic instruments [RFAs and shielded pickups (SPU)] were removed. A 24-hr 150°C bakeout was carried out to the NEG-coated beam pipe string, with RFAs and SPU inserted, prior to the installation in the L3 experimental region. These NEG-coated beam pipes replaced the PEP-II EC text chambers in the drift section of L3 region.

Fiberglass insulated heating tapes were wrapped around and along the NEG beam pipe string for the activation. Six large bore (11-inch diameter) Helmholtz coils, evenly spaced along the beam pipe string (shown in Figure 2.28) replace the normal solenoid winding, found on most of the CESR beam pipes, as the solenoid windings are incompatible with the high temperature heating required during the activation of the NEG coating. The NEG coating was activated at 250°C for a duration of 24 to 48 hours. After each venting of the L3 region and to preserve pumping capacity of the NEG thin film, the activation was normally carried out following the initial period of beam conditioning of the beam pipes.

Vacuum performance of the NEG coated beam pipes was monitored by four CCGs and an RGA (see Figure 2.26). Figure 2.29 plots the measured SR-induced pressure rises ($\frac{dP}{dI}$) as a function of accumulated beam dose. As expected, the RGA showed a residual mass spectrum (Figure 2.30) that was dominated by hydrogen.

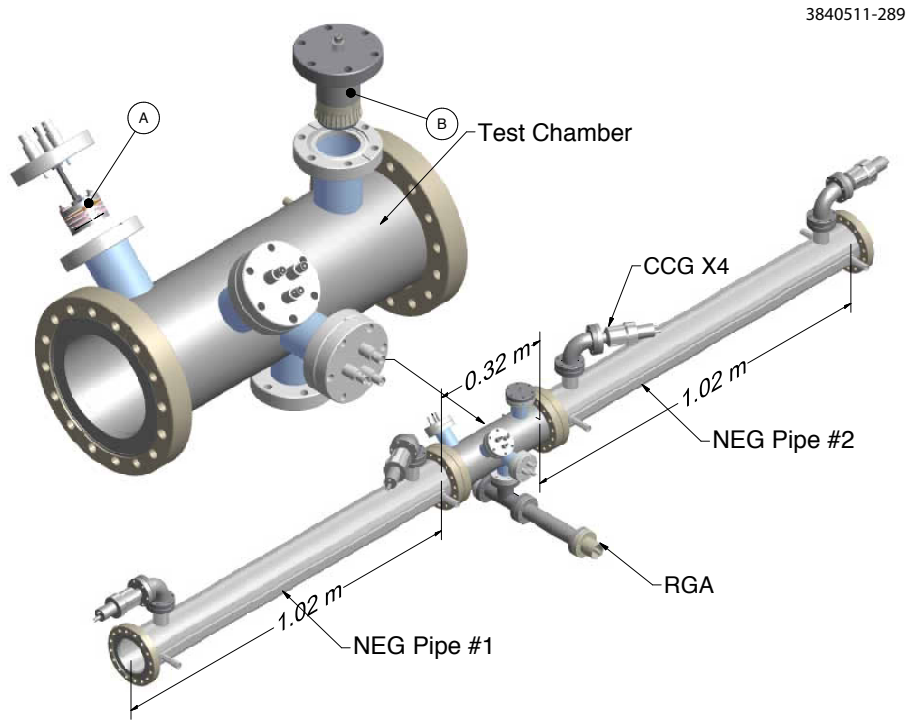

Figure 2.26: Vacuum chambers with NEG thin film coating in the drift section of the L3 experimental region. The test chamber included: (A) 3 units of APS-style RFAs; (B) RF-shielded pickup assembly supplied by LBNL.

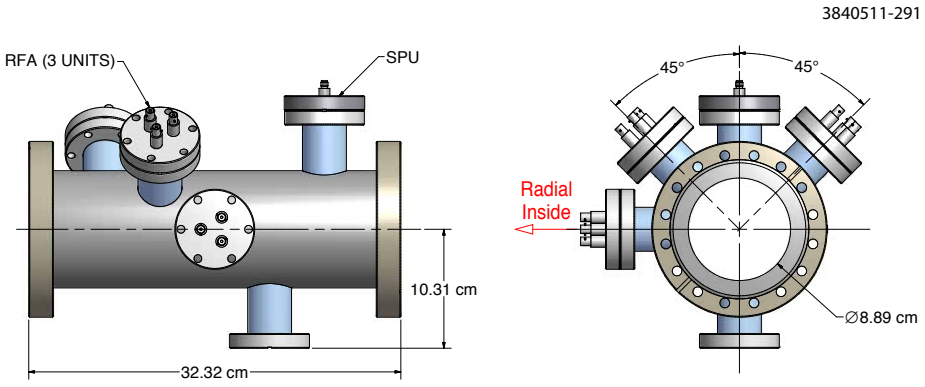

Figure 2.27: EC Diagnostic chamber with NEG thin film coating.

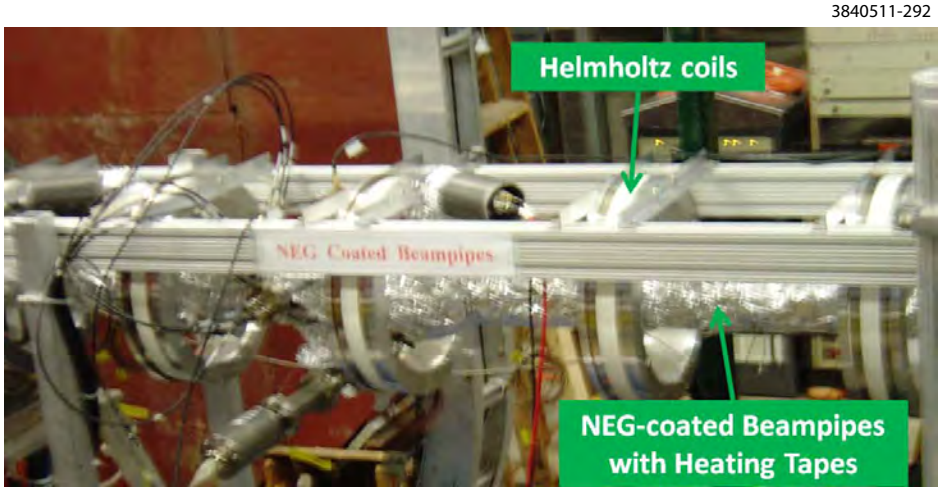

Figure 2.28: NEG-coated beam pipes in L3 after installation of Helmholtz Coils.

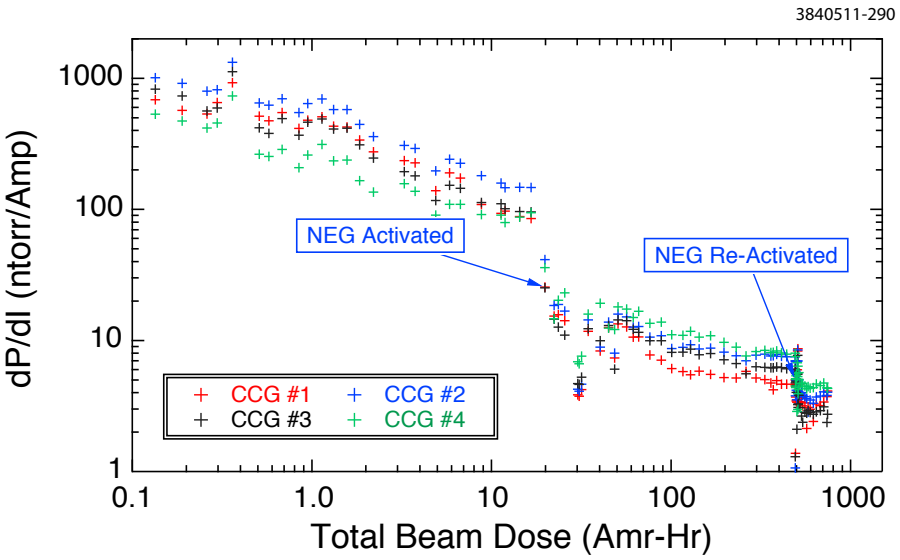

Figure 2.29: Beam conditioning of the NEG coated beam pipes in L3.

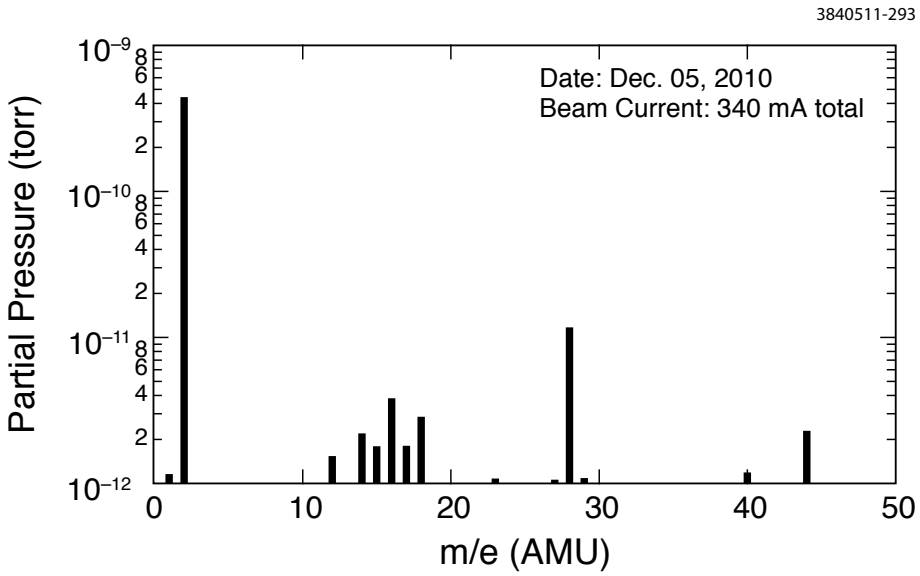

Figure 2.30: A typical RGA spectrum taken with full stored beams in CESR, with accumulated beam dose of ∼900 Amp·hour.

2.2.3.2 Dipole Chambers

CESR Arc Chamber A thin-style RFA design was developed and implemented in a standard CESR dipole chamber at the B12W location. The major design challenge of the RFA design is the very limited vertical space available in order to fit the RFA-equipped chamber within the existing CESR dipole magnet's iron poles.

Figure 2.31 gives an overview of the CESR dipole chamber with the two RFA assemblies. In installation, one of the RFA is placed in the dipole field, while the other in the field-free drift. Figure 2.32 illustrates the structure of the dipole RFA. As shown in the cross-section view, the entire RFA structure is fitted within approximately 3-mm vertical space. Some of the key steps of the dipole RFA construction are summarized as follows:

1. Two RFA openings (see top-left insert in Figure 2.31) were machined into the top of a CESR dipole chamber. The dipole chamber used in this project was a fully functional spare beam pipe, containing the inserted distributed ion pump elements in the ante-chamber and a RF-shielded bellows assembly. The machining of the RFA openings were done completely dry (i.e.with out any cutting fluids) with a cleaned NC-milling machine and cleaned cutting tools. In addition special fixtures were designed and used to contain metal chips and particulates within the opened section and to, thus, prevent them from entering the DIP channels.

2. RFA housing blocks made of 6061-T6 aluminum alloy were placed at the openings and welded to the beam pipe (see photo A in Figure 2.35). The CAD model of the RFA housing block is shown in Figure 2.33. Grouped into 9 segments on three flats, 396 small through-holes (0.75 mm diameter) allow electrons (from the electron cloud), coming from within the beam space, to drift into the RFA space, while blocking out the beam RF EMI. A vacuum leak check was performed after welding the RFA housing to ensure the UHV quality.

3. Three retarding grids, made of stainless steel mesh and sandwiched into ceramic frames, were

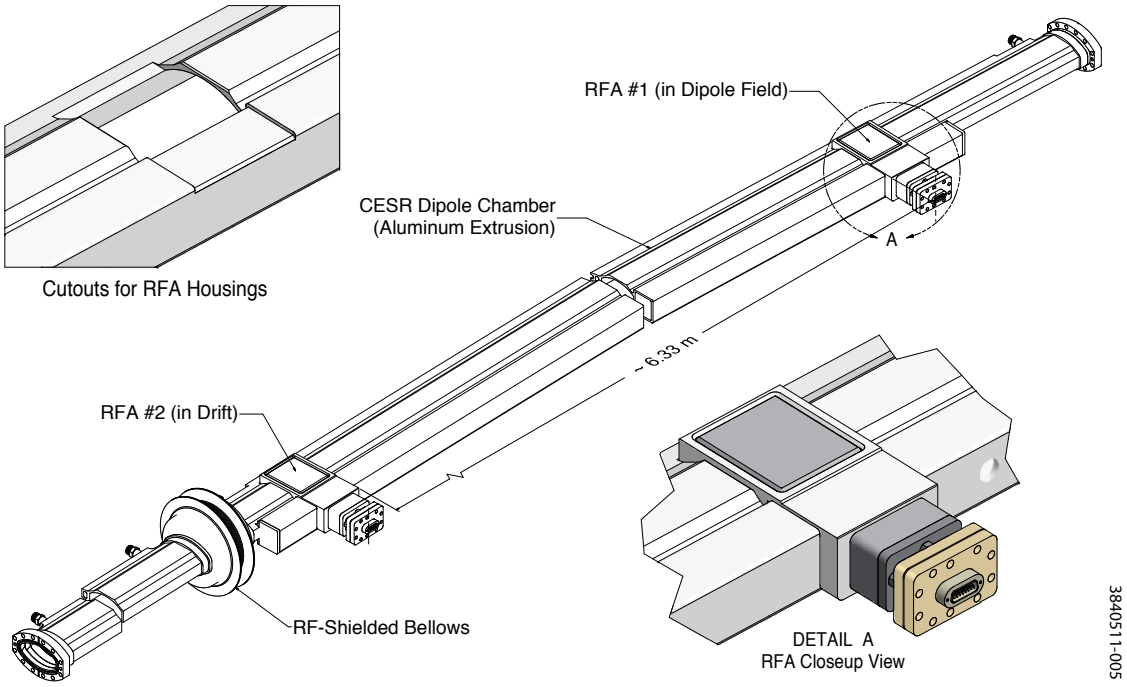

Figure 2.31: A CESR dipole chamber with 2 RFAs.

mounted on the three flats (see Photo B in Figure 2.35). The three grids were individually wired, using Kapton-coated copper wires, which were fed through a 'tunnel' (formed by the RFA housing block) to the connection port. Small amounts of Kapton tape with silicone adhesive were used to keep the grids in place.

4. Thin (approximately 0.15 mm thick) copper-coated-Kapton flexible circuits were used as the RFA collectors. As shown in Figure 2.34, it has 9 segmented copper patches that match with the 9 groups of RFA holes on the housing block. Kapton-coated wires are soldered onto the circuit. After soldering, each flexible circuit was cleaned and vacuum baked (at 150°C) before assembling into the RFA. The flexible circuit was precisely placed on top of the retarding grid frames with ceramic head-pins (see Photo C in Figure 2.35). The pinned circuit was further clamped down with two stainless steel bars, also utilized to avoid over-heating of the circuit in the final step of the assembly, the welding of the RFA vacuum cover. The end of the circuit, containing the external electric connections for the circuit, was fed through the 'tunnel' into the connection port with the 9-pin D-type vacuum feedthrough.

5. After a thorough electrical checkout of the RFA assembly, an aluminum (6061-T6 alloy) cover was welded to seal the RFA. Heat-sinks were used to prevent over-heating of the RFA collector circuit as shown (see Photo D in Figure 2.35).

The RFA dipole chamber was then leak checked and a 150°C pre-installation bakeout was carried out. The chamber was successfully installed in CESR at B12W location during a one-week shutdown in May 2008. Both RFAs on the dipole chamber have been continuously functioning since their installation.

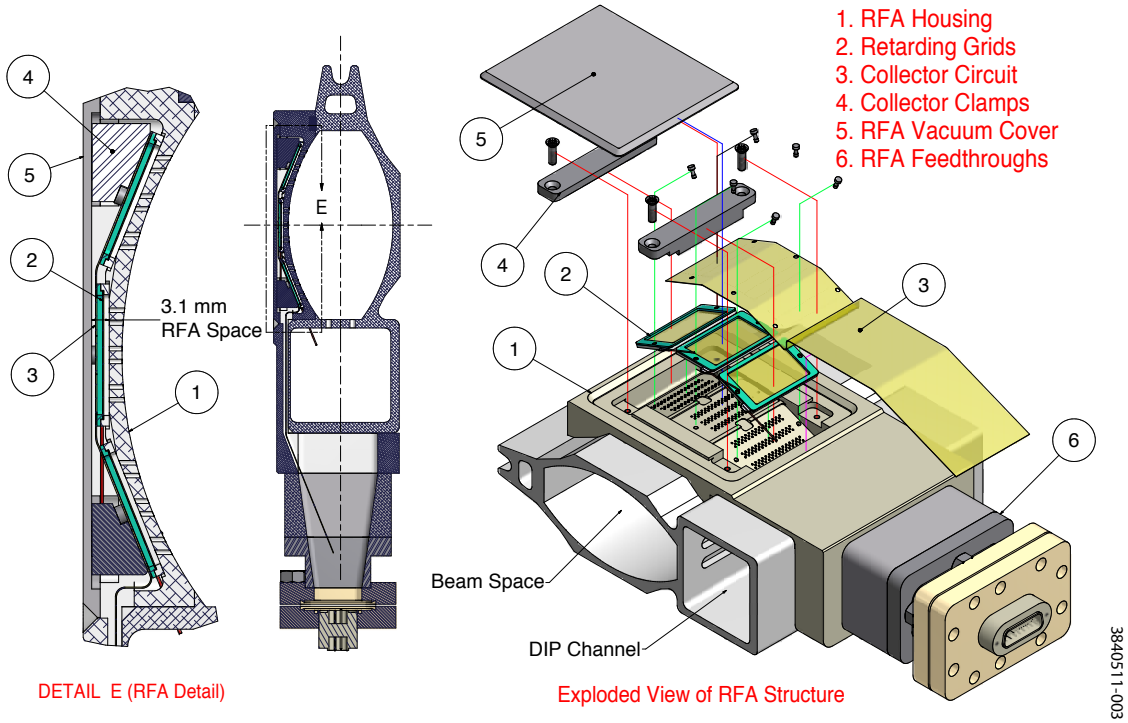

Figure 2.32: RFA design detail for a CESR dipole chamber.

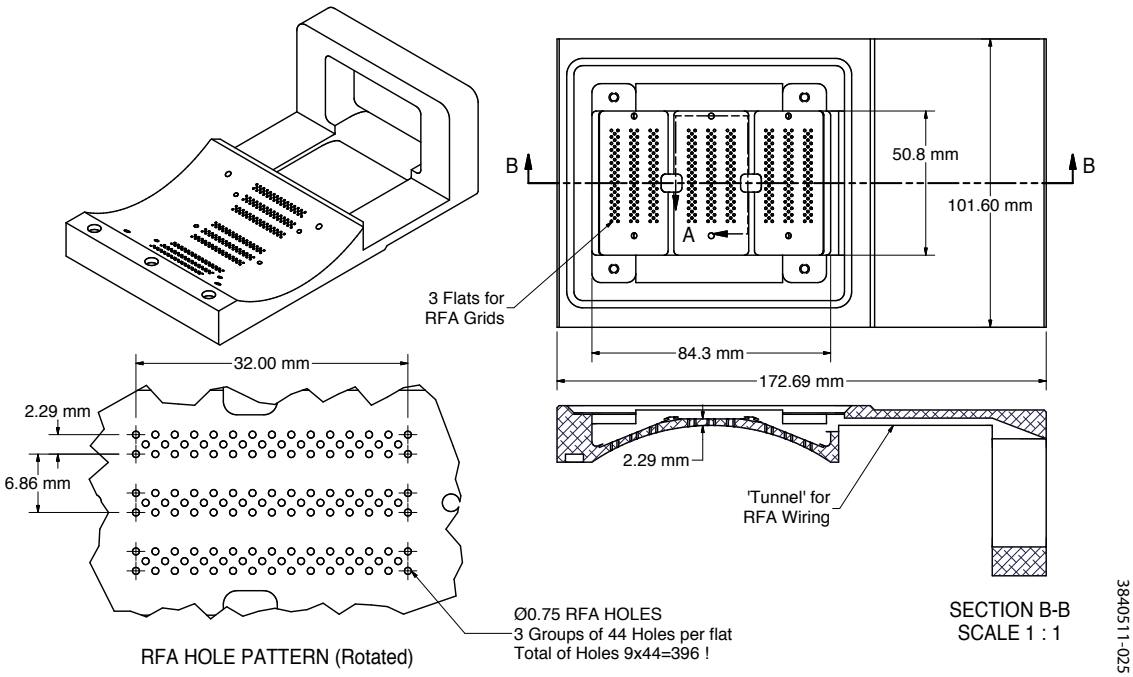

Figure 2.33: RFA Housing block for a CESR dipole chamber.

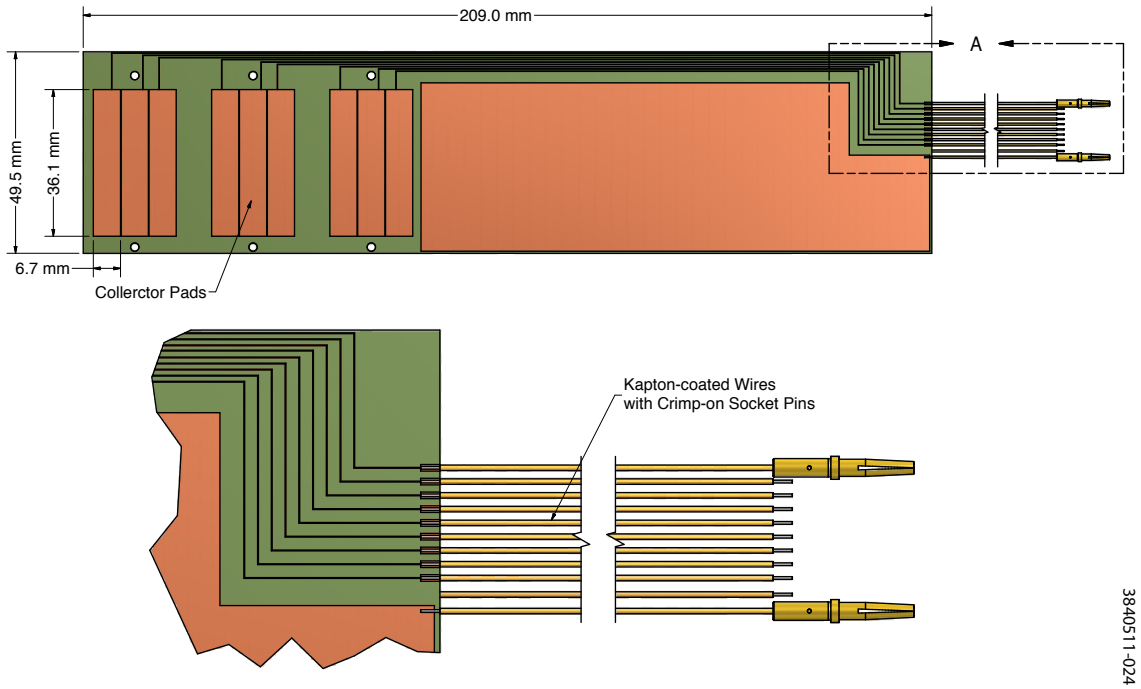

Figure 2.34: RFA flexible circuit collector for a CESR dipole chamber.

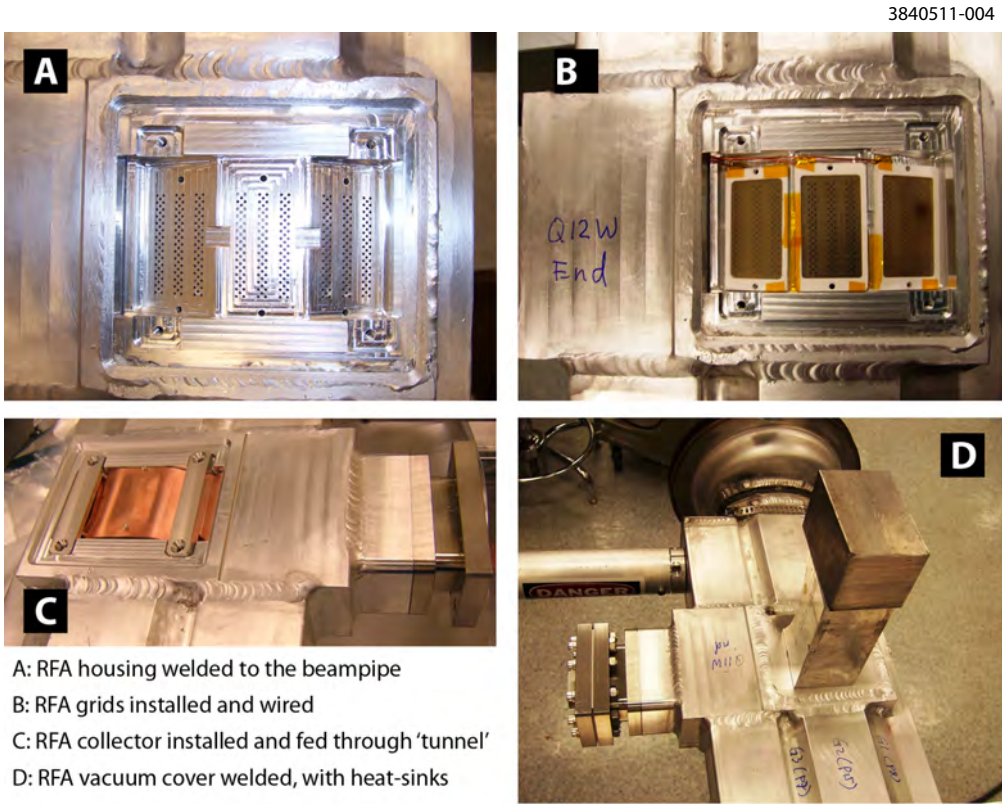

Figure 2.35: CESR dipole RFA assembly and welding photos.

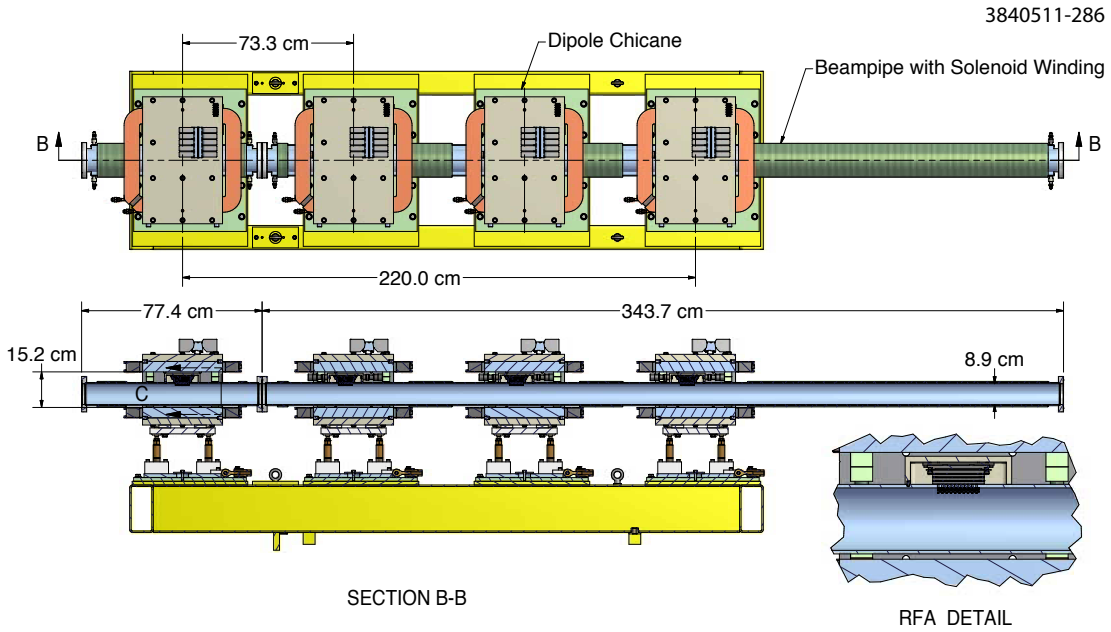

Figure 2.36: PEP-II 4-dipole magnet chicane and RFA-equipped EC chambers.

PEP-II Chicane Chambers A PEP-II 4-element dipole-magnet chicane was installed in the CesrTA L3 experimental region (see Figure 2.10) for the continuation of studies of EC in a dipole field. The field of the chicane dipoles can be varied over the range of 0 to 1.46 kG, the top limit corresponding to the nominal magnetic field strength of the ILC DR arc dipoles. As shown in Figure 2.36, the 4 dipoles are spaced 73 cm apart, with two aluminum beam pipes for a total length of ∼4.2 m. The beam pipes have smooth inner surfaces with TiN coating. Four RFAs were installed on these test chambers, with each of the RFAs located within the dipole magnets. Figure 2.37 shows the structure of these RFAs.

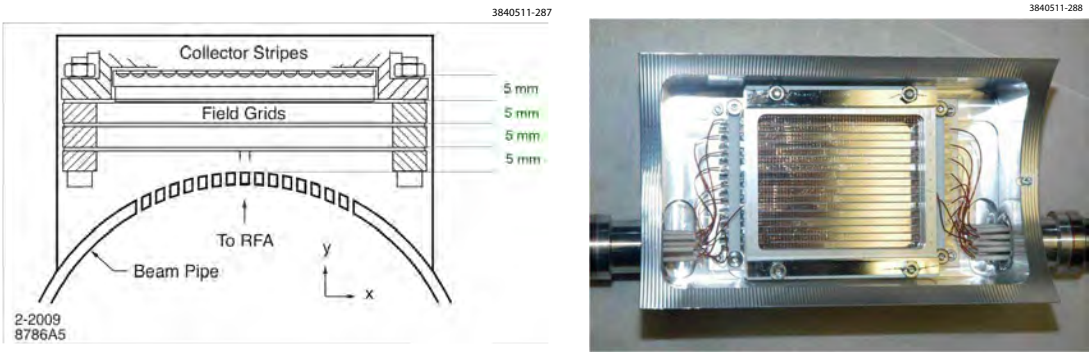

Figure 2.37: Four RFAs were welded onto the chicane beam pipes. LEFT: Cross-section view showing the structure of these RFAs. RIGHT: Photo showing the assembled RFA in its aluminum housing, welded on the top of the chicane beam pipes.

2.2.3.3 Wiggler Chambers

Design Considerations and RFA Structure Superconducting wigglers (SCWs) were designed and fabricated for the CESR-c/CLEO-c program. The CESR-c wigglers are 8-pole super-ferric magnets with main period of 40 cm and trimming end poles. The SCWs provide a very uniform transverse field up to 2.1 T, closely matching the ILC DR wiggler requirements. Therefore, these SCWs are ideal test vehicles for the study of EC growth and suppression in the wiggler field. With this motivation, a thin-style RFA design was developed for the wiggler beam pipe and a set of diagnostic chambers was constructed by a collaboration including Cornell, KEK, LBNL and SLAC.

Figure 2.38 illustrates the structure of the SCW. The details regarding the design of the CESR-c SCWs can be found in [11]. In the original SCW production, the beam pipe was assembled into the magnet's cold-mass, and the cold-mass with the beam pipe was in turn inserted in the isolation vacuum vessel. 16 SCWs were constructed for the CESR-c program on a specially designed SCW assembly line in a dedicated facility that no longer exists. Therefore, the following design constraints were imposed on the RFA beam pipe design and construction.

- The RFA beam pipe must fit inside the space in the cold-mass thermal shield (see Figure 2.38), while still providing sufficient beam aperture.
- The removal of the existing beam pipe and the insertion of the RFA beam pipe must be accomplished without disassembling or disturbing the wiggler magnet structure.
- The RFA beam pipe (including all material used) must be UHV-compatible.

With these requirements the vertical aperture of the RFA beam pipe was reduced from the standard 50 mm to 43.5 mm to provide space for the RFAs, as shown in Figure 2.39. The copper extrusions were split into top and bottom halves. After trimming the vertical edges, the two halves were re-joined (via EB-welds) to form the RFA beam pipe. As detailed later in this section, the top half beam pipe houses the RFA assemblies, while a variety of EC suppression techniques were implemented on the bottom half beam pipe.

Simulations [12] predicted distinct longitudinal and transverse EC density distributions in wiggler beam pipes. The design goal of the wiggler RFA beam pipe is to place RFAs at strategic longitudinal locations in the wiggler magnetic field to measure corresponding transverse EC density distributions.

The RFA beam pipe design is illustrated in an exploded view in Figure 2.40. As mentioned earlier the RFA beam pipe is constructed from the top and bottom halves of the original vacuum chamber. Along the longitudinal direction of the beam pipe, three pockets were machined into the top half of the beam pipe to form housings for the three RFAs. The three RFAs' locations together with the vertical field map of the SCW are depicted in Figure 2.41. After installation in the wiggler magnet, the RFA #1 is at boundary between two center poles (zero vertical magnetic field), #2 at center of a pole (maximum vertical magnetic field) and #3 at 'edge' of a pole (longitudinal B-field).

Electrons from the EC in the beam pipe drift through transmission holes to the RFA detector. There are 240 small holes in each of the three RFAs. As shown in Figure 2.42, they are grouped into 12 segments in the transverse direction to the beam pipe. These holes have a diameter of 0.75 mm ($\frac{1}{3}$ of wall thickness) to reduce the EMI into the RFA signals.

The retarding grids are nested in ceramic frames with the frames bolted to the RFA housing

pockets. Two generations of metallic meshes were used as the retarding grids. The first generation was made of photo-chemically etched 0.15 mm-thick stainless steel (SST) mesh, with an optical transparency of approximately 38%. The SST mesh is easy to handle and inexpensive. However, the SST mesh has two drawbacks. Its relatively low transmission not only directly translates to low EC detection efficiency, but also limits the EC diagnostic accuracy due to significant interaction the transmitted electrons with the grid. To reduce the secondary emission from the grid, the SST meshes were coated with approximately 0.3 μm of gold. The second generation grids (by Precision EForming, Inc) were electroformed copper meshes, bonded to SST frames (supplied by Cornell). The electroformed copper meshes were also coated with gold (approximately 0.3 μm in thickness) via electroplating to reduce secondary electron emission. The electroformed meshes consist of 15 μm wide and13 μm thick copper wires with spacing 0.34 mm in both transverse directions and an optical transparency of approximately 92%. The disadvantage of the copper mesh is that it is very expensive and fragile.

Similar to the thin RFA design, used in the dipole RFA, a flexible copper-clad/Kapton circuit was used as RFA electron collector. As shown in Figure 2.43, three sets of RFA pads each contain 12 transverse collectors to match the hole patterns on the RFA beam pipe. After tinning the soldering pads, the flexible circuits were cleaned and degassed with a 150°C vacuum bakeout before insertion in the RFA beam pipe. The flexible circuit strip was laid on top of the ceramic frames of the grids and precisely positioned with ceramic head-pins. After positioning the flexible circuit and feeding its connection pad through a 'duck-under' channel (see 'Detail B' in Figure 2.40) into the RFA connection port, UHV-compatible Kapton-coated copper wires (42 wires per assembly) were soldered to the connection pads. The final RFA connections are wired to three 15-pin D-type vacuum feedthroughs on a 4.5 inch ConFlat© flange. A copper RFA vacuum cover was electron-beam welded to the beam pipe's top half to complete the RFA assembly. Figure 2.44 shows the cross-section of the RFA beam pipe at one of the RFA locations. The entire RFA structure is contained within a total vertical space of 2.5 mm.

Preparation of SCW for RFA Beam Pipe Preparations must be undertaken for a CESR-c SCW to receive an RFA beam pipe assembly. The main task is to extract the existing beam pipe from a CESR-c SCW without disturbing the magnet's structure. As shown in Figure 2.38, the CESR-c SCW beam pipe is attached to the insulating vacuum vessel via two thin stainless steel disks. The major portion of these disks is about 1.5 mm thick. Called flexible disks, they allow for differential thermal expansion and contraction of the beam pipe relative to the vacuum vessel. The flexible disks completed the insulation vacuum envelope after being welded to the beam pipes and the large end flanges of the vacuum vessel. The sequence of the beam pipe extraction from a CESR-c SCW is described in Figure 2.45. After the extraction of the beam pipe, all debris from the extraction operation was thoroughly removed from the magnet and a pair of large end flanges (with O-ring seals) were mounted to the insulation vacuum vessel. Then the vacuum vessel was leak checked. The integrity of the wiggler magnet was also verified.

Coated and Uncoated Chambers Over the past three years, four SCWs equipped with RFA beam pipes were constructed and installed for the CesrTA program. In the first two units, one has a bare copper beam pipe and the other has a copper beam pipe coated with a TiN thin film (prepared by the SLAC shop). In the third and fourth units, a grooved plate and an EC clearing electrode were implemented on the bottom half of the beam pipe. More details on the third and fourth assemblies are given later.

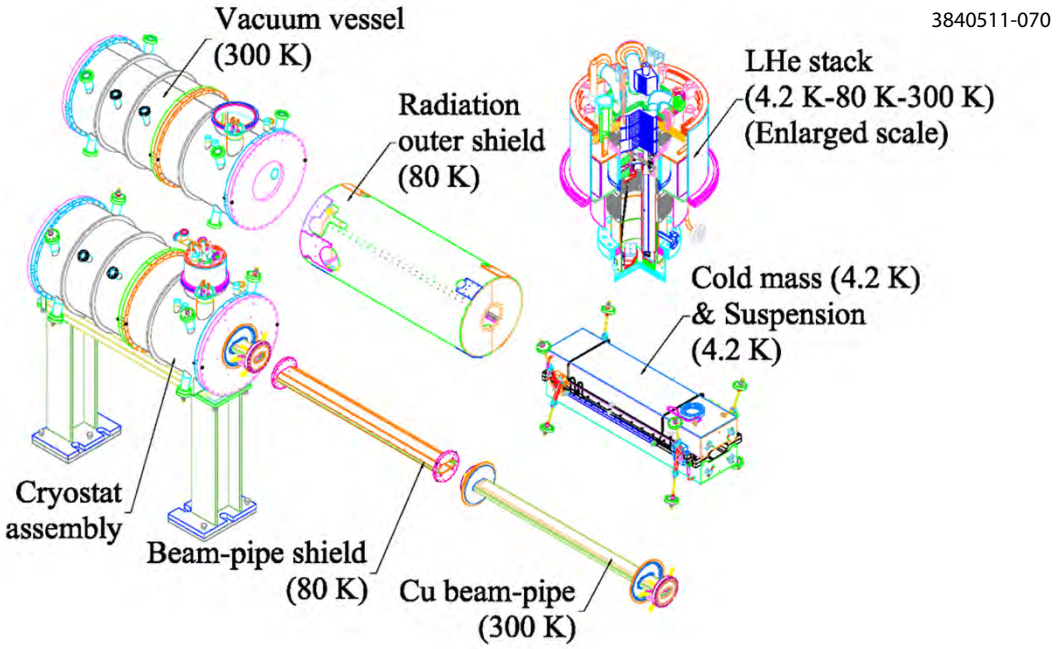

Figure 2.38: Exploded view of the structure of a CESR-c superconducting wiggler assembly.

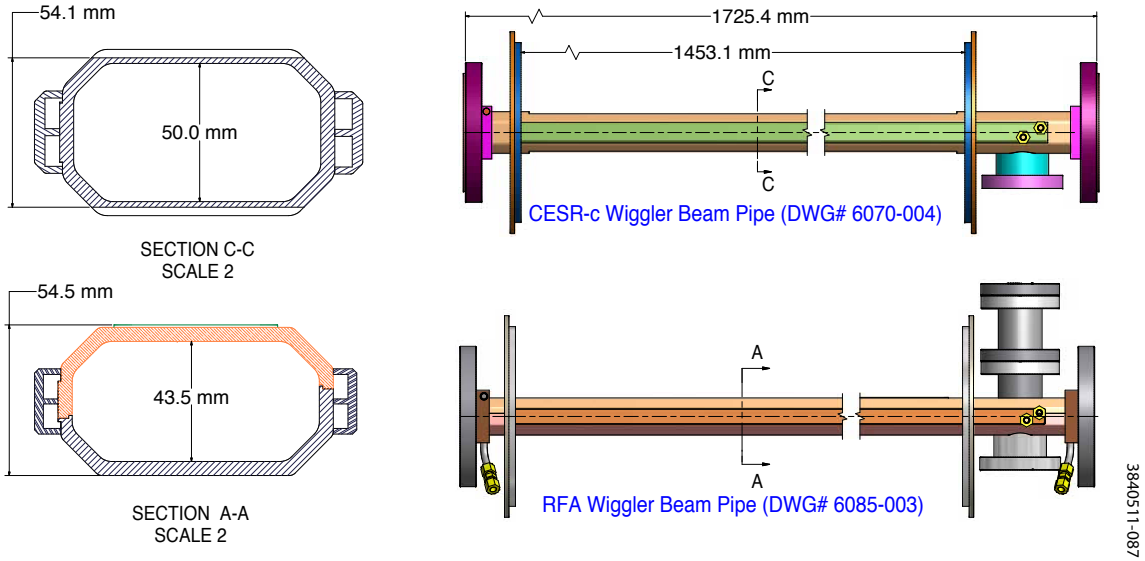

Figure 2.39: Cross section comparison between a 'standard' CESR-c SCW beam pipe and a CesrTA RFA-equipped SCW beam pipe.

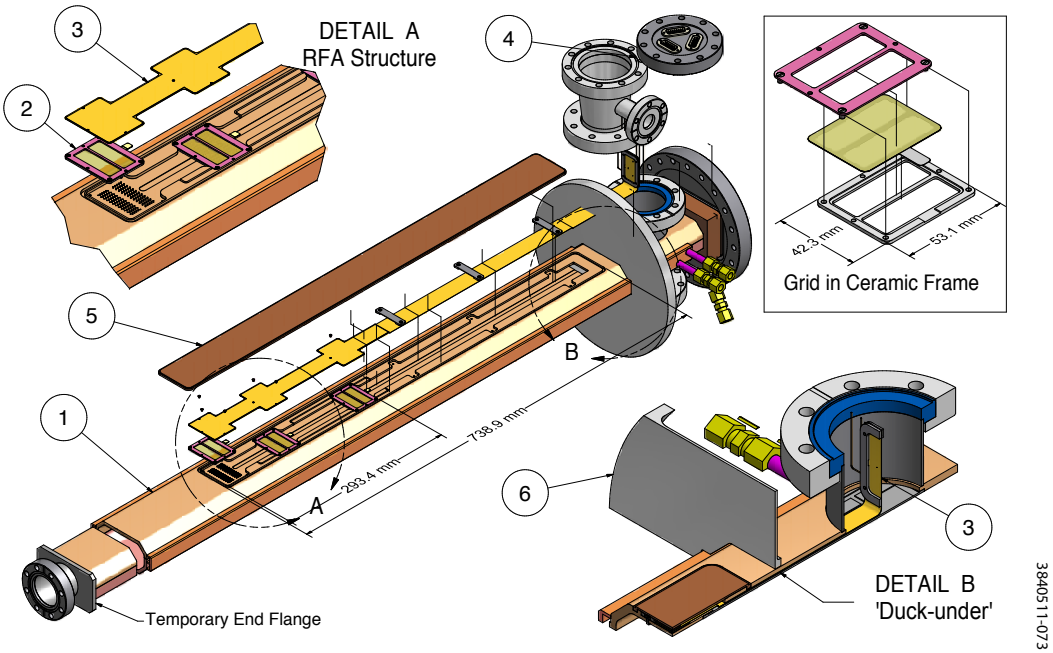

Figure 2.40: Exploded View of a SCW RFA beam pipe Assembly. The key components are: (1) beam pipe top half, housing the RFAs; (2) RFA grids (see upper right inset); (3) RFA collector on a flexible printed circuit board; (4) RFA connection port; (5) RFA vacuum cover. The 'duck-under' channel, through which the kapton flexible circuit is fed after all heavy welding is complete, is shown in detail B.

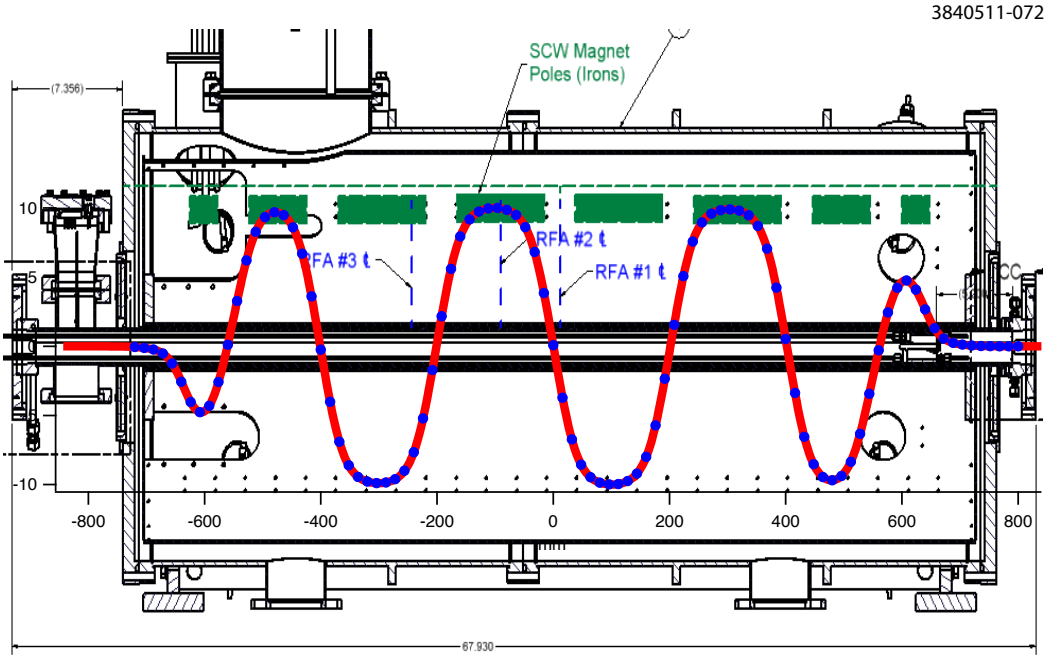

Figure 2.41: Three RFAs are built into each SCW RFA beam pipe. A plot of the B-field along the wiggler (red line with blue dots) is superimposed on the drawing of the wiggler. The RFAs are located at three strategic B-field locations, as shown.

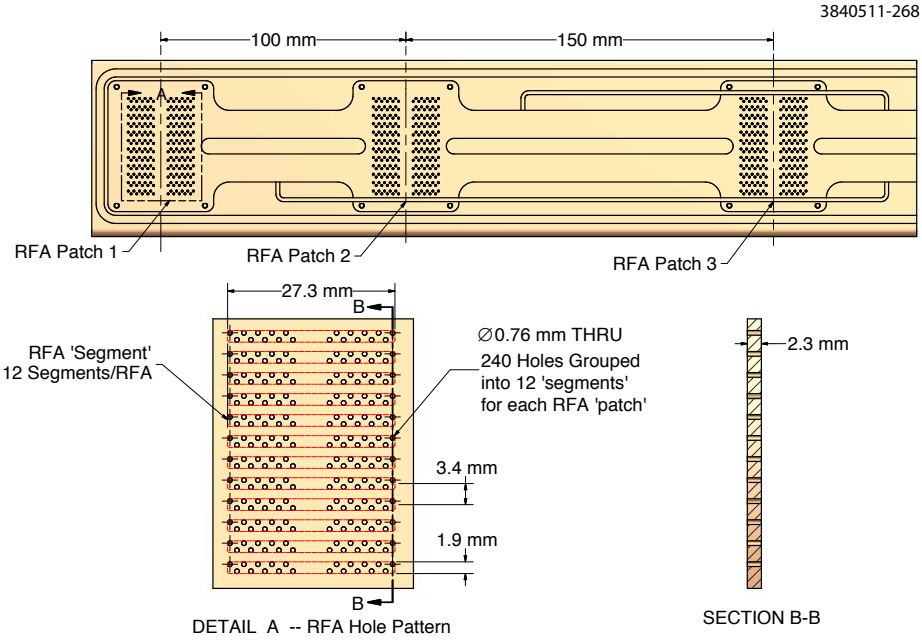

Figure 2.42: Small holes are drilled through top beam pipe to allow electrons in the beam pipe drift into RFAs. There are 240 holes for each RFA, and they are grouped into 12 segments to sample transverse EC density distribution.

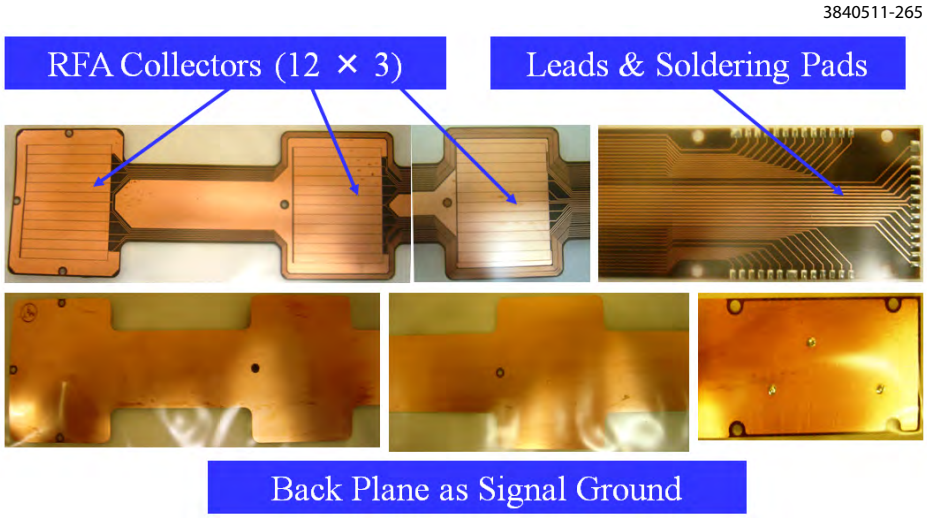

Figure 2.43: Photos of the flexible circuit used as RFA electron collectors in the SCW RFA beam pipe. The flexible circuit is made of a thin Kapton sheet with copper cladding on both sides, having a thickness of 0.15 to 0.20 mm and length of 886 mm.

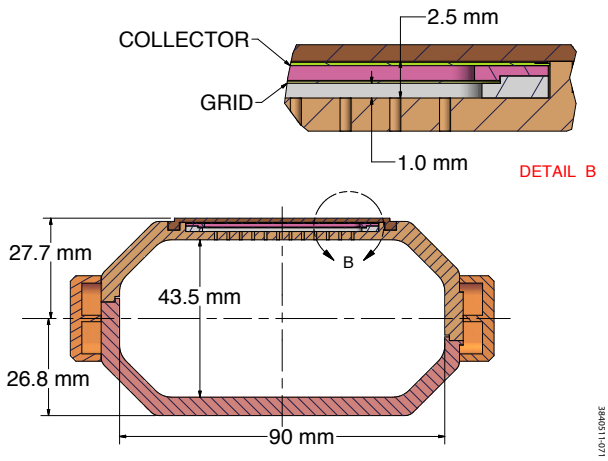

Figure 2.44: Cross section view of a RFA structure on the SCW beam pipe

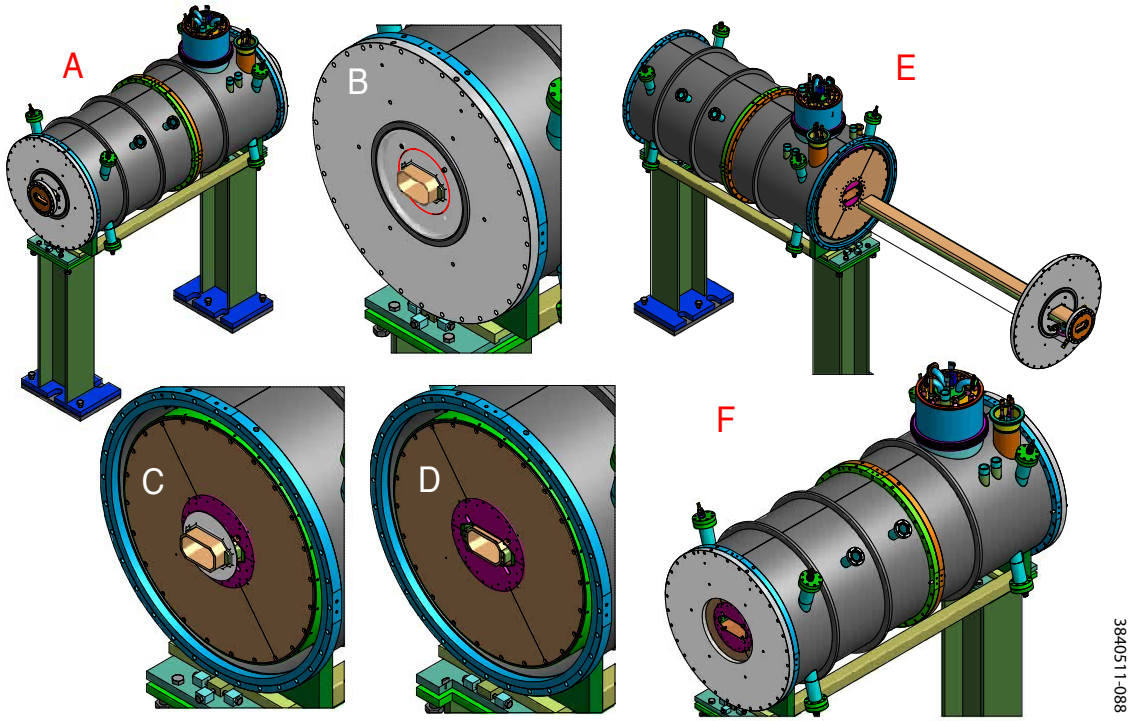

Figure 2.45: Sequence of the extraction of the beam pipe from CESR-c SCW Assembly. (A) One of end beam pipe flanges is cut off with a saw; (B) A circular cut is made through the flexible disk (indicated by red line) with a hole saw; (C) The large insulation vacuum vessel flange is demounted; (D) Another saw cut is made on the beam pipe behind the remainder of the flexible disk; (E) The remaining beam pipe is then pulled out of the SCW's warm-bore using the large flange at other end; (F) Both large vacuum vessel end flanges are remounted, after some surface machining to remove remnants of the flexible disks.

Many steps of heavy welding are required as part of the RFA wiggler beam pipe construction. As illustrated in Figure 2.40, we have designed the equipment in a such way so as to have all the welding that may overheat the portions of the beam pipe near the RFA flexible circuit completed prior to the installation of the flexible circuit. This Kapton©-based circuit has a temperature rating of 220°C. To allow for this requirement, a 'duck-under' channel was created beneath the stainless steel flexible disk, which later will be welded to the wiggler insulation vacuum vessel. During the construction process, all vacuum welds, except the final RFA vacuum cover, can be completed and leak checked prior to the installation of the heat-sensitive flexible circuit. Utilizing the 'duck-under' channel, one can feed the flexible circuit from the RFA portion of the beam pipe (i.e. inside wiggler insulation vacuum space) to the RFA connection port.

The beam pipe fabrication began by splitting the fully annealed OFE copper extrusion into two halves. The copper extrusions are the same type used for PEP II LER Quad beam pipe and the original CESR-c SCW beam pipes. All RFA-related features on the top half were machined at LBNL's machine shop with CNC machinery. These include the RFA grid pockets, 720 electron transmission holes, the 'duck-under' channel, and all the EB weld-preps (see photos in Figure 2.46). After cleaning, an 'under cover plate' was EB welded to the top half of beam pipe to form the 'duck-under' channel. Then two finished halves were joined together using a CNC EB welder, with approximately a 1 mm E-beam penetration at the seams. After passing a leak check of the beam pipe seams, two side cooling channels were also EB welded to the beam pipe (see photos in Figure 2.47). Measurements using NC coordinate machine found that amount of distortion of the EB-welded beam pipe is well within design tolerances. Subsequently, all other vacuum components (including end flanges and transitions, RFA connection port and vacuum pumping port) were manually welded to the beam pipes with tungsten inert gas (TIG) welding in an argon atmosphere to avoid the oxidation of the copper beam pipes. A temporary flange was welded to the end of the beam pipe, which is away from the RFA locations, to facilitate initial leak checking, bakeout and coating. At this stage all the UHV joints of the beam pipes, with exception of the top RFA vacuum cover plate, were finished and were ready for the final RFA component assembly. To ensure the required UHV quality, both beam pipes were baked to 150°C under vacuum. After the bakeout, one of the two RFA beam pipes produced at LBNL was coated with TiN thin film on the beam pipe's interior by the SLAC team. By comparing with the TiN coated and bare copper chambers using the CesrTA diagnostics, the effectiveness of TiN coating in suppressing EC in wiggler magnetic fields can be evaluated.

The first two partially finished wiggler beam pipes at LBNL were shipped to Cornell (in September 2008) for final RFA component assembly and integration into the SC wiggler assemblies. Photos in Figure 2.48 show some of the key steps of the RFA installation. The entire RFA installation was performed in a Class 1000 Clean Room. After thorough electrical checks the RFA installation was finished by E-beam welding on the OFE copper RFA vacuum cover. The finished RFA beam pipes were baked to 150°C for 48 hours before final insertion into the prepared wiggler magnet assemblies.

Before integrating the RFA beam pipe into the SCW, the temporary flanged end (end away from the RFAs) must be machined off using a clean milling machine with clean cutting tools. Extreme care was taken in this final machining step, which included blocking metallic debris from entering the RFA section of the beam pipe and constant purging of the chamber with N_2. The RFA beam pipe was inserted into the wiggler warm-bore and precisely positioned with respect to the wiggler magnet by optical survey. Extreme care was also taken in the final welding stages (including final beam pipe flange and seals to the wiggler insulation vacuum vessel) to prevent overheating of the

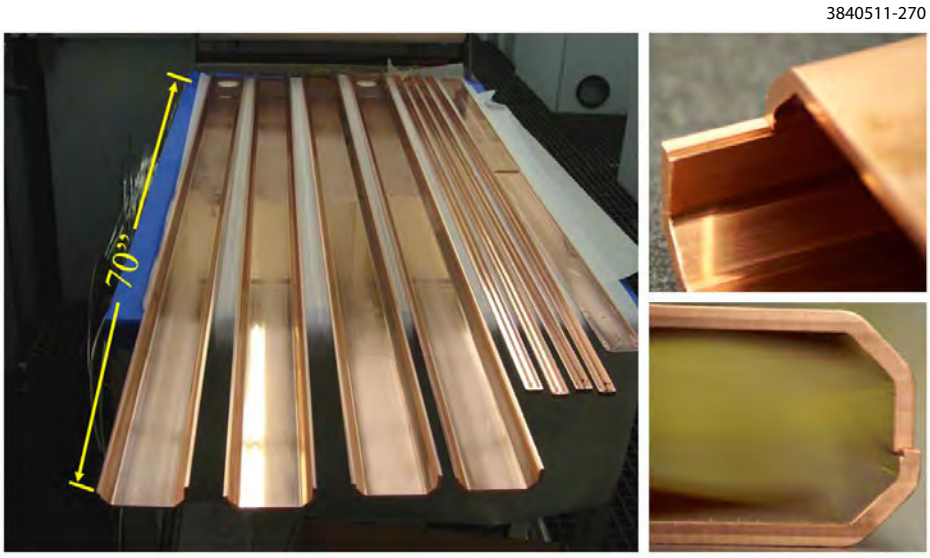

Figure 2.46: The copper beam pipes are split into two halves with EB-weld preps ready for cleaning and EB-welding. (Photos: courtesy of Dawn Munson of LBNL)

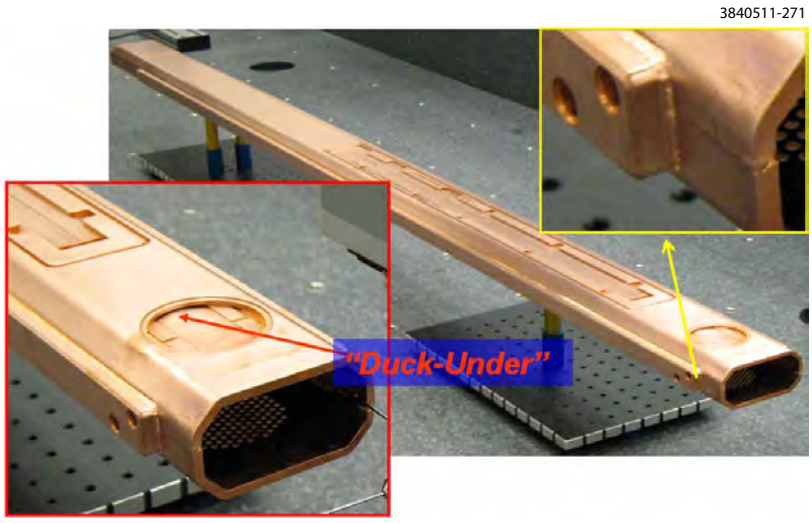

Figure 2.47: The beam pipe halves were EB-welded with approximately a 1 mm beam penetration. Two side cooling channels were also EB-welded to the beam pipes. The inserts show close-up views of the 'duck-under' channel for the RFA flexible circuit (lower right) and the EB-welds (upper left). The welded beam pipe is shown here on a CMM (coordinates measuring machine), which gave the total measured distortion of less than 0.15 mm. (Photos: courtesy of Dawn Munson of LBNL)

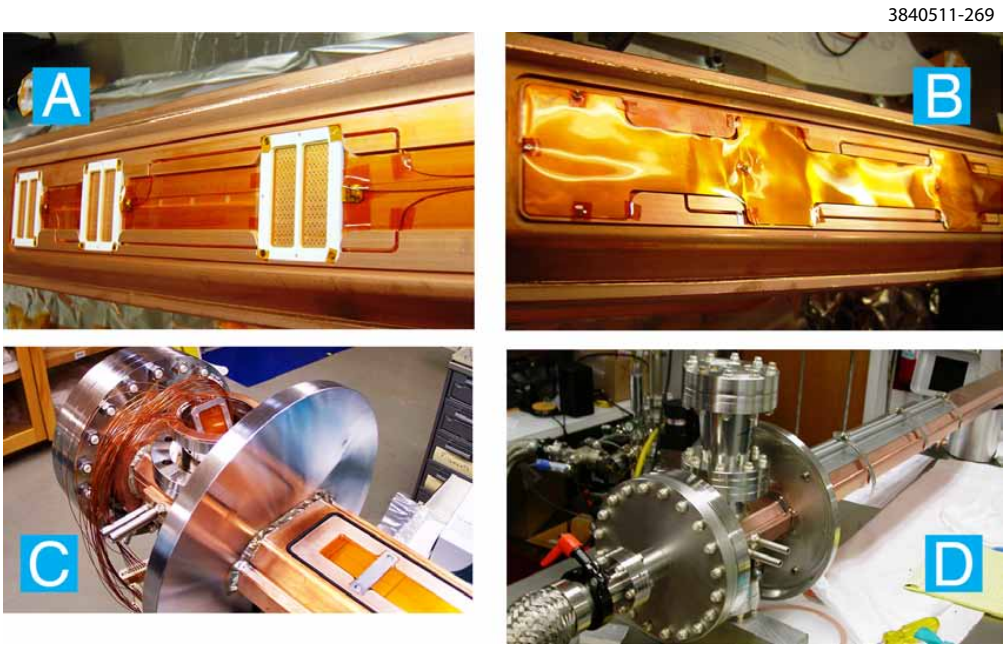

Figure 2.48: Photographs of the key steps in the RFA installation on a wiggler beam pipe: (A) Three grids are installed and individually wired to the connection port; (B) The flexible circuit collector is installed and located with 5 ceramic head-pins; (C) With the circuit through the 'duck-under' tunnel, all signal wires are attached in the connector port; (D) After making the final RFA connections, a vacuum leak-check is performed and a final RFA electrical check-out is done under vacuum before EB-welding of the RFA cover.

RFA components.

Finally, the completed SCWs with RFA beam pipes were 'baked' at 70°C for 2 days by circulating hot water through the beam pipe cooling channels in an effort to de-gas the vacuum components after the prolonged air exposure during the final RFA beam pipe insertion and welding. The first two SCWs with RFA beam pipe were successfully installed in the west side of the L0 Experimental region in CESR in October 2008 (see Figure 2.49) in the SCW02WA and SCW02WB locations (refer to Figure 2.2 in Section 2.2.2.1).

Grooved Chamber Using grooved surfaces to lower effective SEY is a well-known [5–8] passive technique to suppress EC growth in a magnet field. Having successfully implemented RFAs into SCWs in CESR, we studied the effects of grooved chambers by constructing an RFA-equipped SCW chamber with a grooved insert installed on the bottom surface. Figure 2.50 shows the design of the RFA beam pipe. This beam pipe assembly is basically identical to the design as shown in Figure 2.40 with the exception that a copper plate with triangular grooves has been attached to the bottom half via EB-welding. The same procedure (described previously in this section) was followed for the RFA installation to the beam pipe and the beam pipe integration into the SCW.

The implementation of a grooved surface in a copper vacuum chamber was found to be quite challenging. Practical considerations dictated the implementation of the grooved surface using an

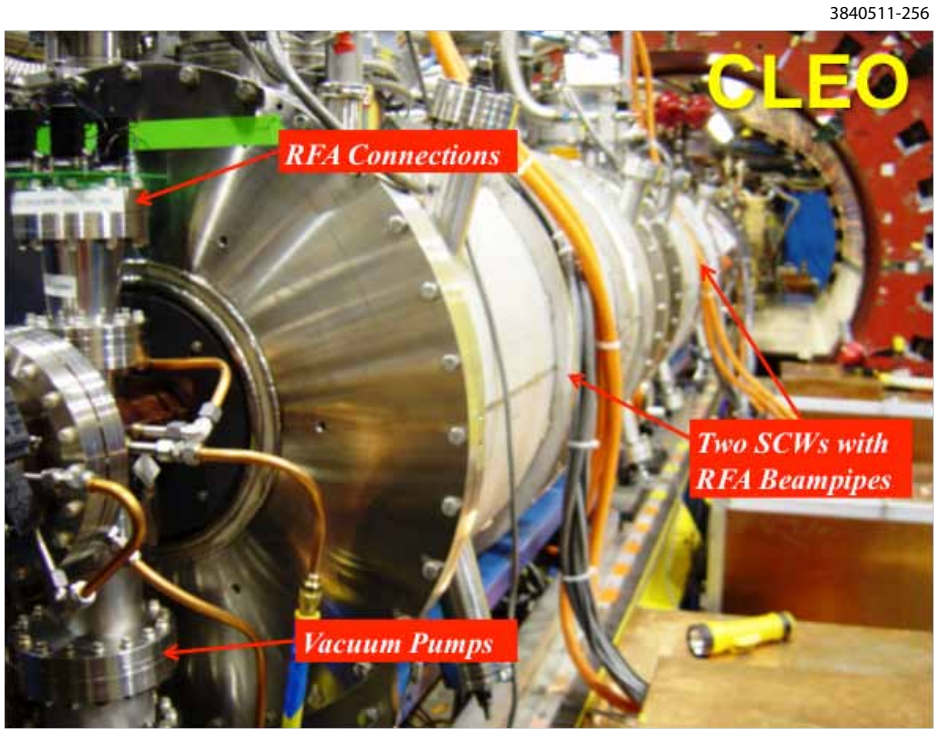

Figure 2.49: SCWs with RFA beam pipes were installed in the L0 Experimental region.

inserted plate. First, it was determined (through test machining) that the copper extrusions used for the SCW beam pipe were fully annealed, and too soft for machining the tiny groove geometry. Thus the grooves were machined in a separate plate of harder alloy which could be electron-beam welded into the vacuum chamber. A further limitation was that, even in the case of machining a separate plate, it was too costly to machine grooves for the entire length of the chamber. Thus, for the experimental tests, a grooved plate of sufficient length to span the RFAs was used.

The geometry and dimensions of the grooves are shown in the 'Detail F' in Figure 2.50. A cut-out opening was machined for the grooved plate into the bottom half of the beam pipe (Figure 2.51). 30° slope cuts were made on both ends of the groove plate and on the beam pipe wall (shown in 'Detail D' in Figure 2.50), which provide a smooth transition from the flat surface to the triangular groove tips in order to minimize HOML.

The triangular grooves were made with a milling technique using specially designed cutters. In practice there will be finite radius on the tips and valleys of these grooves. The effective peak SEY on these triangular grooves was simulated as a function of the tip/valley radius by Wang [13]. As shown in Figure 2.52 for the grooved surfaces to be effective in suppress SEY, it is essential to produce these triangular grooves with average radius of their tips and valleys smaller than 0.003" (75 μm). To qualify this groove fabrication technique, a prototype groove plate (of same width, but 150 mm long) was produced for inspection. Figure 2.53 shows the prototype groove plate, and images from optical inspections. The resulted tip and valley radii were approximately 25 μm and 60 μm, which were satisfactory.

The RFA beam pipe assembly, having the RFA features on the top half and the grooved plate on the bottom half, was fabricated at LBNL and delivered to Cornell in May 2009. The thin RFAs

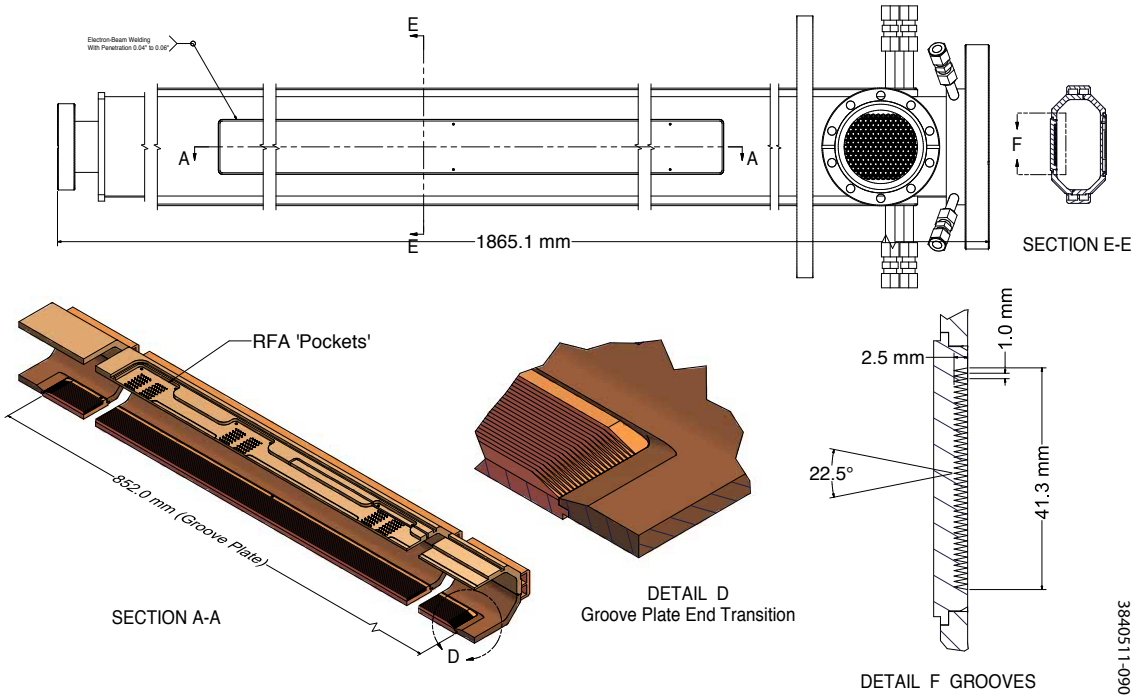

Figure 2.50: SCW RFA beam pipe with a groove plate EB welded to the bottom beam pipe.

were assembled into the beam pipe and then the RFA beam pipe was inserted into a SCW, following a similar procedure as describe previously in this section. Extra measures were taken to protect the sharp grooves at the bottom of the beam pipe throughout the final stages of assembly. The completed SCW was successfully installed for the CesrTA program in the L0 EC experimental region in July 2009 in the SCW02WB location (refer to Figure 2.2 in Section 2.2.2.1).

The SCW beam pipe assembly, containing the grooves and their associated RFAs, was successfully operated through two CesrTA experimental runs (July 2009 to September 2009, and November 2009 to December 2009) and two CHESS runs (September 2009 to November 2009, and January 2010 to March 2010), accumulating total beam doses of approximately 940 Amp·hr. During the April 2010 CESR shutdown, this SCW assembly was replaced with a SCW assembly fitted with RFA beam pipe, having an EC clearing electrode (see the subsequent topic in this sub-section). After its removal from CESR the following procedures were performed on the grooved RFA beam pipe as a continuing effort in studying EC suppression in wigglers.

- During the CHESS runs (and some of the CesrTA experimental runs), short electron/positron bunches with high bunch current were stored. Therefore, concerns were raised as to whether the high image current density on the sharp groove tips may have caused over-heating that resulted in damage. Close-up optical inspection of the grooves was carried out with a combination of a specially design 'trolley' (that locates a mirror above the grooves in the beam pipe) and a high-zoom digital camera. The entire length of the groove plate was inspected for damage to the groove tips. No damage was observed.

- Using a DC sputtering technique, a TiN thin film coating was applied to the interior surfaces of the beam pipe, including the grooved portion at the bottom beam pipe. The coating setup is shown in Figure 2.54. Figure 2.55 displays the uniform discharge during the TiN thin film

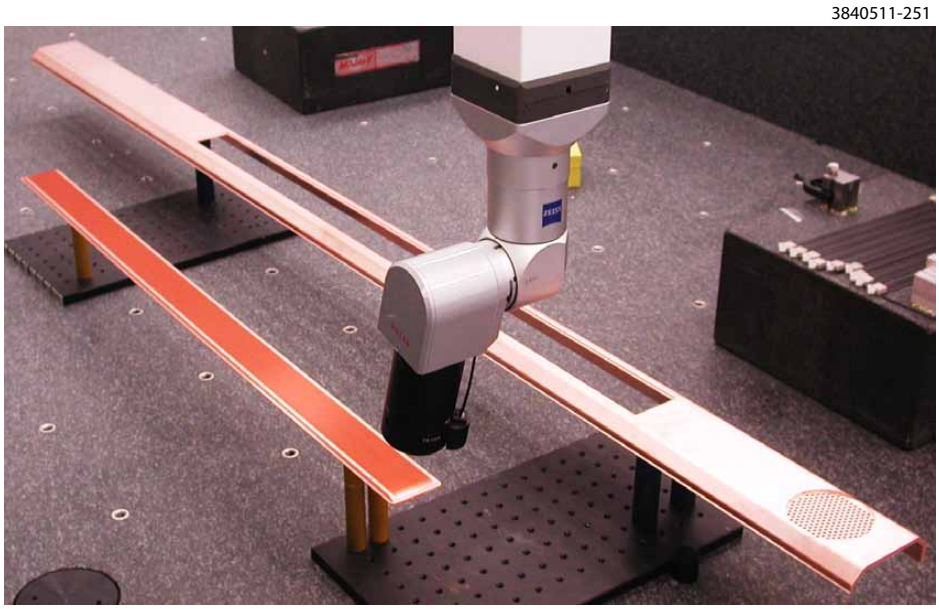

Figure 2.51: Bottom half of an SCW beam pipe with a cut-out and the groove plate during inspection on a CMM (Photo courtesy of Dawn Munson of LBNL)

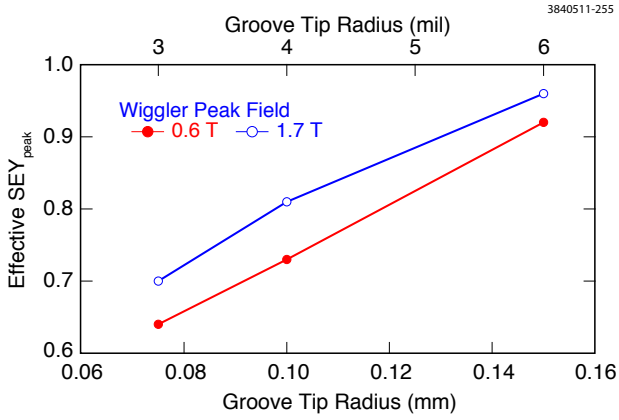

Figure 2.52: Simulated effective peak SEY on triangular grooves on copper as a function of groove tip/valley radius (sharpness) for two typical wiggler peak fields. (The simulation assumed the tips and valleys to have the same radius.) The two peak wiggler fields correspond to CESR beam energies of 1.8 GeV and 5.2 GeV.

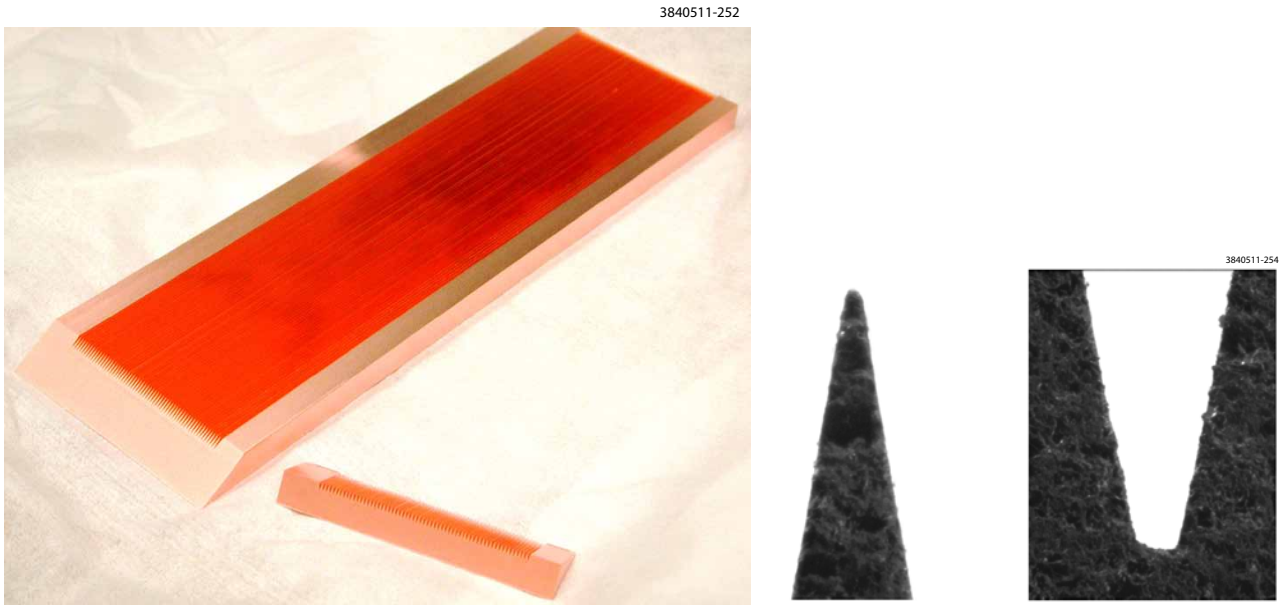

Figure 2.53: LEFT: A prototype groove plate was fabricated with full-hard OFC copper. A precision wire-cut across the grooves was performed for groove sharpness inspection. RIGHT: Images of prototype groove tip and valley, taken with a high-resolution camera on the CMM at LBNL with back-lighting. The tip radius is estimated to be approximately 0.001" (25 μm) and the valley approximately 0.0025" (63 μm). (Photo courtesy of Dawn Munson of LBNL)

deposition. The TiN deposition was undertaken in two stages with the titanium cathodes shifted transversely to minimize the geometric shadowing of the steep grooves. The estimated TiN film thickness was 150 to 500 nm, based on the on-line measurements of a QCM (Quartz Crystal Micro-balance) and the off-line measurements of witness coupons.

- Close-up optical inspection of the grooves was done after the TiN coating. Figure 2.56 shows typical inspection images of a portion of the grooves before and after the TiN coating. Although the camera did not possess sufficient acuity to resolve the fine features of the sharp tips/troughs, no obvious sign of over-heating and damage to the grooves were visible. The image also showed relatively uniform TiN coating with no significant shadowing within the groove troughs.

The TiN coating process was performed in the presence of RFA assemblies with all RFA grids and collectors grounded. The RFAs were found to be fully operational after coating in this manner. The TiN coated, grooved RFA SCW assembly was reinstalled in the L0 EC experimental region in SCW02WA location in January 2011.

Electrode Chamber One of the electron cloud mitigation methods studied at CesrTA makes use of a clearing electrode, operating with a positive bias voltage to attract the electrons, which would ordinarily collect around the positron beam. To investigate its EC suppression efficacy in the wiggler field, a clearing electrode was installed on the bottom of an RFA-equipped beam pipe in an SCW. The structure of the beam pipe is shown in Figure 2.57. The beam pipe consists of a top half with three RFAs (identical to the design as shown in Figure 2.40) and a bottom half with a clearing electrode assembly.

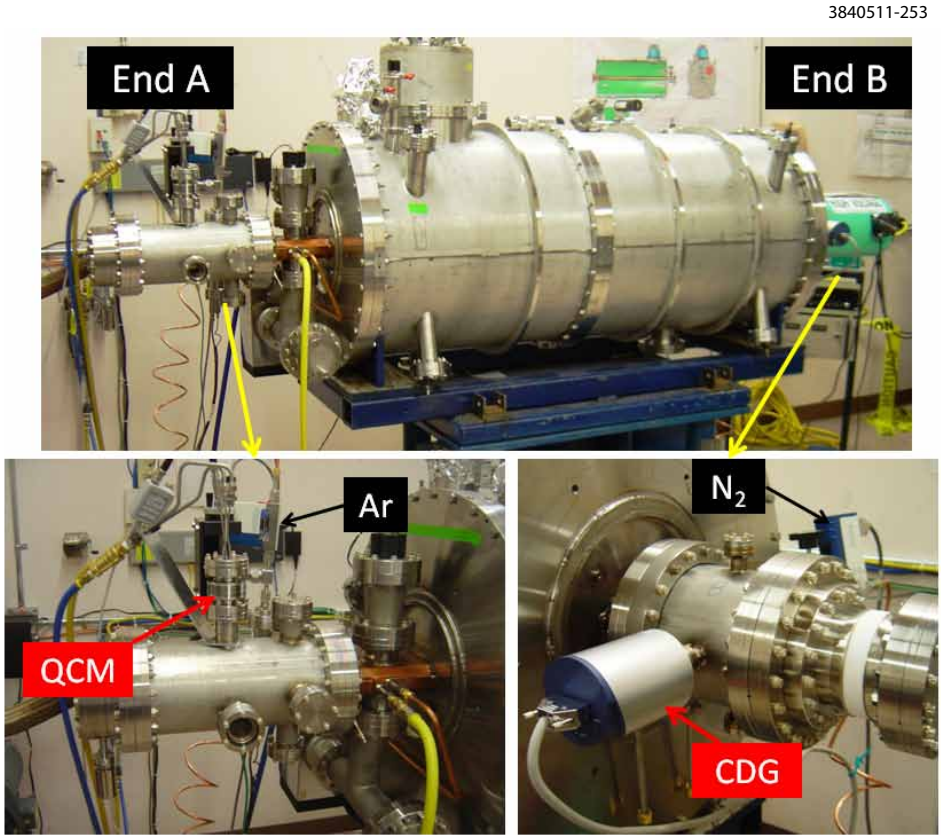

Figure 2.54: TiN coating setup of the SCW RFA beam pipe with bottom grooved plate. Solid grade 1 titanium rods were used as cathode, biased at a DC voltage of 1.5 kV. Flow rates of sputtering gases (Ar and N_2) were controlled with flow meters, and the sputtering pressure was controlled at approximately 0.10 torr. A Quartz Crystal Micro-balance (QCM) was used to monitor film thickness.

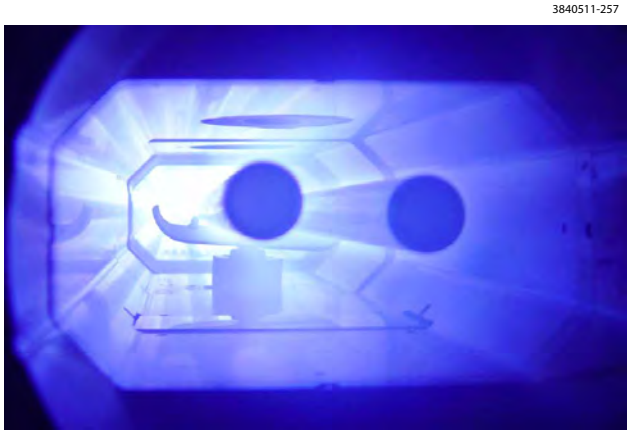

Figure 2.55: Glowing discharge during TiN coating of the grooved RFA beam pipe. The coating was performed in two stages, the first stage using two Ti rods (as shown) and the second stage with three rod (located in different transverse positions.) The two-stage coating is to minimize shadowing effects from the steeply grooved troughs.

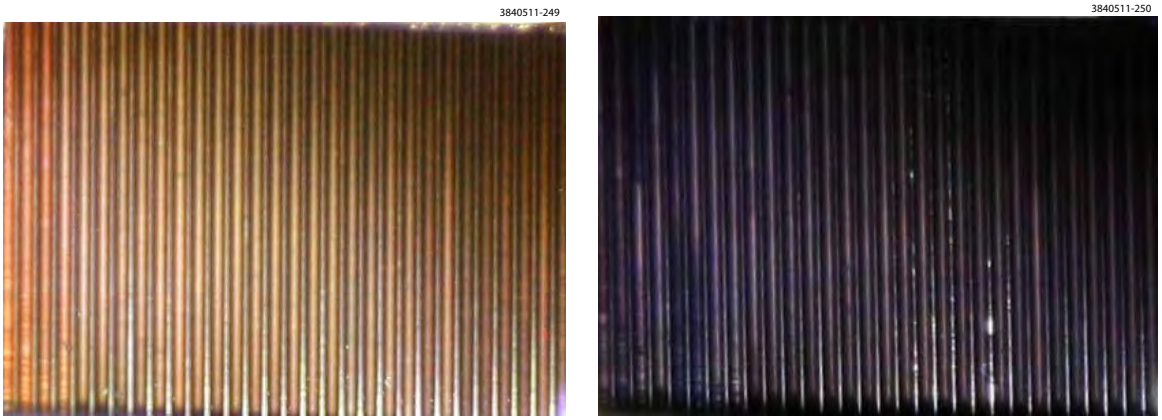

Figure 2.56: The grooves of the SCW RFA beam pipe were inspected optically. LEFT: Before TiN coating; RIGHT:After TiN coating.

The geometry of the clearing electrode is a thin stripline [14], which consists of an alumina ceramic layer on copper surface (of approx. 0.2 mm in thickness) as an insulator and a thin layer of tungsten on the ceramic surface (of approx. 0.1 mm in thickness) as the electrode. The area of the alumina ceramic layer was larger than that of the electrode, so that the required DC voltage could be applied to the electrode in vacuum. These two layers were deposited via a thermal spray technique and were tightly bonded to the copper chamber. Tungsten was chosen as the electrode material owing to its small thermal expansion rate (as compared to the alumina ceramics), good thermal and electrical properties, and substantial experience in the utilization of thermal spray applications. The photograph in figure 2.58 shows the finished bottom beam pipe with its deposited electrode. The insulation resistance between the electrode and the copper chamber was about 5 MΩ (in dry air) and the electrode is capable of withholding DC voltages above 1 kV.

Since the magnetic field within the wiggler magnet is vertical, electrons will stream along field lines, impacting the top and bottom walls of the vacuum chamber and produce secondary electrons, which will again stream to the opposite vacuum chamber wall. Thus the clearing electrode is designed to have a width of 40 mm and is placed on the lower wall of the vacuum chamber, extending for 1.09 m along the beamline, in order to intercept electrons impacting the bottom of the vacuum chamber. However, from the beam-impedance point of view, the narrower the electrode is, the smaller the impedance. To minimize HOML induced by the electrode, the ends of the electrode are tapered at a 42° angle down to a 3 mm radius at its tip. The HV connection is made by a coaxial line coming through a port located underneath one of the tapered ends of the electrode. The electrical connection to the electrode is made via a convex button washer (having a 26 mm diameter) on the top of the electrode, as shown in Figure 2.57 and Figure 2.59. The connection was designed to make the inner surface (visible to the beam) as smooth as possible, while keeping a secure electrical contact. Although the effects of the low profile of the discontinuity, the tapered ends of the electrode and the hidden HV connection have not be calculated in detail, they are expected to produce a HOML parameter of less than a few times 0.001 V/pC for the 7 to 10 mm bunch length of CESR. Any heating from the wall currents flowing on the surface of the electrode is easily handled by conduction to the beam pipe through the thin alumina dielectric layer, which has good thermal conductivity. Thermocouples mounted on the bottom beam pipe near the electrode assembly have detected no increase in heating due to HOML at any of the beam currents during operations.

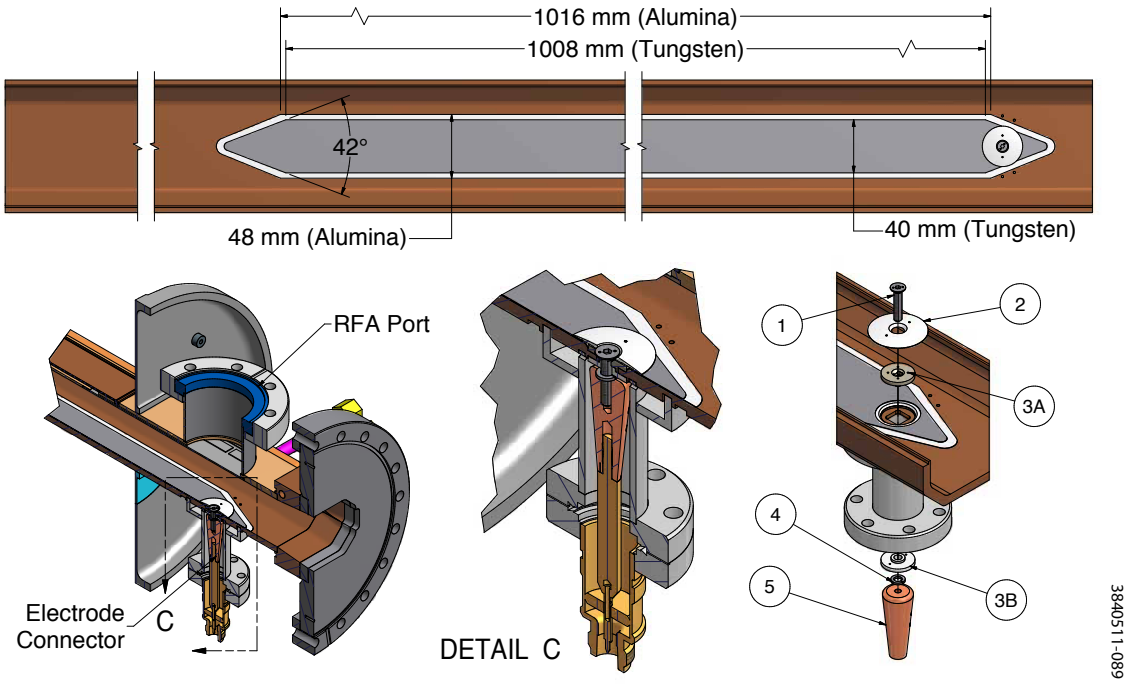

Figure 2.57: SCW RFA beam pipe with clearing electrode assembly. Top: sectional view and clearing electrode as seen from the top. Bottom left: sectional view of the clearing electrode and the HV input port. Bottom middle: detail of HV coupling port. Bottom right: exploded view of HV port; electrical contact is made with a vented screw (1), an aluminum alloy button (2), insulation spacer made of PEEK (3A, 3B), a stainless steel spring washer (4), and a tapered copper pin (5).

At LBNL the bottom half of the beam pipe (containing the thermal-sprayed electrode) was EB-welded with the top half beam pipe (with all RFA features as shown in Figure 2.40) to form the pre-RFA beam pipe assembly and then delivered to Cornell in February 2010. Following the same procedures described earlier, RFAs were assembled to the electrode beam pipe, integrated into an SCW and then installed in the L0 experimental region for CesrTA experimental runs beginning April 2010. After operations for three CesrTA runs and two CHESS X-ray User runs (from April to December 2010), a visual inspection of the electrode and the electric contact was done during the January 2011 shutdown. With an accumulated total beam dose exceeding 1000 Amp·hr over the CesrTA and CHESS runs, the electrode and the electrical contact were found to be in excellent condition with no sign of arcing or over-heating.

During stored beam operation one concern with the electrode design was the peak voltage induced by a bunch's passing. There are two parts to this particular concern. First is that the peak voltage is high enough to either break down the dielectric layer or produce an electrical discharge in the vacuum, which could cause metal to be plated onto the dielectric, either of which will degrade the high voltage standoff capability of the electrode. The second is that the voltage induced onto the electrode might couple to subsequent bunches causing enhanced HOML or transverse kicks possibly destabilizing later bunches in the train. This could be particularly a concern for the clearing electrode, since its structure resembles that of a stripline pickup or stripline kicker. Since the transmission line impedance of the electrode structure is difficult to match to the external coupling

Figure 2.58: Photo of deposited electrode on the bottom of the SCW beam pipe.

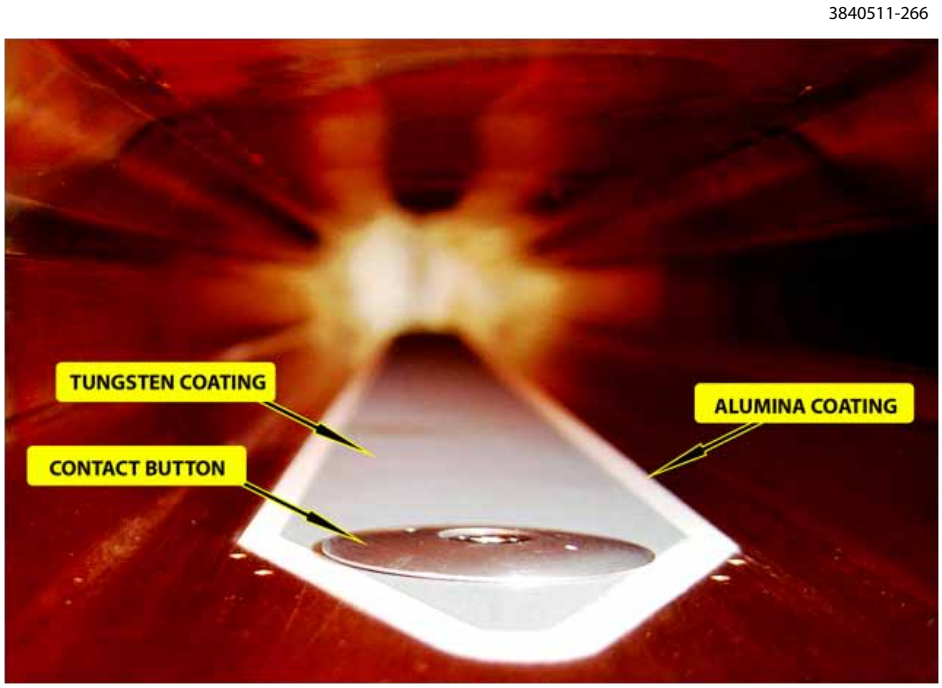

Figure 2.59: Photo of electrode connection button on the bottom of the SCW beam pipe.

port, there can be many reflections of the induced voltage before it damps out. If the transmission line-electrical length of the electrode is chosen poorly, a resonant excitation of the beam-induced voltage could result in large voltages occurring on the electrode with respect to ground. This resonant enhancement of the voltage could lead to a sizable multiplication of all effects. Therefore the 1.05 m length of the clearing electrode was designed, after taking into account the dielectric constant of alumina of 9.8 (a reduction of the propagation delay of the signal in the stripline by a factor of 3.13 from the speed of light in vacuum), to have a round trip delay of 21.9 ns, which is not a multiple of either 4 ns or 14 ns, the primary bunch spacings employed for CesrTA.

To reduce the peak induced voltage, the ends of the electrode are tapered. As a bunch passes by the tapered end of the electrode the induced wall currents in the electrode spread out over a time equal to the difference of the propagation delay of the signal in the electrode's stripline transmission mode and the transit time of the bunch. With a taper length of 31.3 mm, the duration of the induced signal at both ends will spread out over 0.2 ns in the forward transit direction and 0.4 ns in the reverse direction. Since the temporal standard deviation of the bunch ranges between 20 and 35 ps, spreading the induction of the signal in the electrode over more than ten times the bunch's rise time will reduce the peak signal by a comparable factor. Since the wall currents traveling with the beam are induced into the transmission line composed of the electrode resting on the dielectric layer on top of the vacuum chamber wall, the induced voltage will be proportional to the impedance of the transmission line. With a dielectric thickness of 0.2 mm and a maximum electrode width of 44 mm, the transmission line impedance is 0.59 Ω. At the tapered ends the impedance increases to 3.6 Ω, thus the reflections off of the ends will cause additional (somewhat more complicated) spreading of the transmission line signal.

Some care was taken to make a reasonable match of the impedance of the external coaxial HV connection to the clearing electrode. The effective impedance of the electrode at the point where

the external port attaches to the electrode's taper is 0.78 Ω. The hole through the beam pipe under the taper plus the HV connection post (sticking through the hole) have an impedance of 6.2 Ω, making it impossible to match the clearing electrode's impedance at the connection point. However, some improvement to the mismatch to the 50 Ω type-N connector was accomplished by tapering the center conductor with a conical taper from the 50 Ω connector to 11.5 Ω where the center conductor attaches to the HV connection post. So in the final design there are two mismatches between electrode and the type-N connector: 1) between the electrode and the HV post and 2) between the HV post and the tapered coaxial feed line, giving reflection coefficients, respectively, of -0.80 and -0.30. Lastly, for thermal expansion there is a sliding contact where the conical coaxial center conductor attaches to the constant diameter, 50 Ω center conductor.

After the construction and assembly of the electrode and the coaxial HV connection port, time domain reflectometer (TDR) measurements were made. The TDR allows a basic check of the impedance of the entire structure using a step function-signal with a rise-time of 25 ps. However, since the electrode's transmission line impedance is so low, only an upper limit may be placed on its impedance. At the input side, the type-N connector had a reflection of + 6%, while the sliding contact had additional ± 4% reflections. Neither of these is very serious as they are relatively small and are contained within regions of less than 0.15 ns propagation delays. The estimated upper limit of the transmission line impedance of the central section of the clearing electrode itself is 2.6 Ω, which is consistent with the expected 0.59 Ω.

With 5 mA single bunch stored beams, measurements have been made to observe the signal coming from the type-N connector at the HV input port. The orientation of the clearing electrode after it was installed in CESR has the HV input port such that the electron bunches pass the end with the input port first and then the end with no connection afterwards. A positron bunch circulates in the opposite direction as compared with an electron bunch. All measurements were made with 26 dB of attenuation for signal before connecting to a LeCroy Model Wavemaster 804ZI, 4 GHz bandwidth oscilloscope. In the subsequent figures the scales have been corrected for the 26 dB of attenuation. Figures 2.60 and 2.61 show the signal from the positron single bunch on longer and shorter time scales, respectively. The signal from the positron bunch has a peak value of 13 V at the time of the bunch's passage by the HV coupling port as is indicated by the 2.9 GHz burst. Although a detailed model for the coupling from this tapered stripline has not yet been constructed, this frequency appears to be characteristic of the propagation delay along the taper. Figure 2.61 shows in more detail the signals induced at the HV coupling port (as described above) and the open taper at the far end. Although the signal from the positron bunch was induced at the open taper earlier, due to the propagation delay from the dielectric insulator this signal arrives at the HV coupling port 0.61 ns later than the signal induced in the tapered end connected to the HV coupling port. The time segment marked in figure 2.61 is approximately the delay from the $v = c$ beam transit velocity and the $v = 0.31\ c$ signal propagation velocity. Likewise the signal observed from the 5 mA electron bunch, seen in figures 2.62 and 2.63 (viewed on longer and shorter timescales, respectively), shows the same high frequency burst from the taper at the HV coupling port followed by the lower bandwidth pulse from the open tapered end of the electrode. In this case the peak signal observed in the HV input port is 9 V and the delay between the signals at the two ends has increased to 1.33 ns. The longer delay is caused by the fact that the bunch must transit the length of the electrode at $v = c$ and then the signal induced in the open taper must propagate back at $v = 0.31\ c$. By comparing the delays between these two signals for positrons and electrons, it is possible to determine the measured propagation delay in the transmission line defined by the clearing electrode and, hence, the dielectric constant for the alumina. These measurements yield a dielectric constant of 2.93 in good agreement with the expected 3.13 value.

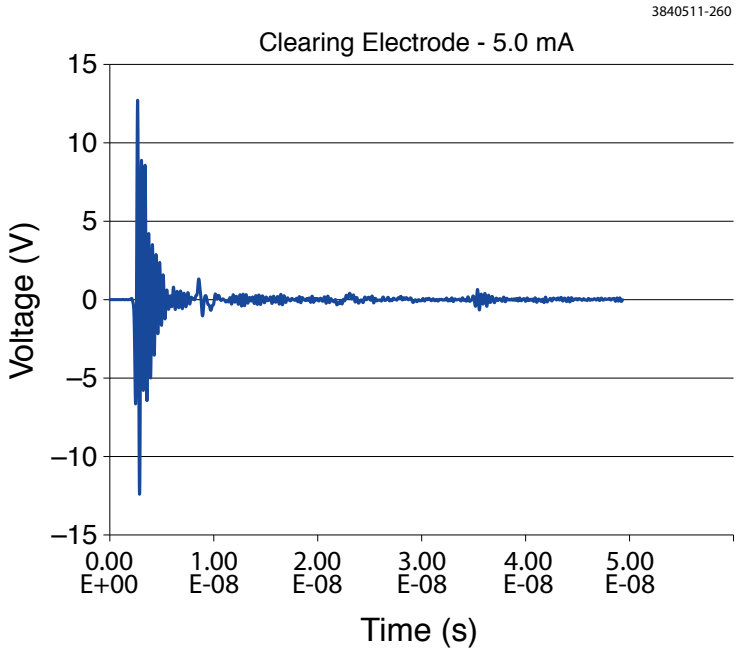

Figure 2.60: Clearing electrode HV port signal for a single 5 mA positron bunch

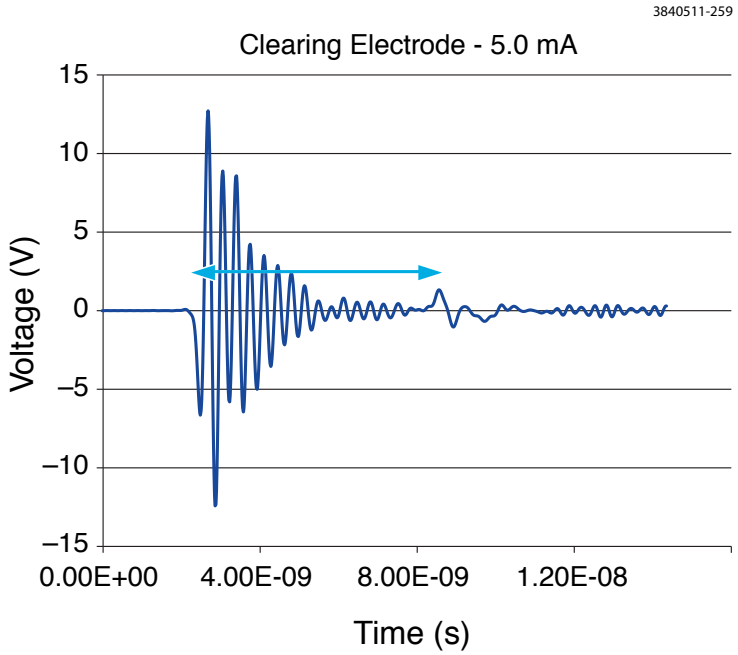

Figure 2.61: Clearing electrode HV port signal for a single 5 mA positron bunch on an expanded time scale. The time segment marked with the arrows represents the delay between signals induced at the HV coupling port end and the far end of the electrode.

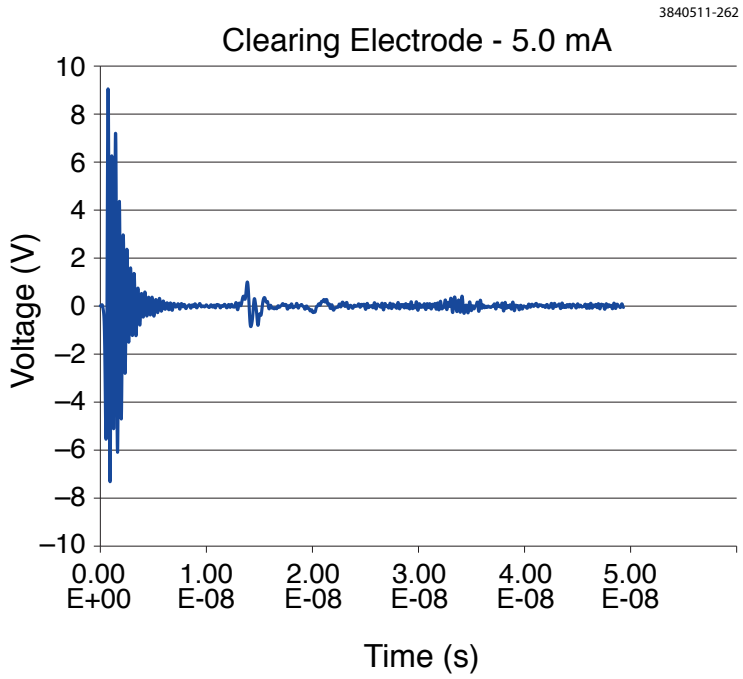

Figure 2.62: Clearing electrode HV port signal for a single 5 mA electron bunch.

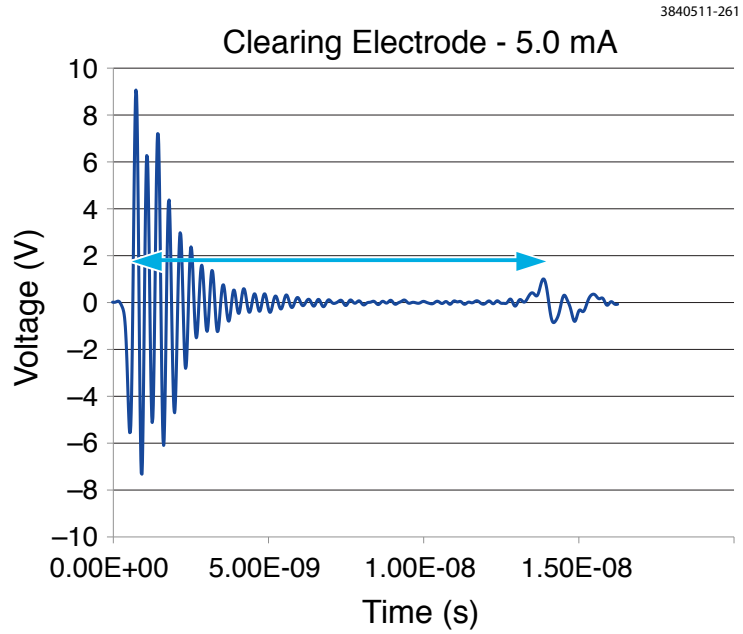

Figure 2.63: Clearing electrode HV port signal for a single 5 mA electron bunch on an expanded time scale. The time segment marked with the arrows represents the delay between signals induced at the HV coupling port end and the far end of the electrode.

Neither of the positron or electron beam induced signals, as viewed at the HV coupling port, suggest serious peak voltages for the electrode at any typical operating currents for CesrTA. They also suggest that the reflections die out in only a small number of traversals along the electrode and that taken with the measured propagation delays imply that resonant build-up of the signals from multiple bunches within trains will not be a problem.

The last of the installation-related measurements was made after attaching the HV coupling network and measuring the electrode current vs. electrode voltage for a given beam current. The coupling network and its HV DC power supply are shown in figure 2.64; the network is constructed from bias tees, which were purchased from MECA (part number 200N-MF-1) and rated to handle 200 V DC bias, with 300 W average RF power and 3 kW peak RF power. Two of these were cascaded to obtain the needed 400 V bias capability for the CesrTA studies. During bench testing of the MECA units, it was apparent that they had an unpleasant notched response just below about 100 MHz. Anticipating that this could be a problem, the bias tees that were modified by replacing the originally installed inductor with a 1 kΩ resistor. The frequency response is improved and now has a single pole high pass cutoff frequency of about 30 MHz. Figure 2.65 gives the measured clearing electrode current as a function of bias voltage for a train of 20 positron bunches at 5.3 GeV, while the superconducting wiggler is unpowered. Note that 100 V of bias is enough to saturate the clearing electrode's collection current.

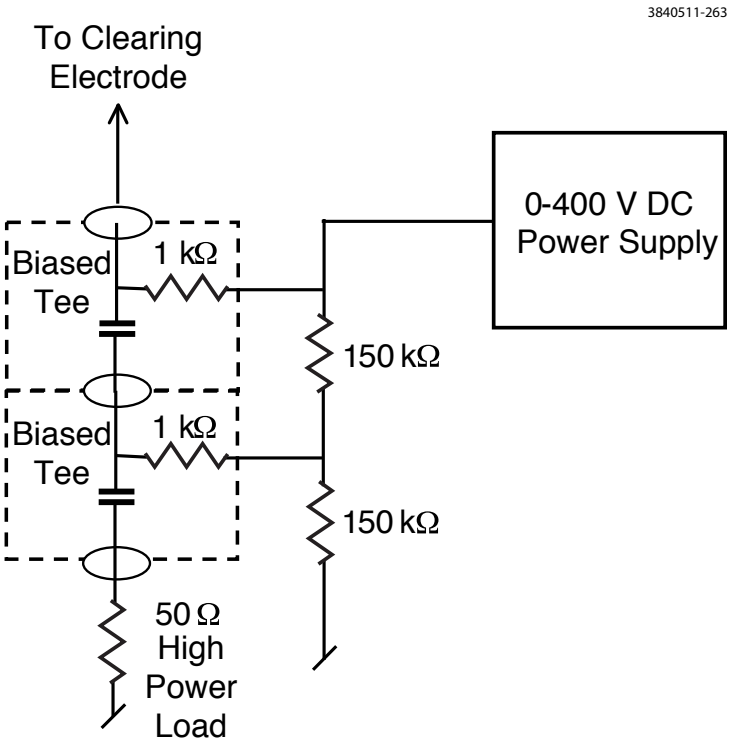

Figure 2.64: Coupling network for the clearing electrode's HV coupling port.

After eight months the vacuum chamber housing the clearing electrode was opened for a visual inspection after operating in CESR for CesrTA studies and for CHESS operations with the higher peak bunch currents of over 9 mA. A visual inspection showed no sign of any arcing or plating of material anywhere inside of the vacuum chamber. The clearing electrode's appearance was the same as it was during its installation.

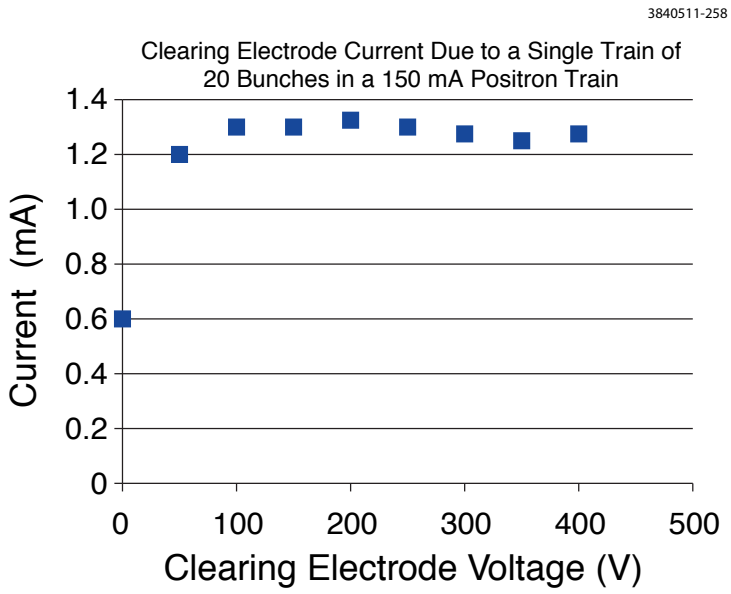

Figure 2.65: Beam induced clearing electrode current as a function HV bias setting for a 20 bunch train of a total current of 150 mA at 5.3 GeV with the wiggler turned off.

2.2.3.4 Quadrupole Chambers

Thin-style RFAs were implemented in beam pipes in a quadrupole magnet in CESR in the L3 experimental region (see Figure 2.10). The design of the quadrupole RFA beam pipe is illustrated in Figure 2.66. The beam pipe is constructed from thick wall aluminum tube (6061-T6 alloy, 4.5" outside diameter, 3.5" inside diameter), allowing room for a machined RFA housing pocket. A channel was also machined as a part of the RFA housing pocket for wires connecting the grid and RFA collectors to the vacuum feedthrough port, which must be outside of the quadrupole magnet. The structure of the RFA consists of high-transparency gold-plated copper meshes nested in PEEK frames and a segmented collector made of flexible circuit, similar to the RFA designs used in the CESR dipole and wigglers. Many small holes (1740-0.75 mm diameter holes) were drilled through the beam pipe to allow electrons to reach the RFA, while filtering out beam-induced RF EMI. These 1740 holes are grouped into 12 angular segments, matching the 12 RFA collector elements on the flexible circuit (Figure 2.67). The angular coverage and resolution of the RFA is shown in Figure 2.68.

Photos in Figure 2.69 show key steps in the RFA assembly process. Before any RFA assembly the RFA quadrupole beam pipe vacuum components (minus the RFA vacuum cover) were TIG-welded, including the cooling channels. A vacuum leak check was performed using a specially constructed Viton gasket to seal off the RFA pocket to ensure the vacuum integrity for all the major vacuum welds. Then to ensure that the temperature sensitive RFA parts (the flexible circuits, PEEK grid frames, etc.) were not subjected to heating from any heavy TIG-welding, water-cooled bars were added to the cover before welding. The RFA electrical properties (including capacitance measurements) were checked repeatedly at every step of the assembly. The finished RFA beam pipe was leak checked, and an 150°C/24-hr vacuum bakeout was carried out before back-filling with dry N_2 in preparation for installation.

Two RFA quadrupole beam pipe assemblies were constructed during the CesrTA Phase 1 program.

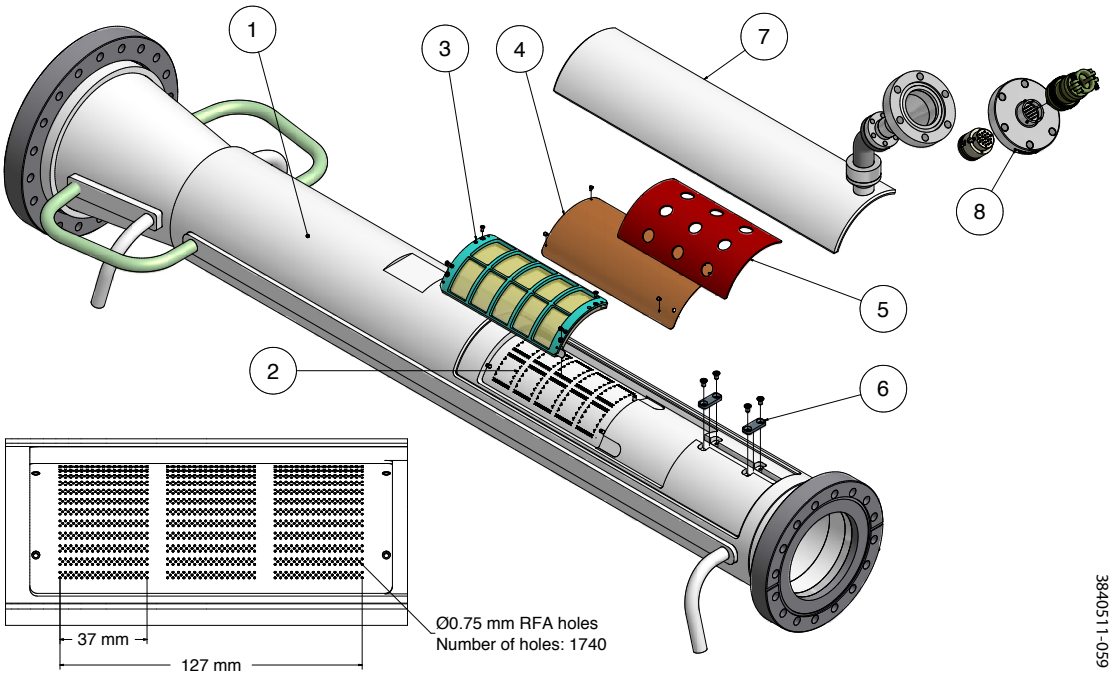

Figure 2.66: Exploded view of the structure of the RFA within a CESR quadrupole beam pipe. The major components of the RFA beam pipe include: (1) Aluminum beam pipe with cooling channels; (2) RFA housing and wiring channels; (3) Retarding grids, consisting of high-transparency gold-coated meshes nested in PEEK frames; (4) RFA collector flexible circuit; (5) Stainless steel backing plate; (6) Wire clamps; (7) RFA vacuum cover with connection port; (8) 19-pin electric feedthrough for RFA connector

The first assembly was with a bare aluminum beam pipe. It was installed in the L3 experimental region (in the Q48W quadrupole magnet) in July 2009 and tested in CesrTA experimental runs between July 2009 and March 2010. With the first quadrupole RFA beam pipe successfully assembled and tested in CESR, the second assembly was built with a TiN-coated aluminum beam pipe. The TiN coating (of 150 nm to 200 nm in thickness) was applied via DC sputtering to the inner surfaces of the beam pipe before the assembly of the RFA. The same RFA assembly procedure was followed as was employed for the first assembly. The TiN-coated RFA beam pipe replaced the bare aluminum RFA beam pipe in April 2010, and has remained in the L3 experimental region since.

2.3 Electron Cloud Diagnostics

2.3.1 Retarding Field Analyzers

2.3.1.1 Introduction

In order to characterize the distribution of the electron cloud build-up around CESR, retarding field analyzers have been deployed at multiple locations in the ring. Local EC measurements provided by these devices represent a central element of the CesrTA experimental program:

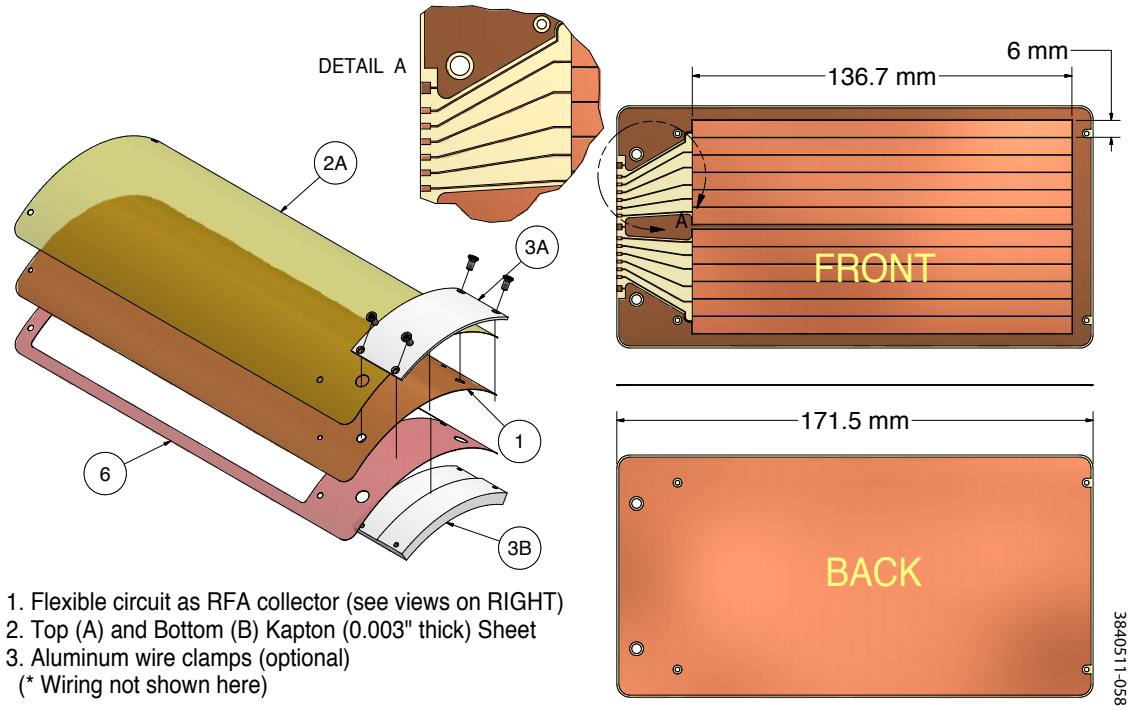

Figure 2.67: The flexible circuit used for the quadrupole RFA collector.

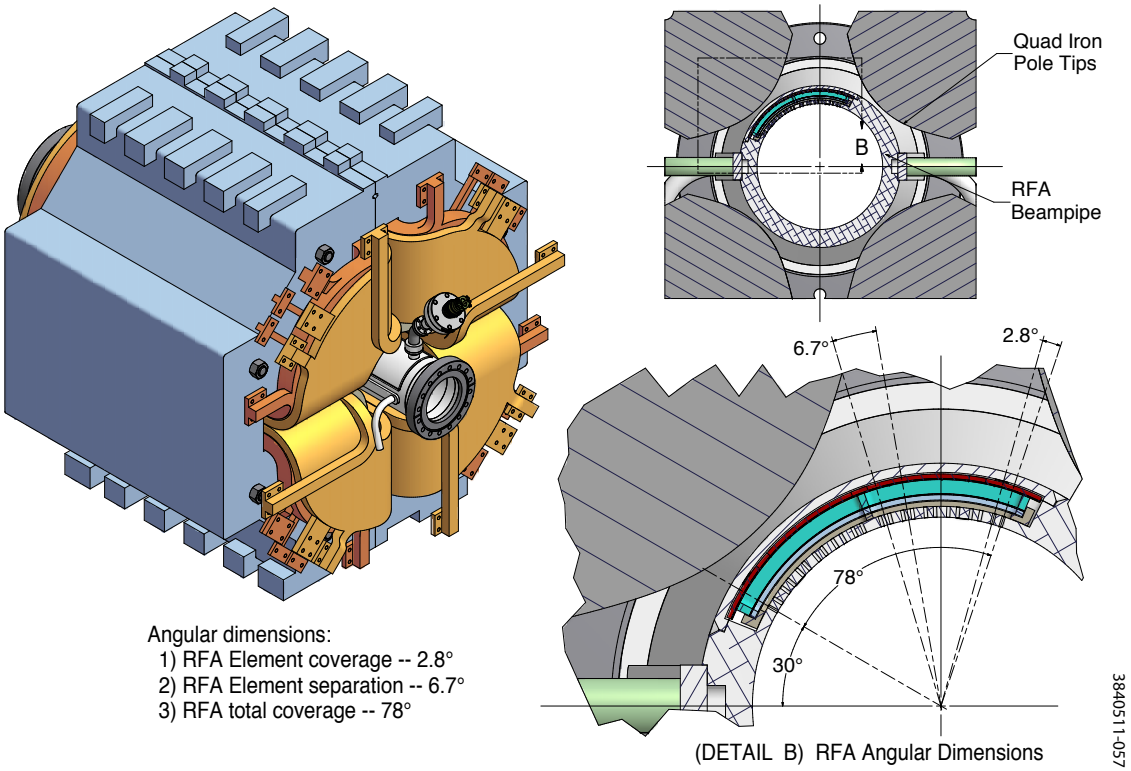

Figure 2.68: The RFA beam pipe in the Q48W quad (left). The RFA angular coverage (right).

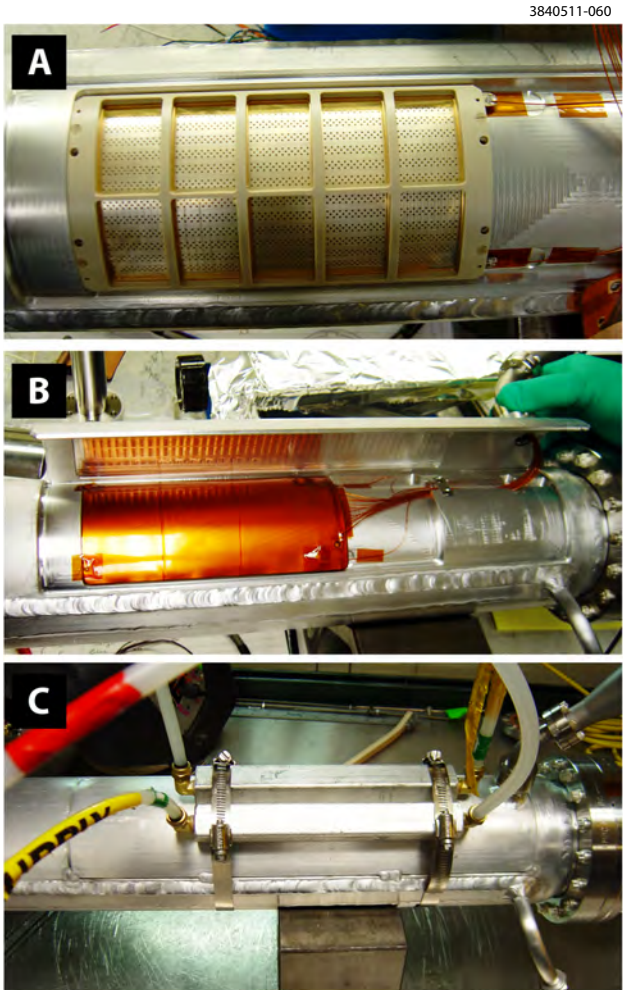

Figure 2.69: Photos of quadrupole RFA beam pipe construction, showing key steps: (A) Gold-coated meshes in PEEK frames are mounted and wired; (B) Flexible collector circuit installed. The circuit is electrically isolated with clean Kapton sheets; (C) Water-cooled bars were used during final welding of the RFA vacuum cover.

- They provide a baseline measurement of the EC densities and energy spectrum in each of the major vacuum chambers and field regions in CESR;
- By using segmented designs, each RFA provides detailed information about the transverse distribution of the EC in each vacuum chamber;
- In combination with non-local techniques, such as bunch-by-bunch tune measurements of long trains, the information obtained from these devices can be used to constrain the primary photoelectron yield and the secondary electron yield models which describe the overall development of the EC;
- Finally, when employed in vacuum chambers with EC mitigation, these devices directly measure the efficacy of various mitigation techniques being considered for the ILC Damping Rings.

This section basically describes the instrumentation for these local measurements of EC buildup. The hardware description found in this section is supplemented in Chapter 5 with further details of the hardware, the analysis methodology and the results of measurements.

2.3.1.2 Hardware Design

The RFAs, designed for use in CESR, are primarily intended for vacuum chambers where detector space is severely limited due to magnet apertures. Thus the design minimizes the thickness of the structure although this has performance implications for the device. In particular, the maximum retarding voltage will be limited to a few hundred volts with a somewhat degraded energy resolution. A self supporting 0.006" thick stainless steel with an etched bi-conical hole structure (0.007" diameter holes with a 0.01" pitch) was chosen for the grids while the electron collector pads were laid out on copper-clad Kapton sheet using standard printed circuit board fabrication techniques. These layers can be supported with machined ceramic or PEEK structures. RFAs for various vacuum chamber configurations have been created for CesrTA :

- The drift chamber RFAs are found in Figures 2.13, 2.17 and 2.18 for example for the Q15E location.
- An example of the RFAs for the CESR dipole chamber are seen in Figures 2.31, 2.32, 2.33, 2.35 and 2.35.
- RFAs have been incorporated into the vacuum chambers within the L3 chicane magnets and one of these is displayed in Figure 2.37.
- Special RFAs were developed for use within superconducting wiggler chamber and these are found in Figures 2.40, 2.42, 2.43, 2.44 and 2.48.
- A quadrupole RFA has been developed and installed in one of the L3 quadrupoles and is seen in Figures 2.66, 2.67, 2.68 and 2.69.

The specific RFA structure that was used both for bench testing with an electron gun and for beam testing in CESR is shown in Figure 2.70. Typically, the grid layers are vacuum-coated with a thin gold layer (several hundred nm) to reduce their secondary electron yield. Operating voltages are typically $20 - 100$ V on the collector and retarding voltages in the range of $+100$ to -300 V.

A modular high voltage power supply and precision current monitoring system has been designed to support RFA measurements at multiple locations around CESR. A block diagram is shown in Figure 2.71. Each HV supply contains two four-quadrant grid supplies and a single unipolar collector supply. The standard grid supply can operate from −500 V to +200 V and can provide −4.4 mA to 2.4 mA at 0 V. The unipolar collector supply can operate from 0 V to 200 V and is rated for 50 mA. A digital control loop is used to set and stabilize the output of the each supply with a feedback resolution of 60 mV. The feedback is specially configured to enable high precision current measurements while the feedback loop is quiescent. Upon receipt of a voltage command, the HV control sets the voltage and allows it to stabilize. At that point, all feedback corrections are suspended for a 20 second data acquisition window. The controls for the two grid and single collector supplies in a full HV supply are configured to make this quiescent period simultaneous.

The RFA data boards distribute bias voltages to the detector elements (up to 17) and measure the current flow in each. The current is measured by an isolation amplifier looking at a series resistor (selectable as 1, 10, 100 or 1000 kΩ) in the high side of the circuit with the output going to a 16-bit digitizer. The various resistors correspond to full scale ranges of 5000, 500, 50, and 5 nA. The finest resolution is 0.15 pA.

The readout system is in a 9U VMEbus crate with a custom P3 backplane that distributes bias voltages to the databoards. This backplane is divided into three segments, each with its own HV power supply. A common controller board controls all of the HV supplies and incorporates voltage and current trip capability. The entire crate is connected to the CESR control system through the local fieldbus. Data acquisition code running on the CESR control system is capable of running energy scans and continuous current monitoring by way of this communications path. Separate data acquisition servers operate for each of the crates deployed in CESR. Code to support central control of all servers for simultaneous scanning is currently being implemented.

2.3.1.3 Calibration Studies

Non-beam and beam-based checks of the new RFA design have been performed. Figure 2.72 shows the results of a number of scans acquired with an electron gun. The RFA configuration which was tested used a front 'grid', which was a slab of copper with holes corresponding to those in the vacuum chamber of a diagnostic wiggler [15]. Simulations which include the effects of secondary electron generation in the 'vacuum chamber' holes, secondary generation on the surface of the grid, and a focusing effect of the grid holes when a retarding field is applied are shown overlaid with the data in each plot in Figure 2.72. Overall, the simulations replicate all of the major features observed in the data including: the relatively higher collector efficiency than would be expected from the geometric transparency of the grids (Figure 2.72 top plot); an excess of low energy electrons created in the holes which is observed as excess low energy current in both the retarding grid and the collectors (Figure 2.72 middle and bottom plots); as well as the tendency of the net grid current to plummet or even switch signs due to secondary emission when retarding voltages are applied (bottom plot). (Figure 2.73 shows beam measurements which compare the performance of a segmented detector of the new design in a drift region with two adjacent APS-style RFAs [16]. The vacuum chamber ports were designed so that the outer and inner pairs of collectors in the segmented RFA would measure the same region as a corresponding RFA of the APS design. Overall the current response (top plot) and the energy response (bottom plot) of the devices show excellent agreement.

2.3.1.4 Conclusions

Overall, the thin RFA design appears to provide the necessary performance for application in CesrTA. Variants of the design have been deployed in drift, dipole and wiggler regions [15, 17] and are providing useful data [18]. An important conclusion of our studies to date is that the detailed properties of the RFAs must be included in our physics simulations. This is a particularly important issue for RFAs deployed in high field magnets.

2.3.2 TE Wave Diagnostics

2.3.2.1 Summary

The analysis of the propagation of electromagnetic waves excited within the accelerator's beampipe has recently emerged as a powerful method for the study of the electron cloud [19–22]. Since this technique does not require the installation of any hardware inside the vacuum chamber, we were able to implement this method for different sections of the CesrTA ring. Although the fundamental physical principles of the technique are well understood, its practical implementation requires understanding and limiting several potential sources of errors for the quantitative determination of the electron cloud density. It is worth stressing the fact that at the beginning of the CesrTA program, the technique had only been demonstrated at the PEP-II Low Energy Ring, making CesrTA only the second accelerator, on which it was successfully implemented. Therefore, a substantial effort has been dedicated to reaching a better understanding of the technique itself, going beyond simply measuring the cloud density in a number of locations around the ring. As an additional result of this effort, we conceived and tested some novel schemes, which could avoid some of the intrinsic limitations of the original technique.

2.3.2.2 Introduction

The use of microwaves for diagnostic purposes is well established in plasma physics [23]. The unique characteristics of an accelerator environment and of the electron cloud excited by a circulating beam make it necessary to adopt different techniques from what is traditionally used, although the fundamental physics principles are the same. In its simplest formulation, the technique measures the change in phase delay of an electromagnetic wave propagating in a waveguide mode inside of a length of the accelerator vacuum chamber. The expression for such a phase delay is particularly simple when a single waveguide-mode is excited and, since lowest set of TE modes always propagate at the lowest frequencies in any metallic beam pipe, the method is referred to as 'TE wave technique'. In principle, one could also use TM modes or higher TE waveguide modes, after utilizing the proper phase delay expression, but cross-coupling of the electric field patterns between TE and TM modes, generated by the numerous discontinuities in an accelerator vacuum chamber, would require a much more detailed understanding of the beam pipe geometry. This would render the evaluation of the cloud density from the phase delay data very difficult, if not impossible. Similar coupling is possible between higher propagation frequencies of the lowest TE mode and those overlapping the next set of TE modes (occurring at frequencies above that next mode's cutoff frequency), so for ease of evaluation this consideration in practice places a frequency bound for the method within a range of frequencies between the fundamental mode's cutoff and the next higher waveguide mode's cutoff frequency.

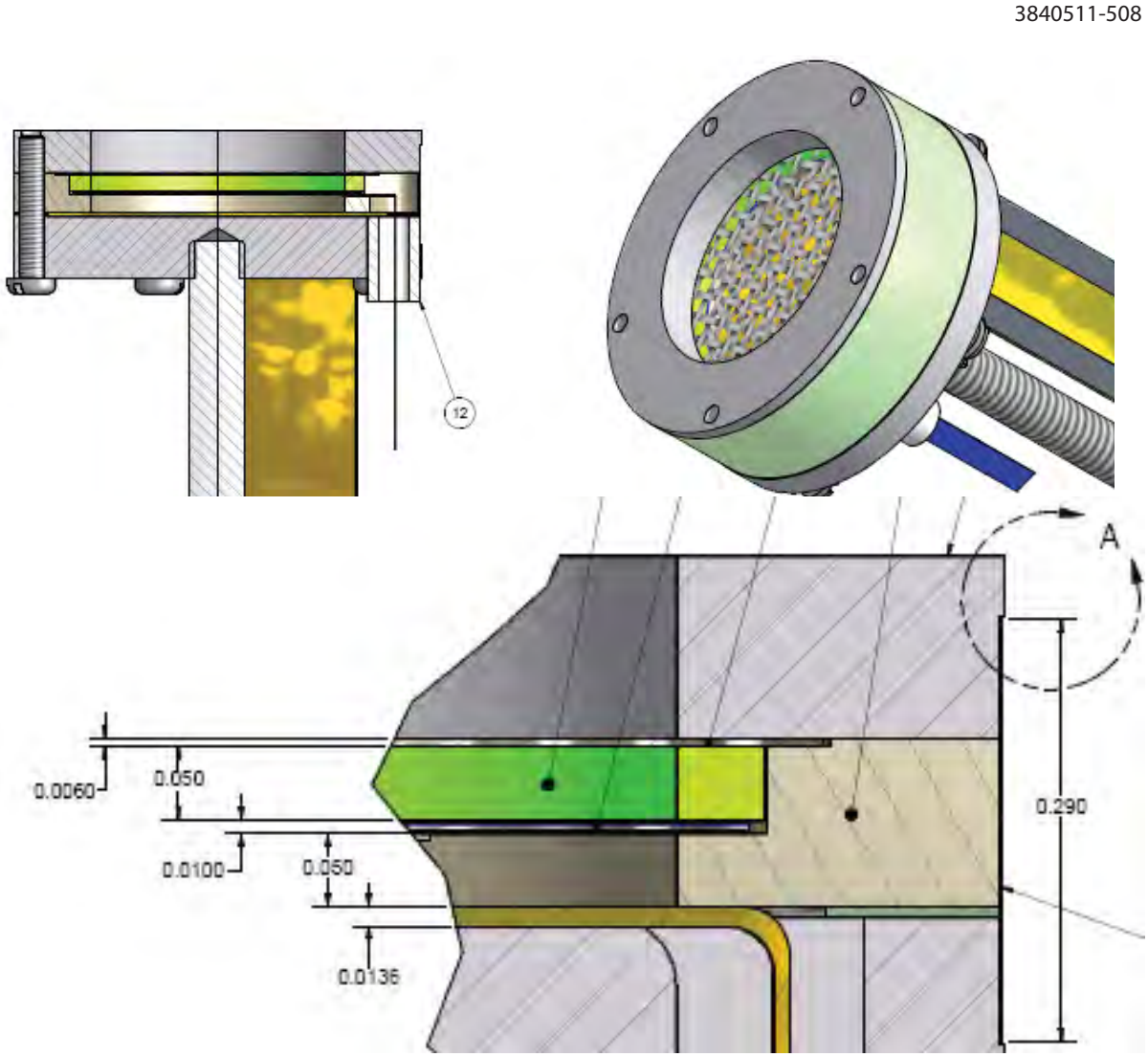

Figure 2.70: The basic retarding field analyzer structure for use in vacuum chambers with limited external aperture. Two variants of this design have been tested. In the first variant (shown), two grids are employed in front of a collector made of copper-clad Kapton. In the second variant, the front grid is replaced by a block of copper with a hole pattern of the same type as implemented in the walls of the CesrTA diagnostic wiggler vacuum chambers. In these designs, the layers are supported by a ceramic structure with an interlayer spacing of approximately 1 mm.

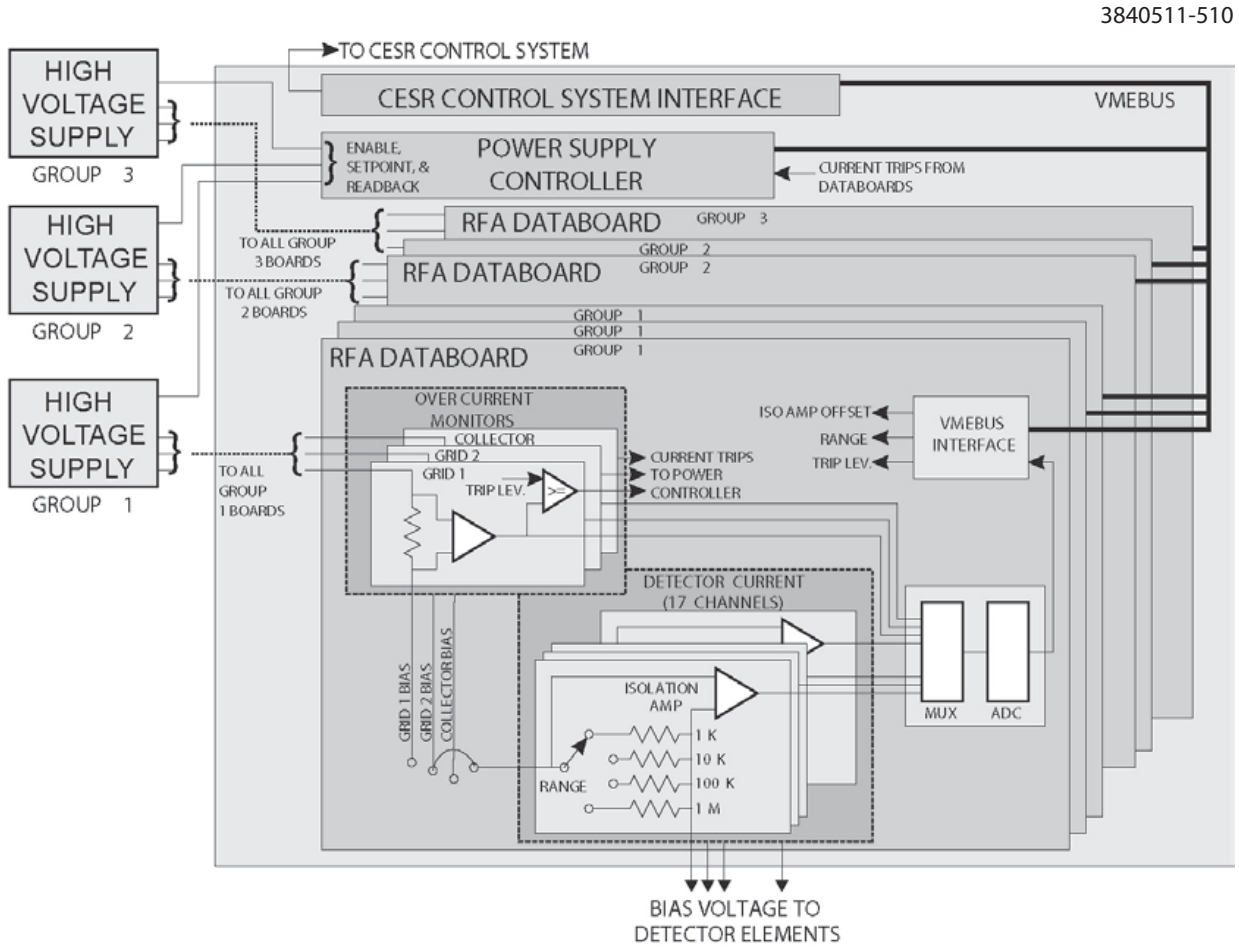

Figure 2.71: Schematic showing the high voltage power supply system and the RFA current monitor boards.

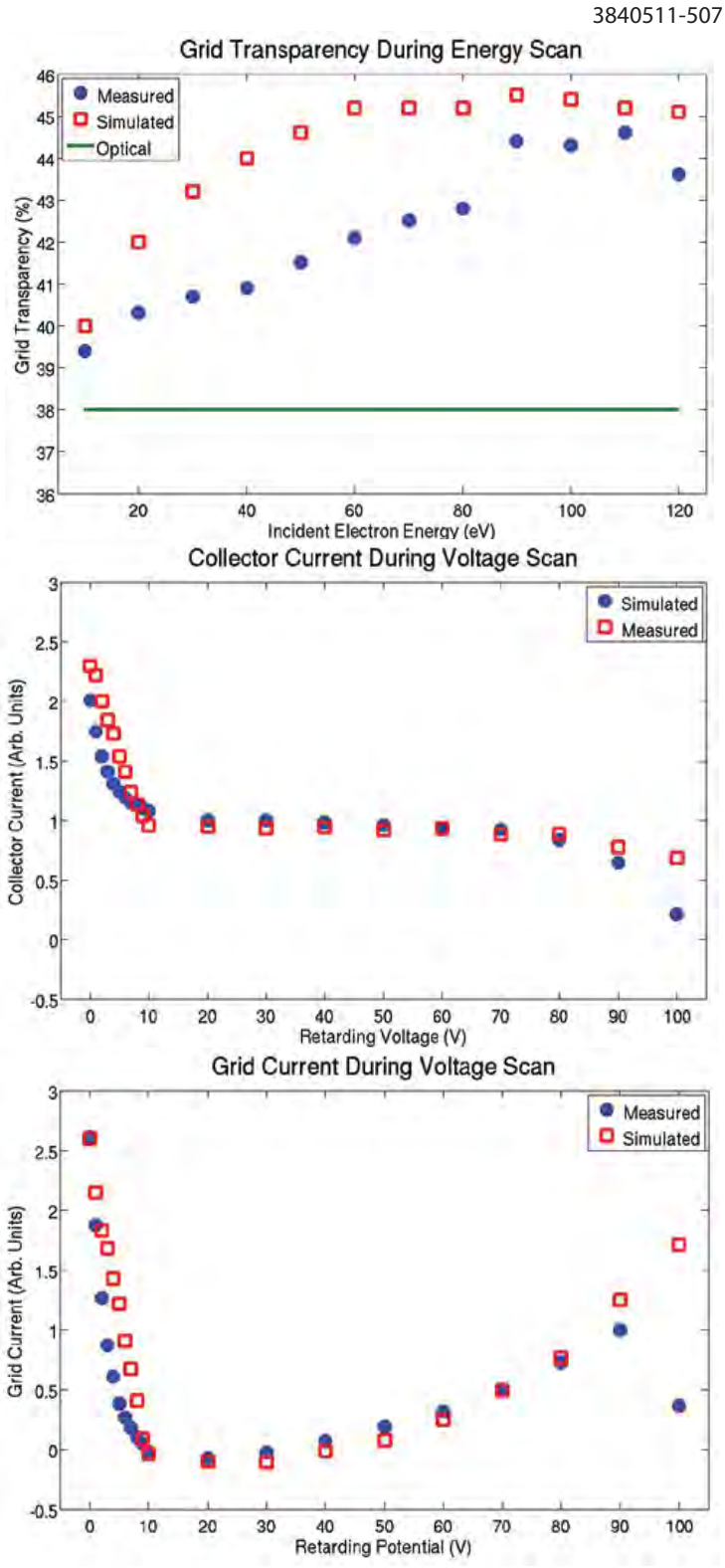

Figure 2.72: Plots showing electron gun studies of the performance of the thin RFA structure with a front plate with holes matching the wiggler vacuum chamber specifications. The top plot shows the fraction of electrons reaching the collector versus the energy of the incident electrons. The bottom pair of plots show the collector and grid currents observed during a retarding voltage scan with 110 eV incident electrons.

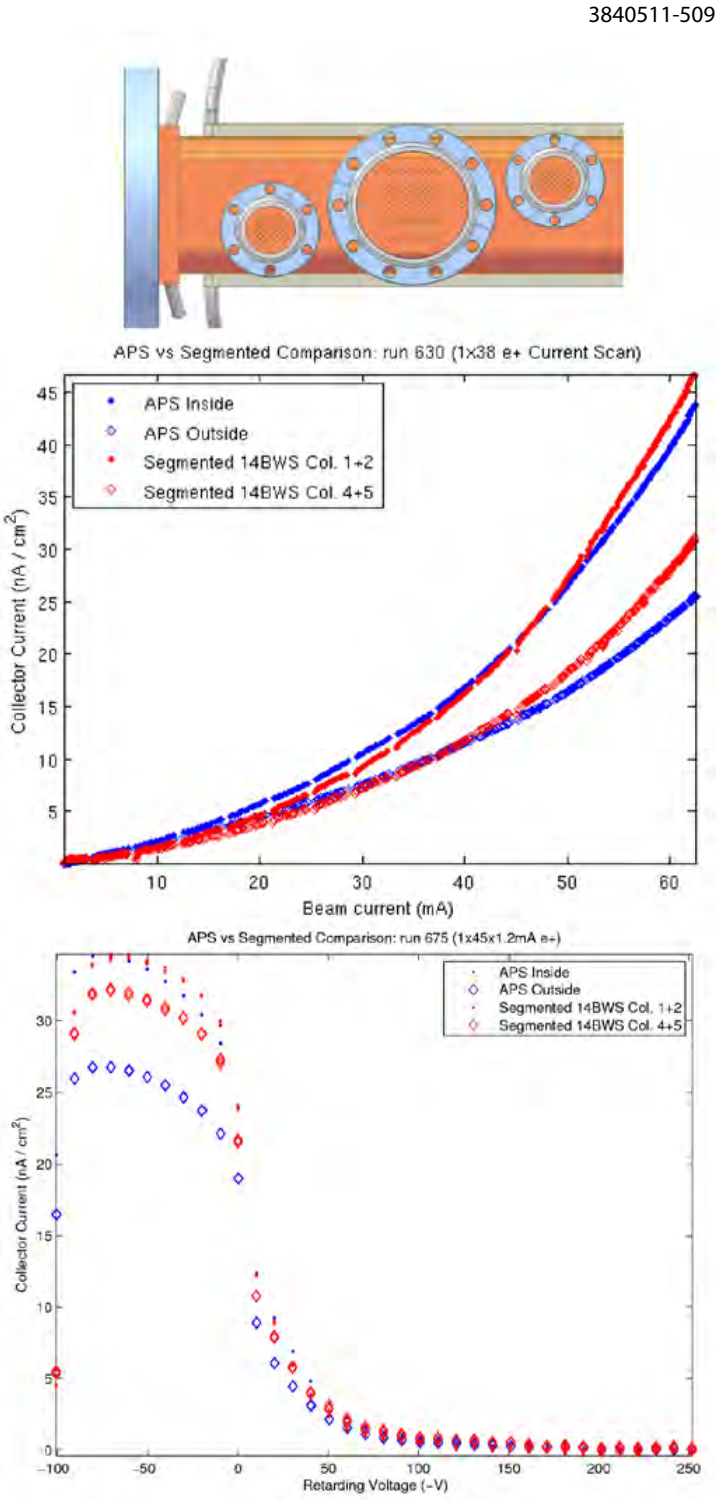

Figure 2.73: Beam comparisons of segmented RFAs with APS-style structures. Top drawing shows the arrangement of a segmented RFA and 2 APS-style ports where the response of the 2 outer and 2 inner segments can be directly compared with the 2 APS RFAs. Middle plot compares the current response and the bottom plot compares the energy response of the detectors.

In the ideal case the choice would be to utilize this lowest set of TE modes for investigation and to limit the region between the input and output coupling ports for the beam pipe to have the same cross sectional profile. Furthermore we would assume that the energy in the waveguide mode would propagate outward from the input coupling port in both directions without any reflections from upstream and downstream discontinuities in the beam pipe shape. In practice there are discontinuities in the beam pipe causing reflections and these produce standing waves in addition to the traveling waves in the experimental region. Another alternative and often the much easier technique is to study the resonant modes from these standing waves and to measure the tune shift of the stationary electric field pattern associated with the presence of the electron cloud. This leads to two potential methods (traveling and standing waves) for using the TE-wave methodology for studying the electron cloud density within a vacuum chamber. The initial work of this collaboration has focused on TE Wave studies utilizing the traveling wave technique and so the majority of this report focuses on this effort.

For the case of a beam pipe filled with an electron cloud of uniform density and in the absence of an external magnetic field, the plasma-modified dispersion relation causes an additional term ω_p^2 to be introduced into the expression for the propagation constant for the guided wave, giving

$$k_z = \sqrt{\frac{\omega^2 - \omega_c^2 - \omega_p^2}{c^2}} \tag{2.1}$$

where ω_c is the beampipe cutoff angular frequency for the lowest frequency TE mode and $\omega_p = \sqrt{n_e\ e^2\ /m_e\ \varepsilon_0}$ is the the plasma angular frequency, which is proportional to the square root of the electron density n_e. In the absence of an electron plasma, Eq. 2.1 reduces to the usual dispersion relation for waveguide propagation. When there is an electron density n_e along a length L of the vacuum chamber, there will be an additional phase delay $\Delta\varphi$ occurring for a travelling wave's propagation due to the plasma. The phase delay per unit length is then

$$\frac{\Delta\varphi}{L} = k_{z0}\left[\sqrt{1 - \frac{1}{k_{z0}^2 c^2}\left(\frac{n_e\ e^2}{m_e\ \varepsilon_0}\right)} - 1\right] \tag{2.2}$$

where the mode propagation constant is given by $k_{z0} = \frac{1}{c}\sqrt{\omega^2 - \omega_c^2}$. Thus the electron density is directly related to the measured phase shift. For $\Delta\varphi/L \ll 1$, Eq. 2.2 can be approximated as

$$\frac{\Delta\varphi}{L} \simeq -\frac{1}{2k_{z0}c^2}\left(\frac{n_e\ e^2}{m_e\ \varepsilon_0}\right) \tag{2.3}$$

One of the most attractive features of this technique is the ability of excite and detect the propagating wave almost anywhere in an accelerator without the need of any installation of additional components within the vacuum chamber. Ordinary beam position monitor (BPM) electrodes, which are generally widely distributed around the storage ring, can be easily converted to this use by just connecting them to the appropriate RF instrumentation.

Figure 2.74 is a schematic diagram illustrating the principle of the technique. A traveling electromagnetic wave is excited using the electrodes of a BPM and detected on another BPM after propagating through a section of the beam pipe containing an electron cloud. The signal is then

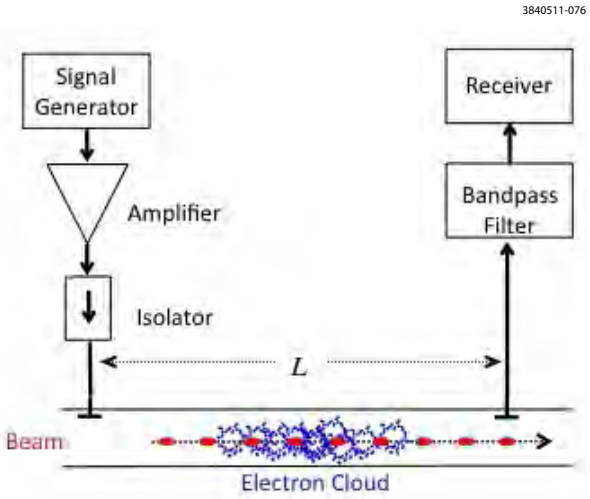

Figure 2.74: Schematic view of the TE-wave transmission technique for measuring the electron cloud density.

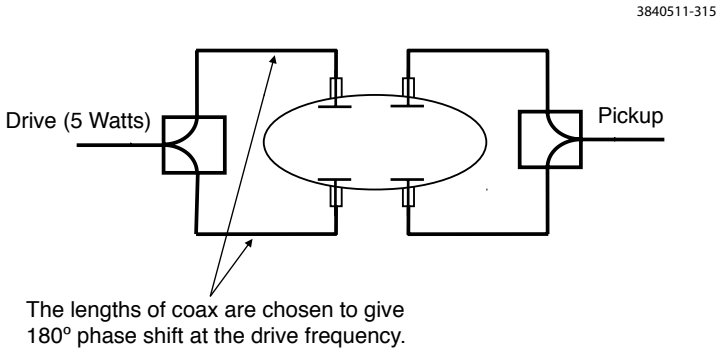

Figure 2.75: Signals from pairs of BPM electrodes are subtracted to improve coupling to the $TE_{1,0}$ mode electric field and reject direct beam signal. At most locations, pairs are available for both excitation and/or detection of the waveguide modes.

analyzed to determine the amplitude of the phase modulation, typically using a spectrum analyzer. For the optimal driving of the $TE_{1,0}$ mode's electric field, the drive signal is coupled into the beam pipe via a top/bottom pair of BPM electrodes with excitations, phase shifted from each other by 180° (as shown in Figure 2.75.) Similarly the $TE_{1,0}$ mode's electric field is detected at the down stream BPM using a top/bottom pair of BPM electrodes, again phase shifted from each other by 180°; this configuraion has the side benefit of yielding some level of rejection of the direct beam-induced pickup signal.

2.3.2.3 Phase Modulation

Given the level of the electron cloud densities typically present in an accelerator, electron cloud induced phase delays are of the order of a few milli-radians. So a direct measurement, comparing the small phase shift with and without a circulating beam (and hence the electron cloud), is problematic due to comparable phase delays introduced by other effects, e.g. temperature variations. TE wave

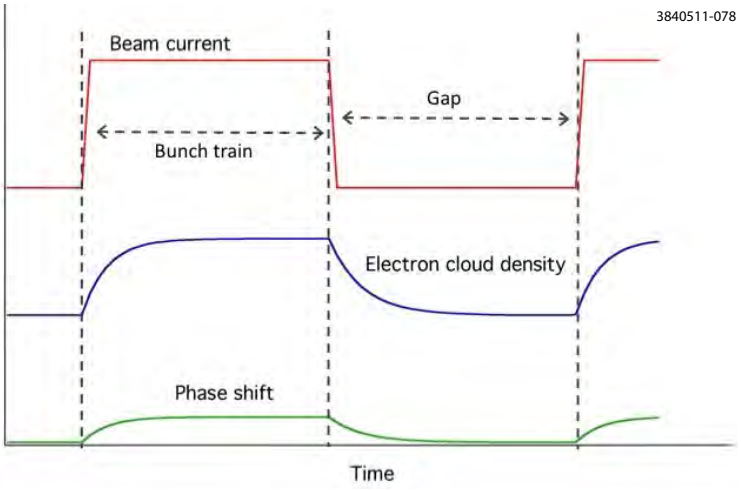

Figure 2.76: Qualitative time evolution of beam current (red), electron cloud density (blue) and phase shift (green).

measurements take advantage of the gaps due to the bunch train, which occupies only a fraction of the revolution time and thus introduces a periodic modulation in the phase of the propagating wave. The frequency of this modulation is the ring revolution frequency f_{rev} (or a multiple of it in the case of multiple trains of bunches) and its depth is essentially the phase delay that we wish to measure, provided the gaps between trains are long enough to clear the electron cloud (Fig. 2.76).

The spectrum of the signal measured on the receiving BPM contains not only the information about the modulation depth $\Delta\varphi$, which allows us to estimate the electron cloud density via Eq. 2.3, but also the electron cloud's evolution in time. A typical observed spectrum is shown in Fig. 2.77. The peak corresponding to the TE wave frequency (carrier) and the modulation sidebands are mixed with the direct beam-induced signal (at the revolution harmonics), which are also spaced at f_{rev}. The carrier excitation frequency can be conveniently chosen so that revolution harmonics and modulation sidebands are separated in frequency.

The modulation depth can be calculated by comparing the height of the sidebands to the height of the carrier. The wave attenuation in the propagation between the two BPM's and the measurement noise floor are critical for determining the minimum, measurable phase shift, and therefore the smallest electron cloud density the instrument is able to detect.

2.3.2.4 CesrTA Experimental Setup

An overview of the regions of the CesrTA ring where TE wave measurements have been performed is given in Fig. 2.78. The 12W-15W region, which is composed of a dipole and a wiggler replacement straight section chamber, was the location, where the technique was first studied. After the initial studies, more interest developed for observations in the L0 region (wiggler straight) and the L3 region (having a chicane and a section of straight circular pipe with a clearing solenoid.) The instrumentation on these regions have been connected to an online data acquisition system. Software/hardware has been configured so that changes in beam conditions can trigger a full set of measurements, which are then archived in the control system database. Data can also be taken on

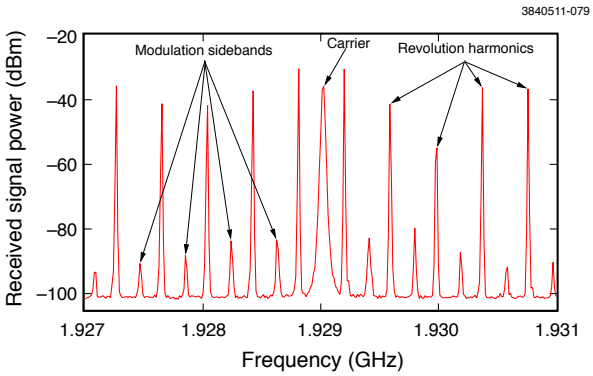

Figure 2.77: Example of phase modulated TE wave and direct beam-induced signal observed in a CesrTA beam position monitor.

demand (when the automated software has been disabled) to permit using the same hardware for specialized measurements.

2.3.2.5 L0 Region

Fig. 2.79 shows the connections permitting the signal generator's output to three locations in the L0 region, as well as the routing of the pickup signals from each of these BPM locations to the spectrum analyzer. Each detector has four available buttons. Vertical pairs of buttons are combined using RF splitters and unequal lengths of coax, so that the signals from the two buttons will be exactly out of phase at the drive frequency in order to provide the top/bottom difference signal. In any given BPM, one vertical pair is used for the drive and the second for the detected signal. The system uses two RF relays to select excitation/detection pairs. In this way data can be taken using any excitation/detection combination including driving and detecting at the same location.

2.3.2.6 L3 Region

Fig. 2.80 shows the connection of the signal generator output to four locations in the L3 region, as well as the routing of the BPM pickup signals from these locations to the spectrum analyzer. The beam pipe is circular and the buttons available for TE wave measurements are generally on the same flange as those used for beam position measurements. There are fewer available buttons in this region as compared to L0. Due to the interest in exploring electron cyclotron resonances via TE waves, the chosen orientation excites a horizontal electric field. At the detector in the Chicane magnet, horizontal pairs of buttons are used to excite/detect signals. The central detector near Q49 has only a single drive pair of buttons (a vertical pair is also available but not used). At both Q48E and Q48W, the two available horizontal buttons are used individually to give drive and detection signals.

2.3.2.7 Alternative Microwave Techniques

In the course of our efforts to implement the TE wave experimental methods at CesrTA and further develop its theoretical background, we also expanded its original concept. This allowed us

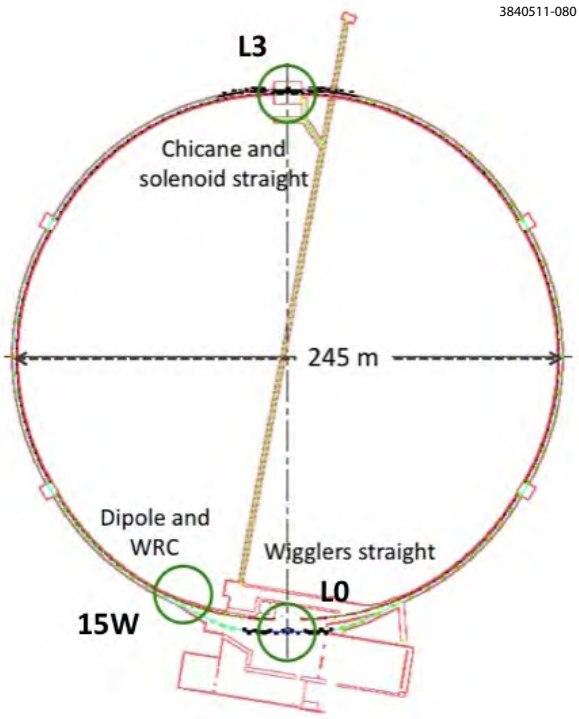

Figure 2.78: TE wave measurement locations in the CesrTA ring. WRC designates the wiggler replacement chambers for the newly constructed drift space.

to develop new techniques, which circumvent some of the problems that emerged during our earlier experimental work. These techniques still take advantage of the interaction between electron cloud and electromagnetic fields: in one adaptation the TE field is non-propagating, while in another case a constant magnetic field is superposed on the beam pipe.

Resonant BPM As will be discussed in Section 5.2.1 our experimental studies detected a significant influence to the measurements from reflections and standing waves within the beampipe. This influence complicates the simple theoretical model of a wave propagating from the transmitting to the receiving BPM, making it difficult to properly analyze the measurements, since the effective propagation length L is difficult to determine.

A new class of studies, called TE wave resonance measurements, treat the beam pipe and its reflections as producing a standing wave structure (analogous to a cavity) (Ref. [24]) in order to estimate the EC density. In this case the TE wave may propagate some distance in both directions before being fully reflected. The vacuum chamber may be configured with the drive/pickup at the same BPM. There is an additional special case for this type of excitation when the drive frequency is below the cutoff frequency causing a trapped evanescent mode, in which the TE fields are highly localized.

Magnetic Resonance During the TE wave measurements in the chicane in the L3 region, we detected a resonance between the TE wave and the magnetically trapped electron cloud in the chicane dipoles (Ref. [25]). This resonance has been studied extensively by plasma scientists and

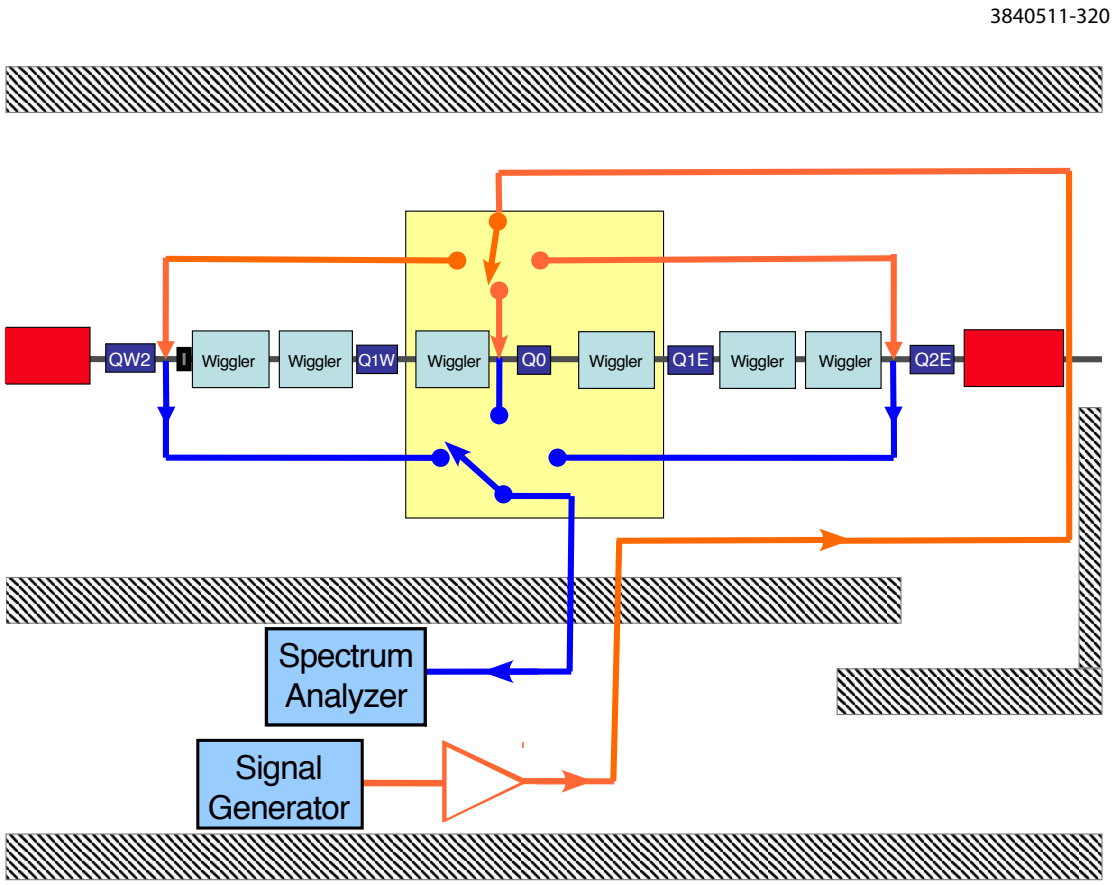

Figure 2.79: TE wave hardware in the L0 region uses RF relays to route signals to/from the BPMdetectors.

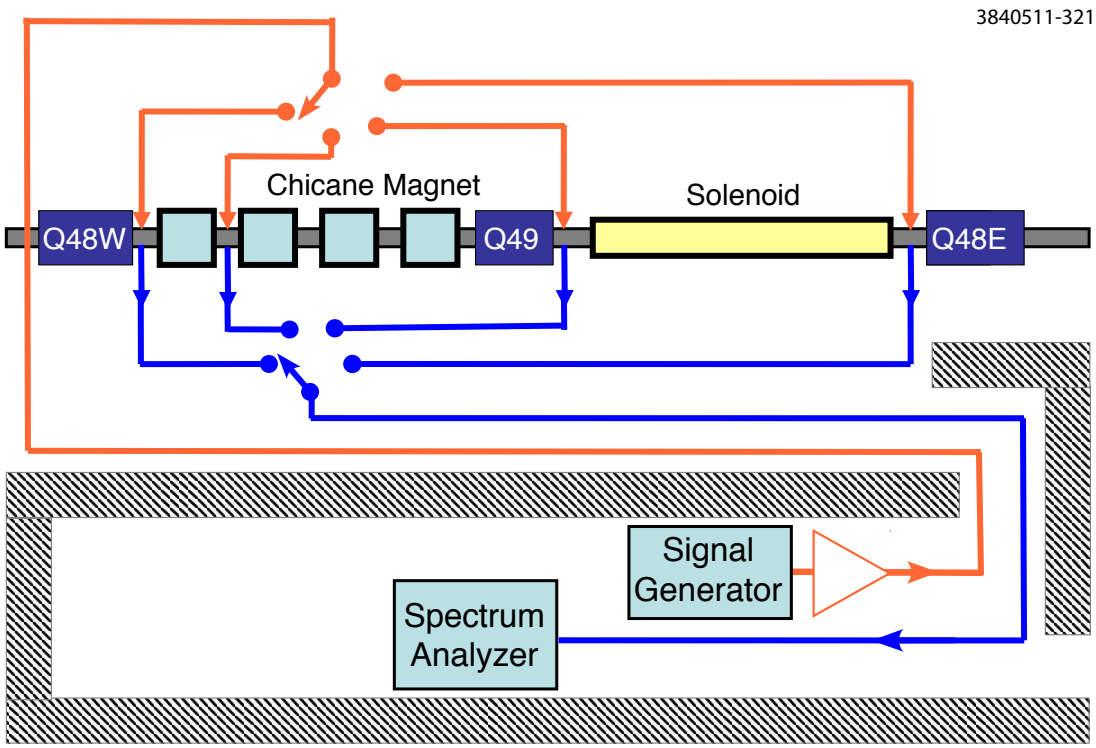

Figure 2.80: TE wave hardware in the L3 region uses RF relays to route signals to/from the BPM detectors.

has been given the name of the upper hybrid resonance: The propagation constant of a wave with a linearly polarized electric field perpendicular to both the magnetic field and its direction of propagation exhibits a singularity when

$$\omega_{TE}^2 = \omega_p^2 + \omega_{cycl}^2 \tag{2.4}$$

where the cyclotron frequency is $\omega_{cycl} = \frac{eB}{m_e c}$. In principle, by measuring the resonance frequency and knowing the magnetic field value, it is possible to calculate the plasma frequency and therefore the cloud density in the region of the static magnetic field.

2.3.3 Shielded Pickups

Shielded pickup detectors have been installed at three locations in CesrTA for the purpose of studying time resolved electron cloud build-up and decay. The detectors are located at 15E, 15W and L3 (see Fig. 2.1). The initial configuration for this pickup uses a BPM, whose button electrode is recessed back beyond the pipe's wall that is penetrated with many small holes. This design provides electromagnetic shielding from the beam wakefield while allowing cloud electrons to enter the vacuum space of the detector [26]. This section describes the hardware configuration and capabilities of these detectors at CesrTA.

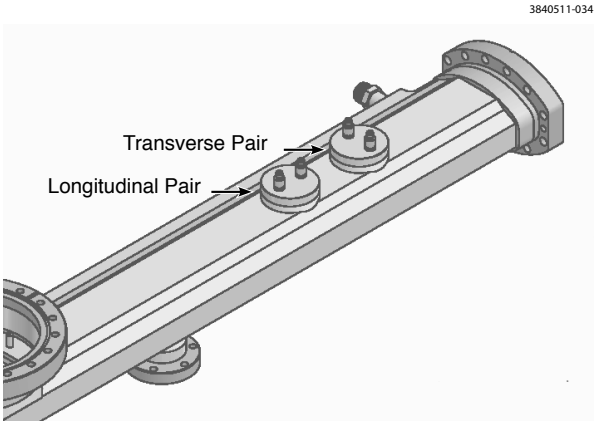

Figure 2.81: Shielded pickups are assembled in pairs. The longitudinal pair provide redundant measurement of the cloud along the beampipe centerline.

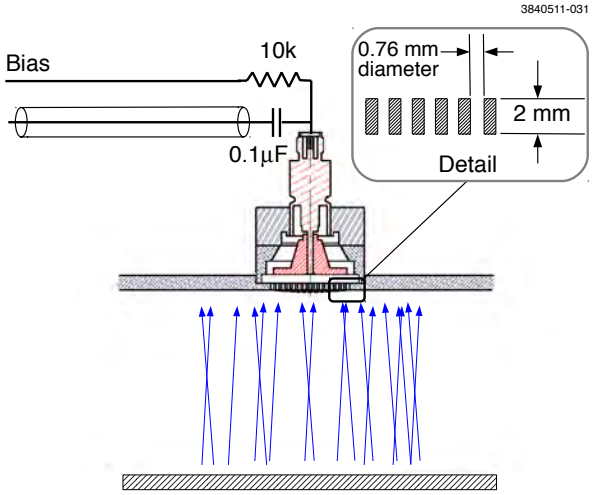

Figure 2.82: Photoelectrons pass through the holes in the beampipe and enter the evacuated detector volume.

2.3.3.1 Vacuum Chamber

Several chambers have been constructed with various vacuum surfaces: bare aluminum, amorphous-carbon and TiN, so that their electron cloud growth/decay can be measured and compared [1] [17].

The upper beampipe wall is perforated with a circular pattern of 169 small diameter vertical holes for each button, and a button assembly welded on top. Typically two pairs of buttons are installed at a given location with one pair in the 'normal' configuration of a position monitor and the other rotated to put the two button inline with the center of the chamber, the combination allowing measurements at three transverse positions in the beampipe(Fig. 2.81). So although the buttons are in the vacuum space, they are electromagnetically isolated from the main beampipe by the perforated beampipe wall [26] (see Fig. 2.82). The hole geometry favors the detection of electrons with nearly vertical trajectories.

2.3.3.2 Signal Routing and Electronics

A button bias voltage with a range of +/- 50 V is provided through a 10k ohm resistor mounted at the vacuum feedthrough. The buttons are typically biased with about +50 V in order to minimize the emission of secondary electrons from the button.

The voltage induced on the button by the cloud charge is AC coupled via a 0.1 microfarad capacitor to a coaxial cable as shown in Fig. 2.82. A nearby coaxial relay selects the button signal that is to be routed outside of the storage ring to a data acquisition station. There, two Mini-Circuits ZFL-500 amplifiers having a bandwidth of 0.05 to 500MHz are connected in series for a total voltage gain of 100. These amplifiers are at the input of an Agilent 6054A (500MHz) digital oscilloscope that is also provided with a trigger at the revolution frequency for signal averaging(Fig. 2.83). At each location one button at a time is connected to the common cable run, amplifiers and oscilloscope.

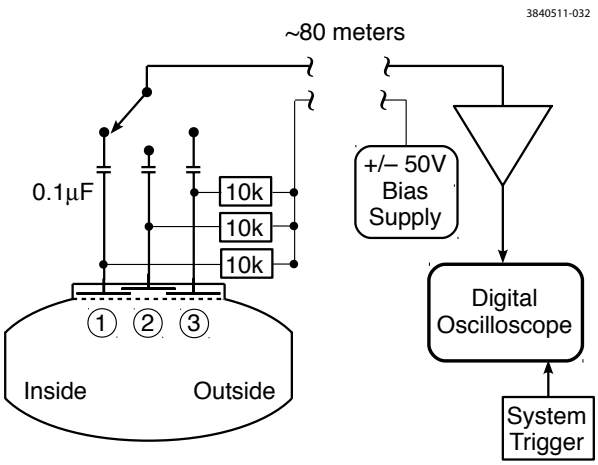

Figure 2.83: The shielded pickup signal is selected with a relay and routed to amplifiers and oscilloscope.

Figure 2.84: Photo of Shielded Pickups installed at 15E with the installed solenoid winding

This relatively simple hardware configuration[27] was chosen to provide reliable signals for long-term comparisons of the different chamber coatings.

Low field solenoids had been installed in CesrTA that are intended as a mitigation technique to be studied[28]. In the region of the shielded pickups, bipolar power supplies have been connected to these solenoids so that they can produce approximately +/-40 Gauss fields(Fig. 2.84). These solenoids have been used to estimate the energy spectrum of primary electrons and this method is described in more detail in (Section 5.2.1.3.)

2.3.3.3 Data Collection

Data acquisition software provides control of the relay (which selects of the button to be measured), the bias voltage, the solenoid field and the scope configuration. Data collection can be either on demand or triggered by changes in machine conditions, such as a change in the beam current. When taking data, a text file determines the detector configuration, scope horizontal and vertical scaling, etc. The software enters information for each measurement as a row in a web table, including links to the data file and plot, beam currents, bunch spacing, bias, etc. This information is also entered into a searchable database.

2.3.4 In-Situ SEY Station

We developed and deployed an in-situ system for measurements of the secondary electron yield (SEY). An in-situ system allows us to observe beam conditioning effects that change the SEY as a function of exposure to direct synchrotron radiation (SR), scattered synchrotron radiation, and electron cloud bombardment. Additionally, the in-situ system allows us to compare the SEY between bare metal surfaces and surfaces with coatings, grooves, or other features for SEY reduction, in a realistic accelerator environment.

A two-sample SEY system has been installed in the CesrTA beam pipe in CESR. The system

is installed in the L3 East area of the ring; the bending magnets are located such that the SEY samples are exposed predominantly to SR from the electron beam. The typical CESR conditions for the SEY studies are a beam energy of 5.3 GeV and beam currents of 200 mA for electrons and 180 mA for positrons.

Both samples are positioned flush with the inner diameter of the round beam pipe, with one sample positioned horizontally in the direct radiation stripe, and the other sample positioned at 45°, beneath the radiation stripe. The SEY of both samples can be measured repeatedly without having to remove them from the vacuum system. Measurements can be taken in approximately 1.5 hours. This allows us to use the (approximately) weekly tunnel access for SEY measurements to study the SEY as a function of SR dose.

The design and commissioning of the in-situ system is described in this section. The initial SEY results are discussed in Section 5.1.5. Additional information can be found in recent papers [29, 30].

2.3.4.1 In-Situ System

Our in-situ measurement system, shown in Figure 2.85, consists of a sample mounted on an electrically isolated linear magnetic actuator[1] and a dc electron gun.[2] The electron gun and the sample actuator are attached to a 316 stainless-steel crotch, with the gun at 25° to the sample actuator axis. The gun is mounted onto a screw-based linear motion actuator[3] to allow us to move it out of the sample actuator's path when the sample is inserted into CESR beam pipe (Figure 2.85b). When the sample is in the SEY measuring position (Figure 2.85c), the gun is moved forward, such that the gun-to-sample distance is 32 mm for the SEY measurements. The crotch has a special port for changing the samples in-situ while flowing nitrogen gas. The SEY system's vacuum is isolated from the beam pipe vacuum via gate valves when the sample is changed. With the gas purge, the ultra-high vacuum fully recovers within 24 hours.

As shown in Figure 2.85d, two samples can be installed in CESR, one mounted at the horizontal radiation stripe and one mounted at 45°, below the stripe. A photograph of the horizontal SEY system after installation into the L3 section of CESR can be seen in Figure 2.85e.

The SEY measurements are taken at 9 points of a 3×3 grid (7.4 mm $\times$ 7.4 mm) on each sample using the xy deflection mode of the gun, as can be seen in Figure 2.86. The sample has a curved surface to conform to the circular beam pipe cross-section in this part of CESR.

The SEY measurement circuit is the same as that used in previous studies [31]. A picoammeter[4] is used to measure the current from the sample; the sample dc bias is provided by a power supply internal to the picoammeter. (The data acquisition system is described in detail in Section 5.1.5.2.) During the SEY measurements, the two gate valves are closed to isolate the CESR vacuum system from the SEY system.

[1] Model DBLOM-26, Transfer Engineering, Fermont, CA.
[2] Model ELG-2, Kimball Physics, Inc., Wilton, NH.
[3] Model LMT-152, MDC Vacuum Products, LLC, Hayward, CA.
[4] Model 6487, Keithley Instruments, Inc., Cleveland, OH.

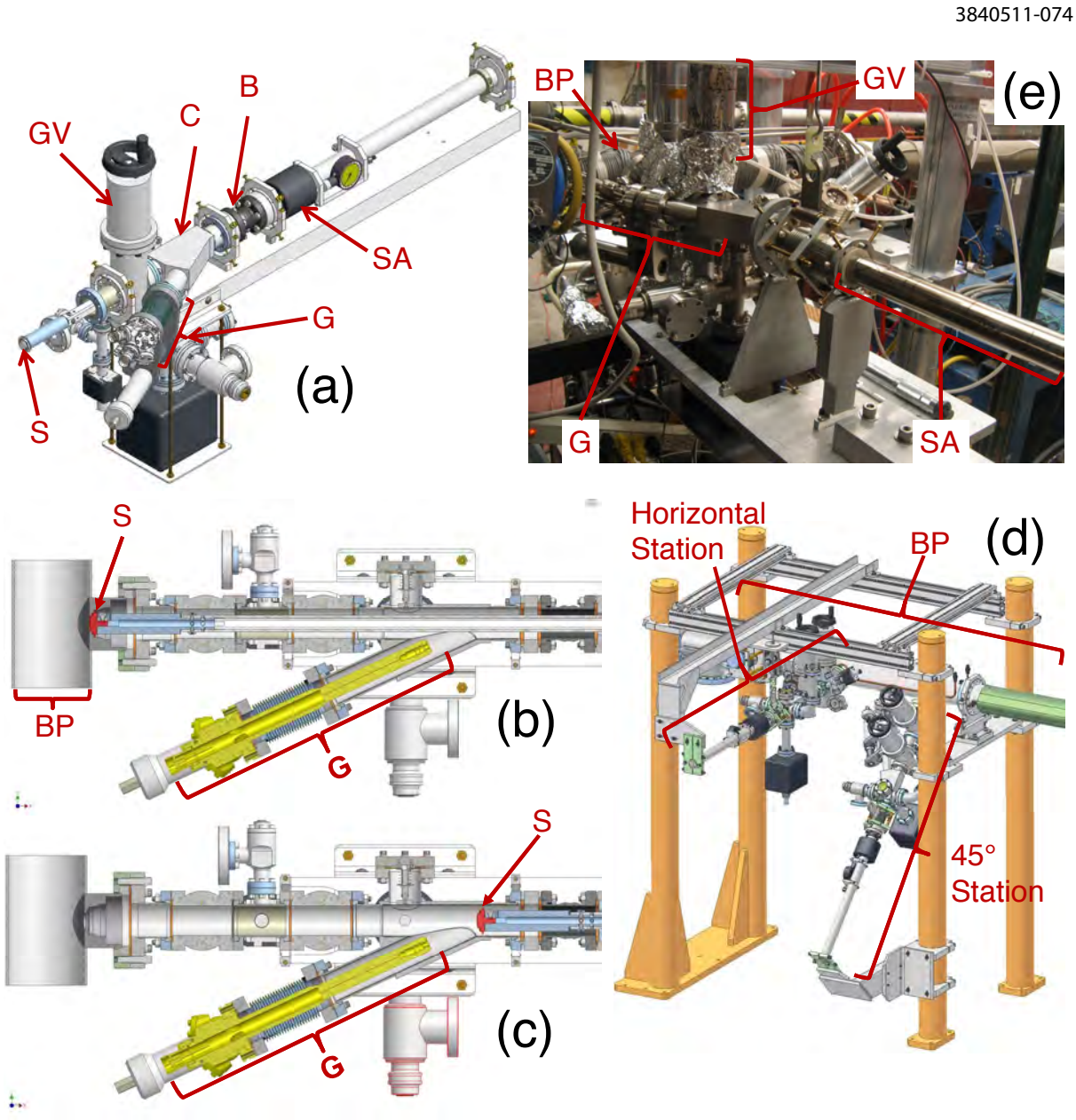

Figure 2.85: Drawings and photograph of the in-situ SEY system. (a) Isometric view of the horizontal station; the beam pipe and connecting tube are not shown. Cross-sectional views of in-situ station with (b) sample inserted in beam pipe and (c) sample retracted for SEY measurements. (d) Isometric view of the horizontal and 45° stations in the ring. (e) Photograph of the horizontal SEY station in the ring. (S: sample; G: electron gun; BP: beam pipe; C: vacuum crotch; B: ceramic break; SA: sample actuator; GV: gate valve.)

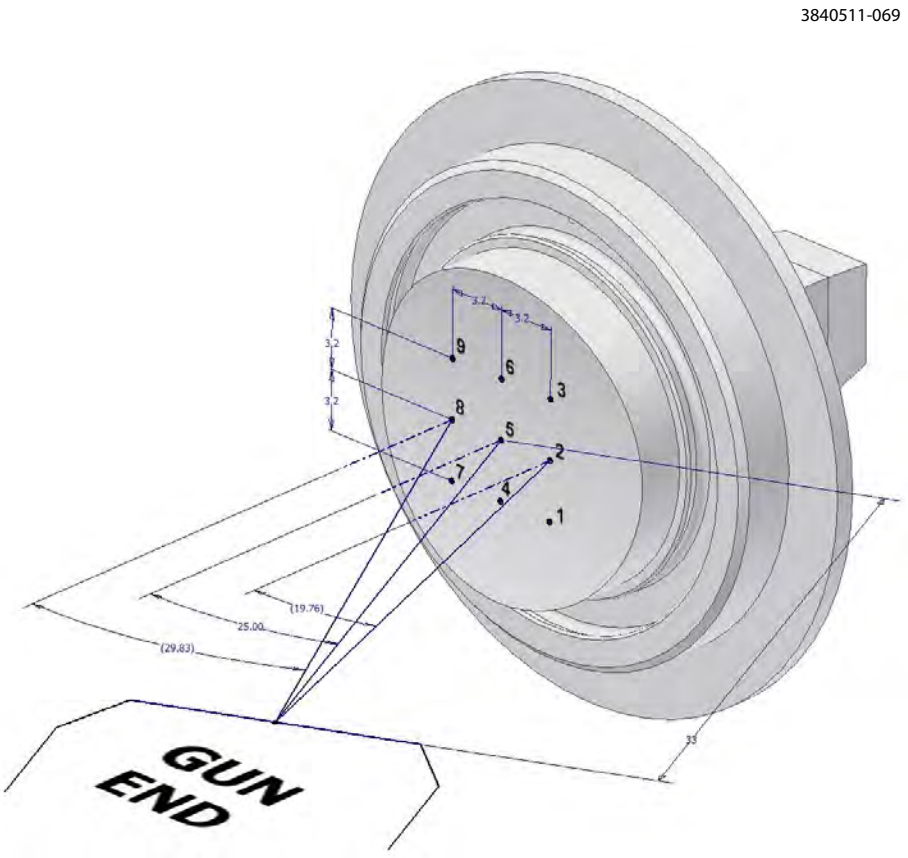

Figure 2.86: Isometric view of a sample showing the 9 grid points where the SEY is measured.

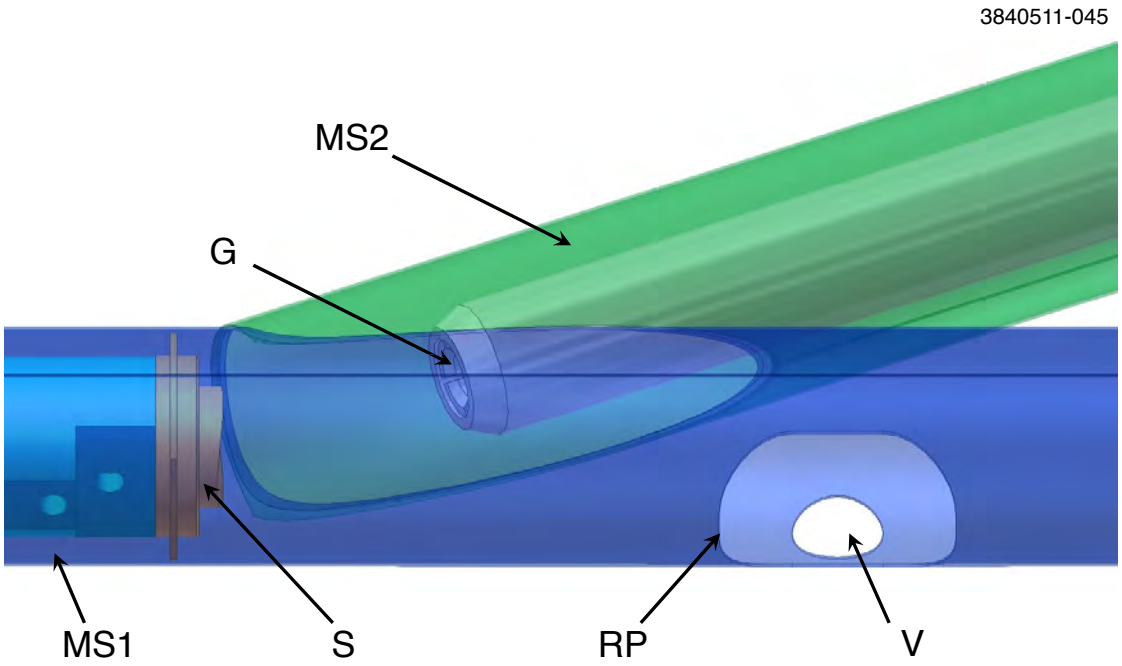

Figure 2.87: Magnetic shielding for SEY system. The sample (S) is inside Magnetic Shield 1 (MS1). The electron gun (G) is inside Magnetic Shield 2 (MS2). Magnetic Shield 1 has a Sample Replacement Port (RP; the patch is not shown) and a hole at the pumping port for vacuum pumping (V).

2.3.4.2 Electron Gun Spot Size and Deflection

At low energy (0 to 100 eV), the electrons can be deflected by up to a few millimeters by the stray magnetic field. To mitigate this problem, we inserted a mu-metal tube inside the crotch and the electron gun port, as shown in Figure 2.87. The mu-metal shields reduce the stray magnetic field to about 0.1 gauss or lower. To quantify the deflection after the shielding was installed, a collimation electrode with a 1 mm slit was positioned in front of the sample. The sample was biased with +20 V and was used as a Faraday cup. The collimator was electrically isolated from the sample and centered in front of the sample, with the slit oriented in the y direction. With the electron gun 32 mm from the sample, two picoammeters were used to measure the electron current reaching the collimator and reaching the sample. At each electron beam energy, the beam was scanned across the slit using the gun's x deflection electrode to center the beam spot on the slit by maximizing the current to the sample and minimizing the current to the collimation electrode. Over the full range of electron beam energy (0 to 1500 eV), the value of the x deflection voltage to center the beam spot on the slit was zero, which confirms that the stray magnetic field is well shielded. At each energy, the gun's focusing voltage was adjusted to minimize the beam spot size at the sample location (based on previous measurements).

Figure 2.88 shows the current reaching the sample divided by the total current (current to sample plus current to collimator) as a function of energy. For beam energies between 200 eV and about 800 eV, nearly all of the current reaches the sample, indicating that the beam spot size is smaller than 1 mm. Follow-up measurements were done to better characterize the beam spot size. The measured beam spot size is less than or equal to 0.75 mm for beam energies in the range of 250 eV

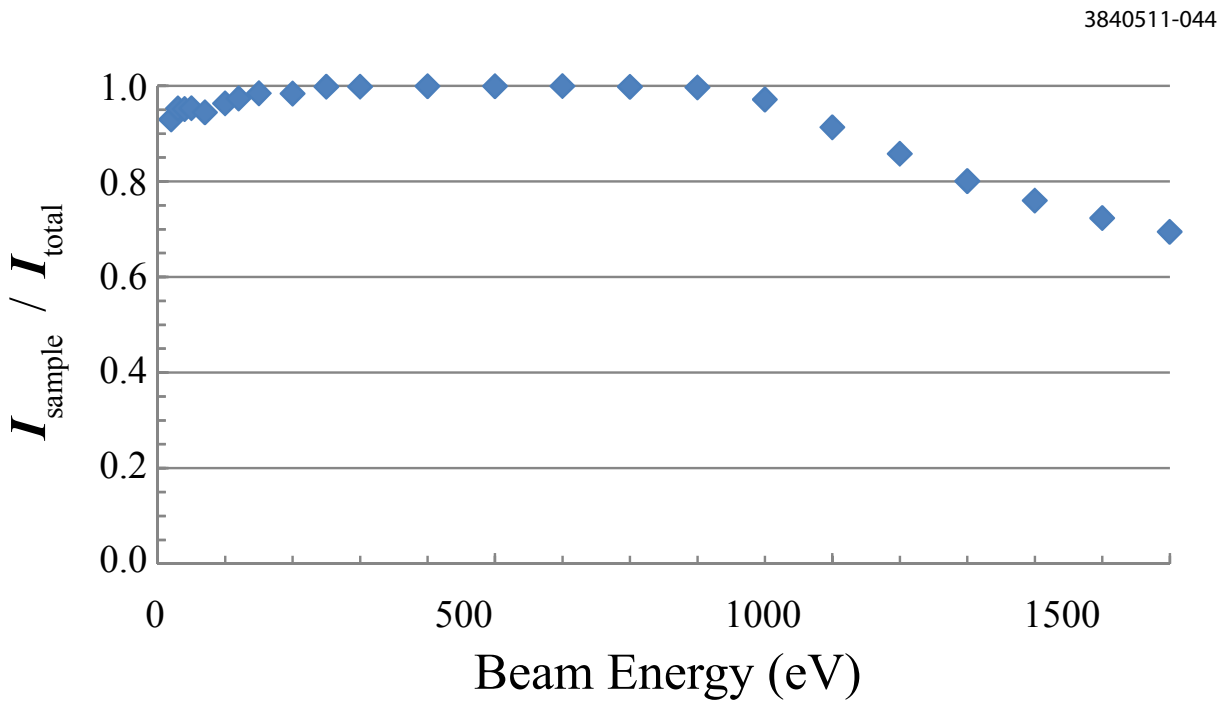

Figure 2.88: Slit collimation measurements for the SEY system. For the vertical axis, I_{sample} is the current reaching the sample and I_{total} is the current reaching the sample plus the current reaching the collimation electrode.

to 700 eV. Between 20 eV and 200 eV, the spot size is slightly larger than 1 mm; from 800 eV to 1500 eV the beam spot size increases with energy, reaching about 1.2 mm at 1500 eV. For the 3×3 grid for measurements on the sample, the distance between adjacent grid points is 3.7 mm, which is at least 2.6 times larger than the beam spot size at the sample.

2.4 Beam Instrumentation and Feedback Systems

The undertaking of the CesrTA project required the development or upgrading of several accelerator operating systems. The significant improvements to beam instrumentation are summarized as follows:

- A major upgrade to the beam position monitor system, which replaced an older relay-based position monitor system with individual readout modules for each monitor capable of turn-by-turn and bunch-by-bunch trajectory measurements for bunches spaced as closely as 4 nsec.
- The installation of positron and electron x-ray beam vertical size monitors designed for turn-by-turn and bunch-by-bunch beam size measurements for 4 nsec spaced bunches.
- Implementation of positron and electron visible-light monitors to measure the horizontal beam size, including the addition of optical elements to allow streak camera measurements of both electron and positron bunches.
- Development of software to extract bunch-by-bunch tunes utilizing the new modules for the

beam position monitors and a second method, which employed video gating of signal from a few beam position monitors from the older relay system.

- An upgrade for the tune tracker, which is phase locked to the betatron tunes of a bunch. This device allows the measurement of the betatron phase advance and the horizontal-to-vertical coupling of CESR permitting their correction.
- Installation of a new beam-stabilizing feedback system, which damps 4 nsec-spaced bunches for horizontal, vertical and longitudinal motion.

2.4.1 Beam Position Monitors

An upgraded beam position monitor (BPM) system that provides high resolution measurement capability has been designed and deployed. This system is capable of turn-by-turn measurements of individual bunches within bunch trains with spacings that are multiples of either 4 ns or 14 ns. The system provides the ability to make betatron phase, coupling and dispersion measurements via synchronous detection of a driven beam.

2.4.1.1 System Requirements

The core operational requirements for the CESR BPM (CBPM) system include:

- The ability to operate with counter-rotating beams of electrons and positrons in a single vacuum chamber for CHESS operations;
- High resolution for low emittance optics correction and tuning;
- Turn-by-turn readout capability for multiple bunches to support beam dynamics studies;
- Capability for digitizing single species bunch trains with bunch spacing as small as 4ns and dual beam digitization for bunch trains with 14 ns spacing.

The need for dual beam operation of the system places a unique constraint on the CESR BPM specifications. Since the relative arrival time of the bunches from the two beams varies widely from location to location around the ring, standard RF processing techniques to optimize resolution and minimize timing sensitivity cannot be applied to the full system. As a result, the CESR design utilizes peak sampling with a high bandwidth digitizer and incorporates hardware and software design features to optimize the system timing performance. Table 2.2 summarizes the design specifications for the high resolution measurements required for low emittance optics correction.

2.4.1.2 System Design

The CESR BPM system consists of a network of local sensors and processors. Each location has four beam buttons arranged in a mirror symmetric fashion as shown in Figure 2.89 which provide relative amplitude signals for a processing module. All modules share a common controls database, timing and synchronization controls, and networked data storage. This allows for accelerator-wide

Table 2.2: CESR BPM Module Requirements

Parameter	Specification
Front End Bandwidth (for 4 ns bunch trains)	500 MHz
Absolute Position Accuracy (long term)	100 μm
Single Shot Position Resolution	10 μm
Differential Position Accuracy	10 μm
Channel To Channel Sampling Time Accuracy	10 ps
BPM Tilt Errors (after correction)	10 mrad

coordinated measurements.

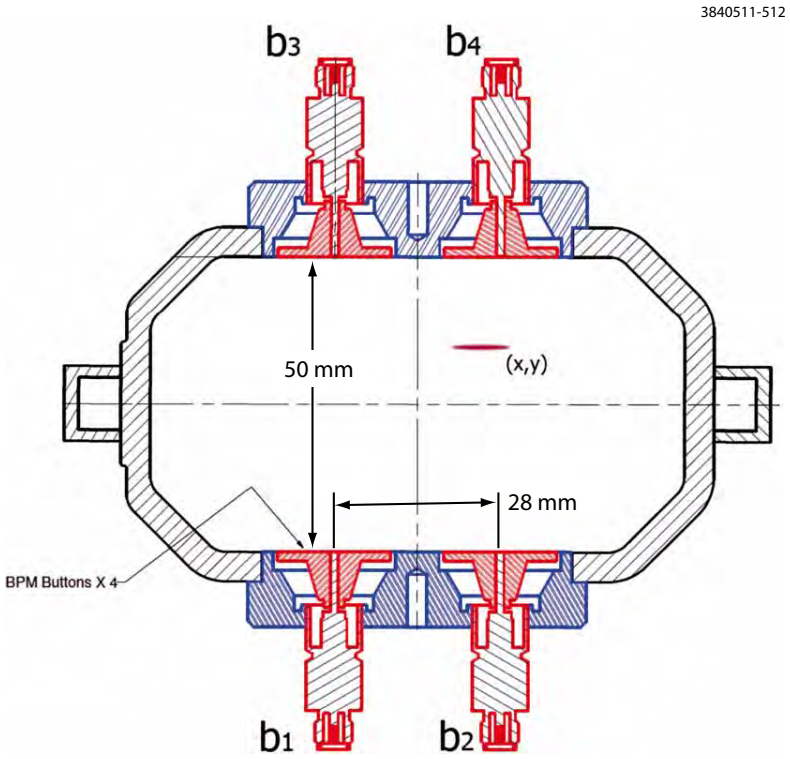

Figure 2.89: BPM module functional diagram

Figure 2.90 shows a block diagram of the digital BPM readout modules developed for CESR. Each module incorporates four front end boards with dual parallel 16-bit digitizer chains based on the Analog Devices AD9461 operating to digitization rates of 125 MHz. When operating with 4 ns bunch trains, digitizing is interleaved between the two chains. For 14 ns dual species operation, each digitizer chain handles a single species. The front end boards have both a fixed gain amplifier optimized for precision measurements for bunches with $N_b \sim 1\times10^{10}$ particles and a digital variable gain amplifier for measurements over a wide dynamic range. Timing configuration is carried out by a dedicated timing board integral to each module. This board takes a turn marker signal from the CESR master timing system and provides overall digitization rate control, adjustment capability for channel-to-channel digitization times, and global adjustment capability for the module digitization

time relative to the bunch arrival time at the detector. This fine degree of local timing adjustment is required in order to maintain the resolution and noise performance of each device. Communications, operational control, and onboard data processing for each device is provided through a digital board and TigerSharc digital signal processor (DSP). Communication is supported for both ethernet and dedicated CESR field bus.

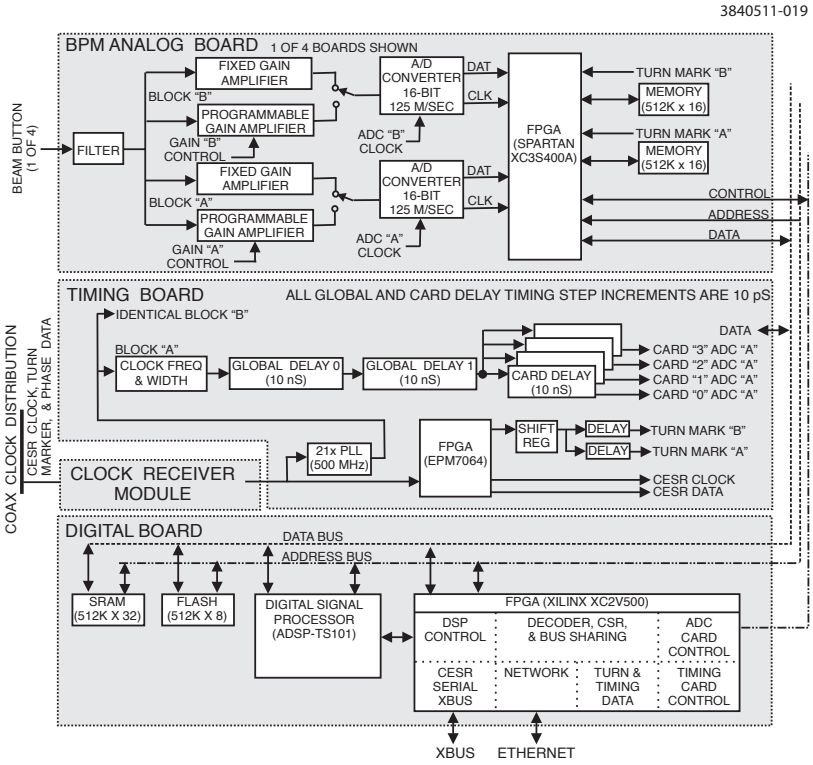

Figure 2.90: BPM module functional diagram

The CESR BPM system is controlled via a custom server application running on the CESR control system cluster. All system parameters, including pedestal and gain scale calibration values, delay tables for all supported bunch spacing configurations, and various identification and management data is stored in a central location. The server application is responsible for loading, managing, and saving this information with new values generated within the instruments. All control and data readback is performed via a custom network protocol running over 10-base-T ethernet.

Rapid measurements taking advantage of on-board averaging, pedestal subtraction, and gain scaling can be requested of all or a subset of instruments or detailed turn-by-turn data can be acquired for an arbitrary combination of bunches and turns in 14 ns or 4 ns bunch spacing modes. The software on board the instruments is also capable of automatically determining appropriate delays to use for sampling at the optimal point of the incoming waveform on all channels.

Data from all detectors is stored in a centrally-located data file. Raw ADC values, along with pedestals and gain scale factors for all channels and amplifier settings are stored in the data files. Sufficient information is provided to allow analysis of raw ADC or pedestal-subtracted and gain-

scaled turn-by-turn button data and/or physical beam positions for every bunch stored and detector location in the machine.

2.4.1.3 Status and Performance

Presently there are 104 digital BPM readout modules installed in CESR. These modules are in routine use for beam diagnostics and machine studies. The BPM system has regularly been used to measure the bunch by bunch positions of a train of 4 ns spaced bunches with a minimum of cross talk between bunch signals. A special diagnostic triplet location has been used to study the resolution and stability of the system. The triplet consists of three sets of detectors mounted in close proximity on a single vacuum chamber. Figures 2.91 shows vertical orbit differences between pairs of triplet detectors. The histograms include 256K turns of data (0.67 s duration) taken simultaneously with each detector. The effective resolution corresponds to the standard deviation of each distribution is consistent with our target single shot resolution.

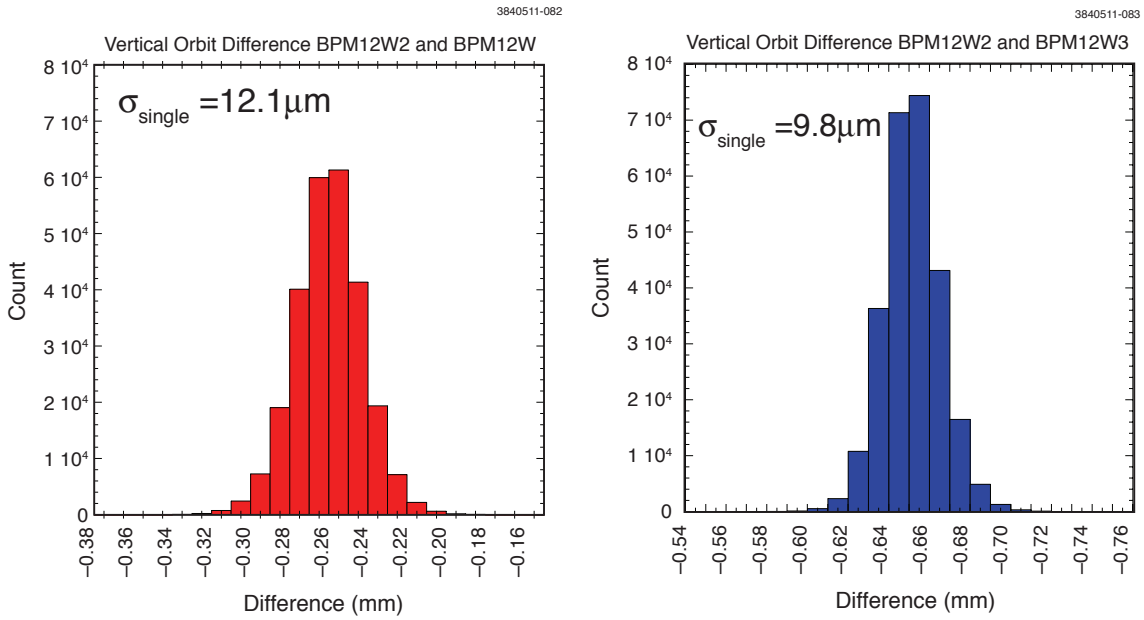

Figure 2.91: Vertical orbit differences between closely located detectors

In summary, the hardware and infrastructure of the CESR BPM system is functioning and in active use at this time. Development continues on data storage, analysis and diagnostic software. Other sections of this report discuss various aspects of the performance of the system.

2.4.2 X-Ray Beam Size Monitors

In the CesrTA 2 GeV ultra-low emittance optics configuration, a high resolution x-ray beam size monitor (xBSM) is required to measure vertical beam sizes of order 10 μm and characterize the

vertical beam emittance. These measurements are done by imaging 2-4 keV synchrotron radiation photons emitted from a source point in a dipole magnet onto a one-dimensional photodiode array. Three types of x-ray optics have been utilized to do this imaging. First, a vertically-limiting heavy metal (W) slit is used for pin-hole (PH) imaging in the vertical dimension. This slit can be used over the full range of CesrTA operating energies (1.8-5.0 GeV).

using various types of x-ray optics. Instrumentation in the evacuated x-ray beam line includes upstream interchangeable optics elements, a monochromator and an InGaAs photodiode detector. The interchangeable optics include a 'vertical pin-hole (PH)', that is a vertically-limiting tungsten slit, as well as coded aperture and Fresnel zone plates. The signal readout is based on a beam-synchronized fast analog-to-digital converter, that is capable of parallel measurement of consecutive bunches with as little as 4 ns spacing.

2.4.2.1 Conceptual Overview

In the x-ray beam size monitor (xBSM), we use synchrotron radiation to measure the vertical bunch size and thereby vertical emittance. Separate xBSMs have been successfully commissioned in x-ray beam lines to measure the sizes of the electron and positrons.

2.4.2.2 X-Ray Line

The layout of the positron x-ray beam size monitor beam line is shown in Figure 2.92. Synchrotron radiation x-rays are emitted in a dipole magnet to the right of the figure. Optical elements vertically focus an image of the beam onto a detector mounted in the enclosure at the left. In the positron (electron) line, the optical elements are located 4.36 m (4.23 m) from the x-ray source point and 10.19 m (10.67) from the detector giving a magnification of 2.34 (2.52). Three optical elements are available for use in 2 GeV stored beam operation. These include include a vertically limiting slit, a Fresnel Zone Plate (FZP), and a Coded Aperture (CA). These elements reside in the storage ring vacuum and can be selected and aligned remotely to meet the requirements of various measurements. At 2 GeV, the typical power load on the optical element is of order 1 mW/mA; the optical elements are in contact with actively cooled copper supports to remove this heat.

2.4.2.3 X-Ray Optics

The FZP and CA are manufactured on a common silicon substrate. For the positron line, the patterns are cut into 0.7 μm Au and are supported by a 2.5 μm Si membrane. The FZP pattern has 120 transmitting rings in a diameter of 1200 μm. The CA pattern has 8 transmitting elements with total dimensions 310 μm in the imaging direction by 1200 μm wide. For the electron line, the absorbing material is 4 μm Ta and 0.02 μm Ru. While the FZP pattern is identical, the CA is reduced in size to limit distortions due to angular misalignment of the CA to the beam plane. This CA pattern has 8 transmitting elements with total dimensions 155 μm in the imaging direction by 500 μm wide. For 4 GeV stored beam operation, there is a coded aperture designed for higher power in each line as well as the vertically limiting slit.

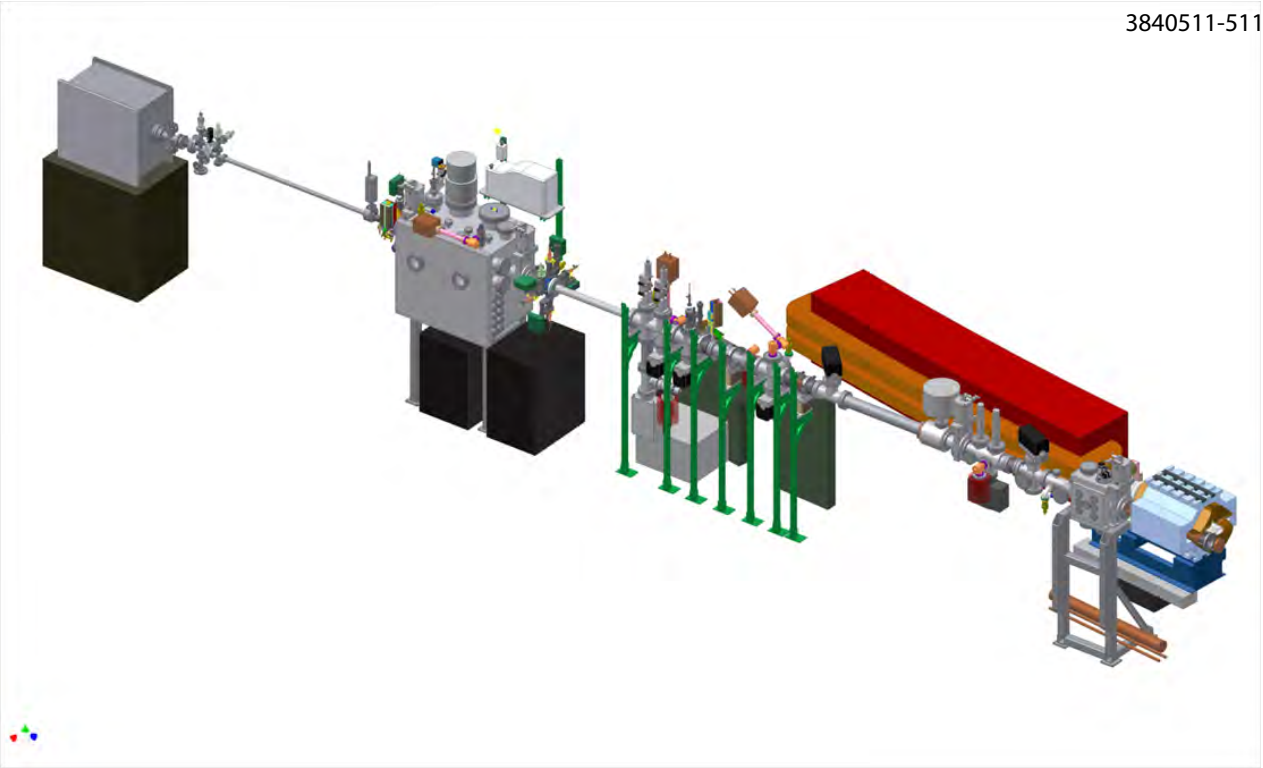

Figure 2.92: Layout of the positron x-ray beam size monitor beam line. The positron beam travels from the right through the quadrupole (blue magnet) and then the dipole (red magnet). x-ray photons emitted from the positrons within 10 cm of the entrance of the bend magnet pass through the beam line on their way to the detector box at the far left.

2.4.2.4 Detectors and Data Acquisition

The detector is a vertical array of 32 InGaAs diodes with a 50 μm pitch and horizontal width of 400 μm. The InGaAs layer is 3.5 μm thick, which absorbs 73 percent of photons at 2.5 keV; there is a 160 nm Si3N4 passivation layer. The time response of the detector is sub-nanosecond.

The data acquisition system used in the xBSM is a collection of custom designed hardware and software. This design uses a modular approach and occupies space both inside and outside of the detector box. Figure 2.94 presents an overview of this system.

The signals from the diode detector are received, amplified and converted to differential signals prior to being delivered out of the detector box in bundles of 8 channels of twin-axial cable. The bundle of 8 differential signals is received by a carrier board which contains 8 channels of signal conditioning and digitization. Each channel provides 12 dB of fixed gain and -4 dB to 20 dB of digitally controllable gain. Figure 2.95 shows the functional blocks of a single channel s signal chain.

A 300 MSPS, 10 bit analog to digital converter is utilized to provide the capability of digitizing 4 ns spaced bunches. The data from the converter is streamed through a local FPGA and is stored

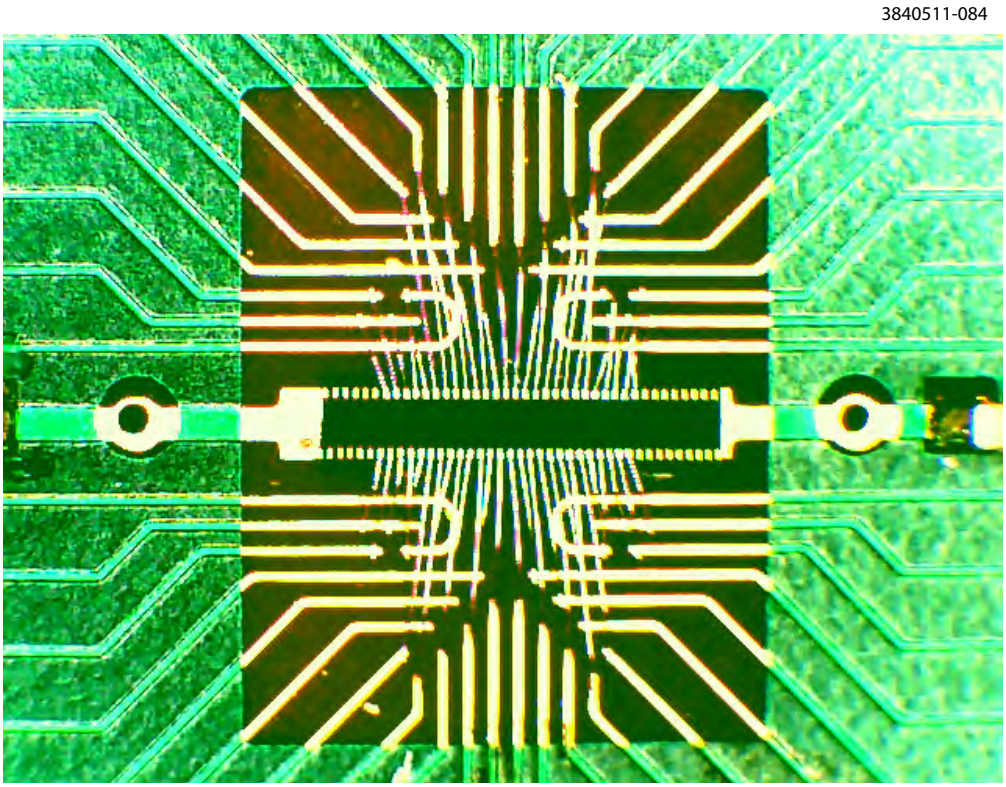

Figure 2.93: xBSM diode detector

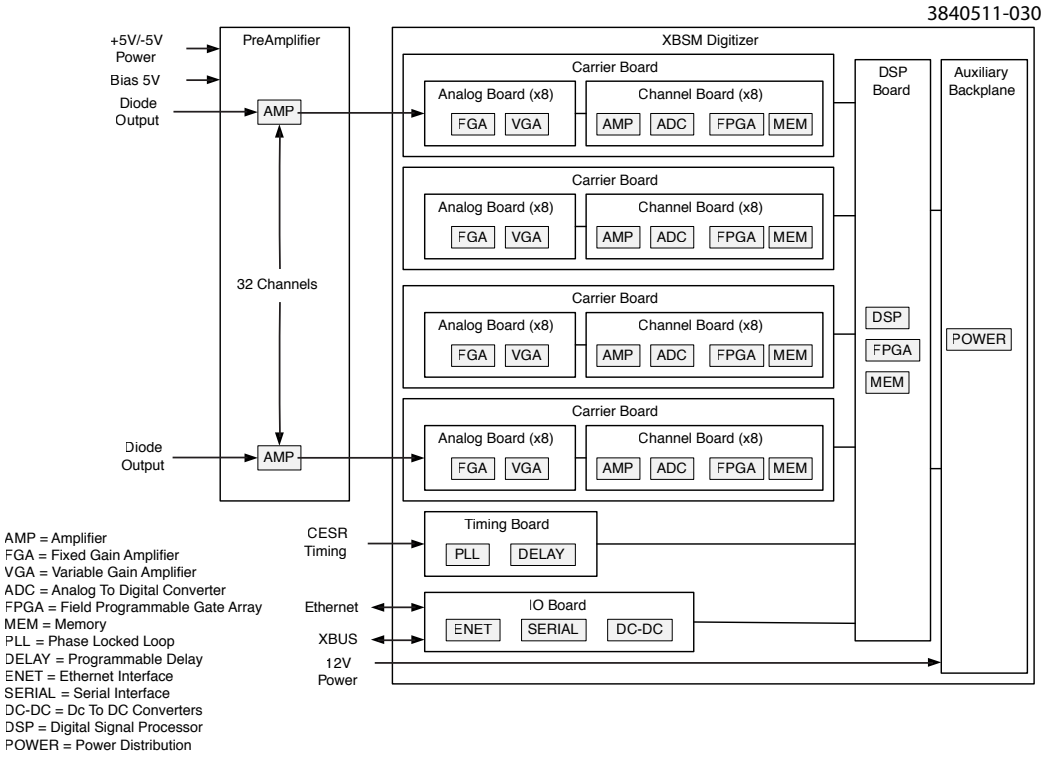

Figure 2.94: xBSM data acquisition system

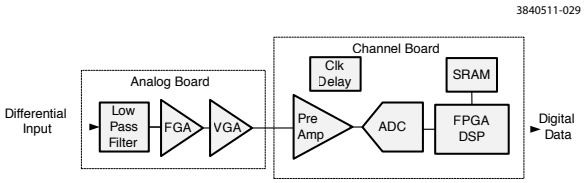

Figure 2.95: xBSM signal chain

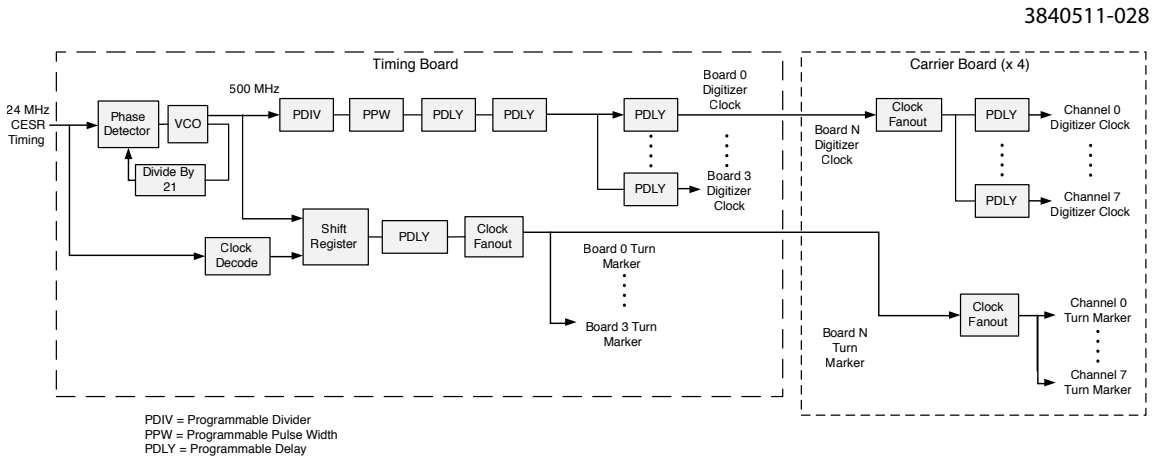

Figure 2.96: xBSM internal timing

locally for each channel in an 18 Mbit SRAM. This allows for 1 million samples to be captured on each channel (without data compression). Each channel receives its own sampling clock and has an in-channel configurable delay to allow for channel to channel synchronization, as described below. The digital data from each channel is funneled into the digital signal processing board. This board allows for on-instrument processing and data manipulation. It also provides the link to the ethernet interface which is contained on the input-output board. All controls and data retrieval are accomplished via the ethernet interface. A diagnostic interface is provided via a serial field-bus (XBUS) connection on the input-output board. Power is delivered to the various boards via the auxiliary backplane.

Machine Timing And Synchronization The xBSM is synchronized to the CESR accelerator timing system via a 24 MHz encoded data signal provided from the CESR timing system. This signal is synchronized to the CESR RF system and also contains revolution markers (turn markers) as well as acquisition triggers. This same signal is also delivered to all of the storage ring beam position monitors. This allows for synchronized turn by turn measurements between the two systems.

xBSM Internal Timing An overview of the internal timing control and distribution is provided in Fig 2.96. The 24 MHz encoded signal is received by the timing board. This signal is used to synchronize an on board voltage controlled oscillator which generates a 500 MHz source clock. This

clock drives a programmable divider with a programmable pulse width to provide a fully configurable sampling clock. The sampling clock passes through a series of programmable delays prior to being fanned out to each of the four carrier boards. Each carrier board then fans the clock out to the 8 sampling channels. Every channel has its own programmable delay which allows for precise adjustment of the sample point. The timing board also extracts the turn marker from the 24 MHz encoded signal. The turn marker then passes through its own set of programmable delays and is fanned out to all 4 carrier boards where it is delivered to the individual channels. Each channel can be synchronized to the accelerator revolution frequency. The digitizers run continuously and a bunch pattern is provided to all channels and serves as a gating signal which determines when the sample is to be stored in the local SRAM.

2.4.2.5 Performance

As described in section 2.4.2.1, the beam size is measured by analyzing the image of synchrotron radiation x-rays on a 32 element linear pixel detector. The image is formed by one of the three available optics elements placed between the source point in the storage ring and the detector; these are a pin-hole, a Fresnel Zone Plate, and a Coded Aperture as described in section 2.4.2.3.

Images for each of the three optics elements, for a beam with a size of about 16 μm, are shown in Fig. 2.97. The pinhole image is characterized by a gaussian distribution with a width that is a convolution of the pinhole size and the beam size. The Fresnel zone plate image has two components: a narrow peak, with width due only to the beam size, and a wide background which is due to the chromatic aberration of the focus. The coded aperture image is a complex diffraction pattern due to the eight transmitting slits in the device. Details of extracting the beam size for each of the optics elements are described below.

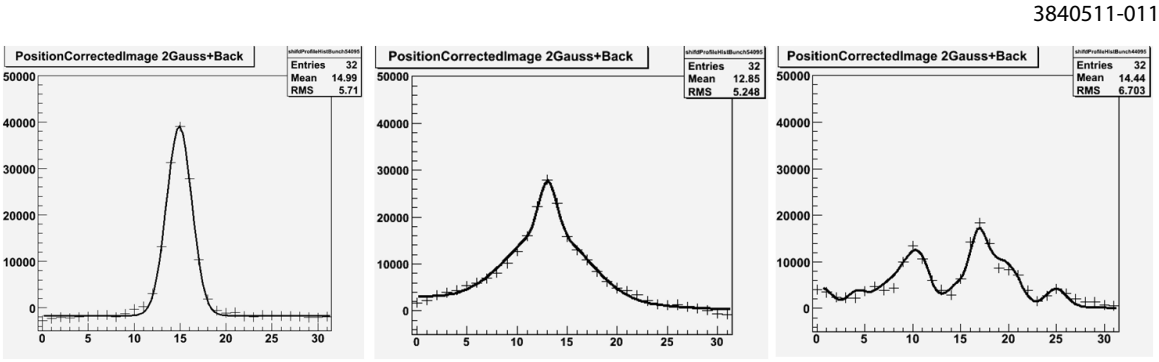

Figure 2.97: Typical images for pinhole, Fresnel zone plate and coded aperture, each with 16 μm beam size.

The images shown in Fig. 2.97 are taken with 0.75 mA, 0.50 mA, and 0.5 mA per bunch respectively. Analysis of the turn-by-turn fluctuations of the pulse peak pulse height indicates that the readout value of 30000 counts corresponds to about 110 photons. Single turn images have about 10% RMS pulse height fluctuations of the peak. To reduce statistical fluctuations, the images in Fig. 2.97 are averages of 4096 turns for a single bunch within a train of bunches within the storage ring. With the onset of instabilities, there can be significant turn-to-turn beam motion. As shown in Fig. 2.98,

the motion can be several pixel spacings when measured at the detector. For each of the optics elements, a beam position is determined in a preliminary fit. This motion is removed in building the average images shown in Fig. 2.97.

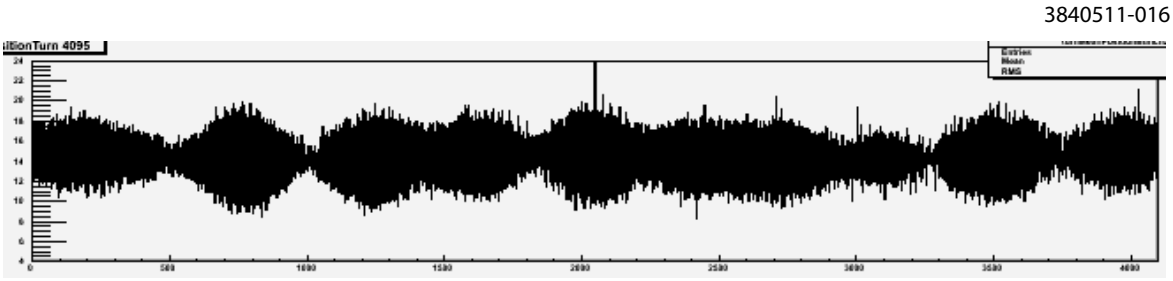

Figure 2.98: Beam position as a function of turn number for 4096 storage ring turns. Units are 50 μm pixels measured at the image. The high frequency motion is due to betatron motion. In this example, with a maximum variation of ± 4 pixels, and a magnification of 2.34, the beam motion at the source is ± 85 μm.

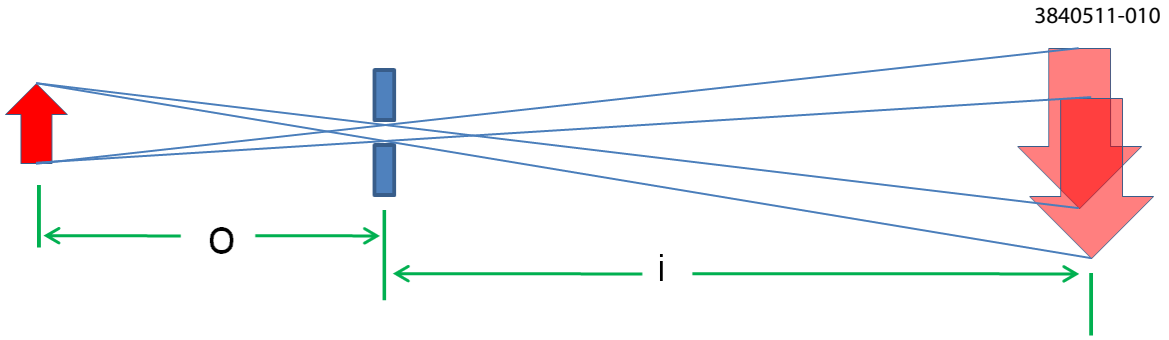

Figure 2.99: Schematic showing the convoluted image in pinhole focusing.

As shown in Fig. 2.99, the pinhole image is a convolution of the pinhole size and the beam size. For large pinhole size, the image approaches a projection of the pinhole and increases linearly with increasing pinhole size; for small pinhole size, the image approaches a diffraction pattern and increases with the inverse square of the pinhole size. Thus, the pinhole size is set to the value which results in a minimum image size and minimum correction as shown in Fig. 2.100. The minimum image size for the mean x-ray energy of 2 keV is about sigma = 49 μm, found with a pinhole full-height of 45 μm. The pinhole size, referred to the source, is the minimum image size divided by the magnification and is estimated to be 21 μm. This sets a limit for accurate measurement of the beam size. The image is fit to a Gaussian and a flat background. The Gaussian describes the convolution of the two contributions. The floating background is necessary because the individual pixels are not independent; charge measurement in illuminated channels results in a baseline depression in the others. As the image is typically covering only a fraction of the detector pixels, the baseline is well determined. The beam size is then extracted by subtracting the pinhole size from the image size, in quadrature.

The Fresnel Zone Plate is a diffractive focusing element; paths through successive rings differ by one wave length. Unlike the case of refractive focusing, chromatic aberration is severe; calculations show that the bandwidth is about 0.1 keV, while the x-ray energy distribution has a width

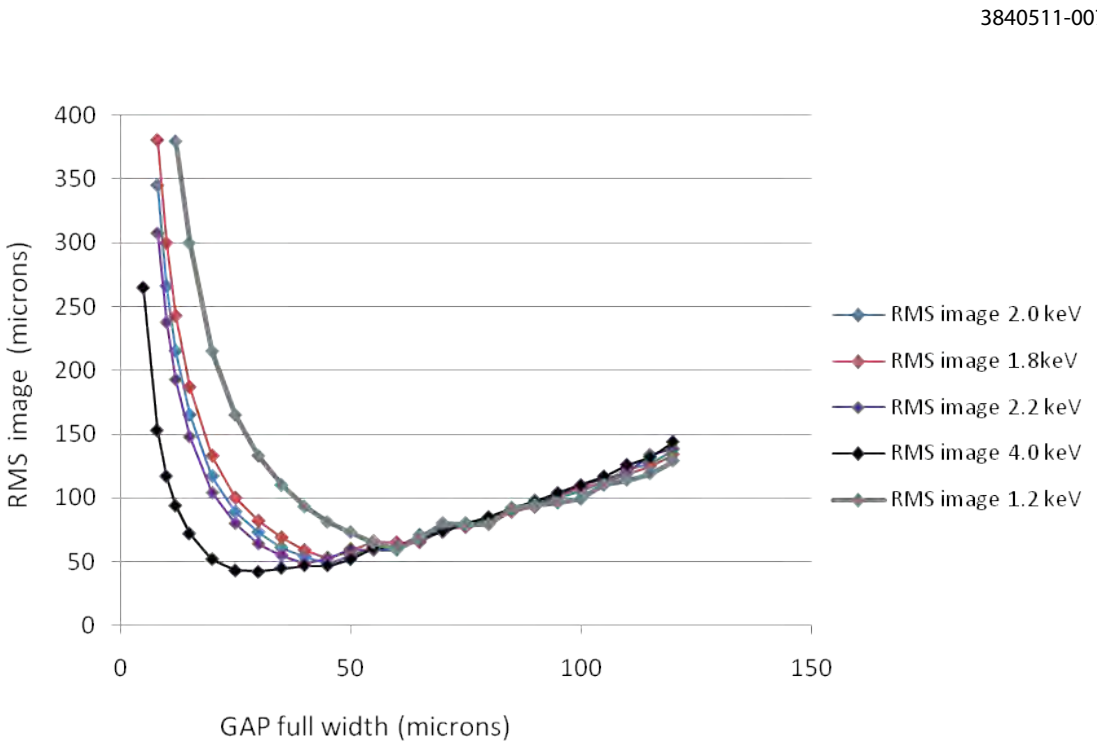

Figure 2.100: Image size vs pinhole size. The pinhole size (labelled GAP full width) is set to provide minimum image size for the x-ray energy distribution.

of sigma 0.5 keV. Thus, roughly 20% of the x-ray energy distribution is focused by the Fresnel zone plate, consistent with the image shown in Fig. 2.97. This causes complications in extracting the beam size from the image. Attempts to use a monochromator to eliminate the out-of-focus component resulted in a reduction of the peak intensity to 1%, about one photon per turn at the peak of the distribution with 0.5 mA per bunch. Analysis of fluctuation in the background indicates that the electronic noise, for the 14 ns readout, corresponds to about 0.3 photons. With this significant reduction of the in-focus signal, the resulting signal-to-noise ratio leads to decreased sensitivity. Fresnel zone plate measurements are made without the monochromator. The image is fit to a narrow Gaussian representing the in-focus signal. The out-of-focus contribution has a fractional area, intrinsic width, and position relative to the in-focus image that are assumed to be independent of the beam size. The background is well determined with constant and linear terms. Thus, the image is fit to five parameters. The beam size is extracted from the narrow Gaussian width, corrected by removing the pixel size, 6.2 μm (referred to the source).

The Coded Aperture is an array of 8 slits ranging in size from 10 μm to 40 μm at the optics element. As described for the single slit, diffraction effects become significant for a slit width less than 45 μm. Thus, the coded aperture image is a complex diffraction pattern. Extracting the beam size from the coded aperture image requires a parameterization of the image for all beam sizes. This has been accomplished via two methods. In the first, the images are directly calculated for many representative values of the beam size and values of the image position with respect a pixel center. The set of calculated images are then used as the templates in a template fit. In the second method, only the image for zero beam size is calculated. The result is parameterized by an ensemble

of Gaussians with fixed values for the widths, relative areas, and relative positions. Fig. 2.101 shows the parameterization overlaid on the calculation of the zero beam size image. Using Gaussians for the basis of the parameterization, it is straightforward to extend the parameterization to any beam size for use as the function is a chi squared fit, as is shown for a beam size of 15 μm. Either of the fitting methods provides the beam size, image location and overall normalization. Since the image spreads over the entire detector size, it is difficult to independently extract a background level.

3840511-009

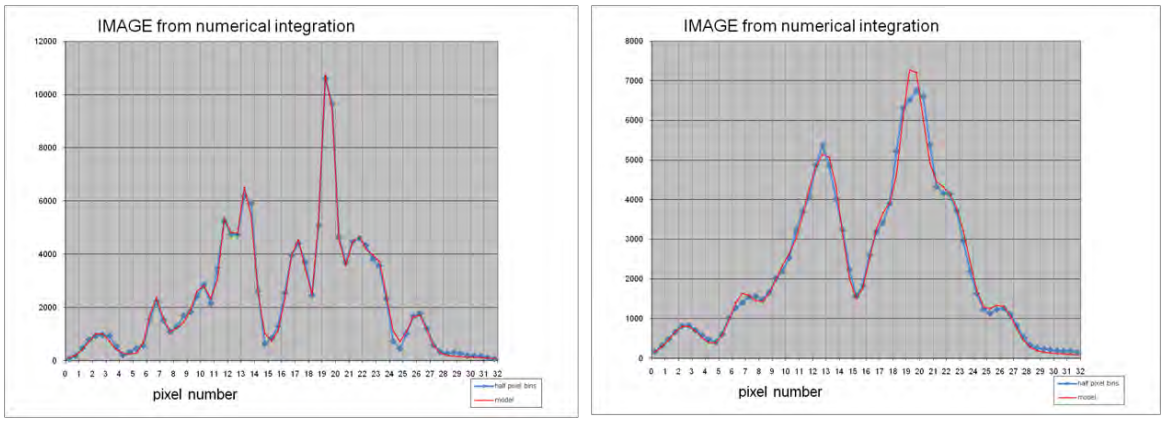

Figure 2.101: Coded aperture calculated image for zero beam size and for a beam size of sigma = 15 μm.

Measurements of the beam size, using the three optics elements, are overlaid in Fig. 2.102. In each sub-figure, beam conditions were similar for the measurements with each of the optics elements. There is good agreement between the results for the three optics elements for beam sizes below about sigma = 50 μm. There are discrepancies in some details. For example, in (c), the beam size for the first two bunches is higher when measured with the coded aperture. However, this is not the case in the other examples. It has been shown that the increased size of the first bunches is sensitive to the level of vertical and horizontal feedback. Another detail discrepancy is that, in (a), for bunches 2 through 15, the beam size is about 1 μm higher when measured with the coded aperture. Again, this is not the case in the other examples. Thus, both of these discrepancies are not systematic effects; the effects are due to small differences in the actual beam conditions. Of significance is that the onset of beam growth is the same for each of the beam conditions when measured with each of the optics elements, starting at bunch 20 in (a), at bunch 9 in (b), at bunch 11 in (c) and at bunch 13 in (d).

For beam size above about sigma=50 μm, the measurements using the different optics elements have significant disagreements. The precision of the beam size measurement is affected by several factors. Electronic noise and photon statistics contribute to random fluctuations in individual channel measurements. Inexact pedestal determination and channel-to-channel gain calibration lead to systematic distortions of the image that can be correlated with the image position. Image measurements in a storage ring bunch can be distorted by the signal from preceding bunches if the characteristic amplifier settling time is significant compared to the inter-bunch spacing. Finally, each of the optics elements has inherent limitations that are described below.

Fig. 2.103 shows the images for the three optics elements with larger beam size. The pinhole, even

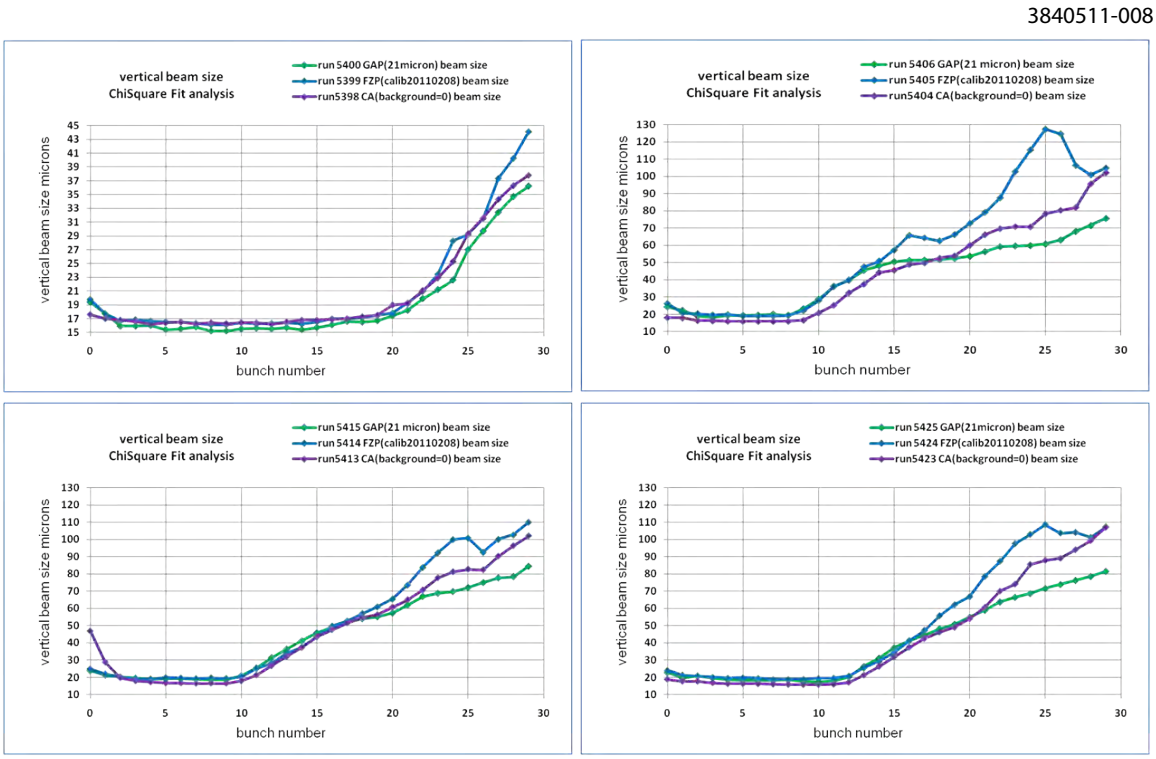

Figure 2.102: Beam size measurements with three optics elements, in four running conditions: (a) tuned for small beam size with 0.50ma/bunch, (b) same, 0.75 ma/bunch, (c) high chromaticity, (d) high chromaticity with precursor bunch 182ns before train.

with a beam size of 85 μm, has a well determined background. It is expected that systematic errors due to the fit if the image will allow accurate measurements to about 100 μm. The lower limit is determined by the pinhole size. As the size, referred to the source, is 21 μm, the correction leads significantly increased uncertainty for beam size below about 11 μm. With the Fresnel zone plate, the beam size is extracted from the width of a narrow gaussian which accounts for only about 13% of the image area. The out-of-focus contribution to the image has a fixed width that corresponds to beam size of about 83 μm. For a beam size of 40 μm, the in-focus contribution is not well separated. More significantly, the modeling of the out-of-focus contribution could be improved to increase the sensitivity of the fit to the beam size. At this time, measurements with the Fresnel zone plate are expected to be useful up to 40 μm. With the coded aperture, for a beam size of 60 μm, the separation of the two major features is significantly reduced. In addition, background is not well determined because the image fills the detector. Measurements with the coded aperture are expected to be useful up to this beam size. The lower limit is determined by the width of the features of the image calculated for zero beam size. As this typical feature size, referred to the source, is 15 μm, accurate measurements can be made for a beam size as low as about 8 μm.

2.4.3 Other Beam Diagnostics

Several instruments have been added or modified for use with the CesrTA program. They include visible light beam size monitors, position detectors, which measure the tunes and detect some of

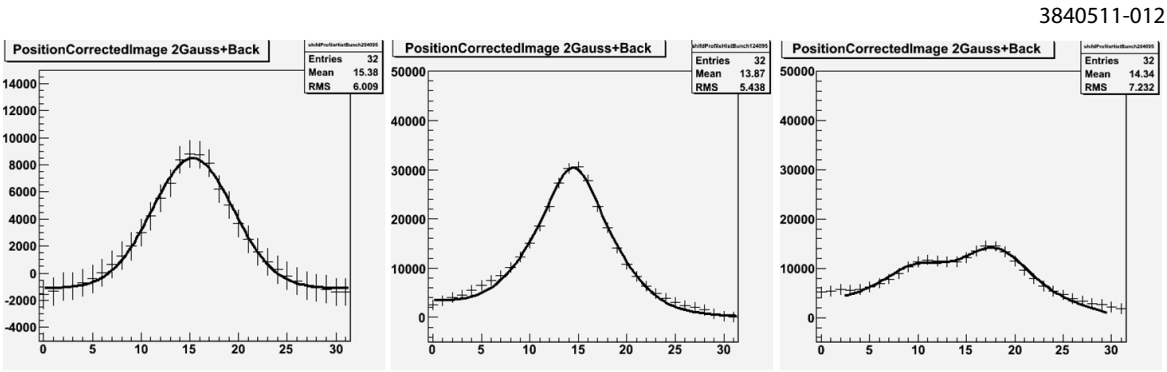

Figure 2.103: Typical image for pinhole, Fresnel Zone Plate and coded aperture, with beam sizes 80 μm, 40 μm and 60μm respectively.

the internal modes of oscillation, beam kickers and tune trackers, which lock on to the bunch's betatron or synchrotron tunes.

2.4.3.1 Visible Light Beam Size Monitors

The two visible light beam size monitors (vBSM) are located in the L3 area of the storage ring. The vBSMs are placed symmetrically at east and west ends of the north area straight, in order to image visible synchrotron light from the positron and electron beams, respectively. The visible SR from bending magnets 48E/W (140 m bending radius) is reflected by a Beryllium mirror located inside the vacuum chamber through a vacuum window out of the chamber and into an optics box. The angular acceptance of the mirror for light from the source in the bend magnet is 2.5 x 2.2 mrad (H x V). On exiting the vacuum window, the SR photons pass through an iris with an adjustable aperture into the optics box. The optics box contains several sets of double slits with different slit spacings and orientations for interferometric measurement of vertical or horizontal beam size. The slits are followed by a focusing lens (f=5 m). The lens is 6 m from the source. The light is then reflected by multiple mirrors, overhead, across the tunnel and eventually through the wall of the accelerator tunnel to an optical table in an experimental hall. At this point the light has traveled 27 m from the source in the bend magnet. The path of the light, from vacuum window through tunnel wall, is indicated in Fig. 2.128 . On the optical table in the experimental hall, the SR light passes through a second lens (f=1 m), a polarizer, a 500-nm narrow bandpass filter and is finally incident on a CCD camera. A beam splitter can be placed in the path to direct a fraction of the light into a streak camera, to measure the bunch length. The optical layout is shown schematically in Fig. 2.104.

The diameter of the iris in the optics box can be varied from 3.0 mm to 22 mm, corresponding to an acceptance of visible light from a minimum of 0.5 mrad with depth of field 70 mm to 3.5 mrad and depth of field of 350 mm. The three sets of double slits (vertically and horizontally aligned) each with fixed slit separation, were machined in a single piece and mounted on a motorized translation stage and a rotation stage. The stages inside the optics box are remotely controlled. Different sets of slits can be chosen by appropriate setting of the translation stage. The slits can also be rotated away from the SR beam to image the beam profile directly. The optics box is shown in Fig. 2.105.

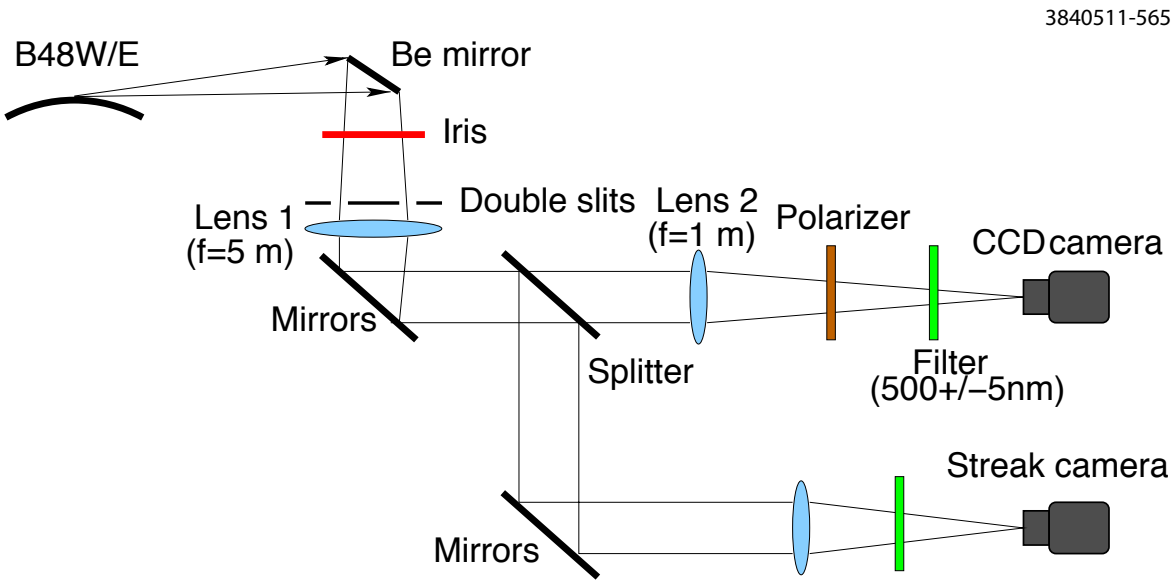

Figure 2.104: Visible synchrotron light monitor optics.

On the optical table in the experimental hall the optical elements can be adjusted during machine operation. The polarizer can be rotated 90 deg to select either the 0-polarized or π-polarized component of SR light. The position of the CCD camera can be adjusted so as to view different image planes. The CCD camera can be located to image the source point where direct images of the beam profile or the interference fringes can be recorded. Alternatively the CCD camera images the double slits, providing a means to determine slit alignment and the imbalance factor.

We are experimenting with both inferometry and π-polarization for measuring vertical beam size, and direct imaging and interferometry for measuring horizontal size. The streak camera is used to measure bunch length and longitudinal particle distribution. Our goal is simultaneous measurement in all three planes.

2.4.3.2 Tune and Motion Detection

The variation of the tunes of individual bunches carries information about the global electron cloud density. Different methods have been employed to measure the tunes of the bunches during the beam dynamics studies.

A simple method for determining the tunes for each bunch in a train of bunches is to use a subset of the complete number of CBPM modules to measure the beam position turn-by-turn for each bunch. The block diagram for this configuration is shown in Fig. 2.106. The data is read out from the CBPM modules and written into a raw data file. Each BPM's position data is then analyzed offline by performing a Fourier transform, which yields the spectral lines of the beam's transverse motion. This method is most often used in conjunction with a kicker that deflects all of the bunches within the train.

A second method is shown in the block diagram in Fig. 2.107. This detection method makes use of a few BPM detectors, which are still connected to CESR's original relay-based BPM system

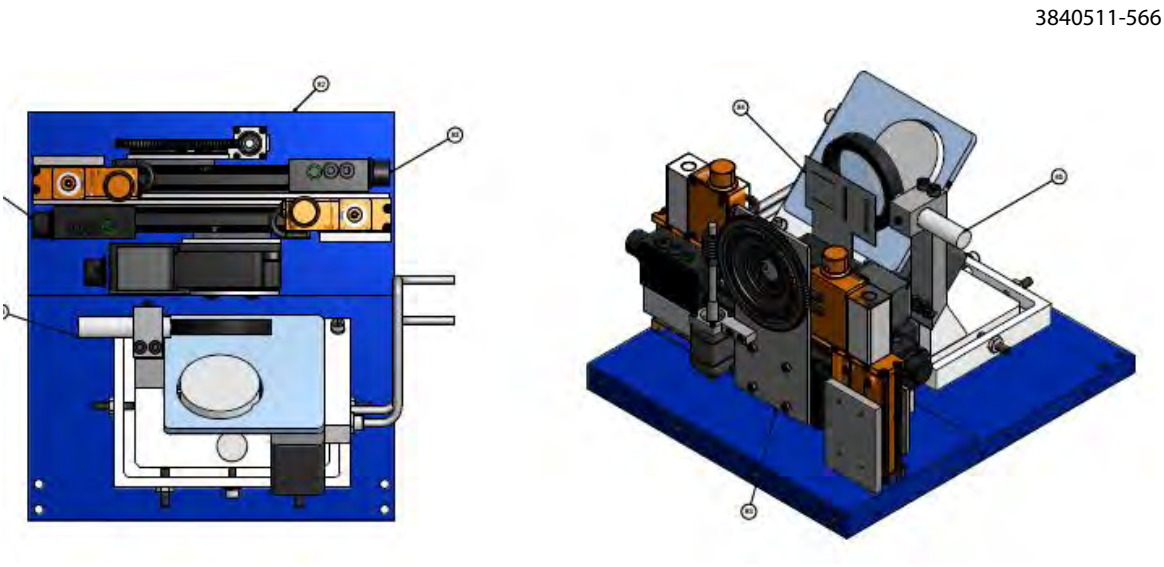

Figure 2.105: Visible synchrotron light monitor optics box. The optics box contains an aris with adjustable aperture, a double slit, a lens, and a mirror.

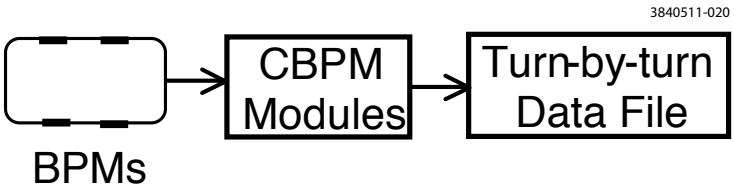

Figure 2.106: Block diagram of a betatron tune receiver utilizing the bunch-by-bunch and turn-by-turn readout capabilities of the CBPM system.

processors. The signal from one BPM button is routed via coaxial relays to one of the analog processors, where fixed gain amplifiers and/or attenuators may be inserted in the signal path to maintain the peak signal level within a factor of five over a wide range of currents. After the gain adjustment the signal passes on to an RF gating circuit, which is triggered by the Fast Timing System, allowing the selection of the signal from a single bunch, sending it to a peak rectifier circuit (with approximately 700 MHz bandwidth) and then routing its output video to a spectrum analyzer in the Control Room. In Fig. 2.108 the timing aperture for the gating circuit was measured by sweeping the gate delay for the signal coming from a single bunch to observe the signal amplitude vs. gate delay. A second method for observing the signal crosstalk between bunches is seen in Fig. 2.109. This plot is obtained by shaking the beam vertically and observing the spectrum analyzer's signal amplitude as a function of gate delay. This second observation gives the base timing aperture as 7.5 ns wide, giving more than 20 dB isolation of the signal crosstalk from adjacent 4 ns-spaced bunches and a signal isolation of greater than 50 dB for 14 ns-spaced bunches.

The initial setup of the storage ring parameters for the tune measurements is performed with a single stored bunch. The betatron tune instrumentation configuration, capable of detecting the beam's tune in both planes, is shown in the block diagram in Fig. 2.110. In this mode the single bunch is excited with the relatively narrow bandwidth shaker magnets (described below) and detected with

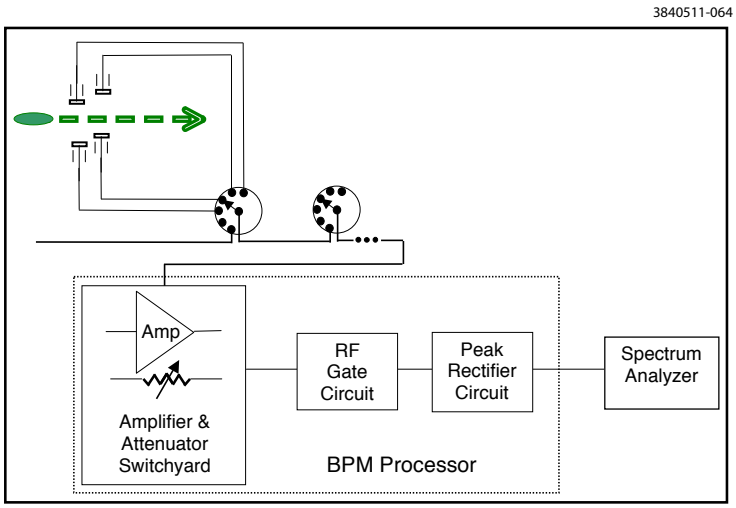

Figure 2.107: Block diagram of a betatron tune receiver utilizing the bunch-by-bunch and turn-by-turn readout capabilities of the CBPM system.

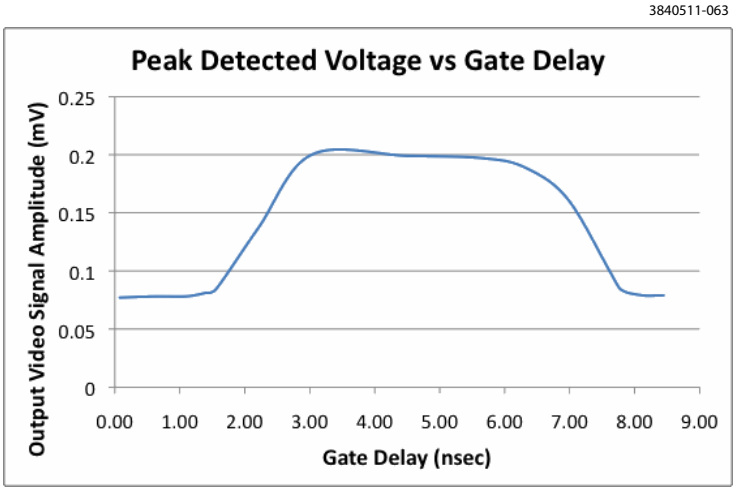

Figure 2.108: Relay BPM processor's gate timing aperture as measured with the video signal in the Control Room showing a 77 mV DC offset from its peak rectifier circuit.

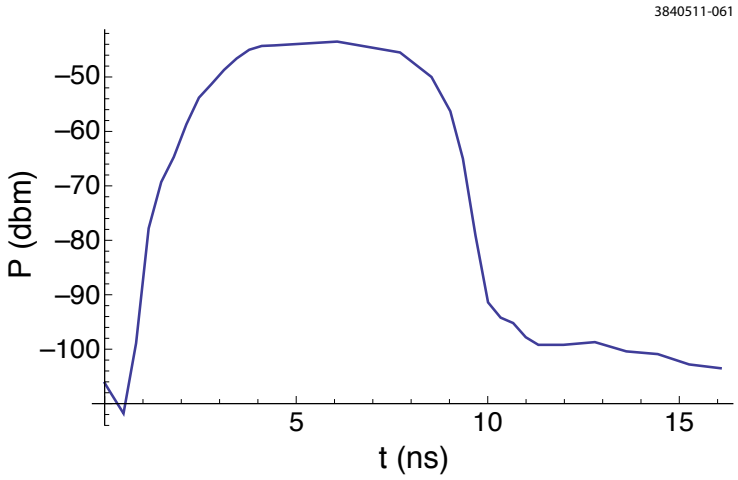

Figure 2.109: Relay BPM processor's gate timing aperture as measured by driving a single bunch vertically and measuring its response vs. gate delay.

a swept spectrum analyzer.

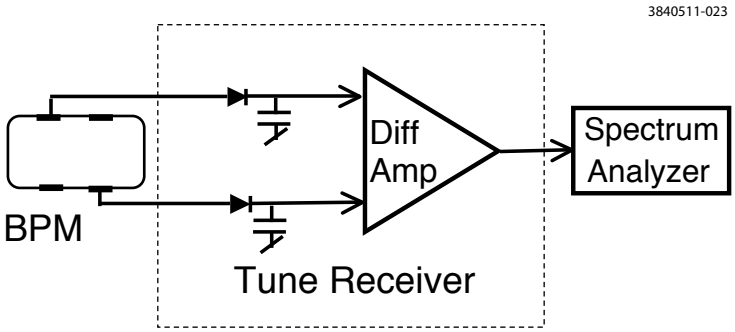

Figure 2.110: Simple block diagram of a narrow-band tune receiver, shown in the mode where it can detect both the horizontal and vertical betatron tunes.

2.4.3.3 Beam Excitation

To measure the tune spectra of bunches it is necessary to observe them undergoing coherent motion. In some cases their self-excitation is sufficient for a good tune measurement, but in other cases the beam must be driven with some type of dipole kicker to cause the bunch(es) to undergo centroid motion. There are three types of dipole kickers used in CESR for the measurements described here.

One type of kicker is called a pinger magnet and it is used for single impulse deflection for the beam. There are three pingers installed in CESR: two are horizontal and one is vertical. A horizontal pinger is shown in Fig. 2.111 as a single-turn ferrite-core pulsed magnet, which surrounds a Kovar-coated ceramic vacuum chamber. The horizontal pingers are excited using a thyratron with a approximately square pulse, having a flattop region about a 2 μsec long. This is more than long enough to deflect all bunches in one train with the same angle. The pulse shape for the vertical

pinger has a different waveform; the magnet is driven with a half sine-wave pulse of approximately 2.5 μsec duration. The pingers can be triggered via CESR's Fast Timing System at repetition rates as high as 60 Hz and the triggers can be synchronized with the CBPM turn-by-turn and bunch-by-bunch data acquisition. Because of its half sine-wave shape, the vertical pinger is timed to have the train of bunches arrive straddling the peak of its deflection.

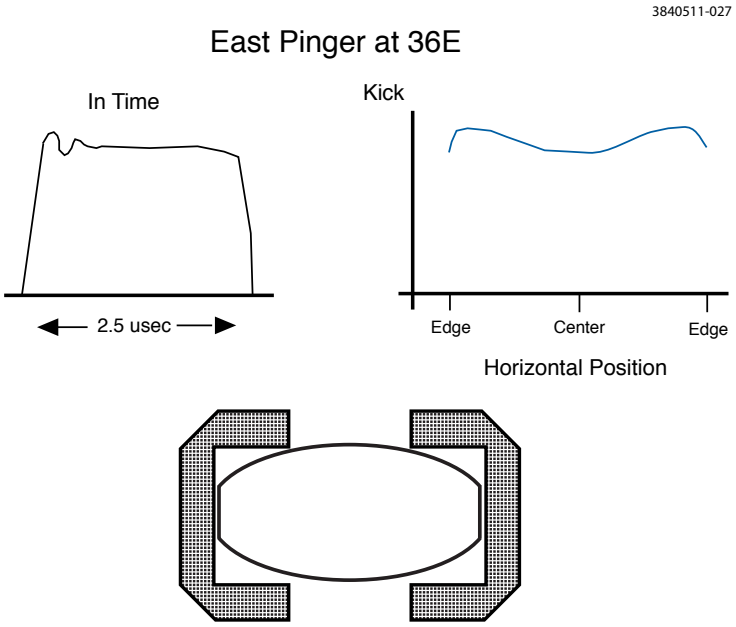

Figure 2.111: Horizontal pinger. This is a pulsed ferrite magnet surrounding a metallized coated ceramic vacuum chamber, which provides deflection to the beam with a single turn's duration. The upper two plots display qualitatively the deflection to the beam as a function of time (on the left) and spatially across the vacuum chamber's aperture (on the right.)

The second type of deflection element, utilized for beam dynamics measurements, is a stripline kicker, an example of which is shown in Fig. 2.112. There are two (one horizontal and one vertical) stripline kickers installed in CESR. They are the deflectors for the transverse dipole bunch-by-bunch BSF systems for the ring. They have a 3.5 ns long transit time and are excited with 250 W 250 MHz RF amplifiers. As a part of the transverse feedback system for 14 ns-spaced bunches, the amplifiers are modulated with 14 ns single period sine-wave, producing a constant (± 5 %) deflection to the beam for about 1 ns. Each feedback system modulator has an external modulation input and when it is enabled, the input will allow the deflection of any combination of 14 ns-spaced bunches. For beam dynamics measurements, the stripline kickers are most often used to deflect individual bunches within the train.

For completeness we will mention a third type of deflection component in the storage ring. This is low-frequency shaker magnet, a multi-turn coil wound around a H-frame ferrite core surrounding a metallized coated ceramic vacuum chamber. Although this shaker magnet is not in use during beam dynamics measurements, since it is unable to distinguish motion of individual bunches, it is important for the detection of the tunes as conditions are re-established at the beginning of each measurement period.

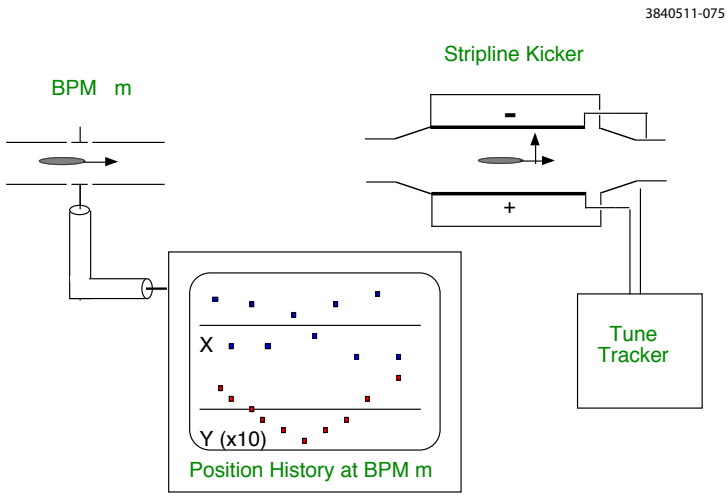

Figure 2.112: Stripline kicker, having two plates that are driven differentially to deflect the bunch.

2.4.3.4 Tune Tracker Techniques

Numerous storage ring diagnostic operations require synchronous excitation of beam motion. An example is the lattice phase measurement[32], which involves synchronous detection of the driven betatron motion. In the CESR storage ring, the transverse tunes continuously vary by several times their natural width. Hence, synchronous beam excitation is impossible without active feedback control. The digital tune tracker [33] consists of a direct digital frequency synthesizer which drives the beam through a transverse kicker, and is phase locked to the detected betatron signal from a quad button position detector. This ensures synchronous excitation, and by setting the correct locking phase, the excitation can be tuned to peak resonance. The fully digital signal detection allows a single bunch amid a long train to be synchronously driven, which allows lattice diagnostics to be performed which include collective effects.

The feedback unit operates at a clock frequency of 71.4 MHz, and this clock is used for beam sampling, filtering, and synthesis of the betatron drive signal. Since only a single bunch is to be used for phase locking, the instrument can be used with any bunch configuration.

The position signal is taken from a set of microstripline electrodes, which are separated into amplitude and displacement signals with a network of sum and difference combiners. The difference signal is digitized with a 10 bit ADC which is timed to peak signal amplitude, and the signal from the selected bunch is latched for one turn. The latched amplitude signal is digitally mixed at 71.4 MHz with two square wave representations of the betatron drive signal in quadrature phase. This produces a vector representation of the phase difference between the synthesized betatron drive and the actual betatron motion of the beam. The betatron clock is represented as square waves to eliminate the need for real-time multiplication. The demodulated position signals are filtered in a pair of single pole IIR (infinite impulse response) filters. Only one of the filtered signals is used to represent betatron phase error, and the other is only used to reconstruct signal amplitude.

The DDS (direct digital synthesizer) is straightforward, consisting of a phase register which is incremented by the frequency command at the 71.4 MHz clock rate, a sinusoidal lookup table implemented in a high speed cache RAM, and a 14 bit DAC. Adjustments of drive phase and amplitude are effected by changing the contents of the RAM, and the 14 bit output resolution

gives sufficient dynamic range for all applications without the need for analog attenuation. The betatron drive signal is coupled to the beam via the feedback kicker, which allows the isolated drive of a single bunch in the 14 ns spacing configuration. In closer bunch configurations, there is some crosstalk of the drive signal to bunches adjacent to the one selected for phase locking.

The phase locked loop requires a proportional channel and an integrating channel. The proportional channel shifts the betatron frequency command by an amount proportional to phase error. This is necessary to maintain loop stability, and to give the loop sufficient agility to track the tune fluctuations of the storage ring in real time. The integrating channel increments the frequency command on every revolution by an amount proportional to phase error. This is necessary to bring the phase error to zero, and thus provide a stable phase reference for lattice measurements.

The DDS phase register value is latched once per accelerator revolution, and the phase is sent by a parallel digital link to the clock modulator for the CBPM system[34]. The BPM clock modulator imposes both the vertical and horizontal phase values from the two tune trackers on the BPM clock using a pulse width modulation system. The individual BPM modules then extract the phase values and use them to reconstruct the drive signal, typically one of the three normal mode frequencies, which is used to synchronously detect corresponding phase at each BPM station. The synchronous phase measurement is used to determine the phase advance between BPM stations, and hence the phase function of the entire lattice. The relative phase of horizontal and vertical motion at each BPM is used to extract coupling information.

The operating configurations of the tune trackers, including center frequencys, gains, and filter settings, are saved and restored along with the storage ring configuration. This gives a high probability of successful phase lock without adjustment. The signal acquisition and locking functions can be operated through a GUI (graphic user interface), and the same functions can be executed automatically by other system processes using control system subroutines.

The tune tracker can initially acquire a betatron signal by sweeping the drive frequency through a band, typically 20 kHz wide, and recording betatron amplitude and phase error relative to the DDS. A fit of center frequency, center phase, peak width, and peak amplitude is then automatically done to a Lorentzian resonance model as shown in Figure 2.113.

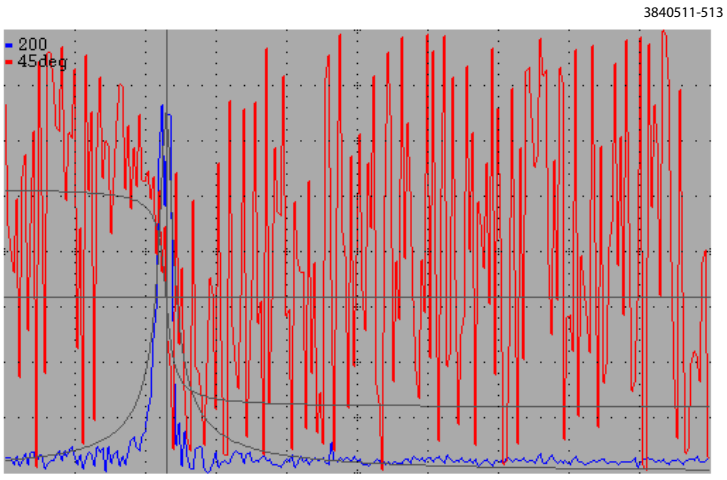

Figure 2.113: Frequency sweep over 10kHz. Blue trace is amplitude and red trace is phase error, showing fit to Lorentzian resonance model.

Only a rough fit is possible to the tune of an unlocked beam because of the tune noise of the storage ring, which is approximately several hundred Hz. Acquisition of phase lock is accompanied by a large increase in betatron amplitude. Once phase lock is established, a fine fit to the resonance can be done by sweeping the betatron drive phase, and recording betatron amplitude and drive frequency. A fit of the same four parameters is automatically done to the Lorentzian model by the same method described above. This consists mainly of fitting the amplitude to a cosine function, and gives the closest possible approach to the resonance peak.

2.4.4 Feedback System Upgrade

Three Dimtel iGp-1281F signal processor systems have been added to the CESR ring to supplement the existing feedback systems. Previously CESR was capable of 14 ns, multiple bunch, turn-by-turn feedback. The 14 ns system was designed for and constrained by having electrons and positrons in the ring simultaneously. The Dimtel systems add faster processing capability to the same detection and kicker hardware to provide feedback for bunches spaced down to 4 ns. This gave CesrTA the flexibility to transversely and longitudinally stabilize bunch trains with a bunch spacing of any integer multiple of 2 ns greater than 4 ns.

2.4.4.1 14 ns Feedback System

The 14 ns feedback system uses a standard set of four CESR beam position buttons as the input. Pairs of button signals are connected to hybrid combiners which output both the sum and difference of the two signals. The vertical feedback system uses the signals from combining the top and bottom button signals together, thus yielding a difference signal which is sensitive to vertical position. Likewise, the horizontal system uses the difference of the combined inner and outer button signals. The sum of all four button signals is used as the longitudinal system input. The horizontal system block diagram is nearly identical to the vertical system block diagram and can be seen in Fig. 2.114.

Signals are acquired at 71.4 MHz by a direct sampling 10 bit analog to digital converter (ADC). This rate allows sampling at the traditional CESR bunch spacing of 14 ns. Longitudinal signals are processed with displacement or phase detection, sample and hold, displacement or phase offset correction, and filtering circuits. Transverse signals are filtered then sampled in a DSP. The output is the beam error signal represented by a ± 500 mV analog signal that is updated every 14 ns[35].

For the transverse systems, the error signal is modulated into a bipolar pulse. The pulse is amplified by an ENI3200L 200 watt power amplifier with bandwidth from 250 kHz to 150 MHz. The amplified pulse is sent to a 1.16 m stripline kicker. The kicker is shorted at one end, with an electrical length of 3.5 ns. The kicker has an impedance of 50 ohms and is constructed from OFHC (oxygen free, high thermal conductivity) copper sheet. The stripline kicker is further described and illustrated in section 2.4.3.3.

The longitudinal error signal is amplified by a 1 kW solid state amplifier. The signal is transmitted to the beam through an 1142 MHz resonant frequency cavity kicker. The cavity kicker has three coupling ports for drive and three coupling ports for load, for a total of six ports. The cavity has a loaded Q of about 14 and a field decay time of 3.9 ns[36]. A block diagram overview of the longitudinal system is in Fig. 2.115.

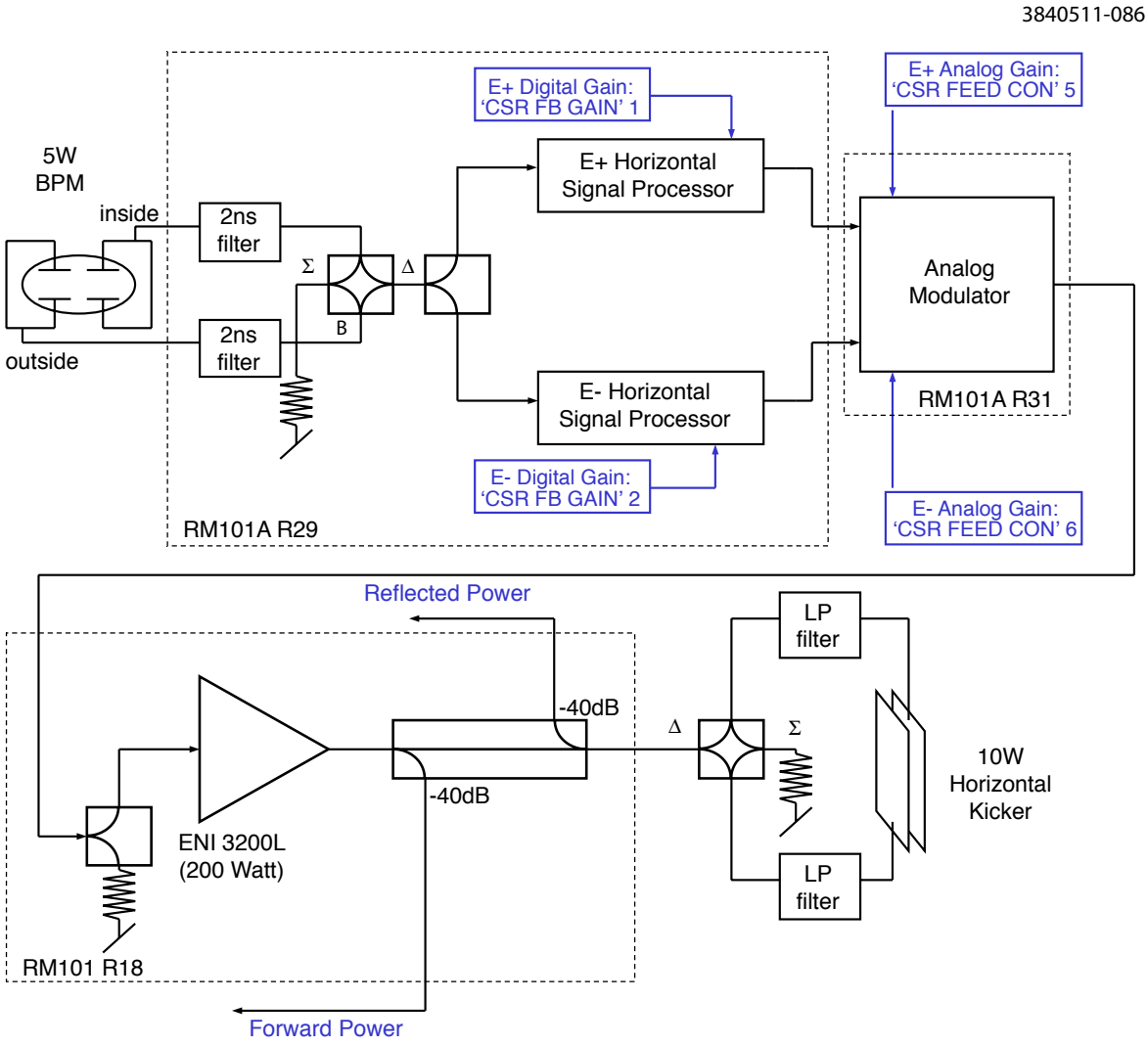

Figure 2.114: System overview of the horizontal 14 ns feedback.

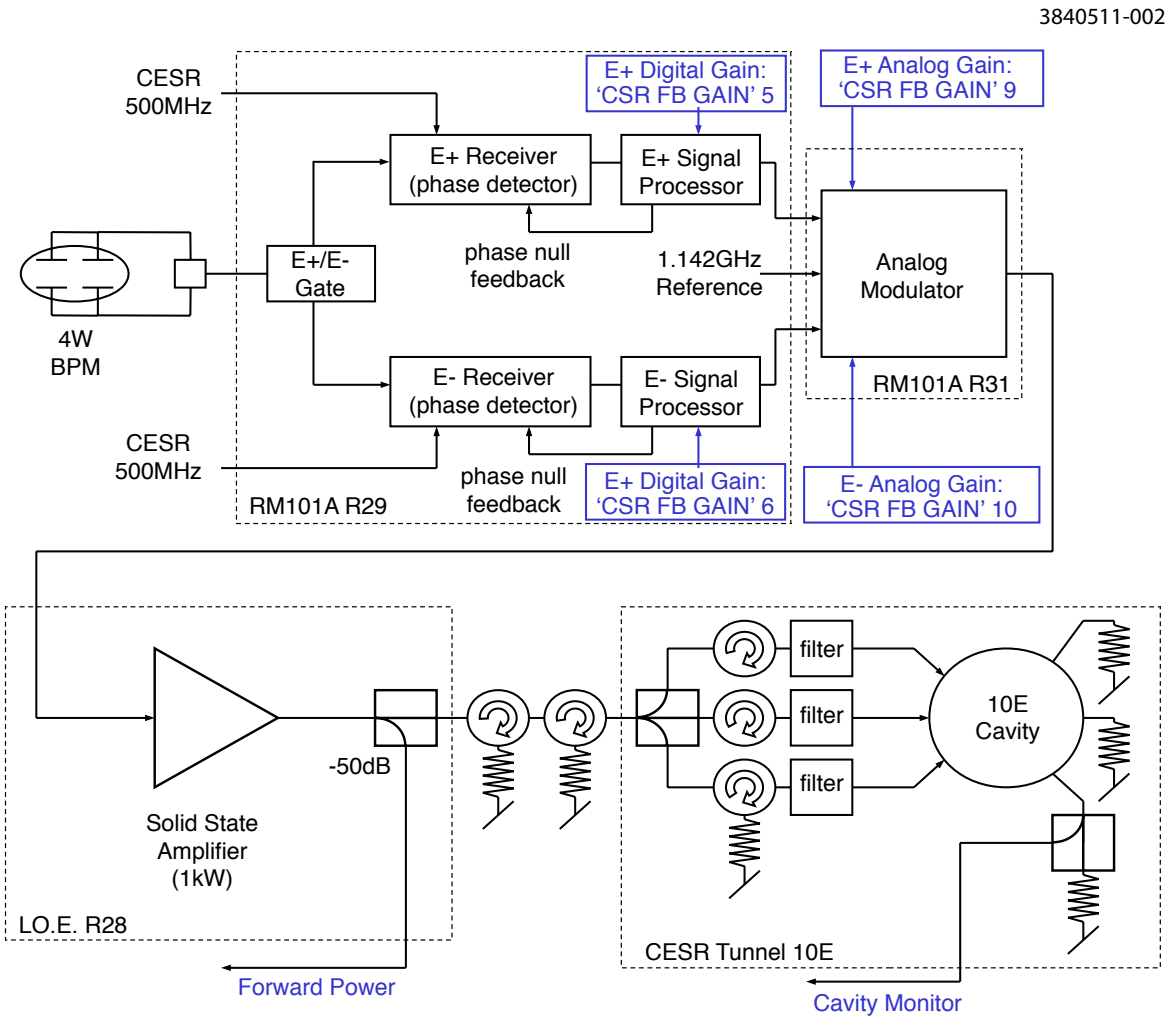

Figure 2.115: System overview of the longitudinal 14 ns feedback.

The 14 ns feedback system is controlled through the CESR control system multi-port memory (MPM). The MPM allows many devices to share a memory space. The DSPs access the shared memory for information on the gains and delays necessary for different CESR ring configurations.

2.4.4.2 4 ns Feedback System

The pre-existing feedback system described above was augmented to provide stability for bunches spaced down to 4 ns by adding three Dimtel iGp-1281F signal processors, one each for horizontal, vertical and longitudinal. The processors use the same beam input signals as the 14 ns feedback system as well as the same stripline and cavity kickers. A block diagram of the iGp is in Fig. 2.116.

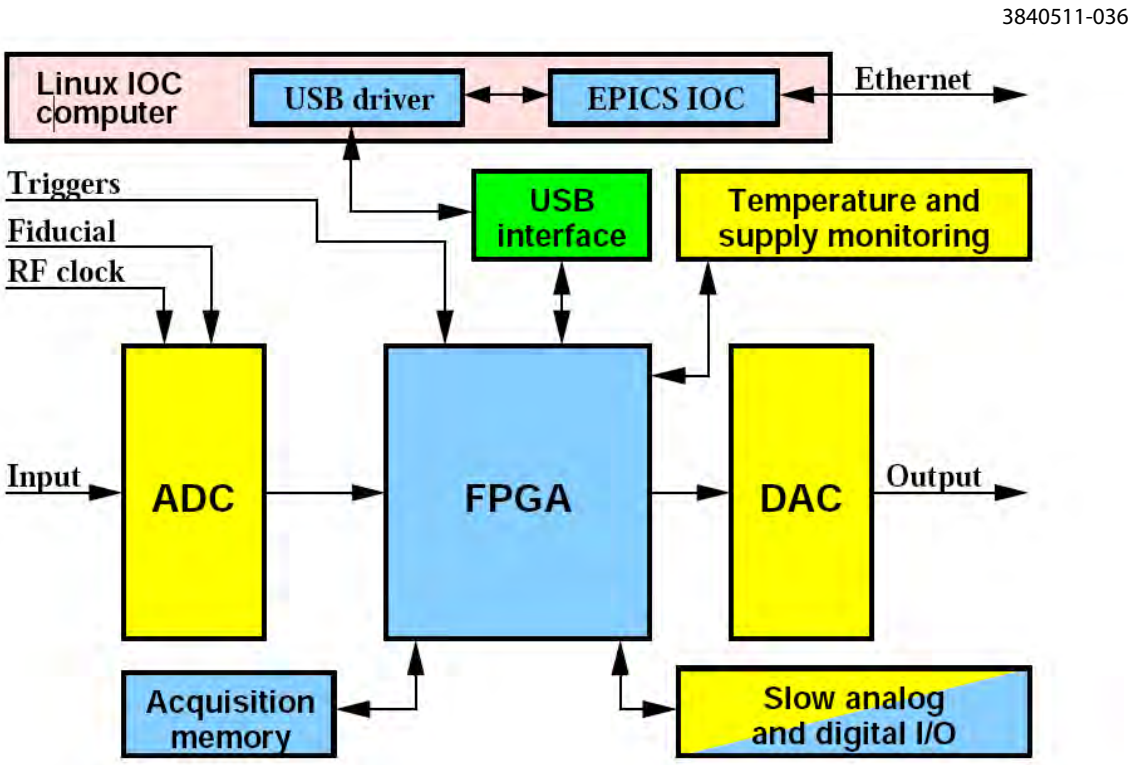

Figure 2.116: System overview of the Dimtel iGp 4 ns signal processor.

The new signal processors operate at 500 MHz and acquire the input signals with 1.26 GHz bandwidth with high speed 8 bit ADCs. The signals are processed by a dual port memory field programmable gate array (FPGA) for control computations including applying a finite impulse response (FIR) filter with up to 16 taps. A high speed DAC drives the output signal with 12 bit resolution, a rise time under 250 ps and a fall time under 350 ps.

The FPGA is controlled by an embedded EPICS (experimental physics and industrial control system) input-output controller (IOC). The IOC is connected to the FPGA by universal serial bus (USB) and to the CESR control system via Ethernet[37]. Computing scripts and display screens, on the CESR control system, are used to control the parameters of the signal processor and to acquire

and analyze data. An additional software EPICS IOC running on the CESR control system and a service program provide an interface from the CESR MPM to the iGp devices.

Completely configurable bunch control allows the setting of any combination of the 1281 available RF buckets in CESR for feedback or excitation. The 1281 buckets are spaced 2 ns apart and the iGp has the ability to resolve the individual bunches, however, the system is limited by the electrical length of the stripline kickers and the field decay time of the cavity kicker to provide differing feedback kicks 4 ns apart.

2.4.4.3 Feedback System Results

The Dimtel iGp upgrade proved successful in stabilizing both electron and positron beam (separately), in a wide array of bunch patterns and spacings. For example, at 5.3 GeV the single bunch damping in the horizontal system is shown in Fig. 2.117. In this drive-damp measurement, the beam is driven for 3 ms and then allowed to damp. The black curve shows the natural damping without any horizontal feedback. The blue curve shows the result with the 4 ns feedback on. The feedback drops the maximum excitation by about 15 dB and the beam is damped back to its noise floor within 500 μs.

2.5 General Accelerator Modifications and Upgrades

2.5.1 Alignment and Survey Upgrades

Meeting the more stringent alignment tolerances specified by the CesrTA project required an upgrade to both the survey monument hardware and the survey equipment. All upgrade changes essentially revolved around the conversion of main surveying instrument from a Leica TDM5005 total station to an API Tracker III laser tracker with interferometer. The laser tracker required monument hardware which would accept the 1.5 inch spherically mounted reflectors (SMR's), and also supporting instruments which could accurately measure the gravity based heights of the reference target, since at the time of purchase no laser tracker had an integrated high precision gravity based level and compensator. Thus, a Leica DNA03 digital level and staffs completed the survey instrument upgrade.

After some study of the available hardware, and a training and observation trip to Lawrence Berkeley National Laboratory's Advanced Light Source we chose to use Hubb's Machine and Manufacturing, Inc. drift nests and floor targets. (see Fig. 2.118, Fig. 2.119 and Fig. 2.120 below). Tack welding the drift nests onto Uni-Strut gussets resulted in cost effective and very stable wall targets, which attached to our existing Uni-Strut ribs in the tunnel walls. The floor targets were permanently epoxied into holes drilled in the concrete floor of the tunnel with a core drill. The o-rings covers and stainless steel construction of the floor targets provided good protection against water infiltration and corrosion. Triplets of two wall targets (on inside and outside tunnel walls) and one floor target (near the center of the tunnel floor) spaced at approximately 8 to 10 meters apart provided the necessary geometry to meet the alignment tolerances.

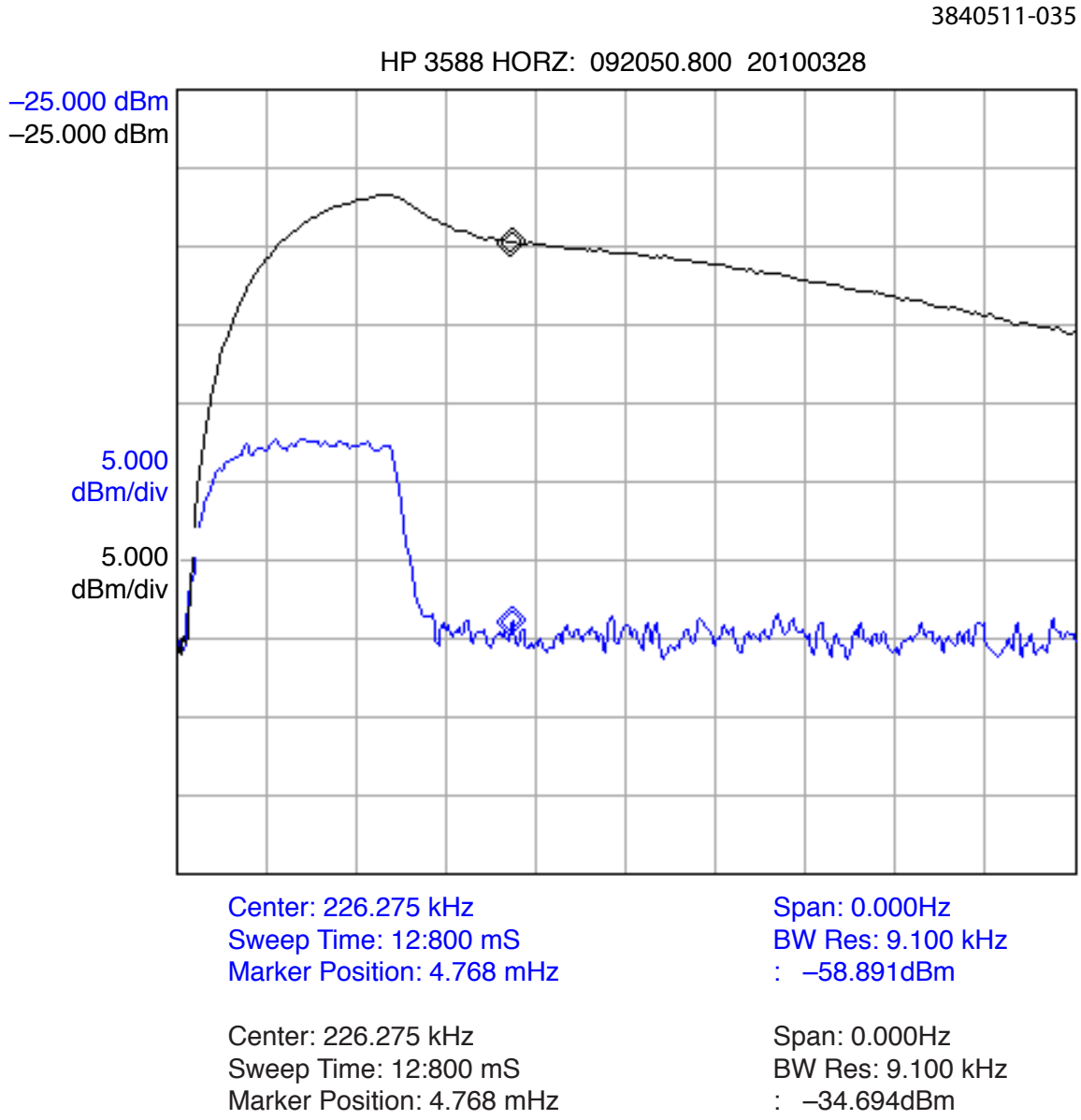

Figure 2.117: A drive-damp measurement with the horizontal 4 ns feedback.

3840511-347

Figure 2.118: Wall Target attached to tunnel Uni-Strut.

Figure 2.119: Floor target.

Figure 2.120: Floor target with cover removed.

2.5.2 Wiggler Straight Section

The CESR storage ring required extensive modifications for the straight section that contained the CLEO-c high energy physics (HEP) experimental detector[1]. During HEP operation this straight section was a micro-beta insert utilizing four superconducting quadrupoles and two permanent magnet final focus quadrupoles, all of which were oriented with approximately 4° tilts to compensate the CLEO solenoidal magnetic field. There was an additional pair of skew quadrupoles within the interaction region straight section to complete the solenoid compensation. During HEP operations the electron and positron bunches crossed at the interaction point with approximately a ±2 mrad crossing angles, created by four horizontal separators placed symmetrically in the arcs of CESR. The layout of the HEP interaction region straight section is displayed in Fig. 2.121.

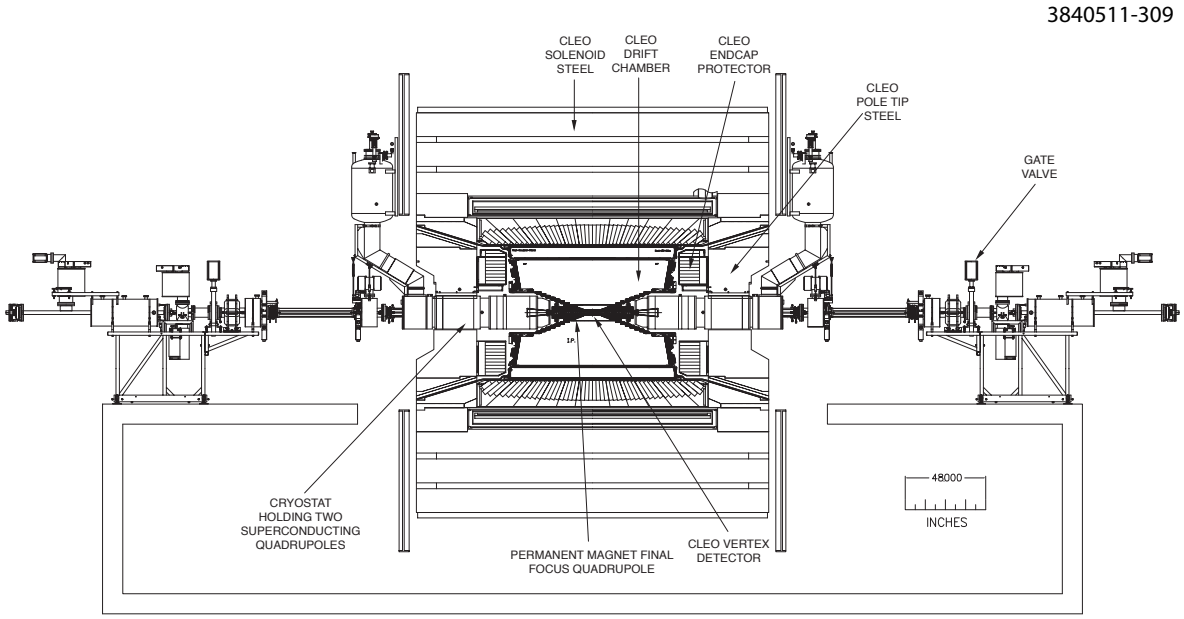

Figure 2.121: An elevation view of the CESR-c/CLEO-c interaction region before reconfiguration as the wiggler straight section for CesrTA. The central section of the CLEO-c detector, the final focusing superconducting quadrupoles and the connecting vacuum chambers were removed during the CesrTA installation.

As a part of the CESR-c/CLEO-c HEP program, twelve superconducting wigglers (SCWs) were installed in the southern one third of CESR[38]. For 2.1 GeV operation, these wigglers provided 90% of the radiation damping in CESR and, in their original arc locations, could be used for emittance control of the colliding beams. During CESR-c/CLEO-c HEP operations, 6 of the 12 SCWs were installed as two triplet SCWs, located at two straight sections, namely L1 and L5, and the remaining 6 SCWs were in shorter straight sections between L0 and L1, and between L0 and L5. For ultra low emittance operation for CesrTA, all twelve wigglers must be located in regions with zero dispersion. The CesrTA lattice provides for zero dispersion regions in the L0, L1 and L5 straight sections, which are shown above in Fig. 2.1. Therefore six of the CESR-c wigglers needed to be relocated to the CESR L0 straight, in place of the CLEO detector. The other six wigglers, located in the L1 and L5 straight sections, were permitted to remain in place.

During the July 2008 shutdown, the central portion of the CLEO detector was decommissioned

by removing the superconducting, normal conducting and permanent quadrupoles, the steering magnets for CESR, the CLEO endcap detectors, the vertex detector, the drift chamber and all of their associated cabling along with approximately 17 meters of vacuum chambers, all of which were located between the soft bend dipole magnets. A pair of bridging I-beams was installed through CLEO iron to support the quadrupole and steering magnets and the SCWs, which were positioned in the central portion of the L0 straight section. The six SCWs originally in the short straight sections between L0-L1 and L0-L5 were the wigglers relocated to the L0 long straight section. With the relocation, all 12 SCWs are positioned in the long straight sections, in which the optics can be configured for zero dispersion, to produce the smallest possible beam emitances. Fig. 2.2 shows the beam pipe, the conventional magnets and the six SCWs placed within the vacated CLEO detector's solenoid iron yoke. Fig. 2.122 and Fig. 2.123 display two different views of the wiggler straight section.

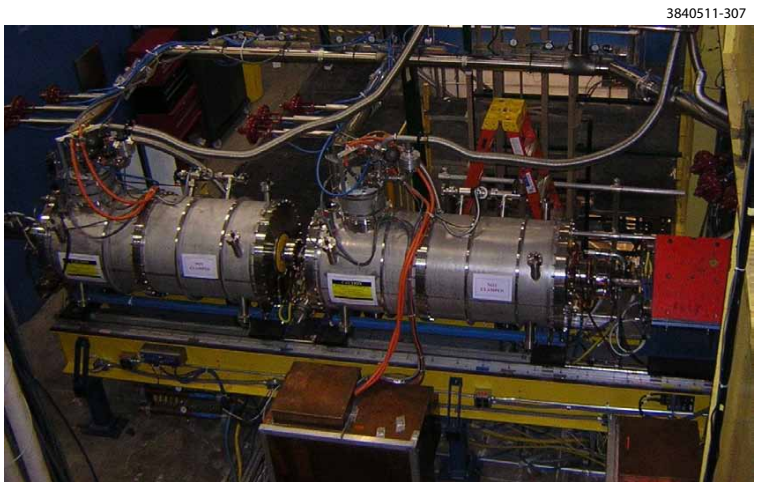

Figure 2.122: View of the wiggler straight section during the operation of CesrTA from the North on the East side of the wiggler straight section. Two of the wiggler cryostats are visible as is a part of Q01E (orange magnet to the right of the cryostats.)

2.5.3 L3 Straight Section

During CESR-c/CLEO-c HEP operations the straight section diametrically opposite to the wiggler straight section was configured to have a pair of electrostatic vertical separators, necessary to separate electron and positron bunches at the second horizontal angle crossing point for CESR, plus an additional six quadrupoles forming a mini-beta insert. A schematic of the original optics layout for the central region of the L3 straight section is found in Fig. 2.124. To accommodate the planned experimental regions in this straight section, a major change to the accelerator optics was undertaken. After the removal of the pair of electrostatic vertical separators (outboard of the Q48W and Q48E quadrupoles), a long experimental straight section was established in the north region of CESR (L3). This 12-meter section, as shown in Fig. 2.125, is currently hosting many SLAC EC beam pipes for study and diagnostics, including a set of 4-dipole chicane magnets with beam pipes equipped with EC detectors, and an aluminum beam pipe with grooved interior. A pair of retractable synch-light mirrors (highly polished beryllium) are set up for diagnostics and are used for beam profile measurements. A load-lock system for different surface samples was also installed in this section for measurements of secondary electron emission yield (SEY) as a

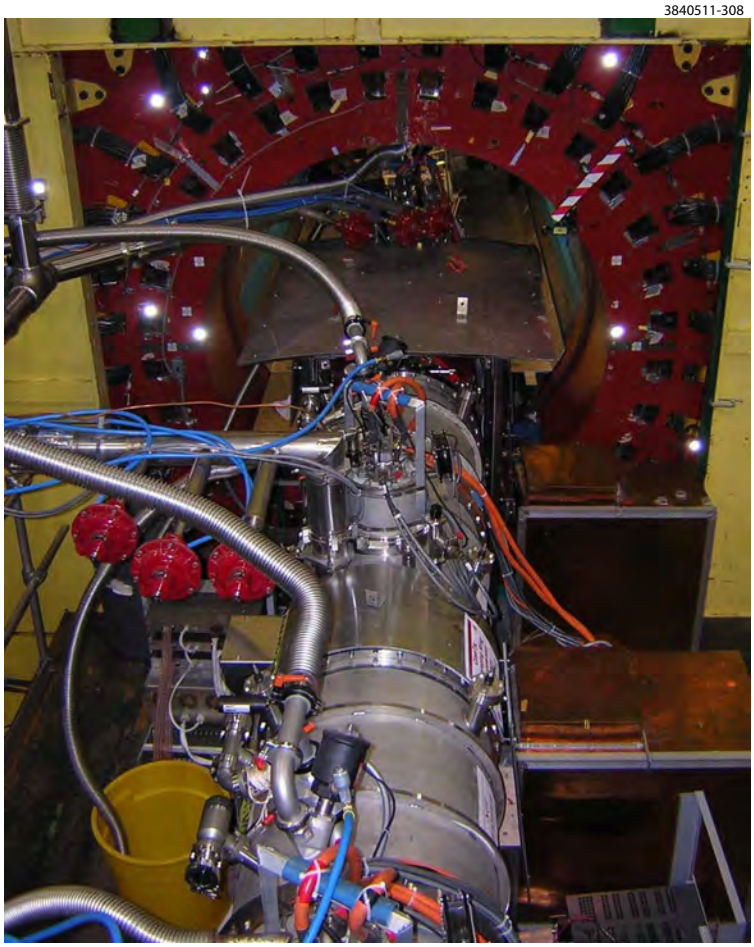

Figure 2.123: View of the wiggler straight section taken from the West side of the wiggler straight section looking into the former CLEO detector's pole tip.

function of synchrotron beam doses for commonly used vacuum chamber materials. Pictures of the experimental region are found in Fig. 2.126 and Fig. 2.127 and an assembly drawing of the L3 region is found in Fig. 2.128.

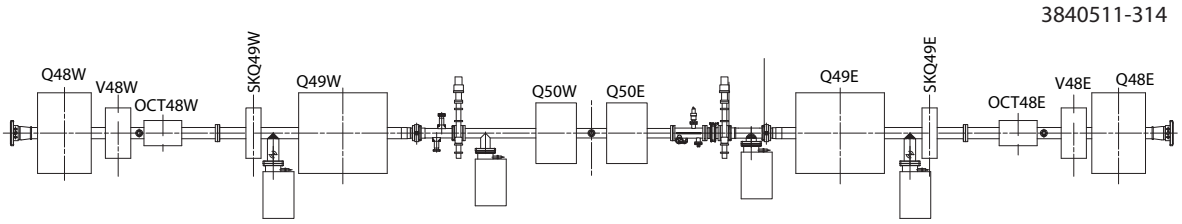

Figure 2.124: Schematic layout of the L3 optics between the vertical separators before reconfiguration for CesrTA operations.

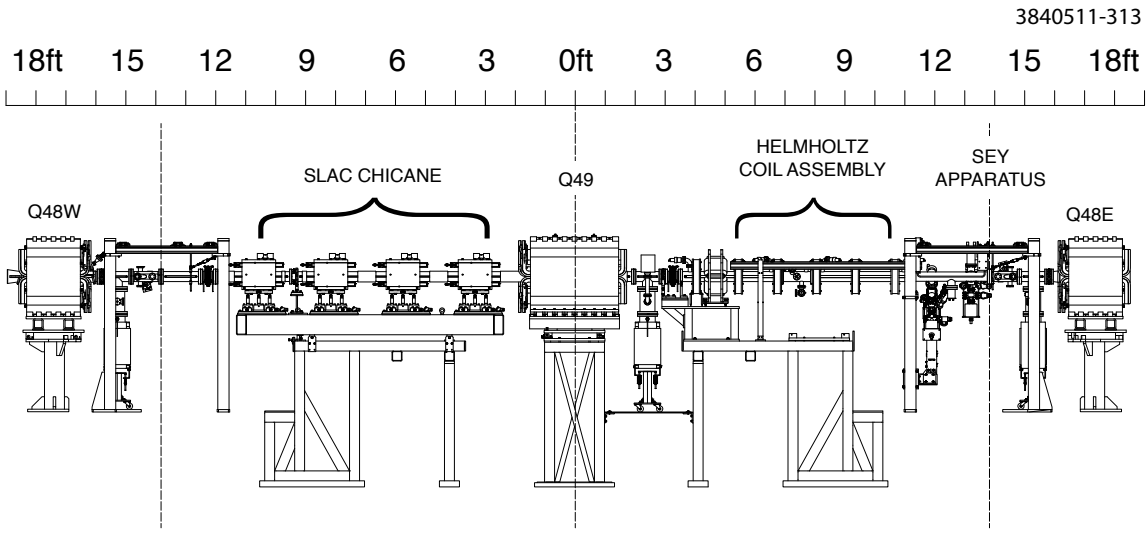

Figure 2.125: Schematic layout of the L3 experimental region. The experimental area includes the following vacuum chamber test regions: a chicane section, a region that has Helmholtz coils around the beam pipe to allow for chamber processing via bakeout etc., and an SEY apparatus with a lock-load mechanism to permit easy access for changing vacuum chamber wall surfaces.

2.5.4 Solenoid Windings

Solenoid windings on drift sections of storage rings have been successfully employed to reduce the effect of electron clouds in other storage rings.[39],[40]. Although the total drift section length of CESR is only approximately 15% of the circumference and is not expected to play a major role in the electron cloud dynamical effects for the entire ring, elliptical solenoid windings have been added to cover approximately 80% of this drift length. The windings were wrapped directly on the CESR vacuum chamber after a thin Kapton insulating layer was added around the radial outside of the chamber to enlarge the radius of these corners. In a few sections of the storage ring the beam pipe is circular so in these places the windings are cylindrical solenoids. In the experimental region in the L3 straight section, several Helmholtz coils were employed to allow better access to

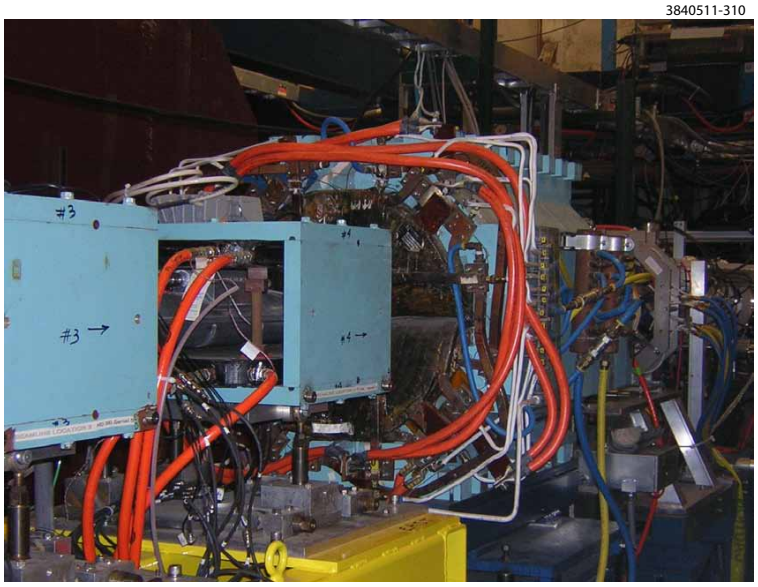

Figure 2.126: View of the L3 experimental region looking to the East and showing two of the chicane magnets in the foreground followed by Q49.

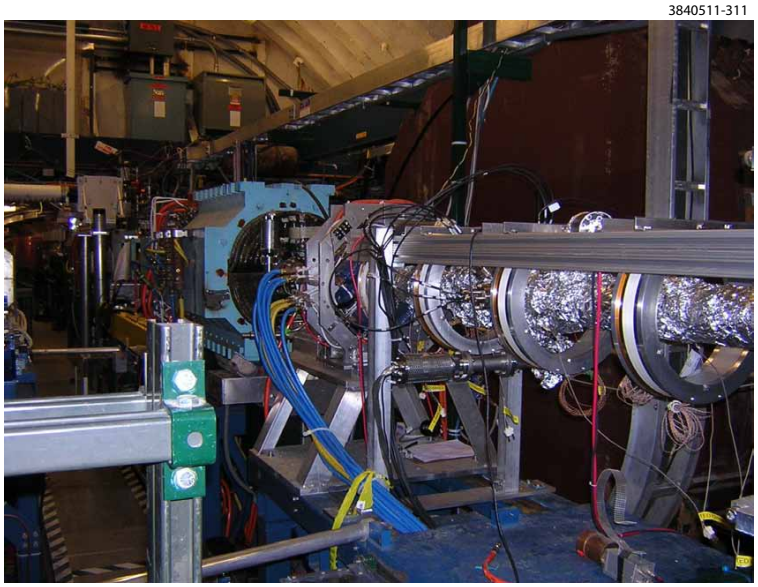

Figure 2.127: L3 experimental region viewing Q49 from the East and having the Helmholtz coils around the beam pipe for studies of Electron Cloud suppression. The picture also shows the Helmholtz coils surrounding the vacuum chamber as it is being prepared for a bakeout.

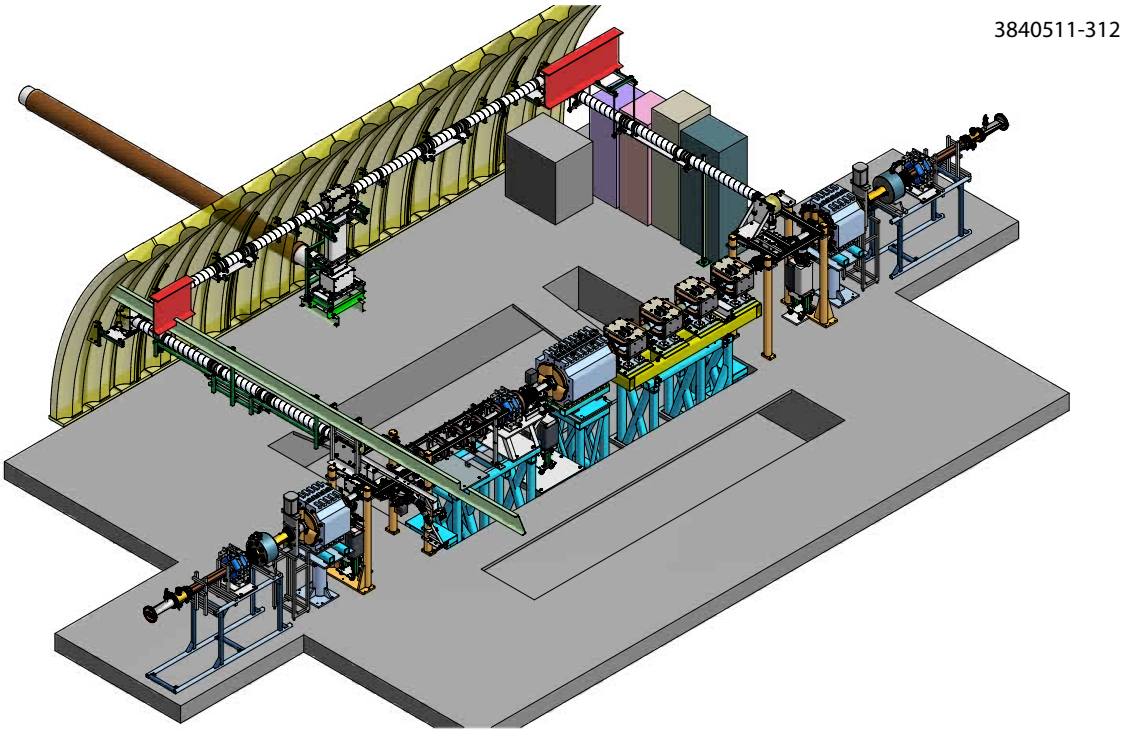

Figure 2.128: Final assembly drawing of the CesrTA beam line viewing L3 from above and the North and East. The pipes coming off of the CESR beam line to the south, transport the light from the vBSM's mounted just to the North (center of straight section) of the Q48W and Q48E quadrupoles (the outermost large blue magnets.)

the vacuum chamber; the spacing between the coils was set to have the longitudinal field for these coils approximately the same as in the standard solenoid windings. The cable, employed for the windings wrapped directly on the beam pipe, is radiation hard number 10 (AWC) gauge insulated wire, which is wound in a single close-packed single layer. A few examples of the solenoid windings maybe seen in Fig. 2.127, Fig. 2.129, Fig. 2.130 and Fig. 2.131. Windings in adjacent drift sections are clustered together and connected in series to one switching DC power supply, where an effort has been made to reduce the net longitudinal magnetic field by arranging the polarity of the windings to roughly balance the number of turns which have the current flowing clockwise around the vacuum chamber with those where it is flowing counter-clockwise. This reduces the local horizontal-vertical coupling of the beam's motion caused by each supply powering an individual cluster of solenoid windings.

The power supplies are generally unipolar 25 A switching DC power supplies operating off of the common 65 VDC ring magnet power supply bus. The power supplies function with the same control system hardware and software as the CESR steering power supplies. The winding resistance for the adjacent drift sections, as clustered together and connected in series, is less than 2.5 Ω. This resistance is low enough to allow the full 25 A of current. In two instances where the solenoid windings surround the shielded pickups, 100 A bipolar supplies were installed (and limited to ± 25 A operation) to permit sweeping the solenoid field over both polarities for the shielded pickup measurements.

During installation the polarities of the windings for all of the separate drift sections was verified to have the required alternation needed to reduce the horizontal-vertical coupling effects. After installation the magnitude of the longitudinal magnetic field was measured to be approximately 40 G for a 25 A excitation in the standard CESR beam pipe windings. A positron single bunch in 2 GeV conditions was used to check the coupling error caused by each of the 16 clusters of windings. After adjusting the minimum tune split on the coupling resonance to be less than 0.0002, the change in the global coupling of the bunch was measured when all of the solenoid power supplies were excited to their full currents. With all solenoid power supplies at full current the accelerator minimum tune split on the coupling resonance was 0.0027. Since the solenoids were installed primarily to study their effect on the cloud's density, they are usually powered only during mitigation or shielded pickup measurements.

2.5.5 Controls and Software Upgrades

The conversion of CESR to a test accelerator to study low emittance beams and the effects of electron clouds has required significant additions or changes to the accelerator controls. The first set of changes is obvious from the preceding sections: the reconfiguration of the magnet controls for the convention accelerator magnet system. The change to CESR's optics and steering controls required the removal, installation, reconfiguration or re-cabling of 48 separate magnets in the ring for the wiggler and L0 straight sections. The elements, which are presently installed for CesrTA operations, are summarized in Table 2.3.

In addition to the aforementioned magnet supplies several other types of magnets were either moved or installed around the ring for CesrTA use. These include the wigglers that were moved into the wiggler straight section from their location in the storage ring's arcs between L0 and either L1 or L5 straight sections. Fig. 2.132 presents a view of some of the wigglers in the wiggler straight section and Fig. 2.133 shows one of the power supply control racks. The wiggler straight section's

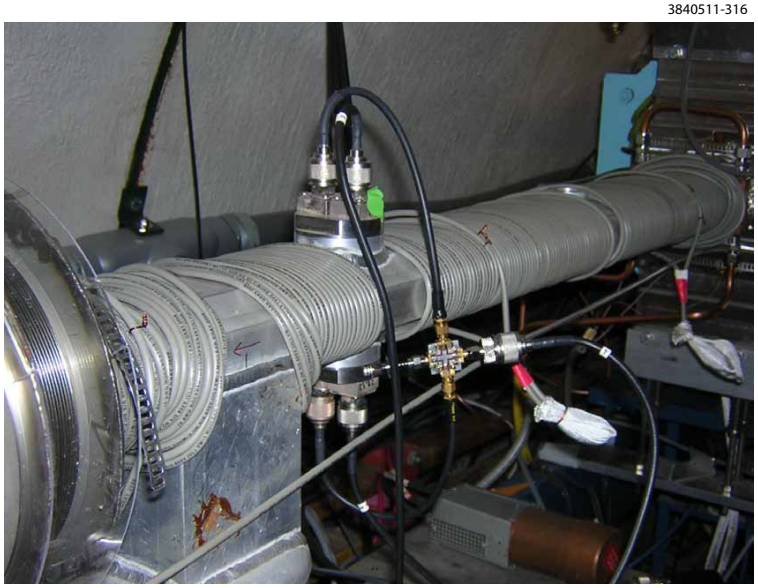

Figure 2.129: View of solenoid windings on one typical arc vacuum chamber.

Figure 2.130: View of solenoid windings on a second typical arc vacuum chamber.

Table 2.3: Listing of standard CESR accelerator elements, which were installed, re-cabled or reconfigured for CesrTA operation.

Name(s) of CesrTA Element	Type of Power Supply	Maximum Current	Maximum Voltage	Quantity
Q00W	Linear Pass-bank Regulated	250 A	28 V	1
Q01W, Q01E	Precision Chopper Switching Regulator	80 A	55 V	2
Q02W (16T), Q02E (16T)	Precision Regulated EMI PS	1000 A	20 V	2
Q48W (6T dipole PS) Q48E (6T dipole PS)	In series with dipole magnets - Transrex PS's	700 A	300 V	1
Q48W (22T), Q48E (22T)	Linear Pass-bank Regulated	250 A	28 V	2
Q49W (22T)	Precision Regulated EMI PS	1000 A	20 V	1
H01W	Bipolar Chopper Switching Regulator	±12.5 A	±55 V	1
V01E	Bipolar Chopper Switching Regulator	±12.5 A	±55 V	1
V02W, V02E	Bipolar Chopper Switching Regulator	±12.5 A	±55 V	2
SQ01E	Bipolar Chopper Switching Regulator	±12.5 A	±55 V	1
SQ02W, SQ02E	Bipolar Chopper Switching Regulator	±12.5 A	±55 V	2
H49E	Bipolar Chopper Switching Regulator	±12.5 A	±55 V	1
V49E	Bipolar Chopper Switching Regulator	±12.5 A	±55 V	1
V48W, V48E	Bipolar Chopper Switching Regulator	±12.5 A	±55 V	2
SQ48W, SQ48E	Bipolar Chopper Switching Regulator	±12.5 A	±55 V	2

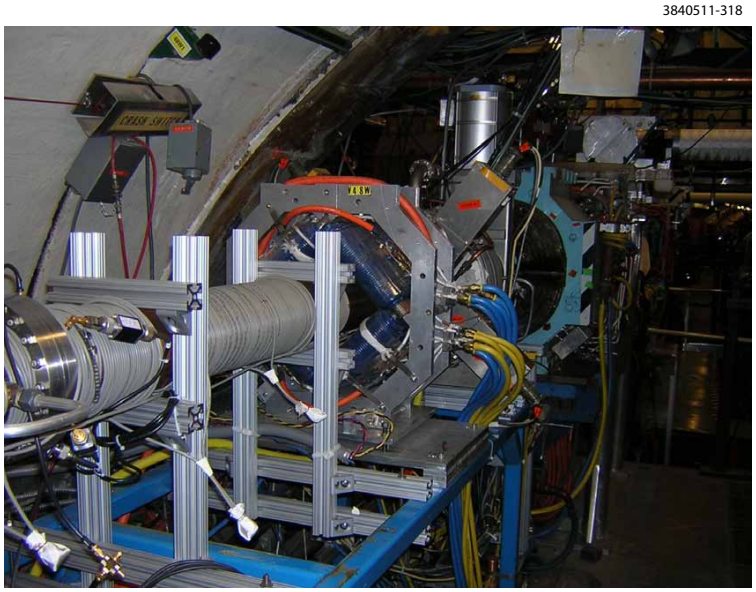

Figure 2.131: View of solenoidal field windings on the L3 straight section vacuum chambers.

construction required the relocation of six wigglers, their cryogenic controls and power supplies. The rack of control electronics includes a number of control and monitoring functions. The first is the "Ready Chain" for the protection of the magnets and power supplies, which requires such elements as the primary power, water and cryogenic cooling, the quench protection be enabled and heat sink temperature monitor be below its trip level, in order for the power supplies to turn on. The power supplies are a 300 A-3.3 V wiggler main supply and an 8 A-15 V steering trim supply. There is also monitoring circuitry including 16 channels of cryogenic temperature readouts, 20 channels of voltage, current, cryogen level and pressure sensor slow readouts, 8 channels of fast quench protection readouts.

The chicane magnets and their power supplies in the L3 experimental area are on loan from SLAC during the CesrTA experimental run. The chicane consists of four dipole magnets wired with field polarities of +, -, -, and +. They are powered with two DC supplies having a total of 235 A at 56 V. The system is current regulated using a Danfysic current transformer connected to a modified CESR 16-bit unipolar regulator card, which provides a 10 V maximum control signal to the main DC power supplies. The integrator in the lead-lag circuit of the regulation loop is adjusted to compensate the magnets' time constant of 0.074 sec. The modified CESR 16 bit magnet controller card was chosen as it has a common connection to the CESR magnet clock, which allows for coordinated excitation of the chicane magnets with other CESR magnets. This permits the simultaneous scaling of the current command to the chicane magnets with any other CESR magnet, e.g. to have coordinated scaling of the chicane field with other CESR steering elements.

During most of its operations, CESR stored beams with bunches spaced in multiples of 14 ns. As a result, all of the current monitoring instrumentation was configured for 14 ns as the minimum spacing. To accommodate the multiple of 4 ns-spaced bunches for CesrTA, a new current monitor was developed. This current monitor utilizes a standard BPM button position monitor connected to one of the new CBPM modules (section 2.4.1), which was programmed specifically to return a constant times the sum of the button signals as the bunch current. This monitor is capable of measuring all stored bunches with a minimum of a 4 ns-spacing over the desired bunch current

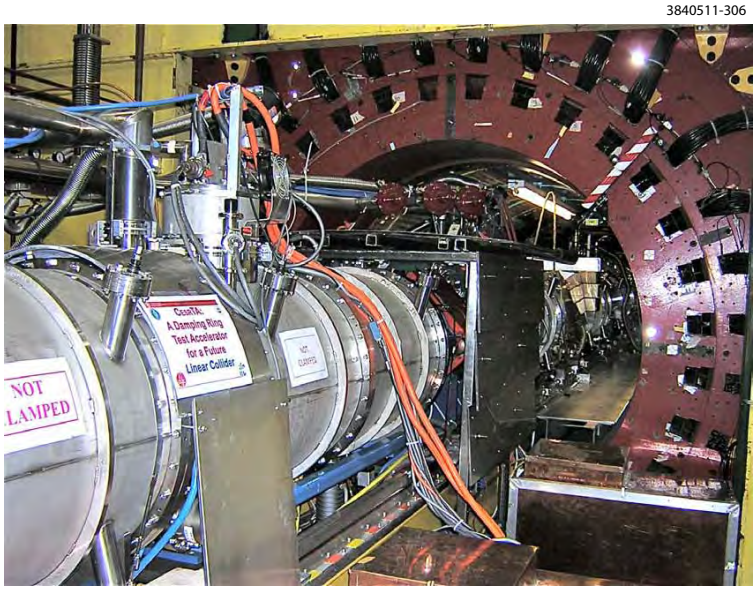

Figure 2.132: Wigglers in the wiggler straight section with their controls. The picture shows a view looking into the former CLEO detector with two of the three wigglers displayed to the left and the cabling of rightmost of these two in the center of the picture.

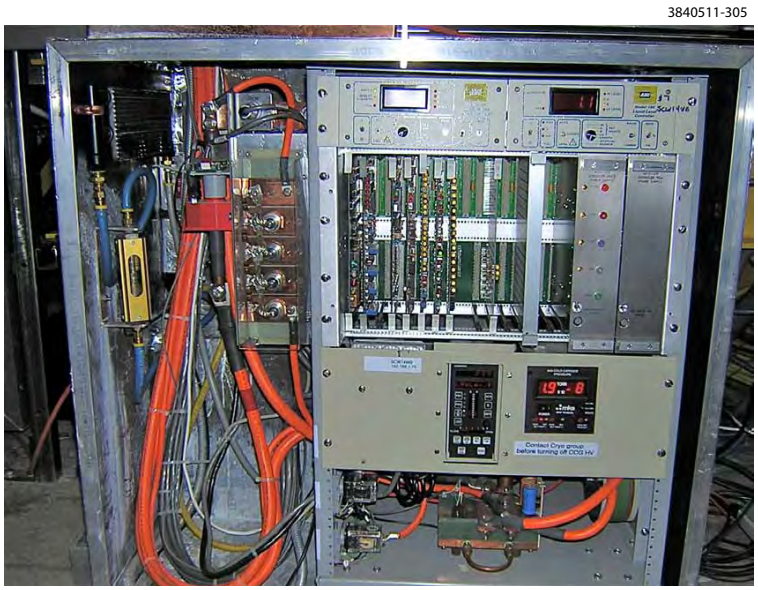

Figure 2.133: This picture presents view of the wiggler control rack containing all of the controls and the power supplies for the wiggler and its steering trim coils.

range with an update rate of 3 to 4 Hz.

The current monitor is an integral component utilized by the injection software. This program reads the current monitor to obtain the charge in each of the bunches, it then turns on the appropriate triggers to the gun pulser in order to accelerate a set of bunches to fill the storage ring. Substantial revisions were needed for this software to accommodate more general timing patterns for the stored bunches in CESR. This is the case since the lowest common harmonic frequency shared by the LINAC injector RF, the LINAC RF accelerator cavities, the synchrotron accelerator cavities and CESR's RF system is 71.4 MHz, equaling a bunch spacing of 14 ns. Injecting any multiple of 14 ns-spaced bunches only requires turning on triggers for the gun pulser at the correct time and the bunches can be accelerated and be stored in CESR with no change of any RF system phase. However, injecting 4 ns-spaced bunches requires an additional shift of all of the injector's RF phases for bunches to line up with proper CESR RF buckets. The upgraded injection software employed a new operator interface to specify which RF buckets were to be filled in CESR while accomplishing the required triggering for the gun pulser and injector RF phase shifts to store these bunches.

The injection software had new protection algorithms added, which limit the total current that can be stored in CESR. This is necessary for several reasons. When the superconducting wigglers are powered, software interlocks limit the total beam current to prevent their X-ray flux from damaging the downstream vacuum chamber walls. When the xBSM's optics chip is inserted in the X-ray beam, both software and hardware interlocks limit the total stored beam current. Also as a failsafe mechanism for communications failure of the bunch-by-bunch current monitor, the injection triggers are disabled whenever the sum of the bunch currents significantly disagrees with the DC current monitor.

Additionally hardware and software infrastructure was created for for xBSM, CBPM and RFA detectors. This included the installation of modest bandwidth and wide bandwidth interfaces to all of these detectors. It also included the software interfaces and data structures to operate this hardware and to communicate their data to the data acquisition software.

Chapter 3

Low Emittance Tuning Program

3.1 Introduction

Investigation of electron-cloud effects relevant to the performance of positron damping rings for linear colliders requires that we be able to circulate low emittance positron beams in CESR. We are interested especially in exploring the sensitivity to the emittance growth induced by electron cloud to the zero current equilibrium emittance. The specifications for the ILC damping ring are vertical and horizontal geomtric emittances $\epsilon_v = 2$ pm-rad and $\epsilon_h = 0.5$ pm-rad respectively. The CESR layout, with rather long dipoles and relatively few quadrupoles, is not by design a low emittance machine. In order to achieve horizontal emittance of a few nm-rad we exploit the installed superconducting damping wigglers which at 1.9T peak field reduce the radiation damping time by an order of magnitude. Lacking the precision girder based magnet alignment and stability of modern low emittance synchrotron light sources, we set our vertical emittance target at 10-20 pm-rad, anticipating that target to be both realistic and sufficient to the requirements of the electron cloud R&D program. We note that in recent years, order 1 pm-rad vertical emittance has been achieved in electron storage ring sychrotron light sources [41, 42].

The goals of the CesrTA low emittance tuning program are to develop beam based techniques for measuring sources of emittance dilution, and correction algorithms for minimizing the residual vertical emittance. Ideally, the procedure will routinely yield vertical emittance less than 10 pm and require only a few minutes (perhaps 10) of dedicated machine time. There are a variety of strategies that have proven effective at synchrotron light sources for extracting information about lattice errors from beam based measurements. Our technique is predicated on the requirement that it be readily extended to a ring with larger circumference (several kilometers) and many more magnetic elements than CESR. To that end we exploit the turn by turn capability of the precision beam position monitors to measure orbit, betatron phase advance and transverse coupling, and dispersion. We measure and then minimize closed orbit errors with dipole correctors, and focusing errors by adjustment of the independent quadrupole power supplies. Transverse coupling is minimized with skew quadrupoles. There are 25 skew quads in the storage ring, strategically located adjacent to the wiggler straights. Finally we minimize vertical dispersion using vertical steering magnets and skew quadrupoles.

Vertical dispersion is the principle source of vertical emittance and accurate measurement is obviously essential in order to minimize it. In CesrTA the accuracy of the dispersion measurement is

limited by systematics associated with the beam position monitors. The systematic effects include BPM button to button gain variation and physical tilt of the monitors. Beam based techniques for measuring gain and tilt are described in Section 3.3.

The low emittance tuning techniques that we are developing are applicable to all of the various lattice configurations deployed in CESR. But the development of the tuning methods is based almost exclusively on the 2.085 GeV lattice with 2.5 nm-rad horizontal emittance, that being the minimum that can be achieved in the storage ring with 12 damping wigglers operating at 1.9 T peak field. We routinely achieve vertical emittance less than 10 pm-rad, corresponding to an effective emittance coupling of $< 0.4\%$.

We have developed elaborate modeling and simulation codes to test the capability of the beam based diagnostics and the correction algorithms. When the simulation includes a random distribution of magnet misalignments consistent with known survey errors, and measurement errors based on the established BPM resolution and systematics, we find that the modeled results are consistent with the emittance that we measure after correction.

The simulations indicate that the effectiveness of the correction is indeed limited by the accuracy of the beam position monitor systematics, the sources of the BPM error being timing jitter, and as note above, button to button gain variation and BPM tilt.

Simulations further suggest that the number and placement of corrector magnets is more than adequate, and that additional skew quads for example would not yield better correction. We also find that the measured misalignments of quadrupoles, dipoles, wigglers and sextupoles, that are the principal source of vertical emittance, do not at present limit the emittance that we can achieve with our correction procedure. If, for example, the BPMs returned exact positions, then our tuning procedure would yield vertical emittance of order < 1 pm-rad.

It should be noted that the goal of the Phase I program is vertical emittance less than 20 pm-rad. The resolution of the beam position monitors and the tuning techniques we have developed readily yield vertical emittance below the 20 pm-rad target.

3.2 Sources of Vertical Emittance

We consider sources of emittance dilution in the zero current limit. Here we ignore electron cloud interactions, intrabeam scattering and other collective effects. In the ideal machine, the closed orbit lies in the horizontal plane. There are no vertical kicks and therefore, there is no vertical dispersion. Vertical emittance arises exclusively from coupling and vertical dispersion generated by magnet misalignments. (In fact that is not quite true. The emission of photons contributes to emittance via dispersion due to the change in energy of the emitting particle. But in addition to the change in energy, the emission of a photon at a finite angle with respect to the particle trajectory changes the transverse momentum of the particle, generating a finite emittance even in the ideal machine. We estimate that the vertical emittance in the limit of zero coupling and zero vertical dispersion is ~ 0.1 pm-rad [43, p. 19-22])

It is important to distinguish the normal mode emittance from the horizontal/vertical emittance that we measure in the laboratory. We identify the A-mode with horizontal motion and the B-mode with vertical. Transverse coupling will in general locally increase vertical beam size at the expense of horizontal, but it has no effect on the B-mode emittance unless it occurs in dipoles or wigglers where

there is synchrotron radiation. Otherwise, the vertical/horizontal aspect ratio can be restored by suitable decoupling. Transverse coupling that propagates into regions of finite horizontal dispersion will of course generate vertical dispersion. If that vertical dispersion is permitted to propagate through a bending magnet or a wiggler then the B-mode emittance is increased.

3.2.1 Misalignments

As noted, vertical dispersion can be generated directly by vertical dipole kicks, and indirectly via coupling of horizontal dispersion into the vertical plane. Sources of vertical kicks include quadrupoles vertically offset from the plane of the orbit and horizontal dipole magnets with non-zero roll. Wigglers produce no net dispersion, but do generate dispersion internally. A wiggler that is rotated (tilted) about the beam axis will generate vertical dispersion internally.

Tilted quadrupoles couple horizontal dispersion into the vertical plane as do sextupoles that are vertically offset from the plane of the ideal orbit. In addition, even perfectly aligned sextupoles introduce coupling if the vertical orbit is distorted by offset quadrupoles or rolled dipoles.

In order to quantify the sensitivity to alignment errors we consider the contributions to vertical dispersion, transverse coupling and vertical emittance of misalignments of the various guide field elements in turn. The procedure is to create a large number (N) of sets of randomly generated misalignments. We apply each set of misalignments to the lattice and compute dispersion, coupling and vertical emittance.

3.2.2 Machine Model

Lattice parameters and the effect of misalignments are modeled using the BMAD library[44]. The linear guide field elements are characterized by 6×6 matrices. Sextupoles are treated using a kick-drift-kick model. The wiggler magnet is modeled as a symplectic map that is based on an expansion of the field in terms of trigonometric and hyperbolic functions [45] . Misalignments are included by offseting and/or rotating the relevant phase space coordinates that are tracked through the misaligned element. Once the closed orbit has been computed, magnet matrices are recalculated so that offset and tilted quadrupoles include dipole and skew quad components, etc., yielding Twiss parameters and dispersion function appropriate to the orbit. The determination of the normal mode emittances is then based on that set of lattice functions that corresponds to the real closed orbit.

3.2.3 Quadrupole Offsets and Dipole Rolls

We begin by quantifying the effect of quadrupole vertical offsets and dipole rolls on the vertical closed orbit. We suppose that there is a distribution of alignment errors. That distribution will be based on the real survey of magnet positions. The measured distribution of quadrupole offsets (as of May 2011) is shown in Figure 3.1(left). The standard deviation of the distribution is 35 μm. The measured distribution of rolls for all of the storage ring dipoles is shown in Figure 3.1(right) and the standard deviation is 152 μrad. We assume that the standard deviation of the measurements is representative of the fundamental uncertainty of the magnet positions and roll angles. We generate a large number of configurations (1000) each with a Gaussian distribution of vertical quad offsets

and dipole rolls and compute the closed orbit for each configuration and the root mean square of the residual vertical orbit error, namely

$$\sigma_y = \sqrt{\frac{1}{N}\sum_{i=1}^{N} y_i^2} \tag{3.1}$$

where N is the number of beam position measurements.

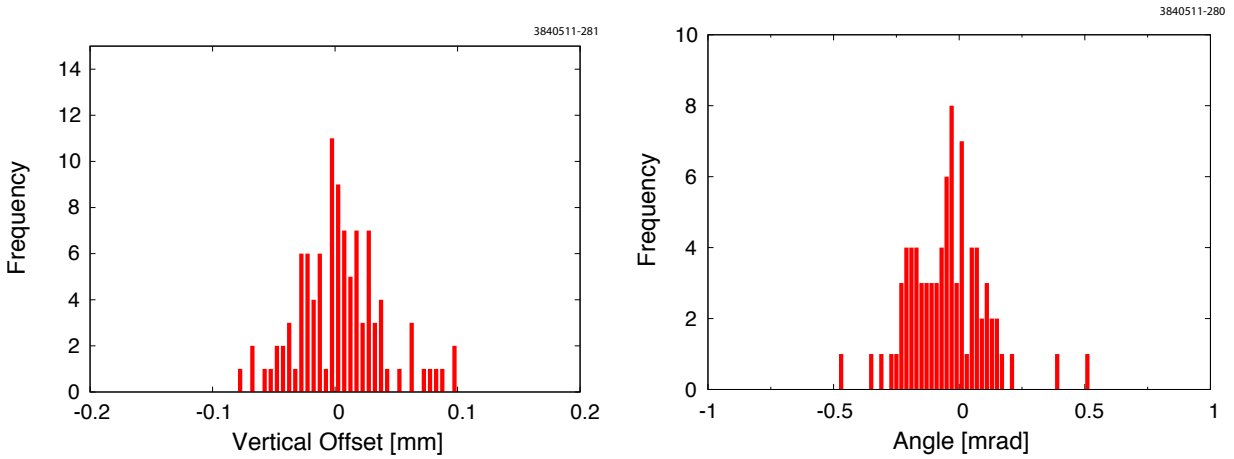

Figure 3.1: (Left) Distribution of measured vertical offsets of ring quadrupoles. The root mean square of the distribution is 35 μm. (Right) Distribution of measured rolls of ring dipoles. σ_θ = 152 μ-rad.

Figure 3.3 is a histogram of the rms vertical orbit error for the 1000 seeds with quadrupole and dipole alignment errors summarized in Table 3.1. The measured, uncorrected CESR orbit is shown in Figure 3.2. The rms residual vertical orbit error is 1.06 mm, near the peak of the distribution of possible orbit residuals for the 1000 seeds shown in Figure 3.3. We see that the measured zero corrector orbit is consistent with the measured distribution of quadrupole and bend misalignments.

In order to appreciate the sensitivity of vertical emittance to misalignments and the critical role of emittance tuning, it is useful to consider the effect of the quadrupole offsets. We compute the vertical emittance for 200 different machines, each with a distribution of vertical quadrupole offsets with standard deviation corresponding to the measured value of $\sigma_v = 35$ μm. The resulting distribution of emittances is shown in Figure 3.4. Over 90% of the seeds have vertical emittance greater than our 20 pm-rad target. Evidently beam-based measurement and compensation of emittance diluting misalignments will be essential to achieve our emittance goal.

Table 3.1: RMS quadrupole and dipole misalignments

Parameter	RMS
Quad vertical offset [μm]	35
Dipole roll [μrad]	152

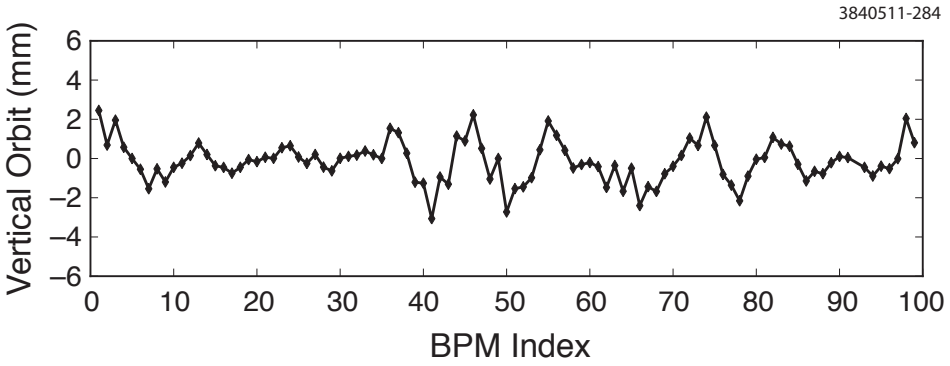

Figure 3.2: Measured vertical orbit in CESR with all vertical correctors turned off. The rms of the residual is 1.06 mm

3.2.4 Sextupoles

In CESR, the sextupoles are mounted on the same tables as the quadrupoles on keyed aluminum blocks. There is no independent means of adjusting sextupole position with respect to the quadrupole. Furthermore, as there are no survey monuments on the sextupole magnets, precision alignment is not practical. We estimate that the uncertainty of the alignment of sextupole centers is 250 μm.

3.2.5 Wigglers

Because of the very high dipole field in the wigglers, even small amounts of residual vertical dispersion can contribute significantly to the vertical emittance. The equilibrium vertical emittance in the storage ring is given by

$$\epsilon_y = C_q \frac{\gamma^2}{J_y} \frac{I_{5y}}{I_2} \tag{3.2}$$

where the quantum constant $C_q = \frac{55}{32\sqrt{3}} \frac{\hbar}{mc} = 3.84 \times 10^{-13}$ m, J_y is the vertical damping partition number, $\gamma = E/mc^2$, and

$$I_{5y} \quad = \quad \int \frac{(\eta_y^2 + (\beta_y \eta_y' + \alpha_y \eta_y)^2)/\beta_y}{|\rho^3|} ds. \tag{3.3}$$

The contribution to I_{5y} due to residual vertical dispersion in the wigglers is

$$\Delta I_{5y} \quad \sim \quad \frac{\langle \eta_y^2 \rangle}{\beta_y} \int \frac{|\cos^3(k_p s)|}{\rho_w^3} ds \tag{3.4}$$

$$\sim \quad \frac{\langle \eta_y^2 \rangle}{\beta_y} \frac{4l}{3\pi \rho_w^3} \tag{3.5}$$

In the CesrTA wigglers, $\lambda = 0.4$ m, and in the low emittance 2.085 GeV optics $\rho_w = 3.66$ m at $B_{max} = 1.9$ T , $\beta_y \sim 10$ m, and the wiggler length l =1.3 m. Then we find that the contribution to I_{5y} due to dispersion in the wiggler is

$$\Delta I_{5y} \sim 1.1 \times 10^{-3} \langle \eta_y [\mathrm{m}]^2 \rangle \, \mathrm{m}^{-1}$$

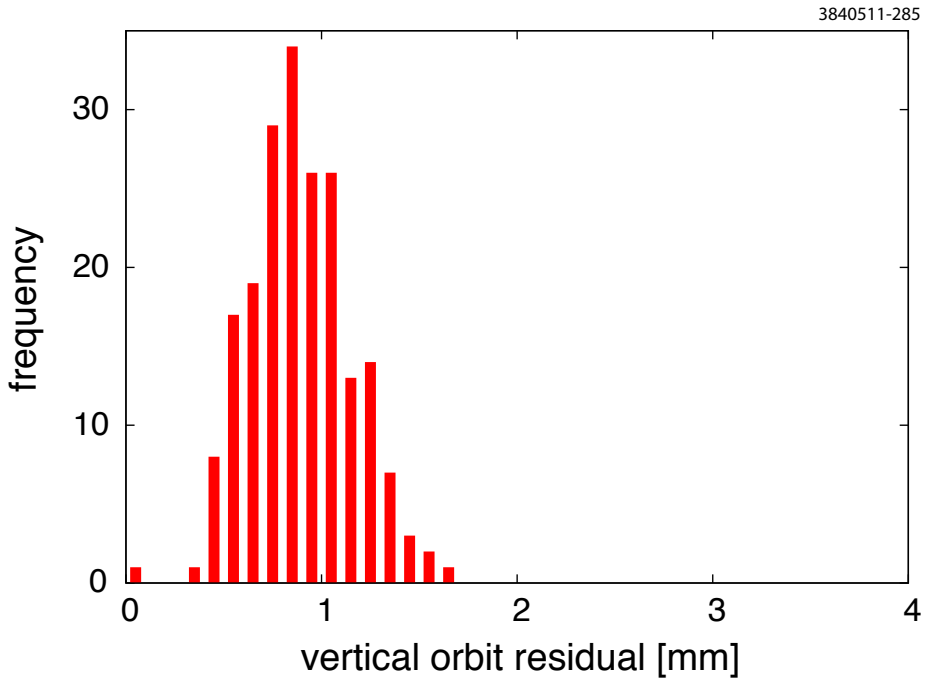

Figure 3.3: Distribution of residual vertical orbit offset for 200 configurations each generated with gaussian vertical quadrupole offsets with $\sigma_y = 35\,\mu$m and bend rolls with σ_θ =152 μm.

For a typical $E = 2.085$ GeV CesrTA lattice, $I_2 \sim 0.71$ m^{-1}. Therefore the contribution to the vertical emittance due to residual vertical dispersion in one of the 12 damping wigglers in the CesrTA lattice is

$$\Delta\epsilon_y \sim C_q \frac{\gamma^2}{J_y} \frac{\Delta I_{5y}}{I_2} \sim 10 \langle \eta_y[\mathrm{m}]^2 \rangle \,\mathrm{nm-rad}$$

A residual vertical dispersion of 1 cm in a single wiggler will generate a vertical emittance of 1 pm-rad.

The on axis integrated wiggler kick is zero. Rotation about the beam axis (tilts) and horizontal displacements do not generate closed orbit or dispersion errors. But because there is a vertical focusing component, vertical displacement of the wiggler generates vertical orbit and dispersion in the same manner as a vertically focusing quadrupole. In addition the internally generated dispersion can contribute directly to the emittance. Internally generated horizontal dispersion and the associated emittance is the principal component of the horizontal emittance for this wiggler dominated lattice. If the wiggler is tilted, so that there is a component of the nominally vertical magnetic field in the horizontal plane, then it will generate vertical dispersion and emittance. If we assume that the radiation is overwhelmingly generated by the wigglers (as is the case in CesrTA at 2.085 GeV and in the ILC damping ring), then the contribution to the vertical emittance if all of the wigglers are tilted by θ about the beam z-axis, is

$$\Delta\epsilon_y \approx C_q \frac{\gamma^2}{J_y} \frac{8\beta_y}{15\pi k_p^2 (\rho_w^y)^3} \tag{3.6}$$

where ρ_w^y is the peak wiggler bending radius in the vertical plane:

$$\rho_w^y = \rho_w / \sin\theta$$

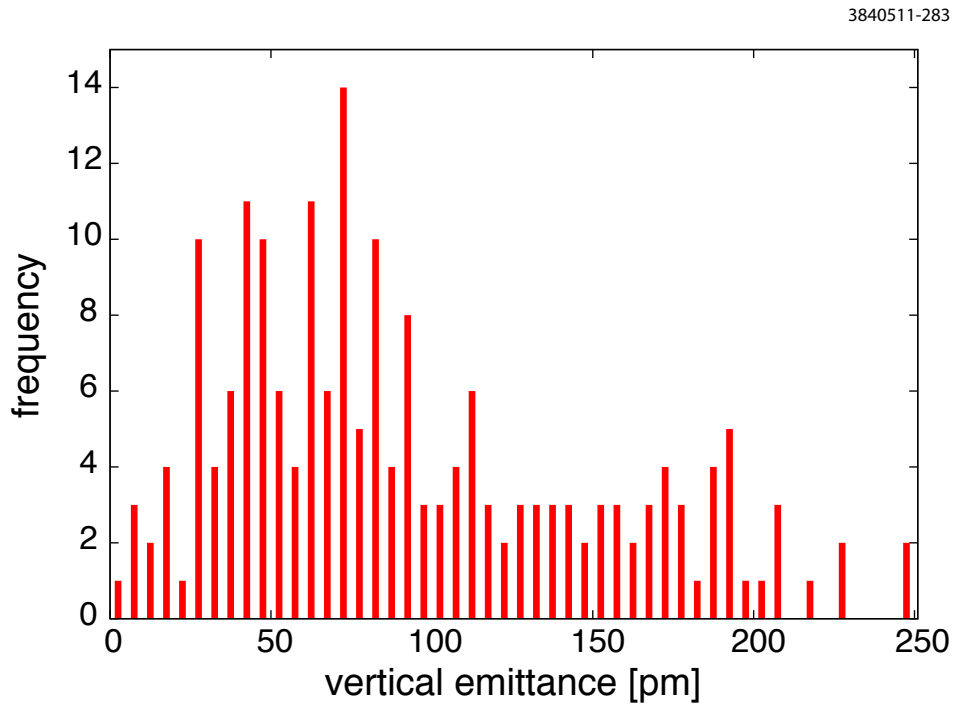

Figure 3.4: Vertical emittances of 200 configurations in the case that quadrupoles in each configuration are vertically offset with a Gaussian distribution with $\sigma_y = 150$ μm.

Then

$$\Delta\epsilon_y \approx (3.8 \times 10^{-13}\,\mathrm{m})(4080)^2 \frac{8(10\,\mathrm{m})}{15\pi(15.71\,\mathrm{m}^{-1})^2(3.66\,\mathrm{m})^3} \sin^3\theta = 0.9\sin^3\theta\ \mathrm{nm-rad} \tag{3.7}$$

If the wiggler is tilted (rotated about the beam axis) by $\theta = 100$ mrad, it will generate $\Delta\epsilon_y \sim 1$ pm. We believe the actual tilt angle to be less than $\sim 200\,\mu$rad. Therefore the contribution to vertical emittance from wiggler misalignment is negligible.

3.2.6 Survey

The alignment tolerances for the guide field magnets are summarized in Table 3.2. The table gives the root mean square of the measured distribution of positions for the elements for which data is available. The distribution of quadrupole tilts is shown in Figure 3.5. The values for sextupoles and wigglers are estimates. As noted above, the misalignments associated with vertical orbit errors, namely quadrupole offsets and dipole rolls, are consistent with the measured zero corrector orbit.

3.3 Beam-based Measurements

The low emittance tuning procedure relies on beam based measurements both to calibrate the beam position monitors and to determine sources of emittance dilution. The tuning procedure typically

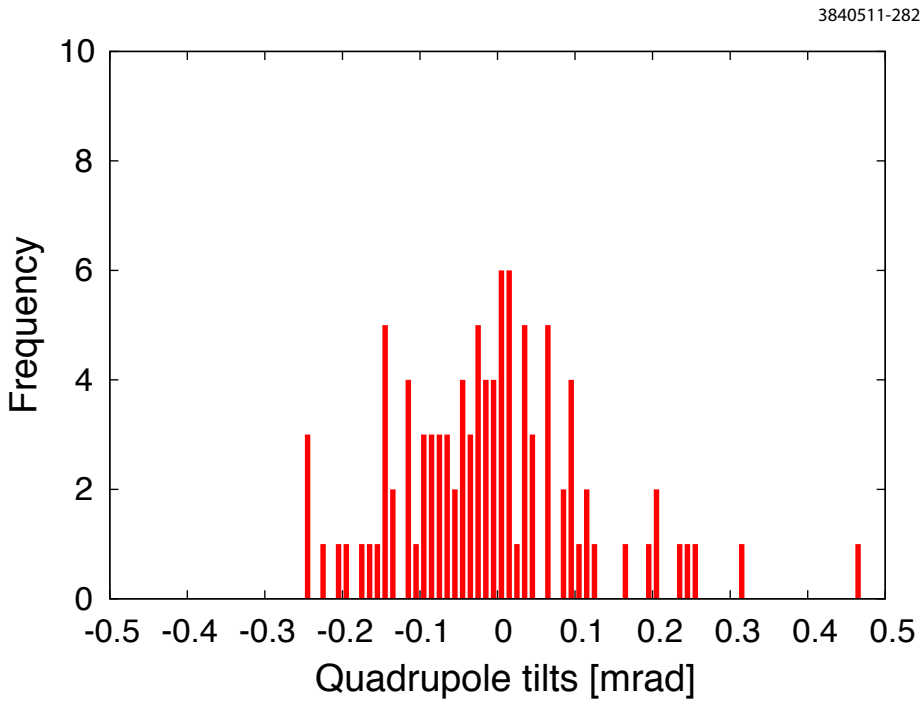

Figure 3.5: Distribution of measured tilt of ring quadrupoles with root mean square 133 μrad.

Table 3.2: Alignment tolerances after survey

Parameter	RMS
Quad tilt [μrad]	133
Quad vertical offset [μm]	35
Dipole roll [μrad]	152
Sextupole vertical offset [μm]	250
Wiggler roll [μrad]	200

begins with a measurement of the closed orbit. As described in Chapter 2 of this report, the beam position monitors have a single shot resolution of about 10 μm. After correcting closed orbit errors we measure and correct betatron phase and coupling, and finally vertical dispersion. Techniques for measuring the linear lattice functions are described in the remainder of this chapter.

Systematic effects limit the accuracy of our measurements of closed orbit, vertical dispersion, and to some extent, transverse coupling. The most significant systematic in the measurement of the closed orbit is a result of the uncertainty of the offset of the BPM with respect to the center of the adjacent quadrupole. Beam based BPM/quad centering is discussed below. The accuracy of the measurement of vertical dispersion is limited by variations in the gains of the BPM button electrodes and related electronics, and the physical tilt of the beam position monitors. We attempt to resolve these systematics with beam based measurement techniques.

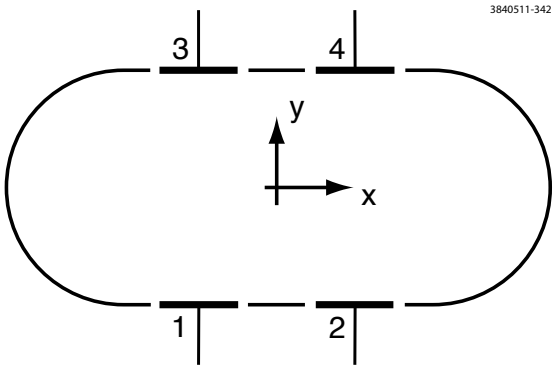

Figure 3.6: Button layout at a beam position detector

3.3.1 Phase and Coupling Correction

Betatron amplitude, phase and transvserse coupling are measured simultaneously. A circulating bunch is driven resonantly with magnetic shakers with the aid of a tune tracker at the transverse normal mode tunes.

At each of the four button electrodes (see Fig. 3.6) of each beam position monitor, we measure the intensity of the signal on each turn. Typically $N = 30,000$ turns of data are recorded. For the motion at the "horizontal" frequency the amplitude and phase of the motion at each button is extracted as follows

$$A_{j,sin,h} = \frac{2}{N}\sum_{i=1}^{N} \sin(\theta_{t,h}(i))\, a_j(i)$$
$$A_{j,cos,h} = \frac{2}{N}\sum_{i=1}^{N} \cos(\theta_{t,h}(i))\, a_j(i) \tag{3.8}$$

where $A_{j,sin,h}$ and $A_{j,cos,h}$ are the "in-phase" and "out-of-phase" components of the horizontal beam motion at button $j = 1, \ldots, 4$. In the above equation $\theta_{t,h}(i)$ is the phase of the reference signal from the horizontal tune tracker at turn i and $a_j(i)$ is the signal on button j at turn i. There is a similar equation for the vertical motion. In order to speed up the data taking process, horizontal and vertical measurements are done simultaneously. The above analysis depends upon the tunes being well enough separated from any low-order resonance so that the "cross-talk" between the horizontal and vertical mode sums in Eqs. 3.8 is negligible. In practice it is always easy to satisfy this condition.

After the button amplitudes have been measured and summed, the in-phase amplitudes in the x and y planes are given by

$$A_{x,sin,h} = C_x \frac{A_{4,sin,h} + A_{2,sin,h} - A_{3,sin,h} - A_{1,sin,h}}{A_{4,sin,h} + A_{3,sin,h} + A_{2,sin,h} + A_{1,sin,h}}$$
$$A_{y,sin,h} = C_y \frac{A_{4,sin,h} + A_{3,sin,h} - A_{2,sin,h} - A_{1,sin,h}}{A_{4,sin,h} + A_{3,sin,h} + A_{2,sin,h} + A_{1,sin,h}} \tag{3.9}$$

Similar equations describe the out-of-phase component at the horizontal tune and then a corresponding set gives the in-phase and out-of-phase response to vertical shaking. C_x and C_y are

constants dependent upon the geometry of the BPM. Here we are writing the dependence of position on button amplitude assuming linear dependence for illustration. In practice we include nonlinear depenence with the help of a nonlinear model of the BPM pickup response [46].

The next step is to turn the sine and cosine components into phase and amplitude

$$\begin{aligned} A_{x,h} &= \sqrt{(A_{x,sin,h})^2 + (A_{x,cos,h})^2} \\ \phi_{x,h} &= \tan^{-1} \frac{A^h_{x,sin,h}}{A^h_{x,cos,h}} \end{aligned} \tag{3.10}$$

and similarly for vertical shaking. In general, the horizontal mode motion of the beam can be written in the form [47]

$$\begin{aligned} x &= \gamma_c \, a_x \, \sqrt{\beta_h} \, \cos(\psi_{h,i}) \\ y &= -a_x \, \sqrt{\beta_v} \, [\overline{C}_{22} \, \cos(\psi_{h,i}) + \overline{C}_{12} \, \sin(\psi_{h,i})] \end{aligned} \tag{3.11}$$

where β_h and β_v are the beta functions at the BPM, $\overline{C}_{ij}$ are components of the coupling matrix, and

$$\psi_{h,i} = i \, \mu_h + \phi_{h,\beta} + \phi_{h,0} \tag{3.12}$$

with i being the turn number, μ_h being the horizontal tune, $\phi_{h,\beta}$ being the horizontal betatron phase at the BPM, and ϕ_0 being an overall phase offset independent of the BPM. In the above equation γ_c is a parameter dependent upon the coupling. γ_c is generally near 1 and can be ignored.

Comparison of Eq. 3.11 with the measured beam amplitude components gives

$$\begin{aligned} \beta_h &= k_{h,\beta} \, A^2_{x,h} \\ \phi_{h,\beta} &= \phi_{x,h} + d\phi_h \\ \overline{C}_{12} &= \sqrt{\frac{\beta_h}{\beta_v}} \, \frac{A_{y,h}}{A_{x,h}} \, \sin(\phi_{y,h} - \phi_{x,h}) \\ \overline{C}_{22} &= -\sqrt{\frac{\beta_h}{\beta_v}} \, \frac{A_{y,h}}{A_{x,h}} \, \cos(\phi_{y,h} - \phi_{x,h}) \end{aligned} \tag{3.13}$$

where $k_{h,\beta}$ and $d\phi_h$ are overall constants dependent upon the amplitude and phase of the shaker drive. A similar analysis is carried out for the vertical shaking data. Here the x and y motions are

$$x = a_y \, \sqrt{\beta_h} \, [\overline{C}_{11} \, \cos(\psi_{v,i}) - \overline{C}_{12} \, \sin(\psi_{v,i})] \tag{3.14}$$

$$y = \gamma_c \, a_y \, \sqrt{\beta_v} \, \cos(\psi_{v,i}) \tag{3.15}$$

where $\psi_{v,i}$ is the analog of $\psi_{h,i}$ in Eq. 3.12

$$\psi_{v,i} = i \, \mu_v + \phi_{v,\beta} + \phi_{v,0} \tag{3.16}$$

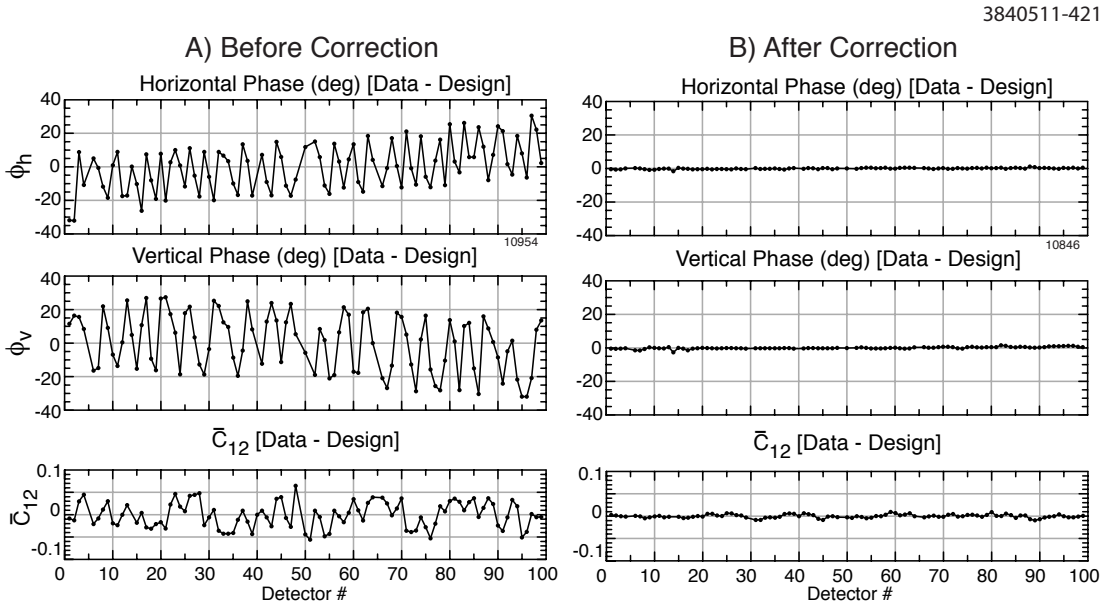

Figure 3.7: Example betatron phase and coupling correction. A) Measured betatron phase and $\overline{C}_{12}$ coupling matrix element before a correction. Plotted are the difference between the measured values and the design values as computed from the theoretical design lattice. B) Measured values after correction. A perfect correction would result in the measured values being equal to the design ones.

Comparison of this with the measured beam amplitude components gives

$$\begin{aligned} \beta_v &= k_{v,\beta}\, A_{x,v}^2 \\ \phi_{v,\beta} &= \phi_{x,v} + d\phi_v \\ \overline{C}_{12} &= \sqrt{\frac{\beta_v}{\beta_h}}\,\frac{A_{x,v}}{A_{y,v}}\,\sin(\phi_{x,v} - \phi_{y,v}) \\ \overline{C}_{11} &= -\sqrt{\frac{\beta_v}{\beta_h}}\,\frac{A_{x,v}}{A_{y,v}}\,\cos(\phi_{x,v} - \phi_{y,v}) \end{aligned} \tag{3.17}$$

The data is collected and analyzed for all 100 BPMs in less than 10 seconds.

Once a measurement is completed, the strengths of the quadrupoles and skew quadrupoles can be adjusted to correct the Twiss parameters and coupling. This is done using a software model of the CesrTA lattice. The correction procedure is in two steps. The first step is to vary the quadrupole and skew quadrupoles in the model until the betatron phases and the $\overline{C}_{12}$ as computed from the model most closely match the measured phases and measured $\overline{C}_{12}$. The measured beta is generally ignored since the betatron phase gives a cleaner signal. This is true since the betatron phase is insensitive to variations in the gains of the button signals. Similarly, the $\overline{C}_{11}$ and $\overline{C}_{22}$ data is typically ignored since the $\overline{C}_{12}$ data is generally cleaner. This is due to the insensitivity of the $\overline{C}_{12}$ data to button gain errors and rotations of the BPM in the x-y plane.

An example correction is shown in Fig. 3.7. Fig. 3.7A shows the difference between measured and design betatron phase and coupling before correction. Since the betatron phase can always be

scaled by an arbitrary additive constant, the phase constants $d\phi_h$ and $d\phi_v$ are taken to be such that the average measured phase is equal to the average phase as calculated from the design lattice. Fig. 3.7B shows the measured phase and coupling after correction. The deviation between actual and design values is now quite small. The vertical emittance ratio ϵ_v/ϵ_h due to coupling effects is roughly $\sigma^2_{\overline{C}_{12}}$ - the square of the RMS sigma of $\overline{C}_{12}$. After correction, $\sigma_{\overline{C}_{12}}$ is 0.004 so ϵ_v/ϵ_h due to coupling is of order 2×10^{-5} which is very small. The RMS betatron phase deviation after correction is about 0.5 degrees which translates to an RMS deviation of the actual β relative to the design β of less than 1%.

3.3.2 DC Dispersion

We have developed two techniques for measuring dispersion. The conceptually most straightforward method and the one that is conventionally used at other machines, is to measure the change in the closed orbit for a given change in beam energy. The beam energy is related to the RF frequency via the momentum compaction, typically $\alpha_p = 6.8 \times 10^{-3}$ for low emittance CesrTA optics. RF cavity bandwidth and energy aperture limit the frequency change to ± 4 kHz and energy offset to about 0.24%. Sensitivity to a vertical dispersion of 1 cm, requires that we measure an orbit difference of $24\,\mu$m. The CesrTA beam position monitors nominally have turn by turn reproducibility of order $10\,\mu$m and the orbit measurement is based on an average of several thousand turns. (The accuracy of the orbit measurement is limited by systematic rather than statistical effects.)

The disadvantage of this so-called DC measurement is that the speed with which the RF frequency can be changed is very slow. It is limited by the speed with which the cavity tuners can respond. A single measurement takes of several minutes.

3.3.3 AC dispersion

The AC dispersion method is a generalization of the phase and coupling measurement described above. A single tune tracker is set to lock on the synchrotron tune, so that we drive the beam on the synchrotron resonance via modulation of the RF phase. From the phase and amplitude of the horizontal and vertical components of the motion at each of the beam position monitors we extract the horizontal and vertical dispersion. The amplitude of the energy oscillations is determined by fitting the measured horizontal dispersion signal to the design values. We also rely on the design values of the longitudinal phase at each BPM, as it is not measured. Because the overall longitudinal phase advance is much less than a wavelength ($\nu_s \sim 0.05$), the error from using calculated rather than measured phase is small.

The amplitude of the energy oscillation is limited by the electronics that modulate the RF phase. It is typically of order 0.2% so that the measurement accuracy is comparable to that obtained from the DC technique. The AC measurement of dispersion is subject to somewhat different systematic limitations than the DC measurement. The AC dispersion is based on the BPM response exclusively at the synchrotron tune, whereas noise is filtered out of the DC measurement by averaging a large number of turns. Perhaps the most important advantage of the AC measurement is that as no change in RF frequency is required, the data can be collected in la few seconds.

3.3.4 BPM/quad centering

To reach the lowest vertical emittance it is necessary for the vertical closed orbit to be as close to the centers of the quadrupoles as possible to minimize vertical kicks which would contribute to the vertical dispersion. Correction of the closed orbit can be compromised by offsets between the magnetic center of a quadrupole and the electrical center of a near-by BPM.

To correct for this, these offsets are measured with the circulating beam. The standard beam based technique involves measurement of orbit changes with variation of the quadrupole's strength k [48]. One common method for determining the quadrupole center involves taking measurements at various beam positions and then interpolating the results to find the quadrupole center which is the position where the beam orbit does not change with variation of the quadrupole strength. This method can be slow due to the number of measurements needed. For large rings, this technique is not practical.

The measurement method developed at Cornell uses a variation of this technique:

1. Betatron phase and orbit are measured at two different strength settings for a given quadrupole at some location s_q. To differentiate the two measurements, one measurement is called the "base" measurement and is denoted with a subscript "0" and the other is called the "non-base" measurement.

2. The change in vertical orbit $dy \equiv y - y_0$ due to the variation in quadrupole strength is given by
$$dy(s) = dy' \frac{\sqrt{\beta_y(s)\,\beta_y(s_q)}}{2\,\sin\pi\nu_y}\,\cos(|\phi_y(s) - \phi_y(s_q)| - \pi\nu_y) \tag{3.18}$$
where dy' is the kick due to the change in quadrupole strength, and the Twiss parameters β, ϕ and ν are evaluated in the non-base configuration. From the phase data, the Twiss parameters can be calculated. Using the calculated Twiss parameters, a fit to the orbit difference data gives a measurement of dy'.

3. Using a fit to the betatron phase data, the change in quadrupole strength dk and the beta at the quadrupole can be calculated. The change in orbit dy can be written in the form
$$dy(s) = [y_{qc} - y_0(s_q)]\,dk\,L\,\frac{\sqrt{\beta_y(s)\,\beta_y(s_q)}}{2\,\sin\pi\nu_y}\,\cos(|\phi_y(s) - \phi_y(s_q)| - \pi\nu_y) \tag{3.19}$$
where y_{qc} is the quadrupole center, and L is the quadrupole length. Comparing the above two equations gives
$$y_{qc} = \frac{dy'}{L\,dk} + y_0(s_q) \tag{3.20}$$
A similar analysis holds for the horizontal plane.

4. The accuracy of the calculation depends upon the displacement of the beam from the quadrupole center dy_{beam}. This separation is given by
$$dy_{beam} = y_{qc} - y_0(s_q) = \frac{dy'}{L\,dk} \tag{3.21}$$
The closer the beam is to the quadrupole center, the more accurate the calculation of y_{qc}. If the beam is too far off from the center, an orbit bump is used to steer the beam towards the center and the measurement cycle is repeated until $|dy_{beam}|$ is within a set tolerance. Typically this is 300 μm.

The important innovation here is that the analysis incorporates the phase measurement which leads to a more accurate determination of the Twiss parameters and dk. This, in turn, leads to to a more accurate determination of y_{qc}. The result is that the tolerance on dy_{beam} can be increased which leads to a reduced number of measurement cycles and hence a shorter measurement time. The entire procedure in CESR — calibrating all 100 or so BPMs — has been automated and takes somewhat less than two hours.

3.3.5 BPM gains

The principal systematics limiting the accuracy of our measurement of vertical dispersion are variation of BPM button gains and BPM tilts. There are several effects that will contribute to gain errors, beginning with the button itself and extending through the cabling and electronics. Small variations in how the button is seated in the BPM block will affect the response to the beam signal, as will cable and connector dependent attenuation. Finally, each of the four BPM button electrodes drives a dedicated front end amplifier, each of which do not in general respond identically.

It is easy to see that our measurement of vertical dispersion is especially sensitive to gain errors. Suppose for example, at a particular detector there is finite horizontal but identically zero vertical dispersion. If there is any variation in button gains, a component of vertical dispersion will appear in the measurement.

We estimate sensitivity of the measurement of vertical dispersion to gain errors with a simple example. Consider a BPM where there is finite horizontal dispersion η_x and zero vertical dispersion, and the on energy orbit is at precisely zero in both horizontal and vertical. The position for an energy offset $\Delta E/2$, is given by

$$x^+ = x_0 \left(\frac{B_4^+ - B_3^+ + B_2^+ - B_1^+}{\sum B_i} \right)$$

where $x_0 = 19.6$ mm is the BPM horizontal scale factor and the labels are defined in Figure 3.6. We assumed that there is zero vertical orbit offset, and since there is zero vertical dispersion and no change in vertical position with the energy, it must be that $B_4^+ = B_2^+$ and $B_3^+ = B_1^+$ so that

$$x^+ = 2x_0 \left(\frac{B_4^+ - B_3^+}{\sum B_i} \right)$$

Then with energy offset $-\Delta E/2$,

$$x^- = x_0 \left(\frac{B_4^- - B_3^- + B_2^- - B_1^-}{\sum B_i} \right)$$

By symmetry, $B_3^- = B_4^+$ and $B_1^- = B_2^+$. Therefore

$$\Delta x = x^+ - x^- = 4x_0 \left(\frac{B_4^+ - B_3^+}{\sum B_i} \right) \tag{3.22}$$

and $\eta_x = \Delta x/\Delta E$. Now suppose that there is a fractional gain error f for B_3 so that $B_3 \to (1+f)B_3$. Then we will measure

$$y^+ = y_0 \left(\frac{fB_3^+}{\sum B_i} \right), \quad y^- = y_0 \left(\frac{fB_3^-}{\sum B_i} \right) = y_0 \left(\frac{fB_4^+}{\sum B_i} \right), \quad \text{since } B_4^+ = B_3^-.$$

Finally

$$\Delta y = y_0 \left(\frac{f(B_3^+ - B_4^+)}{\sum B_i} \right) \tag{3.23}$$

($y_0 = 26$ mm for the CESR BPM.) Combining the equations 3.22 and 3.23 we find that

$$\Delta y = \frac{f}{4} \Delta x \frac{y_0}{x_0} \rightarrow \Delta \eta_y \sim 0.34 f \eta_x.$$

The peak horizontal dispersion in the CesrTA lattice is about 2 m. Therefore a 1% gain error on a single button will introduce an error in the measurement of the vertical dispersion of $\Delta\eta_y \sim 6.8$ mm.

To calibrate the gains, we take advantage of the fact that a position measurement in a 4 button detector is over constrained. Indeed, the signals on any three of the four buttons locates the beam in the detector. We find that the four button signals are related as follows [49]

$$B_1^i - B_2^i - B_3^i + B_4^i = \frac{c}{I}(B_1^i - B_2^i + B_3^i - B_4^i)(B_1^i + B_2^i - B_3^i - B_4^i) \tag{3.24}$$

where B_j^i is the intensity on the j^{th} button on the i^{th} measurement. c is a constant determined by the BPM geometry and I the bunch current. If we suppose that there is a variable gain associated with each button then we can write

$$g_1 B_1^i - g_2 B_2^i - g_3 B_3^i + g_4 B_4^i = \frac{c}{I}(g_1 B_1^i - g_2 B_2^i + g_3 B_3^i - g_4 B_4^i)(g_1 B_1^i + g_2 B_2^i - g_3 B_3^i - g_4 B_4^i) \tag{3.25}$$

The next step is to measure response to the beam over the entire active area of the detector so that we have a set B_j^i, for $i = 1, \ldots, N$ where N is a large number. Then we fit the g_j to minimize

$$\chi^2 = \sum_{i=1}^{N} \left(g_1 B_1^i - g_2 B_2^i - g_3 B_3^i + g_4 B_4^i - \frac{c}{I}(g_1 B_1^i - g_2 B_2^i + g_3 B_3^i - g_4 B_4^i)(g_1 B_1^i + g_2 B_2^i - g_3 B_3^i - g_4 B_4^i) \right)^2 \tag{3.26}$$

In order to sample the active region of all of the BPMs, we resonantly drive the beam simultaneously at the horizontal and vertical tunes, and collect turn by turn data. Because the measurement and fitting can be completed in just a few minutes, it is straightforward to maintain up-to-date gain calibrations. An example of fitted gains for all 100 beam position monitors is shown in Fig. 3.8.

A histogram of the individual gains is shown in Fig. 3.9a. The accuracy of the beam based method for determining button gains is reflected in the reproducibility of the fitting procedure. Fig. 3.9b shows the distribution of the variation in fitted gains for seven distinct sets of turn by turn data. Evidently we characterize gains with fraction of a percent precision.

3.3.6 BPM Tilts

BPM tilts couple measured horizontal and vertical dispersion. In particular for a BPM tilt θ, $\Delta\eta_y \sim \eta_x \theta$. Peak horizontal dispersion in the CesrTA lattice is about 1-2 m. In order that the error in measured vertical dispersion be less than 10 mm, we require that uncertainty in BPM tilts be less than 10 mrad. BPM tilts can be extracted from the coupling measurements by taking advantage of the fact that the out of phase component of the coupling matrix $\overline{C}_{12}$ is insensitive to

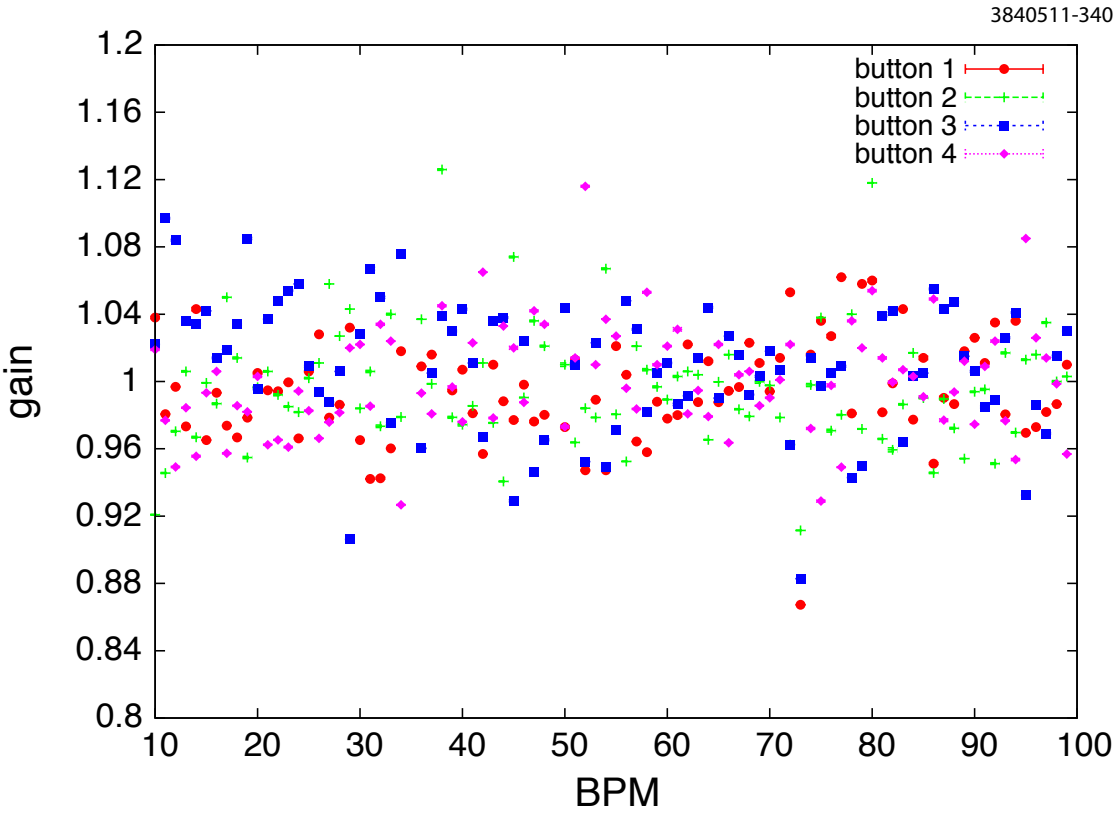

Figure 3.8: Measured BPM button gains. Note that there are four data points for each BPM.

tilt. Then if $\overline{C}_{12}$ is corrected with skew quads, the in phase components $\overline{C}_{11}$ and $\overline{C}_{22}$ provide a direct measure of the physical tilt.

The algorithm for extracting BPM tilt from the coupling data is as follows:

1. Measure and correct coupling based on $\overline{C}_{12}$

2. Remeasure coupling, specifically $\overline{C}_{11}$ and $\overline{C}_{22}$.

3. Model the measured $\overline{C}_{11}$ and $\overline{C}_{22}$ by fitting BPM tilts.

The procedure has been applied to 58 sets of coupling data, all collected during the course of the June 2011 run. The 58 data sets include measurements in five distinct lattice configurations and at four different beam energies. The average along with the rms of the residuals of the fitted tilts are shown in Fig. 3.10a. A histogram of the rms of the residuals is shown in Fig. 3.10b. Uncertainty in the measured tilts is less than 10 mrad.

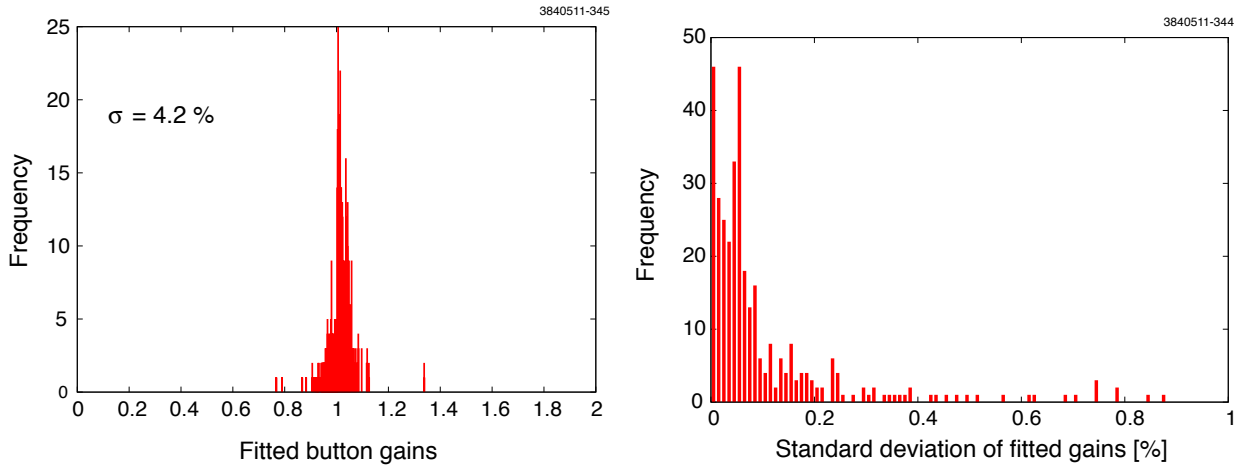

Figure 3.9: (Left) Distribution of measured button gains, with standard deviation 4.2%. (Right) Distribution of the variation in fitted button gains for seven sets of turn by turn data.

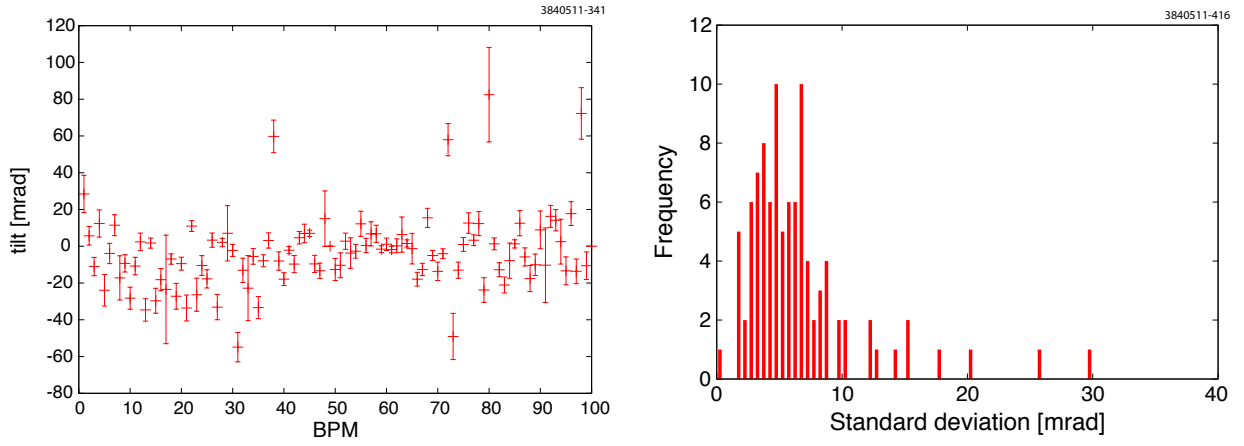

Figure 3.10: (Left) Measured BPM tilts. The error bars are $\sigma = \frac{1}{N}\sqrt{\sum_{i=1}^{N}(\theta - \langle\theta\rangle)^2}$ of 58 data sets. (Right) The distribution of the rms residuals.

3.4 Performance of Low Emittance Instrumentation

3.4.1 Orbit

We estimate the intrinsic resolution of the orbit measurement in terms of reproducibility. The variation in the measured positions for twenty consecutive measurements is shown in Figure 3.11. The standard deviation of horizontal and vertical position measurements is 7.8 μm and 5.8 μm respectively.

3.4.2 AC & DC Dispersion

The distribution of the variation of the measured horizontal and vertical dispersion is shown in Figure 3.12. The standard deviations are 4.6 mm for horizontal and 2.3 mm for vertical dispersion,

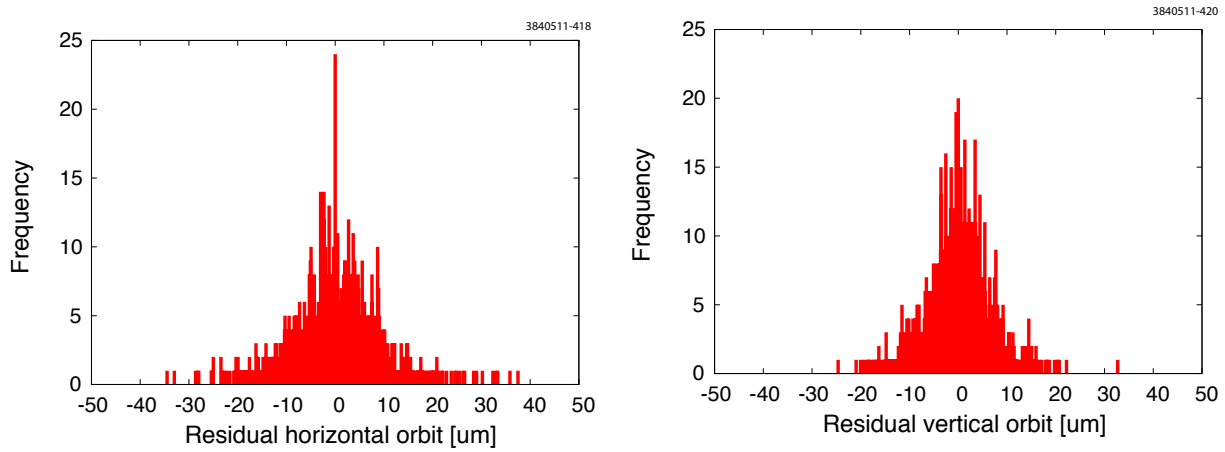

Figure 3.11: Reproducibility of horizontal (left) and vertical (right) orbit measurements. The standard deviation of the measurements is 7.8 μm and 5.8 μm respectively.

corresponding to the intrinsic resolution of the dispersion measurement. The accuracy of the dispersion measurement is limited by the systematics described above, rather than the instrinsic resolution of the beam position monitors.

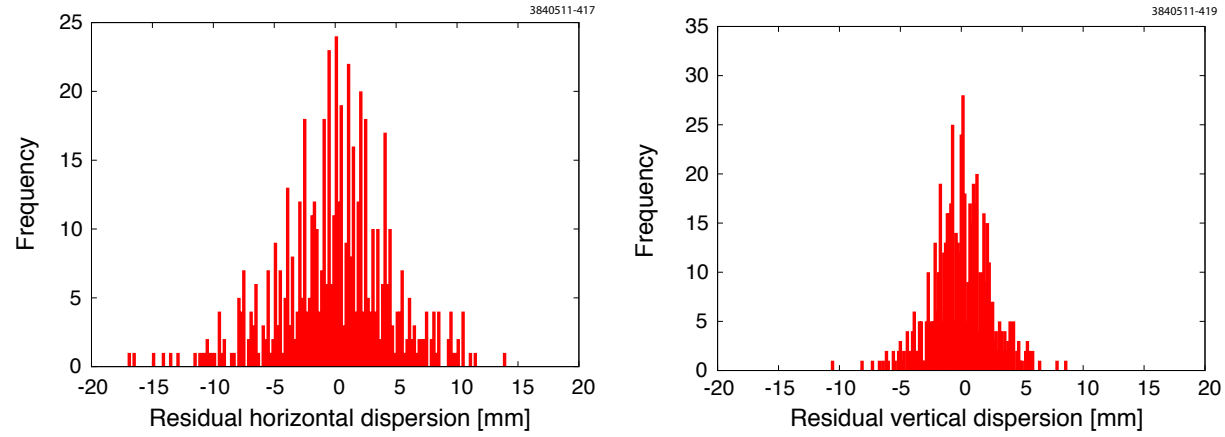

Figure 3.12: Reproducibility of horizontal (left) and vertical (right) dispersion measurements. The standard deviation of the measurements is 4.6 mm and 2.3 mm respectively.

3.4.3 Phase/coupling

In order to determine the intrinsic resolution limit of the phase and coupling measurement, we repeat the measurement 20 times consecutively. Differences from one measurement to the next are due either to some machine instability or statistical limitation of the technique. The distribution of the residuals with respect to the average measurement of vertical phase for each BPM is shown in Figure 3.13a, and the distribution of residuals with respect to the average coupling ($\overline{C}_{12}$) are shown in Figure 3.13b.

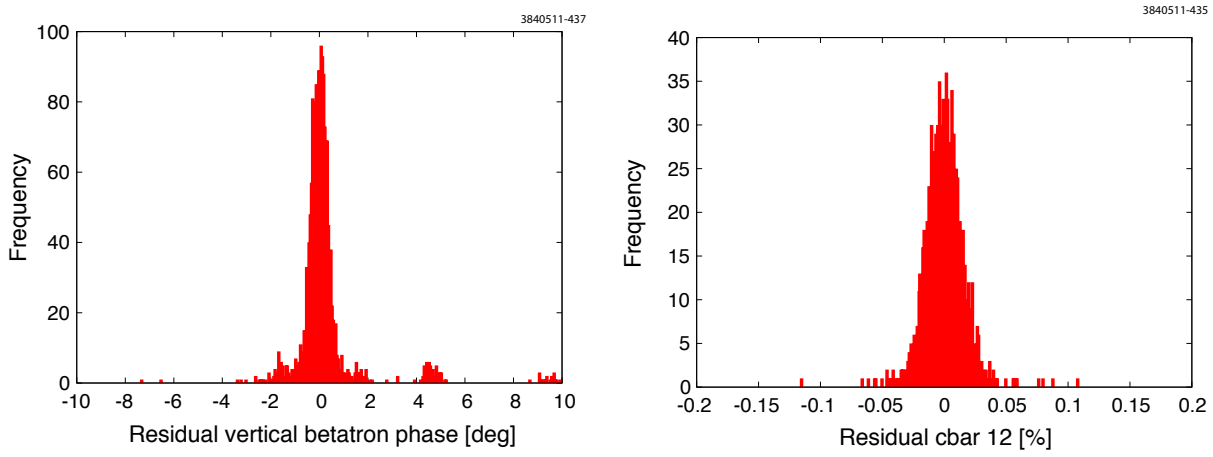

Figure 3.13: Reproducibility of vertical (left) betatron phase measurements, and transverse coupling (right).

3.4.4 xBSM - vertical beam size

The X-ray beam size monitor images synchrotron radiation x-rays emitted in a hard bend dipole onto a linear array of 32 photodiodes (see section 2.4.2). The xBSM is the principle tool for measurng vertical emittance and determining the effectiveness of our low emittance tuning.

The pinhole image (as compared to that of the Fresnel zone plate and coded aperture) is the most straightforward to interpret and is the basis for most of the low emittance tuning studies. (The optic that we refer to as the pinhole is in reality a horizontal gap with adjustable width.) Neglecting diffraction, light from a point source passing through a slit of width G produces an image of width $\sigma_{pointsource} = \frac{G}{x_s}(x_i + x_s)$, where x_i and x_s are distances from optic-to-image and source-to-optic, respectively. The "effective height" of the pinhole can then be taken to be $\sigma_p = \sigma_{pointsource}/M$, where $M = x_i/x_o$ is the magnification of the pinhole. The pinhole (gap height) is set to give minimum image size for the mean X-ray energy of 2 keV (at 2.085 GeV beam energy). The effective height, $\sigma_p = 21 \pm 2\,\mu$m, is defined as the convolution of magnified gap image and diffraction distribution.

The final beam image will be computed as the convolution of the image of the source from an infinitely small pinhole and the image of a finite-width gap from a point source σ_p. The width of the final image will therefore be ${\sigma_{im}}^2 = M^2 \cdot \left({\sigma_y}^2 + {\sigma_p}^2\right)$. Solving this for the source size yields

$$ {\sigma_y}^2 = \frac{{\sigma_{im}}^2}{M^2} - {\sigma_p}^2 \tag{3.27} $$

Systematic uncertainties that contribute to the error in the measurement of the beam size include the location of the source point and the effective gap width. The magnification is inversely proportional to the distance from the pinhole to the source and the effective gap width is subtracted in quadrature to determine source size.

We estimate the uncertainty in the location of source point as follows. We note that X-rays are emitted in a narrow cone with axis tangential to the orbit. The result is that there will be no

light on the detector unless the X-ray beam-line corresponds to an orbit tangent. Now suppose the angle of the orbit as it enters the bend is changed by $\Delta\theta$ due to some change to the closed orbit. The X-ray beam-line will no longer be tangent to the orbit at the nominal source point. There will be some new point along the orbit whose tangent is parallel to the beam-line. In general that new point will be displaced from the X-ray beam-line but we assume that the orbit can always be translated radially to compensate for that displacement. We want to determine the distance along the orbit from the nominal source point to the new tangent point.

The angle of the closed orbit varies through the bend by $\theta(s) = s/R$ where R is the radius of curvature. The angle corresponding to the nominal source point is $\theta_n = s_n/R$ where s_n is the location of the source. Now due to the shift in the closed orbit, the angle of every point along the orbit inside the bend is shifted to $\theta \to \theta(s) + \Delta\theta$. The angle of the X-ray beam line does not change, (and that angle is θ_n), so the position of the source does. The change in position Δs to the point along the orbit with the original angle θ_n is given by

$$\theta_n = \frac{s_n}{R} + \frac{\Delta s}{R} + \Delta\theta \to \frac{\Delta s}{R} + \Delta\theta = 0 \to \Delta s = -R\Delta\theta$$

Therefore, the uncertainty in s corresponds to the uncertainty in the orbit angle offset $\Delta\theta$. And in general, angle errors translate to position errors as $\Delta s = -R\Delta\theta$.

An inspection of a typical measured orbit with the xBSM bump shows that the angle of the orbit through the bend is about 3 mrad. The uncertainty in the angle is certainly no more than 3 mrad. (If we tried to increase the angle from 3 mrad to 6 mrad we would lose the beam since that would correspond to a 30 mm displacement.) So let $\Delta\theta_{co} = 3$ mrad due to uncertainty in the closed orbit, or we could take something larger for the angle uncertainty to be more conservative. But with $\Delta\theta = 3$ mrad, according to the above, $|\Delta s| = R\Delta\theta = (33\,\mathrm{m})(3\,\mathrm{mrad}) = 10\,\mathrm{mm}$.

Now consider the effect of the uncertainly in the direction of the beam-line. The beam-line is defined by the aperture of the optical element (1.2 mm) and the detector width (0.5 mm). We estimate the uncertainty in their positions very conservatively to be ± 1 cm. A 1 cm uncertainty in the location of the optic and another 1 cm uncertainty in the location of the detector, corresponds to an uncertainty in the angle of the line by $2\,\mathrm{cm}/L_{line}$, where $L_{line} = 10.19$ m is the distance from optic to detector. Therefore the uncertainty in the angle of the line is $\Delta\theta_l < 2$ mrad.

We note in addition, that there is some finite angular spread in the light emitted by the beam which means that the orbit at the source does not have to be precisely tangent to the beam line. The angular spread is the quadrature combination of the angular divergence of the beam $\theta_{div} = \sqrt{\frac{\epsilon_x}{\beta_x}}$ and the opening angle $\theta_{open} = \frac{1}{\gamma}$.

Putting all the pieces together we have

$$\Delta\theta = \sqrt{(\Delta\theta_{co})^2 + (\Delta\theta_l)^2 + (\theta_{div})^2 + \theta_{open}^2} = \sqrt{3^2 + 2^2 + (0.00025) + (0.25)^2}\ \mathrm{mrad} = 3.6\,\mathrm{mrad}$$

(To compute θ_{div} we assume $\epsilon_x = 2.5$ nm and $\beta_x = 10$ m. For θ_{open} we use $\gamma = 2\,\mathrm{GeV}/0.51\,\mathrm{MeV}$). Then the uncertainty in position is

$$\Delta s = \pm\Delta\theta R = \pm 12\,\mathrm{cm}$$

The nominal distance from source to lens is $x_s = 4$ m and the fractional uncertainty is $\Delta s/s \sim 3\%$. Finally the uncertainty in the magnification is $\Delta M/M = \Delta s/s \sim 3\%$.

The combined systematic uncertainty is computed from Equation 3.27:

$$\Delta\sigma = \sqrt{\left(\frac{1}{\sigma}\frac{\sigma_{im}^2}{M^2}\frac{\Delta M}{M}\right)^2 + \left(\frac{1}{\sigma}\sigma_p^2\frac{\Delta\sigma_p}{\sigma_p}\right)^2} \sim 2.5\,\mu\text{m}$$

Evidently the systematic error is dominated by uncertainty in the width of the gap.

3.4.5 Measurement resolution summary

The resolution of measurements of beam position, dispersion, coupling, betatron phase advance, and vertical beam size are summarized in Table 3.3.

Table 3.3: Accuracy of beam based measurements

Parameter	RMS
BPM position (absolute) [μm]	100
BPM position (differential) [μm]	10
Dispersion [mm]	10
Coupling($\overline{C}_{12}$)[%]	0.2
Betatron phase [deg]	2
Vertical beam size [μm]	1

3.5 Ring Correction Methods

3.5.1 Tuning algorithm

The CesrTA low emittance tuning technique relies on a complete characterization and then correction of lattice errors. The procedure is to:

- Measure and correct closed orbit using all steerings.
- Measure betatron amplitudes, phase advance and coupling and correct with all skew quads and lattice quads. The phase and coupling derives from turn by turn position data of a resonantly excited beam[32] as described above.
- Remeasure closed orbit, phase and coupling, and measure dispersion. Simultaneously minimize closed orbit errors, coupling and vertical dispersion using vertical steerings and skew quadrupoles.

The efficacy of the low emittance tuning algorithm is explored with simulations. We introduce random misalignments of quadrupoles, sextupoles, wigglers, beam position monitors and quadrupole focusing errors into the machine model. The standard deviations of the misalignments are consistent with the survey as summarized in Table 3.2. We model the correction process by simulating first the measurement of orbit, betatron phase, coupling, dispersion etc., including measurement errors as given in Table 3.3. The vertical emittance at the conclusion of each step of the emittance tuning process, for 1000 seeds, is shown in Figure 3.14.

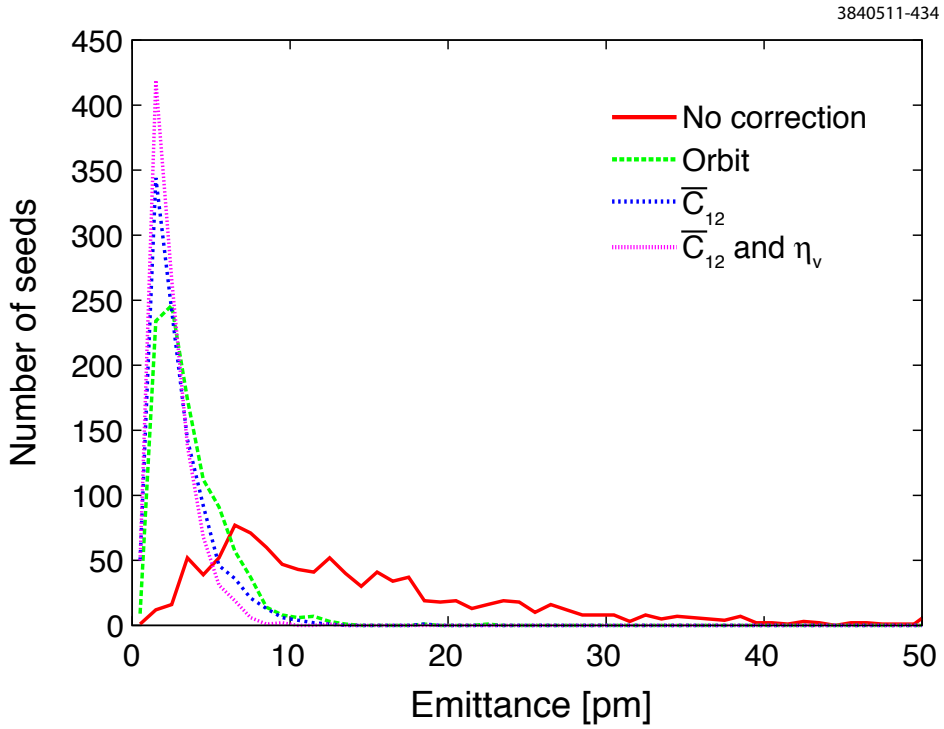

Figure 3.14: Simulation of effectiveness of low emittance tuning algorithm for machines with misalignments as in Table 3.2 and measurement accuracy from Table 3.3, for 1000 seeds. The red line is the distribution of vertical emittance in the event of no correction. The green line corresponds to emittance after correction of closed orbit, blue after correction of closed orbit and coupling and purple after correction of orbit, coupling and dispersion.

With these assumptions the low emittance tuning procedure yields $\epsilon_y < 8.9$ pm-rad for 95% of seeds, consistent with our control room experience where we routinely achieve sub 10 pm-rad vertical emittance.

The simulations also show that if the BPM tilt is reduced from 22 mrad to 10 mrad, then 95% of the seeds yield a corrected emittance less than 5 pm-rad. If, in addition, the differential resolution of the BPMs is reduced from 10 μm to 4 μm, then 95% of the seeds can be corrected to less than 2 pm-rad. Clearly the ability to identify sources is limited by the differential BPM resolution and systematics, and not by the number or position of correctors. Absolute BPM position is not a fundamental limit, as the measurement of dispersion is independent of BPM offsets. The systematic that limits the quality of the dispersion measurement in CesrTA is the BPM tilts, and the energy aperture that restricts the amplitude of the energy offset.

3.5.2 Normal Mode Dispersion Measurement and Correction

An alternative technique for low-emittance tuning, based on calibration of the BPMs with respect to the beam normal modes, has been developed at CesrTA. Although this technique was initially suggested by the turn-by-turn data provided by the new BPM digital signal processing electronics, the necessary data can also be acquired using the well-established betatron phase measurement

Table 3.4: Magnet misalignment and beam position measurement resolution

Parameter	Initial
Quadrupole vertical offset [μm]	250
Quadrupole tilt [μrad]	300
Bend roll [μrad]	300
Sextupole vertical offset [μm]	250
Wiggler tilt [μrad]	200
BPM absolute resolution [μm]	100
BPM differential resolution [μm]	10
BPM tilt [mrad]	22

method. The basic principle behind the technique is that quantum excitation of betatron oscillations in a particular mode results from photon emission at a location in the ring where the dispersion has some non-zero component along an axis corresponding to motion in that mode. For example, in a perfectly aligned planar ring without coupling, horizontal dispersion in a dipole leads to excitation of the horizontal emittance. With zero vertical dispersion, there is no excitation of vertical betatron motion, and the vertical emittance will damp to a (very small) value determined by the opening angle of the synchrotron radiation. Alignment errors in a storage ring will lead to generation of vertical dispersion and betatron coupling. If the coupling is reasonably small, then it may be characterized by a (local) rotation of the axes corresponding to betatron motion in each of the two transverse normal modes, which we denote mode I (close to the horizontal) and mode II (close to the vertical). However, if the vertical dispersion is such that the total dispersion vector in a dipole is parallel to an axis corresponding to mode I, then photon emission will lead to excitation of motion in only this mode. If the BPMs can be calibrated to measure the beam motion along the normal modes (rather than purely horizontal and vertical motion), then they can be used to measure directly the components of the dispersion parallel to the normal mode axes. Correction of the mode II dispersion should then minimize the mode II emittance. Of course, the BPM calibration will be dependent on the coupling, and is therefore likely to change after an applied correction. However, if the calibration can be performed quickly and easily, then it should be possible to iterate the correction procedure, including re-calibration at each step, to minimize the mode II emittance. Calibration of a BPM to measure the motion along the normal mode axes may be achieved by exciting beam motion in each of the normal modes in turn, while observing the response on the BPM buttons. The relative changes in the button signals when the beam is observed over many turns can be used to characterize the BPM response to motion in the corresponding normal mode. Since collection of turn-by-turn data can be carried out simultaneously for all BPMs, the calibration can be performed quickly and easily. Fig. 3.15 shows an example of calibration data collected for BPM 7W with resonant excitation in mode I. The BPM calibration (which allows changes in beam position along the normal mode axes to be calculated from measured changes in button signals) is obtained from the gradients of line fits to the correlation plots. With high-resolution BPMs (capable of turn-by-turn position measurements with resolution of order 10 μm), it is possible to obtain high quality calibration data while maintaining an excitation amplitude below the point where the nonlinear response of the BPM buttons becomes significant. The effectiveness of the calibration may be tested by computing the Fourier spectra of the turn-by-turn data for excitation in each normal mode. For a correct calibration, the spectrum obtained from each coordinate should contain only a single peak, for the corresponding normal mode. Fig. 3.16 shows an example for data collected with BPM 7W.

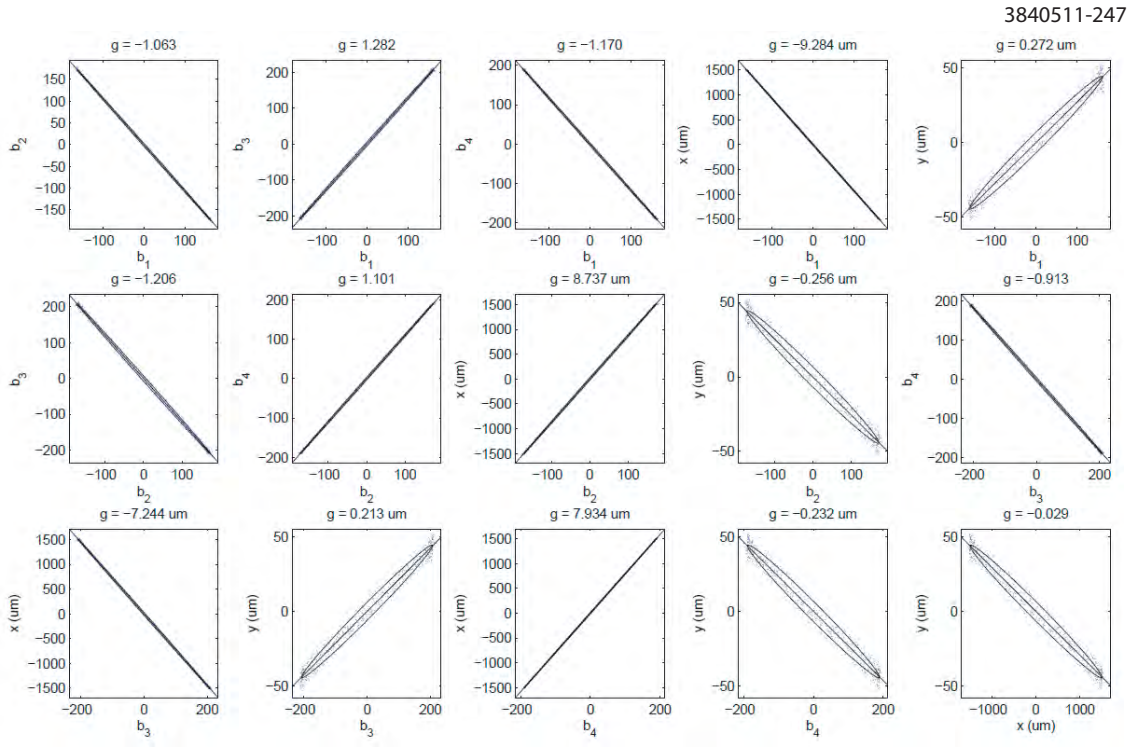

Figure 3.15: Correlations between turn-by-turn button signals on BPM 7W during resonant excitation of mode I. The beam is driven by the tune tracker at the mode I (horizontal) tune. The five plots along the top of the figure show the signals on buttons b_2, b_3, b_4, and horizontal and vertical position versus the signal on button b_1. Button signals are given in digitizer units. Horizontal and vertical positon are in microns. The next four plots give dependencies of buttons b_3, b_4 and horizontal and vertical position on button b_2. The next three plots give dependencies on button b_3 and the next two on button b_4. The last plot is vertical versus horizontal position. The number g for each is the fitted gradient.

Following calibration, the normal mode dispersion may be measured in the conventional way, by varying the RF frequency and observing the resulting change in closed orbit. Correction of the mode II dispersion can be achieved using skew quadrupoles: the appropriate changes in strength of the skew quadrupoles can be determined from a response matrix relating the skew quadrupole strengths to the normal mode dispersion. In CesrTA, measurements have been made of the response of the mode II dispersion to changes in strength of the skew quadrupoles. The results suggest that a response matrix computed from an ideal model of the machine should be good enough to calculate the skew quadrupole strengths needed to achieve correction of the mode II dispersion in the real machine.

It should be emphasized that correction of the mode II dispersion effectively minimizes the quantum excitation of particle motion in normal mode II: thus, there is no need to correct separately the dispersion and the coupling. Also, since the BPMs are calibrated with respect to the normal modes using direct observations of beam motion, the correction is insensitive to BPM gain errors. Fig. 3.17 shows the results of simulations of low-emittance tuning of CesrTA using correction of the mode II dispersion. The technique is robust (correction was achieved for all seeds) and effective (in the great majority of cases, the correction results in a mode II emittance below 20 pm).

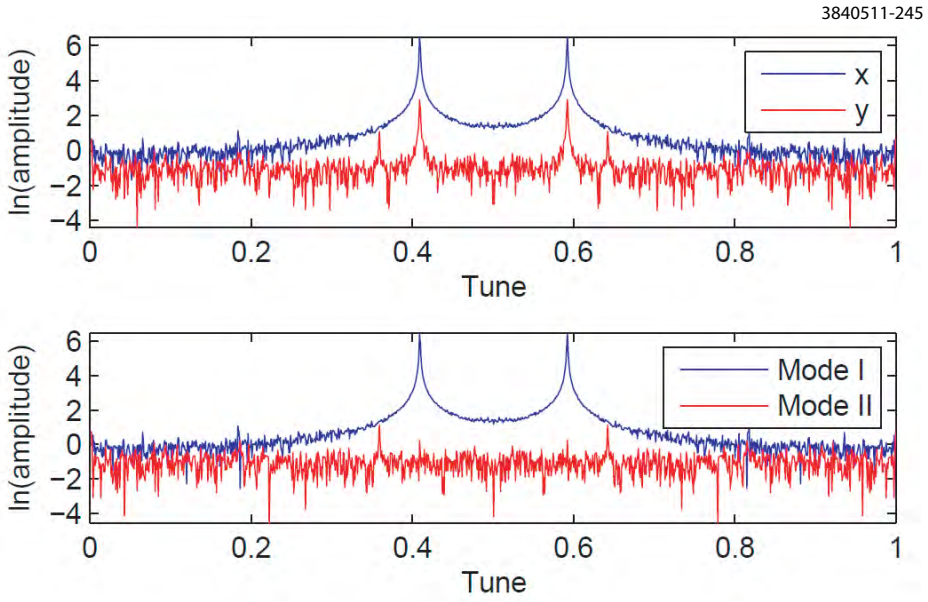

Figure 3.16: Fourier spectra of turn-by-turn signals recorded on BPM 7W. Top: "nominal" $(x-y)$ calibration, showing peaks corresponding to the mode I frequency in both x and y coordinates. Bottom: "normal mode" calibration, showing the normal mode frequencies appearing in only the corresponding normal mode coordinate.

Tests at CesrTA have demonstrated that normal mode calibration of the BPMs can be achieved using either turn-by-turn data (with excitation in each normal mode successively), or using phase advance data (with excitation in both normal modes simultaneously). The normal mode dispersion can be measured with calibrated BPMs, using either the conventional method of RF frequency variation, or using the AC dispersion technique. Tests indicate that the resolution of the measurement should be around 6 mm. Application of the technique to reduction of the mode II emittance was tested by starting from a condition in which the machine was tuned to a vertical emittance of about 14 pm (based on measurements using the fast X-ray beam size monitor), then turning off the skew quadrupoles. At this point, the emittance increased to 24 pm. After normal mode BPM calibration, measurement and correction of the normal mode dispersion using new skew quadrupole settings, the vertical emittance of 14 pm was restored. However, after a further iteration (re-calibration of the BPMs, then further measurement and correction of the mode II dispersion), the vertical emittance increased to 21 pm. This may have been because the correction was applied with equal weight given to the mode II dispersion at each BPM: however, it is really the mode II dispersion at the locations where synchrotron radiation is generated (i.e. the dipoles and, in particular, the wigglers) that really counts for the excitation of mode II emittance. It is possible that overall reduction of the mode II dispersion results in a (maybe small) increase in the mode II dispersion in the dipoles and wigglers, and hence in an overall increase of the mode II emittance.

Further tests of low-emittance tuning based on measurement and correction of mode II dispersion could be carried out using an optimized algorithm, in which greater weight is put on the mode II dispersion measurements close to the dipoles and wigglers. The performance of the technique in simulation is encouraging. Also, it has a number of advantages over other low-emittance tuning techniques (such as orbit response matrix analysis), in that the required data can be collected quickly and easily (within a few minutes), and the technique can be applied to a large ring as

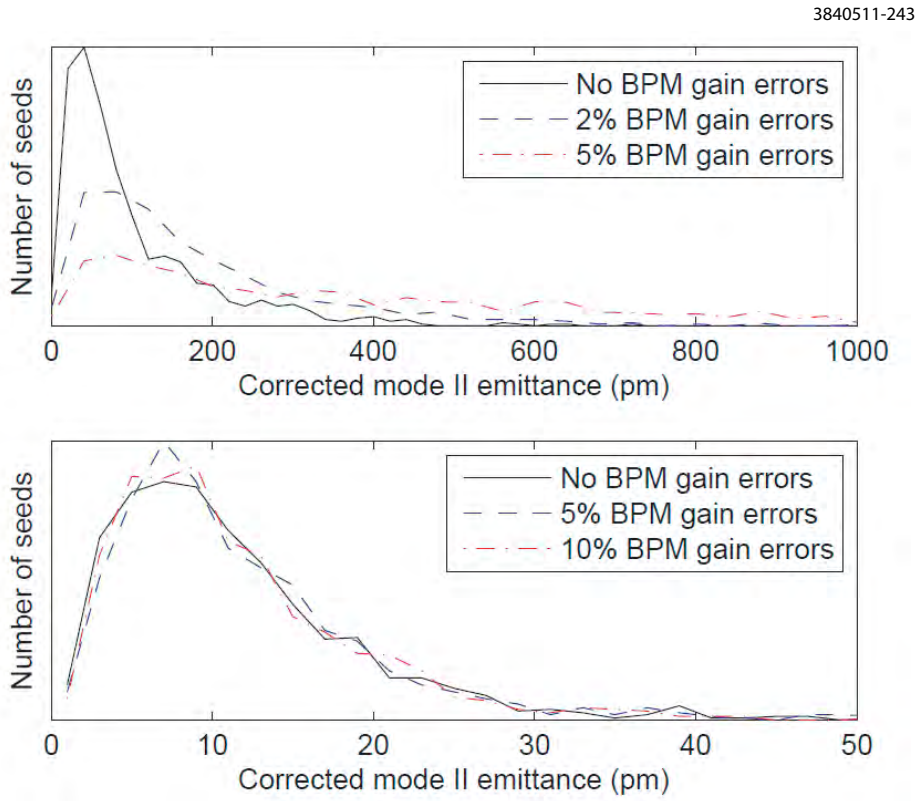

Figure 3.17: Results of simulation of low-emittance tuning in CesrTA using: (top) correction of vertical orbit and vertical dispersion; (bottom) correction of mode II dispersion, using BPMs calibrated to measure beam motion in the normal modes. The lines show the distribution of final mode II emittance over 1000 seeds of random machine errors, for different cases of BPM gain errors.

easily as to a small ring. The insensitivity of the technique to BPM gain errors is also an attractive feature.

3.6 Results

3.6.1 Effectiveness of Corrections

We summarize the effectiveness of our low emittance tuning in terms of corrections of betatron phase and coupling, vertical dispersion and the resulting vertical emittance.

3.6.1.1 Betatron Phase and Coupling

Figures 3.18 and 3.19 show typical betatron phase and coupling measurement ($\overline{C}_{12}$) after performing low-emittance tuning. We routinely correct betatron phase to an RMS (measurement - design) of less than 2 degrees. Typical levels of RMS coupling after correction are $\overline{C}_{12} < 0.01$.

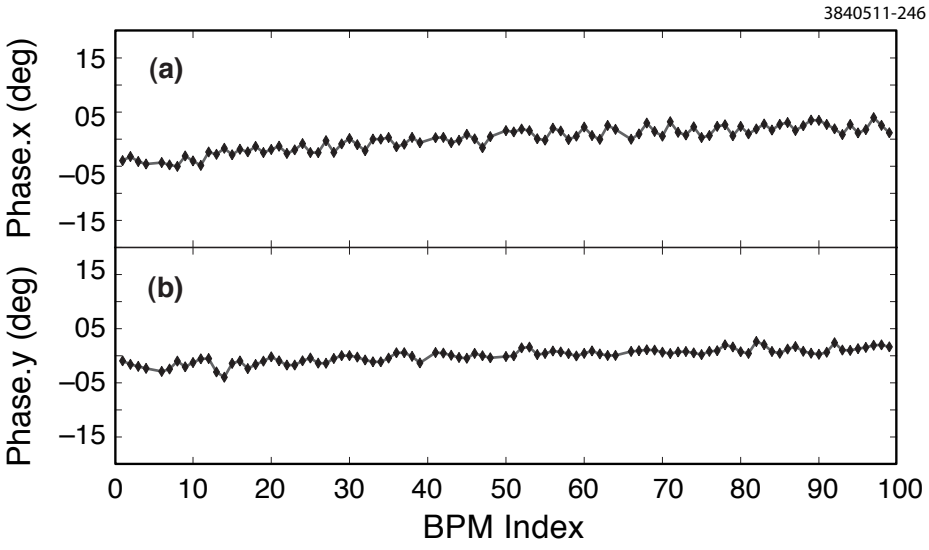

Figure 3.18: Typical horizontal and vertical betatron phase measurements (measured - design) after corrections. The constant slope indicates a difference in measured and design tunes, which is usually intentional when exploring a different working point. Accounting for the tune difference, RMS (measured - design) $\phi_a = 1.7°$, $\phi_b = 0.64°$. This corresponds to a beta beat of $\sim 3\%$ and 2%, respectively.

3.6.1.2 Dispersion

The low-emittance tuning procedure typically reduces the vertical dispersion by a few millimeters. Figure 3.20 shows a typical vertical dispersion measurement after the low-emittance tuning procedure, using both AC dispersion and traditional dispersion methods. The two measurements were taken within five minutes of each other, and in identical machine conditions.

The residual of the measured vertical dispersions and the best fit model using standard corrector magnets, quadrupole offsets and tilts, defines the noise level of both the AC dispersion and traditional dispersion measurements.

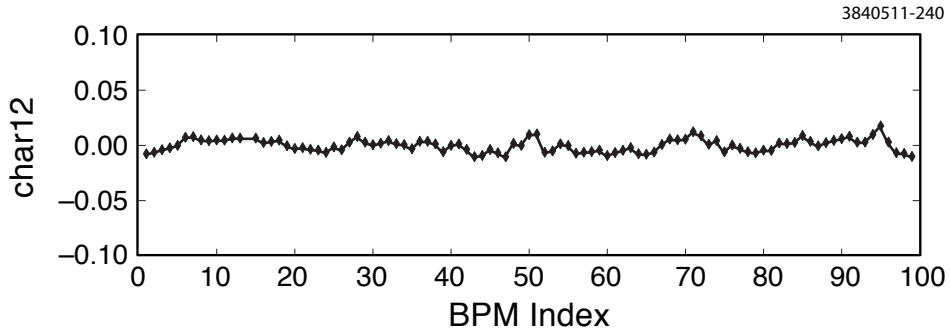

Figure 3.19: Cbar12 coupling after a typical low-emittance correction. The RMS is 0.006.

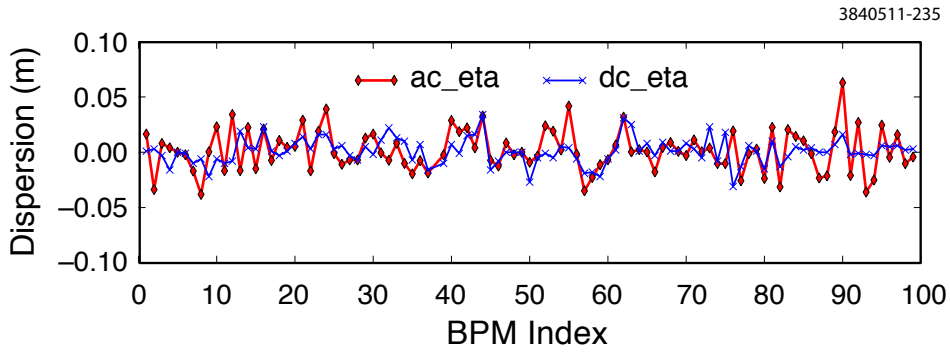

Figure 3.20: Typical vertical dispersion after a low-emittance correction, measured using both resonant excitation ("AC" dispersion) and traditional orbit difference ("DC" dispersion) techniques. For AC dispersion, RMS = 19 mm. For traditional dispersion measurement, RMS = 12 mm.

3.6.1.3 Emittance

The vertical emittance ϵ_y is related to beam size σ_y according to

$$\sigma_y = \sqrt{\beta_y \epsilon_y + \left(\eta_y \frac{\sigma_E}{E}\right)^2} \quad , \quad \text{or} \tag{3.28}$$

$$\epsilon_y = \frac{{\sigma_y}^2 - \left(\eta_y \frac{\sigma_E}{E}\right)^2}{\beta_y} \tag{3.29}$$

For maximal sensitivity to small emittance, we typically employ a lattice with the relatively large $\beta_y^{source} = 40$ m to image using the pinhole optic.

After low-emittance tuning, we routinely measure beam sizes below 20 μm with 0.75 mA in a single bunch (1.2×10^{10} positrons). With $\beta_y^{source} = 40$ m and assuming zero dispersion, this yields $\epsilon_y = 10$ pm. From Eq. 3.29, for a fixed beam size measurement, any vertical dispersion at the source point will reduce the contribution to the beam size from emittance. We therefore conclude this is an upper bound on the typical emittance correction.

As a test of the veracity of the vertical beam size monitor we arrange skew quads to introduce closed vertical dispersion bumps in the damping wigglers so that we can vary the beam size in a controlled way. These coupling/dispersion bumps are designed to couple the large horizontal dispersion (adjacent to the wiggler straight) into the vertical plane such that $\eta_y \neq 0$ in the wigglers, thus increasing vertical emittance and beam size in a predictable way (see Fig. 1.3). The bumps are closed such that the global coupling and dispersion outside the bump remain unaffected, in particular at the xBSM source point. The actual response of the beam size to the coupling knob will depend on the residual vertical emittance. An example of a scan of beam size vs. the dispersion bump is shown in figure 3.21 for measurements made in April 2011.

There are a number of systematic uncertainties associated with interpretation of emittance from measurements of beam size. Emittance depends on vertical beta at the source. We determine β_y by fitting to the betatron phase advance and amplitude data and extrapolating to the source point. There is some uncertainty in the location of the source point, as discussed in Sec. 3.4.4. Vertical dispersion is measured with a resolution of order 5 mm and it too depends on the location of the source. Dispersion affects the emittance asymmetrically: that is, any nonzero dispersion will lead to

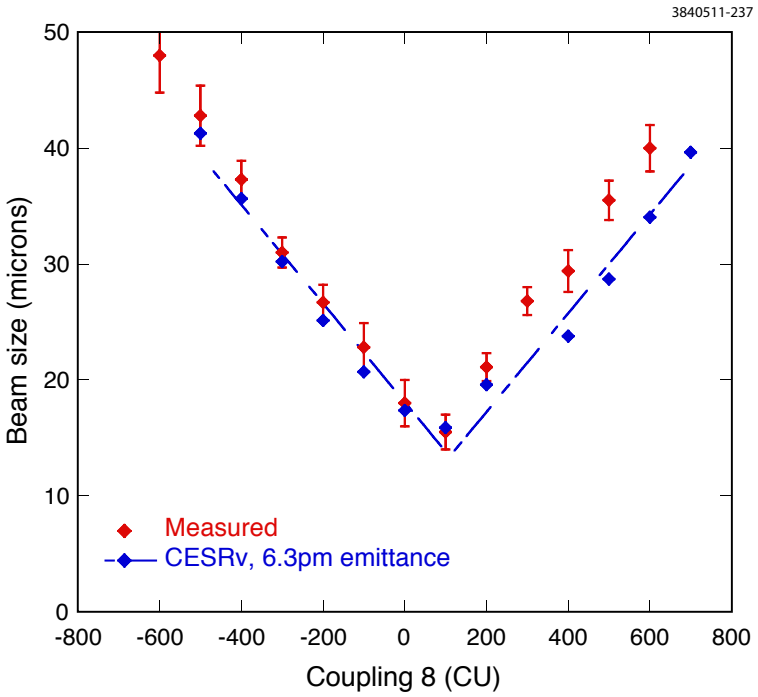

Figure 3.21: Beam size as a function of a closed dispersion and coupling bump through one of the arc wiggler triplets. The units of the horizontal scale are arbitrary Computer Units, proportional to the strength of the coupling bump. Here, $\beta_y^{source} = 40$ m. Data is shown in red, with error bars from fitting the beam profile from the xBSM for 100 consecutive turns. The blue points correspond to the beam size calculated in a model lattice given the skew quad values used to generate the bump. The model lattice includes a Gaussian distribution of vertical quadrupole offsets that generate a residual emittance (with the dispersion bump off) of 6.3 pm of vertical emittance. Residual vertical emittance of 6 pm is typical after low emittance tuning. The agreement between data and model confirms the calibration and resolution of the beam size monitor

an overestimate of the emittance. In addition there are systematics associated with the instrument itself. There is some uncertainty in the effective height of the gap ("pinhole") as noted in Sec. 3.4.4. We also need to evaluate possible intensity dependence of the detector response, channel to channel bleedthrough between photodiodes, backgrounds, etc.

The parameters used to compute the error in the emittance measurement are summarized in Table 3.5 below. Table 3.6 shows uncertainties on those parameters, and their contributions to the emittance uncertainty.

3.6.1.4 Zero current emittance

As noted above, we typically, we execute the emittance tuning with about 0.75 mA (1.2×10^{10} particles) in a single bunch. At this bunch current, the beam position monitors operate in a fixed gain mode and are optimally sensitive. We expect that collective effects that might generate emittance growth will be very small.

Table 3.5: Parameter values used for calculating beamsize.

Parameter	Value
σ_{im}	60.6 μm
σ_p	21 μm
β_y	39.2 m
η_y	0.75 mm
$\partial\beta_y/\partial s$	-8.98 m/m
$\partial\eta_y/\partial s$	0.52×10^{-3} m/m
$\partial M/\partial s$	0.6/m
σ_E/E	8.125×10^{-4}

Table 3.6: Parameter uncertainties used for calculating uncertainty in emittance, and their relative contributions to $\delta\epsilon_y$. The statistical uncertainties in optics functions are determined by recording several consecutive measurements in identical machine conditions, and noting the scatter between measurements.

Parameter	Value	$\lvert\partial\epsilon_y/\partial x_i\rvert \times \delta x_i$	Reference
$\delta\sigma_{im}$	$\pm$2.2 μm	$\begin{cases} +1.21 \text{ pm} \\ -1.08 \text{ pm} \end{cases}$	100 consecutive turns; $\langle\sigma_y\rangle = 14 \pm 1.6\,\mu$m
$\delta\sigma_p$	$\pm$2.0 μm	$\begin{cases} +2.04 \text{ pm} \\ -2.25 \text{ pm} \end{cases}$	Analytic estimate
$\delta\beta_y^{sys}$	$\pm$0.75 m	$\pm$0.09 pm	RMS residual (measured - model)
$\delta\beta_y^{stat}$	$\pm$0.75 m	$\pm$0.09 pm	See caption
$\delta\eta_y^{sys}$	$\pm$7mm	$\begin{cases} +1.00 \text{ pm} \\ -0.65 \text{ pm} \end{cases}$	Fitting model to measurement
$\delta\eta_y^{stat}$	$\pm$2 mm	$\begin{cases} +0.67 \text{ pm} \\ -0.80 \text{ pm} \end{cases}$	See caption
δs^{sys}	$\pm$2 cm	$\pm$0.14 pm	Analytic estimate
δs^{stat}	$\pm$0.2 cm	$\pm$0.01 pm	Analytic estimate

3.6.2 Tune Scans

We explore the dependence of vertical beam size on betatron tunes with scans. A scan relies on an automated measurement of beam size, as the tunes are varied across a grid.

For the scan shown in Figure 3.22 we use a lattice with $\beta_y^{source} = 16.8$ m at the x-ray beam size monitor source point. Chromaticity is compensated to $\sim +1$ in both horizontal and vertical using a simple two-family sextupole distribution. The low-emittance tuning algorithm is applied prior to intitiating the scan.

The width of various resonances in general depends on the details of the misalignments and the deployment of compensating correctors. Tune scans are used to find a region of the tune plane in which vertical beam size is a minimum, and is sufficiently clear of resonances so that measurements of current (and other dependencies) will not be complicated with simple tune dependencies. From the tune scan shown in Fig. 3.22, we identified the working point $(Q_x, Q_y) = (0.584, 0.639)$, which after application of the low-emittance tuning procedure, yielded emittance < 5 pm with 0.5 mA bunch current.

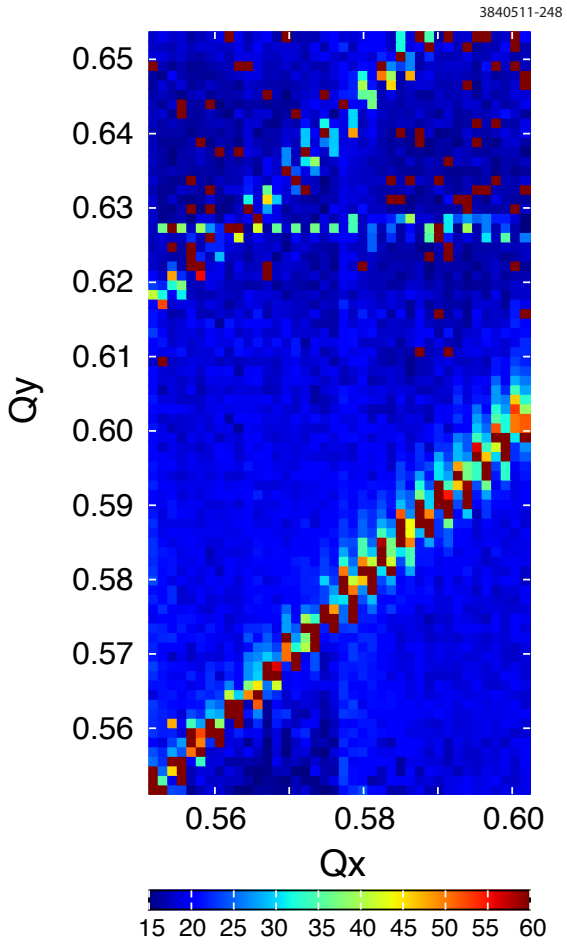

Figure 3.22: Beam size measured across a grid of working points. Each data point represents a 100-turn average. The color scale shows beam size in microns, where $\beta_y^{source} = 16.8$ m.

3.7 Summary and Further Investigations

We have developed a procedure for tuning for low emittance that routinely yields vertical emittance of less than 10 pm (and as low as 5 pm), as measured with the X-ray beam size monitor. Correction is based on measurements of closed orbit, betatron phase and coupling, and vertical dispersion. Simulation of the tuning procedure applied to model machines with misalignments also yields vertical emittance less than 10 pm when BPM accuracy is as summarized in Table 3.3.

The measurement of the vertical dispersion, essential to its correction, is limited by the systematic uncertainty of the BPM tilt angles and BPM button to button gain variation. With the development of beam based techniques for calibrating both BPM tilt and gains, we have been able to reduce these systematics to the point where other sources of emittance blowup are beginning to appear. For example, we observe a significant contribution to vertical size due to coherent motion of the beam. Spectral analysis of turn by turn position data collected with the BPM system, and position and size data from the x-ray beam size monitor, indicate beam motion with amplitude on the order of the vertical beam size at the betatron tunes. We are in the midst of a thorough investigation to identify the drivers of that motion. The possibilities include high frequency (10-100 kHz) noise

from corrector magnet power supplies, feedback amplifiers, RF klystrons, etc. We believe that the CesrTA instrumentation provides the capability to consistently achieve vertical emittance less than 5 pm-rad, once coherent beam motion is eliminated. We further note that the emittance tuning algorithm developed for CesrTA is easily extrapolated to a much larger ring. All of the data from each of the beam position monitors is collected in parallel, so the time required for a complete characterization with beam based measurements is essentially independent of the size of the ring.

Chapter 4

Description of the Electron Cloud Model

4.1 Description of the EC Model

4.1.1 Brief Historical Context

The buildup of high densities of low-energy electrons produced by the intense synchrotron radiation in electron and positron storage rings has been under active study since the phenomenon was identified in the mid-90's in the KEK Photon Factory (PF) when operated with a positron beam [50]. While this phenomenon did not present an operational limitation at the PF under nominal conditions, the observation raised immediate concerns for both B Factories, then under design, and triggered significant simulation efforts [51] and analytical work [52] aimed at quantifying the phenomenon and designing mitigation techniques. Indeed the luminosity in the B-Factories was eventually limited by the electron cloud effect (ECE). Mitigating this effect at both machines was essential to reach, and then exceed, the design luminosity [40].

Almost concurrently with the above-mentioned developments at the PF and the B Factories, concerns arose in 1995-96, based on prior experience at the ISR, that electrons might spoil the LHC vacuum [53]. Early 1997 calculations showed that the LHC would be subject to an ECE [54], chiefly because the beam emits copious synchrotron radiation upon traversing the dipole bending magnets, in analogy with e^+e^- storage rings. Indeed, the LHC is the first proton storage ring ever built in which synchrotron radiation is significant: although the critical photon energy is only ~ 44 eV at 7 TeV beam energy (as opposed to several keV in typical e^+e^- storage rings), this value is well above the work function of the chamber metal, hence photoemission inside the chamber is unavoidable. A straightforward calculation yields an estimate of 0.4 photons emitted per proton per dipole magnet traversal, also at 7 TeV beam energy. Although ~50% of these photons have energies below the work function of the metal, the remaining 50% lead to a substantial number of photoelectrons. Further calculations [54, 55], including the effects of secondary electron emission, quickly revealed the possibility of a substantial ECE. In the case of the LHC, the primary concern from the ECE is the power deposited on the beam screen by the electrons as they rattle around the chamber under the action of successive bunch passages. This power must be dissipated by the cryogenic system if the LHC superconducting magnets are to work as specified. Since the cryogenic system was designed before the prediction of the ECE in the LHC, a significant "crash

programme" was launched in 1997[1] to better estimate the power deposition, to identify the conditions under which the cooling capacity might be exceeded, and to devise mitigation mechanisms if necessary [56]. As part of this effort, the ECE has been experimentally studied at the SPS and the PS at the high beam intensities required for nominal LHC operation (recent experience at the LHC has confirmed the expectation of a significant ECE, even though the beam energy is presently only 3.5 TeV [57]). The LHC EC crash programme was almost certainly the single most comprehensive effort to understand the electron cloud in a hadron machine, and was comparable in scope to the present program at CesrTA for an e^+e^- machine.

The above-mentioned ECE's are related to previously observed electron-proton dynamical effects such as beam-induced multipacting (BIM), first observed at the CERN proton storage ring ISR [58] when operated with bunched beams. Closely related to BIM is trailing-edge multipacting observed at the LANL spallation neutron source PSR [59], where electron detectors register a large signal during the passage of the tail of the bunch even for stable beams. All ECEs in e^+e^- as well as in hadron storage rings have precursors in the e-p instabilities for bunched and unbunched beams first seen at BINP in the mid-60s [60]. Another precursor to the presently observed EC phenomena was a coupled-bunch instability observed at CESR, although in that case the photoelectrons were trapped and localized in a section of the ring rather than spread out over most of the circumference [61].

For the above reasons, 1995 marks the beginning[2] of the Common Era (CE) of the ECE, i.e., common to lepton and hadron rings. Before the Common Era (BCE), the only beam dynamics phenomena that were understood to be caused by electrons pertained to proton beams. As far as we know, 1997 was the first year in which ECEs from both positron and proton storage rings were discussed at the same meeting [62, 63].

The interest generated by the observations at the PF published in 1995 triggered a series of dedicated workshops the most recent of which was held in Italy in 2012 [64]. The similarities of the ECE's in e^+e^- and hadron storage rings is evidenced by the simultaneous and comparable participation, since 1997, of both communities in these workshops. Phenomena related to electron cloud buildup have been reported, and in some cases have been a performance- limiting factor, at the Advanced Photon Source at ANL [65], BEPC [66], the Spallation Neutron Source at ORNL [67], the Relativistic Hadron Collider at BNL [68], the Proton Storage Ring at LANL [69], the DAΦNE Φ-factory at the INFN-LNF in Frascati [70], PEP-II at SLAC [71, 72], the Tevatron Main Injector at FNAL [73], the CERN Proton Synchrotron [74], the Super Proton Synchrotron [75], and the LHC [57].

The enhanced understanding of electron cloud physics has identified the phenomenon as a primary potential limiting factor in the operation of damping rings for future e^+e^- linear colliders [76–78]. The determining physical phenomena governing the characteristics of the clouds are the generation of photoelectrons, their trajectories in the transient and ambient electric and magnetic fields, and the secondary electron yield properties of the vacuum chamber. Thus the RF structure of the beams, their intensities, the shape and dimensions of the vacuum chamber, and especially the electronic properties of those chambers affect the production of electrons by incident electrons, and are therefore important factors in the rates of buildup and decay. A variety of mitigation techniques have been experimentally studied and implemented in other operating storage rings, such as grooves

[1] The website `http://ab-abp-rlc.web.cern.ch/ab-abp-rlc-ecloud/` provides documentation and software tools related to this effort.

[2] We choose the dividing line to be the publication year, 1995, even though the PF instability had been under study well before publication.

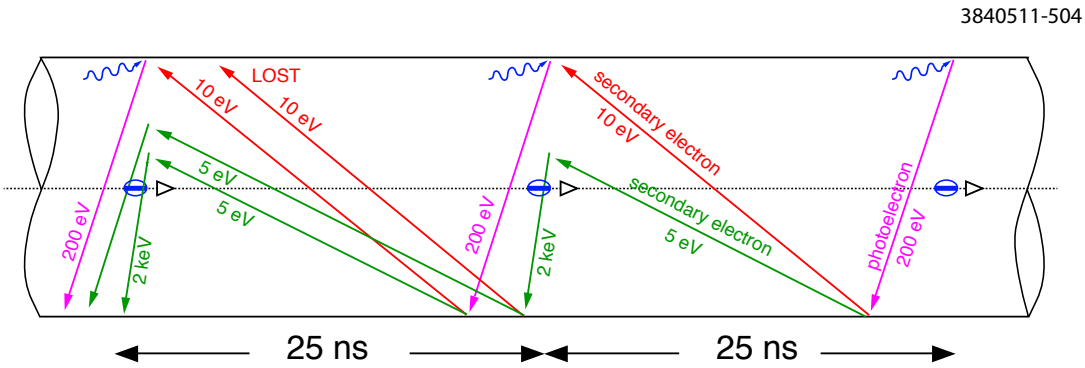

Figure 4.1: Cartoon illustrating the build-up of the electron cloud in the LHC for the case of 25-ns bunch spacing. The process starts with photoelectrons and is amplified by the secondary emission process. This cartoon was generated by F. Ruggiero.

on the chamber surface of the LHC arcs, TiN coating in the PEP-II ring [79] and at the Spallation Neutron Source, and the use of weak solenoidal magnetic fields at both B Factories [72, 80].

4.1.2 The Basic Physical Picture

The qualitative description of the development of an electron cloud for a bunched beam is as follows:

1. Upon being injected into an empty chamber, a beam generates electrons by one or more mechanisms, usually referred to as "primary," or "seed," electrons.

2. These primary electrons get rattled around the chamber from the passage of successive bunches.

3. As these electrons hit the chamber surface they yield secondary electrons, which are, in turn, added to the existing electron population.

Figure 4.1 illustrates the build-up of the electron cloud in the LHC.

In essentially all cases of practical interest, it is the secondary electron emission process that dominates the build-up of the electron cloud because this process leads to a compounding effect of the electron density under the action of successive bunches traversing the chamber: the more electrons are present in the chamber, the more electrons are generated upon striking the chamber walls. A notable exception to this general rule is CesrTA because the beam can be adjusted in length, energy, bunch spacing and bunch intensity so as to make either the primary or the secondary component dominate the electron cloud.

As successive bunches go by, the EC density n_e grows until a saturation level is reached. The density gradually decays following beam extraction, or during the passage of a gap in the beam. In many cases of interest, the net longitudinal motion of the electrons, i.e., along the beam direction, is not significant; therefore, in first approximation, it makes sense to study the electron density and its distribution at various locations around the ring independently of the others.

The above considerations lead us to define "the EC model," for the purposes of this report, as follows: a set of physical formulas and specific parameter values, combined with a calculational method, that allows one to determine the intensity, 6D distribution and time evolution of the electron cloud in a given region of a ring, for a given vacuum chamber, under the action of a given beam.

It should be clear that, with this definition, we are excluding from consideration the combined action of the beam and the electron cloud (except in very limited circumstances—see below) under their mutual influence. For example, the beam can become unstable under the action of the electron cloud it generated, hence it can no longer be considered "given." The full-fledged, fully coupled beam–electron-cloud dynamical system is interesting in its own right, and advanced simulation tools exist to study it [81], but is outside the scope of the research program presented here. In any case, a fully unstable beam is of limited practical use, hence our interest is more in identifying the conditions under which the instability arises, and/or to investigate the initial stages of the unstable dynamics, and/or to investigate the effects from the EC on the beam in those cases when the beam–electron-cloud coupling is sufficiently weak and the beam instability has small amplitude. Such cases are discussed in Chapter 6. In all cases when the beam instability is relatively weak, a detailed knowledge of the EC density and distribution is an essential first step to understand the response of the beam.

4.1.3 Simulation Programs

As implied by the above physical picture, the codes employed in the simulation of the EC build-up consist of some or all of the following actions:

1. Simulate the emission of photons off the beam particles as the beam traverses magnetized sections of the storage rings, especially bending magnets and wigglers.
2. Track each of the simulated photons until they hit the vacuum chamber downstream of the emission point. Decide whether any given photon yields a photoelectron, or whether it is reflected. If it is reflected, keep tracking it.
3. Simulate the emission of photoelectrons at the photon-wall collision point.
4. Compute the forces that act on the electrons (from the beam, space-charge and external fields).
5. Apply these forces to the electrons and track their motion.
6. Simulate the emission of secondary electrons as the electrons hit the walls of the chamber.

Simultaneously with the above actions, collect individual or statistical electron data via multiple diagnostic modules interspersed throughout the simulation. These yield many details of the electron distribution as a function of time, or time-averaged quantities.

Each of the above steps is performed during a time interval Δt sufficiently small (typically $10^{-12} - 10^{-10}$ s) to resolve the relevant ingredients of the physical model. The above processes are iterated as needed, for a sufficiently long time (typically $10^5 - 10^7$ time steps), in order to simulate the overall development of the EC for a sufficiently long time that a comparison with experimental data becomes possible and meaningful (typically $10^{-9} - 10^{-6}$ s).

Since the electron motion in the cloud is usually negligible in the longitudinal direction (as compared to the transverse dimension), the codes are typically 2D, and thus simulate the EC build-up and decay at a given, short, section of the storage ring. The overall picture for the entire ring is obtained by stitching together, in the post-processing phase, the results for each section with the appropriate weight. The 2D approximation is a particularly good one for field-free regions, and for dipole and quadrupole magnets provided they are significantly longer than the transverse size of the chamber. In certain cases, the 3D-ness of the EC has been shown to be important, and hence not amenable to 2D simulations. For example, the electron cloud has significant longitudinal motion at the edge of quadrupole magnets; the resulting electron "leakage" into adjacent regions is important in understanding the EC build-up in such regions [82, 83]. Wiggler magnets have magnetic fields whose characteristic range of variation is typically comparable to the transverse size of the chamber in all 3 dimensions. For the case of the CesrTA wigglers, detailed 3D simulations show that the electron dynamics in the regions where the vertical magnetic field B_y is maximum is qualitatively different from that in the regions where B_y is minimum [84]. In the maximum-B_y regions, not surprisingly, the electron dynamics is similar to that in a dipole magnet. In the minimum-B_y regions there is significant drift of electrons across the mid plane of the chamber, leading to horizontal electron density stripes, a phenomenon somewhat analogous to the generation of vertical stripes in dipole magnets. The relative electron density in vertical vs. horizontal stripes in a wiggler is sensitive to the photon reflectivity; therefore, the relative contributions to the vertical vs. horizontal coherent tune shifts from the electron cloud in a wiggler is sensitive to the photon reflectivity. Not only the distribution, but also the longevity of the electron cloud is different in these two regions. The stripes in the maximum-B_y regions dissipate much faster than those in the minimum-B_y regions. These long-lived electrons are trapped within the magnetic field, mirroring back and forth in the longitudinal direction along field lines. Therefore, although these minimum-B_y regions are of limited length, they may have a disproportionate effect on the beam.

The simulation codes employ the macroparticle method to represent the electrons in the cloud, and a prescribed function of space and time to represent the beam. The computation of the forces on individual electrons (due to the beam, external fields and the EC self-field), as well as the tracking of individual macro-electrons under the action of such forces, are carried out via well-known techniques [85]. Action 3 is implemented via a Monte Carlo algorithm by virtue of which macro-electrons are generated randomly given the value of the quantum efficiency and the energy-angle emission spectrum. A similar method is used to simulate the generation of secondary electrons in action 6. In the case of the code POSINST [55, 71, 86, 87], a very detailed phenomenological model of the secondary yield and the emission spectrum is implemented [86], some of whose parameter values are obtained by fitting simulation results to the measurements. Other codes used simpler models, although the basic physical model is the same.

At present, there is no single code that encompasses all 6 above-mentioned actions. All codes we know about, however, do encompass, in various degrees of detail, actions 3-6. Actions 1-3 are typically implemented via a simplified model for the photoemission spectrum and quantum efficiency. A major advancement of the CesrTA program over the past 2 years has been the development of the simulation code Synrad3D [88] (see detailed description below), which implements in great detail actions 1-3; the resultant temporal, geometrical and energetic distribution of the photoelectrons is then used in the Monte Carlo simulation of the generation of macro-photoelectrons in the codes.

A broad-based program of developing, comparing and benchmarking electron cloud buildup simulation codes was initiated in the CesrTA collaboration in 2008 and continues today. We have used

CesrTA input parameters as input to the simulation codes ECLOUD [89, 90], `CLOUDLAND` [91, 92], `POSINST` [71, 86], `WARP/POSINST` [93] and `PEHTS` [94], and compared the results against measurements. By iterating this process, we are able to pin down parameters that are not well known and thereby make more reliable extrapolations to the future ILC damping rings. The main parameters that are not well known are those pertaining to the electronic surface properties, i.e. photon reflectivity, photoemission yield (QE) and photoemission spectrum, and secondary electron yield and spectrum.

4.1.4 Primary Electron Sources

In lepton storage rings, including CesrTA and the proposed ILC damping rings, the beam typically emits copious synchrotron radiation with a ∼keV critical energy upon traversing the dipole bending magnets and/or the wigglers. On striking the vacuum chamber the synchrotron radiation photons emit photoelectrons. For this reason, in such machines, the primary electrons are essentially all photoelectrons. In hadron rings, with the notable exception of the LHC (see above), photoemission is negligible; in such cases the primary electrons are typically generated by ionization of residual gas, or by stray beam particles striking the chamber walls. In this report we will wholly ignore these two latter sources.

4.1.4.1 Photon Transport

Introduction The Bmad software library [44] has been used very successfully at Cornell for modeling relativistic charged particles in storage rings and linacs. Associated with this library are a number of programs used for lattice design and analysis. Recently, a new program that uses the Bmad library, called `Synrad3D` [88], has been developed to track synchrotron radiation photons generated in storage rings and linacs.

The motivation for developing `Synrad3D` was to estimate the energy and position distribution of photon absorption sites, which are critical inputs to codes which model the growth of electron clouds. `Synrad3D` includes photon scattering from the vacuum chamber walls, based on X-ray data from an LBNL database [95] for the smooth-surface reflectivity, and an analytical model [96, 97] for diffuse scattering from a surface with finite roughness. `Synrad3D` can handle any planar lattice and a wide variety of vacuum chamber profiles. A simpler, earlier code [98] was applied to the synchrotron radiation in the LHC.

In the following sections, the general approach used in `Synrad3D` will be described.

Approach `Synrad3D` uses Monte Carlo techniques to generate simulated photons based on the standard synchrotron radiation formulas for charged beam particles traversing dipoles, quadrupoles and wigglers, in the lattice of an accelerator. Any planar lattice can be handled. The lattice can be specified using Bmad, MAD, or XSIF formats. Photons are generated with respect to the particle beam's closed orbit, so the effect of variations in the orbit can be studied. In a linear accelerator lattice, since there is no closed orbit, the orbit is calculated from the user supplied initial orbit. The particle beam size is also taken into account when generating the photon starting positions. The emittance needed to calculate the beam size can be supplied by the user or is calculated from the standard synchrotron radiation formulas.

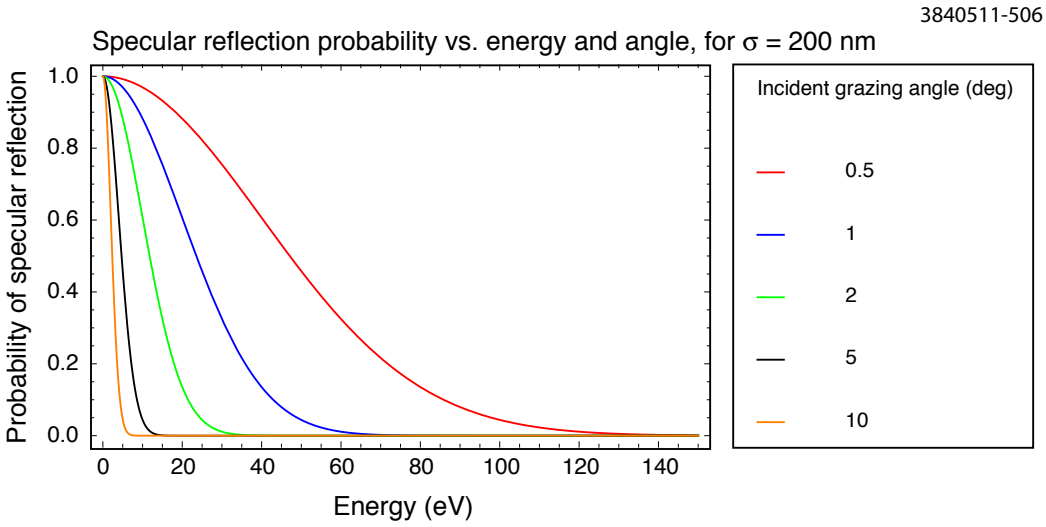

Figure 4.2: Specular reflection probability [96], vs. photon energy and angle, for an rms surface roughness of 200 nm.

Scattering Model Simulated photons are tracked until they hit the wall, where the probability of being scattered, and the scattering angle, are determined by their energy and angle of incidence. This section describes the scattering model.

Generally, the probability of specular reflection of a photon from a rough surface depends on the the rms surface roughness σ, the photon wavelength λ, and the grazing angle. An explicit formula for this probability is [96]

$$P_{\text{spec}} = \mathrm{e}^{-g(x,y)}, \tag{4.1}$$

in which

$$g(x,y) = \frac{4\pi^2\sigma^2(x+y)^2}{\lambda^2} \tag{4.2}$$

where x is the cosine of the incident polar angle, and y is the cosine of the scattered polar angle. For a typical technical vacuum chamber surface, the rms surface roughness $\sigma \gtrsim 200$ nm is greater than most of the X-ray wavelengths of interest, for all except the lowest energy photons. In this regime, except at very small grazing angles, diffuse scattering from the surface dominates over specular reflection. This is illustrated in Fig. 4.2.

The theory of diffuse scattering of electromagnetic waves from random rough surfaces is a well-developed subject, and is covered in detail in references [96] and [97]. The model we use here is based on scalar Kirchhoff theory; this model has been used successfully to describe the scattering of soft X-rays from metal surfaces [99, 100]. In our case, we assume a Gaussian distribution for both the surface height variations (rms σ) and for the transverse distribution (equal in both transverse directions, with autocorrelation coefficient T).

The most general expression for the diffusely scattered power is complex, and involves an infinite sum. However, the expression simplifies substantially in the limit $g(x,y) \gg 1$. For very rough surfaces corresponding to technical vacuum chambers, for which typically $\sigma \gg \lambda$, this condition is satisfied over much of the region of interest. In this limit, the diffusely scattered power per unit

solid angle is given by

$$\frac{dP_{\rm diff}}{d\Omega} = P_0 \frac{\langle R\rangle}{4\pi y} \frac{(1+xy)^2}{(x+y)^4} \tau^2 \mathrm{e}^{-\frac{(2-x^2-y^2)\tau^2}{4(x+y)^2}} (1 - a\cos\phi)^2 \mathrm{e}^{b\cos\phi}, \tag{4.3}$$

with

$$a = \frac{h(x,y)}{1+xy}, \tag{4.4}$$

$$b = \frac{2h(x,y)\tau^2}{4(x+y)^2}, \tag{4.5}$$

$$h(x,y) = \sqrt{1-(x^2+y^2)+x^2y^2}. \tag{4.6}$$

In this expression, P_0 is the incident power, and $\langle R\rangle$ is the smooth-surface reflectivity, which is determined by the atomic structure of the surface material. ϕ is the scattering angle out of the plane of incidence. Note that the relative power depends on the ratio $\tau = T/\sigma$, and not on the T or σ separately.

The smooth-surface reflectivity $\langle R\rangle$ depends on the atomic structure of the surface materials (including any thin layers which may be deposited on the surface). The surface roughness parameters σ and T depend on the geometry of the surface deviations from a perfect plane. These parameters may be determined from inspection of the vacuum chamber surface, for example, using an atomic force microscope.

To derive a working model for the smooth surface reflectivity and the surface parameters for a typical vacuum chamber surface, we have relied on measurements [101] of X-ray scattering from an aluminum vacuum chamber surface made at `DAPHNE`. For these measurements, the rms surface roughness of the sample was reported to be 200 nm.

The theory of diffuse scattering discussed above has been used, together with smooth surface reflectivity results taken from an X-ray database [95], to predict the scattering and compare with the measurements. From these comparisons, the best-fit value for the transverse autocorrelation parameter, T, was found to be 5500 nm. In addition, it was found that the smooth-surface reflectivity corresponding to a 10 nm carbon film on an aluminum substrate was needed to fit the data. The assumption of an aluminum oxide surface film was not consistent with the data. The data and the corresponding fits are shown in Fig. 4.3, 4.4, and 4.5.

With the smooth-surface reflectivity determined, and the surface parameters established, the scattering model in `Synrad3D` is completely determined. The model currently in use has a smooth-surface reflectivity illustrated in Fig. 4.6. Diffuse scattering distributions for 30 eV photons are shown in Fig. 4.7 and Fig. 4.8. At this low photon energy, the approximation $g(x,y) \gg 1$ does not hold in general, and the full diffuse scattering formalism is used to compute these distributions. Diffuse scattering distributions for high energy photons, for which $g(x,y) \gg 1$ are shown in Fig. 4.9 and Fig. 4.10. These distributions have been computed from Eq. 4.3.

Vacuum Chamber Model The vacuum chamber wall is characterized at a number of longitudinal positions by its cross-section. The cross section model is shown in Fig. 4.11. As shown

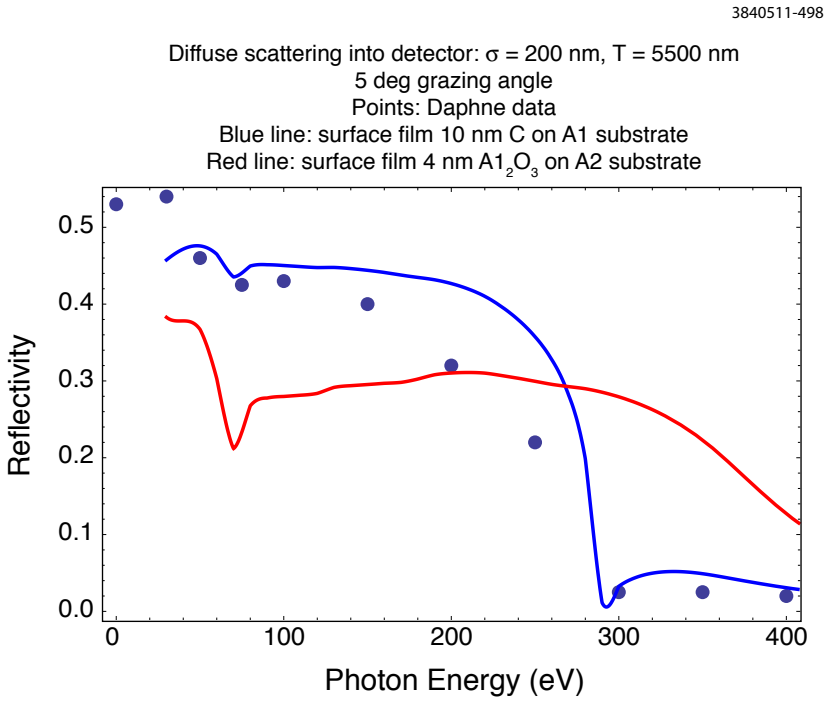

Figure 4.3: Diffuse scattering at 5 deg from a surface layer on an aluminum substrate: comparison of data and model

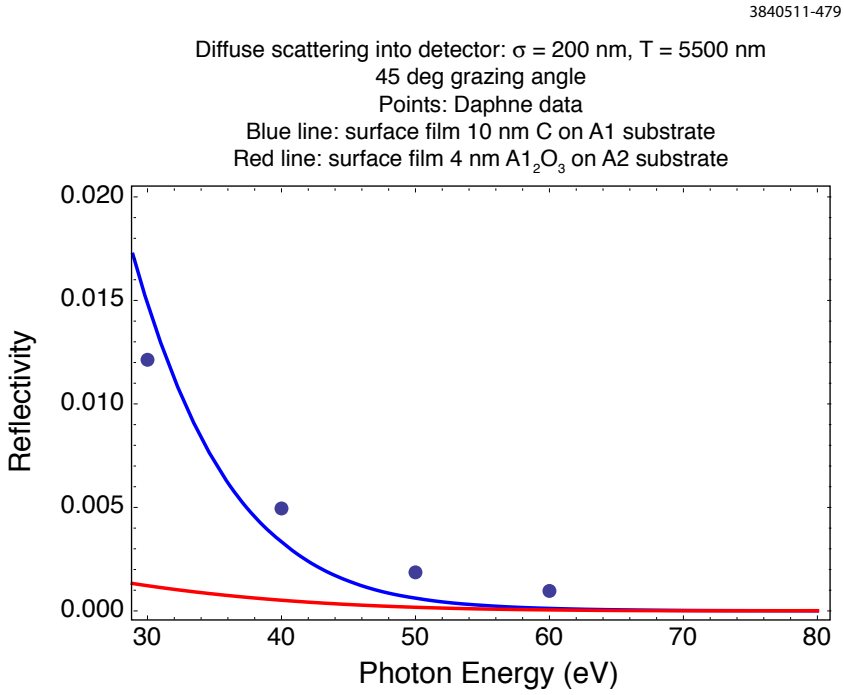

Figure 4.4: Diffuse scattering at 45 deg from a surface layer on an aluminum substrate: comparison of data and model

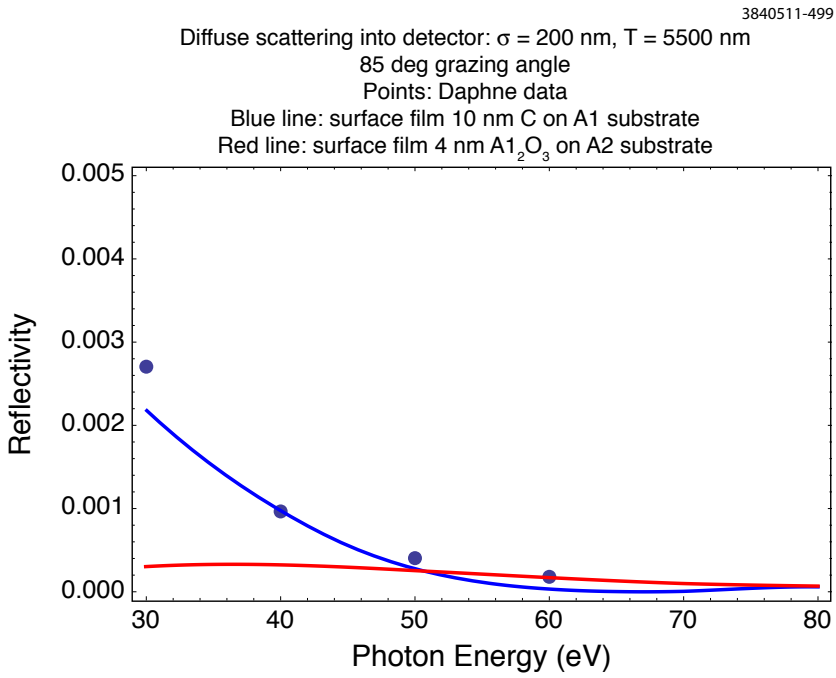

Figure 4.5: Diffuse scattering at 85 deg from a surface layer on an aluminum substrate: comparison of data and model

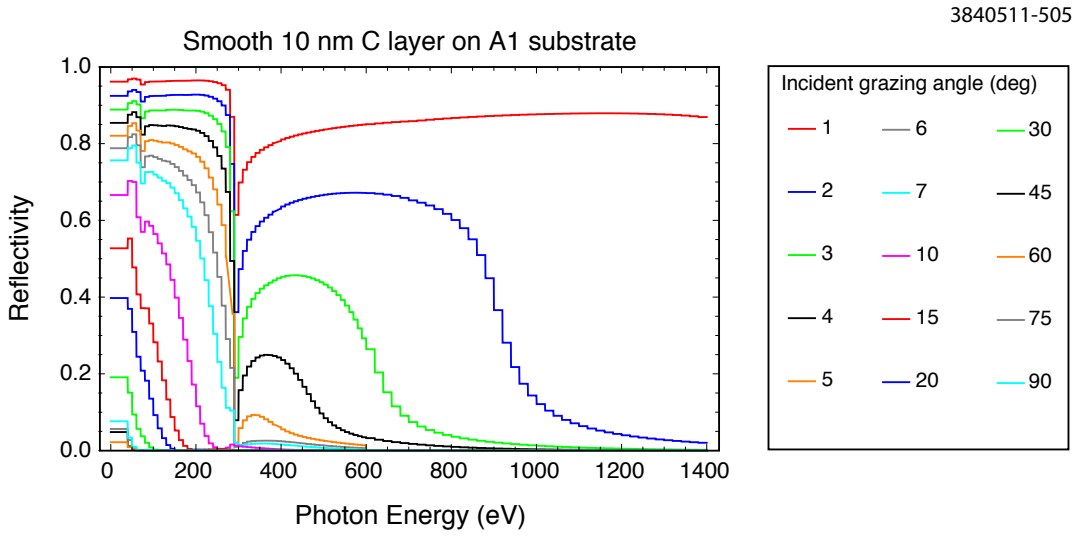

Figure 4.6: Smooth surface reflectivity for a 10 nm C film on Al substrate: from [95]

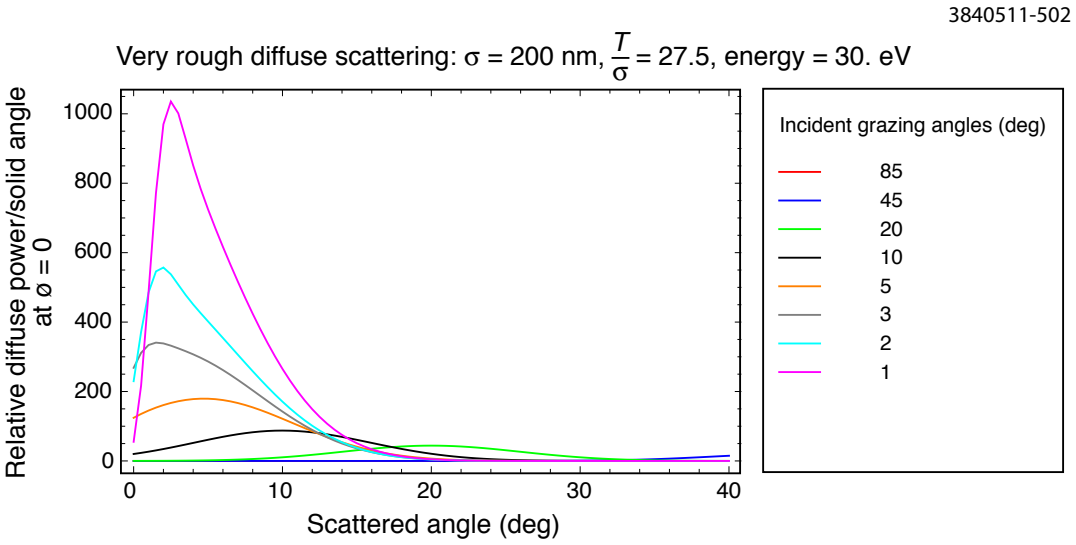

Figure 4.7: Diffuse scattering polar angular distributions for 30 eV photons

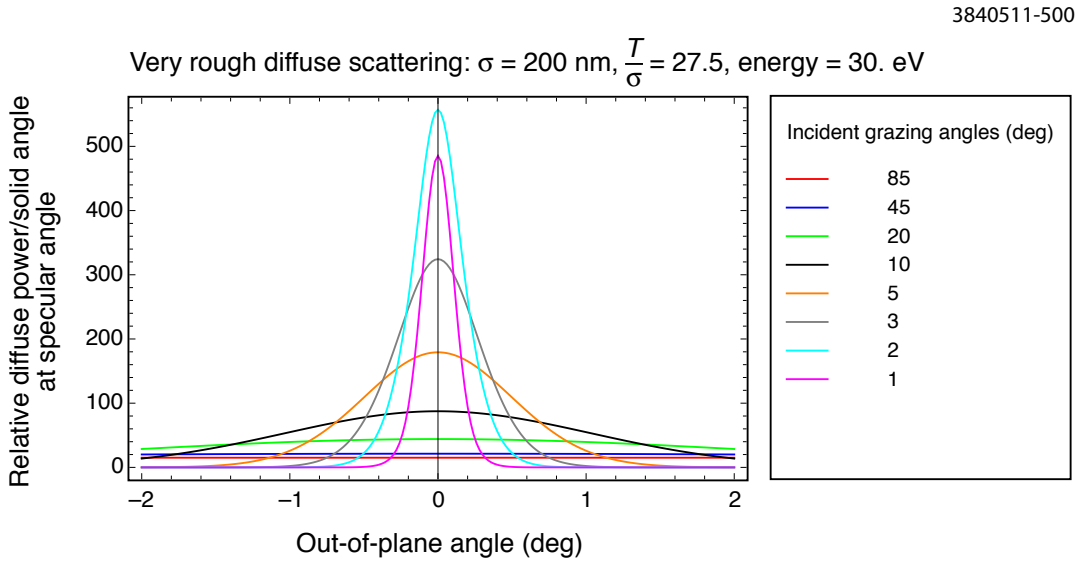

Figure 4.8: Diffuse scattering out-of-plane angular distributions for 30 eV photons

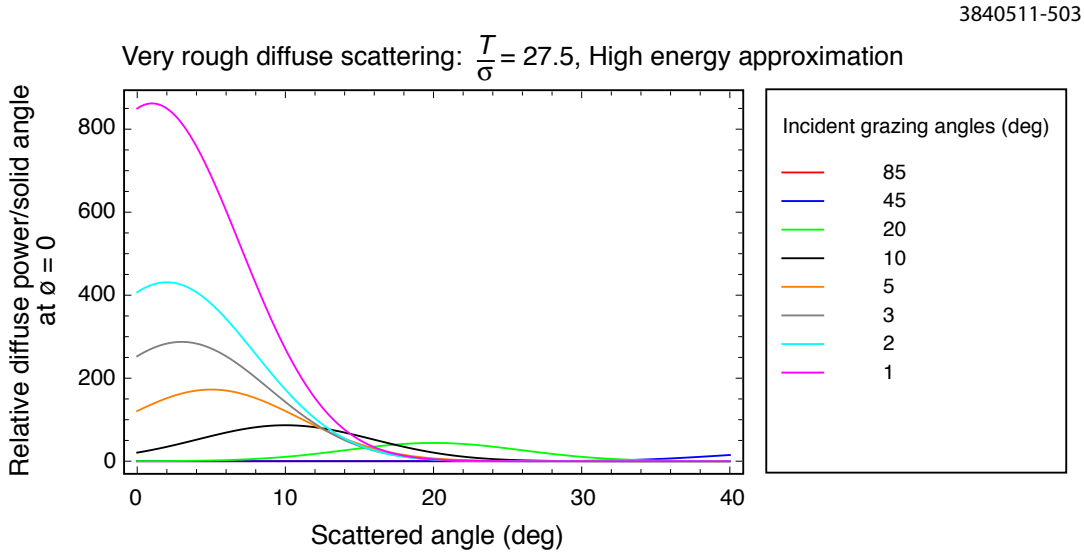

Figure 4.9: Diffuse scattering polar angular distributions for high energy photons

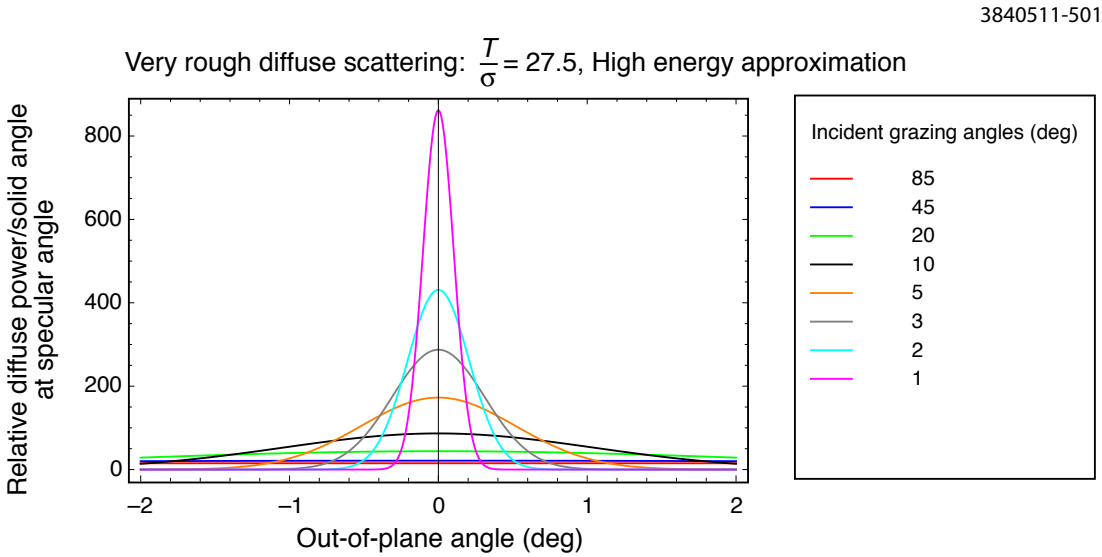

Figure 4.10: Diffuse scattering out-of-plane angular distributions for high energy photons

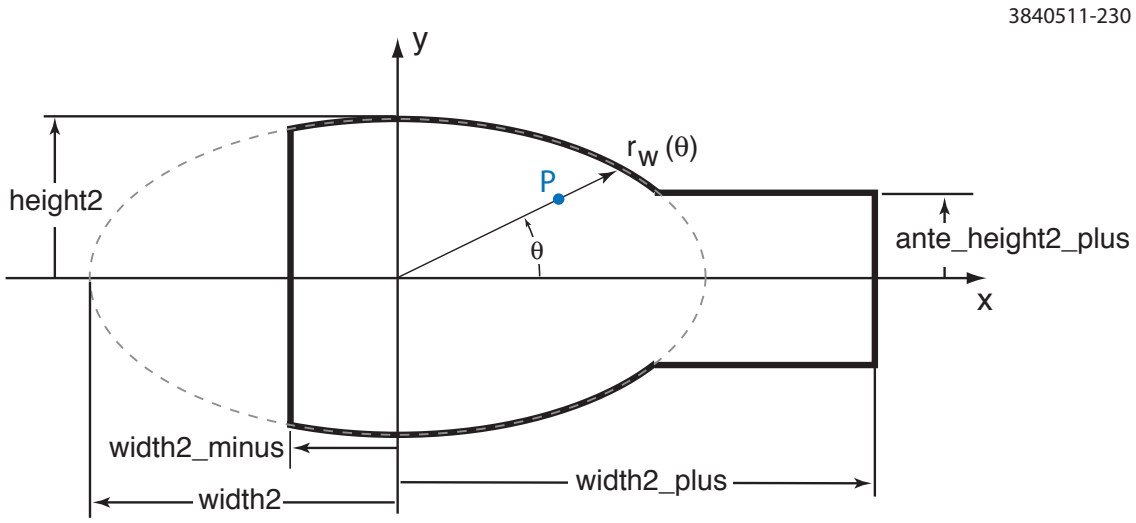

Figure 4.11: Vacuum chamber model

in the figure, antechambers can be included. A vacuum chamber wall cross-section may also be characterized using a piecewise linear outline.

In between the cross-sections, linear interpolation or triangular meshing can be used. Linear interpolation is faster but is best suited for convex chamber shapes.

4.1.4.2 Photoelectron Models

The simple photoelectron generation model implemented at present uses a single energy-independent value for the quantum efficiency, ignores the incident photon energy spectrum and generates an ad-hoc photoelectron energy distribution which must be re-tuned for each set of beam conditions under study. The reasonableness of these empirically determined values may be checked by comparing with direct measurements of the quantum efficiency. Since the quantum efficiency is a function of the energy of the absorbed photons, we need to know the photon energy spectrum to do this. This spectrum is provided by the photon transport simulations described in Section 4.1.4.1.

In connection with studies of electron cloud effects for the LHC, direct measurements [102] have been made of the quantum efficiency, and the photoelectron energy spectrum, for VUV photons in the energy range up to about 120 eV. The measurements were made for a variety of surfaces, including aluminum. To estimate the relative quantum efficiency above 120 eV, we refer to tables of the photoabsorption cross section as a function of energy, as given in the Atomic Data and Nuclear Data Tables [103, p.34]. The relative quantum efficiency obtained in this way for an aluminum surface is shown in Fig. 4.12.

The information from Fig. 4.12 can be folded with the photon energy spectrum from the photon transport simulations to estimate the effective quantum efficiency for different beam energies at different points in the CesrTA ring. This provides additional information that is useful in constraining the quantum efficiency when comparing with CesrTA data, and in extrapolating electron cloud effects to future positron rings.

Absolute quantum efficiencies, averaged over a VUV photon energy spectrum, were also measured

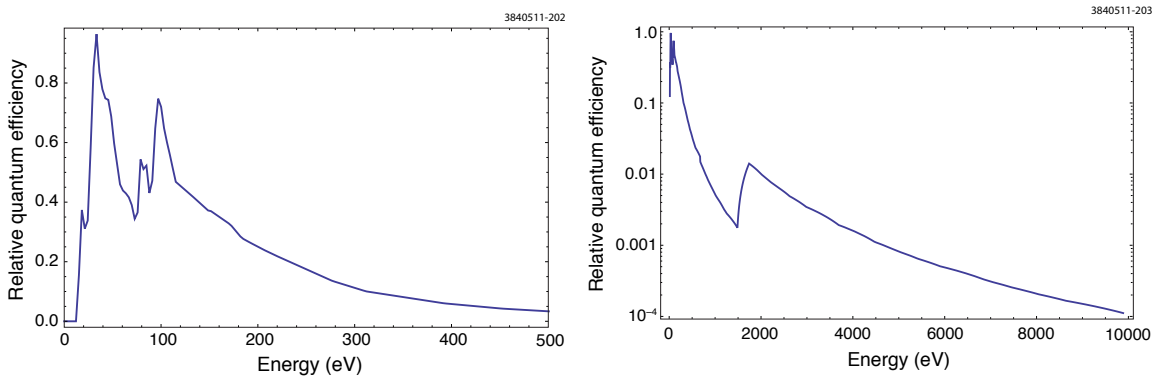

Figure 4.12: Relative quantum efficiency for an aluminum surface vs. photon energy. Left: energy range up to 0.5 keV. Right: energy range up to 10 keV. The L- and K-edges are evident at energies near 0.1 keV and 2 keV, respectively.

in Ref. [102]. These results were quite sensitive to the surface material and conditioning, but were in the range of 4% to 11%. Quantum efficiency values found for the best fits to the CesrTA data are roughly similar to these numbers.

4.1.5 Secondary Electron Emission

The above-mentioned primary mechanisms are usually insufficient to lead to a significant EC density. However, the average electron-wall impact energy is typically ∼100–200 eV, at which secondary electron emission is significant. As implied by the above description, secondary emission readily exponentiates in time, which can lead to a large amplification factor, typically a few orders of magnitude, over the primary electron density, and to strong temporal and spatial fluctuations in the electron distribution [104]. This compounding effect of secondary emission is usually the main determinant of the strength of the ECEs, and is particularly strong in positively-charged bunched beams (in negatively-charged beams, the electrons born at the walls are pushed back into the wall with relatively low energy, typically resulting in relatively inefficient secondary emission).

We remind the reader, however, that the broad flexibility of the CesrTA beam allows the establishment of experimental conditions in which one can selectively emphasize either the primary or the secondary electron components of the electron cloud.

The ECE combines many parameters of a storage ring such as bunch intensity, size and spacing, beam energy [105], vacuum chamber geometry, vacuum pressure, and electronic properties of the chamber surface material such as photon reflectivity R_γ, effective photoelectric yield (or quantum efficiency) Y, secondary electron yield (SEY), characterized by the function $\delta(E)$ (E =electron-wall impact energy), secondary emission spectrum [106, 107], etc. The function $\delta(E)$ has a peak $\delta_{\max}$ typically ranging in $\sim 1-4$ at an energy $E = E_{\max}$ typically ranging in $\sim 200-400$ eV.

A convenient phenomenological parameter is the effective SEY, δ_{eff}, defined to be the average of $\delta(E)$ over all electron-wall collisions during a relevant time window. Unfortunately, there is no simple a-priori way to determine δ_{eff}, because it depends in a complicated way on a combination of many of the above-mentioned beam and chamber parameters. If $\delta_{\text{eff}} < 1$, the chamber walls act as net absorbers of electrons and n_e grows linearly in time following beam injection into an empty chamber. The growth saturates when the net number of electrons generated by primary mechanisms balances

the net number of electrons absorbed by the walls. If $\delta_{\text{eff}} > 1$, the EC grows exponentially. This exponential growth slows down as the space-charge fields from the electrons effectively neutralize the beam field, reducing the electron acceleration. Ultimately, the process stops when the EC space-charge fields are strong enough to repel the electrons back to the walls of the chamber upon being born, at which point δ_{eff} becomes $= 1$. At this point, the EC distribution reaches a dynamical equilibrium characterized by rapid temporal and spatial fluctuations, determined by the bunch size and other variables. For typical present-day storage rings, whether using positron or proton beams, the spatio-temporal average n_e reaches a level $\sim 10^{10-12}$ m^{-3}, the energy spectrum of the electrons typically peaks at an energy below ~ 100 eV, and has a high-energy tail reaching out to keV's.

If there is a gap in the beam, or if the beam is extracted, the cloud dissipates with a fall time that is controlled by the low-energy value of $\delta(E)$ [108]. In general, there is no simple, direct correlation between the rise time and the fall time.

In regions of the storage ring with an external magnetic field, such as dipole bending magnets, quadrupoles, etc., the EC distribution develops characteristic geometrical patterns. For typical fields in the range $B = 0.01 - 5$ T and typical EC energies < 100 eV, the electrons move in tightly-wound spiral trajectories about the field lines. In practice, in a bending dipole, the electrons are free to move in the vertical (y) direction, but are essentially frozen in the horizontal (x). A cloud electron in a dipole field gets a kick from a bunch which is proportional to the bunch charge and inversely proportional to the distance from the beam orbit to the cloud electron (assuming the electron is outside the core of the bunch). Secondaries produced when that electron strikes the top or bottom of the chamber are trapped at the same horizontal position, and these secondaries will be subjected to the same x dependent kick. As a result, the x dependence of the kick imparted by the beam on a given electron is remembered by the electron for many bunch passages. It often happens that for a given value of the bunch charge, the kick imparted by the bunch, which corresponds to the electron-wall impact energy, equals $E_{\max}$. At this location $\delta(E) = \delta_{\max}$, hence n_e is maximum, leading to characteristic high-density vertical stripes symmetrically located about $x = 0$ [109]. For quadrupole magnets, the EC distribution develops a characteristic four-fold pattern, with characteristic four-fold stripes [110].

The secondary emission yield (SEY) function $\delta(E_0, \theta_0)$ is the average number of electrons emitted when an electron of kinetic energy E_0 impinges on a surface at an incident angle θ_0 (conventionally measured relative to the normal to the surface). The SEY reaches a peak value $\delta_{\max}$ (conventionally specified at normal incidence) at an energy $E_0 = E_{\max}$. A fairly detailed phenomenological probabilistic description of the secondary emission process is presented in Refs. [86, 87], upon which we base our analysis.

Closely related to δ is the emitted-energy spectrum of the secondary electrons, $d\delta/dE$ at given incident energy E_0, where E is the emitted electron energy. The spectrum covers the region $0 \leq E < E_0$, and it exhibits three fairly distinct main components: elastically reflected electrons (δ_e), rediffused (δ_r), and true secondaries (δ_{ts}). The SEY is given by $\delta = \delta_e + \delta_r + \delta_{ts}$. The three components are emitted with qualitatively different energy spectra. Depending upon various features of the storage ring considered, the three components can contribute differently to various aspects of the ECE. Detailed analyses are presented in Ch. 5 and Ch. 6.

4.2 Summary

In summary, the electron-cloud model:

- Is characterized by rich physics, involving many ingredients pertaining to the beam and its environment.
- Involves a broad range of energy and time scales.
- Is always undesirable in particle accelerators.
- Is often a performance-limiting problem, especially in present and future high-intensity storage rings.

As a consequence, the physics of the formation and dissipation is challenging to accurately quantify, predict and extrapolate. The main goals of current research in electron-cloud physics are, in no particular order of importance or relevance:

- Identify the relevant variables in each case.
- Estimate the electron density, time dependence, incident flux at the walls of the chamber, etc.
- Compare predictions against measurements as thoroughly as possible; iterate the process and pin down the values of the relevant parameters.
- Predict the magnitude of the effect in other cases; if possible, minimize the effect at the design stages of new machines.
- Define a relatively simple set of rules of thumb, or a simple effective theory, to approximately determine the severity of the effect.
- Design and implement mitigation or suppression mechanisms.

The R&D program on electron cloud at CesrTA described in this Phase-I Report addresses all the above.

Chapter 5

Studies of Electron Cloud Growth and Its Mitigation

5.1 Local EC Build-Up and Mitigation Studies

5.1.1 Overview

The buildup of high densities of low-energy electrons produced by the intense synchrotron radiation in electron and positron storage rings has been under active study since it was identified in the mid-90's in the KEK Photon Factory (PF) when operated with a positron beam [50]. While this phenomenon did not present an operational limitation at the PF under nominal conditions, the observation raised immediate concerns for both B Factories, then under design, and triggered significant simulation efforts [51] aimed at quantifying the phenomenon and designing mitigation techniques. Several years later, as the luminosity performance in the B Factories was pushed towards its specified goal, the electron cloud became at some point the most significant limitation. Mitigating this effect at both B Factories then became essential to reach, and then exceed, the design performance [40]. For a more complete historical summary, see Sec. 4.1.1.

Simple analytic examinations of the electron dynamics under the influence of the beam soon revealed that, for essentially all the high-energy storage rings in which the phenomenon has been observed, the electron motion takes place predominantly in the transverse plane, i.e., in the plane perpendicular to the beam direction. While a certain amount of longitudinal electron drift is always present, it is generally a good approximation to analyze the electron-cloud density locally, independently of the other regions of the ring. This is particularly true in regions where there is no external magnetic field, or when this field is uniform. For the same reasons, the analysis of the build-up and decay of the electron cloud at any given location is quite amenable to a 2D analysis. For this reason, 2D build-up codes have been extensively used and have led to substantial progress in the field. It should be kept in mind, however, that there are regions in the machine, particularly in small rings, in which the 3D nature of the external field demands 3D simulation codes. Such is the case, for example, of wiggler magnets and the ends of dipole bending magnets. In case that the bunch is very long, such as in the spallation neutron source PSR [59], the $\mathbf{E} \times \mathbf{B}$ drift of the electrons is significant, and a 3D analysis become necessary in many cases.

5.1.2 Special Features of the CesrTA EC Program

The CesrTA program is the single most comprehensive effort to measure and characterize the EC, and to assess techniques for its mitigation, in e^+e^- storage rings to date [1]. Mitigation techniques studied include low-emission coatings such as TiN, amorphous carbon and diamond-like carbon on aluminum chambers; grooves etched in copper chambers; clearing electrodes; and more. Combined with an extensive array of instrumentation and diagnostic tools such as retarding-field analyzers and shielded-pickup detectors, much has been learned to date about the physics governing the buildup of electron clouds. While some of these diagnostics instruments had been employed in previous studies elsewhere in various combinations, the CesrTA program includes all of them in a single storage ring, with measurements analyzed by the same group of researchers. In addition, several pre-existing simulation codes have been augmented, cross-checked, and in some cases debugged, and applied to the analysis of the data.

In essentially all cases of practical interest, it is the secondary electron emission process that dominates the build-up of the electron cloud because this process leads to a compounding effect of the electron density under the action of successive bunches traversing the chamber: the more electrons are present in the chamber, the more electrons are generated upon striking the chamber walls. The flexibility of the beam formatting at CesrTA affords the unique and valuable possibility of studying the electron cloud formation and dissipation with a beam consisting of an almost arbitrary fill pattern and bunch intensity. This flexibility allows, in principle, to tease out the contributions to the electron cloud due to photoemission from those due to secondary electron emission. This is a consequence of the fact that short bunch trains (typically fewer than 10 bunches) lead to an electron cloud dominated by photoemission, while long bunch trains (say, more than 40) lead to an electron cloud typically dominated by secondary electron emission (unless the peak value of the SEY is unusually low, say < 0.9). In addition, an isolated "witness bunch" can be placed at varying distances from the end of the train, thus affording the possibility of studying the dissipation of the electron cloud as a function of time.

In addition, the beam energy can be varied in the range $\sim 2 - 5$ GeV, which provides a powerful handle on the synchrotron radiation intensity and hence on the photoelectron creation rate. As if the above features were not enough, the instrumentation installed at CesrTA allows the measurement of the electron cloud density bunch by bunch, which provides yet another handle to disentangle the intensity of the photoelectrons from the secondaries, as well as a more detailed and time-resolved analysis of the build-up of the EC density.

5.1.3 Simulation Program

A broad-based program of developing, comparing and benchmarking electron cloud buildup simulation codes was initiated in the CesrTA collaboration in 2008 and continues today. We have used CesrTA parameters as input to the simulation codes `ECLOUD` [89, 90], `CLOUDLAND` [91, 92], `POSINST` [71, 86], `WARP/POSINST` [93] and `PEHTS` [94], and compared the results against measurements. By iterating this process, we are able to pin down parameters that are not well known and thereby make more reliable extrapolations to the future ILC damping rings. The main (indeed, the only) parameters that are not well known are those pertaining to the electronic surface properties, i.e., photon reflectivity, quantum efficiency, and secondary electron emission.

5.1.3.1 EC Build-Up Modeling

Essential components of the codes are photoelectron generation models, time-sliced calculations of macroparticle dynamics including beam kicks, the space charge force from the cloud itself, the Lorentz forces of ambient magnetic fields, and the the model describing the various components of the secondary yield (SEY). The `ECLOUD` and `POSINST` models use two-dimensional approximations for the electric fields and have successfully reproduced a variety of coherent tune shift measurements, as well as local RFA and shielded-pickup measurements. These 2D codes are relatively fast, and are generally successful in predicting the features of the electron cloud in regions of the ring that are essentially 2D, namely field-free regions and long magnets, especially dipoles. The `CLOUDLAND` [111] and `WARP/POSINST` [84] codes are 3D and therefore far more computationally expensive, and have been used to model the electron cloud in essentially 3D regions such as the ends of quadrupoles and sextupoles, and wiggler magnets, providing information on the long-term trapping of electrons. In addition, it should be pointed out that `ECLOUD` and `POSINST` are build-up codes. They assume that the beam is a prescribed function of space and time and therefore does not respond to the electron cloud. `CLOUDLAND` and `WARP/POSINST`, in addition to being 3D, have the option of describing the beam fully dynamically, so that the beam and the electron cloud respond to their mutual simultaneous influence.

5.1.3.2 Photon Production, Transport and Absorption

In Section 4.1.4.1, we have described the code `Synrad3D`, which models photon production, transport, scattering, and absorption in beam lines and storage rings. In this section, we present five examples of `Synrad3D` photon production, transport and absorption simulations using CesrTA lattices and vacuum chambers. The examples are presented in order of increasing sophistication.

Example 1: Photon Emission in a Dipole As the first example, we consider the CesrTA ring with a 5.3 GeV positron beam, and use `Synrad3D` to simulate photon emission only in the arc dipole at B12W. The vacuum chamber is a simple ellipse (dimensions 9 cm horizontal by 5 cm vertical), and the scattering is purely specular. The photons are generated only in the upstream end of this dipole but propagate downstream and can scatter.

In Fig. 5.1, we show a collection of photon trajectories, projected onto the bend plane. Photons generated by the beam in B12W strike the B12W vacuum chamber a short distance downstream. Some are absorbed here, but most scatter and strike the vacuum chamber further downstream, in B13W. More are absorbed here, but many others scatter again.

These photon trajectories in three dimensions are shown in Fig. 5.2. Photons from the source (on the right) propagate and strike the vacuum chamber. Blue dots represent absorption sites. For this simple example, in which the photon source is localized longitudinally, the absorption site locations tend to be clumped in several clusters (at the location of downstream dipoles), with decreasing intensity as we get further from the source.

Other features of the photon scattering and absorption process are shown in Fig. 5.3 and Fig. 5.4.

In Fig. 5.3(left), a histogram of the number of reflections is presented. Many photons suffer no reflections, that is, they are absorbed as soon as they hit the vacuum chamber, but most are reflected several times before being absorbed. The mean number of reflections is 5.1.

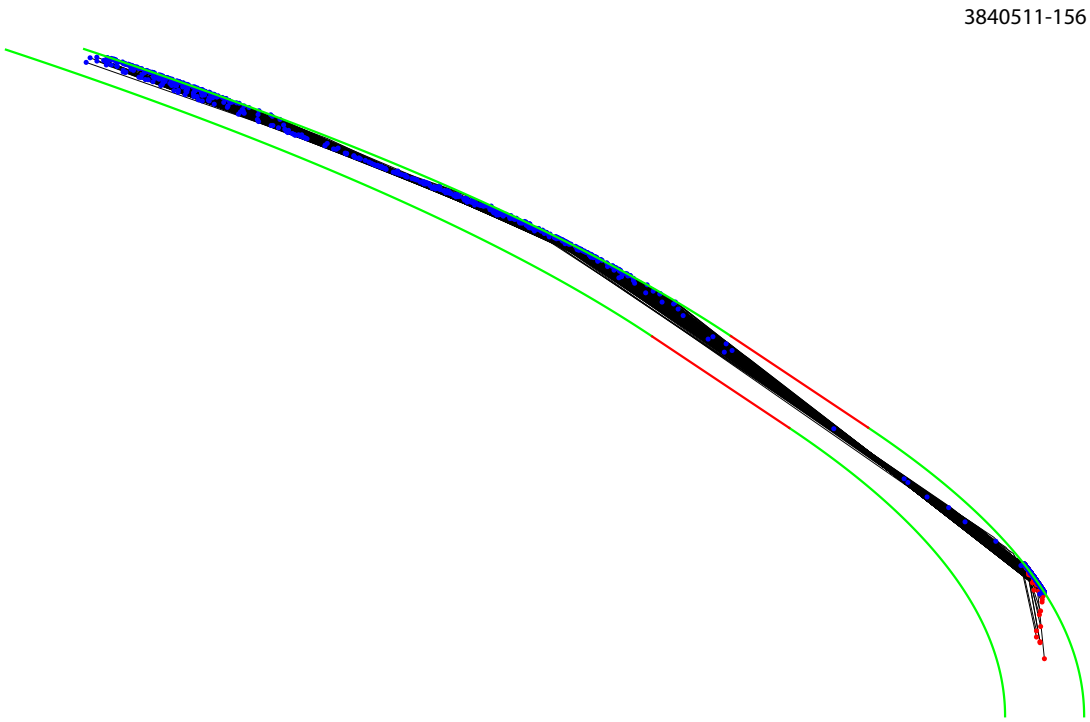

Figure 5.1: Photon trajectories from B12W: projections onto bend plane. The red dots at the lower right are the photon source (the radiating beam in a section of the dipole). Black lines are photon trajectories, and blue dots are photon absorption sites. The green lines in the lower right are the edges of the vacuum chamber in B12W; the red lines are the edges in a straight section, and the green lines on the left are the edges of the vacuum chamber in the next dipole, B13W. The geometry has been distorted for purposes of illustration.

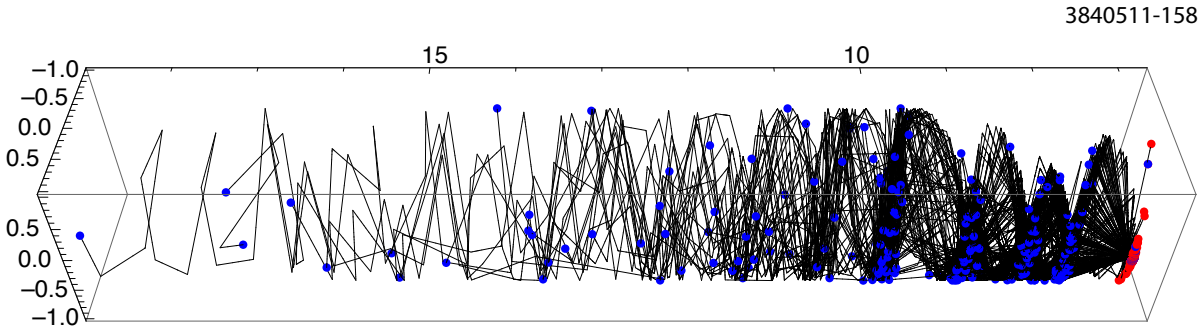

Figure 5.2: Photon trajectories from B12W in three dimensions. The photon source is on the right. Black lines are trajectories, and blue dots are photon absorption sites. The transverse geometry has been distorted from an ellipse to a circle, and the longitudinal dimension has been rectified and divided by 10, for purposes of illustration.

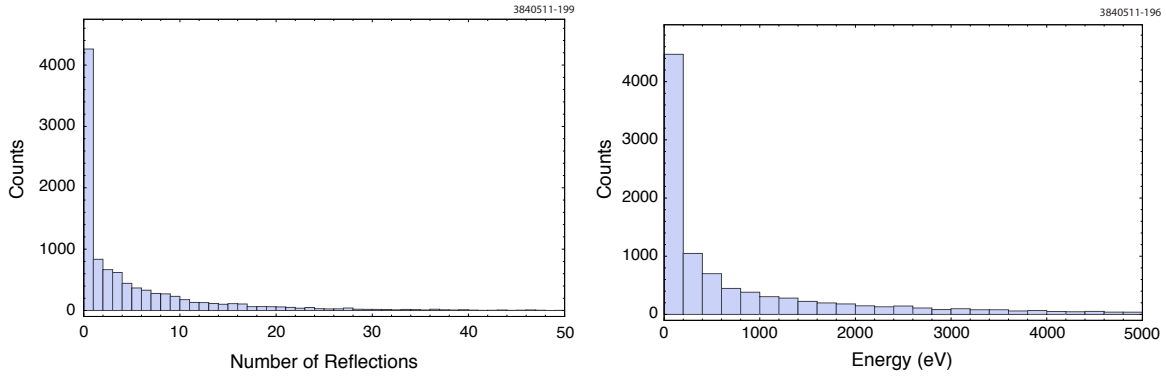

Figure 5.3: Reflection distribution (left) and energy distribution (right). The mean number of reflections is 5.1.

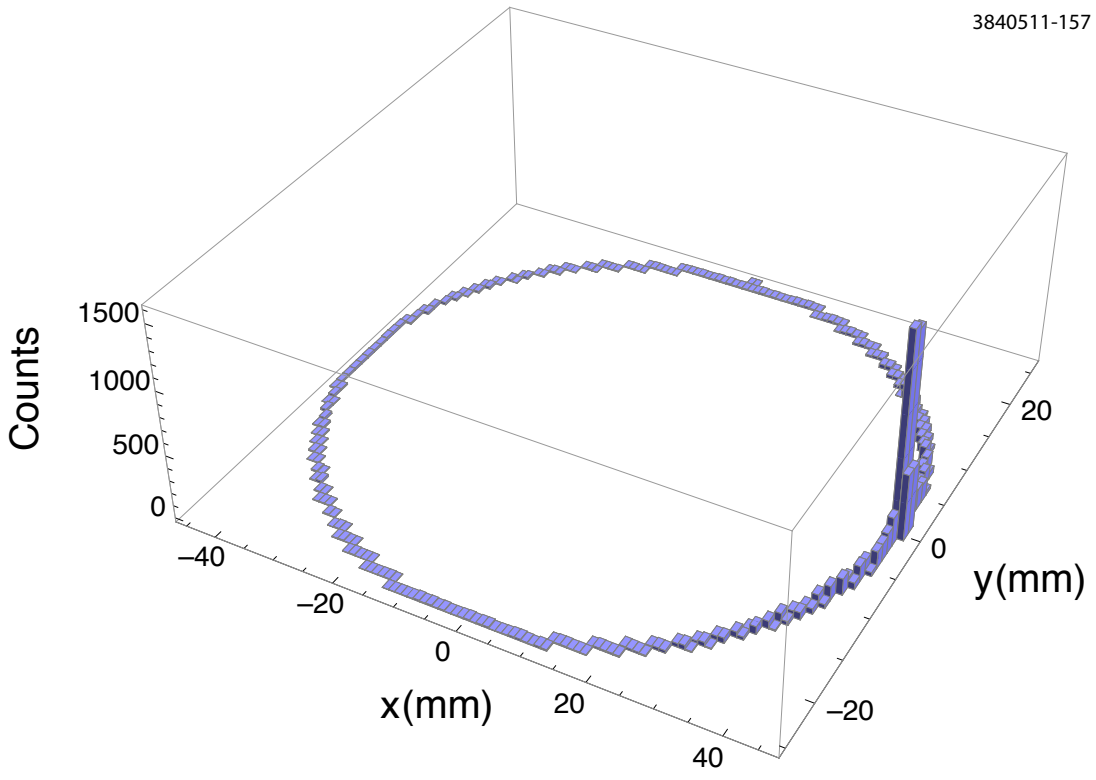

Figure 5.4: Distribution of photon absorption sites around the vacuum chamber perimeter

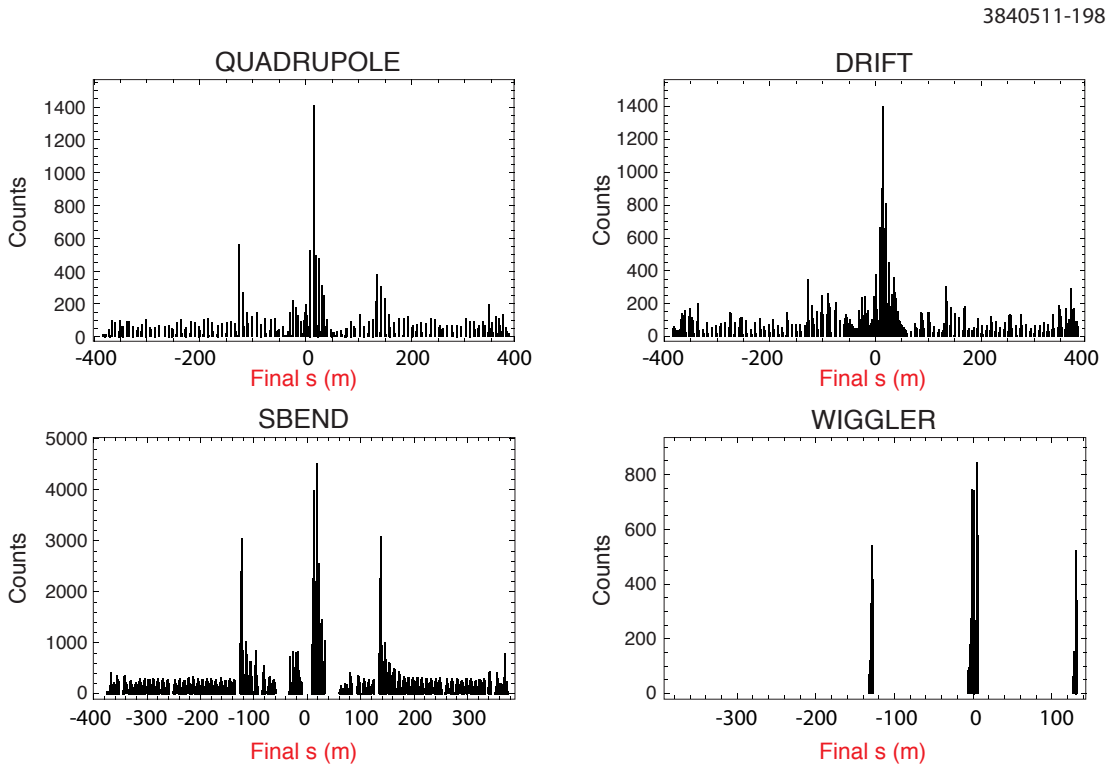

Figure 5.5: Distribution of photon absorption sites vs. longitudinal position, for different magnetic environments. The origin for the longitudinal coordinate is the center of the L0 straight section. The ring circumference is about 760 m.

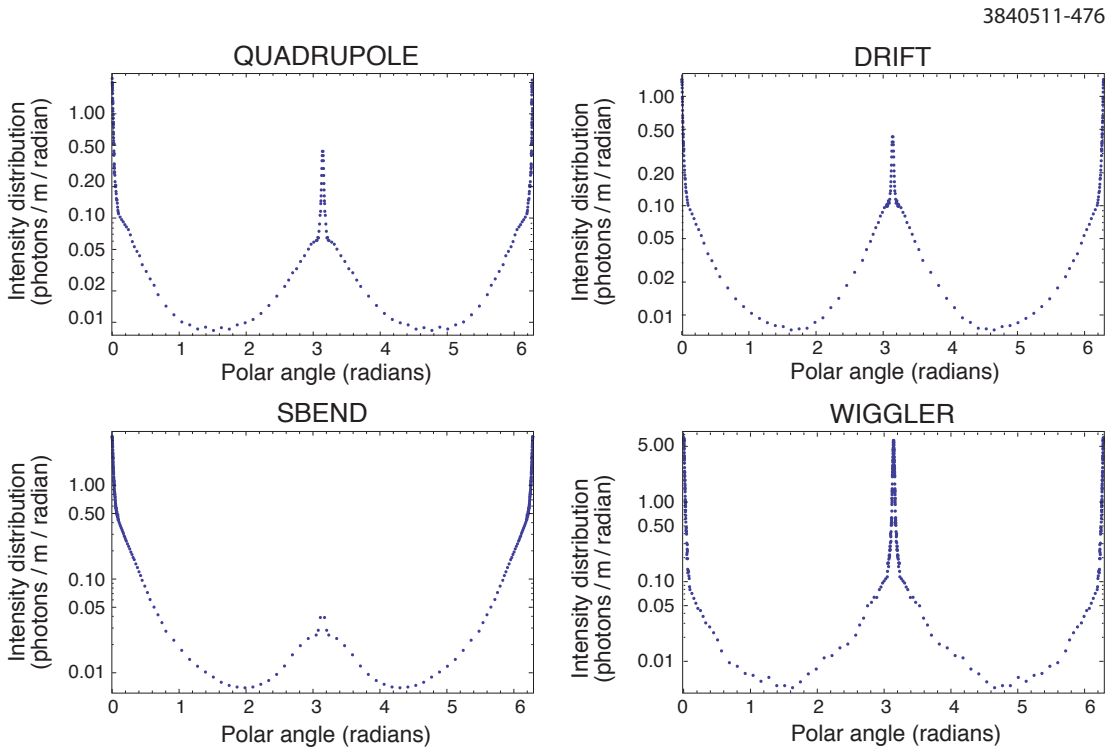

Figure 5.6: Photon intensity distribution (in photons/meter/radian) vs. polar angle (measured around the vacuum chamber, with zero angle corresponding to the radial outside direction), averaged over each type of magnetic environment. A 9 cm (horizontal) by 5 cm (vertical) elliptical vacuum chamber profile is assumed throughout the ring, and all scattering is specular. Top-bottom symmetry is assumed.

In Fig. 5.3(right), a histogram of the energy of all absorbed photons is presented. This is strongly peaked at zero but has a long tail out to at least 5 keV.

In Fig. 5.4, a two dimensional histogram of the number of photons vs. location of the absorption site along the vacuum chamber perimeter is presented. This is is peaked at the outside edge of the vacuum chamber, where the direct photon strikes occur, but there is long tail extending around the entire surface of the vacuum chamber, due to the reflected photons.

Example 2: Photon emission throughout the ring, elliptical vacuum chamber, no diffuse scattering For the second example, photon emission throughout the CesrTA ring from a 2.1 GeV positron beam is simulated. (The lattice name is `2085mev_20090516`). The vacuum chamber is again a simple ellipse, and the scattering is purely specular.

In Fig. 5.5, the distribution of photon absorption sites around the ring is shown, sorted by the type of magnetic environment in which the absorption occurs. This information is important for simulations of electron cloud growth, which is strongly influenced by the magnetic environment.

The wigglers in the L0 straight section are responsible for the large peaks near $s = 0$. The large peaks near $s = \pm 130$ m are due to wigglers in the arcs near these locations. The small peaks in the arcs are due to the regular CesrTA dipoles.

In Fig. 5.6, we present the photon intensity distribution (in photons/meter/radian) vs. polar angle (measured around the vacuum chamber, with zero angle corresponding to the radial outside direction), averaged over each type of magnetic environment.

In the wigglers, most of the photons come from the radiation fans in an upstream wiggler region, so there are strong peaks on both edges of the vacuum chamber. In the bends, most of the radiation is from direct strikes from upstream dipoles, so there is only a strong peak on the radial outside edge, together with a long tail, due to scattering. In the quadrupoles and drifts, there are two peaks, with the higher one at the radial outside, and a distribution between the peaks due to scattering.

Example 3: Photon emission throughout the ring, realistic vacuum chamber, no diffuse scattering For the third example, photon emission throughout the CesrTA ring from a 2.1 GeV positron beam is simulated again, with a realistic vacuum chamber profile. The scattering is purely specular, as in the previous example.

In Fig. 5.7, we present the photon intensity distribution (in photons/meter/radian) vs. polar angle (measured around the vacuum chamber, with zero angle corresponding to the radial outside direction), averaged over each type of magnetic environment.

Compared to the previous example, the photon intensity on the top and bottom of the chamber (polar angles of $\pi/2$ and $3\pi/2$) is substantially suppressed, while the radiation striking the radial inside edge of the vacuum chamber (polar angle near π) is enhanced. This is primarily due to the local shape of the vacuum chamber at the strike point of the direct synchrotron radiation. For the elliptical chamber, the wall is curved at the radiation strike point, which, for a finite sized radiation stripe, enhances scattering out of the median plane. For the real CesrTA chamber, for most of the ring, the wall is vertical at the radiation strike point (see Figure 2.32), so that scattering out of the median plane is limited.

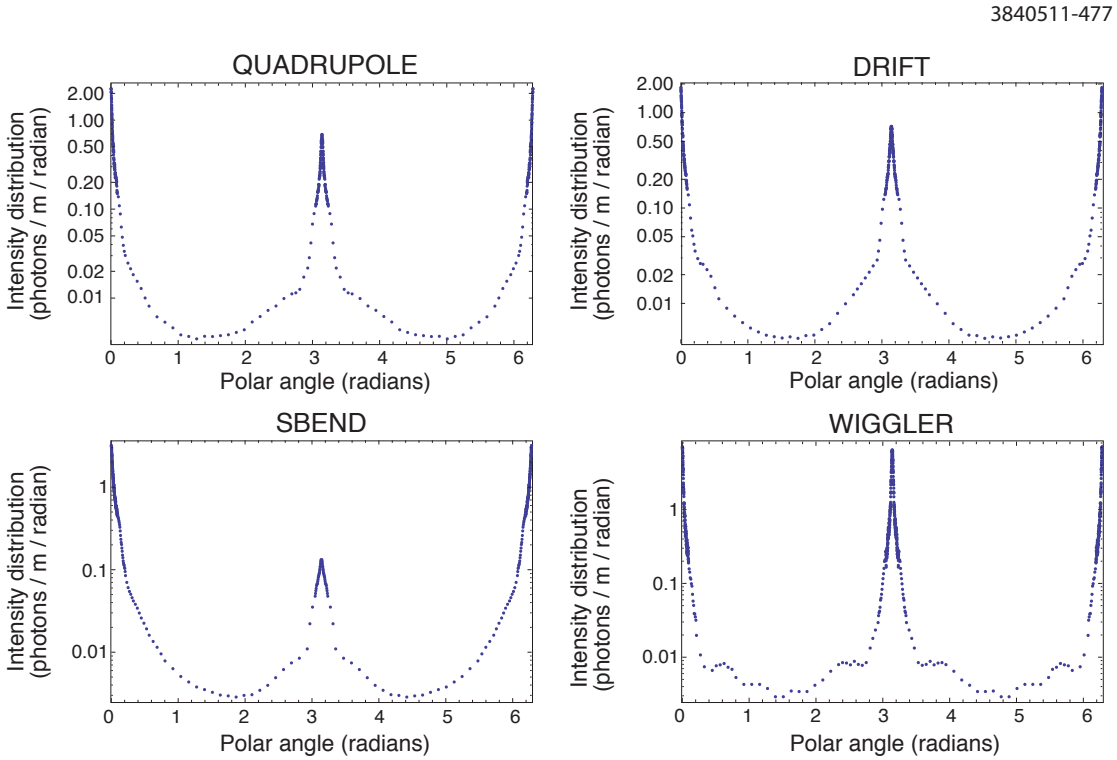

Figure 5.7: Photon intensity distribution (in photons/meter/radian) vs. polar angle (measured around the vacuum chamber, with zero angle corresponding to the radial outside direction), averaged over each type of magnetic environment. A realistic model for the CesrTA vacuum chamber throughout the ring is used. All scattering is specular. Top-bottom symmetry is assumed.

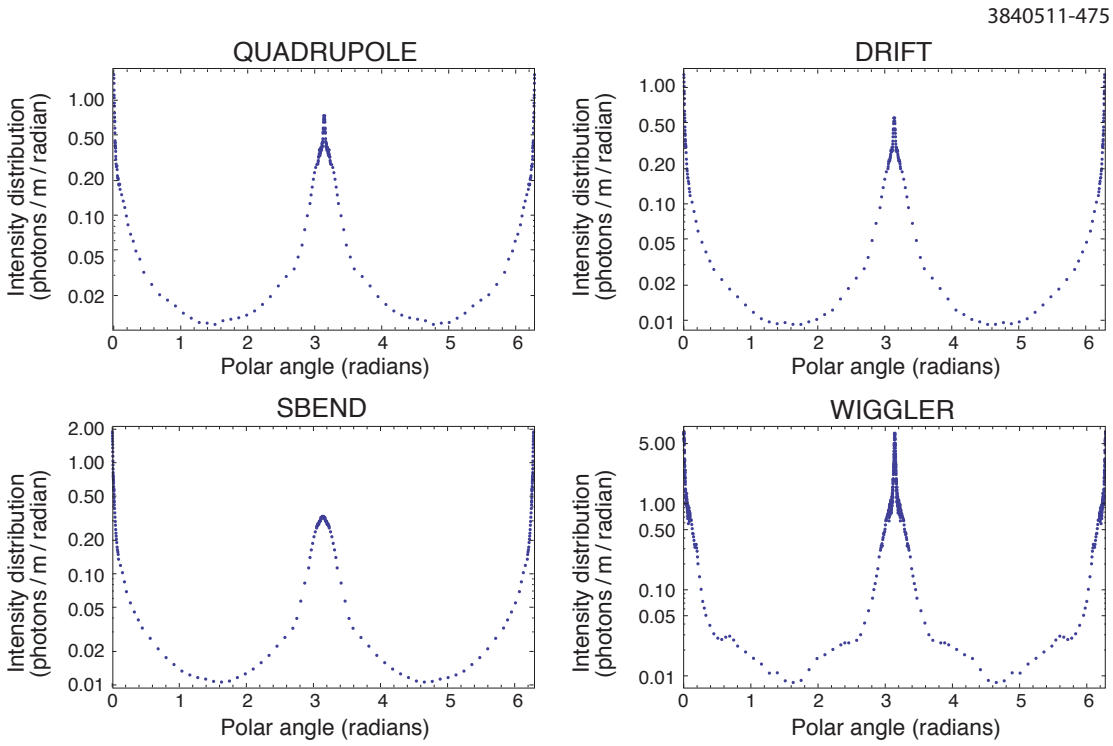

Figure 5.8: Photon intensity distribution (in photons/meter/radian) vs. polar angle (measured around the vacuum chamber, with zero angle corresponding to the radial outside direction), averaged over each type of magnetic environment. A realistic model for the CESR vacuum chamber throughout the ring is used, and diffuse scattering is included. Top-bottom symmetry is assumed.

Example 4: Photon emission throughout the ring, realistic vacuum chamber, diffuse scattering included. For the fourth example, photon emission throughout the CesrTA ring from a 2.1 GeV positron beam is simulated again, with a realistic vacuum chamber profile. In this case, diffuse scattering is included, using the parameters and model described in Sect. 4.1.4.1.

In Fig. 5.8, we present the photon intensity distribution (in photons/meter/radian) vs. polar angle (measured around the vacuum chamber, with zero angle corresponding to the radial outside direction), averaged over each type of magnetic environment.

Compared to the previous example, the photon intensity on the top and bottom of the chamber (polar angles of $\pi/2$ and $3\pi/2$) is now much higher, and is comparable to that seen in Example 2. This is due to the out-of-plane diffuse scattering, which results in substantial amounts of radiation scattering out of the median plane. In addition, the radiation striking the radial inside edge of the vacuum chamber (polar angle near π) is also increased.

Example 5: Effect of variation of the diffuse scattering parameters For the fifth example, photon emission throughout the CesrTA ring from a 2.1 GeV positron beam is simulated again, with a realistic vacuum chamber profile. In this case, the effects of varying the diffuse scattering parameters (using the model described in Sect. 4.1.4.1) is illustrated.

In Fig. 5.9, the photon intensity distribution, averaged over each type of magnetic environment,

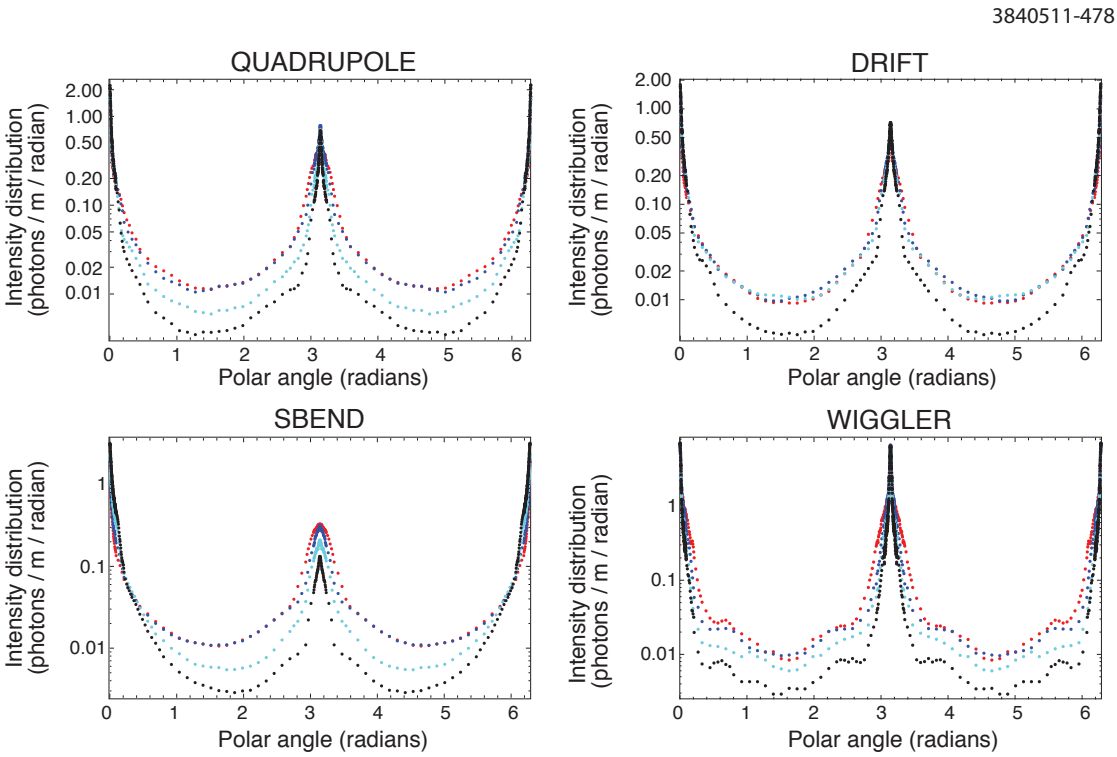

Figure 5.9: Photon intensity distribution (in photons/meter/radian) vs. polar angle (measured around the vacuum chamber, with zero angle corresponding to the radial outside direction), averaged over each type of magnetic environment. A realistic model for the CESR vacuum chamber throughout the ring is used. The different colors correspond to: red, diffuse scattering parameters $\sigma = 200$ nm and $T = 5500$ nm; blue, diffuse scattering parameters $\sigma = 100$ nm and $T = 5500$ nm; cyan, diffuse scattering parameters $\sigma = 4$ nm and $T = 200$ nm; black, pure specular scattering. Top-bottom symmetry is assumed.

is shown, for four different cases. The red points correspond to the diffuse scattering parameters $\sigma = 200$ nm and $T = 5500$ nm (same as Fig. 5.8). The black points correspond to pure specular reflection (same as Fig. 5.7). Two intermediate cases are also shown: the blue points correspond to still a rough surface, but with $\sigma = 100$ nm, and $T = 5500$ nm; and the cyan points correspond to a polished surface ($\sigma = 4$ nm, with $T = 200$ nm).

It can be seen that there is not much dependence on σ for the two rough surface cases. A polished surface gives considerably less scattering, as expected, but there is still a significant difference between this case and pure specular reflection.

5.1.3.3 Photoelectron Models

The components of the photoelectron generation model are the quantum efficiency as a function of photon energy, the angular function governing the initial momentum direction of the photoelectrons, and their kinetic energy spectrum. The azimuthal distribution of photoelectrons produced on the wall of the vacuum chamber is the same as that of the absorbed photons, and is provided by the photon transport simulations discussed in the previous section. The code benchmarking

project revealed that reconciliation of the time structure of density buildup in the ECLOUD and POSINST codes for CesrTA conditions required a modification of the ECLOUD model for the angular distribution to match that employed by POSINST. The simple model implemented at present uses a single energy-independent value for the quantum efficiency, ignores the incident photon energy spectrum and uses an ad-hoc photoelectron energy distribution which must be re-tuned for each set of beam conditions under study.

While the modeling for the coherent tune measurements proved to be rather insensitive to the assumed photoelectron energy distribution (see Section 6.3.1.7), the local RFA measurements, and especially the time-resolved shielded-pickup pulse shapes have been shown to impose strict constraints on the photoelectron generation model. These results are described in Sect. 5.2.2 below.

On the other hand, the modeling of the coherent tune shift measurements depends critically on the azimuthal distribution of the produced photoelectrons. As the bunch current increases, the contribution from the dipole regions begins to dominate the total tune shift, since the cloud electrons are trapped on field lines near the vertical plane of the beam. If photon reflection were to be ignored in the model, this dominant contribution would be absent, since no photoelectrons would be produced on the top or bottom of the beampipe. The CesrTA cloud modeling effort thus required a substantial effort to develop a photon transport model, as described in Section 4.1.4.1.

5.1.3.4 RFA Modeling

In principle, a single RFA voltage scan, in which data is collected while the retarding voltage is varied (see Section 2.3.1), gives a great deal of information about the local behavior of the electron cloud. In practice, however, it is a highly nontrivial task to map a data point from a voltage scan to any physical quantity, such as cloud density. Typically, this gap is bridged through the use of cloud simulation programs, which track the motion of cloud particles during and after the passage of a bunch train (Section 5.1.3.1). Generally speaking, there are two ways to obtain a predicted RFA signal from a cloud simulation program: by post-processing the output of the program, or by integrating an RFA model into the actual code. Both methods are discussed below.

Drift RFA Simulations The simplest method for simulating the output of an RFA for a given set of beam conditions is post-processing the output of a cloud simulation program, such as POSINST [86] or ECLOUD [112]. More specifically, these codes can output a file containing information on each macroparticle-wall collision, and one can perform a series of calculations on this output to determine what the RFA would have seen had one been present.

A basic post-processing script does the following:

- Determine if the macroparticle has hit in the azimuthal region where one of the RFA collectors exists.
- Calculate an efficiency (probability of passing through the beam pipe hole) based on the incident angle and energy of the particle.
- Choose an energy "bin" for the particle based on its transverse energy.

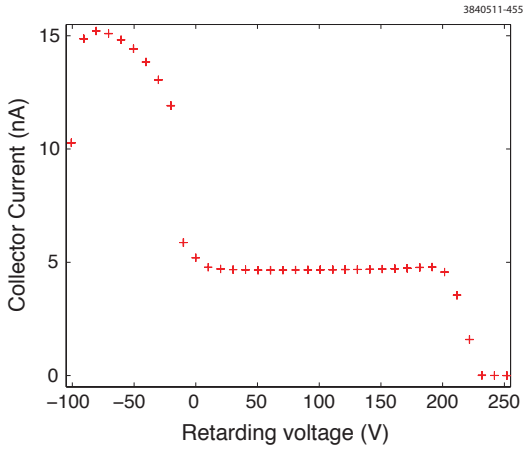

Figure 5.10: Bench measurement of RFA efficiency, showing an enhancement at low energy.

- Deposit the final charge (equal to the macroparticle charge times the overall RFA efficiency) into the appropriate and collector and energy bin

- To replicate an RFA measurement at a given retarding voltage, add up all the signal in bins with higher energy than the voltage.

Note that by proceeding in this way one implicitly assumes that the presence of the RFA has no effect on the development of the cloud. This assumption is probably justified for a drift RFA, but may not be in the presence of a magnetic field. The latter case is discussed in the next subsection.

Bench measurements of RFA efficiency have shown an enhancement of the signal at low retarding voltage due to the production of low energy secondary electrons inside the beam pipe holes [113]. An example bench measurement is shown in Fig. 5.10. It was taken using a monoenergetic beam of 200 eV electrons, and shows a large increase in the signal at positive retarding voltage, where these low energy secondaries are guided into the RFA. We have developed a specialized particle tracking simulation to quantify this effect. It uses a Monte Carlo method to calculate the average efficiency for an incident electron, as a function of energy and angle, including beam pipe hole secondaries. Fig. 5.11 shows the effect of this enhancement for two different incident energies. This is included in the analysis as an additional charge added to the simulated RFA signal at zero retarding voltage. We are currently doing more rigorous bench measurements to fully quantify this effect.

In a drift region, qualitative agreement between data and (post-processed) simulation can generally be obtained without fine tuning of the simulation parameters. For example, Fig. 5.12 shows the measured and simulated (with `POSINST` [86]) RFA signal for voltage scan done under a typical set of beam conditions. The plots give collector signal as a function of collector number and retarding voltage. Here the data and simulation are similar both in general shape and magnitude. Getting closer quantitative agreement, however, requires a more systematic approach; see Section 5.1.4.2 for details.

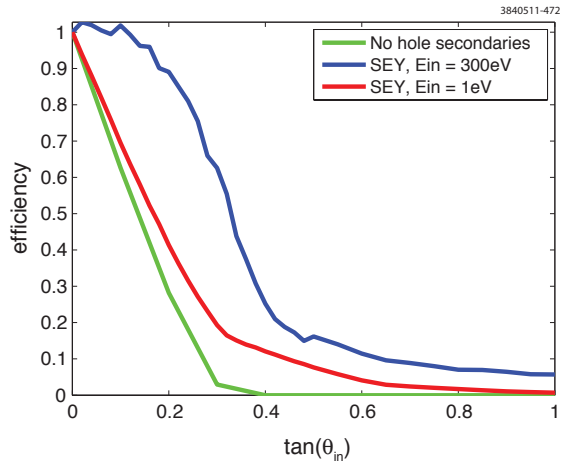

Figure 5.11: Simulated RFA efficiency vs incident angle, including secondary electrons produced in the beam pipe holes. The geometric efficiency (not including secondaries) is shown for comparison.

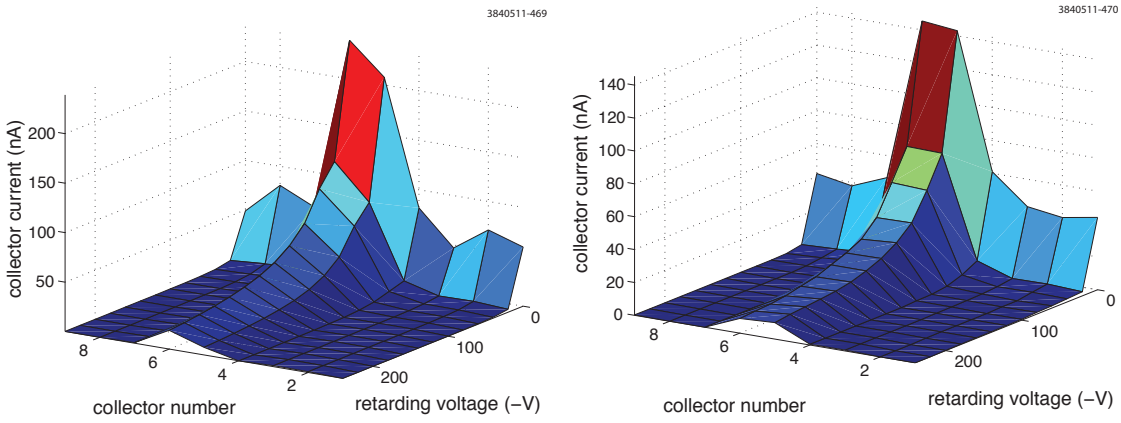

Figure 5.12: Comparison of data (left) and un-optimized simulation (right), Aluminum drift RFA. Beam conditions are 45 bunches of positrons at 1.25 mA/bunch, 14 ns spacing, 2.1 GeV.

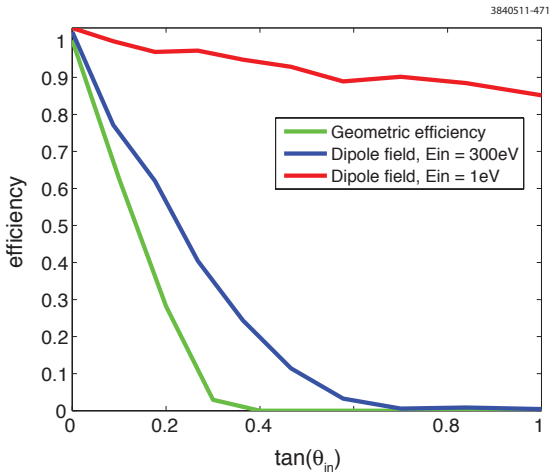

Figure 5.13: Simulated RFA efficiency vs incident angle for a CESR dipole RFA, with a 790 G magnetic field. This corresponds to operation at 2.1 GeV.

Dipole RFA Simulations Simulations have also been done for an RFA located inside a CESR dipole (see Section 2.3.1), using the same method described above. Simulated efficiency curves for different incident energies are shown in Fig. 5.13. The simulation gives a very high efficiency for low energy electrons, due to their small cyclotron radius.

Fig. 5.14 shows a typical example of a simulation done for a dipole RFA. The results are again roughly consistent with the data, except at low energy ($V_{ret} = 0$). Here, the simulation significantly overestimates the signal observed by the RFA. One possible explanation for this discrepancy is an over-counting of the effect of individual macroparticles in the simulation. If a macroparticle collides with the vacuum chamber wall in the area covered by the RFA and creates a signal there, it should lose a corresponding amount of charge. However, this cannot be accomplished with a post-processing method. In a dipole region, a single macroparticle will move up and down along the same field line, potentially striking the RFA area several times. The post-processing script will treat each of these collisions separately, and obtain a spuriously high signal. This effect will be become worse as the macroparticle becomes more tightly constrained along the field line (i.e. as its cyclotron radius becomes smaller). So we expect it to be worse for low energy electrons (as in Fig. 5.14), and for high magnetic fields (as we will see in the section on wiggler simulations).

Quadrupole RFA Simulations Some preliminary simulations have been done for the quadrupole RFA installed in CESR. The simulations generally reproduce the behavior, discussed in section 5.1.4.1, where the majority of the signal is concentrated in one collector. Interestingly, they also give some indirect evidence that the cloud can become trapped in the quadrupole for long periods of time.

Fig 5.15 shows the signal in collector no. 10 for a voltage scan done with a 45 bunch train of positrons at 1 mA/bunch. Also plotted are simulations done in `ECLOUD` [112] of these conditions. If one does a simulation for only one beam revolution period (2.56 μs), the simulated signal is too low at all energies by over an order of magnitude. However, if one continues the simulation for multiple turns, one finds that the data and simulation start to get closer. By 19 turns, they are in very good agreement at high energy, and within a factor of 2 at low energy. This implies that the

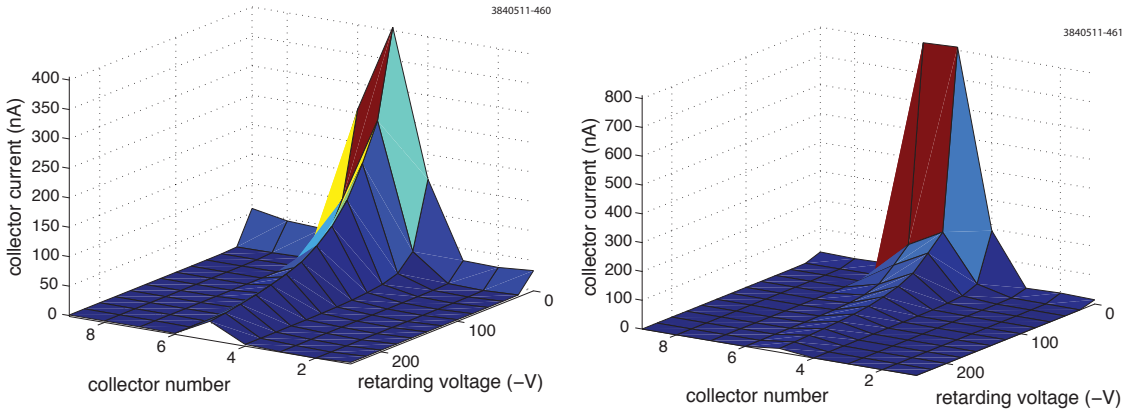

Figure 5.14: Comparison of data (left) and un-optimized simulation (right), Aluminum dipole RFA. Beam conditions are 45 bunches of positrons at 1.25 mA/bunch, 14 ns spacing, 2.1 GeV.

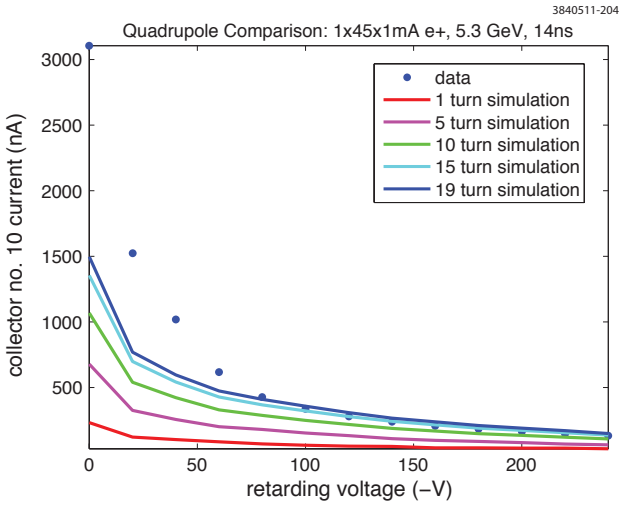

Figure 5.15: Quadrupole RFA simulation showing long term cloud buildup: 45 bunches, 1 mA/bunch, e+, 5.3 GeV, 14 ns

cloud is building up over several turns, and that the RFA is sensitive to this slow buildup.

Wiggler RFA Simulations One major disadvantage of using a post-processing RFA model is that one cannot accurately model any interaction between the RFA and the cloud. For an example of such an interaction, see Fig. 5.16. It shows a voltage scan done with an RFA in the center pole of a wiggler (approximated by a 1.9 T dipole field). Here one can see a clear enhancement in the signal at low (but nonzero) retarding voltage. Since the RFA should simply be collecting all electrons with an energy more than the magnitude of the retarding voltage, the signal should be a monotonically decreasing function of the voltage. So the RFA is not behaving simply as a passive monitor. Furthermore, the spike in collector current is accompanied by a corresponding dip in the grid current, suggesting that the grid is the source of the extra collector current.

We believe this spurious signal comes from a resonance between the bunch spacing and retarding

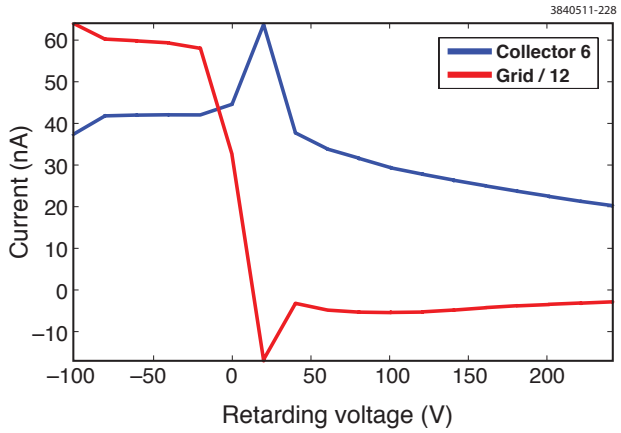

Figure 5.16: Resonant enhancement in wiggler data, 45 bunches, 1.25 mA/bunch, e+, 2.1 GeV. Note that there are 12 collectors, so collector 6 is one of the central ones. Also note that the grid signal is divided by 12.

voltage. To understand this, consider an electron which collides with the retarding grid and generates a secondary. Because electrons are so strongly pinned to the magnetic field lines in a 1.9 T field, this electron is likely to escape through the same beam pipe hole that the primary entered. In other words, the motion of the electrons is approximately one-dimensional. An electron ejected from the grid will gain energy from the retarding field before it re-enters the vacuum chamber. If it is given the right amount of energy, it will be near the center of the vacuum chamber during the next bunch passage, and get a large beam kick, putting it in a position to generate even more secondaries. The net result is a resonance condition for the retarding voltage that is inversely proportional to the square of the bunch spacing, since the shorter the bunch spacing, the more kinetic energy an electron needs to arrive at the beam in time for the next bunch passage [114]. Fig. 5.17 shows that this dependence is (roughly) present in the data, though the low energy spike in the 4 ns data is not predicted by this model.

Motivated by these measurements, we have incorporated into `POSINST` a model of the RFA geared toward reproducing the geometry of the devices installed in the vacuum chambers of the CesrTA wigglers. The motion of the electrons within the RFA, including the electrostatic force from the retarding field, is tracked using a special routine. The grid is modeled realistically, and secondary electrons can be produced there, with the same secondary yield model used for normal vacuum chamber collisions. The peak secondary electron yield and peak yield energy can be specified separately for the grid.

Because the actual retarding field is included in this model, the retarding voltage must be specified in the input file, and a separate simulation must be run for each voltage desired. Fig 5.18 shows the result of running this simulation for a series of different retarding voltages, for one set of beam conditions. Notably, the simulation reproduces the resonant enhancement seen in the data, at approximately the same voltage ($\sim$ 10 V for 14 ns spacing).

The resonant enhancement is present in much of the wiggler data, so an integrated RFA model will be needed to obtain a more complete understanding of the cloud behavior in a wiggler magnet. This effect is also present to a lesser extent in our dipole data, indicating that a post-processing model may not be sufficient there either.

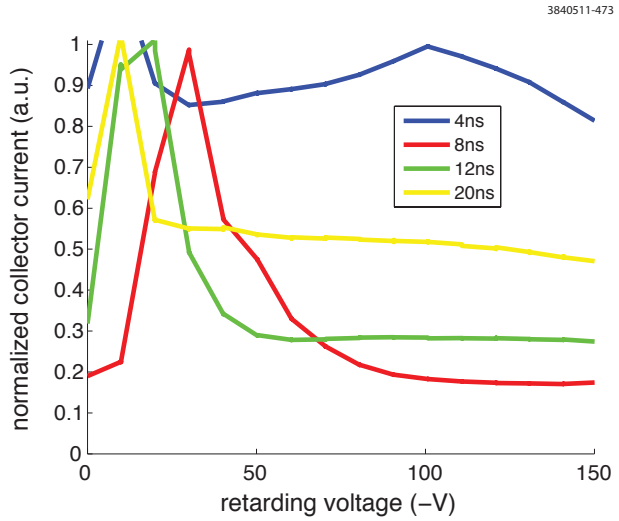

Figure 5.17: Resonant spike location at different bunch spacings, 45 bunches, 1.25 mA/bunch, e+, 5 GeV. Only the signal in the central collector is plotted

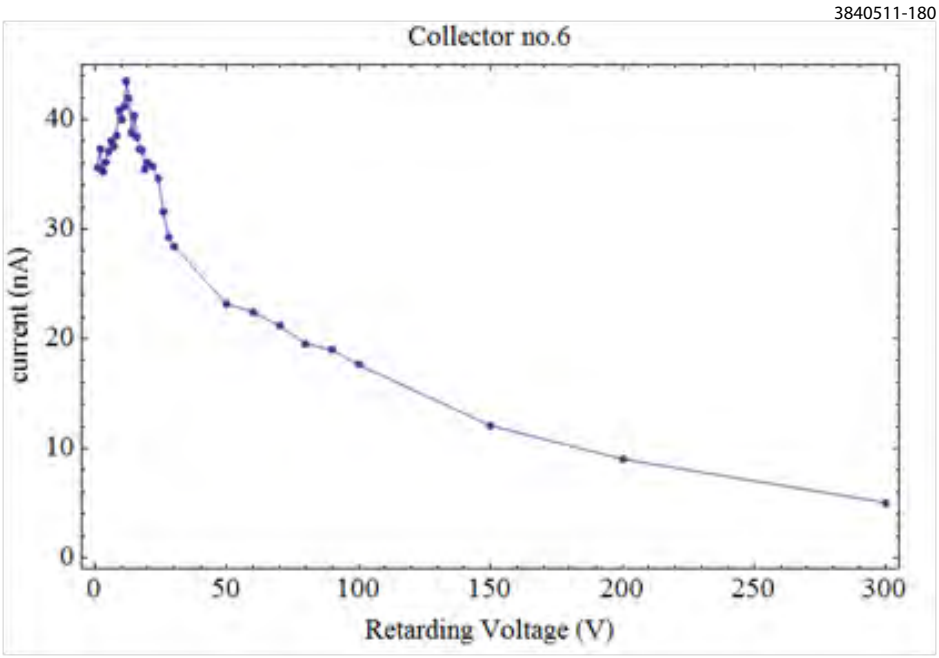

Figure 5.18: `POSINST` simulation showing resonant enhancement, 45 bunches, 1.2 mA/bunch, e+, 2.1 GeV, 14 ns, central collector

Table 5.1: RFA styles deployed in CESR

Type	Magnetic Field	Grids	Collectors
APS	Drift	2	1
Insertable I	Drift	2	5
Insertable II	Drift	3	11
Thin	Drift, Dipole	1	9
SLAC	Dipole	3	17
Quad	Quadrupole	1	12
Wiggler	Wiggler	1	12

Table 5.2: Common beam conditions for electron cloud mitigation studies

Parameter	Typical Values	Units
Number of bunches	9, 20, 30, 45	-
Bunch current	.75, 1.25, 2.8, 3.8, 10	mA
Bunch spacing	4, 14, 280	ns
Species	Electron, positron	-
Beam energy	2.1, 4, 5.3	GeV

5.1.4 EC Mitigation Observations in RFAs and Comparison with Simulations

5.1.4.1 Measurements

We have used RFAs to probe the local behavior of the cloud in different magnetic field elements, and in the presence of different mitigation schemes. Table 5.1 gives a list of the various RFA types discussed in this section. Most of the data presented here is one of two types: "voltage scans," in which the retarding voltage is varied while beam conditions are held constant, or "current scans," in which the retarding grid is set to a positive voltage (typically 50V), and data is passively collected while the beam current is increased.

At CesrTA, we have been able to study the electron cloud under a wide variety of beam conditions, varying the number of bunches, bunch current, bunch spacing, beam energy, and species. As described in Section 5.1.4.2, this is very helpful for independently determining the photoelectron and secondary electron properties of the instrumented chamber. Table 5.2 lists some of the more common (but by no means only) beam parameters used for electron cloud mitigation studies with RFAs.

Drift Data Many of our earliest detailed measurements were done with "Insertable I" style RFAs (Table 5.1). Fig 5.19 shows an example of a voltage scan done with one of these RFAs, in typical CesrTA beam conditions. It plots the RFA response as a function of collector number and retarding voltage. Roughly speaking this is a description of the transverse and energy distribution of the cloud. In this example, the signal is fairly broad across all five collectors, indicating that the cloud density is not strongly peaked around the beam. It also falls off quickly with retarding voltage, indicating that the majority of cloud particles have low energy. The RFA signal is expressed in terms of current density in nA/mm^2, normalized to the transparency of the RFA beam pipe and grids. In principle, this gives the time averaged electron current density incident on the beam pipe

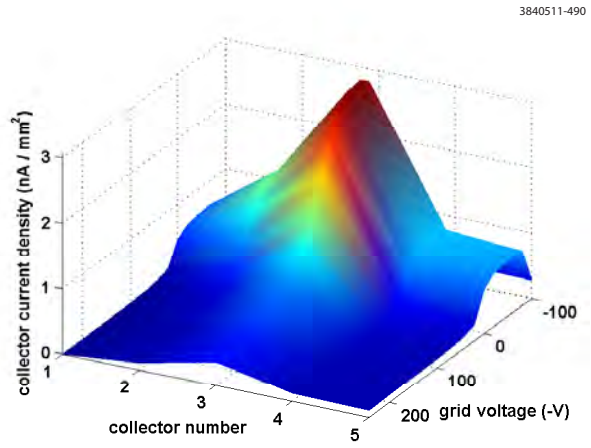

Figure 5.19: RFA voltage scan with an insertable segmented drift RFA in a Cu chamber, 1x45x1.25 mA e+, 14 ns, 5.3 GeV

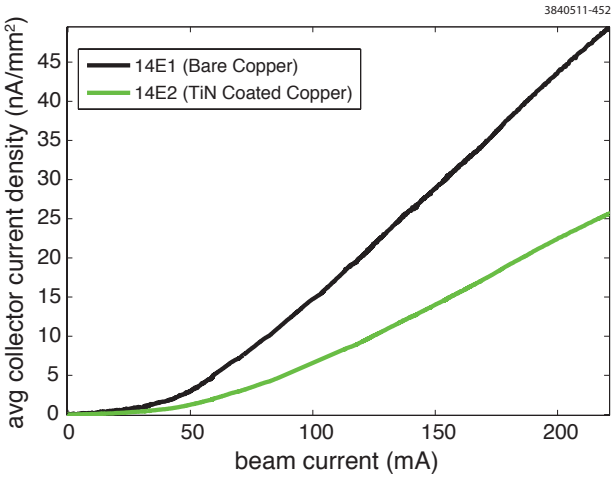

Figure 5.20: Comparison of insertable drift RFAs, 1x20 e+, 5.3 GeV, 14 ns

wall. The beam conditions are given as "1x45x1.25 mA e+, 14 ns, 5.3 GeV." This notation, which will be used throughout this section, indicates one train of 45 bunches, with 1.25 mA/bunch (1 mA $= 1.6 \times 10^{10}$ particles), with positrons, 14 ns spacing, and at beam energy 5.3 GeV.

Fig 5.20 compares a current scan measurement done with two adjacent RFAs, one in a bare Copper chamber, and one in a TiN coated Copper chamber. Here we compare the average collector current density in the two detectors, as a function of beam current, and find that it is lower in the coated chamber by a factor of two.

"Thin" style RFAs (Table 5.1) were developed to fit inside the aperture of a CESR dipole, but they have also been deployed in drift regions. These RFAs have since been replaced by "Insertable II" style detectors, which have more collectors and can support higher voltages. Example measurements done with both of these RFA styles, in a TiN coated chamber, can be found in Fig. 5.21.

We have installed RFAs in arc drift sections adjacent to the 15E and 15W quadrupoles in CESR.

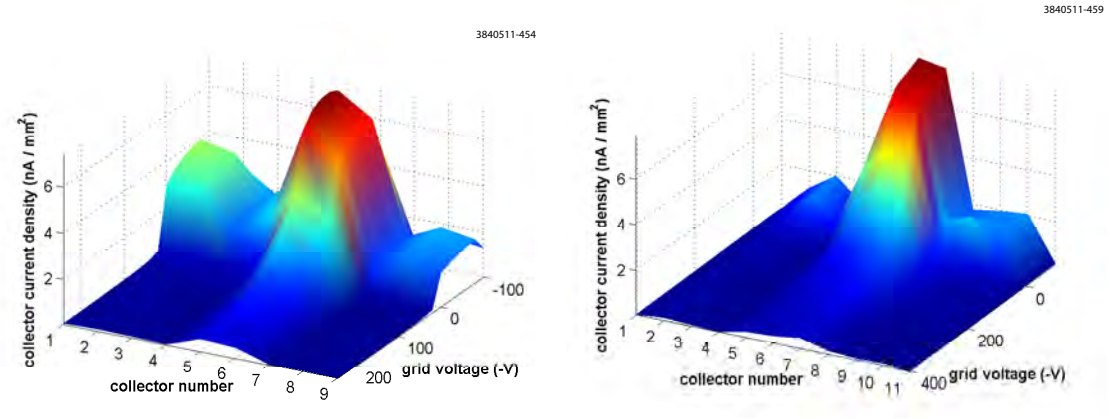

Figure 5.21: Example voltage scans with thin (left) and insertable (right) style drift RFAs in the same location. Both are TiN coated, beam conditions are 1x45x1.25 mA, 5.3 GeV, 14 ns.

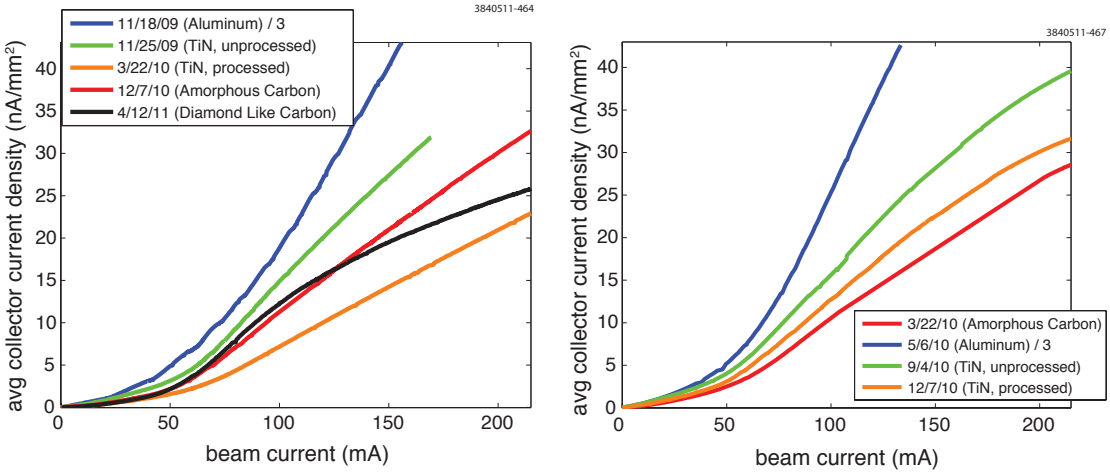

Figure 5.22: Comparison of different beam pipe coatings, 15E (left), and 15W (right) drift RFAs. Plots show average collector signal vs beam current for **20 bunches** of **positrons** with **14 ns** spacing, at beam energy **5.3 GeV**. Note that the aluminum chamber signals are divided by 3.

The photon flux for a positron beam at 15W is about twice that of 15E, and vice versa for an electron beam. Measurements have been taken at both locations with TiN and amorphous carbon coatings, as well as with an uncoated aluminum chamber. In addition, a chamber with diamond-like carbon (DLC) coating has recently been installed at 15E. By comparing measurements taken at the same location in CESR, we ensure the comparisons can be made under identical beam conditions, including photon flux. Figs. 5.22 through 5.24 compare the RFA signal with each of these coatings for typical sets of CesrTA beam conditions. We have generally found that data taken with 20 bunches of positrons at high current shows the biggest difference between the different chambers. It is under these conditions that we expect to be most sensitive to the peak secondary electron yield (δ_{max}).

All coated chambers show a sizeable reduction in signal when compared to uncoated aluminum. After extensive processing, both TiN and amorphous carbon coated chambers show similar mitigation performance. The details of the small difference between 15E and 15W (where in one case

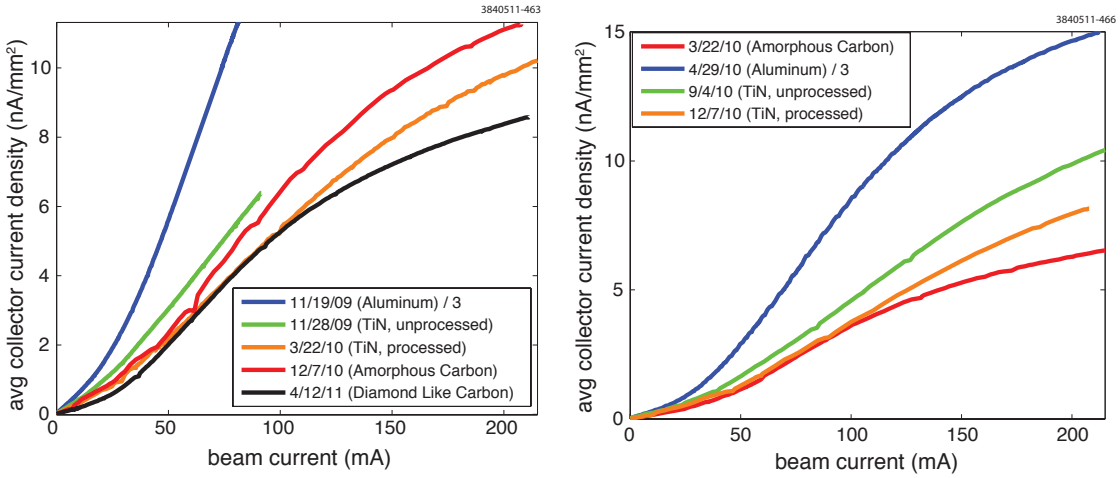

Figure 5.23: Comparison of different beam pipe coatings, 15E (left), and 15W (right) drift RFAs. Plots show average collector signal vs beam current for **20 bunches** of **electrons** with **14 ns** spacing, at beam energy **5.3 GeV**. Note that the aluminum chamber signals are divided by 3.

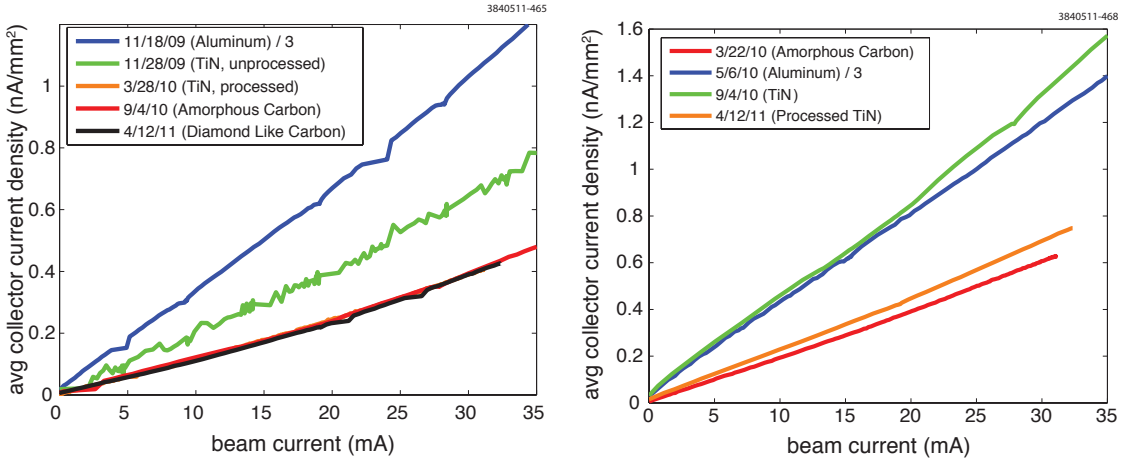

Figure 5.24: Comparison of different beam pipe coatings, 15E (left), and 15W (right) drift RFAs. Plots show average collector signal vs beam current for **9** equally spaced (**280 ns**) bunches of **positrons**, at beam energy **5.3 GeV**. Note that the aluminum chamber signals are divided by 3.

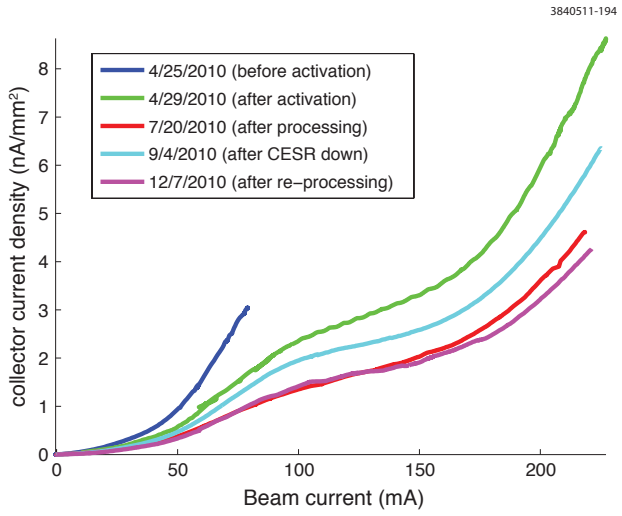

Figure 5.25: NEG RFA comparison, 1x20 e+, 5.3 GeV, 14 ns.

TiN appears slightly better and in the other amorphous carbon does) require further analysis to understand fully.

Diamond-like carbon may perform better than other coatings at very high beam current. It should be noted that bench measurements of the Secondary Electron Yield (SEY) of DLC have found that the material can retain charge if bombarded with a sufficiently high electron flux, thus modifying the apparent SEY performance (Section 5.1.5). This effect may also be influencing the in situ measurements presented here.

We have also installed a NEG coated chamber in our L3 straight region. This chamber is instrumented with three single collector RFAs, located at different azimuthal positions. Fig. 5.25 compares the current measured by one of these RFAs on several different dates, corresponding to different states of activation and processing of the NEG coating. It was observed that both activation and initial processing reduced the signal measured by this RFA. After a CESR down (during which the NEG was activated again), the signal rose somewhat, but it processed back down to its minimum value after a few months of beam time. The other two detectors showed a similar trend.

Dipole Data RFA data have been taken in the presence of a dipole field, both in a standard CESR dipole (the "Thin" style in Table 5.1), and in a specially designed chicane which was built at SLAC [115]. The field in the chicane magnets is variable, but most of our measurements were done in a nominal dipole field of 810 G. Of the four chicane chambers, one is bare Aluminum, two are TiN coated, and one is both grooved and TiN coated. The grooves are triangular with a depth of 5.6 mm and an angle of 20°. Fig. 5.26 shows a retarding voltage scan done with both the CESR dipole and Aluminum chicane RFAs. In both cases, one can see a strong multipacting spike in the central collector.

Mitigation studies Fig. 5.27 shows a comparison between three of the chicane RFAs. We found the difference between uncoated and coated chambers to be even stronger than in a drift region.

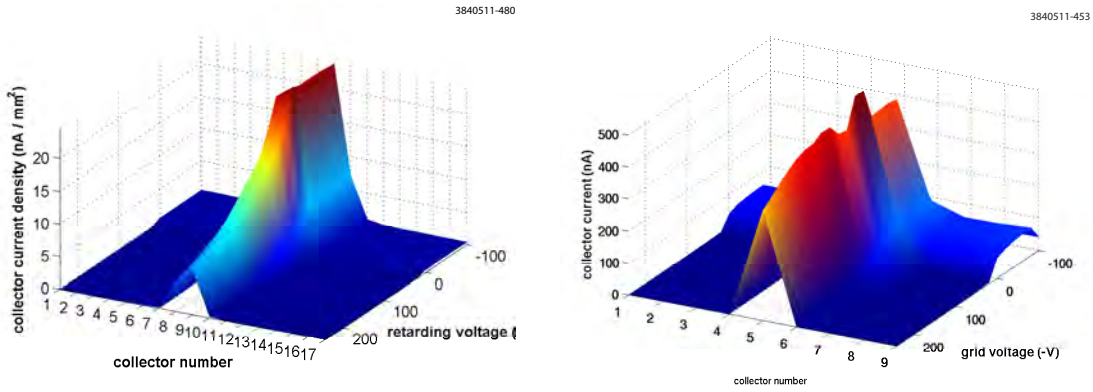

Figure 5.26: Typical Al dipole RFA voltage scans: 1x45x1.25 mA e+, 5.3 GeV, 14 ns. Left: SLAC chicane RFA; Right: CESR dipole RFA

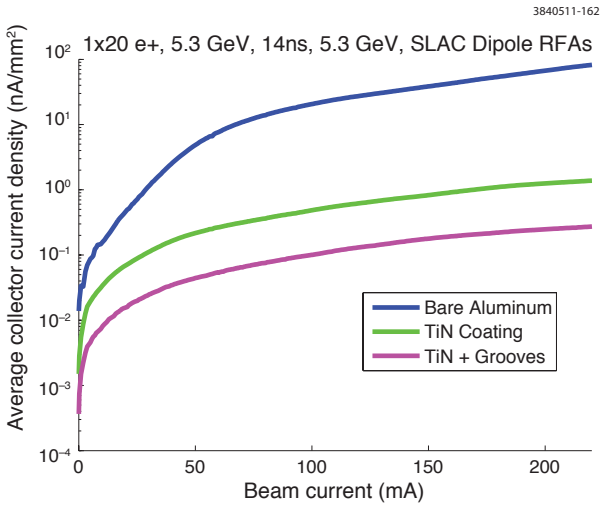

Figure 5.27: Dipole RFA mitigation comparison, 1x20 e+, 5.3 GeV, 14 ns

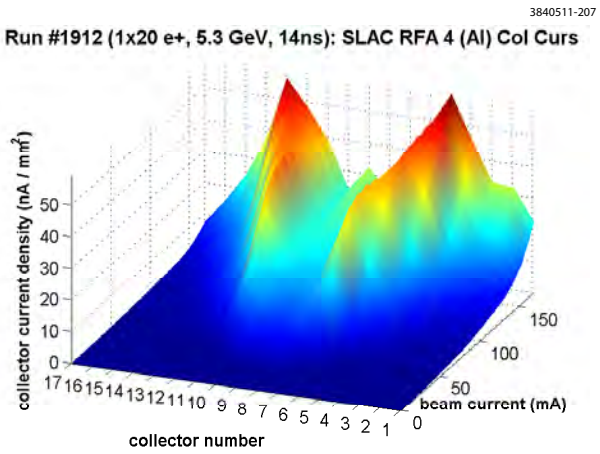

Figure 5.28: Bifurcation of peak cloud density in a Al dipole: 1x20 e+, 5.3 GeV, 14 ns

At high beam current, the TiN coated chamber shows a signal smaller by two orders of magnitude than the bare Al chamber, while the coated and grooved chamber performs better still.

Central peak bifurcation For high bunch currents, we have observed a bifurcation of the central multipacting peak into two peaks with a dip in the middle. This is demonstrated in Fig 5.28, which shows the signal in all 17 RFA collectors vs beam current. Bifurcation occurs when the average energy of electrons in the center of the beam pipe is past the peak of the SEY curve, so that the transverse location of the effective maximum yield is actually off center. The higher the bunch current, the further off center these peaks will be.

Cyclotron resonances By varying the strength of the chicane magnets, we can also study the behavior of the cloud at different dipole magnetic field values. Fig. 5.29 shows an example of RFA data taken as a function of magnetic field strength. The most prominent feature of the data is regularly occurring spikes or dips in all three plotted chambers. These correspond to "cyclotron resonances," which occur whenever the cyclotron period of cloud electrons is an integral multiple of the bunch spacing [116]. For 4 ns bunch spacing we expect them every 89 Gauss, which is what is seen in the data. Another interesting feature of this measurement is that these resonances appear as peaks in the RFA signal in the Aluminum chamber, but as dips in the coated chambers. The cyclotron resonance measurements corroborated the earlier SLAC measurements made under very different beam conditions [115–117]. The electron cloud modeling program `POSINST` successfully modeled the SLAC measurements, showing that the resonant cloud buildup enhancements observed for the uncoated aluminum vacuum chamber can follow from higher energy electrons striking the bottom and top of the vacuum chamber at more grazing angles [116, 117]. We have undertaken similar modeling studies with the `ECLOUD` program package, extending them to describe the resonant suppression mechanism observed in the TiN-coated chamber which is shown in Fig. 5.29. Figure 5.30 shows the `ECLOUD` result around the first cyclotron resonance (n=1, B=89 G) in 2 G steps for the case of an uncoated aluminum chamber.

This simple model defines each collector signal by the impact position of electrons on the top of the vacuum chamber. The collector current is derived by the collector area, a transparency factor of 15%, and the size of the time interval. No kinematic RFA acceptance function is applied, nor

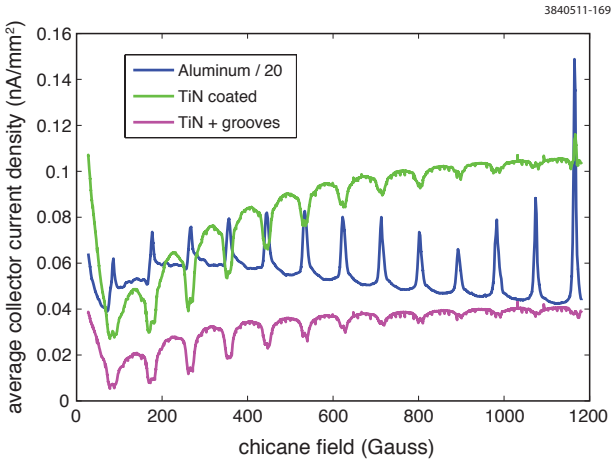

Figure 5.29: RFA signal as a function of chicane magnetic field: 1x45x1 mA e+, 5 GeV, 4 ns. Cyclotron resonances are observed every 89 G. Note that the Aluminum chamber signal is divided by 20.

is any interaction between the RFA and the cloud taken into account. Collector signal sums are accumulated over a time span of 360 ns, the first half of which comprises 45 4-ns-spaced bunches populated with 1.44×10^{10} 2-GeV positrons. A secondary yield value of 2.0 is assumed, as is an elastic yield of 1.0. No rediffused component in the secondary yield is included in the model. The sum of the 17 collector signals clearly show the resonant behavior. The individual collector contributions show that the central collector (collector 7-11) signals vary little with magnetic field, while the resonant effect is clear in the outer collectors. Figures 5.31 and 5.32 show how the increased signal on resonance arises. The upper plots show the secondary yield as a function of incident electron energy, while the lower plots show the distribution of incident energies. The plot on the upper right shows that on resonance there is a class of electrons with increased energies between about 50 and 300 GeV, resulting in higher yields since for this bunch population the cloud energies are generally below the peak energy of the secondary yield curve (300 eV). In addition, the spread in true secondary yields near the peak energy is larger. This spread shows the range of incident angles, since the peak yield value of 2.0 is increased by a factor of up to 1.5 at more grazing incidence. The resonance is enhanced by the circular shape of the vacuum chamber in the chicane, since the beam kicks from the centered beam are radial. A model with an elliptical vacuum chamber showed negligible RFA signal increase on resonance, since the incident angles were more grazing both on and off resonance, raising the off-resonance signal relative to the on-resonance signal.

This simple explanation for the resonant RFA signals is apparently contradicted by the resonance suppression exhibited in a TiN-coated chamber (see Fig. 5.29) under the same beam conditions. Since the cloud electron energy distribution and incident angles must be very similar, we investigated the possibility of a secondary yield curve decreasing with energy below the peak yield. We chose a value of 1.0 for the elastic yield at low incident energy and a value of 0.5 for the peak true secondary yield. The result, shown in 5.33, demonstrates that the resonant suppression effect can be modeled in this manner. Figures 5.34 and 5.35 show the corresponding secondary yield population curves. Further modeling studies showed the transition from resonant suppression to enhancement observed in the PEP-II data [115] in the same field scan over multiple resonances can also be reproduced.

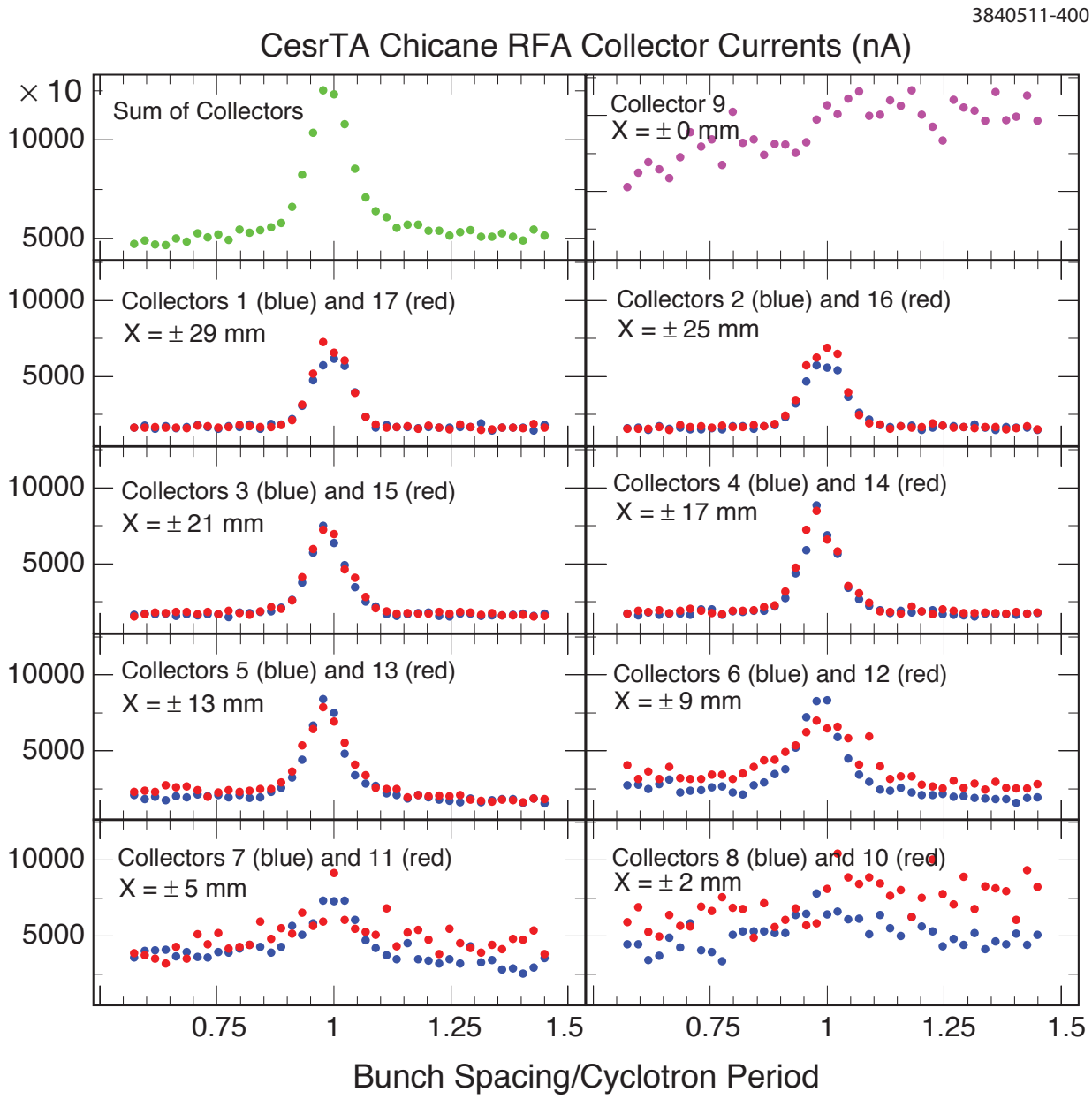

Figure 5.30: `ECLOUD` model for the RFA signals measured with the SLAC RFA in the PEP-II chicane for a 45-bunch train of 2 GeV positrons. The sum of the 17 collector signals is shown in green in the upper left plot as a function of the ratio of bunch spacing to dipole magnetic field as the field is varied in 2 G steps around the resonant value of 89 G. The central collector signal is shown in the upper right plot. The signals from the remaining 16 collectors are shown in left-right symmetric pairs. This result showing the resonant enhancement of the RFA signal was obtained with a secondary yield model appropriate for an uncoated aluminum chamber.

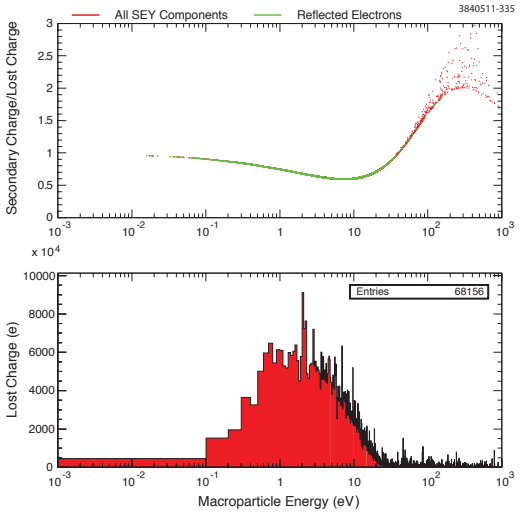

Figure 5.31: Population of the modeled secondary yield curve for the case of an uncoated aluminum chamber and a chicane magnetic field value of 129 G, halfway between the first and second cyclotron resonances for the 4 ns bunch spacing.

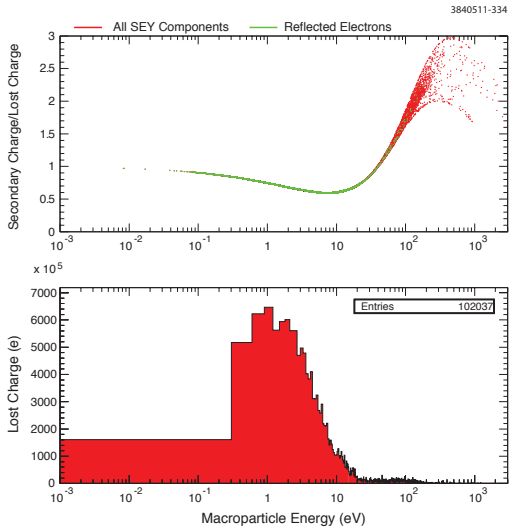

Figure 5.32: Population of the modeled secondary yield curve for the case of an uncoated aluminum chamber and a chicane magnetic field value of 89 G, which corresponds to the first cyclotron resonance for the 4 ns bunch spacing.

However, there is no independent empirical evidence for such behavior in the secondary yield for a TiN-coated chamber. The *in situ* measurements of TiN-Al samples described in Sect. 5.1.5 have measured true secondary yield values near 1.0, not 0.5. And the shielded pickup measurements of cloud lifetime described in Sect. 5.2.2 clearly exclude values for the elastic yield greater than 0.1. Further modeling studies will be needed to understand the physical basis for the resonant suppression.

Multipacting resonances Because the properties of the electron cloud can change significantly over the course of nanoseconds, it is interesting to investigate its behavior as a function of bunch spacing. At CesrTA we have taken RFA data with bunch spacings varying from 4 ns to 112 ns.

Fig. 5.36 shows the signal in the central collector of two dipole RFAs as a function of bunch spacing. The left plot is for the Aluminum SLAC chicane RFA; the right is for the CESR dipole RFA (see Fig. 5.26). The SLAC chamber has a half-height of 4.4 cm, while the CESR RFA has a half-height of 2.5 cm.

For the SLAC RFA, we observe two distinct peaks in the positron data, at approximately 14 ns and 60 ns. The electron beam data shows almost no signal before 36 ns, and is peaked around the same place as second the positron peak. The enhancement of the signal at 60ns could be due to a resonance between the bunch spacing and the cloud development (often called a "multipacting resonance"). This effect will be enhanced by the dipole field, which renders the motion of the electrons mostly one dimensional.

A very simple model for a multipacting resonance is that if the time for a typical secondary electron

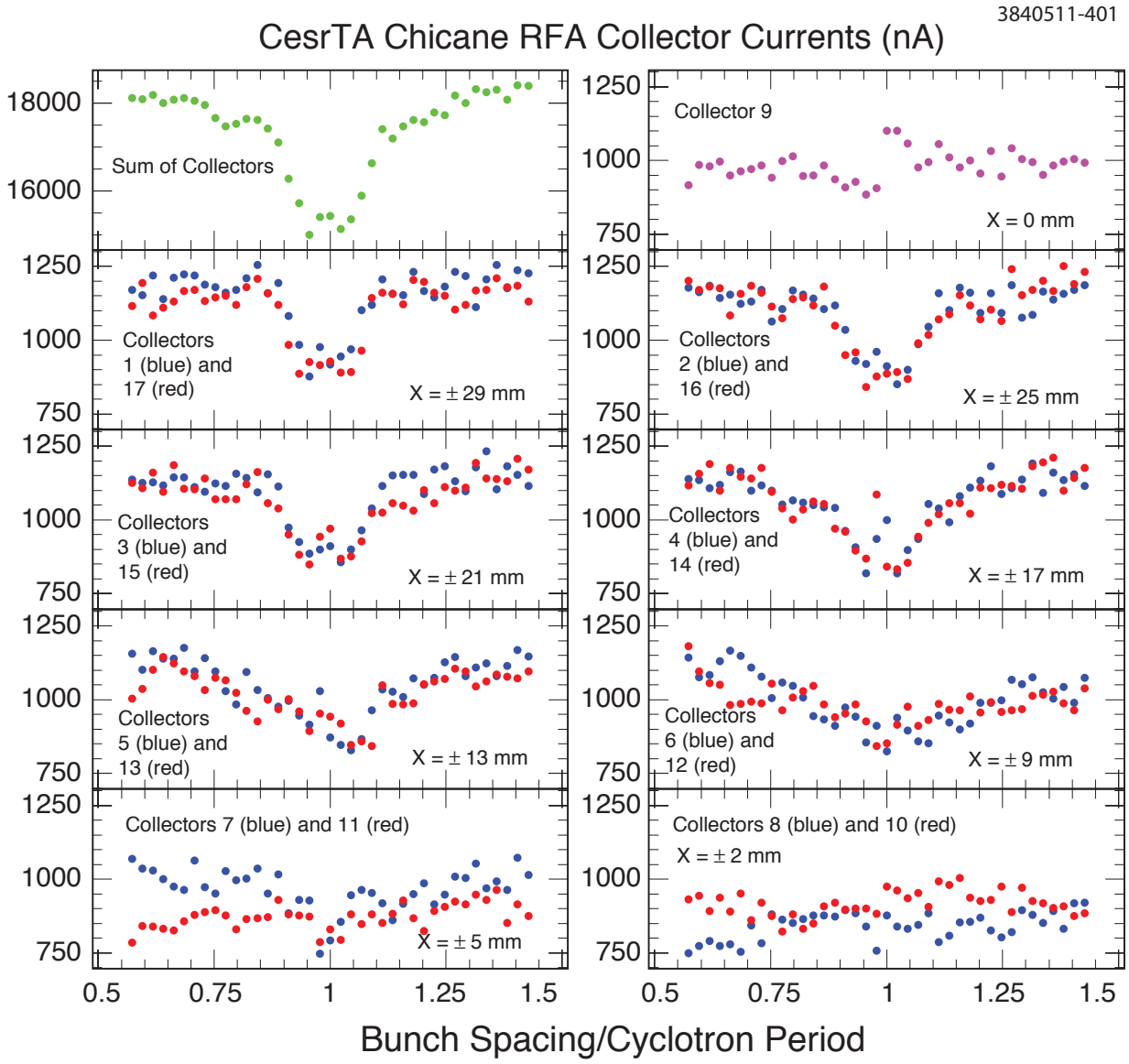

Figure 5.33: `ECLOUD` model for the resonant suppression observed in the TiN-coated chamber in the PEP-II chicane. This result was obtained under the assumptions of a peak secondary yield of 0.5 and an elastic yield value of 1.0.

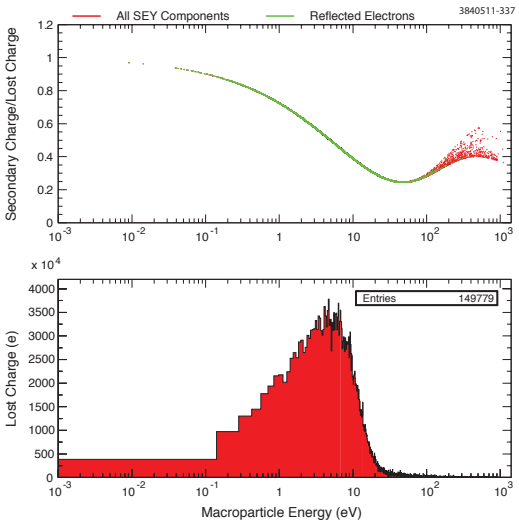

Figure 5.34: Population of the modeled secondary yield curve for the case of a TiN-coated aluminum chamber and a chicane magnetic field value of 129 G, halfway between the first and second cyclotron resonances for the 4-ns bunch spacing.

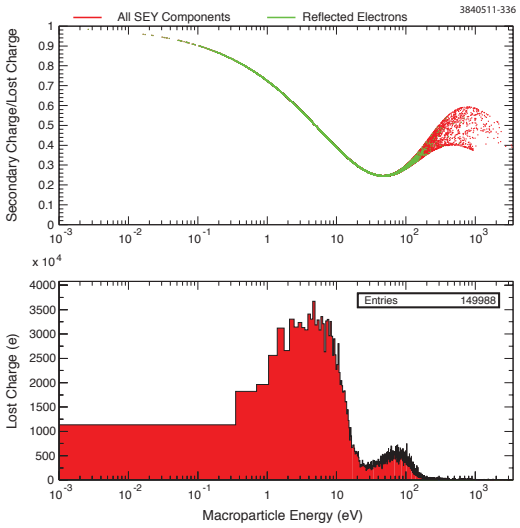

Figure 5.35: Population of the modeled secondary yield curve for the case of an TiN-coated aluminum chamber and a chicane magnetic field value of 89 G, which corresponds to the first cyclotron resonance for the 4 ns bunch spacing.

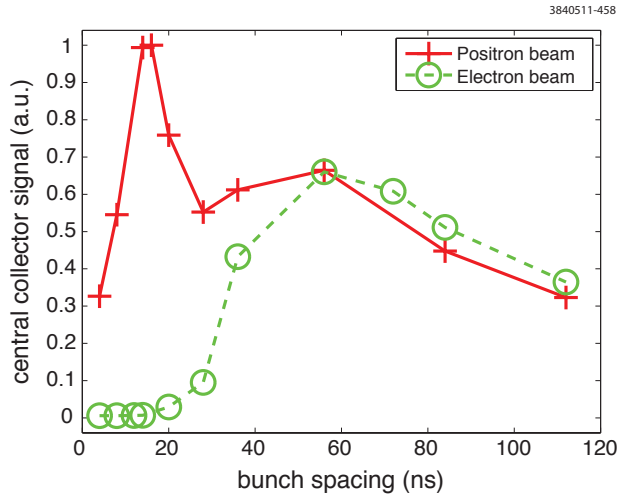

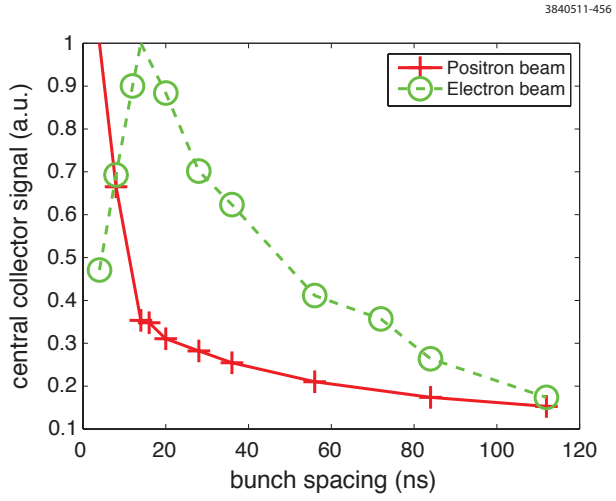

Figure 5.36: Central collector signal in a dipole RFA as a function of bunch spacing, for a 20 bunch train with 3.5 mA (5.6×10^{10} particles) per bunch, at 5.3 GeV. Left: SLAC chicane RFA, right: CESR dipole RFA

to travel to the center of the beam pipe is equal to the bunch spacing, this electron will be kicked strongly by the beam, and is likely to produce more secondary electrons. In reality, peak secondary production will occur when this electron is given an amount of energy corresponding to the peak of the SEY curve. However, for aluminum the SEY is greater than 1 well into the keV range, so an electron anywhere near the beam is a candidate to produce more secondaries. Thus we expect the "resonance" to be somewhat broad.

If we ignore the time for the kicked electron to travel to the beam pipe wall (which will be small if the kick is strong), the resonance condition is simply $t_b = a/v_{sec}$, where t_b is the bunch spacing, a is the chamber half-height (i.e. the distance from the wall to the beam), and v_{sec} is a characteristic secondary electron velocity. For a 1.5 eV electron, this peak will occur at 61 ns. The fact that there is a finite width to the secondary energy distribution will further smear out the peak.

The lower energy peak in the positron data could be a higher order multipacting resonance, where it takes two bunch passages to set up the resonance condition. Here we consider the case where the first bunch gives some additional energy to the electron, so that it makes it to the center of the chamber in time for the second bunch. If we again neglect the time for the kicked electron to reach the beam pipe wall, the resonance condition becomes:

$$t_{b,2} = \frac{a - r_1}{v_{\rm sec}} = \frac{r_1}{v_2} \tag{5.1a}$$

$$v_2 = v_{\rm sec} + \frac{2cN_b r_e}{r_1} \tag{5.1b}$$

Here r_1 is the distance from the electron to the beam during the first bunch passage, v_2 is the velocity of the electron after it is kicked by the first bunch, N_b is the bunch population and r_e is the classical electron radius. Solving for $t_{b,2}$ gives us Eq. 5.2, where we have defined $k \equiv 2cN_b r_e$.

$$t_{b,2} = \frac{k + 3av_{\rm sec} - \sqrt{k^2 + 6kav_{\rm sec} + a^2 v_{\rm sec}^2}}{4v_{\rm sec}^2} \tag{5.2}$$

For a 1.5 eV secondary electron, $t_{b,2}$ is 11 ns, somewhat less than the 14 ns that is observed. A more sophisticated model (which would include, among other things, the time for the kicked electron to reach the wall) may yield a more accurate result. Note that this resonance condition applies only to positron beams, so only one peak is predicted for the electron data (which is what we find). Overall, a multipacting scenario with a 1.5 eV peak secondary energy is approximately consistent with the SLAC chicane data, for both the positron and electron beam data.

The predictions for our CESR dipole (Fig. 5.36, right) would then be $t_b = 34$ ns and $t_{b,2} = 4$ ns. The former is higher than what is observed, though the latter is consistent with the data. A better fit would be for an 8 eV electron, then $t_b = 15$ ns and $t_{b,2} = 3$ ns. It is also possible that a more sophisticated model would fit the CESR dipole data better.

Quadrupole Data Another development at CesrTA has been the incorporation of an RFA into a quadrupole chamber. This RFA wraps azimuthally around the chamber, from about 70 to 150 degrees (taking zero degrees to be the source point). A typical quadrupole RFA measurement is shown in Fig. 5.37. We find that the collector that is lined up with the quad pole tip (no. 10) sees a

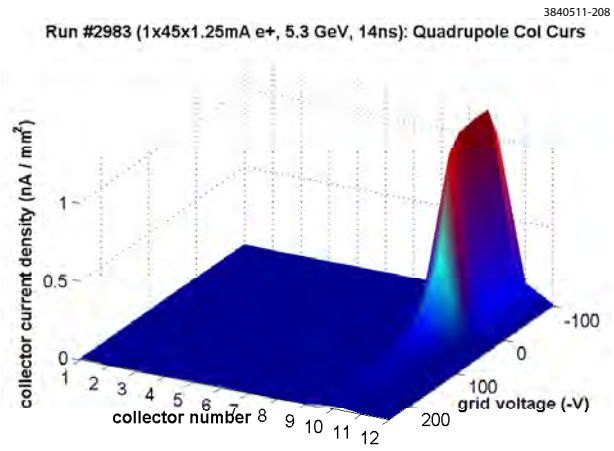

Figure 5.37: Quadrupole RFA voltage scan: 1x45x1.25 mA e+, 5.3 GeV, 14 ns

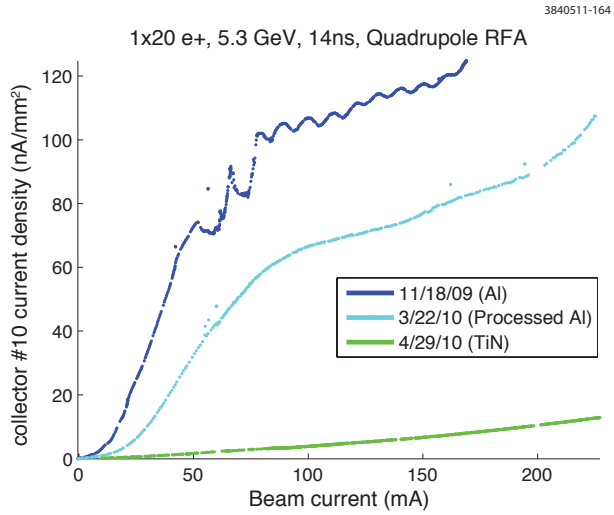

Figure 5.38: Quadrupole mitigation comparison, 1x20 e+, 5.3 GeV, 14 ns

large amount of current, while the rest of the collectors see relatively little. This suggests that the majority of the cloud in the quad streams along the field lines between adjacent pole tips.

Fig. 5.38 shows a comparison of a bare Aluminum (both processed and unprocessed) quadrupole chamber with the TiN coated chamber that has replaced it. In this comparison only collector 10 is being plotted. The signal in the TiN chamber was found to be reduced by well over an order of magnitude.

One potential side effect of the cloud mirroring between the quad pole tips is that it may become trapped for a long time. As seen in Fig. 5.39, for a positron beam we do not observe a strong dependence on bunch spacing, though there does seem to be a modest enhancement around 14 ns. The data for an electron beam is even more surprising, actually showing a monotonic increase with bunch spacing. Both of these measurements point to a timescale for cloud development in the quad that is much longer than 100 ns.

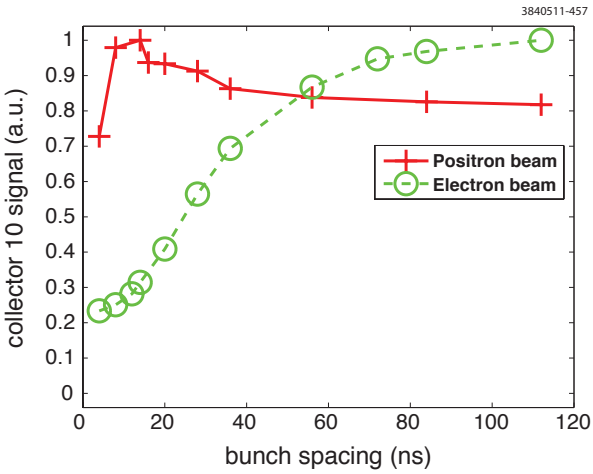

Figure 5.39: Signal in a quadrupole RFA as a function of bunch spacing, for the same beam conditions as in Fig. 5.36. The collector which is in line with the quad pole tip is plotted.

Wiggler Data The L0 straight section of CESR has been reconfigured to include six superconducting wigglers, three of which are instrumented with RFAs (see Section 2.3.1). Each wiggler has three RFAs: one in the center of a wiggler pole (where the field is mostly vertical), one in between poles (where the field is mostly longitudinal), and one in an intermediate region. Fig. 5.40 shows a typical voltage scan done in the center pole RFA of a Cu wiggler chamber, for a 45 bunch train of positrons at 1.25 mA/bunch, 14 ns spacing, and 2.1 GeV. The signal is fairly constant across all the collectors at low retarding voltage, but does become peaked at the center at high energy. There is also an anomalous spike in current at low (but nonzero) retarding voltage; we believe this is due to a resonance between the bunch spacing and retarding voltage (see Section 5.1.3.4).

As with the drift RFAs, cycling the location of the different wigglers has allowed us to compare the RFA response with different mitigation techniques at the same longitudinal position in the ring. We have tested chambers with bare Copper, TiN coating, triangular grooves, TiN coating on grooves, and a clearing electrode. Fig. 5.41 shows an example voltage scan from the grooved chamber; it is interesting to note that the RFA is sensitive to the grooved structure. The grooves have 2 mm depth and 20° angle, and the spacing between the RFA collector strips is 3.4 mm (see Fig. 2.42)

Fig. 5.42 compares the average collector current (in the center pole RFA) vs. beam current for different mitigation schemes, at both the 2WA and 2WB locations. These locations have slightly different photon fluxes, but as the TiN coated chamber has been installed in both, it can be used (roughly) as a reference. Note that TiN coating by itself does not appear to lead to a reduction in the wiggler RFA current relative to bare copper. Grooves do lead to an improvement, and TiN coated grooves are better still. The chamber instrumented with a clearing electrode shows the smallest signal by a wide margin, improving on TiN by approximately a factor of 50. The electrode was set to 400 V for this measurement.

Very little dipole radiation is expected to reach the downstream vacuum chambers in the L0 straight, but they will be illuminated by radiation from the wigglers. Therefore, by varying the field in the wiggler magnets, we can vary the number of photons striking the wall at a given point along the straight. This will also vary the number of photoelectrons produced there, so electron cloud

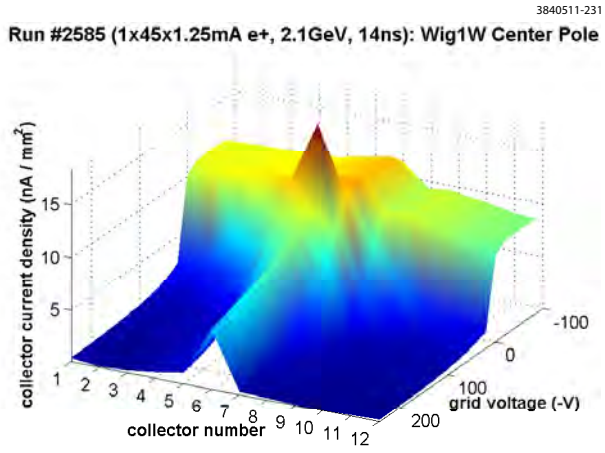

Figure 5.40: Cu wiggler RFA measurement: 1x45x1.25 mA e+, 2.1 GeV, 14 ns

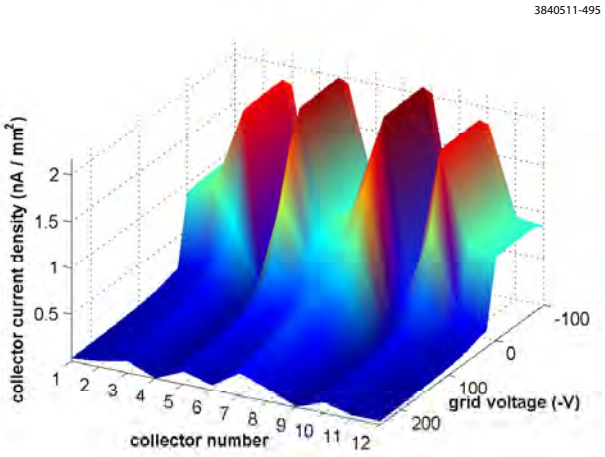

Figure 5.41: Grooved wiggler RFA measurement: 1x45x1.25 mA e+, 2.1 GeV, 14 ns

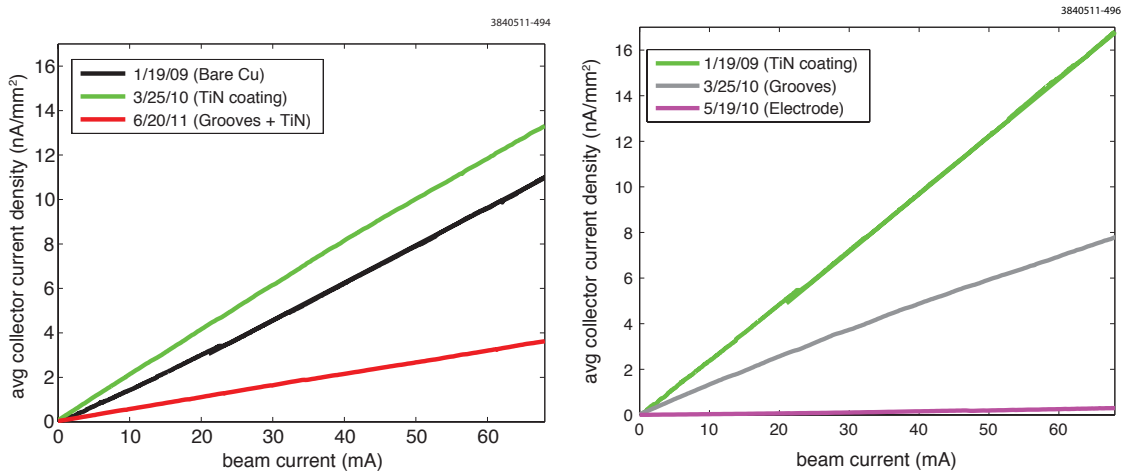

Figure 5.42: Wiggler RFA mitigation comparison: 1x45 e+, 2.1 GeV, 14 ns. Left: 2WA location, right: 2WB location. The 2WB location is further downstream in the wiggler straight, and therefore has a slightly higher photon flux.

diagnostic devices located in L0 can provide an indirect measurement of the properties of the wiggler photons.

Fig. 5.43 shows the signal in three center-pole wiggler RFAs as a function of wiggler field strength. We observe a "turn on" of the signal in each detector at a specific wiggler field value. Note that the detectors that are further downstream (i.e. those with a higher s value) turn on first. This is because as the wiggler field is increased, the radiation fan becomes wider. The farther downstream a detector is, the less wide the fan must be for photons to hit at that location. This measurement can help us understand the scattering of photons in L0, since only photoelectrons produced on the top or bottom of the beam pipe can initiate the build-up of the part of the cloud detected by the RFA.

During normal operation, essentially no signal is observed in longitudinal field detectors, because there are no electrons with sufficient energy to cross the field lines. Fig. 5.44 shows the signal in a longitudinal field RFA (in the uncoated Copper wiggler), as a function of magnetic field strength. The signal is effectively gone by 1000 Gauss, well below the 1.9 T full field value.

Mitigation Summary In terms of the effectiveness of mitigation types, several qualitative comments can be readily made:

- We have found beam pipe coatings (TiN, amorphous carbon, diamond-like carbon, and NEG) to be effective at mitigating the cloud in drifts.
- TiN coating was also found to be effective in a dipole and quadrupole; using a grooved and coated chamber in a dipole is even more effective.
- In a wiggler, a clearing electrode appears to be the most effective mitigation technique.

A systematic study to obtain more quantitative information about the different chambers, in particular the primary and secondary electron yield properties of the surface, is discussed in the next section.

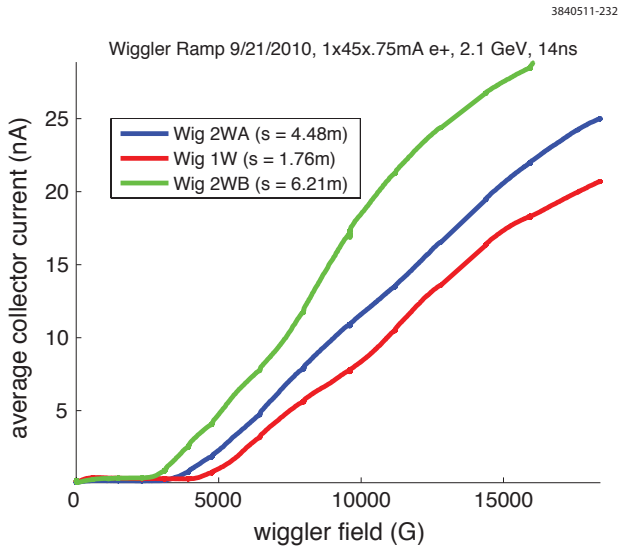

Figure 5.43: Wiggler ramp measurement: 1x45x.75 mA e+, 2.1 GeV, 14 ns

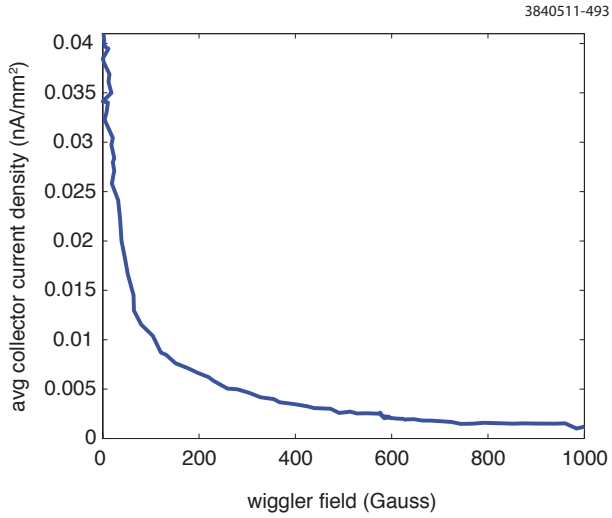

Figure 5.44: Wiggler ramp measurement in longitudinal field region: 1x45x.75 mA e+, 2.1 GeV, 14 ns

5.1.4.2 Comparison with Simulation

The large quantity of RFA data obtained during the CesrTA program necessitates a systematic method for detailed analysis. The goal is, given a set of voltage scan data, to find a set of simulation parameters that bring data and simulation into as close to agreement as possible.

A chi-squared analysis has been employed to accomplish this. In short, we want to minimize χ^2, as defined in Eq. 5.3. Here $\mathbf{y}$ a vector containing the difference between the data and a nominal simulation, $\mathbf{X}$ is the Jacobian matrix, and β is the a vector containing the change in each of the parameters under study. $\mathbf{W}$ is a diagonal matrix whose elements are $\frac{1}{\sigma_i^2}$, where σ_i is the error on the data-simulation difference for point i. Note that both the data and simulation can contribute to this error. The value of β which will minimize χ^2 is given in Eq. 5.4. Once a new set of parameter values is obtained, the process can be repeated with this new set as the "nominal" values. This method will generally need to be iterated a few times before it converges on the actual minimum value of χ^2.

$$\chi^2 = (\mathbf{y} - \mathbf{X}\,\beta)^T\,\mathbf{W}\,(\mathbf{y} - \mathbf{X}\,\beta) \tag{5.3}$$

$$\beta = (\mathbf{X}^T\,\mathbf{W}\,\mathbf{X})^{-1}\,\mathbf{X}^T\,\mathbf{W}\,\mathbf{y} \tag{5.4}$$

There are many subtleties in the precise definitions of the terms in Eq. 5.4. For the RFA analysis, the points in the vector $\mathbf{y}$ come from voltage scan data. To determine the parameters independently, one should use several different voltage scans, which cover a wide range of beam conditions. Since a voltage scan is actually a measurement of the integrated energy spectrum, once should differentiate the signal to obtain a set of independent data points. These points may not individually have enough signal to be meaningful, so one can group them together (i.e. make energy "bins" of varying width) to get one element of the $\mathbf{y}$ vector.

The choice of which simulation parameters to fit is also essential. There are many parameters that characterize the production of secondary electrons in `POSINST` [86], but a few stand out as being especially important. Among them are:

- **dtspk**, the peak true secondary electron yield
- **P1epk**, the low energy elastic yield
- **P1rinf**, the rediffused yield at infinity
- **E0epk**, the energy at which peak secondary production occurs
- **powts**, the "shape parameter," which determines the rise and fall of the SEY curve
- **pangsec**, the angular distribution of secondary electrons

- **enpar** and **pnpar**, which determine the energy distribution of secondary electrons

In general, primary photoelectrons are less well understood than secondary electrons. Some important primary emission parameters include:

- **queffp**, the effective quantum efficiency

- **ek0phel** and **eksigphel**, the peak energy and width of the photoelectron energy distribution

Generally speaking, **dtspk** and **queffp** need to be included in the fitting procedure to get good agreement with the RFA data. Other sensitive parameters include **P1epk**, **P1rinf**, and **powts**, but they are highly correlated with each other (i.e., they have similar effects on the RFA simulation), so only one of the three is needed.

The starting points for several SEY parameters (**dtspk**, **E0epk**, **powts**), were chosen based on fits to the in situ SEY measurements in CESR (Section 5.1.5).

We have found that, in order to have any RFA signal for a high current electron beam, some high energy photoelectrons need to be generated. Currently this is accomplished by using a Lorentzian photoelectron energy distribution (rather than the default Gaussian distribution), with a low peak energy (**ek0phel** = 10eV), but a large width (**eksigphel** = 150 eV). However, the drift RFA data do not seem to constrain the exact shape of the distribution. Measurements with a shielded pickup detector (Section 5.2.2) provide a method to probe these parameters in more detail.

The photon flux and reflectivity at the RFA are kept fixed, based on a 3 dimensional simulation of photon production and reflection in the CesrTA vacuum chamber using the code `Synrad3D` (Section 4.1.4.1). Photoelectron parameters were allowed to be different for different beam energies and species, because the photon energy spectrum at any given location in CESR will be different for the two species. Plans are underway to develop a model for photoelectron production which takes into account the energy of the incident photon.

In order to get a good fit to the data, one should choose parameters which have a strong effect on the simulations, and are relatively independent of each other. We have found that a reasonable fit can be obtained with as little as three parameters, typically the true secondary yield (**dtspk**), elastic yield (**P1epk**), and effective quantum efficiency (**queffp**). The true secondary yield has the strongest effect on data taken with short bunch spacings, high bunch currents, and positron beams. The elastic yield, meanwhile, is best determined by data with large bunch spacing, while the quantum efficiency prefers low beam current. Table 5.3 gives a list of data sets used in one round of fitting, and indicates which parameter is most strongly associated with it.

Several sources of error must be taken into account when constructing the error matrix (**W** in Eq. 5.3). They include:

- Noise in the measurements (typically quite small)
- Statistical errors in simulations. This is a major source of error. It can be reduced by increasing the number of macroparticles used in the simulation, at the cost of increased run time.
- A general error of 10% was added to account for systematic uncertainties in the data. One such uncertainty is unevenness in bunch currents along the train, which is not accounted for

Table 5.3: List of beam conditions used for one round of fitting, and which parameter(s) they help determine

Bunches	Bunch current (mA)	Species	Bunch Spacing	Beam Energy (GeV)	Parameter(s)
45	2.3	e^+	14	2.1	dtspk
20	2.8	e^+	4	4	dtspk
20	7.5	e^+	14	2.1	dtspk
20	2.95	e^+	14	4	dtspk
45	2.67	e^+	14	5.3	dtspk
45	1.25	e^+	4	5.3	dtspk
45	2.89	e^-	4	5.3	dtspk, queffp
20	2.6	e^-	14	2.1	queffp
45	0.8	e^-	14	5.3	queffp
45	0.75	e^+	14	5.3	queffp
45	0.75	e^-	14	2.1	queffp, P1epk
9	3.78	e^+	280	2.1	queffp, P1epk
45	0.75	e^+	14	4	queffp, P1epk
9	3.78	e^-	280	2.1	P1epk
9	3.78	e^-	280	5.3	P1epk
9	3.78	e^+	280	4	P1epk
9	4.11	e^+	280	5.3	P1epk

in the simulation.

- We have observed a slow drift of baseline (zero current value) in measurements, on the order of $\sim 2\%$ of full scale. This amounts to $\sim$20 nA on the lowest gain setting, and $\sim$0.02 nA on the highest one.
- An extra 20% error was added to signal in the simulation caused by beam pipe hole secondaries, to account for uncertainty in the modeling of this phenomenon.
- Since the gradient for Jacobian matrix ($\mathbf{X}$) is determined by simulation, it will also have an associated error. This cannot be included in the $\mathbf{W}$ matrix, because it will be different for each parameter. However, it can still be calculated, and its effect on the final parameter errors can be estimated.

We have found that, in general, one can obtain a reasonable fit to the data with only three (well chosen) parameters. As mentioned above, one good set consists of the true secondary yield, elastic yield, and quantum efficiency. Using more parameters does allow for a slightly better fit, at the cost of uniqueness and clarity.

Fig. 5.45 shows some of the results of the parameter finding method for an uncoated aluminum drift chamber. The plots compare the data and simulation for the signal across the 9 RFA collectors at three different retarding voltages. Overall there is good agreement between data and simulation for a wide variety of beam conditions.

In principle, errors on the final parameter values are readily obtainable during the course of the analysis from the covariance matrix for the parameters, $(\mathbf{X}^T \mathbf{W} \mathbf{X})^{-1}$. Standard errors on each parameter can be derived from the diagonal elements of the covariance matrix, and the correlations between each parameter from the off-diagonal elements. However, it should be noted that this

Table 5.4: Best fit parameters, 15W aluminum chamber

Parameter	Description	Base Value	Final Value
dtspk	Peak true secondary yield	1.37	1.74 ± 0.02
P1epk	Elastic yield at E = 0	0.5	0.43 ± 0.01
P1rinf	Rediffused yield at E = ∞	0.2	0.2
E0epk	Peak yield energy	280 eV	280 eV
powts	Shape parameter	1.54	1.54
queffp	Quantum efficiency, 2.1 GeV, e^-	0.1	0.034 ± 0.004
queffp	Quantum efficiency, other	0.1	0.111 ± 0.006

Table 5.5: Best fit parameters, 15E amorphous carbon coated chamber

Parameter	Description	Base Value	Final Value
dtspk	Peak true secondary yield	0.76	0.55 ± 0.02
P1epk	Elastic yield at E = 0	0.5	0.29 ± 0.02
P1rinf	Rediffused yield at E = ∞	0.2	0.2
E0epk	Peak yield energy	300 eV	300 eV
powts	Shape parameter	1.77	1.77
queffp	Quantum efficiency, 2.1 GeV, e^+	0.1	0.021 ± 0.003
queffp	Quantum efficiency, other	0.1	0.081 ± 0.017

analysis will only seek out the nearest local minimum in parameter space. It is always possible that a better fit can be achieved with a different set of values, especially if one uses many parameters in the fit. Therefore, these errors should be understood as the width of the local minimum, rather than an absolute determination of the uncertainty in the parameter. Nonetheless, the ability of this method to achieve a good fit for data taken under a wide variety of beam conditions strongly implies that the PEY and SEY models used are reproducing reality to a reasonable degree.

The best fit values and confidence intervals for an Aluminum chamber are shown in Table 5.4. This chamber was installed in the drift region adjacent to the 15W quadrupole (see Section 5.1.4.1), and the fit used the data taken during May 2010 (listed in Table 5.3). The values listed for the error bars also include an estimate of the uncertainty introduced by errors in the Jacobian matrix, which is added in quadrature to the standard error. Table 5.5 lists the best fit values for the 15E amorphous Carbon coated chamber, using the same data sets. Finally, Table 5.6 gives the values for a TiN coated chamber, installed at 15W during December 2010. As mentioned above, the starting point for all the listed SEY parameters were taken from fits to measured in situ data. It is worth noting that this analysis indicates a very low secondary yield for both coated chambers.

One somewhat strange result of this analysis is that the quantum efficiency at 2.1 GeV was found to be quite low for positron beams at 15E, and electron beams at 15W. The value for the other species, and for 4 and 5.3 GeV, are all consistent with each other. The anomalous value is quoted separately from the other best fit values. This discrepancy appeared for both the 15W Al chamber and the 15E carbon coated chamber (it did not appear for the 15W TiN chamber, because no 2.1 GeV electron beam data was used in the fit). It is most likely a reflection of the incompleteness of our photon and photoelectron modeling.

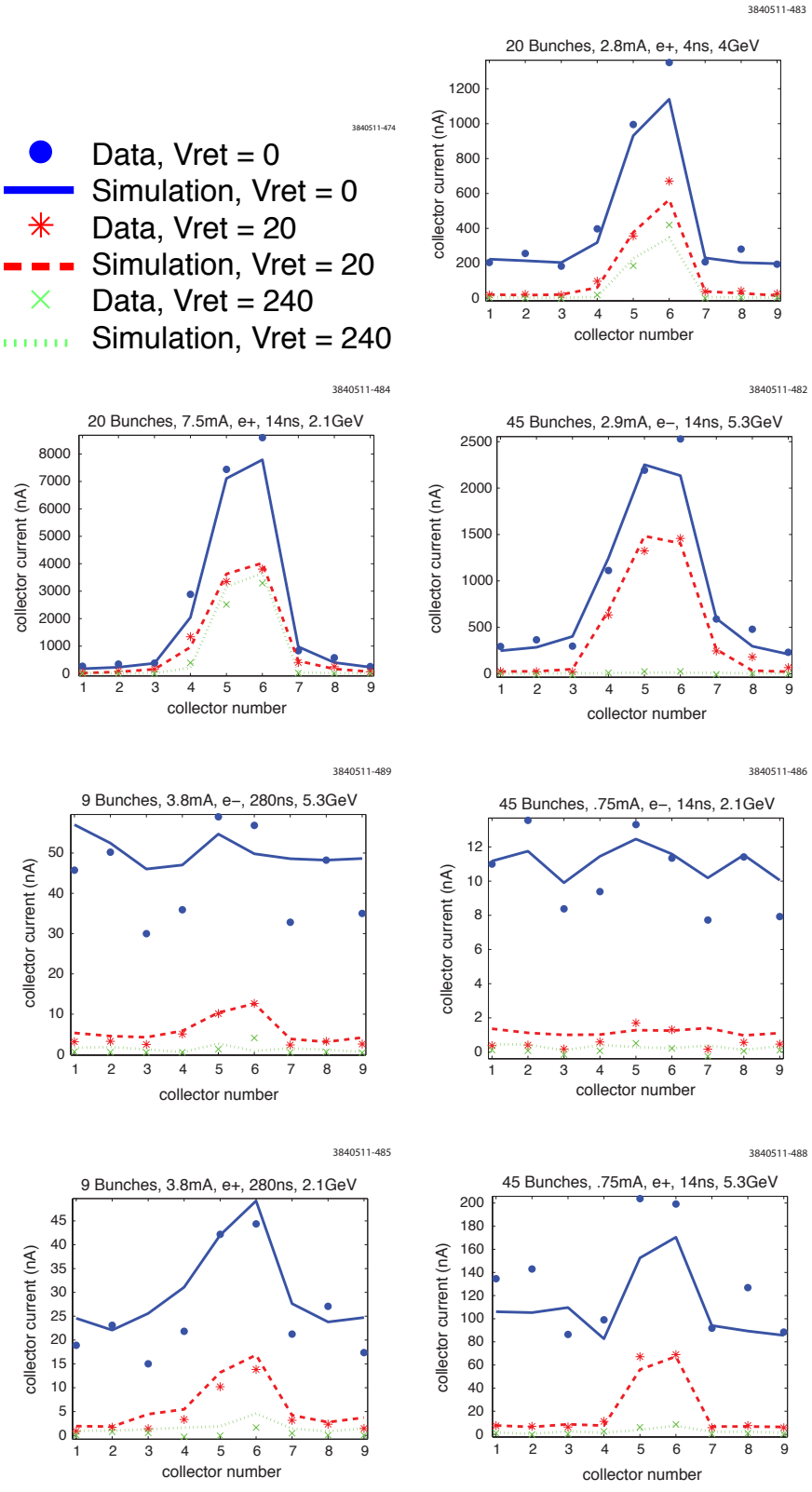

Figure 5.45: Comparison of RFA data and simulation, using best fit parameters. The plots show the signal across the 9 RFA collectors at three different retarding voltages.

Table 5.6: Best fit parameters, 15W TiN coated chamber

Parameter	Description	Base Value	Final Value
dtspk	Peak true secondary yield	0.73	0.54 ± 0.01
P1epk	Elastic yield at E = 0	0.5	0.36 ± 0.01
P1rinf	Rediffused yield at E = ∞	0.2	0.2
E0epk	Peak yield energy	370 eV	370 eV
powts	Shape parameter	1.32	1.32
queffp	Quantum efficiency	0.1	0.068 ± 0.007

Summary A systematic method for fitting RFA simulation to data has been presented, and best fit values for PEY and SEY parameters of some materials have been given. Future work on this topic includes:

- Repeating the analysis for other surface types
- Repeating the analysis for RFAs in magnetic fields, including dipoles, quadrupoles, and wigglers
- Comparing with other local cloud measurements, such as shielded pickups
- Incorporating a more complete description of photoelectron emission

The end result of this analysis will be a detailed and self-consistent description of the in situ primary and secondary emission properties of the materials under investigation.

5.1.5 In situ SEY Studies

We used the in situ secondary electron yield (SEY) station described in Section 2.3.4 to take measurements on samples roughly once a week. Measurements were done on samples coated with SEY-reducing films and bare metal samples.

5.1.5.1 Secondary Electron Yield

The SEY is operationally defined as

$$\mathrm{SEY} = I_{\mathrm{SEY}}/I_p \,, \tag{5.5}$$

where I_p is the current of the primary electrons incident on the sample and I_{SEY} is the current of the secondary electrons expelled by the bombardment of primary electrons. The SEY depends on the energy and angle of incidence of the primary electron beam. The primary current I_p is measured by firing electrons at the sample with the electron gun and measuring the current from the sample with a positive bias voltage. A high positive biasing voltage of +150 V is used to

recapture secondaries produced by the primary beam, so that the net current due to secondaries is zero.

The current I_{SEY} due to secondary electrons is measured indirectly. The total current I_t is measured by again firing electrons at the sample, but with a low negative bias (−20 V) on the sample to repel secondaries produced by the primary electron beam, and also to repel secondaries from "adjacent parts of the system that are excited by the elastically reflected primary beam" [79]. Since I_t is effectively the sum of I_p and I_{SEY} ($I_t = I_p + I_{\mathrm{SEY}}$, with I_{SEY} and I_p having opposite signs), we calculate SEY as

$$\mathrm{SEY} = (I_t - I_p)/I_p \, . \tag{5.6}$$

Some SEY systems include a third electrode for a more direct measurement of I_{SEY}, for example the system at KEK [118]. Our in situ setup cannot accommodate the extra electrode, so we cannot use the more direct method; we must use the indirect method described above.

5.1.5.2 Data Acquisition System

An electrical schematic of the system is shown in Figure 5.46. The current on the sample is measured during three separate electron beam energy scans. Each scan automatically steps the electron gun energy from 20 eV to 1500 eV in increments of 10 eV. For each energy, the focusing voltage is set to minimize the beam spot size on the sample, based on previous measurements. This process is controlled by a LabVIEW interface we developed [29] incorporating existing software from Kimball Physics and Keithley. The first scan is done with a 150 V biasing voltage on the sample to measure I_p, with gun settings for $I_p \approx 2$ nA. This measurement is taken between grid points 5 and 9 to avoid processing the measurement points with the electron beam during the I_p measurement.

The second scan steps through the same gun energies with a bias voltage of −20 V on the sample to measure I_t. At each gun energy, the beam is rastered across all 9 grid points while the program records the current for each point.

To minimize error due to drift in the gun output current, we take a second I_p scan after the I_t scan. The two I_p sets are averaged and the SEY is calculated at each energy. Identical measurements are performed on the 45° system and the horizontal system.

5.1.5.3 Results

In-situ measurements have been done on bare aluminum, titanium nitride, and amorphous carbon surfaces. Preliminary SEY measurements have been carried out in the laboratory for diamond-like carbon (DLC) surfaces, but no in-situ measurements have yet been made.

Aluminum Samples with TiN Coatings Aluminum samples with titanium nitride coatings provided by M. Pivi (SLAC National Accelerator Laboratory) were installed in CESR in both the horizontal and 45° stations from January to August 2010 and their SEYs were measured roughly once a week. These results are summarized in Figure 5.47. There is a peak in the SEY for an incident electron energy near 400 eV. A significant decrease in the SEY is evident between the

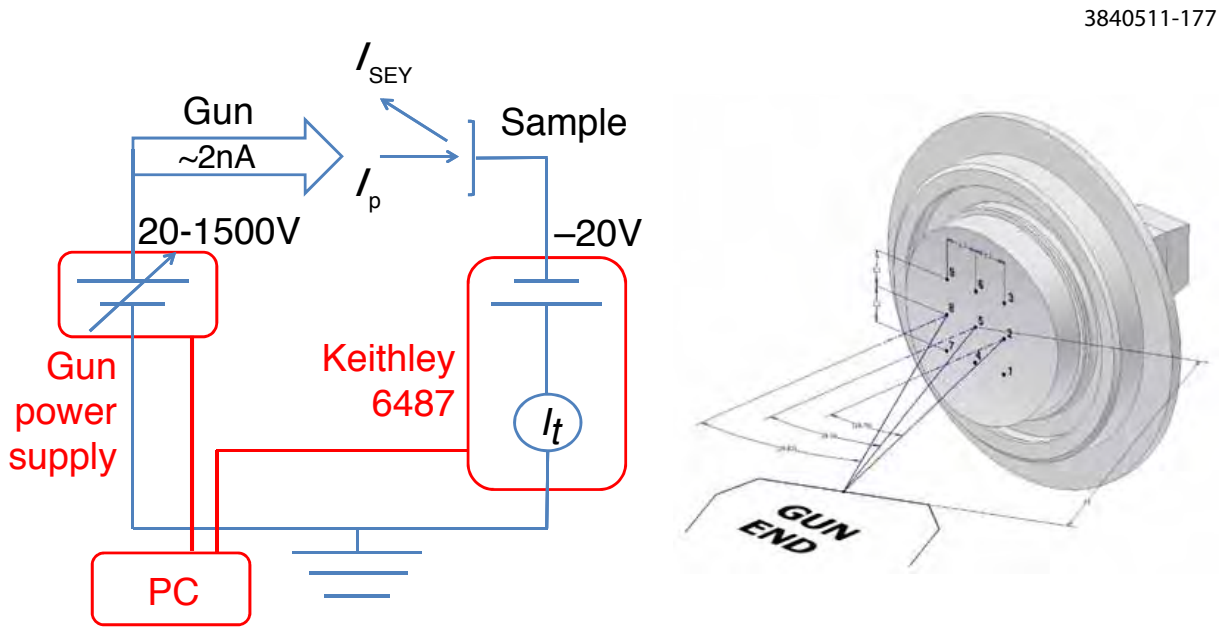

Figure 5.46: Left: Data acquisition schematic. Right: 9 grid points where the SEY is measured.

first round of measurements and subsequent measurements. As the SEY decreases, there is a slight upward shift in the energy at which the peak in the SEY occurs, as indicated by the dotted lines in Figure 5.47.

The value of the SEY peak and the energy $E_{\max}$ at which the peak occurs are useful metrics for tracking the SEY behavior as a function of exposure. The beam conditioning behavior of the samples is illustrated in Figure 5.48, which shows the peak SEY and $E_{\max}$ for the center grid point as a function of accumulated dose. The bottom axis indicates the electron beam current integral in ampere·hours; the top axis indicates the calculated SR dose to the vacuum chamber wall in photons per meter. Neither of these values includes the contribution from the positron beam, because the dominant source of SR for the SEY stations is the electron beam. The SR photon dose in Figure 5.48 accounts for direct SR from the beam onto the chamber wall at the location of the SEY stations: it represents the "source term" and does not attempt to include the effects of scattering of photons (or production of photoelectrons). The dose calculation does not differentiate between the horizontal and 45° stations, even though the 45° station does not receive direct SR and the stations' distance from the bending magnet is not exactly the same.

As can be seen in Figure 5.48, the "fresh" sample in the horizontal setup began with a peak SEY of almost 1.8 and reached a minimum SEY peak of just under 1. At this point the sample remained under ultra-high vacuum (high 10^{-9} torr) for 2 weeks without exposure to beam. Under these conditions, the SEY increased by about 1%. After that, the sample was exposed to nitrogen gas for 1 hour and then the system was pumped down again. The measured peak SEY increased from 1 to 1.12 after exposure to nitrogen. The sample was once again processed in CESR for about 10 weeks, with weekly SEY measurements; the peak SEY decreased to about 1.

The "fresh" sample in the 45° station started with a peak SEY of just above 1.7 and reached a minimum SEY peak of around 1.2. After that the sample in the 45° station was left under ultra-

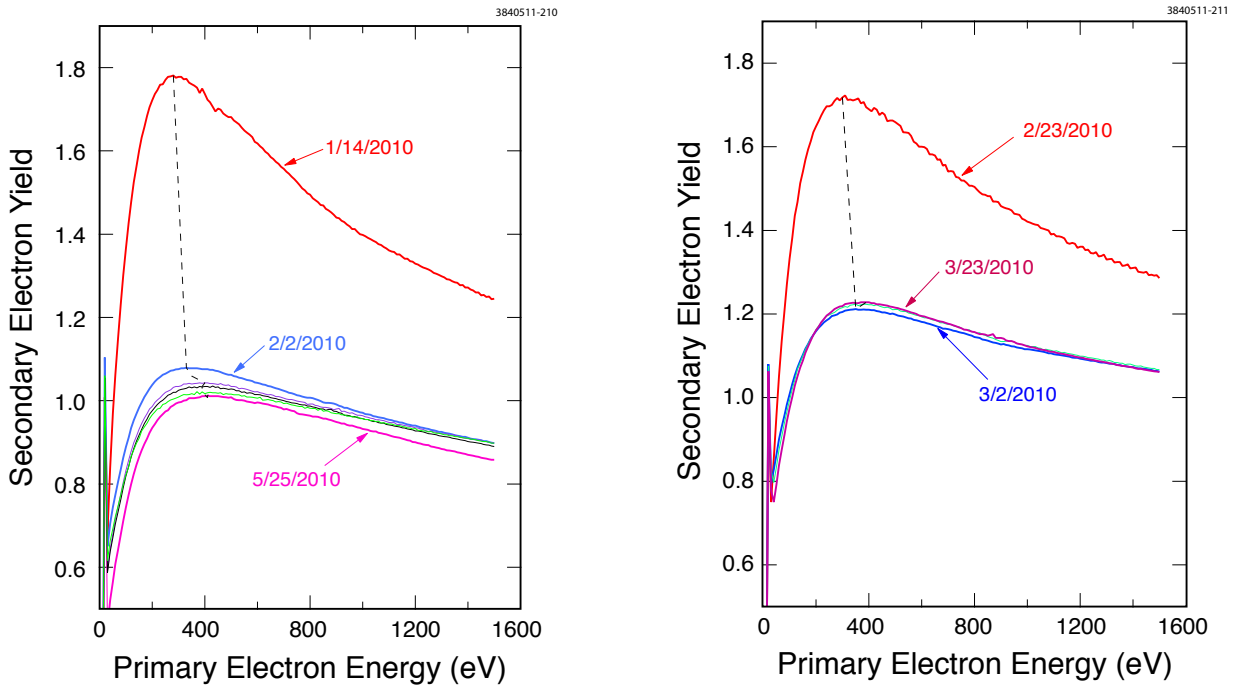

Figure 5.47: Repeated measurements of SEY as a function of energy for TiN-Al samples in the horizontal station (left) and the 45° station (right).

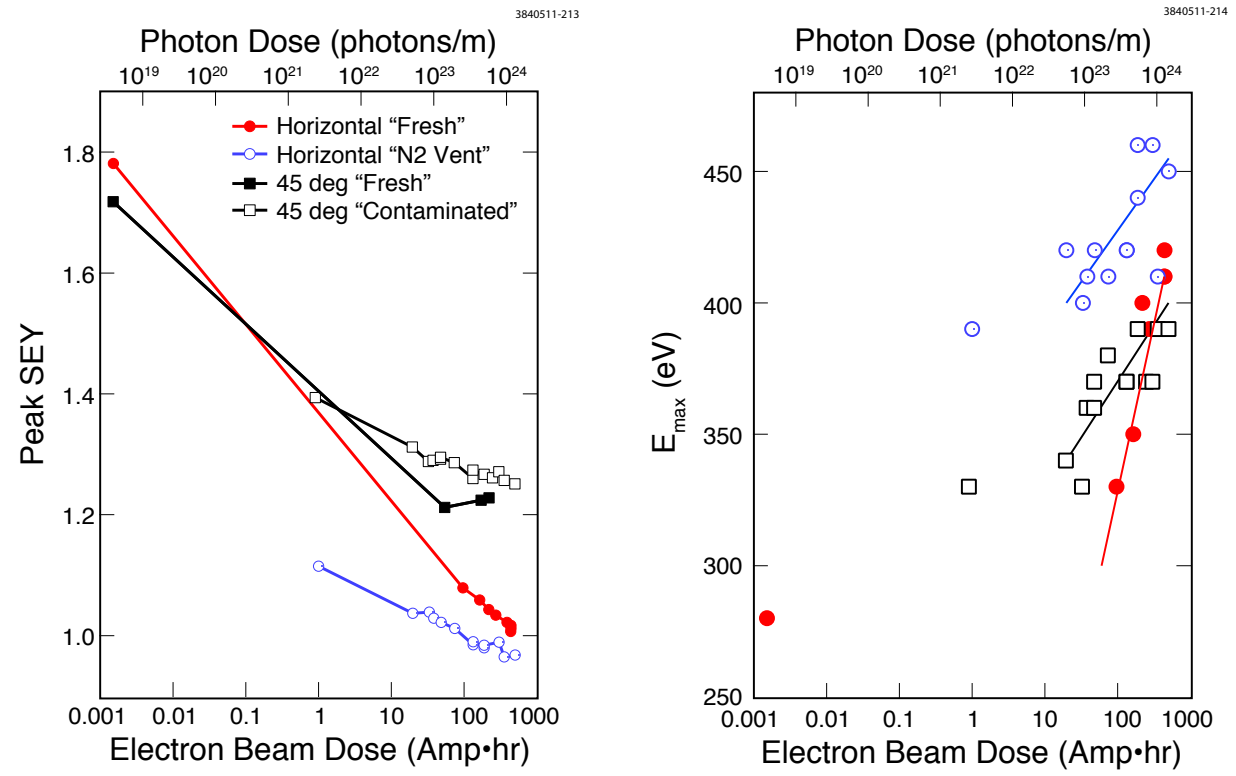

Figure 5.48: Dependence of SEY peak (left) and $E_{\max}$ (right) on dose for TiN-Al samples in the horizontal and 45° stations.

high vacuum in the SEY system for 2 weeks, and the peak SEY increased from 1.2 to 1.4. At that point we realized that the miniature hot filament vacuum gauge of the system had been left on, and that this could explain why the peak SEY of the fresh sample after it reached a peak SEY of about 1.2 was increasing by few percent every week instead of decreasing as the horizontal sample had been by 1 to 2 percent per week. At that point, we turned the hot filament gauge off and processed the sample in CESR for about 10 weeks. The peak SEY decreased to about 1.2, as can be seen in the 45° "contaminated" curve in Figure 5.48.

A test was done to evaluate the effect of vacuum contamination from a vacuum gauge. We found that the emission from a hot-filament vacuum gauge can produce an increase in the SEY of the sample. Based on these results, it is likely that the differences between the final SEY of the samples in the horizontal station and the 45° station are due to contamination of the sample in the 45° station, not due to lack of processing of the 45° sample.

Aluminum Alloy Samples In August 2010, aluminum alloy samples (Al6061-T6) were installed in the in situ systems. The results are summarized in Figure 5.49. The sample in the horizontal station began with a peak SEY of 2.5 for the center grid point, and reached a minimum SEY peak of about 1.6 after 3 ampere·hours of exposure. The sample in the 45° station began with a peak SEY of 2.25 in the center and reached a peak SEY of 1.6 after the same exposure. At this point, the horizontal SEY system was removed because of a malfunction and the spare SEY system with a new Al6061-T6 sample was installed in the horizontal position. This new Al6061 sample had an initial SEY of about 2.9 and, after processing in CESR for about 6 weeks, the peak SEY decreased to 1.9. The peak SEY of the 45° sample decreased from 1.6 to 1.5 during these 6 weeks of processing in CESR. A peak SEY value of 1.5 was achieved after 20 ampere·hours of exposure. There was very little change in the SEY (a slight increase was observed) with additional exposure up to 120 ampere·hours. Similarly, the second sample in the horizontal system had a nearly constant peak SEY (with a slight increase) after 50 ampere·hours of exposure, up to about 100 ampere·hours.

The difference in the initial SEY between aluminum samples is presumably due to differences in the initial surface condition. The Al6061-T6 samples were installed "as received" after cleaning in an ultrasonic bath with alcohol to remove oil residues from machining. The results suggest that the initial peak SEY of bare aluminum samples can vary a lot. This variation may be related to the condition of the surface oxide layer.

Amorphous Carbon-Coated Samples In November 2010, the samples were replaced with amorphous carbon-coated samples provided by S. Calatroni and C. Yin Vallgren (CERN). The substrates were Al6061 (installed in the horizontal station), copper (installed in the 45° station) and stainless steel (not installed in CESR, but measured in an off-line SEY system). The peak SEY of the samples as a function of dose in CESR is shown in Figure 5.50. As can be seen, the peak SEY of both samples is hardly affected by the exposure to the beam.

Initial Measurements on Diamond-Like-Carbon-Coated Samples We have done initial SEY measurements on samples with diamond-like carbon (DLC) coatings on aluminum. The DLC samples were provided by S. Kato (KEK). We have not yet installed any DLC samples in CESR; we have only measured the SEY in the off-line system so far. The measured SEY as function of beam energy for one of the DLC samples is shown in Figure 5.51 (blue circles). The SEY is strongly

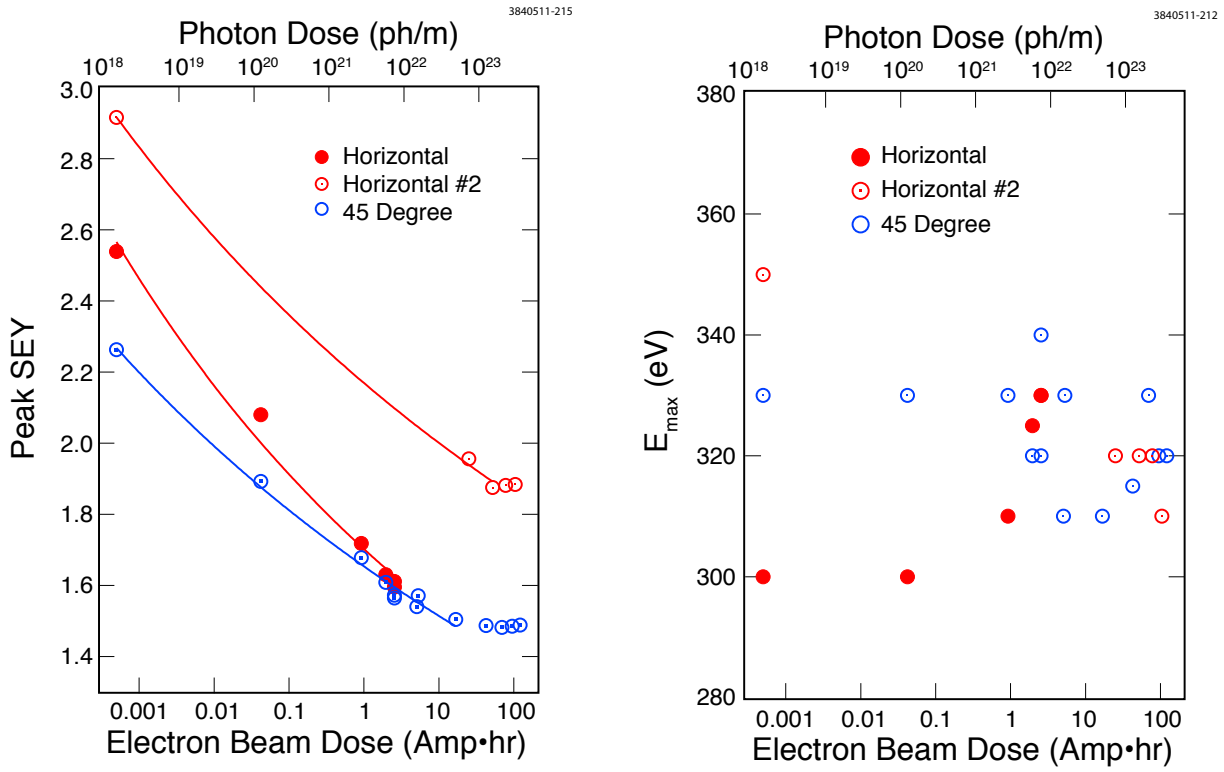

Figure 5.49: Dependence of SEY peak (left) and $E_{\max}$ (right) on dose for Al6061-T6 samples in the horizontal and 45° stations.

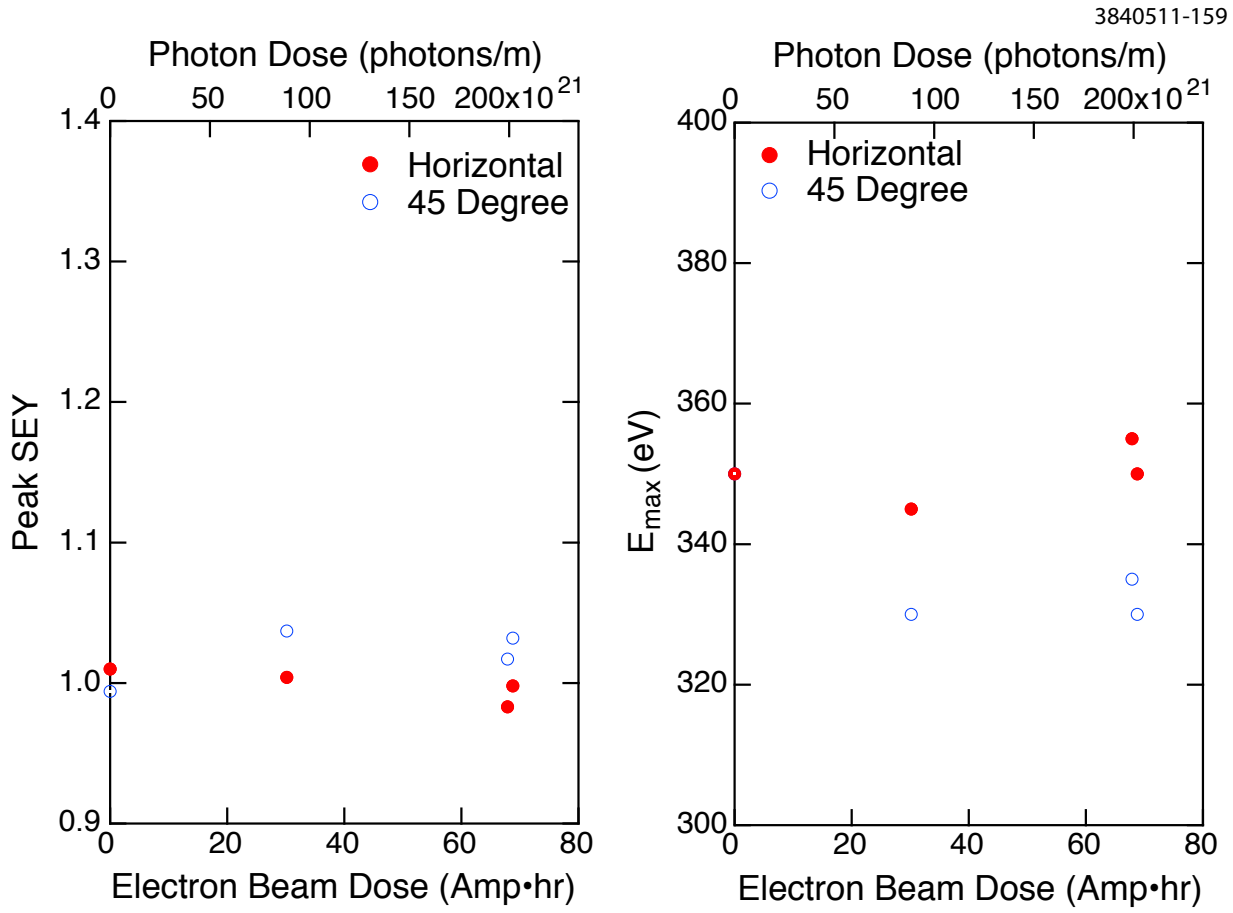

Figure 5.50: Dependence of SEY peak (left) and $E_{\max}$ (right) on dose for amorphous carbon-coated samples in the horizontal and 45° stations.

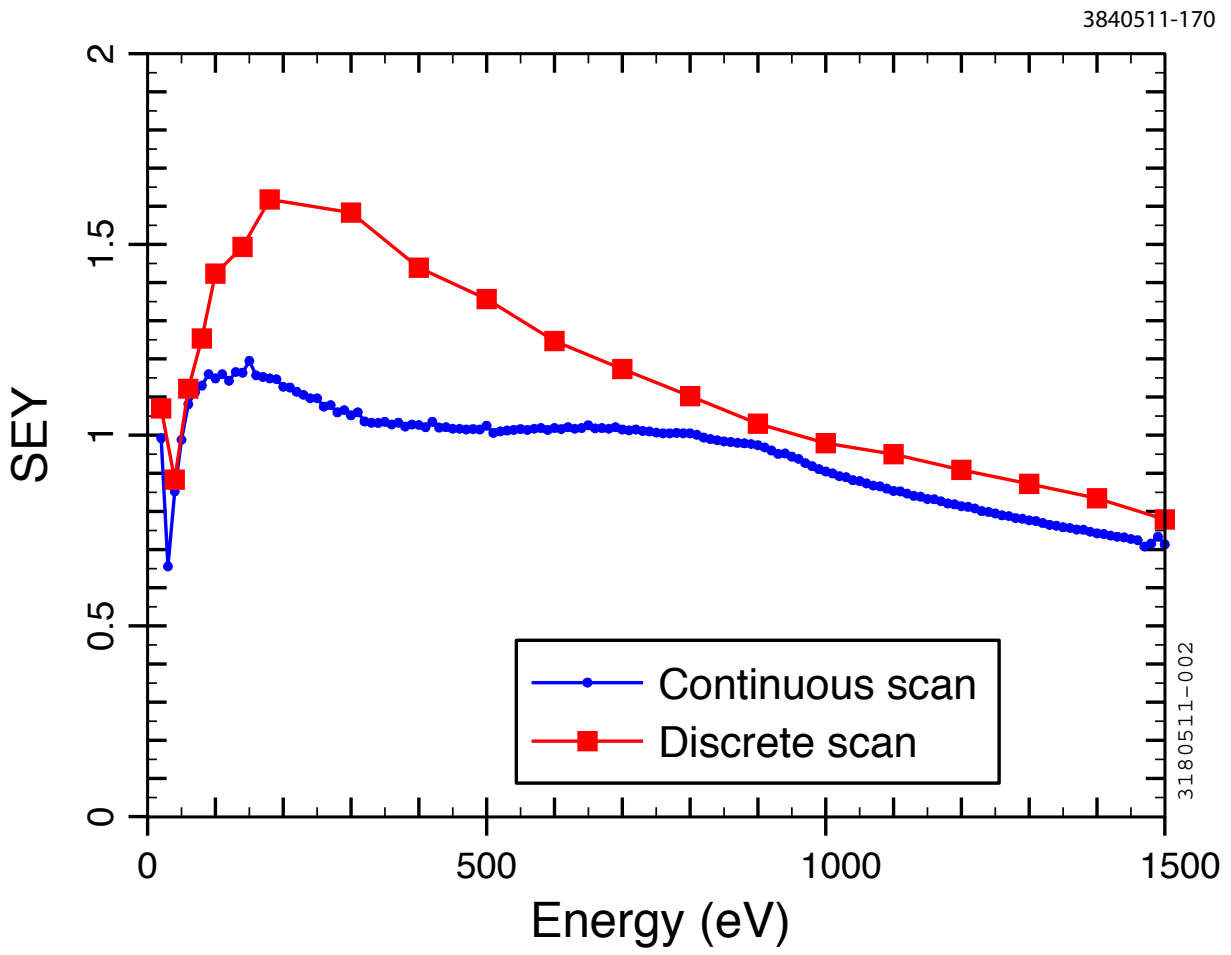

Figure 5.51: SEY as a function of incident electron energy for a diamond-like carbon-coated aluminum sample. The blue circles correspond to a "continuous" scan in energy (5 seconds for each energy, with all 9 grid points measured; Point 5 is shown). The red squares correspond to a "discrete" scan in energy (3 to 4 minutes waiting period with the electron beam deflected away from the point of interest before each measurement; only Point 9 was measured).

distorted due to charging of the DLC-coated surface by the electron beam. To measure the true SEY, we waited a long time (3 to 4 minutes) between each increment in the electron beam energy to allow the surface to discharge and did the scan with a beam current of about 0.5 nA. The results are shown in Figure 5.51 (red squares). As can be seen, the delay time produces a significant change in the measured SEY.

5.1.5.4 Discussion

Our results shows that the initial 80% to 90% decrease in the peak SEY occurs within the first 2 weeks of processing, with a total photon dose of 10^{22} photons/m. This is true for both the horizontal and the 45° systems. After the rapid SEY decrease in the first 2 weeks, the peak SEY decreases about 1 to 2% per week with processing for both the TiN-Al samples and the bare Al6061 samples. On average the peak SEY decreases with increasing beam dosage, D, proportional to $D^{-0.030}$ for

both the bare aluminum and the TiN-coated aluminum samples.

At this point we do not have enough data to draw any strong conclusions about the difference in processing between samples placed in the horizontal system and the 45° system. For the TiN-Al, the sample placed in the horizontal system reached a lower SEY value: a peak SEY of 1 compared to 1.2 in the 45° system. However, we suspect that the higher SEY for the 45° sample is due to contamination from a hot filament vacuum gauge. For the bare Al6061 samples, one set of samples reached the same peak SEY of 1.6. A third sample in the horizontal system started at a higher initial SEY value of 2.9 and reached a minimum peak SEY of 1.9 after an additional 6 weeks of processing in the horizontal system. For comparison, in studies done at PEP-II, a bare Al6063 sample was processed in PEP-II beam line had an initial peak SEY of 3.5 and reached a peak SEY of 2.4 after processing [119]. These measurements suggest that, for bare aluminum samples, the initial value of the peak SEY varies from sample to sample and the final value of the peak SEY after processing depends on the initial value.

The amorphous carbon-coated samples had initial peak SEY values of about 1. They showed almost no change in the peak SEY with processing either in the horizontal or the 45° system.

We observed consistent differences in the peak SEY corresponding to the angle θ between the incident electron gun beam and the normal to the sample surface. We have $\theta = 20°$ for Points 1, 2, and 3; $\theta = 25°$ for Points 4, 5, and 6; and $\theta = 30°$ for Points 7, 8, and 9 (see Figure 5.46). Higher SEYs were observed at points with larger θ. An example is shown in Figure 5.52 for a stainless steel sample with an amorphous carbon coating. The measurements for $\theta = 0$ were done at CERN by S. Calatroni and C. Yin Vallgren on a different sample. The measurements show a small but consistent increase in the peak SEY as θ increases. However, before quantitative conclusions are drawn about the dependence of the SEY on angle, a better evaluation of the systematic errors in our measurement is needed.

Our observation that the SEY depends on angle of incidence is qualitatively consistent with the observations that, as the primary electron angle goes from normal incidence toward grazing incidence, the SEY increases; this has been reported in recent secondary emission studies [79] as well as early experiments [120].

5.1.5.5 SEY Studies Summary and Future Plans

For TiN-Al samples and bare Al6061 alloy samples, we observed that the main processing occurred within the first 2 weeks, with a total photon dose of 10^{22} photons/m, while, after that, the SEY decrease was about 1% per week. For Al6061, we observed that the SEYs after processing are lower than the minimum SEY value of 2.4 for Al6063 reported by SLAC [119].

We are able to observe a small dependence of the SEY on the angle of the incident electron beam. This indicates that the statistical errors are small enough for us to be able to resolve differences of a few percent. However, the systematic errors are likely to be larger than the statistical errors, which will require further investigation.

We are working on mitigating the effects of the current drift of the electron gun. The drift causes a systematic error of around 2 to 4% in the calculated SEY. One method we are investigating is to measure I_p for a given gun energy, and then change the bias voltage to measure I_t at the same energy, before stepping to the next energy and repeating the process. However, we must account for the effects of the stray capacitance of the SEY system, which can dramatically distort our current

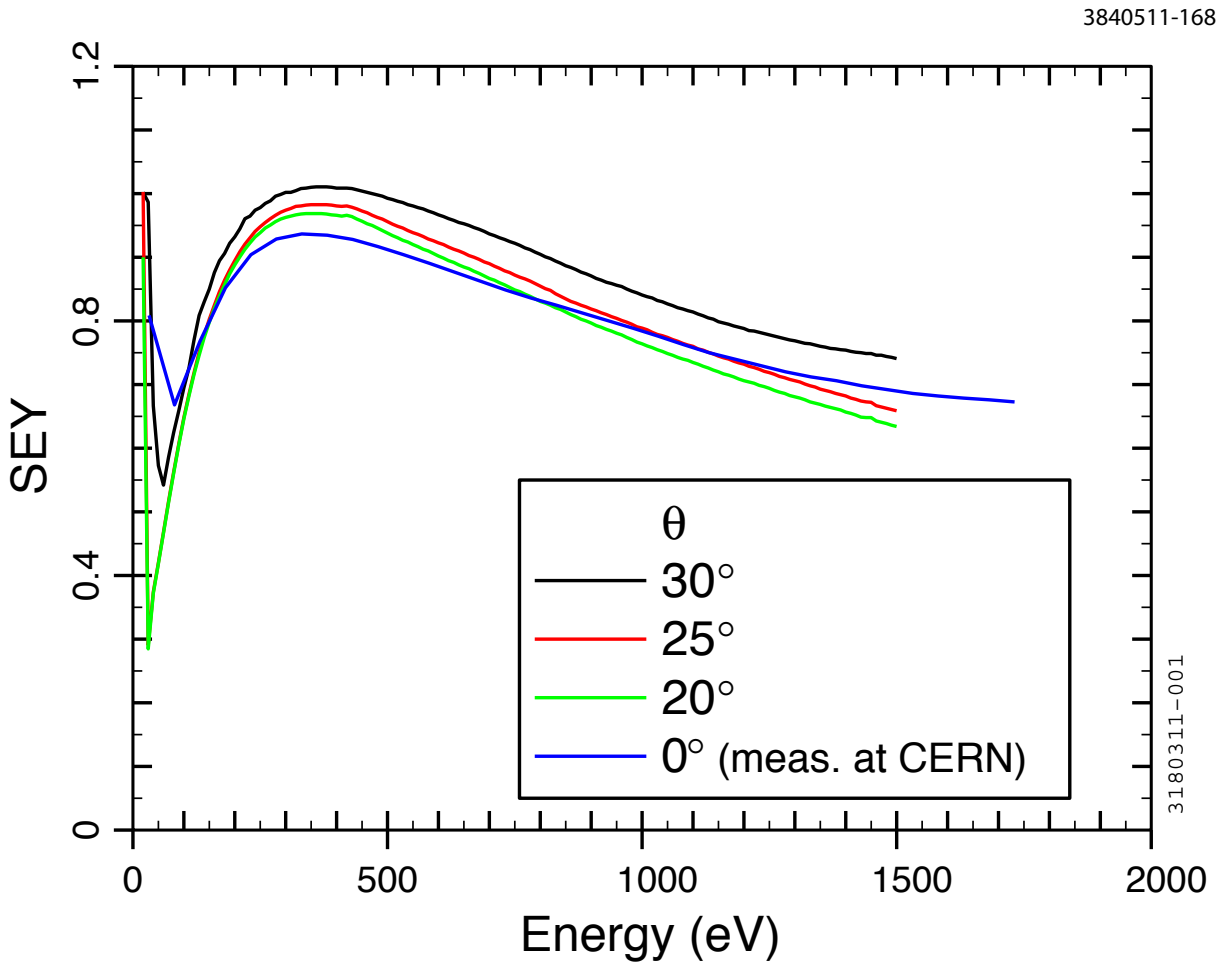

Figure 5.52: Angular dependence of SEY as a function of incident electron energy for amorphous carbon-coated samples.

measurements. Because of the stray capacitance, when we switch the biasing voltage from 150 V to −20 V (or vise-versa), it takes more than 1 minute for the current to reach its steady-state value. In our present method, the biasing voltage is only switched twice, adding just a few minutes to the measurement time. However, the method we are investigating switches the bias voltage at every energy—with 150 gun energy changes per scan, the measurement time may be prohibitively long. We are investigating modifications to minimize the stray capacitance and take fewer energy points.

We plan to compare the Al6063 and Al6061 alloys to better understand the large difference in the peak SEY achieved after processing. Other future work will include the study of other material samples, including samples cut from an extruded, aged (30+ years) 6063 aluminum CESR chamber. In addition, we plan to measure the SEYs of materials coated in non-evaporable getter (NEG) thin film, and continue to study amorphous/diamond-like carbon samples.

We plan to check the reproducibility of the results on TiN-Al samples and do additional checks for systematic effects. We are designing additional experiments to determine whether SR bombardment or electron cloud bombardment is the main source of processing.

5.2 Other Methods to Characterize EC Build-Up

While the RFAs provide the largest number of detectors at CesrTA, other techniques for measuring the electron cloud density are being used at a subset of locations. TE Wave and Shielded Pickup detectors provide data that is complementary to that of RFAs. The Shielded Pickups have a geometry that is similar to that of an RFA, but are designed to measure time resolved signals, while the RFAs measure integrated current. The TE Wave technique — where the periodic electron cloud modulates a carrier transmitted through the beam pipe — is sensitive to the cloud density in the center of the pipe, while both the RFA and Shielded Pickups measure the cloud current that is normal to the pipe surface. The comparison of data taken using these complementary techniques should result in consistent measurements and modeling.

5.2.1 TE Wave Studies

Two versions of TE wave measurements were made at CesrTA. Initial measurements were based on the transmission of microwaves between two points in the accelerator, using the beam pipe as a waveguide. In the course of taking this data, it became clear that a different interpretation of the signals was needed in most cases due to the presence of resonances in the frequency response of the beam pipe. This resulted in the recent development of TE wave resonant measurements where the beam pipe and its reflections are treated as a resonant cavity. Both techniques will be discussed in the sections below. The transmission technique would be most relevant for regions of an accelerator where there are few reflections; the resonant technique for regions where the reflections are significant. These sections also show the historical development of TE wave studies.

5.2.1.1 TE Wave Transmission Measurements

Improvements to the theoretical model The theoretical model of the TE wave measurement proposed by Caspers et al. in [121] only took into account the phase delay induced by the electron

cloud on a propagating TE wave. Moreover, changes in the cloud density were supposed to have a simple sinusoidal evolution. Under such a hypotheses the modulation sidebands amplitude, relative to the carrier SB_c, is simply given by

$$SB_c = \frac{\Delta\Phi}{2} \tag{5.7}$$

if $\Delta\Phi$ is the modulation index, with only one upper and one lower sideband present for low index modulation, which is always the case with cloud densities normally encountered in particle accelerators. In the course of our experimental work, we encountered situations were amplitude modulation, and in general simultaneous phase and amplitude modulation, were present. Additionally, the purely sinusoidal modulation model turned out to be an excessive abstraction in most cases, so that an effort to generalize the theory proved to be necessary. We summarize the result of our effort in the following subsections.

AM/PM modulation To increase the measurement sensitivity, it is good practice to choose the TE wave frequency corresponding to a maximum in the beam pipe transmission function. In most cases those peaks correspond to standing waves trapped by discontinuities in the vacuum chamber [24], and may contain a simultaneous amplitude modulation component. The general formulation for an AM/PM modulation is reported in Ref. [21]. If the standing wave has a narrow resonance (high quality factor Q_0), the modulation indexes are given by

$$\begin{aligned} \Delta M &= \frac{Q_0^2}{2}\left(\frac{\omega_p}{\omega_{\text{res}}}\right)^4 \\ \Delta\Phi &= Q_0\left(\frac{\omega_p}{\omega_{\text{res}}}\right)^2 \end{aligned} \tag{5.8}$$

where $\Delta M = \Delta\Phi^2/2$ is the amplitude modulation index and ω_{res} is the center frequency of the resonance. In the hypothesis $\omega_p \ll \omega_{\text{res}}$ the modulation sidebands amplitude can be written as

$$SB_c \approx \Delta\Phi\left[1 + \frac{1}{2}\left(\frac{\Delta\Phi}{2}\right)^2\right]|F(\omega)| \tag{5.9}$$

where $|F(\omega)|$ is the Fourier transform of the cloud normalized density. In the case of a sinusoidal modulation we can compare Eqs. 5.7 and 5.9 and see that the corrective term in brackets accounts for the AM/PM modulation.

Time evolution of the electron cloud density From Eq. 5.9 one can easily see that the temporal evolution of the electron cloud density is described by the function $F(\omega)$ in the frequency domain, which being the transform of a periodic function will be composed of discrete lines separated by the ring revolution frequency ω_{rev}. In practical cases one usually observes a number of sidebands, even for small modulation depths, as shown in Fig. 5.53. A fairly good approximation can be obtained assuming that rise and fall times of the EC density are much shorter than the bunch train length, but still at least comparable with the bunch spacing. In such a case, a rectangular modulating function with duty factor equal to the train length divided by the machine length, can obviously be seen as a more accurate representation than a sinusoidal one.

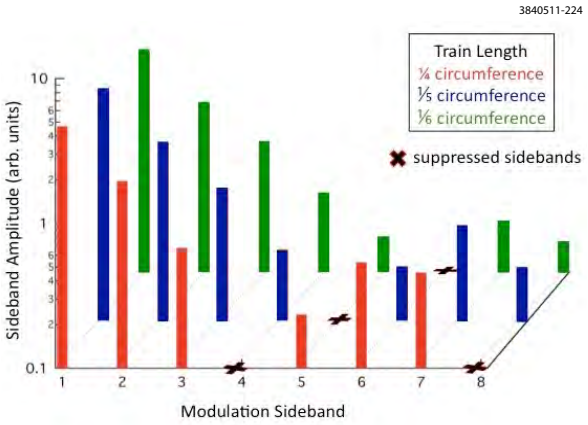

Figure 5.53: Cancellation of modulation sidebands due to different bunch train lengths. Suppressed modulation sidebands due to the rectangular modulation function are indicated for various train lengths.

This hypothesis can find a degree of experimental verification by looking at the sidebands with different train lengths. Figure 5.53 shows a detail of measurements in a dipole region of CesrTA with bunch trains of different lengths equal to one fourth, one fifth and one sixth of the ring circumference. One can see that correspondingly every fourth, fifth and sixth beam harmonic is suppressed. The general properties of the Fourier transform point out how this behavior is evidence of a strong rectangular modulation component. In such a case we can modify Eq. (5.7), by introducing a correction factor that takes into account the rectangular nature of the modulation and we have

$$\Delta\Phi = \frac{1}{2} \times \mathrm{SB}_c \frac{\pi}{\sin(t_b \omega_{\mathrm{rev}}/2)} \tag{5.10}$$

where t_b is the bunch train length. Applying *Carson's Bandwidth Rule* [122], an approximate evaluation of the EC density rise and fall times (t_r) is given by

$$t_r \approx \frac{2}{3} \times \frac{2\pi}{\omega_{\mathrm{rev}} \times N_{\mathrm{SB}}} \tag{5.11}$$

where N_{SB} is the number of visible sidebands.

Beam pipe attenuation compensation Experimental data showed a substantial difference in signal attenuation for different frequencies even on a relatively narrow frequency span such as the 390 kHz between TE wave frequency and first modulation sidebands. These differences need to be compensated in order to correctly evaluate the modulation depth. It is worth stressing that we frequently measured differences of several dB, which would easily cause significant errors if unaccounted for. Furthermore, the attenuation can change substantially with varying beam conditions, due principally to thermal effects, so that a continuous monitoring is necessary.

The relative amplitude of upper and lower sidebands (USB and LSB, respectively) have to be corrected for the difference in transmission function of the measuring system at the carrier and USB and LSB frequencies. This can be done with separate measurements, but we have recently

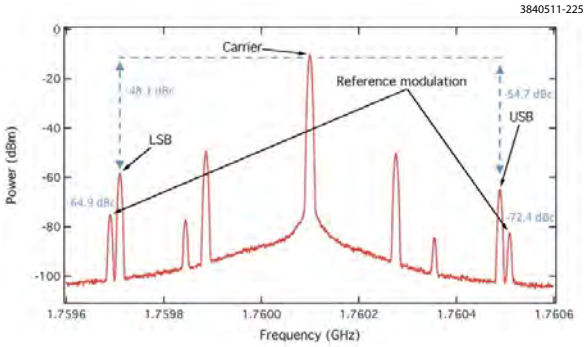

Figure 5.54: Example of sidebands measurement in the wiggler straight. 45-bunch positron train of 60 mA total beam current with 14 ns bunch spacing, with reference modulation sidebands (1 mrad modulation depth at 410 kHz).

introduced a calibration phase modulation of known index at a frequency close to the e-cloud modulation frequency, so that the transmission function is about equal to that for the nearby modulation sidebands. In this case, the reference phase modulation index at 410 kHz was chosen to be 1 mrad, which should generate sidebands at −66 dBc. We observe lower values from which it is possible to infer the attenuation, with respect to the carrier frequency, at the USB and LSB frequencies (390 kHz). We calculate a correction factor equal to $-66.0 - (-64.9) = -1.1$ dB for the LSB and, analogously, +6.4 dB for the USB. The corrected value for the LSB is −49.2 dBc and −48.3 dBc for the USB. It is worth noticing that, while before correction the two sidebands were rather different (6.6 dB), after the correction is applied their values are almost identical, as expected. An example of sideband measurement in the wiggler straight (L0) is shown in Fig. 5.54, where we are measuring the sidebands generated by a 45-bunch positron train of 60 mA total current in a TE wave traveling along the eastern half of the L0 wiggler straight.

As previously stated, being able to continuously monitor the transmission function at the frequencies of interest is quite important during some experiments when beam and/or machine conditions undergo large variations. In such cases the transmission changes due mostly to thermal effects can disrupt the measurement as shown in Fig. 5.55: While ramping the wigglers magnetic field, the emitted synchrotron radiation increase can change the beam pipe transmission function at the sidebands frequency so that USB and LSB amplitudes actually appear to diverge during the experiment until the correction is applied.

To estimate the EC density from the sidebands measured in Fig. 5.54, we can use the average of the two sidebands −48.8 dBc.

5.2.1.2 TE Wave Resonance Measurements

TE wave resonance measurements treat the beam pipe and its reflections as a resonant cavity. Data is generally taken by exciting and receiving at the same detector - so that the value of L used in the transmission technique would be zero, making that interpretation invalid.

As originally proposed, the TE wave technique was based on transmission and reception of microwaves from one point in the accelerator to another using the beam pipe as a waveguide. Button detectors, normally used as part of the beam position monitor (BPM) system are used to couple

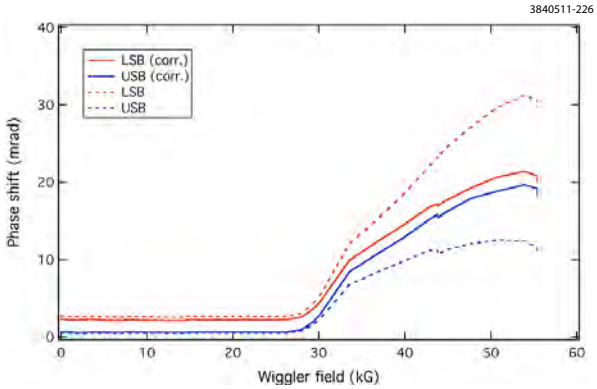

Figure 5.55: Sideband levels relative to the carrier during wiggler ramp in the L0 straight with (solid lines) and without (dashed) correction applied.

microwaves in/out of the beam pipe. In the presence of a plasma (the electron cloud), transmitted microwaves will be phase shifted and the EC density measured [19, 21, 22, 26].

However, in applying this technique to the data at CesrTA, it was noticed that transmission through the beam pipe does not have a flat frequency response. In fact, the large variations in response suggest the presence of resonant excitation of the beam pipe rather than single pass transmission. This interpretation was confirmed by the response when exciting and receiving at the same location, where very large resonances are often seen.

Reflections and Standing Waves The beam pipe at CesrTA was not designed to be a waveguide. In devices such as vacuum pumps, longitudinal slots were used to provide a reasonable vacuum connection, while minimizing the effect of beam-induced fields. However, these longitudinal slots present an obstacle to the propagation of a TE waves. A simple example was found at 43E in CesrTA where a BPM coupler/detector is located between two ion pumps (with slots). The response shown in Fig. 5.56 is consistent with a waveguide of length L having a cutoff frequency f_c and n half wavelengths in the distance L between the pumps [24, 123].

The effect of dielectrics and plasmas on the resonant frequency of a cavity is well established [23]. The effect of small dielectrics on resonant frequency is very useful in mapping the fields of accelerating cavities and plasma densities are routinely measured using resonant cavities [23, 124]. Perturbation techniques provide the following approximation for the shift in resonant frequency due to a dielectric in a resonant cavity [125].

$$\frac{\Delta\omega}{\omega} = \frac{\int_V (1-\varepsilon_r)\, E_0^2\, dV}{2\int_V E_0^2\, dV} \tag{5.12}$$

The effective dielectric constant of a plasma has real and imaginary parts. The imaginary part gives a change in the Q of the resonance, the real part a change in its frequency. For low density plasmas ($\omega_p^2 \ll \omega^2$) with a small collision frequency ($\nu \ll \omega$) and no magnetic field, the real part of the dielectric constant of a plasma can be written as [124]

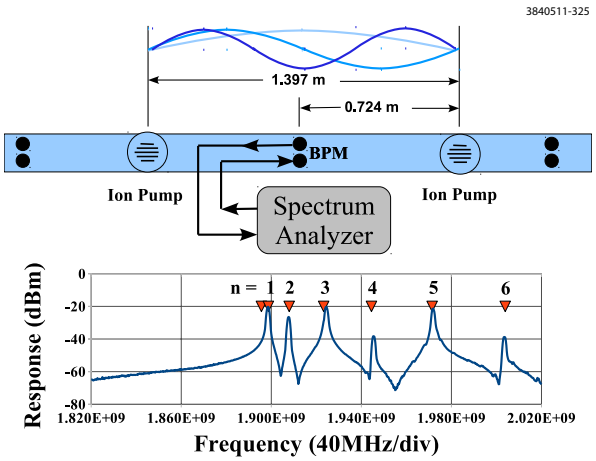

Figure 5.56: Sketch of 43E at CesrTA, where a BPM Detector is located between two ion pumps with longitudinal slots. The measured resonances follow the expected $f^2 = f_c^2 + \left(\frac{nc}{2L}\right)^2$ of a rectangular cavity.

$$\varepsilon_r = \left[1 - \frac{\omega_p^2}{\omega^2\left(1 + (\nu/\omega)^2\right)}\right]. \tag{5.13}$$

The plasma frequency ω_p is related to the electron cloud density n_e by $n_e = \omega_p^2 \varepsilon_0 m_e / e^2$, where m_e is the electron mass [23]. Let the collision frequency be vanishingly small $\nu \to 0$. In this case, the change in resonant frequency becomes

$$\frac{\Delta\omega}{\omega} = \frac{r_e \lambda^2}{2\pi} \frac{\int_V n_e E_0^2 \, dV}{\int_V E_0^2 \, dV}. \tag{5.14}$$

where $r_e = e^2/(4\pi\varepsilon_0 m_e c^2)$ is the classical electron radius and $\lambda = 2\pi c/\omega$ is the wavelength of the TE wave.

The resonant frequency shift is proportional to the local electron cloud density weighted by E_0^2. If there are high local densities where the cavity electric field is zero, they will not have an effect on $\Delta\omega$. If the density is uniform, $\Delta\omega$ is independent of the details of the electric field, since the same integral appears in the numerator and denominator [122]. An EC density of 10^{12} m^{-3} would give a frequency shift of about 20 kHz.

With a train of bunches in the storage ring, the electron cloud will grow and decay each time the bunch train passes a given point – at the revolution frequency $f_{\rm rev}$ (390 kHz at CesrTA). The quantity $\Delta\omega$ is the modulation in the resonant frequency of the waveguide cavity produced by the electron cloud. We now need to determine the effect that this modulation has on the observed signals.

Effect on Signals For most of the TE Wave measurements made at CesrTA, the resonant beam pipe is driven at a fixed frequency and its response measured with a spectrum analyzer. The steady state solution for a driven oscillator is given in the following equations and illustrated in Fig. 5.57.

$$x(t) = A_n \sin(\omega t + \phi_n) \tag{5.15a}$$

$$A_n = Q \frac{A}{[(\omega_n^2 - \omega^2)^2 + \omega^4]^{1/2}} \tag{5.15b}$$

$$\phi_n = \tan^{-1}\left[Q \frac{(\omega_n^2 - \omega^2)}{\omega^2}\right] \tag{5.15c}$$

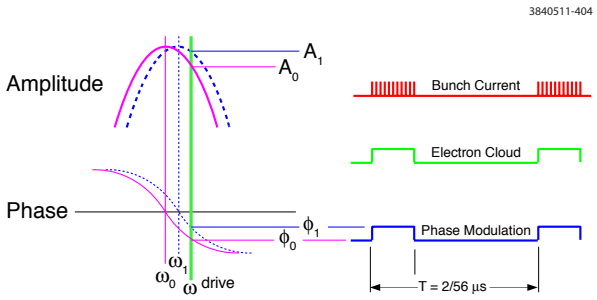

Figure 5.57: Steady state amplitude and phase response as the cavity resonant frequency changes from ω_0 to ω_1.

To obtain a rough estimate of the EC density, a number of approximations will be made: that the steady state solution above applies, the drive frequency ω is close to resonance (this results primarily in phase modulation), the phase modulation, from Eq. (5.15c) using the measured Q of about 3000, is small and a cw modulation would give a ratio of the first sideband to carrier amplitude (S_{ratio}) of $\frac{1}{2}\Delta\phi$. The result of these approximations is given in Eq. (5.16).

$$n_e \approx S_{ratio} \cdot \frac{\omega^2}{Q \cdot 1.59 \times 10^3} = S_{ratio} \cdot 2.5 \times 10^{13} \tag{5.16}$$

Also, the phase modulation is not sinusoidal but modulated by the EC density, so a further approximation needs to be made. Let the duration of the EC density *and its effect on the phase* be of fixed amplitude for the length of the bunch train and zero otherwise. Given these crude approximations, Fig. 5.58 is a plot of the EC density measured in the wiggler region at 2 GeV during a wiggler ramp. The stored beam was a positron 45 bunch train spaced at 14 ns with a total current of 35 mA.

One concern with this approximation is that the beam pipe cavity has damping time of about 500 ns. So the duration of the cloud and the damping time of the cavity are of the same magnitude. We are working on a more correct analysis that would include transient effects. For example, a step in

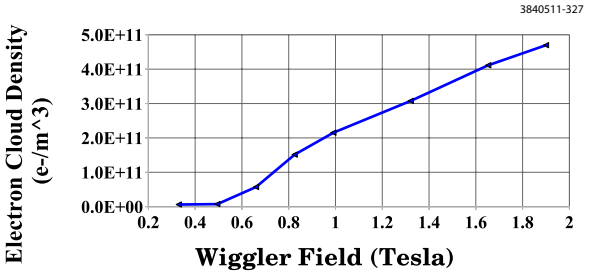

Figure 5.58: Estimate of EC density during a ramp of wigglers

the resonant frequency of the cavity at $t = 0$ would be described by

$$x(t < 0) = A_0 \sin(\omega t + \phi_0) \tag{5.17a}$$

$$x(t \geq 0) = A_1 \sin(\omega t + \phi_1) + e^{-\Gamma t}[A_0 \sin(\omega_1 t + \phi_0) - A_1 \sin(\omega_1 t + \phi_1)]. \tag{5.17b}$$

where Γ is the reciprocal of the cavity damping time. For $t \gg 1/\Gamma$, the exponential vanishes and only the first term (steady state) remains. In the steady state solutions for $t < 0$ and $t \gg 1/\Gamma$ there is a difference both in the amplitude $A_0 \to A_1$ and in phase $\phi_0 \to \phi_1$. But, especially near the resonant frequency, the amplitude change will be quite small and the phase difference will dominate the signal.

The two terms in the brackets are at the new resonant frequency ω_1. For small changes in amplitude and phase this term will be close to zero and decays exponentially with time. To get a better sense of its effect, suppose that the drive frequency ω is between the old and new resonant frequencies. Then the amplitudes A_0 and A_1 will be nearly equal.

Using the $A_0 \approx A_1$ and the trigonometric identity $\sin(a) - \sin(b) = 2\cos(\frac{a+b}{2})\sin(\frac{a-b}{2})$,

$$\begin{aligned}
x(t) &= A_1 \sin(\omega t + \phi_1) + e^{-\Gamma t}[A_0 \sin(\omega_1 t + \phi_0) - A_1 \sin(\omega_1 t + \phi_1)] \\
&\approx A_1 \sin(\omega t + \phi_1) + A_1 e^{-\Gamma t}[\sin(\omega_1 t + \phi_0) - \sin(\omega_1 t + \phi_1)] \\
&\approx A_1 \sin(\omega t + \phi_1) + 2A_1 e^{-\Gamma t}\left[\cos\left(\omega_1 t + \frac{\phi_0 + \phi_1}{2}\right)\sin\left(\frac{\phi_0 - \phi_1}{2}\right)\right] \\
&= A_1 \sin(\omega t + \phi_1) - 2A_1 e^{-\Gamma t}\left[\cos\left(\omega_1 t + \frac{\phi_0 + \phi_1}{2}\right)\sin\left(\frac{\phi_1 - \phi_0}{2}\right)\right] \\
&\approx A_1 \left[\sin(\omega t + \phi_1) - [\phi_1 - \phi_0]e^{-\Gamma t}\cos\left(\omega_1 t + \frac{\phi_0 + \phi_1}{2}\right)\right].
\end{aligned} \tag{5.18}$$

So the term that contains the new resonant frequency is multiplied by the phase difference before/after the change in resonant frequency, which is small. So the change in signal will be primarily that of a phase (and amplitude) shift.

The expression of Eq. (5.18) is more or less of the form $A\sin(x) + B\cos(x)$. For $\omega \approx \omega_1$ and ignoring the fact that the phase terms are not quite equal,

$$
\begin{aligned}
x(t) &\approx A_1 \left[\sin(\omega t + \phi_1) - [\phi_1 - \phi_0] e^{-\Gamma t} \cos\left(\omega_1 t + \frac{\phi_0 + \phi_1}{2} \right) \right] \\
&\approx A_1 \sin\left[\omega t + \phi_1 - (\phi_1 - \phi_0) e^{-\Gamma t} \right] \\
&\approx A_1 \sin\left[\omega t + \phi_1 \left(1 - e^{-\Gamma t}\right) + \phi_0 e^{-\Gamma t} \right] . \qquad (5.19)
\end{aligned}
$$

With all of these approximations, this looks like a rotation of the phase angle from ϕ_0 to ϕ_1 over the damping time. This will have the effect of adding transitions to both the rising and trailing edges of the phase modulation shown in Fig. 5.57, and have a corresponding effect on the Fourier transform of the modulation.

5.2.1.3 TE Wave Alternative Techniques

Finally, we give some other examples of measurements connected to alternative techniques we are developing.

The Cutoff Resonance Bench measurements were made using WR284 waveguide which has a cutoff frequency very similar to the beam pipe of CesrTA near 2 GHz. A 4 meter long section was driven near its longitudinal center using buttons similar in geometry to those in CesrTA. Using metal blocks near the waveguide ends to generate reflections, cavity modes were excited. The $\Delta f \propto E^2$ of these modes were plotted vs. longitudinal position using a dielectric bead, making use of Eq. (5.12) and observing the shifts in resonant frequencies. For measurements with a uniform waveguide, the resonances showed E^2 varying as multiples of half wavelengths, including the lowest $n = 1$ mode.

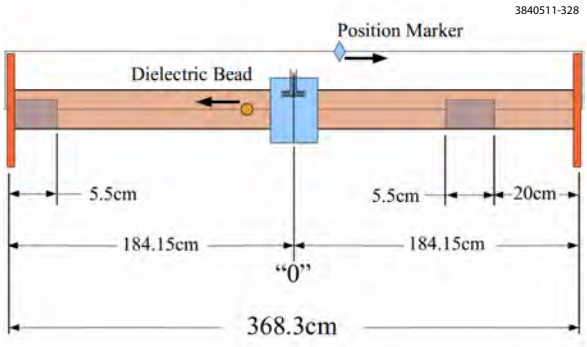

Figure 5.59: For bead pull measurements, a thin monofilament line varies the position of a dielectric bead in WR284 waveguide. The center flange has BPM-like buttons that are used to couple microwaves in/out of the waveguide.

However, a slight modification of the flange used at the drive point resulted in a significant change in the bead pull measurement of the lowest resonance as shown in Fig. 5.63. The inside width of the drive point flange was made 3 mm wider than the waveguide. This portion of the flange is about 2cm long. The lowest '$n = 1$' resonance was then shifted slightly below the cutoff frequency. But rather than a half-sine wave, it has a response consistent with an exponential decrease in E, as with an evanescent wave.

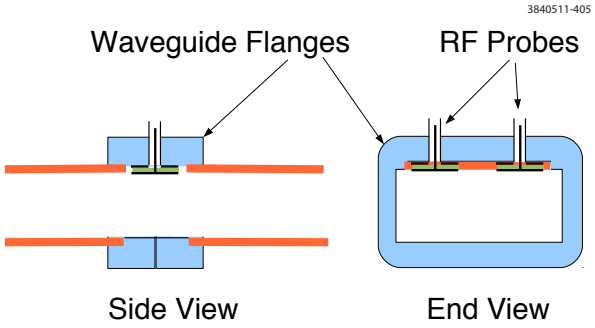

Figure 5.60: Sketch of straight drive flange

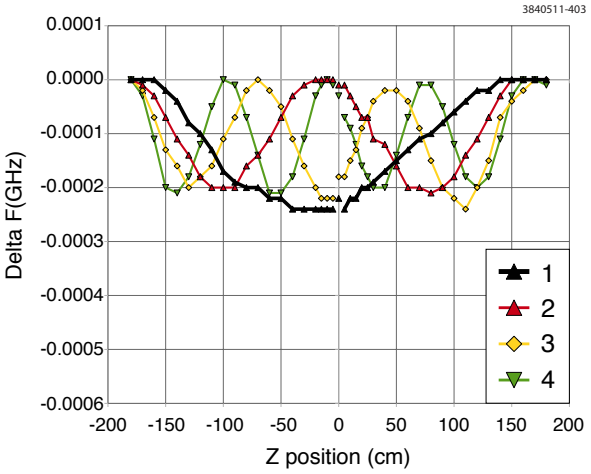

Figure 5.61: Multiple half-wavelength resonances are observed in a section of WR284 waveguide.

If excited in this mode, the response to EC density will occur over a distance of only about two meters and provide a very localized measurement, following Eq. (5.14). This can be a great advantage, especially when trying to cross calibrate with other localized EC density measurement techniques.

There are many details about this cutoff mode that we need to understand. Primarily, we need to be able to tell - without performing a bead pull experiment in the storage ring - whether or not we have excited this resonance vs. the usual half wave $n = 1$ cavity mode. One indication should be the effect on the sequence of resonant frequencies and the extent to which they are different from $f^2 \propto n^2$. For example, the $n = 1$ resonance should be lower than normally expected.

At present, an extensive archive of resonant BPM measurements is available and efforts are underway [24, 122, 123] for a full theoretical model of the relationship between sidebands amplitude and electron cloud density in these conditions.

TE Magnetic Resonance During measurements in the chicane in the L3 region we observed a strong enhancement in the modulation sidebands corresponding to the upper plasma hybrid resonance, generated by a TE wave polarized with its electric field normal to the chicane magnetic field.

Figure 5.64 shows the change in modulation sideband amplitude when the chicane magnetic field is changed so that the TE wave frequency corresponds to the upper hybrid frequency $\omega_{\rm uh} = (\omega_p^2 + \omega_{\rm cycl}^2)^{1/2}$ for the electron cloud plasma. Because in all practical situations, for a wave above cutoff, $\omega_p \ll \omega_{\rm cycl}$ making the evaluating the plasma frequency from the upper hybrid frequency measurement problematic, we are currently studying the phenomenon for waves below cutoff. Preliminary results give us the hope of being able to effectively turn on and off transmission between two BPMs by applying a relatively small dipole magnetic field to the portion of vacuum chamber between them. This could be easily achievable by employing external air-coil magnets, for instance. At that point, the evaluation of the electron cloud density in that region would essentially reduce to the measurement of a resonance peak.

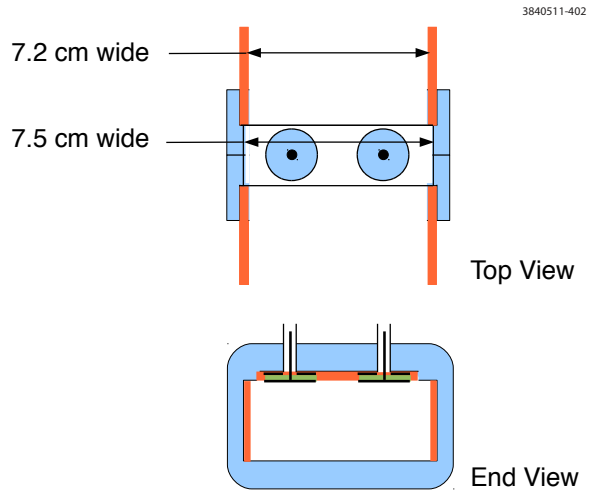

Figure 5.62: Sketch of drive flange modification.

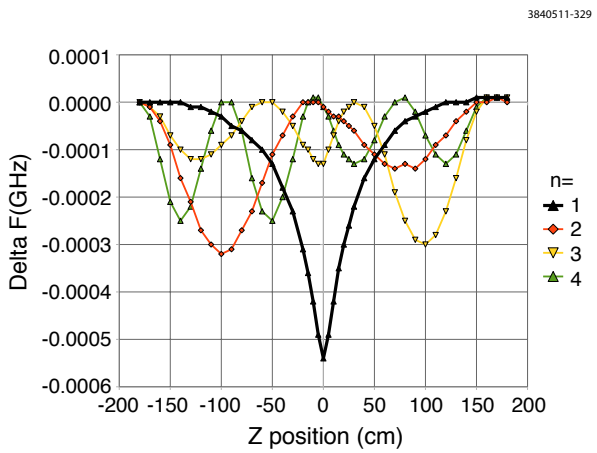

Figure 5.63: The cutoff resonance was observed using a modified drive flange in a measurement with WR284 waveguide.

5.2.1.4 TE Wave Modeling

Vorpal Simulations: The plasma simulation program VORPAL [126], is being used to simulate transverse electric (TE) wave propagation experiments at CesrTA. The electromagnetic particle-in-cell (PIC) routines in VORPAL uses the Yee algorithm [127] for solving Maxwell's equations. In addition to calculations of the evolution of the wave electric and magnetic fields with particles, the program can also include external static fields that affect the particle motion. This helps simulate experiments in the presence of dipole or solenoidal fields.

The regular CesrTA beam pipe geometry may be represented by two circular arcs of radius 0.075 m, connected with flat planes on the sides. The cross-section measures about 9 cm from side to side and the height of the side walls is about 2 cm. In the simulations, the ends of the pipes were either perfect conductors or perfectly-matched layers (PMLs) designed to fully absorb any transmissions. Applying the conducting boundaries created a resonant cavity; using PMLs simulated a section of a longer, continuous beam pipe. PML boundaries, first developed by J. Berenger [128], ascribe a parabolically increasing electrical and (nonphysical) magnetic conductivity to the regions at the ends of the beam pipes. These regions had significant thickness, sometimes as much as one-fourth the length of the entire pipe.

The simulation begins with a specified initial distribution of electrons in the simulation grid and tracks their subsequent motion due to field interactions. The simulation used macro-particles of high mass and charge to represent groups of nearby electrons. Electrons were set to initially have zero velocity (a cold plasma). They were also artificially constrained to cross no more than one cell per time step, a restriction that in practice does not significantly limit the physicality of the simulation. Waves were excited in the simulations by ascribing a transversely oscillating current density to a section of the beam pipe. These sections covered the full cross-sectional area and were two cells thick in the longitudinal dimension. In addition to recording all EM field data at user specified intervals, VORPAL can record the time evolution of a number of different quantities over the entire simulation. Known in the code as Histories, recordable quantities include the potential

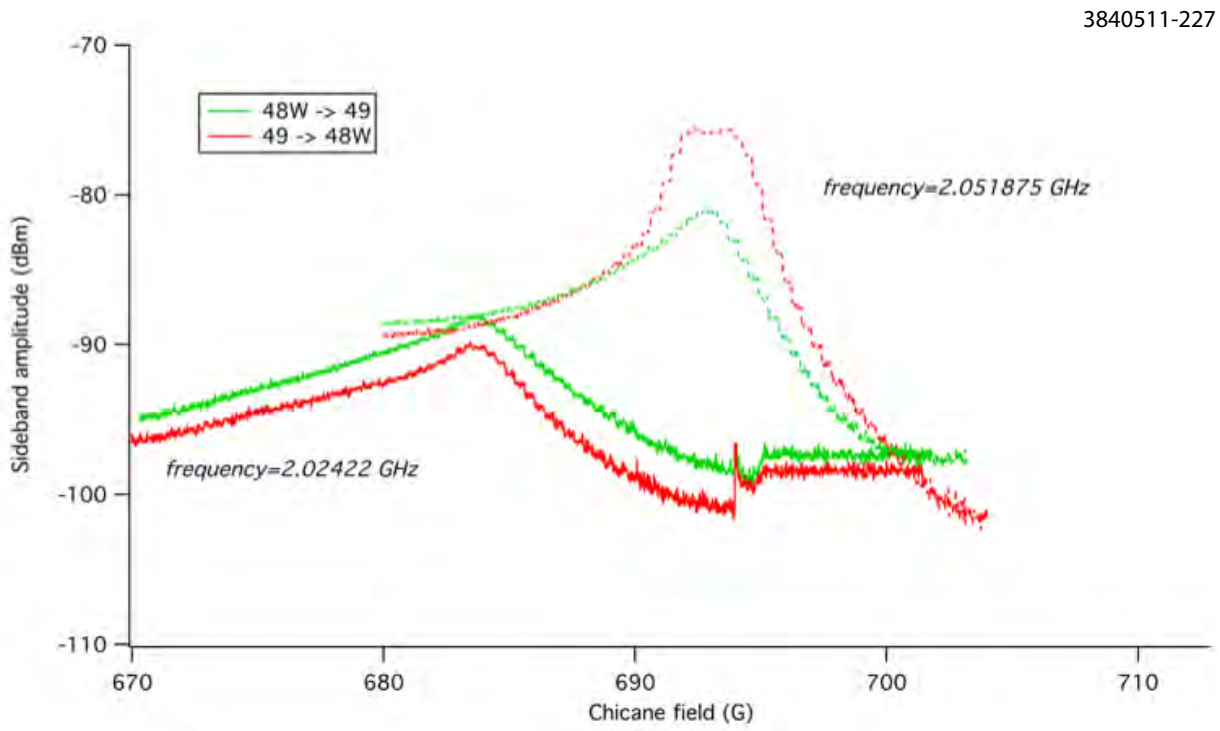

Figure 5.64: Modulation sideband amplitude near the upper hybrid resonance at two different frequencies. Red and green traces correspond to opposite direction of propagation of the TE wave.

difference between two given points, energy flux through a specified cross section, and the number of particles in a given region. The energy flux history is especially useful for testing the effectiveness of the PML boundaries, since all flux is expected to point away from the source current in the absence of reflections along the length of the pipe.

Simulation of phase shift: The calculation of phase shift is performed as follows. Simulations of the wave transmission are performed separately through a vacuum beam pipe and through a beam pipe with electrons respectively. The sinusoidal functions obtained from these simulations are normalized so that their *rms* values are unity. The difference of the two wave functions then gives a sinusoidal wave with an amplitude that is proportional to the phase shift between the first two waves. This may be shown as follows. Suppose the frequency is ω and phase shift δ, then we have

$$w_1 = (1/\sqrt{2})\cos(\omega t) \qquad w_2 = (1/\sqrt{2})\cos(\omega t + \delta),$$
$$(w_2 - w_1)/2 = (1/\sqrt{2})\sin(\delta)\cos(2\omega t + \delta) \tag{5.20}$$

The phase shift for nominal cloud densities is small enough that $\sin(\delta) \approx \delta$. Thus the amplitude of the difference wave is proportional to the phase shift between the two waves.

The phase shift for a pipe without reflection depends upon three quantities, (1) the frequency of the carrier wave ω, (2) the electron plasma frequency, ω_p of the cloud and (3) the cutoff frequency of the vacuum chamber ω_{co}. In the absence of external magnetic fields, the dispersion relationship for a plasma filled waveguide is,

$$k^2 = \frac{\omega^2}{c^2} - \frac{\omega_{co}^2}{c^2} - \frac{\omega_p^2}{c^2} \tag{5.21}$$

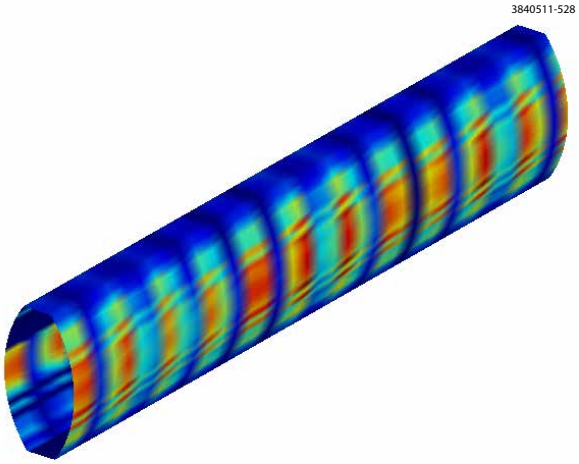

Figure 5.65: Snapshot of a vorpal simulation showing propagation of a TE wave through the CesrTA beam pipe

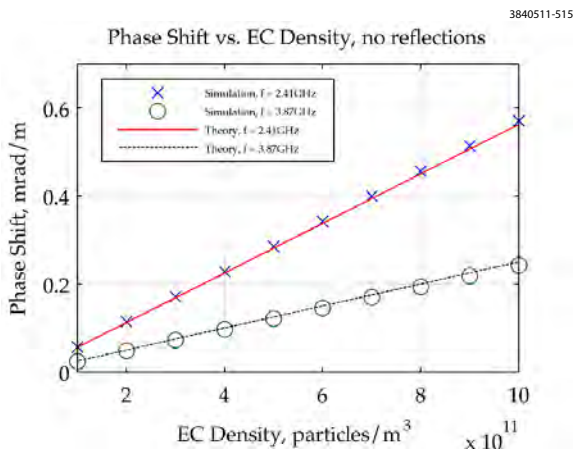

Figure 5.66: Variation of of phase shift with cloud density for a regular CesrTA beam pipe geometry

where $k = 2\pi/\lambda$, ω_{co} is the cut-off frequency of the waveguide and ω_p is the plasma frequency, which is given by $\omega_p^2 = n_e e^2/\epsilon_0 m_e$, with n_e the electron density, e the electron charge, ϵ_0 the free space permittivity and m_e the electron mass. In the limit of small values of plasma frequencies, using the above dispersion relationship, it may be shown that the electron cloud induced phase shift for a unit length of propagation is [129]:

$$\Delta\Phi = \frac{n_e e^2 L}{4\pi c \epsilon_0 m_e \sqrt{f^2 - f_{co}^2}} \tag{5.22}$$

Figure 5.66 shows that simulations agree well with the analytically predicted values of phase shift given by in Eq 5.22. Similar success with a VORPAL-simulated pipe with a square cross-section has been reported before [129].

Simulations with external magnetic fields and the cyclotron resonance: In the presence of an external magnetic field and electron clouds, the medium is no longer isotropic and the polarization of the transmitted microwave plays an important role in the outcome of the measurement. When the wave electric field is oriented perpendicular to the external magnetic field, the mode is referred to as an "Extraordinary" or simply X-wave. In this situation, if the external dipole field corresponds to an electron cyclotron frequency close to the carrier wave frequency, we see an enhanced phase shift. The phenomenon is well understood in the case of open boundaries. It is usually referred to as upper hybrid resonance. The dispersion relationship for the open boundary case is given as follows (see for example ref [130]).

$$\frac{c^2 k^2}{\omega^2} = 1 - \frac{\omega_p^2(\omega^2 - \omega_p^2)}{\omega^2(\omega^2 - \omega_h^2)} \tag{5.23}$$

The term ω_h is the upper hybrid frequency which is given by $\omega_h^2 = \omega_p^2 + \omega_c^2$, $\omega_c = eB/m_e$ being the electron cyclotron frequency for the given magnetic field B. When $\omega \to \omega_h$, it is clear that $k \to \infty$. Since the phase advance is the product of the wave vector k and the length of propagation, we see that the electron cloud induced phase shift will theoretically go to infinity. In the case of electron clouds in beam pipes, the plasma frequency is of the order of a few 10 MHz while the

carrier frequency is around 2 GHz. Thus $\omega_h \approx \omega_c$ and one can state that, for all practical purposes, resonance occurs when $\omega = \omega_c$. The above relationship is not valid for waveguides, which have finite boundaries.

Figure 5.67 shows the enhanced phase shift when the cyclotron frequency approaches the carrier frequency. The beam pipe cross section was circular with a radius of 4.45 cm, which leads to a cutoff at 1.97GHz at the fundamental TE_{11} mode. These parameters match with the beam pipe geometry of the PEP II/CesrTA/ chicane section. The wave frequency was 2.17 GHz. The magnetic field corresponding to this cyclotron frequency is 0.077576T. This magnetic field is tunable in the chicane between 0 to about 0.14T. This effect was first observed when the chicane was located at PEP II [131] and has been confirmed by several follow up measurements after it was transferred to CesrTA.

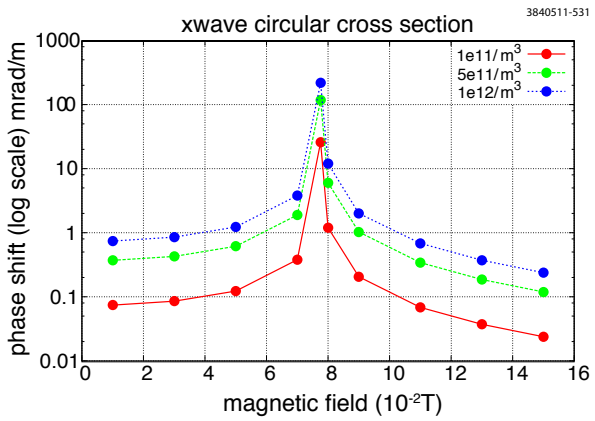

Figure 5.67: Variation of phase shift with external magnetic field (log scale) for different cloud densities

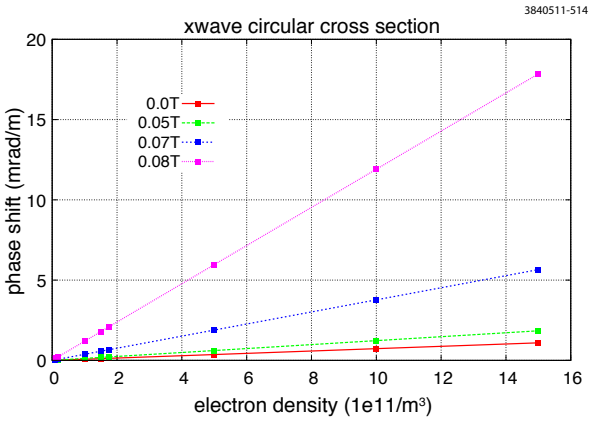

Figure 5.68: Relationship between phase shift and electron density for different settings of external magnetic field

Figure 5.68 shows the variation of phase shift with electron cloud density at different settings of external magnetic fields. These densities are typical of what is produced in CesrTA. The plots show that the variation of phase shift with density remains linear even when one is reasonably close to resonance. This is expected to be true as long as the plasma frequency is much smaller than the wave frequency, regardless of how complex the dispersion relationship of the wave is. Thus, one could easily use an external magnetic field to amplify the signal. Given that the amplification factor of the signal is a constant, one could monitor relative changes in cloud density, if not the absolute density. Thus, simulations have shown that the linear relationship between phase shift and cloud density is retained in the presence of reflections and external magnetic fields.

Simulations with reflections and the resonant cavity method: It is not very likely that one can perform phase shift experiments that are totally free of internal reflections in an accelerator chamber. The presence of internal reflections would affect the value of the phase shift. Thus it became important to study the effects of such internal reflections with the help of simulations. In order to do this, the simulations were altered to include two protruding conductors, which would reflect some of the transmitted wave. The protrusions were slabs in the transverse plane, extending from the bottom to one centimeter above the apex of the lower arc (see Fig. 5.70). They were spaced 0.4 meters apart, and the frequencies 2.41 GHz and 3.87 GHz, the same as those shown in Fig 5.66, correspond to the resonant harmonics ($n = 4$ and $n = 9$, respectively) of a 0.4 meter "resonant

cavity". This was done in order to maximize reflections. As evidence that reflections were in fact occurring between the protrusions, the energy flux (not shown) fell periodically below zero (positive flux points away from the source current) in this region, whereas the flux at the end opposite to the source was always positive. Fig. 5.69 shows the results. The solid shapes represent the data for no reflections and are the same data that appear in Fig. 5.66. The open shapes represent the phase shifts in the presence of reflection. These results clearly indicate that internal reflections modify the expected phase shift. The nature of the alteration of phase shift depends upon the complexities of the transmission-reflection combination, but the linear relationship between phase shift and electron density is always preserved.

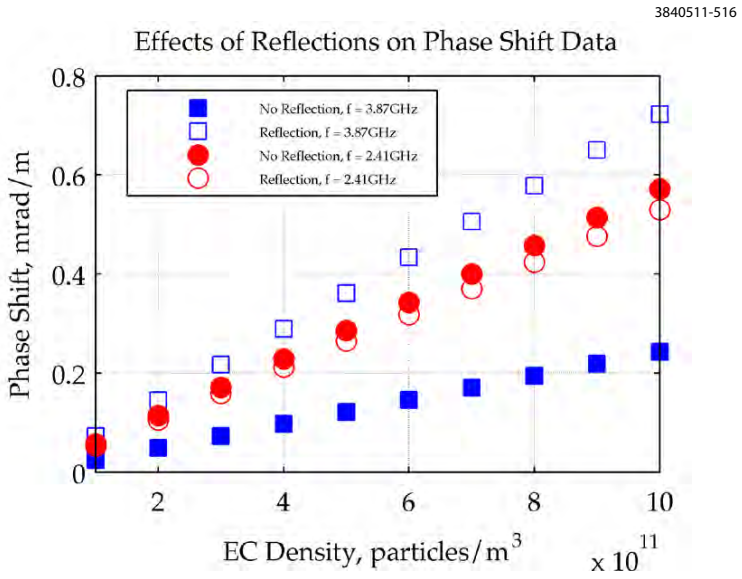

Figure 5.69: Phase shift in the presence of protrusions causing a partial reflection of the wave

The shift in resonant frequency of the carrier wave in the presence of an electron cloud may be calculated from the dispersion relationship given by Eq. (5.21) and the resonance condition for a "cavity" of length L, which is $\frac{n\lambda}{2} = L$. Combining the two in the limit of small values of plasma frequencies, we get

$$\Delta f = \frac{n_e e^2}{8\epsilon_0 m_e \pi^2 f_0} = \frac{n_e r_e c^2}{2\pi f_0} \tag{5.24}$$

in which r_e is the classical electron radius and f_0 is the resonant frequency of the waveguide in vacuum. This shows that the frequency shift is proportional to the electron cloud density. As indicated earlier in this section, an effort is underway to take advantage of this to measure the density of the electron cloud within the beam pipe section where the reflections are occurring. Thus, it became necessary to test this phenomenon with simulations as well, which was carried out as follows: The simulation with reflections was repeated for a number of frequencies and for each of these runs, the energy flux was recorded at every time step at a location in the pipe that was between the two protrusions. This energy flux, which is the Poynting vector integrated over the cross-section area, was then averaged over the whole simulation period, for each frequency. We know that the protrusions will reflect only part of the wave flux while the rest gets transmitted and eventually absorbed into the PML boundary. It can be reasoned that at resonance, the extent of reflection, or trapping of the wave energy is a maximum. This corresponds to a case when the length

between the protrusions is an integer multiple of half a wavelength. Figure 5.71 shows the averaged energy flux transmitted across a location between the protrusions for various frequencies for both an empty beam pipe as well as for a case with electrons in the pipe. At a resonant frequency, when there is an optimized back and forth transmission of the wave, the averaged flux would reach a local minimum. In order to accurately determine this minimum point, we make a parabolic fit in the vicinity of this point using the available points obtained from simulation. The parabolic shape is associated with a Taylor expansion of the function around the minimum. The length of the section between the partial reflectors was 0.898 m and the electron density used in this calculation was 10^{14} m^{-3}, which is rather high, but helps determine the accuracy of the simulation process. For these parameters, the the $n = 2$ resonance occurs at 2.0033 GHz and the expected frequency due to electrons is 2 MHz. Simulations show a shift of 2.05 MHz. Thus we were able to establish that accurate values of frequency shift for such an experiment may be determined from simulations. These simulations may be modified in order to include more features such as a nonuniform cloud density and also an external magnetic fields where analytic expressions for frequency shifts are not readily available.

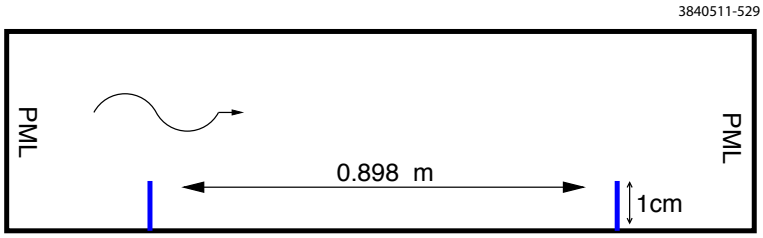

Figure 5.70: A schematic of the simulations with protrusions serving as partial reflectors

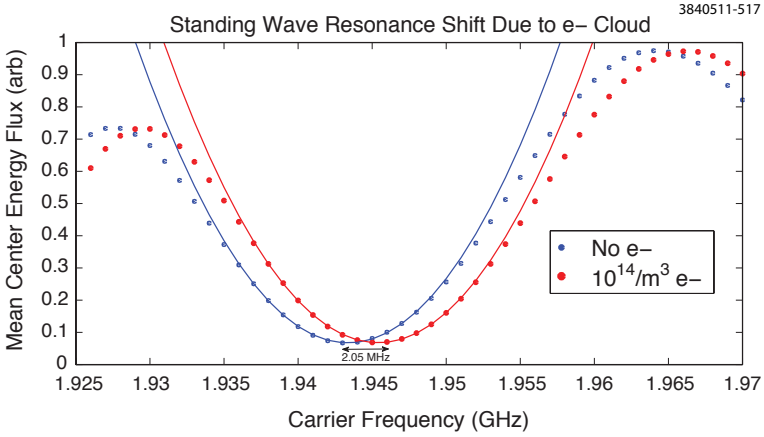

Figure 5.71: Simulation results of a time averaged Poynting vector flux across a plane between the two protrusions. The minimum point indicates corresponds to a standing wave.

Simulations using WARP: Simulations of the EM waves and plasma in the beam pipe were performed using WARP [132]. Parameters roughly corresponded to experiments performed on CesrTA [1, 133]. TE waves of 2.05 GHz are launched into the beam pipe, and propagated at low power through 2 m of electron cloud. The simulation duration is 20 ns, which is sufficient for the entire volume to approach its equilibrium. Typical electron cloud densities are up to 10^{12} m^{-3}, but to enhance

the visibility of the effects the simulations use an average density of 10^{15} m^{-3}. The corresponding plasma frequency of 0.284 GHz is still well below the other relevant frequencies. The beam pipe is chosen to be rectangular with horizontal and vertical dimensions of 0.09 m and 0.05 m, respectively. The lowest mode has vertical polarization and its cutoff is 1.67 GHz. Without electron cloud, $k_z \simeq 8\pi$ m^{-1}, for a wavelength of 0.25 m. Thus, there are 8 periods in the simulated region. A uniform plasma reduces k_z so that there are roughly 7.75 periods. When the plasma is concentrated at smaller $|y|$ there is no change, but when concentrated at smaller $|x|$ the number of periods is further reduced to 7.40. The vertical field on axis for these cases is shown in Figure 5.72.

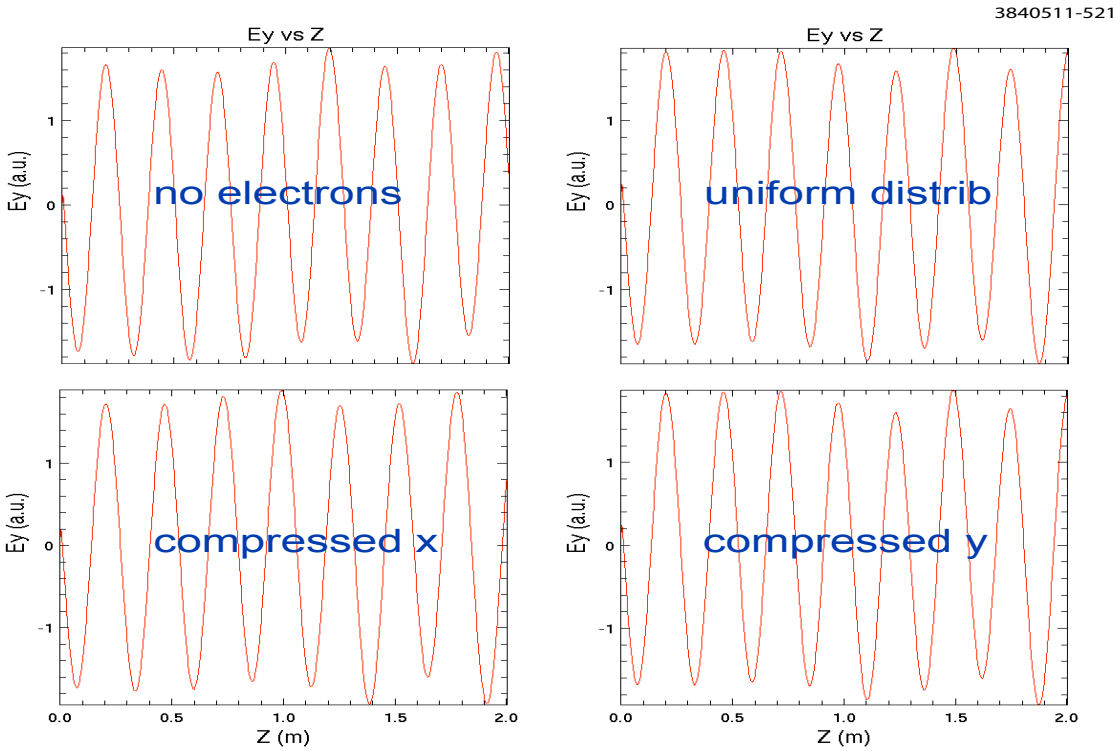

Figure 5.72: A comparison of TE wave propagation for the cases of no electron cloud and distributions that are uniform, compressed horizontally, or compressed vertically. The average electron density is 10^{15} m^{-3} in all cases with electrons.

Large Dipole Field: Simulations were performed using `WARP` with similar parameters as before. A uniform magnetic field of 1.1 T is included, either horizontal, vertical, or longitudinal. The cyclotron frequency is 30.79 GHz. In addition to a rectangular waveguide, a square waveguide with both diameters 0.09 m was used as a simplified model of a cylindrical waveguide. For a cylindrical waveguide, the modes mix components and are more complicated. The cutoff frequency for a circular pipe with diameter 0.09 m would be 1.95 GHz, which is even closer to the input frequency.

When the cyclotron frequency is much higher than the input EM wave frequency, the phase shift from the plasma can be strongly suppressed. When the electric field is aligned with the external magnetic field, there is no effect. When the external field is orthogonal to both the electric fields and the waveguide axis, the phase shift should be reduced by ω^2/Ω_c^2 compared to zero external field. On the other hand, a second polarization component is generated that is out of phase and

a factor of $\omega_p^2/\omega\Omega_c$ smaller in amplitude. The fields are shown in Figure 5.73; note that the wave has close to 8 periods in the simulation volume, very similar to the case with no electron cloud. The horizontal fields might be easier to detect, but will not propagate outside the electron cloud due to their higher-order structure. This effect is only moderately sensitive to the geometry of the waveguide. For a longitudinal magnetic field, Faraday rotation will generate an increasing component of the opposite polarization, so long as the other polarization is able to propagate. The rotation rate is proportional to the electron density and magnetic field. An example for a square waveguide is shown in Figure 5.74 . For a circular beam pipe, the variation of the electric field vector with position further complicates the interaction. By comparing different orientations of the TE wave, one could obtain more detailed information about the location of the electrons. Any decrease in transmission is very weak

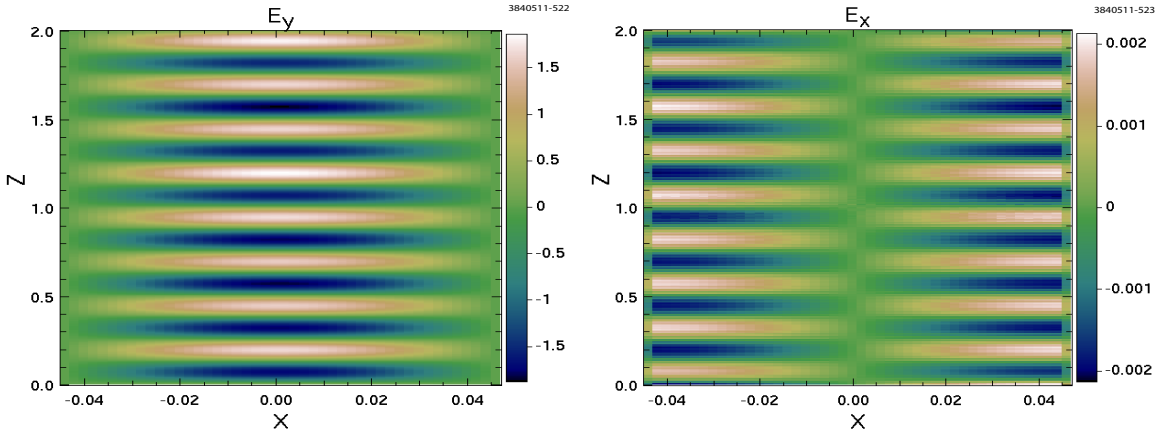

Figure 5.73: Transmission of a vertically-polarized TE wave in a square waveguide with a strong horizontal magnetic field and electron density of 10^{15} m^{-3}.

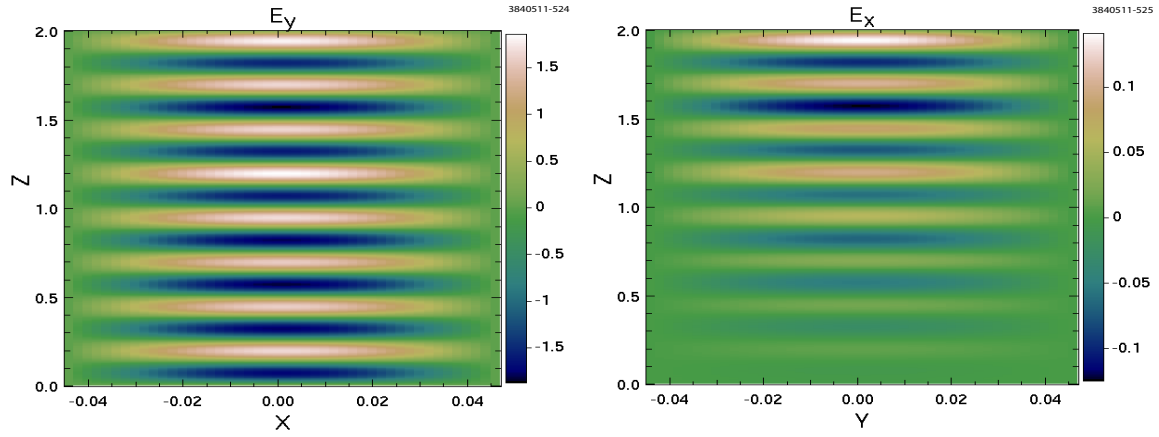

Figure 5.74: Transmission of a vertically-polarized TE wave in a square waveguide with a strong axial magnetic field and electron density of 10^{15} m^{-3}.

Cyclotron Resonance: Close to the cyclotron resonance, there is typically strong damping or reflection due to the mismatch between the normal waveguide modes and the waves allowed by the dispersion equation. There can also be significant heating of the electrons. The frequency for maximal electron heating rather than reflection is the "upper hybrid" frequency, $\omega_{uh}^2 = \Omega_c^2 + \omega_p^2$.

For solenoid fields, where the left-hand circularly polarized mode is insensitive to the resonance, half of the power will still be transmitted if this mode is allowed by the geometry of the waveguide. An example is shown in Figure 5.75 for a magnetic field of 0.07 T, where the cyclotron frequency is 1.96 GHz. The mode is left-hand circularly polarized, and has roughly half the power of the original mode. There is a transition region in the first few wavelengths as the right-hand polarized fields decay.

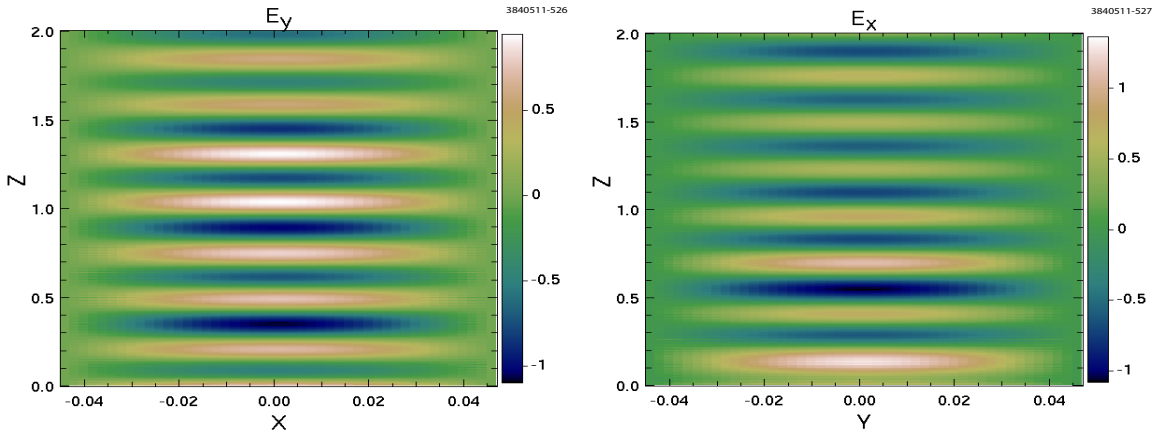

Figure 5.75: Transmission of a vertically-polarized TE wave in a square waveguide with vertical polarization and an axial magnetic field near resonance. The electron density is 10^{15} m^{-3}. A left-hand circularly polarized wave is transmitted at roughly half the original power.

5.2.2 Shielded Pickup Studies

5.2.2.1 Measurements

Time-resolved shielded-pickup measurements provide time structure information on cloud development, in contrast to the time-integrated RFA measurements [134]. However, they have relatively primitive energy selection, since they have no retarding grid and position segmentation is more coarse, the charge-collecting electrodes being of diameter 18 mm. Data has been recorded with biases of 0 and ±50 V relative to the vacuum chamber. The studies described here address exclusively the data a with bias +50 V in order to avoid contributions to the signal from secondary electrons escaping the pickup. Such secondaries generally carry kinetic energy insufficient to escape a 50 V bias. This choice of bias obviously provides sensitivity to cloud electrons which enter the port holes with low kinetic energy. The front-end readout electronics comprise RF amplifiers with 50 Ω input impedance and a total voltage gain of 100. Digitized oscilloscope traces are recorded with 0.1 ns step size.

Two Bunch Data The data shown in Fig. 5.76 was taken with two bunches of equal positron currents, 36ns apart. With a ring revolution period of 2.5 μs, the cloud has presumably fully decayed by the time of the arrival of the first bunch. This first bunch produces a fairly small signal in the detector. The signal from the second bunch is much larger, not because it has produced more photoelectrons, but because its electric field kicks electrons that were produced by the first bunch into the detector.

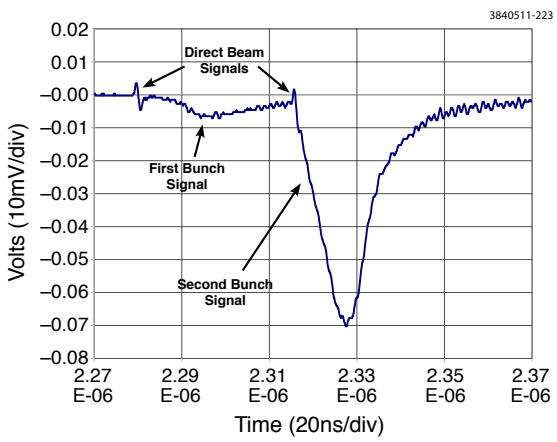

Figure 5.76: Shielded pickup signal from two bunches of positrons spaced at 36 ns

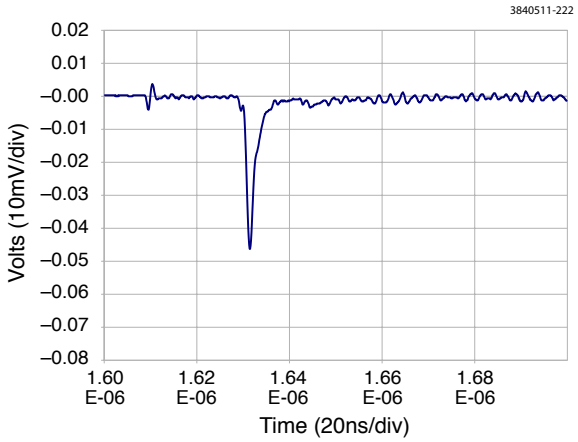

Figure 5.77: The signal from two bunches of electrons spaced at 20 ns

Another feature of the plot in Fig. 5.76 is the presence of what is presumed to be a small direct beam signal. The geometry of the detector holes give reasonably good (but not complete) isolation from the electromagnetic field of the beam. This signal provides a convenient fiducial that can be used to measure the time-of-flight of cloud electrons.

For example, notice that the peak of the signal from the first bunch occurs about 15 ns after its direct beam signal. Given the detector geometry, most of these electrons must be coming from the floor of the beam pipe, a distance of 5 cm, which would require an energy of roughly 30 eV.

After the passage of the second positron bunch in Fig. 5.76, the cloud electrons enter the detector almost immediately. Since this is a positron beam, the electrons kicked into the detector must come from below the beam height in the chamber, at least 2.5 cm from the detector. These initial electrons must have energies of many hundreds of eV and originate close to the beam.

Fig. 5.77 is the signal produced by two electron bunches spaced at 20 ns. Notice that the signal from the first bunch is not visible (except for the direct beam signal) and that the signal from the second bunch has a faster rise time than that of a positron beam.

Two Bunches with Different Spacings The much larger signal after the passage of the second bunch suggests that this signal is dominated by cloud electrons that are already in the pipe and are being kicked into the detector. This kick has an effective duration that is set by the sum of the length of the bunch and the size of the button, about 120 ps. So the second bunch signal is effectively a sample of the electron cloud in the chamber at the time of the second bunch's transit. Following this idea, pairs of bunches with equal currents were injected with different spacings. The result was a mapping of the electron cloud density produced by the first bunch as a function of time as the second bunch samples the cloud. In Fig. 5.78, a number of these measurements are plotted on the same time scale, showing the decay of the cloud.

Single Bunch with Solenoid When the solenoid surrounding the shielded pickup is energized, there is a noticeable effect on the detector signal that generally depends on the sign of the magnetic field. The four plots in Fig. 5.79 show the signal vs. solenoid field for chambers in 15E, 15W, and

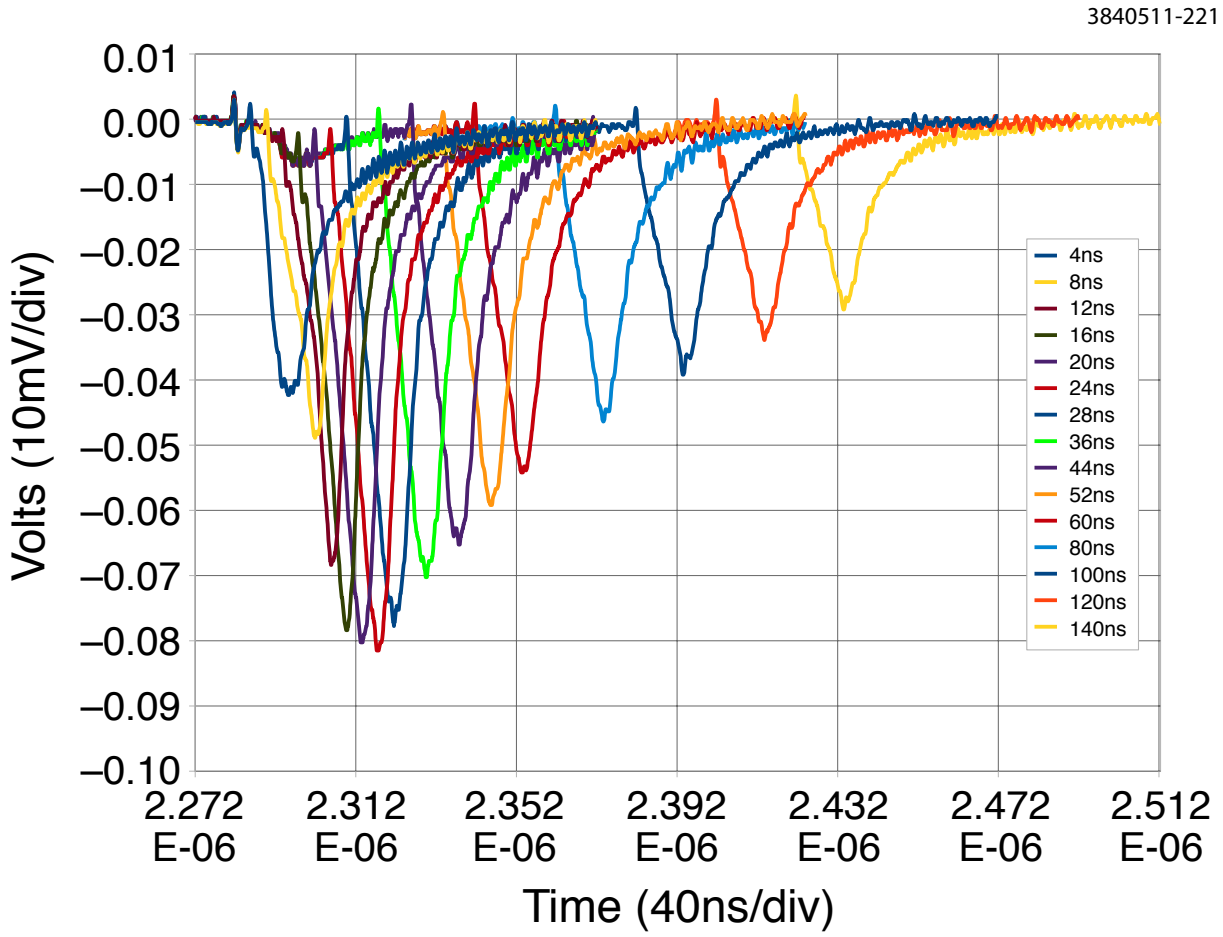

Figure 5.78: Overlay of two bunch data with spacings in multiples of 4 ns at 2.1 GeV with an aluminum chamber

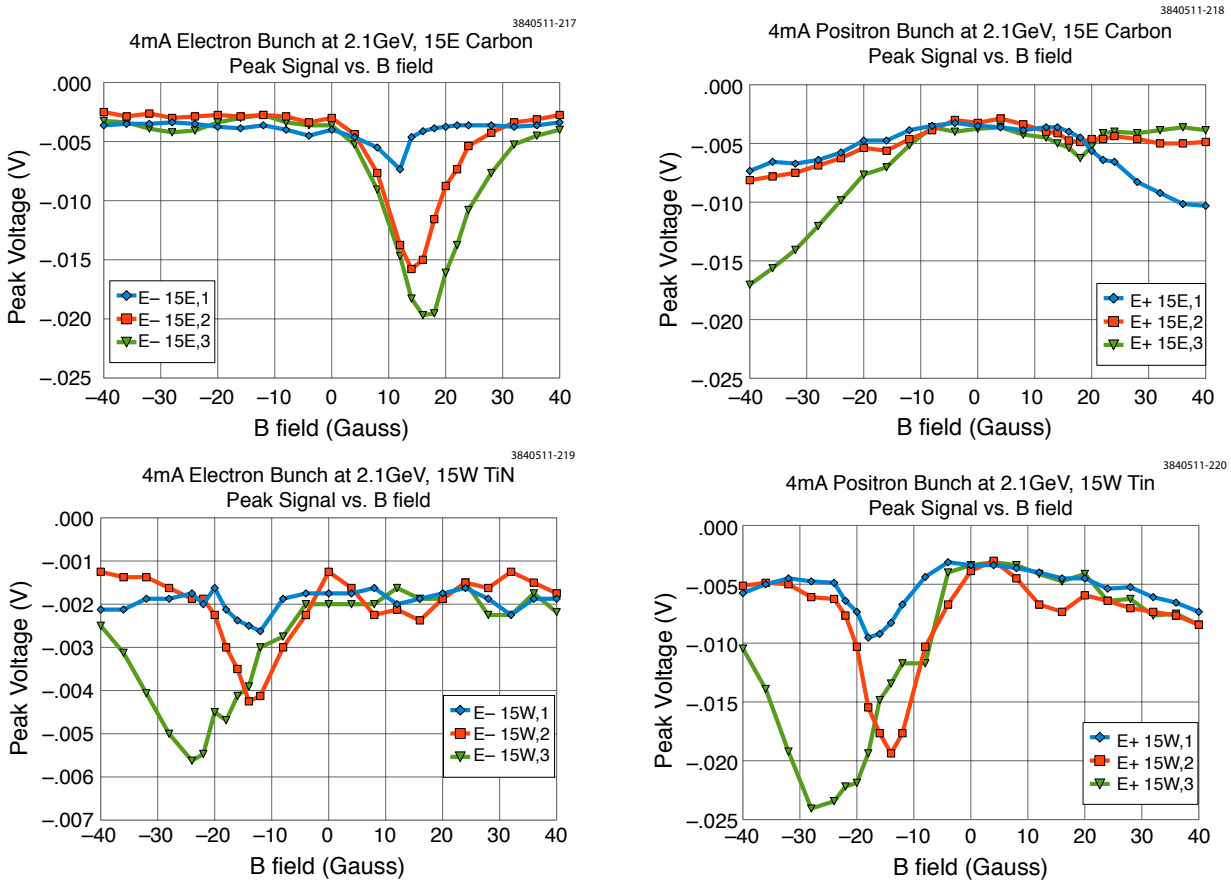

Figure 5.79: Pickup signal vs. solenoid field with a single bunch

for positron and electron beams. In the top left plot of Fig. 5.79 there is a large signal when the sign of the magnetic field positive. This positive magnetic field is such that primary electrons produced at the outside wall would be directed upward into the detector. It is likely that this signal is due to the synchrotron light stripe in the mid-plane of the beam pipe producing a concentration of photoelectrons along that stripe. The magnetic field that gives the largest signal, −14 G, can be used to estimate the electron energy at approximately 150 eV.

So when used with a solenoid, the 15E detector seems to function as a crude spectrometer with an electron bunch. However, data from positrons at 15E or either beam at 15W is inconsistent with this simple interpretation. So while there is hope that the use of a solenoid field can give useful information about electron energies, there are inconsistencies in data interpretation that need to be resolved through more careful modeling.

5.2.2.2 Shielded Pickup Modeling

Sensitivity to Photoelectron Energy Distribution The upper row of Fig. 5.80 shows examples of shielded pickup signals for two bunches of 5.3 GeV positrons (left) and electrons (right) separated by 14 ns. The population of the first bunch is 1.3×10^{11} while that of the trailing bunch varies up to a similar value. The trailing bunch accelerates cloud particles into the detector,

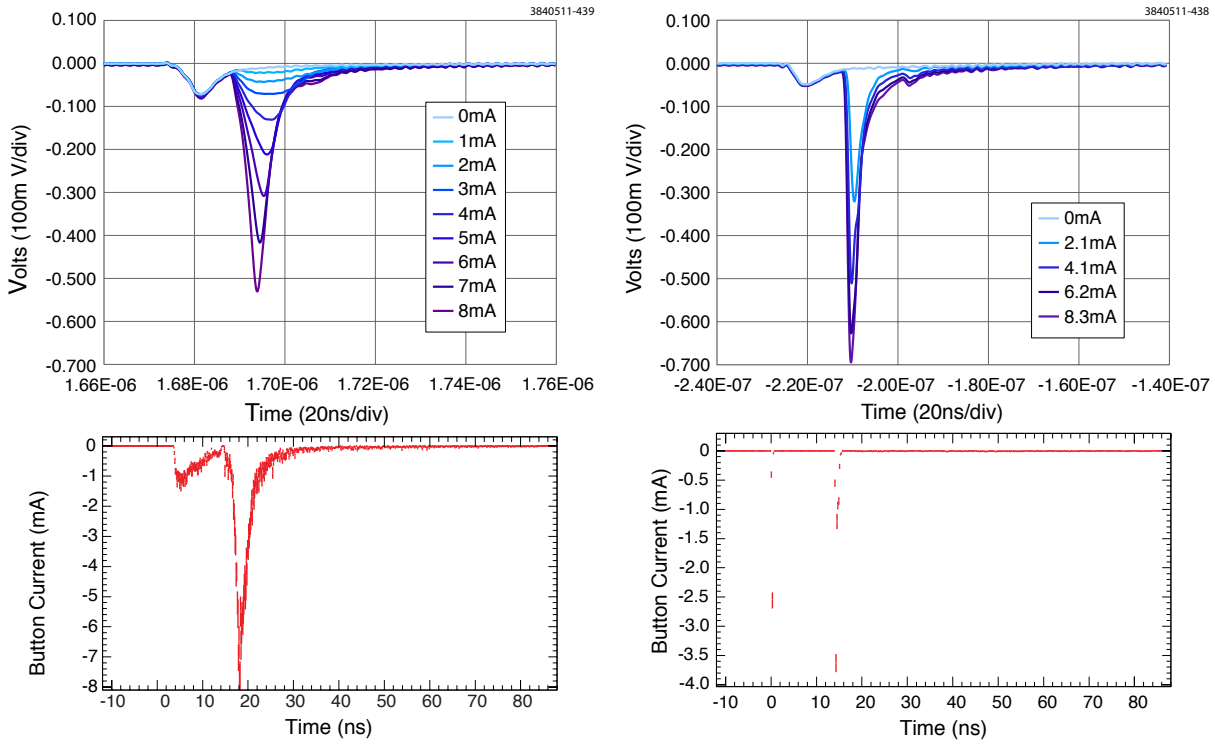

Figure 5.80: Upper row: shielded pickup signals produced by two 5.3 GeV positron (left) and electron (right) bunches separated by 14 ns. The leading bunch population is 1.3×10^{11}, or 8.2 mA. The population of the second bunch varies up to a similar value. Lower row: initial ECLOUD model results exhibiting discrepancies with the measured signals which are quite dramatic in the case of the electron beam.

producing the second signal. The arrival time and structure of the signal from the leading bunch corresponds to photoelectrons produced at the time of bunch passage on the bottom of the vacuum chamber. The kick from the positron bunch accelerates such photoelectrons toward the detector, whereas in the case of an electron beam the signal electrons must be produced with sufficient kinetic energy to overcome the repulsion of the beam bunch.

The lower row of Fig. 5.80 shows an initial attempt to model the case of two 1.3×10^{11} bunches using the electron cloud simulation code ECLOUD [112].

The calculation of cloud kinematics including space charge forces and beam kicks determines arrival times, momentum vectors and charges of the macroparticles reaching the upper surface of the chamber at the positions of the pickups. This early attempt at simulating the observed signals included a rather crude model of the port hole acceptance, leading to poor approximation of the magnitude of the signal, but it was sufficient to diagnose the obviously discrepancy with the observed signals. The positron case shows moderate time structure differences, but the modeling of the electron beam kick exhibited a dramatic discrepancy. The arrival times of the observed signals indicate photoelectron production on the lower wall of the chamber, which is effected in the simulation via a reflectivity parameter distributing 20% of the photoelectrons uniformly in azimuth. The prompt signal from each electron bunch corresponds to photoelectrons produced on the upper wall repelled into the detector during the bunch passage. The photoelectrons produced on the lower wall in the ECLOUD simulation are similarly reabsorbed, and these are the ones needed to produce the

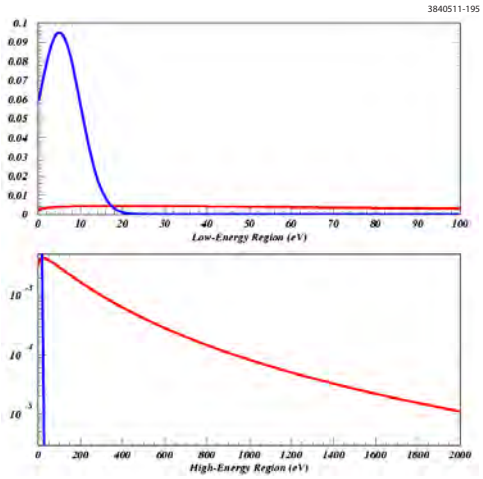

Figure 5.81: Low- and high-energy regions of the photoelectron energy distributions used to model the measured signals shown in Fig. 5.80. The original low-energy distribution shown in blue results in dramatic discrepancy with the signals observed in the case of an electron beam. The modified distribution shown in red provides good agreement with the observed signals.

observed signal! In other words, the measurement shows that photoelectrons of sufficient energy to overcome the repulsion of the beam bunch must be present. The photoelectron energy distribution in this original default model is common to many successful simulations of a wide variety of experimental observations [112, 135, 136], namely a gaussian with average and rms values of 5 eV limited by truncation to positive values. Figure 5.81 compares such a distribution (blue) to a power-law modification adequately reproducing the observed signal shapes (red). Low-energy and high-energy regions are shown normalized on logarithmic scales to illustrate the dramatically higher energies needed.

This new high-energy distribution was determined by matching single-bunch models to the measured signals for various electron bunch currents as shown in Fig. 5.82. The measured signals for a single bunch of 5.3 GeV electrons are shown in the left column. A bunch current of 1 mA corresponds to a bunch population of 1.6×10^{10}.

The model successfully reproduces the increase of signal magnitude with bunch current. While some time structure discrepancies remain, the improvement relative to the results shown in Fig. 5.80 is remarkable. The overall normalization of the modeled signals is proportional to the assumed reflectivity value, which in this case was 20%. In addition, the model also exhibits a prompt signal arising from photoelectrons produced nearby the detector repelled into it during the passage of the bunch, increasing with bunch current similarly to the observed signals.

Detailed Photoelectron Energy Modeling using Bunch Current Scans A detailed model of the photoelectron kinetic energy distribution for photoelectrons produced by reflected photons can be obtained by exploiting SPU data recorded for different bunch current levels. The early SPU signal from the leading bunch for a positron beam is largely due to photoelectrons produced on the bottom of the vacuum chamber. This is the closest production point where the beam kick attracts the photoelectrons toward the SPU. Thus the size and shape of the leading bunch signal is determined by the reflected photon rate, azimuthal distribution, the QE for producing photoelec-

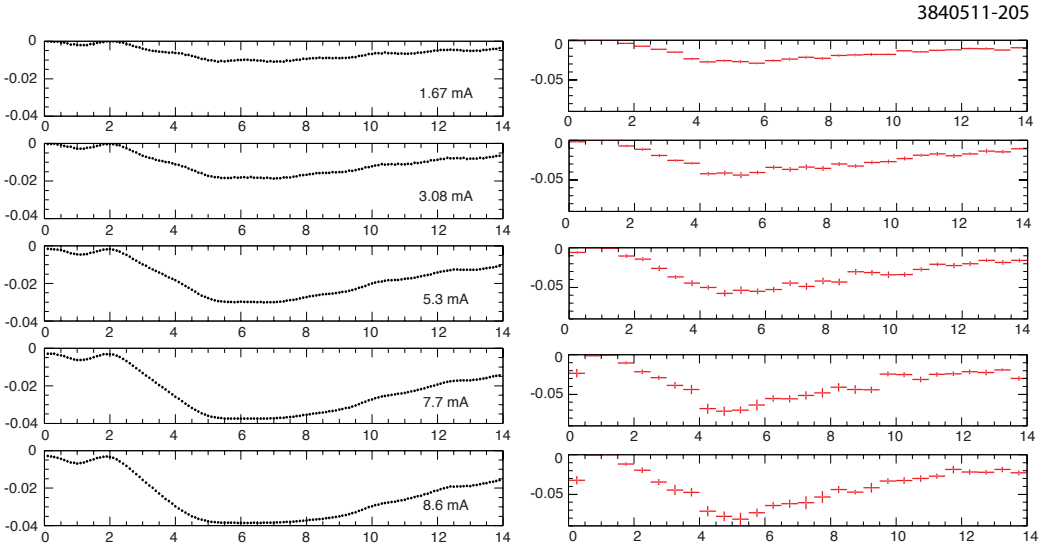

Figure 5.82: Comparison of measured single bunch signals for various electron bunch currents (left column) to the ECLOUD model (right column) after improving the modeled photoelectron energy distributions.

trons, the kinetic energy distribution of the photoelectrons and the strength of the attractive beam kick for a positron beam. In particular, the arrival time distribution determines the shape. By modeling the shape for different strengths of beam kick, we can extract the photoelectron energy distribution. An example of such an analysis is shown in Fig. 5.83. Note that the signal begins just a few nanoseconds after bunch passage even for weak beam kicks, indicating that high-energy photoelectrons were produced (hundreds of eV).

This level of modeling accuracy was achieved with a three-parameter photoelectron energy distribution of the form

$$f(E_{\mathrm{pe}}) \propto \frac{E_{\mathrm{pe}}^{P_1}}{\left(1+\frac{E_{\mathrm{pe}}}{E_0}\right)^{P_2}} \tag{5.25}$$

where the parameter E_0 is related to the value of the energy at the maximum of the distribution E_{peak} by

$$E_0 = E_{\mathrm{peak}}\frac{P_2-P_1}{P_1} \tag{5.26}$$

It was found empirically that two superposed power-law contributions suffice to describe the shape of the signal from the leading bunch. The high-energy component (22%) has a peak energy of 80 eV and an asymptotic power of 4.4 ($P_1 = 4$, $P_2 = 8.4$). Its contribution to the signal is shown as yellow circles in Fig. 5.84. The low-energy component (78%) has a peak energy of 4 eV and an asymptotic power of 2 ($P_1 = 4$, $P_2 = 6$). Its contribution to the signal is shown as magenta triangles. The model with the combined energy distribution is shown on three horizontal scales in Fig. 5.85. Note that these comparisons are complicated by the fact that the cloud development

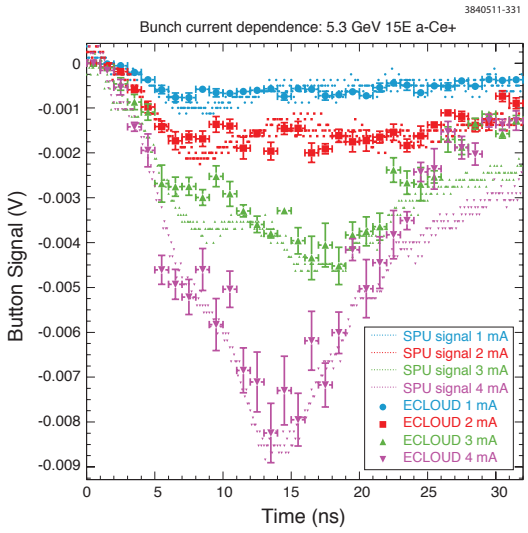

Figure 5.83: Modeled and measured leading SPU signals for bunch currents of 1, 2, 3 and 4 mA/bunch. The dramatically varying amplitudes and shapes are successfully reproduced by tuning the modeled photoelectron energy distribution as described in the text.

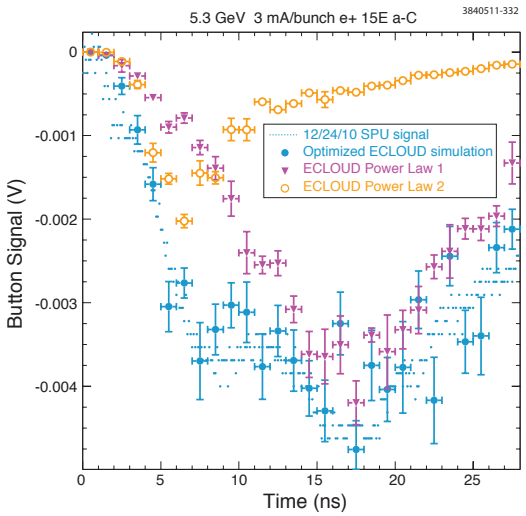

Figure 5.84: Two power-law contributions to the modeled photoelectron energy distribution. The yellow circles show the contribution to the signal from the high-energy photoelectron component, and the magenta triangles the low-energy contribution. The combined result is shown in blue.

for a single photoelectron component is unrealistic. The approximate validity of the superposition shows that space charge forces are weak, as is any contribution from photoelectrons produced at the primary source point on the outside wall of the chamber.

This analysis presents an opportunity to relate the obtained photoelectron energy distribution to the incident synchrotron energy spectrum and thus derive an estimate of the energy dependence of the QE. For example, the power law contributions have been determined in this manner for 2.1 GeV positron beams, showing that the high-energy tails are greatly reduced [137]. These studies also allow us to draw qualitative conclusions on the photoelectron energy distributions for various coatings, as described below in the section on vacuum chamber comparisons under the same beam conditions and radiation environment.

Since these studies pertain to photoelectrons produced by reflected synchrotron radiation photons, the incident photon energy spectrum is a convolution of the critical energy at the source and the energy dependence of the reflection process. Detailed work on modeling reflected photon trajectories is underway [88, 138].

Constraints on the Production Energy Distribution for Secondary Electrons Long after the photoelectrons from the bottom of the beam pipe have produced the peak of the leading bunch signal, secondary electrons produced by photoelectrons from the primary source point in the horizontal midplane on the outside wall of the chamber begin to enter the shielded pickup detector. Their arrival times depend on many characteristics of the model, such as the photoelectron energy distribution for direct (unreflected) photons, their production angular distribution, and, in particular, the energy and production angle distribution of the secondaries. The `ECLOUD` code

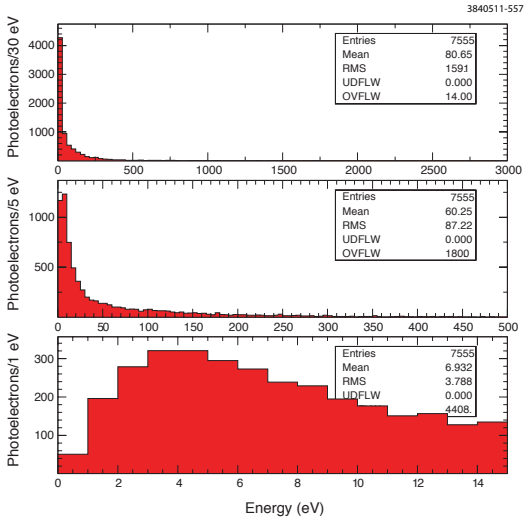

Figure 5.85: Modeled photoelectron energy spectrum resulting from the weighted contribution of the two power laws

provides for a variety of secondary energy distribution parameterizations, many of which could be excluded by studies such as the one shown in Fig. 5.86. For the best parameterization,

$$f(E_{\rm sec}) \propto E_{\rm sec} \exp(-E_{\rm sec}/E_{\rm SEY}) \tag{5.27}$$

an upper bound was obtained on the parameter $E_{\rm SEY}$, which determines the falling exponential slope. For values of $E_{\rm SEY}$ greater than 0.8, the modeled signal exhibits a tail at later times inconsistent with the measured signal.

The signal from a witness bunch following 14 ns after the leading bunch also has a contribution from reflected photons similar to the one that dominates the leading bunch signal. However, it includes additionally a much larger contribution from secondary cloud electrons accelerated into the SPU detector by the beam kick. Those present near the vertical plane containing the beam below the horizontal midplane at the time the witness bunch passes can arrive even earlier than the photoelectrons from the bottom of the beam pipe, so the risetime of the witness bunch signal is faster. Figure 5.87 shows that if the secondary energy distribution does not include sufficiently high energies, the modeled 14 ns witness bunch signal shape is inconsistent with the data.

Remarkably, the two constraints on the secondary electron production kinetic energy distribution described above restrict the $E_{\rm SEY}$ parameter to a narrow range of values around 0.8 eV.

Cloud Lifetime Studies Using Witness Bunches While the awareness of the sensitivity of the shielded pickup measurements to the parameters of photoelectron production was largely motivated by inadequacies of the model discovered in its application to recent measurements, the original intended use of these time-resolved cloud measurements was to provide a quantitative estimate of the elastic yield parameter in the secondary electron yield model. A similar investigation was performed at RHIC [139]. The basic concept is that the mature cloud long after passage of any beam bunch is dominated by low-energy electrons which suffer predominantly elastic interactions

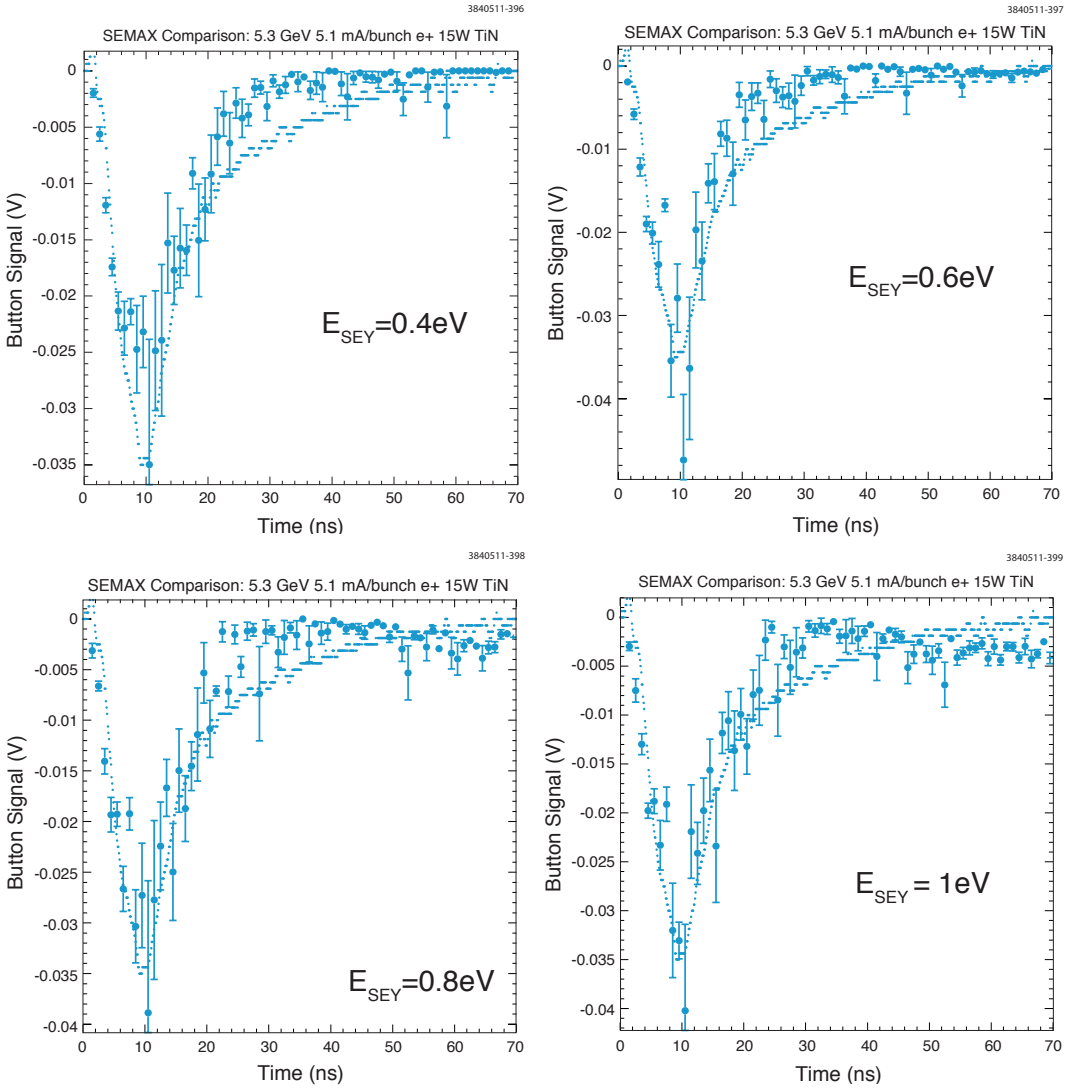

Figure 5.86: Modeled (points with error bars) and measured (dots) leading SPU signals with differing distributions for the parameter E_{SEY} ranging from 0.4 to 1.0. For values of E_{SEY} greater than 0.8, the modeled signal exhibits a tail at later times inconsistent with the measured signal.

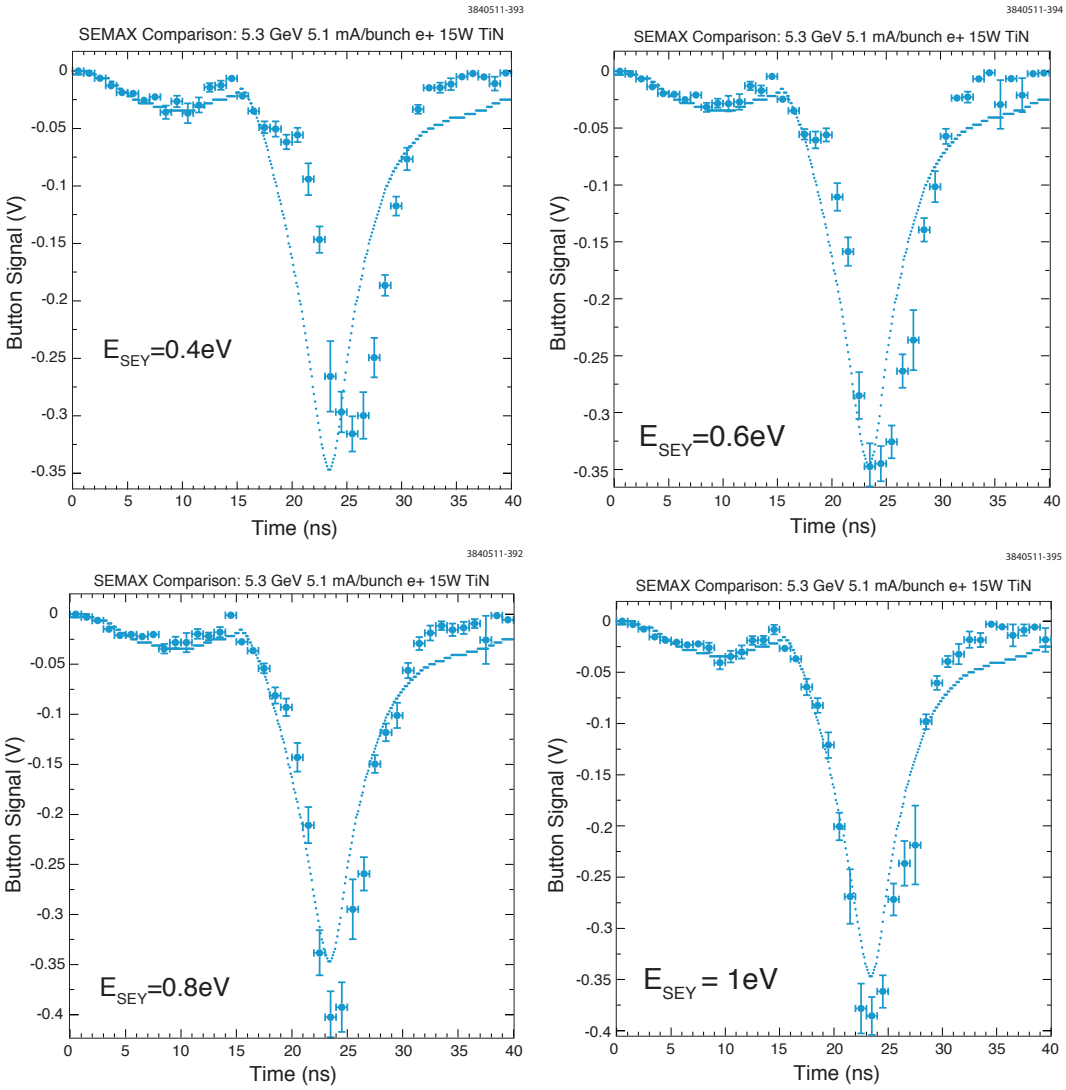

Figure 5.87: Modeled and measured two-bunch signals with values for the parameter E_{SEY} ranging from 0.4 to 1.0. For values of E_{SEY} less than 0.8, the model is inconsistent with the measured witness-bunch signal.

with the vacuum chamber wall. The elastic yield parameter describes the ratio of outgoing to incoming macroparticle charge in probabilistic models [86], and carries a value typically 0.5-0.7, determining the decay time of the cloud density, typically around 100 ns. High-energy electrons of more than 100 eV, produced by synchrotron radiation, beam kicks, or the rediffused component of the secondary yield process, undergo primarily the so-called "true" secondary yield process, in which the produced secondary carries only a few electron volts of kinetic energy, resulting in the dominance of low-energy electrons late in the cloud development.

Figure 5.88 shows an `ECLOUD` secondary yield population curve typical of the shielded pickup signal simulations.The true secondary yield maximum at 400 eV ranges from a minimum of 0.9 to a maximum of 1.5 owing to the dependence on incident angle. At low energy the yield value is dominated by the elastic interactions with the chamber wall. This case exhibits an elastic yield parameter of 0.55.

The witness bunch experimental method consists of generating a cloud with a leading bunch, then accelerating cloud electrons into the shielded pickup detector with a trailing bunch at various delay times. Table 5.7 shows the witness bunch data sets which were recorded from March, 2010 through November, 2011. Additional data sets with delay times restricted to 14 ns and 84 ns at bunch currents of 1, 2, 4, 6, and 8 mA were also taken for systematic checks of the modeling.

The magnitude and time structure of the signal from the leading bunch is determined by the reflective properties of the vacuum chamber and by the energy-dependent QE, as described in the preceding section. The signal induced by the witness bunch has a contribution similar to that of the leading bunch added to the contribution from the existing cloud kicked into the detector. The latter contribution is sensitive to the cloud density and the spatial and kinematic distributions of the cloud electrons. Figure 5.89 shows the results of six sets of simulations with various values for the elastic yield parameter δ_0. In each of the six plots, eleven two-bunch (5.3 GeV, 4.8×10^{10} positrons each) pickup signals are superposed, whereby the delay of the witness bunch varies from 12 to 100 ns. The modeled signals are shown with the statistical error bars corresponding to the number of macroparticles contributing to the signal. The magnitudes of the modeled signals at large witness bunch delay clearly show the dependence on the elastic yield parameter δ_0 as it is varied from 0.05 to 0.95. The most consistent description of the measured signals is given by a value of $\delta_0 = 0.75$. This value can be compared to the value of $\delta_0 = 0.5$ used in the modeling of CesrTA coherent tune shift measurements as described in Refs. [135, 136], where the measurements had much less discriminating sensitivity to the elastic yield.

Figure 5.90 shows a similar study, but for a titanium-nitride-coated aluminum chamber. For each of the six values assumed for the elastic yield, thirteen two-bunch (5.3 GeV, 8.0×10^{10} positrons each) pickup signals are superposed, whereby the delay of the witness bunch is varied from 14 to 84 ns. The optimal value for the elastic yield is clearly less than the value determined for the uncoated aluminum chamber, with $\delta_0 = 0.05$ providing the best description of the measurements.

These comparisons show a number of intriguing discrepancies. The leading bunch signal shape exhibits the need for further tuning of the photoelectron energy distribution. The signal widths tend to be wider than observed. In addition, such a low value of 0.9 for the secondary yield of an uncoated aluminum surface cannot be easily understood, since the tune shift measurements require an average value around the CESR ring of about 1.8. A wide variety of systematic studies have been undertaken since the ECLOUD'10 workshop, discovering sensitivity to many detailed characteristics of the cloud. For example, the signal widths for early witness signals depend strongly

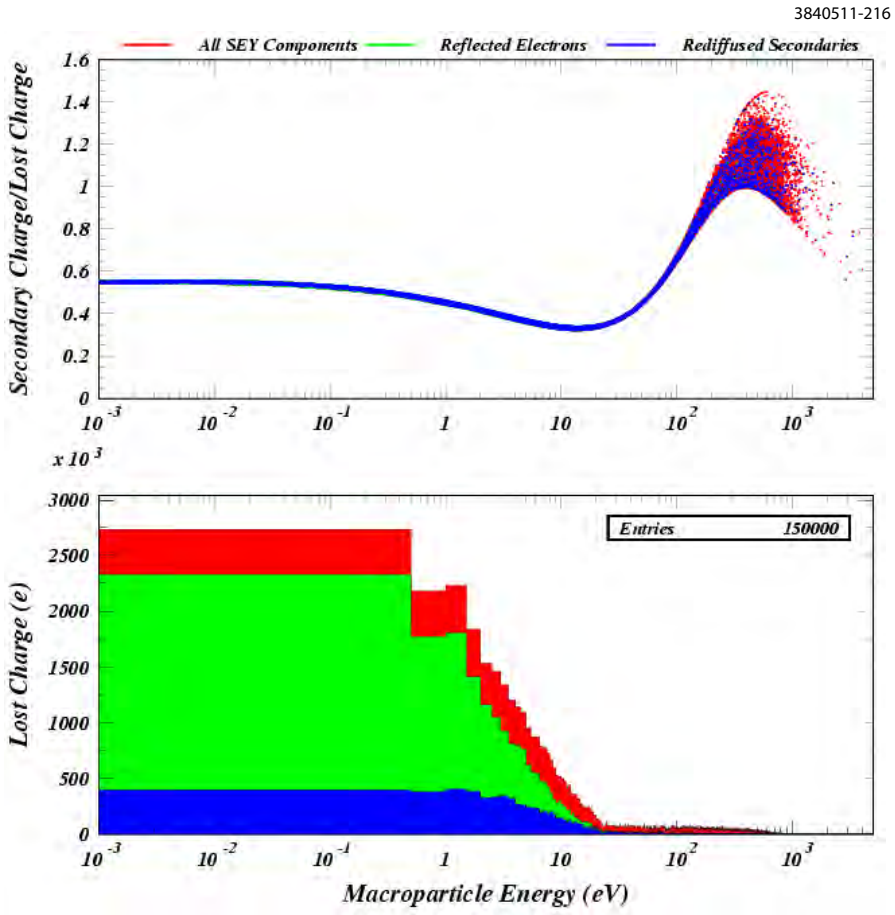

Figure 5.88: Secondary yield population curve typical of the ECLOUD model for the shielded pickup signals. The upper plot shows the yield value (ratio of secondary macroparticle charge to that of the incident charge) as a function of the incident kinetic energy. At low energy the yield value is dominated by the elastic interaction with the chamber wall. This case exhibits an elastic yield parameter of 0.55. The lower plot shows the incident energy distribution. The elastic and rediffused components are shown in green and blue, respectively. The sum of all three components, true, elastic and rediffused, is shown in red. Since the three colors are plotted on top of each other, the upper plot shows primarily blue at low energy, even though the elastic process dominates, as is seen in the lower plot.

Table 5.7: Shielded pickup witness bunch data sets recorded from March, 2010 through November, 2011. Note that the various cloud-mitigating coatings (TiN, a-carbon, and diamond-like carbon) were swapped into the different radiation environments at 15E and 15W. Data sets with differing total radiation dose were obtained as well. Two vacuum chambers with a-carbon coatings were studied, providing information on production reproducibility.

Date	Species	Beam Energy (GeV)	Bunch Current (mA)	15E/W	Mitigation Technique	Bunch Spacing (ns)
03/27/2010	Positrons	5.3	5	W	a-carbon (1)	14-84
				E	TiN	
	Electrons		5	W	a-carbon (1)	14-70
				E	TiN	
05/09/2010	Positrons	2.1	3	W	Al	4-140
				E	a-carbon (2)	
	Electrons		3	W	Al	4-20
				E	a-carbon (2)	
05/17/2010	Positrons	5.3	3	W	Al	4-100
				E	a-carbon (2)	
	Electrons		3	W	Al	4-100
				E	a-carbon (2)	
05/19/2010	Electrons	2.1	1	W	Al	4-120
				E	a-carbon (2)	
09/21/2010	Positrons	5.3	1,2,4,6,8,10	W	TiN	14
				E	a-carbon (2)	
09/24/2010	Positrons	2.1	2,4,6	W	TiN	14
				E	a-carbon (2)	
	Electrons			W	TiN	
				E	a-carbon (2)	
12/10/2010	Electrons	2.1	1,2,3,4,5,6,8,10	W	TiN	14-84
				E	a-carbon (2)	
12/20/2010	Positrons	2.1	1,2,3,4,5,6,8,10	W	TiN	56,84
				E	a-carbon (2)	
12/24/2010	Positrons	5.3	3,5	W	TiN	14-84
				E	a-carbon (2)	
	Electrons		3,5	W	TiN	14-84
				E	a-carbon (2)	
04/07/2011	Positrons	5.3	1,2,3,4,5,6,8,10	W	TiN	14-84
				E	DL carbon	
	Electrons		1,2,3,4,5,6,8,10	W	TiN	14-84
				E	DL carbon	
04/16/2011	Positrons	2.1	1,2,3,4,5,6,8,10	W	TiN	14-84
				E	DL carbon	
04/17/2011	Electrons		1,2,3,4,5,6,8,10	W	TiN	14-84
				E	DL carbon	
06/11/2011	Positrons	2.1	1,2,3,4,5,6,8,10	W	TiN	14-84
				E	DL carbon	
06/12/2011	Electrons		1,2,3,4,5,6,8,10	W	TiN	14-84
				E	DL carbon	
06/18/2011	Positrons	5.3	1,2,3,4,5,6,8,10	W	TiN	14-98
				E	DL carbon	
	Electrons		1,2,3,4,5,6,8,10	W	TiN	14-84
				E	DL carbon	
06/27/2011	Positrons	4.0	1,2,3,4,5,6,8,10	W	TiN	14-98
				E	DL carbon	
	Electrons	2.1	1,2,3,4,5,6	W	TiN	84
				E	DL carbon	
09/27/2011	Positrons	5.3	1,2,3,4,5,6,8	W	a-carbon (2)	14-84
				E	DL carbon	
09/30/2011	Positrons	5.3	1,2,3,4,5,6,8	W	a-carbon (2)	14-84
				E	DL carbon	
10/04/2011	Positrons	5.3	1,2,3,4,5,6,8	W	a-carbon (2)	14-84
				E	DL carbon	
10/11/2011	Positrons	5.3	1,2,3,4,5,6,8	W	a-carbon (2)	14-84
				E	DL carbon	
10/25/2011	Positrons	5.3	1,2,3,4,5,6,8	W	a-carbon (2)	14-84
				E	DL carbon	
11/27/2011	Positrons	5.3	1,2,3,4,5,6,8,10	W	a-carbon (2)	14-98
				E	DL carbon	
	Electrons		1,2,3,4,5,6,8,10	W	a-carbon (2)	14-84
				E	DL carbon	

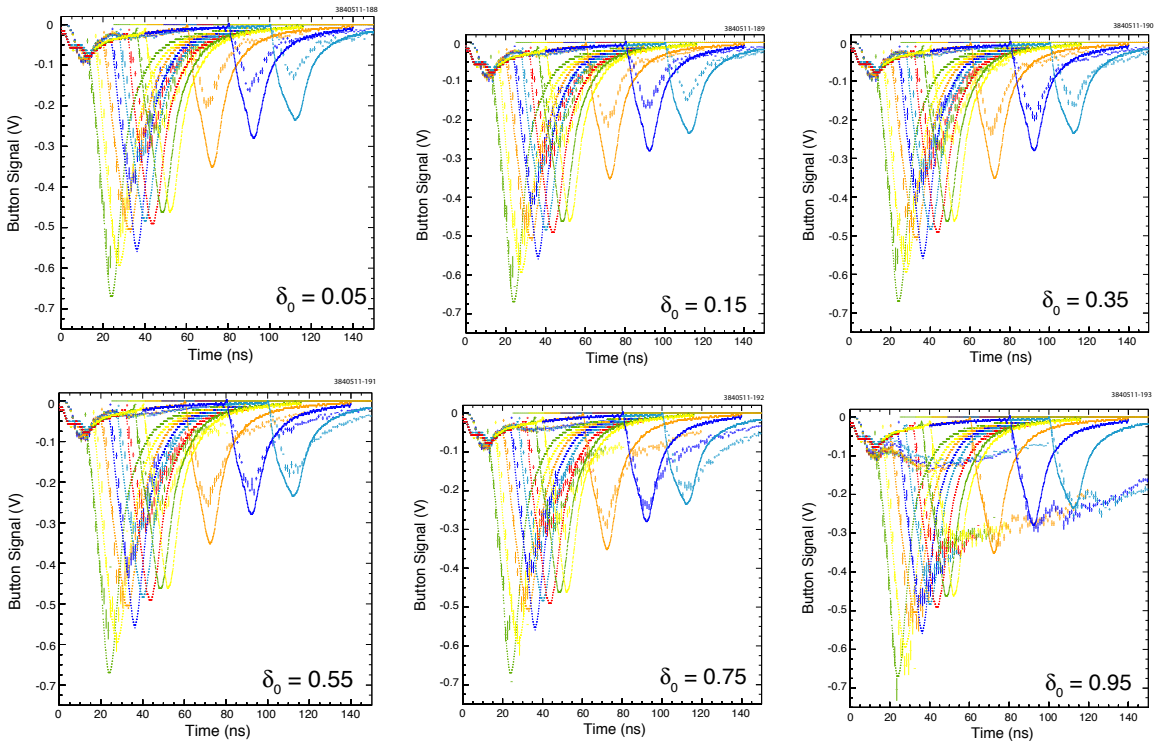

Figure 5.89: Witness bunch study with the uncoated aluminum chamber. Eleven two-bunch scope traces are superposed in each of the six plots, whereby the delay of the witness bunch ranges from 12 to 100 ns. The modeled signals are shown with the statistical error bars corresponding to the number of macroparticles contributing to the signal. The magnitudes of the modeled signals at large witness bunch delay clearly show the dependence on the elastic yield parameter δ_0 as it is varied from 0.05 to 0.95. The most consistent description of the measured signals is given by a value of $\delta_0 = 0.75$.

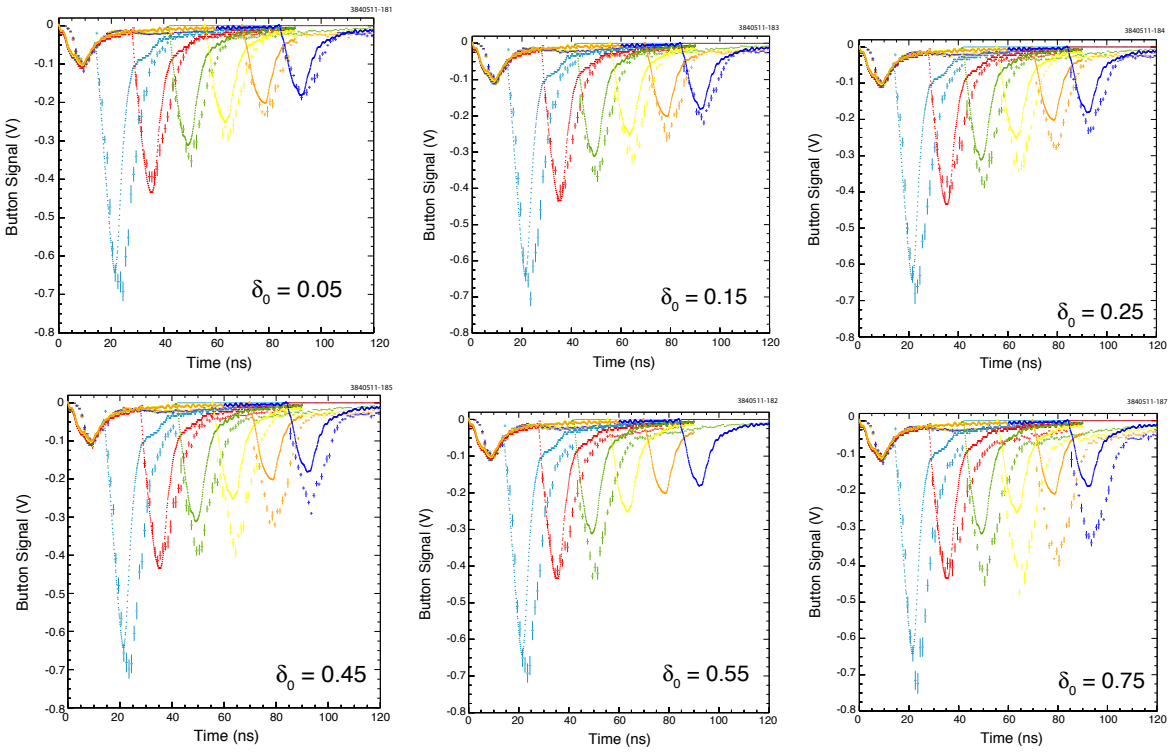

Figure 5.90: Witness bunch study with the titanium-nitride-coated aluminum chamber. The smooth curves are the digitized shield pickup signals. Six two-bunch scope traces are superposed in each of the six plots, whereby the delay of the witness bunch ranges from 14 to 84 ns. The magnitudes of the modeled signals at large witness bunch delay clearly show the dependence on the elastic yield parameter δ_0 as it is varied from 0.05 to 0.75. The most consistent description of the measured signals is given by a value of $\delta_0 = 0.05$.

on the azimuthal production distribution of photoelectrons, as was observed by implementing in ECLOUD the distributions calculated by the photon-tracing reflectivity model for the CESR ring described in Ref. [88]. Nonetheless, the dramatic improvements in consistency obtained via such systematic studies have not changed the quantitative conclusions concerning the sensitivity to the value for the elastic yield. Generally one can say that the choice of peak true secondary yield value relative to the effective reflectivity value determines the ratio of the early witness bunch signal magnitudes to that from the leading bunch. However, for witness bunches late enough that the signal magnitude becomes comparable to that of the leading bunch, there is little sensitivity to the true secondary yield. Instead, those signal magnitudes are determined by the value assumed for the elastic yield.

In situ comparisons of custom vacuum chambers One fruitful analysis strategy has proved to be the comparison of SPU signals in chambers which have been swapped into the same location in the CESR ring and studied under identical beam conditions [140]. The two regions in CESR equipped with SPU detectors differ in radiation environment, since the dominant source points are in dipole magnets of differing strengths. At 5.3 GeV, for example, the source dipole field is 3 kG (2 kG) in the west (east) region for a positron beam, resulting in a critical energy of 5.6 keV (3.8 keV). In addition, the situation with regard to reflected radiation is different. By comparing SPU signals recorded at the same place in the ring with the same beam energy, bunch spacing and bunch population, many systematic contributions to the comparisons are avoided, and relatively simple changes to the modeling suffice to quantify the different properties of the vacuum chambers.

Figure 5.91 shows such a comparison for an a-carbon-coated chamber in May and December 2010 for two 5.3 GeV 28 ns-spaced bunches each carrying 4.8×10^{10} positrons, corresponding to a bunch current of 3 mA.

During the intervening time interval, CESR had operated at high current as an X-ray research facility, with the consequence that synchrotron radiation dose on the chamber had increased by a factor of about 20, from $8.1{\times}10^{23}$ to $1.8{\times}10^{25}$ photons/m. Also shown is the ECLOUD model optimized to reproduce the May measurement. Since the signal from the leading bunch arises from photoelectrons produced on the bottom of the vacuum chamber [140–142], careful tuning of the energy distribution and the QE for photoelectrons produced by reflected photons is required to reproduce the size and shape of the signal. The signal from the witness bunch includes additionally the contribution from secondary EC electrons accelerated into the SPU detector by the witness-bunch kick. The modeled witness signal is therefore crucially dependent on the SEY and production kinematics. Since conditioning affects both signals similarly, we can conclude that the change is in the QE rather than in the SEY. The December measurement is reproduced by a 50% decrease in the modeled QE for photoelectron production. A reduction in the SEY of 25% is inconsistent with the observed effect, since the modeled leading bunch signal remains unchanged.

Guided by the above comparisons, we can assess conditioning effects in the TiN- and DL-carbon-coated chambers in similar fashion. Figure 5.92 compares the SPU signals for two 8×10^{10} e^+ bunches in the TiN-coated chamber in April and June, 2011, with accumulated synchrotron radiation doses of $5.9{\times}10^{24}$ and $1.1{\times}10^{25}$ photons/m, corresponding to integrated beam currents up to more than 730 Amp-hrs. Changes in the QE and SEY are less than a few percent.

Figure 5.93 shows the conditioning effect observed for the DL carbon coating between integrated photon doses of $6.67{\times}10^{24}$ to $2.03{\times}10^{25}$ γ/m over the seven-month period between April and

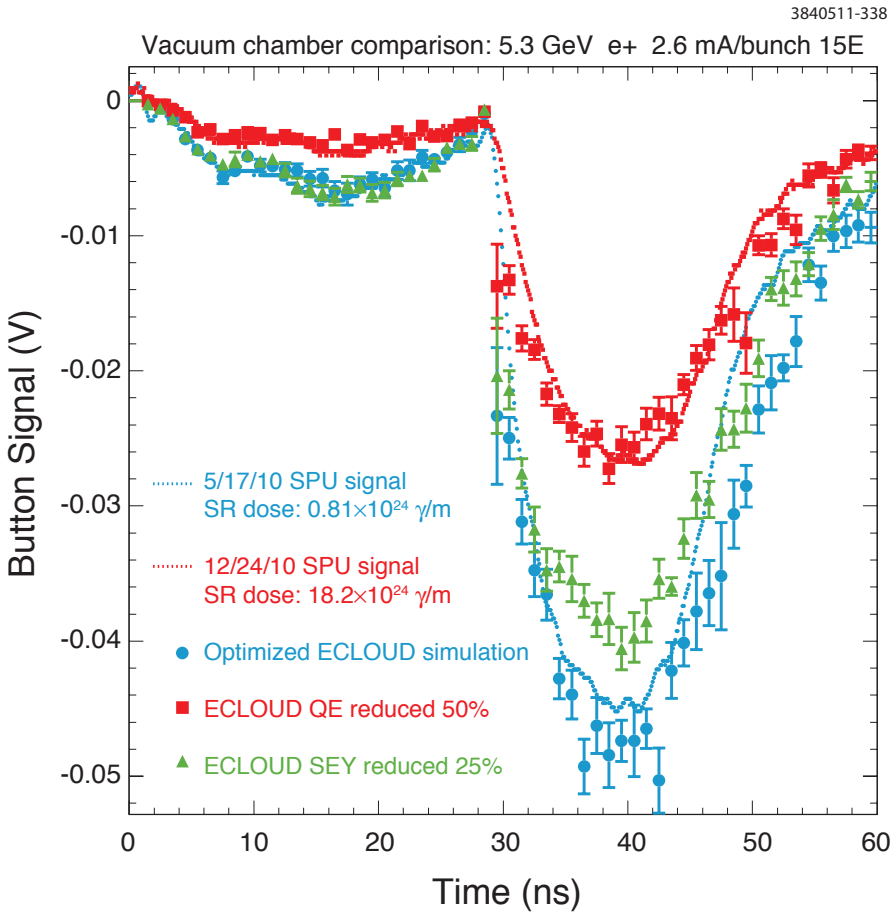

Figure 5.91: Shielded pickup signals measured in an a-C-coated chamber in May (blue dotted line) and December (red dotted line) of 2010 for two 5.3 GeV, 28-ns-spaced bunches each carrying 4.8×10^{10} positrons. The `ECLOUD` model optimized for the May data is shown as blue circles, the error bars showing the signal macroparticle statistical uncertainties.

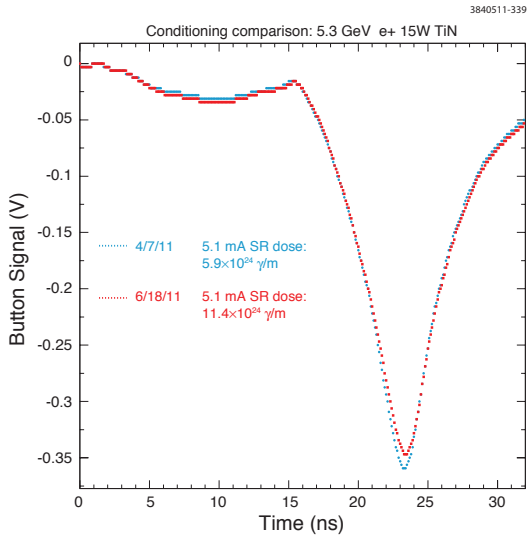

Figure 5.92: SPU signals showing conditioning effects in the TiN-coated aluminum vacuum chamber.

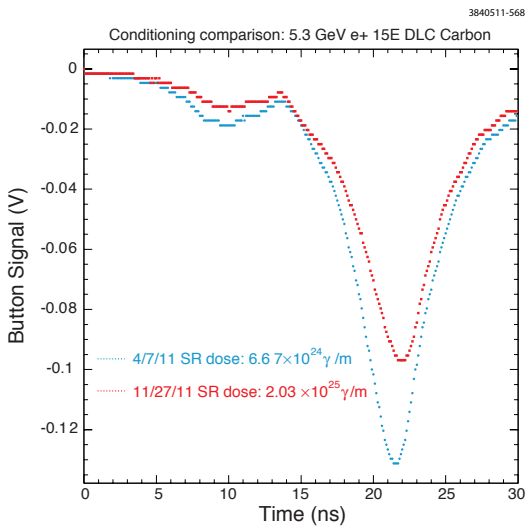

Figure 5.93: SPU signals showing conditioning effects in the aluminum vacuum chamber coated with DL carbon.

November, 2011. The SPU signals from two bunches of 8×10^{10} 5.3 GeV positrons spaced by 14 ns are shown. The decrease in the signal from the leading bunch indicates a conditioning effect in the quantum efficiency for the DL carbon coating similar to that observed for the a-carbon coating[143].

The method of in situ comparison of custom vacuum chambers can also be used to compare the characteristics of different mitigation techniques. Figure 5.94 compares signals from a TiN-coated aluminum chamber and an uncoated chamber with a factor of ten lower synchrotron radiation dose. The shape and size of the leading bunch signal show that the QE for producing photoelectrons from reflected photons is much lower for the TiN coating. The secondary yield is also significantly smaller. A comparison between TiN and amorphous carbon coatings is shown in Fig. 5.95. The later, smaller signal from the leading bunch from the a-carbon chamber shows that the QE is lower, particularly for high-energy photoelectrons. However, the similar magnitudes of the signals from the witness bunch indicate that the secondary yield for TiN is somewhat smaller than that for a-carbon. Further modeling promises to provide quantitative results for these qualitative observations.

Use of a Weak Solenoidal Magnetic Field Another type of measurement which has been explored with the shielded-pickup detectors is illustrated schematically in Fig. 5.96. The vacuum chambers have been outfitted with windings to approximate a solenoidal field in the region of the cloud with magnitude up to 40 G. Since signal contributions require nearly vertical arrival angles, the centers of the corresponding circular trajectories for any given magnetic field value lie in the horizontal plane of the ports. The three trajectories originating at the primary impact point of the synchrotron radiation and leading to the center of each electrode thus select different regions of photoelectron energy and production angle, as shown.

Experiments to date have shown that the 40 G field magnitude range suffices to cover the full energy range of the photoelectrons produced by a 2.1 GeV beam ($E_{critical} \approx 300$ eV) (i.e. no pickup signal is observed for field values of 0 and 40 G), in contrast to the case of a 5.3 GeV

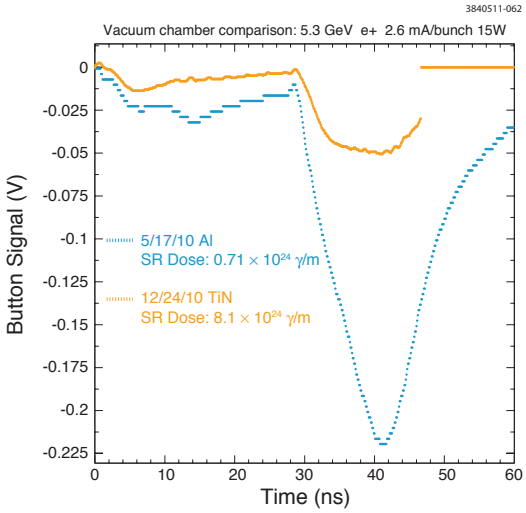

Figure 5.94: SPU signals exhibiting the difference in cloud buildup characteristics between a TiN-coated aluminum chamber and an uncoated aluminum chamber with a factor of ten lower synchrotron radiation dose.

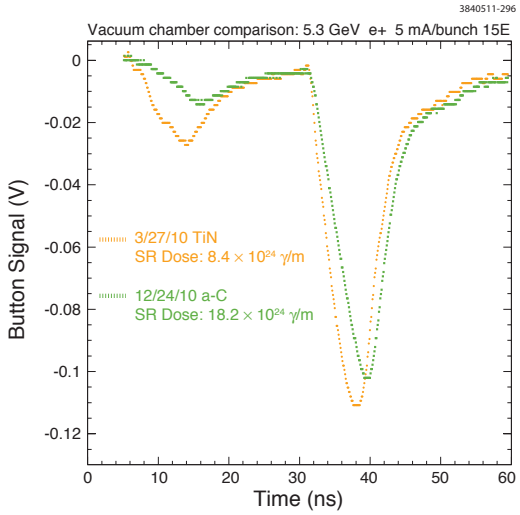

Figure 5.95: SPU signals exhibiting the difference in cloud buildup characteristics between a-carbon-coated and TiN-coated aluminum chambers.

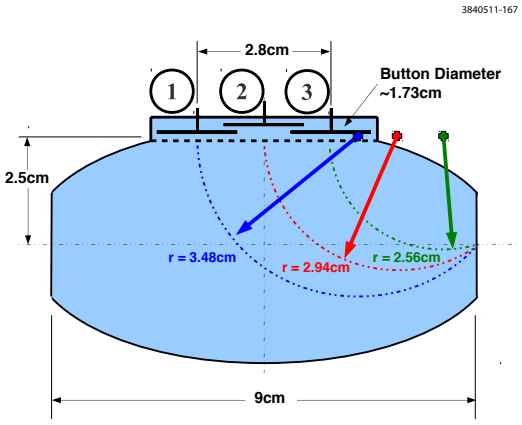

Figure 5.96: Vacuum chamber wall cross section with circular trajectories of photoelectrons contributing to the pickup signals.

beam ($E_{\text{critical}} \approx 5$ keV), where photoelectron energies suffice to produce an observable signal even at 40 G. Furthermore, reversal of the solenoidal field provides information on the production of photoelectrons at a point on the vacuum chamber opposite the primary source point and thus relevant to the reflective characteristics of the vacuum chamber wall.

Summary The shielded pickup detectors installed in the CESR ring in 2010 have begun providing a wide variety of time-resolved measurements of electron-cloud-induced signals. Measurements with custom vacuum chambers incorporating cloud mitigation techniques such as carbon and titanium-nitride coatings have been obtained and compared to the case of an uncoated aluminum chamber. Weak solenoidal magnetic fields have been employed to study photoelectron production kinematics. A model for the shielded pickup acceptance has been developed in the context of the electron cloud simulation code `ECLOUD`. The shielded pickup data have proved remarkably sensitive to model parameters poorly constrained by any other experimental means, such as the azimuthal production distribution for photoelectrons and their energy distributions. The measurements with 5.3 GeV electron and positron beams indicate the need for a high-energy component previously absent in the photoelectron generation model. In addition, the design purpose of the shielded pickup detectors has been experimentally confirmed, as the cloud lifetime has been accurately measured using witness bunches at various delays. Sensitivity to the elastic yield parameter in the secondary yield model has been shown to be less than 0.05 and remarkably robust against variation of other model parameters. Data taken with an uncoated aluminum chamber provide a best estimate for the elastic yield of about 0.75. The cloud lifetime studies in a titanium-nitride-coated aluminum chamber exclude such a high value, yielding an optimal value of 0.05.

5.3 Comparisons Between Methods

5.3.1 Wiggler Ramp Studies

The L0 wiggler straight is instrumented with both RFAs and TE-Wave hardware, which provides an opportunity to compare the two methods. Fig. 5.97 shows a wiggler ramp measurement (see Section 5.1.4.1, under "Wiggler Data"), during which both RFA and TE-Wave data were taken. RFA data is plotted as solid lines, TE-Wave "transmission" measurements with a dashed lines, and TE-Wave "resonant" measurements with dotted lines. Both detectors show the "turn on" behavior described above, and the turn-on points for the two methods are roughly consistent.

5.3.2 Comparison of RFA and Shielded Button Responses

RFA and shielded pickup detectors have been deployed in adjacent locations in the 15E and 15W arc sections of CESR (Section 2.2.3.1). Fig. 5.98 compares the time-averaged signal of the 15W SPU with the central collectors of the 15W RFA. The approximately linear relationship between the signal in the two detectors across a variety of beam conditions implies that their measurements can be directly compared.

RFA and SPU simulations (Sections 5.1.4.2 and 5.2.2.2 respectively) have led to many of the same qualitative conclusions. The most significant of these are a very low secondary emission yield for TiN and amorphous carbon coated chambers, and the necessity of high energy photoelectrons for

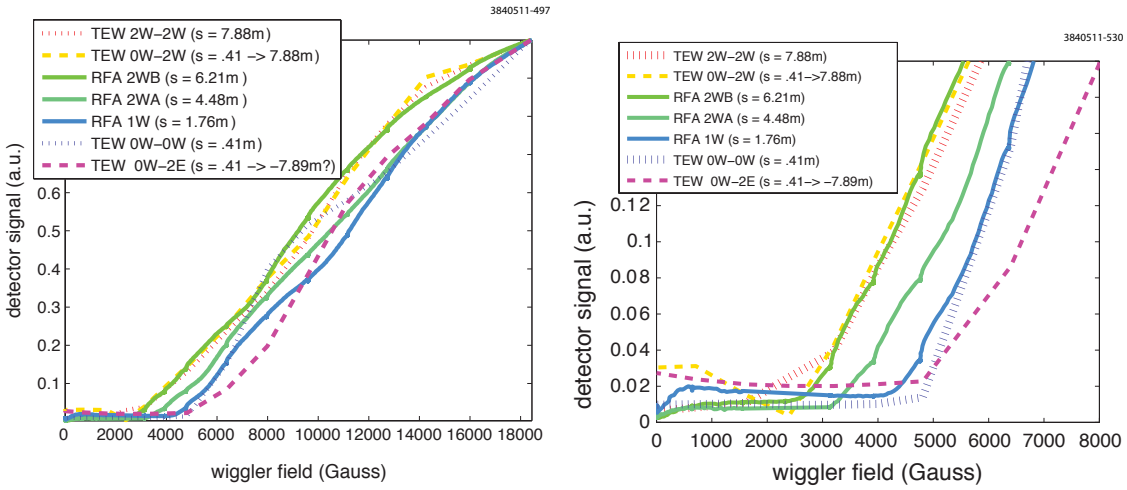

Figure 5.97: RFA/TE-Wave comparison during a wiggler ramp measurement. The right plot is zoomed in, to more clearly show the turn-on behavior. Beam conditions are 45 bunches of positrons at .75mA/bunch, 2.1GeV, 14ns spacing. Each of the signals is normalized to 1 at peak wiggler field (1.9T), because it is difficult to quantitatively compare RFA and TE-Wave data.

reproducing electron beam data. A more detailed comparison of RFA and SPU data and simulations is an important area of future work.

5.3.3 Comparison of TE Wave and SPU Data

Fig. 5.99 shows a particular location at CesrTA where both TE Wave and SPU measurements have been made. While most of the beampipe at CesrTA is bare aluminum, the SPU is installed in a short test section coated with diamond-like carbon. The sensitivity of the TE Wave measurement extends over the region between the pumps, so it samples both the coated and the bare aluminum sections. This complicates the comparison of the two methods since the aluminum section will have a much higher EC density than the coated section.

Fig. 5.101 is an example of the response of these two devices as a function of beam current, using a 20 bunch train of positrons at 5.3 GeV with a bunch spacing of 14 ns (train length 266 ns) and a revolution time of 2563 ns. For TE Wave data, the duration of the cloud was taken to be the roughly the length of the bunch train. The first Fourier component gave a correction of 4.7 to the density calculated by Eq. (5.16), giving the peak EC densities shown. For the SPU data, the voltage gain of 100 was removed and the charge deposited on the electrode for each turn is plotted.

In taking the TE Wave data, the beam-pipe was excited at each of the five resonant frequencies shown in Fig. 5.100. In Fig. 5.101, the measured EC densities for the first three resonances are close to each other, but resonances 4 and 5 give a lower density. According to Eq. 5.14, if the EC density n_e were uniform the frequency shift - and therefore the signal - would be independent of the details of the electric field distribution and all of the TE Wave curves should be the same. The fact that the curves differ suggests that the EC density is non-uniform.

SPU signal is very non-linear at low bunch currents as might be expected. At low bunch currents, the SPU signal can be increased both by a larger EC density and increasing bunch charge. With

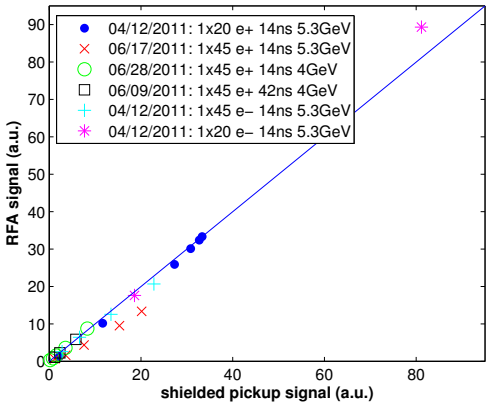

Figure 5.98: Comparison of RFA and SPU measurements, 15W TiN coated chamber. Each point represents a measurement with different beam current.

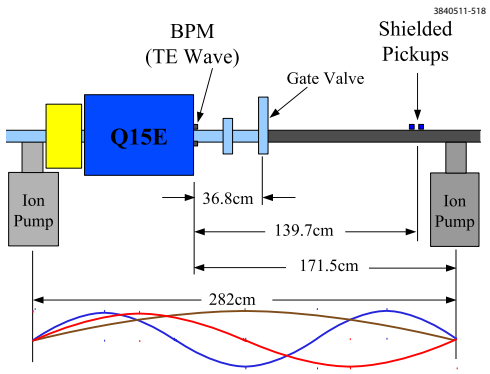

Figure 5.99: The SPU is located in a short test section of chamber where the vacuum surface has been coated with diamond-like carbon (the darker section in the sketch). The TE Wave region spans both the coated and uncoated sections of beampipe.

increased bunch charge, the electron cloud is more effectively kicked into the detector by the beam. So in this low bunch charge region, the SPU signal for a train of bunches should be roughly quadratic with current.

Simulation indicates an approximately linear increase in EC density with beam current as suggested by the TE Wave plots. The full simulation of EC density plus SPU sensitivity is in reasonable agreement with the SPU signal at the location of that detector. A comparison with the EC density given by the TE Wave measurement is complicated by the fact that the resonances span both the aluminum and carbon coated sections of beampipe and the flux of synchrotron radiation photons hitting the wall varies by a factor of three over this region. At 100 mA, the simulation predicts average EC densities of 1.0×10^{13} m^{-3} for the aluminum and 0.58×10^{12} m^{-3} for the diamond-like carbon section. This corresponds to an average value of 5.3×10^{12} m^{-3}, in reasonable agreement with the measurements. Further work is required in order to complete the comparison of TE Wave and SPU data. The results can be used to provide experimental verification of the simulations.

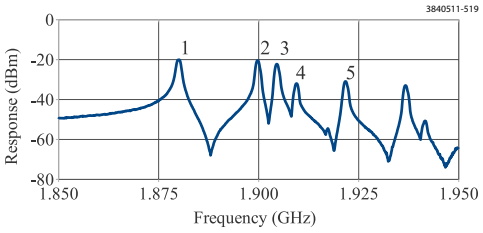

Figure 5.100: Above is the TE Wave response at 15E when resonantly excited. The sideband amplitudes of first five major peaks were used to generate Fig. 5.101 .

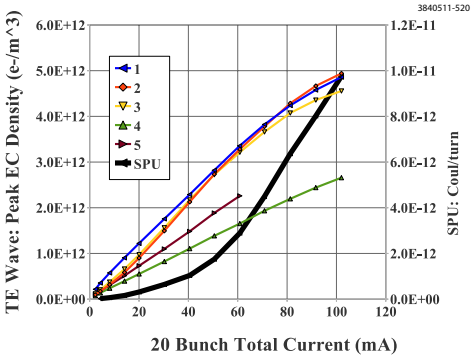

Figure 5.101: Comparison of SPU and TE Wave measurements for a 20 bunch train of positrons. The thick curve is the total charge deposited in the SPU in a single turn; the thinner, numbered curves are based on the TE Wave sidebands of five different resonances shown in Fig. 5.100.

5.4 Summary and Further Investigations

5.4.1 Simulation Program

The simulation program has compared direct measurements of the electron cloud made at CesrTA with the results of simulation codes. Photon production, transport, scattering and absorption has been modeled using the newly developed code `Synrad3D` (described in Section 4.1.4.1). EC-buildup has been modeled using the existing codes `ECLOUD` [89, 90], `CLOUDLAND` [91, 92], and `POSINST` [71, 86]. In order to obtain good agreement with RFA and shielded pickup data, the simple model for the photoelectron energy spectrum contained in these codes (a truncated Gaussian, with a centroid and width in the eV range) has been expanded to allow a significant high-energy tail (up to hundreds of eV) .

5.4.1.1 Drift and Quadrupole RFAs

After post-processing, the output from the build-up codes has been compared with the measurements from RFAs in drift regions. The post-processing scripts incorporate the measured efficiency of the RFA. Generally, qualitative agreement between data and (post-processed) simulation can be obtained with the proper choice of build-up model parameters, such as quantum efficiency and secondary emission yield, without fine tuning of these parameters.

Using this method, comparisons between measurements and simulations for an RFA in a quadrupole have also been made. The simulations show long-term buildup of the cloud in the quadrupoles, which is supported by the data. Simulations limited to a single turn underestimate the measurements by more than an order of magnitude, while agreement between measurements and simulation is good (for electrons with energies > 75 eV) when the simulations are extended to 19 turns.

5.4.1.2 Dipole and Wiggler RFAs

A similar approach, using a post-processing script, is also partially successful when applied to RFA measurements in dipole regions. However, in this case, the simulation significantly overestimates the signal observed by the RFA at low energies. This is due to the interaction between the RFA and the cloud, which is not modeled by the post-processing script, and which is most significant for low energy electrons and for high magnetic fields.

This effect is most pronounced in the RFA measurements made in the high-field wigglers. In this case, it manifests itself as a low-energy peak in the voltage scan of the wiggler's RFA current vs. retarding voltage. The peak appears when a certain resonance condition between the bunch spacing and retarding voltage is satisfied. To properly model this interaction, we have incorporated into `POSINST` a model of the wiggler vacuum chamber, including the geometry and fields of the RFA. The dynamics of the electrons within the RFA, including the electrostatic force from the grid, are fully modeled. This simulation reproduces the resonant enhancement seen in the data, at approximately the observed voltage.

Because of the importance of the cloud-RFA interaction in the wigglers (and to a lesser extent in the dipoles), future work to fully understand the RFA measurements in dipoles and wigglers, and to relate these measurements to detailed surface properties, will need to use buildup codes which include the RFA as an integral part of the simulation.

5.4.2 EC Mitigation Observations in RFAs and Comparisons with Simulations

We have used RFAs to probe the local behavior of the cloud in different magnetic field environments, and in the presence of different mitigation schemes.

5.4.2.1 Drift RFAs

In drift region RFAs, all coated chambers show a sizeable ($\sim \times 5$ or more) reduction in signal when compared to uncoated aluminum. After extensive processing, both TiN and amorphous carbon coated chambers show similar mitigation performance. The RFA signal in TiN-coated copper is about half that of bare copper. Diamond-like carbon may perform better than other coatings at very high beam current.

5.4.2.2 Dipole RFAs

We found the difference between uncoated and coated chambers to be even stronger than in a drift region. At high beam current, the TiN coated chamber shows a signal smaller by two orders of

magnitude than the bare Al chamber, while the coated and grooved chamber performs better still, by another factor $\sim \times 5$.

As has been observed in previous studies, for a fixed value of the dipole field, the RFA shows a bifurcation of the cloud density into two peaks with a transverse separation which increases with beam current.

For fixed beam current, the average RFA collector current exhibits regularly occurring spikes or dips. These correspond to "cyclotron resonances", which occur whenever the cyclotron period of cloud electrons is an integral multiple of the bunch spacing [116]. These resonances appear as peaks in the RFA signal in the aluminum chamber, but as dips in the coated chambers. The peaks measured in the aluminum chamber have been reproduced in `ECLOUD` simulations using the cloud model parameters expected for an aluminum surface. For the coated chambers, the dips can also be reproduced in simulation, by using a value of 1.0 for the elastic secondary yield, and 0.5 for the peak yield at high energies. However, direct measurements of the secondary yield of TiN indicate peak yields near 1.0, not 0.5, and shielded pickup data exclude elastic yields much in excess of 0.1 for TiN.

Measurements of the central RFA collector signal as a function of bunch spacing, for fixed beam current, show peaks which can associated with resonances between the bunch spacing and the transit time of the cloud electrons across the vacuum chamber (often called a "multipacting resonance"). Peaks are seen for both positrons and electrons, both for CESR dipoles and the SLAC chicane dipoles. The positions of the peaks are roughly consistent with a simple model for the multipacting resonance.

5.4.2.3 Quadrupole RFA

Measurements with an RFA in a CESR quadrupole suggest that the majority of the cloud in the quadrupole is streaming along the magnetic field lines between two pole tips. The RFA signal seen in the quadrupole with a TiN surface is reduced by well over an order of magnitude compared to an aluminum surface.

5.4.2.4 Wiggler RFAs

Using RFAs located at the peak field points in high-field wigglers, comparisons have been made of the relative electron cloud signal sizes from surfaces of bare copper, TiN coated copper, grooved and coated copper, and a surface with a clearing electrode. The largest signal is seen for the TiN coated copper surface. As fractions of this signal, the other surfaces give EC signals in the ratios (bare copper, bare copper with grooves, TiN coated copper with grooves, clearing electrode) = (81%, 47%, 28%, $< 1\%$).

RFA observations made in the three wigglers in L0 have been used to measure the growth of the electron cloud signal in the wigglers as a function of the wiggler field. For fixed beam current, we observe a "turn on" of the signal in each detector at a specific wiggler field value. The RFAs that are further downstream turn on first. This measurement is sensitive to the change in the radiation environment, and the associated photoelectron seeds of the cloud, as the wiggler field increases. It should provide a good test of the photon production, transport and absorption simulations. In particular, there may be some sensitivity to the production of fluorescent X-rays in the copper

chambers. Comparison of this data with the simulations will be done as part of the next phase of the program.

5.4.2.5 Comparisons with simulations

A wide variety of drift RFA data have been systematically compared with `POSINST` EC build-up simulations, with post-processing appropriate for the drift RFAs, to extract best-fit cloud model parameters. An iterative chi-squared analysis method has been employed. The photon flux and photoelectron angular distributions are determined from `Synrad3D` simulations. Known sources of error have been included.

For a good description of the high-current electron beam RFA data, a high-energy tail must be present in the photoelectron energy spectrum.

We have found that, in general, one can obtain a reasonable fit to the data by varying only three (well chosen) cloud model parameters. For example, one good set consists of the true secondary yield, elastic yield, and quantum efficiency. Using more parameters does allow for a slightly better fit, at the cost of uniqueness and clarity.

The best-fit model parameters found for an uncoated aluminum chamber are in reasonable agreement with the best-fit parameters determined from the coherent tune-shift data, as presented below in Section 6.3.1. As expected from the mitigation studies, the two coated chambers studied (a-Carbon and TiN), both the true secondary yields and the elastic yields are much lower than for aluminum. There are some unexplained discrepancies in the determination of the quantum efficiencies for certain data sets, which may point to defects in the photon modeling.

5.4.3 In-situ SEY Studies

The in-situ SEY station described in Section 2.3.4 was used to make direct measurements of the secondary emission yield of TiN coated aluminum, several 6061 aluminum, amorphous carbon, and diamond-like carbon surfaces. These measurements were made for different photon doses, to study surface conditioning.

For TiN-Al samples and bare Al6061 alloy samples, we observed that the main processing occurred within the first 2 weeks, with a total photon dose of 10^{22} photons/m, while, after that, the SEY decrease was about 1% per week.

For Al6061, we observed that the SEYs after processing are lower than the minimum SEY value of 2.4 for Al6063 reported by SLAC [119]. Generally, for bare aluminum samples, the initial value of the peak SEY varies from sample to sample.

The amorphous carbon sample had an initial peak SEY of 1 and showed no change with conditioning.

Measurements at varying angles of incidence showed an increase in the surface SEY as the angle goes from normal incidence towards grazing incidence.

Future work will include improvements in the current drift of the electron gun, more study of Al alloys, and measurements of the SEY of NEG films. We also plan to check the reproducibility of the results on TiN-Al samples and do additional checks for systematic effects. We are designing

additional experiments to determine whether SR bombardment or electron cloud bombardment is the main source of processing.

5.4.4 TE Wave Studies

Two versions of TE wave measurements were made at CesrTA. Initial measurements were based on the transmission of microwaves between two points in the accelerator, using the beam pipe as a waveguide. In the course of taking this data, it became clear that a different interpretation of the signals was needed in most cases - due to the presence of resonances in the frequency response of the beam pipe. This resulted in the recent development of TE wave resonant measurements where the beam pipe and its reflections are treated as a resonant cavity.

5.4.4.1 TE Wave Transmission Measurements

Methods have been developed to include both phase and amplitude modulation in the analysis of the response of TE wave transmissions to the time-varying electron cloud in beam pipes. Techniques to continuously monitor the transmission function, and to compensate for beam pipe attenuation, have been worked out.

5.4.4.2 TE Wave Resonance Measurements

The effects of reflections and the generation of standing waves in TE excitation of beam pipes was studied. Methods to extract the EC density signal from beam pipe resonant cavity phase shifts were developed.

5.4.4.3 Other techniques

Other techniques for probing the electron cloud, such as the use of cutoff resonances and TE wave magnetic resonances, are described in this section.

5.4.4.4 TE Wave Modeling

The plasma simulation code `VORPAL` [126] has been used to study TE wave transmission and resonance experiments at CesrTA. The simulated phase shift in a simple transmission experiment (no reflections) in a drift region has been shown to agree well with analytical estimates. Simulations have been done to study TE wave transmission in an external magnetic field, which show an enhanced phase shift for a carrier frequency close to the cyclotron resonance. The enhanced phase shift remains a linear function of the electron density. Simulations were also done of TE wave experiments in the presence of obstacles which cause partial reflection, as will be the case in a real beam pipe. While the phase shifts are modified in this case, the relation between density and phase shift remains linear.

For the case of a large dipole field, as in a wiggler, simulations of TE wave experiments were done using `WARP`[132]. In this case, when the cyclotron frequency is much higher than the carrier frequency, the EC-induced phase shift can be strongly suppressed. However, the longitudinal

magnetic field in the wigglers will rotate the polarization at a rate determined by the product of the field and the electron density, so some information on the density in this region could be obtained by comparing different orientations of the TE wave.

5.4.5 Shielded Pickup Studies

The shielded pickup detectors installed in the CESR ring in 2010 have begun providing a wide variety of time-resolved measurements of electron-cloud-induced signals. Measurements with custom vacuum chambers incorporating cloud mitigation techniques such as carbon and titanium-nitride coatings have been obtained and compared to the case of an uncoated aluminum chamber. Weak solenoidal magnetic fields have been employed to study photoelectron production kinematics. A model for the shielded pickup acceptance has been developed in the context of the electron cloud simulation code `ECLOUD`. The shielded pickup data have proved remarkably sensitive to model parameters poorly constrained by any other experimental means, such as the azimuthal production distribution for photoelectrons and their energy distributions. The measurements with 5.3 GeV electron and positron beams indicate the need for a high-energy component previously absent in the photoelectron generation model. In addition, the design purpose of the shielded pickup detectors has been experimentally confirmed, as the cloud lifetime has been accurately measured using witness bunches at various delays. Sensitivity to the elastic yield parameter in the secondary yield model has been shown to be less than 0.05 and remarkably robust against variation of other model parameters. Data taken with an uncoated aluminum chamber provide a best estimate for the elastic yield of about 0.75. The cloud lifetime studies in a titanium-nitride-coated aluminum chamber exclude such a high value, yielding an optimal value of 0.05.

5.4.6 Comparisons Between Methods

Comparisons have been made of local measurements of electron cloud density using TE waves and RFA's in the L0 wiggler straight. Both types of TE wave measurements (transmission and resonant) have been compared to each other and to RFA measurements made as a function of wiggler current, for fixed beam conditions. All three measurement methods show a similar "turn-on" behavior with wiggler field, and the turn-on locations as a function of longitudinal position of the detectors in the L0 straight are roughly consistent.

TE wave and shielded pickup (SPU) measurements made at the same location in the ring have been compared. This particular comparison is complicated by the fact that the SPU chamber had a diamond-like carbon surface, while the TE wave measurements spanned a longitudinal region which included an uncoated aluminum section of the chamber, as well as the SPU chamber. The SPU signal exhibits a non-linear response to the bunch current for low currents, while the electron cloud density extracted from the TE wave measurements shows a linear response, as expected. Simulations of the expected cloud density at this location, and of the SPU signal size, are in rough agreement with the density extracted from the TE wave measurements and the SPU data.

Chapter 6

Electron Cloud Induced Beam Dynamics

One of the key goals of the CesrTA research program is to improve our understanding of the interaction of the electron cloud with the high energy particle beam. This improved understanding is required to be able to extrapolate with confidence from the experimental conditions of CesrTA to the conditions expected for the ILC damping rings.

The interaction of the particle beam with the cloud can be studied by measuring the properties of the beam in the presence of the cloud. The key beam properties which are influenced by the cloud are the beam's closed orbit distortion (quite small, and not extensively studied with CesrTA), the frequency spectrum of the beam centroid's coherent dipole motion relative to this orbit, and the beam's transverse position distribution.

In CesrTA, the beam is formatted longitudinally into a train of short ($\sim$ 10 mm) bunches separated by an adjustable spacing (variable from a minimum of 4 ns, up to a maximum equal to the revolution period, about 2.5 μs). As described in Chapter 5, for sufficiently closely-spaced bunches, the electron cloud grows along the train, and so the cloud environment is different for each bunch. For this reason, it is critical that the beam dynamics measurement made to probe the cloud be done on a bunch-by-bunch basis.

The frequency spectrum of the coherent dipole motion of each bunch contains a wealth of information. In particular, this information includes

- the amplitude, frequency, and line shape of the betatron lines, which are sensitive to the electron cloud's electric field, to the mode of oscillation of the bunches in the train, and to the presence of multibunch instabilities;
- the amplitude, frequency, and line shape of "head-tail" lines, which are generally separated from the betatron lines by approximately the synchrotron frequency, and are sensitive to internal motion within the bunch driven by electron-cloud-induced single-bunch head-tail instabilities.

In addition, the time dependence of the amplitude of the betatron and "head-tail" lines, after bunch motion has been excited by an external source, provides information on the damping of these lines, which is related to aspects of the effective electron-cloud impedance not probed by tune measurements.

The transverse position distribution of each bunch is sensitive to

- emittance growth driven by single-bunch instabilities. Generally, this growth would be expected to be correlated with the observation of "head-tail" lines described in the previous paragraphs;
- incoherent emittance growth, driven by non-linear components of the electron cloud's electric field, which may take place before the onset of emittance growth driven by single-bunch coherent instabilities.

Incoherent emittance growth, if present, is critical to understand fully, since it could impact achieving the design emittance goals of the ILC damping rings.

For a full understanding of the observational data discussed above, comparison with simulations of the electron cloud is essential. The electron cloud build-up simulation programs discussed in Chapter 5 can be used to compute the expected betatron tune shifts, and comparison with the simulations allows the parameters of the effective ring-averaged electron cloud density sensed by the beam to be determined. Specialized simulation programs([94], [144]) have been written to model the interaction of the cloud and beam responsible for incoherent emittance growth and single-bunch instabilities.

In the sections below, the experimental hardware and techniques used to obtain the measurements are described (Section 6.1); the simulation tools and their applications to the measurements are discussed (Section 6.2); and the most important beam dynamics observations and comparisons with simulations are presented (Section 6.3). The final section presents a summary and discussion of future work.

6.1 Experimental Hardware and Techniques

CesrTA has been studying the effects of electron clouds on stored beams in order to understand their impact on future linear-collider damping ring designs. One of the important issues is the way that the electron cloud alters the dynamics of bunches within the train. Techniques have been developed for observing the dynamical effects of beams interacting with the electron clouds.

There are several beam parameters particularly relevant for the study of electron cloud effects. Since the electron cloud can produce focusing of the stored beam, measuring the betatron tunes of bunches along the train gives information about the density of the cloud along the length of the train. The electron cloud can also produce unstable motion in bunches later in the train. To observe the unstable motion, it is necessary to detect the amplitude of the betatron frequency and any other frequencies representing different modes of oscillation (e.g. head-tail modes) of bunches within the train. The unstable motion may also result in enlargement of the vertical beam size, thus the measurement of the vertical beam size for each bunch in the train is important. Before beam conditions approach the regime for the onset of unstable motion, it is possible to measure the damping of coherent motion of the bunches using drive-damp techniques. This method excites coherent dipole betatron modes or head-tail modes for each bunch within the train and then observes the damping of the motion. Thus it is possible to observe how the coherent motion becomes less stable before the onset of instability. The methodology and examples of typical measurements for these techniques are presented below.

6.1.1 Bunch-by-Bunch Tune Measurements

In the course of the CesrTA project, several different techniques have been utilized for making tune shift measurements for individual bunches within trains of bunches. These techniques, their benefits, and their limitations, will be described in this section.

6.1.1.1 Multi-bunch Large Amplitude Excitation

This method for observing the tunes of different bunches within the train consist of pulsing a pinger magnet with a single-turn excitation to deflect all of the bunches within the train, thereby starting an oscillation of their centroids. The CBPM system (see Sec. 2.4.1) is then is timed to read out a number of BPMs over several thousand turns for all bunches in the train (see block diagram in Fig. 2.106); the data acquisition is synchronized with the triggering of the pinger magnet's deflection. After recording the turn-by-turn bunch positions, the data is analyzed offline with a Fast Fourier transform (FFT), from which the betatron tunes are determined. During these measurements the peak horizontal and vertical beam displacements, for example, were typically 5 mm and 2 mm at 2.1 GeV and 5.3 GeV, respectively.

Since data from all bunches is recorded at the same time, it is relatively rapid to take data in one set of conditions and, since the data from all bunches is taken on the same turn, this method is relatively insensitive to any drifts in the storage ring tunes. However, the fact that all bunches are excited at the same instant implies that the lowest coupled-bunch mode is necessarily excited for the train of bunches. As discussed in Section 6.2.1.3, when the train is oscillating in this mode, the bunch-by-bunch horizontal tune shifts induced by the electron cloud in the dipoles are strongly suppressed, and difficult to measure. It is also the case that the pinger excitations are relatively large with respect to the stored beam's size: e.g., typically the vertical oscillation amplitude may exceed several ten's of vertical sigma. So the beam's oscillation is exploring a fairly large volume of the electron cloud charge distribution.

6.1.1.2 Single Bunch Small Amplitude Excitation

Another approach has been developed for bunch-by-bunch tune measurements. This approach excites only a single bunch in the train, thereby reducing the coupling from earlier bunches to the bunch that one is trying to measure. This is accomplished by driving both the horizontal and vertical stripline kickers (shown schematically for one stripline kicker in Fig. 6.1), using the external modulation input for the beam stabilization feedback system, which allows gating of the input signal into the appropriate timing window in order to excite only the bunch being measured. The source for the signal for the external modulation port comes from a frequency synthesizer, whose output frequency is swept across the range of betatron oscillation frequencies, covering the tunes for the entire ensemble of bunches. The frequency is swept with a saw-tooth at 500 Hz, driving the bunch in its dipole oscillation mode when the excitation frequency crosses the betatron resonance. The turn-by-turn position data is recorded for a number of BPMs using the CBPM system readout (as shown in the block diagram in Fig. 2.106) with the total number of turns sufficiently large to capture at least one excitation and damping cycle. The measurement process is repeated as the excitation's delay is stepped from one bunch to the next, resulting in a set of positions for all bunches at each delay. The data is analyzed offline with an FFT to give the oscillation frequency of the excited bunch and coupling of its motion to subsequent bunches via the electron cloud.

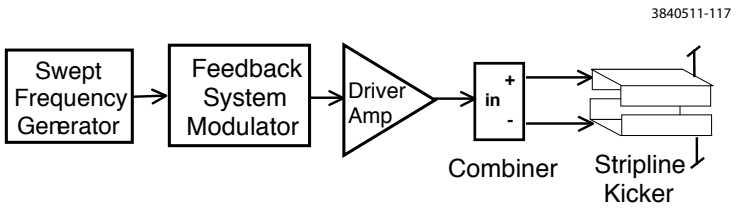

Figure 6.1: Single bunch excitation method using the stripline kicker, driven by a swept frequency source via the feedback systems external modulation port.

Some results are presented here to illustrate this technique; the data were taken with a 10 bunch train with a 14 ns spacing at 2.1 GeV beam energy conditions. Fig. 6.2 shows the horizontal position data for the fourth, fifth and sixth bunch, when only bunch number 5 was being excited. During the 2048-turns of the data-samples taken on simultaneous turns for the three bunches, it is clear that bunch 5 was excited with two complete cycles of the swept signal source. This is even clearer in Fig. 6.3 which shows the horizontal spectra of all 10 bunches when bunch numbers 1, 5 and 10 were being driven individually. The fact that the stripline kicker is driving only one bunch is quite evident in both Figures 6.2 and 6.3.

For comparison with the horizontal data, the matching set of vertical data is presented here for the same storage ring and electron cloud conditions as above. The vertical position data for bunches 4, 5 and 6 is shown in Fig. 6.4, when only bunch 5 is driven. Also the vertical spectra for all bunches are shown in Fig. 6.5, when bunches 1, 5 and 10 are individually excited. An interesting feature, visible in the vertical data, is that even though only one bunch is being driven, its motion couples to subsequent bunches in the train. Fig. 6.5 presents evidence that this coupling increases along the train, suggesting that the electron cloud may be playing a role in this bunch-to-bunch vertical dipole coupling.

This technique has the advantage of avoiding coupling from preceding bunches to the bunch being studied, while also providing information about the coupling of the motion of one bunch to later bunches via the electron cloud. The excitation level can, in principle, be tailored for the bunch that is being driven; the ability to keep a relatively fixed oscillation amplitude of the driven bunch could be important for conditions when the first bunches in the train are more stable but the latter bunches are not. This method has the drawback that it is slower than the preceding method, as it requires collecting turn-by-turn position data for every bunch times the number of bunches within the train. It is, therefore, sensitive to drifts in the tunes of the storage ring.

The sensitivity to drift of the tune during the measurement sequence is being addressed in the future by providing the capability of exciting the first bunch in the train, in addition to the bunch that is being studied. In this way, the tunes of the later bunches are measured with respect to the tune of the first bunch. Another feature which is being added is the ability to turn off feedback for the bunches which are being excited. This permits the train of bunches to be stabilized with feedback, while allowing the bunches which are being measured to have the longest damping time, permitting a more accurate tune measurement.

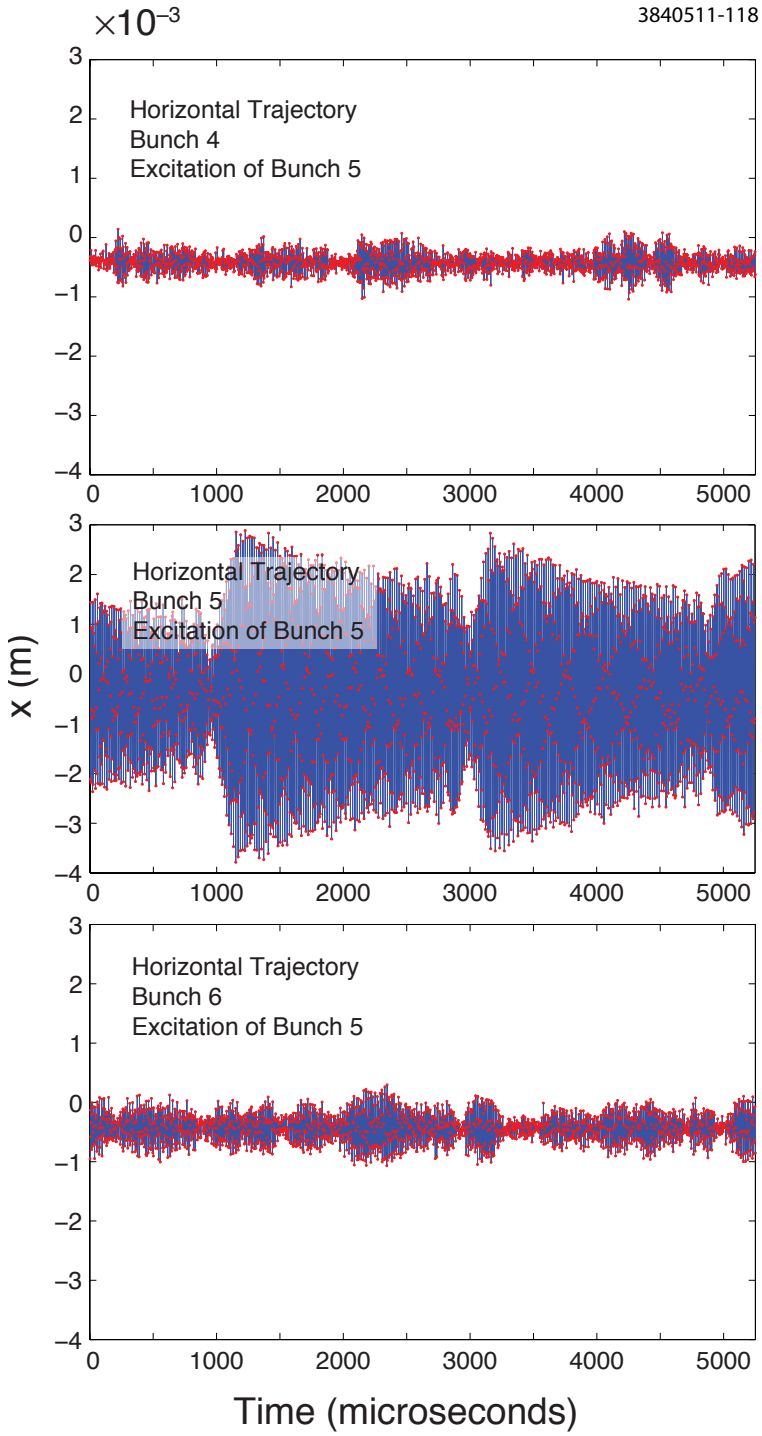

Figure 6.2: Horizontal position of bunches 4, 5 and 6 (respectively for the top, middle and bottom plots) for a 10-bunch train when only bunch number 5 was excited.

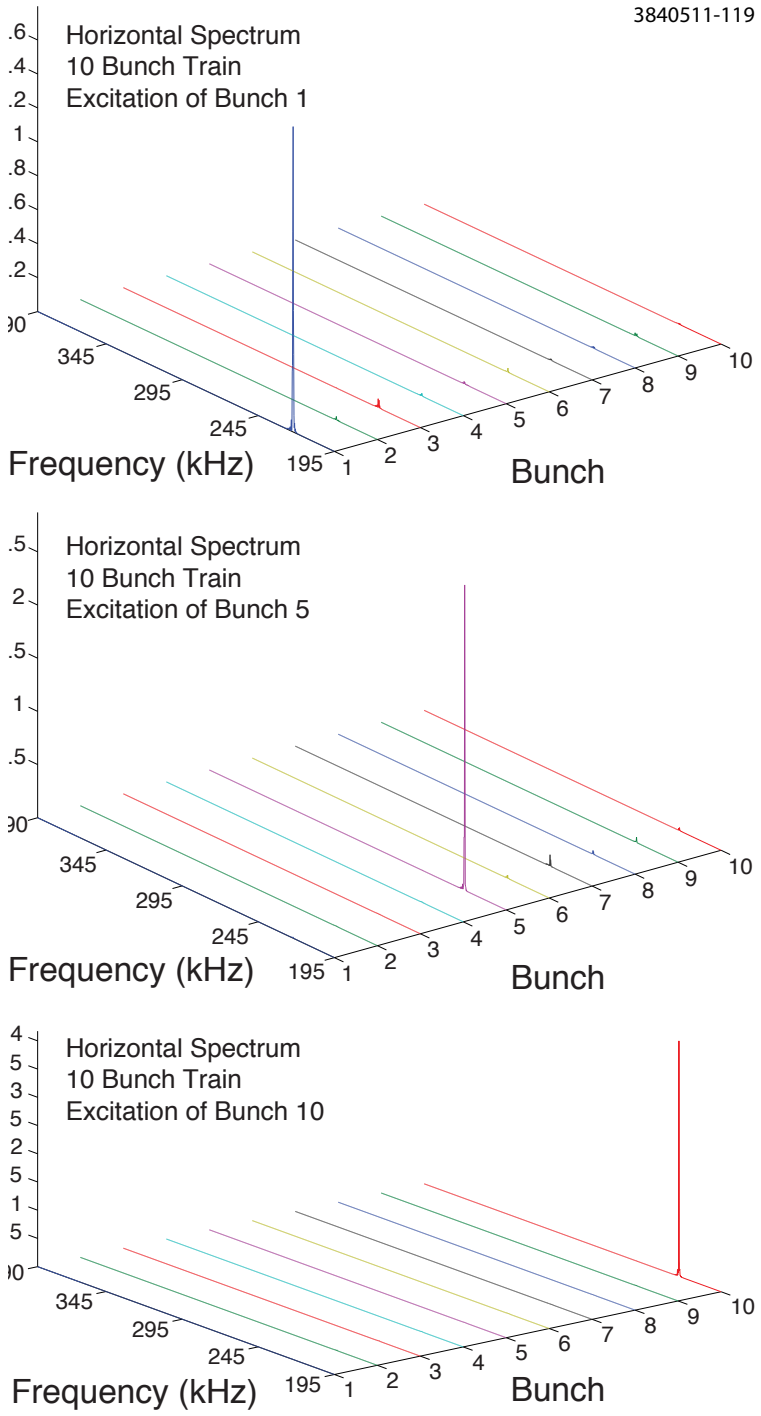

Figure 6.3: Horizontal position spectra of all bunches in a 10-bunch train when bunches number 1, 5 and 10 (respectively for the top, middle and bottom plots) were driven individually.

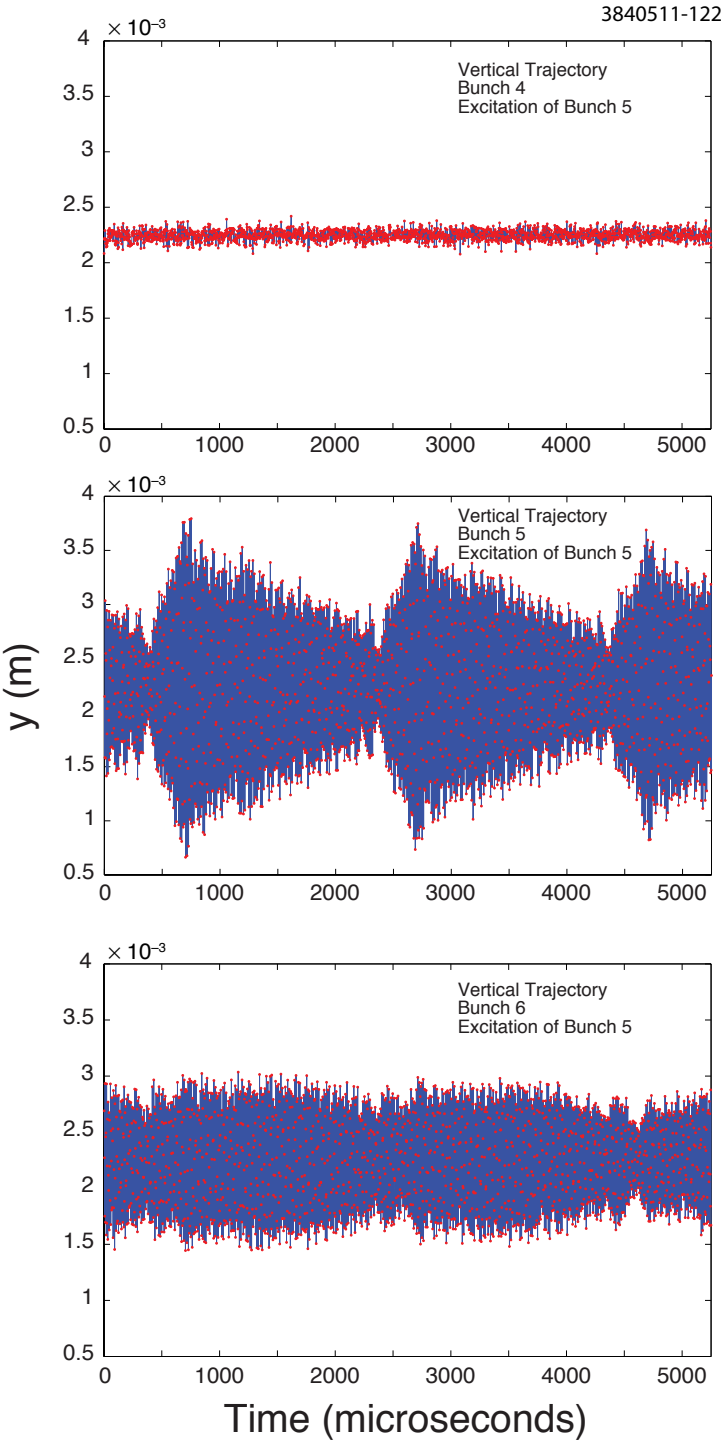

Figure 6.4: Vertical position of bunches 4, 5 and 6 (respectively for the top, middle and bottom plots) for a 10-bunch train when only bunch number 5 was excited.

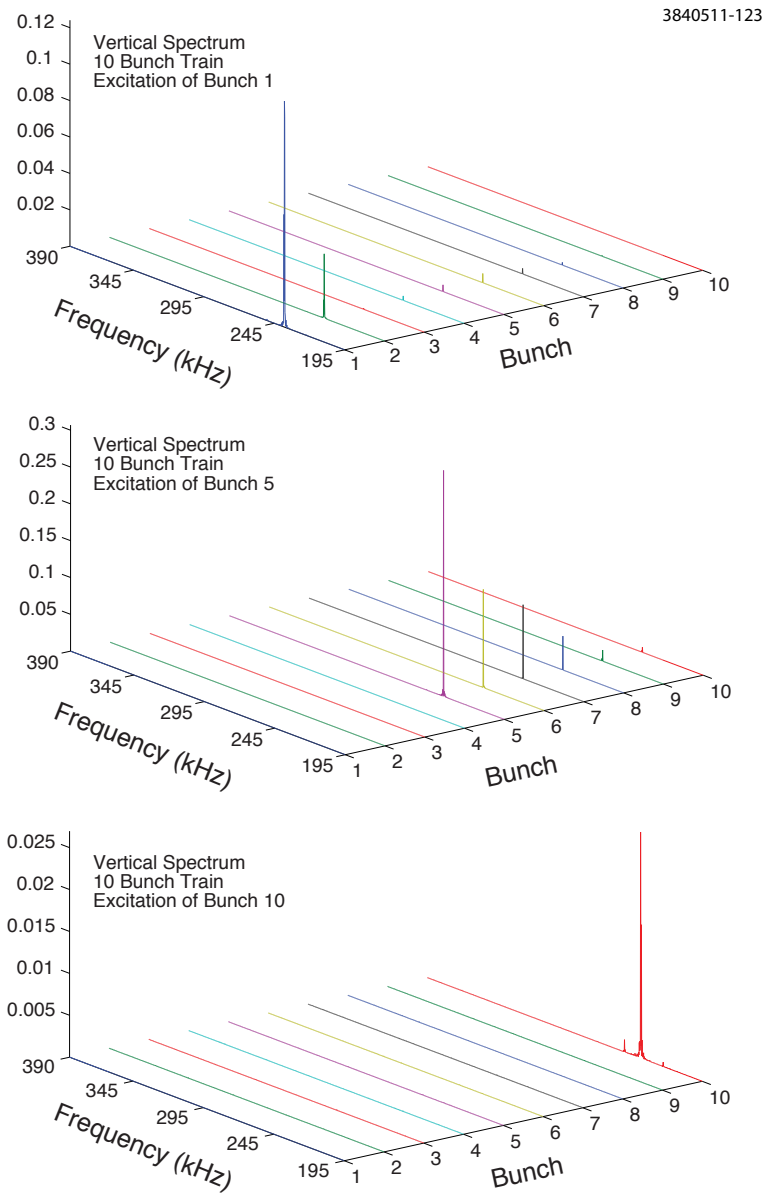

Figure 6.5: Vertical position spectra of all bunches in a 10-bunch train when bunches number 1, 5 and 10 (respectively for the top, middle and bottom plots) were driven individually.

6.1.1.3 Feedback System Response

Another approach for tune measurements became apparent after the installation of the Dimtel[1] feedback electronics, capable of damping bunches with spacings down to 4 ns. While looking at the FFT of the position for a single bunch as part of the feedback system diagnostics, it was observed that the signal amplitude varied as a function of the feedback gain. At low gains the betatron peak is visible, but as the gain is increased the amplitude of the peak decreases until it become a notch in the spectrum at high gain. The notch is created by the feedback system, whose phase is adjusted to suppress the broadband excitation of the beam preferentially at the betatron frequency. When the feedback settings have been fully optimized, the notch in the spectrum for each bunch marks the location of its betatron oscillation frequency.

The position data generally represents the effect of probing the electron cloud in a regime when the bunches are moving at small amplitudes. An example of data taken using this method is seen in Fig. 6.6. There is a very clear trend for the vertical focusing effect from the accumulating electron cloud, which is visible the plot. Although this method is quite appealing, only a few tune shift measurements have been performed via this method. This technique works well for 4 ns-spaced bunches, but it requires fairly exact adjustments of the feedback system parameters to be able to clearly identify the notches in the bunch spectra. To obtain the most accurate spectra, the data for each bunch is averaged typically for 30 seconds, allowing some variation in the tunes due to longer-term drifts in the storage ring focusing.

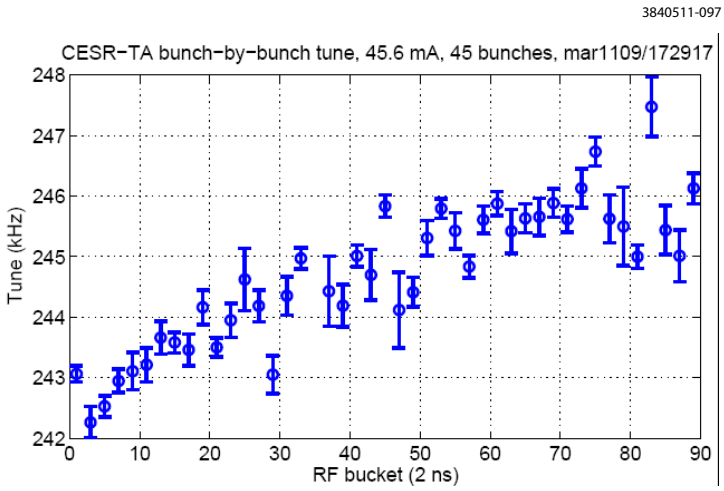

Figure 6.6: Vertical tune vs. RF bucket number for a train of 45 bunches with 4 ns bunch spacing determined from notches in the spectra from the feedback error signal.

6.1.1.4 Self-Excitation

The last method utilized for bunch-by-bunch tune shift measurements is a by-product of the observation of beam instabilities, described in the next section. In this set of measurements the position spectrum of each bunch is measured with a gated spectrum analyzer. Two of the peaks that are visible in these self-excited spectra are the horizontal and vertical dipole modes. The shift of the

[1] Dimtel Inc., www.dimtel.com.

tunes as the gate is moved from bunch to bunch are easily detected via this method. Since most of these measurements are taken in conditions when the beam is above or near an instability threshold for at least some of the bunches within the train, the self-excited amplitudes of the dipole motion will vary along the train. This method is quite sensitive to low signal levels, with the noise floor for small amplitude oscillations at the level of 0.4 μm-rms horizontally and 0.2 μm-rms vertically. Due to averaging in the spectrum analyzer, the data acquisition requires about 1 minute for each bunch, which is long enough to make this method sensitive to drifts in the storage ring tunes.

6.1.2 Instability Measurements

An important set of CesrTA measurements focuses on beam instabilities due to the electron cloud. These studies measure the growth of self-excited oscillation amplitudes of the bunch centroids and the growth of vertical beam size along the train under various accelerator and electron cloud conditions. The first piece of hardware utilized for these measurements is a monitor for the bunch-by-bunch beam position. The other detection system required is the xBSM monitor for determining the vertical beam size of each bunch.

6.1.2.1 Bunch-by-Bunch Position Spectra

For instability studies, the bunch-by-bunch position measurements are accomplished by a BPM detector connected to one of CESR's original relay-based BPM system processors, which in turn passes its video output signal to a spectrum analyzer in the control room. (See Section 2.4.3.2 and Fig. 2.107 for a further description of the hardware.) BPM33W, which is located at a high vertical beta point, has generally been used as the detector for these observations. The signal is taken from one button, making it sensitive to both the horizontal and vertical motion. The data-taking software sets the trigger delay for the sampling gate to select a particular bunch within the train. For almost all of the data, an RG-174 coaxial cable is placed within the signal path to limit the bandwidth of the button signal (giving an effective 20 dB of signal attenuation) and to this an additional 12 dB of amplification is added. The signal is then sent to the biased peak rectifier circuit, which has an effective bandwidth of 700 MHz, and a decay time constant of approximately 5 μs. The resulting video signal is buffered and sent on a wide-band coaxial cable to a spectrum analyzer in the control room.

The spectrum analyzer is a Hewlett Packard model 3588A, operating in the baseband (in these studies the center frequency ranges from 190 kHz to 310 kHz) in "Narrowband Zoom" mode with a 40 kHz span. This mode of operation performs a $\pm$20 kHz FFT on time slices of the signal and these spectra are averaged for 100 time slices, taking about 10 seconds for each 40 kHz step of the center frequency. At 2.1 GeV the position sensitivity of the signal from the BPM at 33W was measured to be

$$\begin{aligned} x_{\rm rms} &= x_0/I_b({\rm mA}) \times 10^{A_x({\rm dBm})/20} \\ y_{\rm rms} &= y_0/I_b({\rm mA}) \times 10^{A_y({\rm dBm})/20} \end{aligned} \tag{6.1}$$

where $x_0 = 81.3$ mm and $y_0 = 45.3$ mm, when the RMS bunch length was approximately 10 mm. A_x and A_y are the amplitudes measured on the spectrum analyzer in dBm. With this gain configuration and over the frequency range of study, the noise baseline falls from -95 dBm to -105 dBm

(corresponding in the vertical direction, respectively, to displacements of 1.1 μm-rms to 0.33 μm-rms for a 1 mA bunch.)

Representative self-excited spectra of the first and last bunch in a 30-bunch positron train at 2.1 GeV are shown in Figs. 6.7 and 6.8. For this train the horizontal tunes are in the range from 212 kHz to 218 kHz, and the vertical tunes are in the range from 224 kHz to 227 kHz. Since this spectrum overlaps the 1/2 integer resonance at 195 kHz, this frequency is a reflection point for the spectra. For bunch 30, additional lines are visible in the ranges 198-201 kHz and 250-252 kHz; these correspond to vertical head-tail modes as their frequencies are plus and minus the synchrotron oscillation frequency added to the vertical tune. The baseline is seen to be falling as roughly a $1/f$ noise spectrum. There are also a number of unrelated noise lines, scattered throughout the spectra assumed to be due to"cultural noise sources." A"mountain-range" plot of the spectra of all 30 bunches within a 30 bunch-long train is shown in Fig. 6.9. A cut of the spectrum has been made at the half integer resonance (195 kHz) to suppress the "reflected" spectral lines. In this plot the self-excited vertical tune amplitude begins to grow at approximately bunch 10 and continues to grow in amplitude until near bunch 20. In this region the two vertical head-tail lines appear above the noise background. Also around bunch 15 the spectral peak of the horizontal tune appears to bifurcate, something which is also seen in Fig. 6.8, and on close examination these data also show bifurcation of the vertical tune and the vertical head-tail lines for the last bunches in the train. Fig. 6.9 also shows a number of "fences", i.e. peaks in the spectrum at fixed frequencies due to external "cultural noise sources."

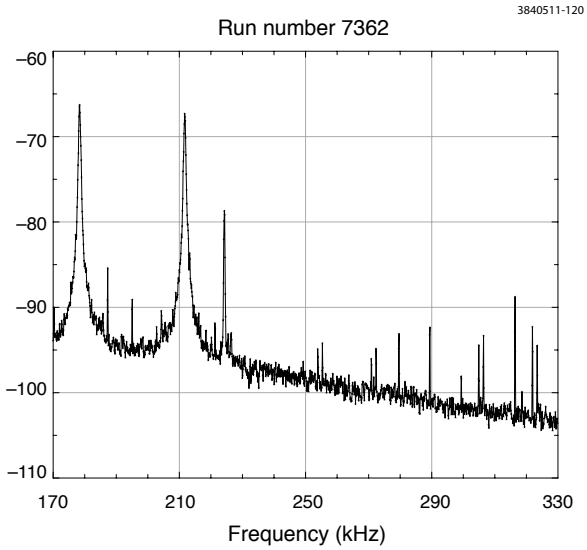

Figure 6.7: Self-excited beam power spectrum for bunch 1 in a 30 bunch-long positron train at 2.1 GeV beam energy. Since this spectrum overlaps the 1/2 integer resonance at 195 KHz, this frequency is a reflection point for the spectra. Thus the peak at 178 KHz is a reflection of the peak at 212 KHz.

Many tests have examined the self-consistency and interpretation of the data. The identification of the vertical and horizontal tunes was checked by changing the controls for each separately and verifying which spectral peak moved. They were also checked using BPMs at other locations, which had buttons summed to produce dominantly horizontally- or vertically-sensitive detectors. The interpretation that the vertical head-tail lines were not inter-modulation distortion components

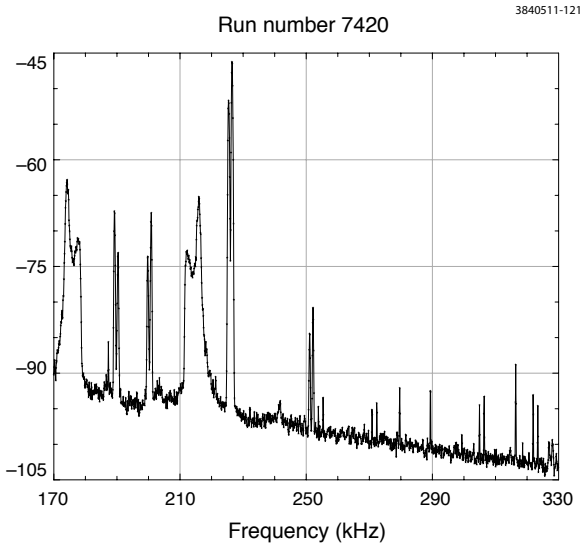

Figure 6.8: Self-excited beam power spectrum for bunch 30 in a 30 bunch-long positron train at 2.1 GeV beam energy.

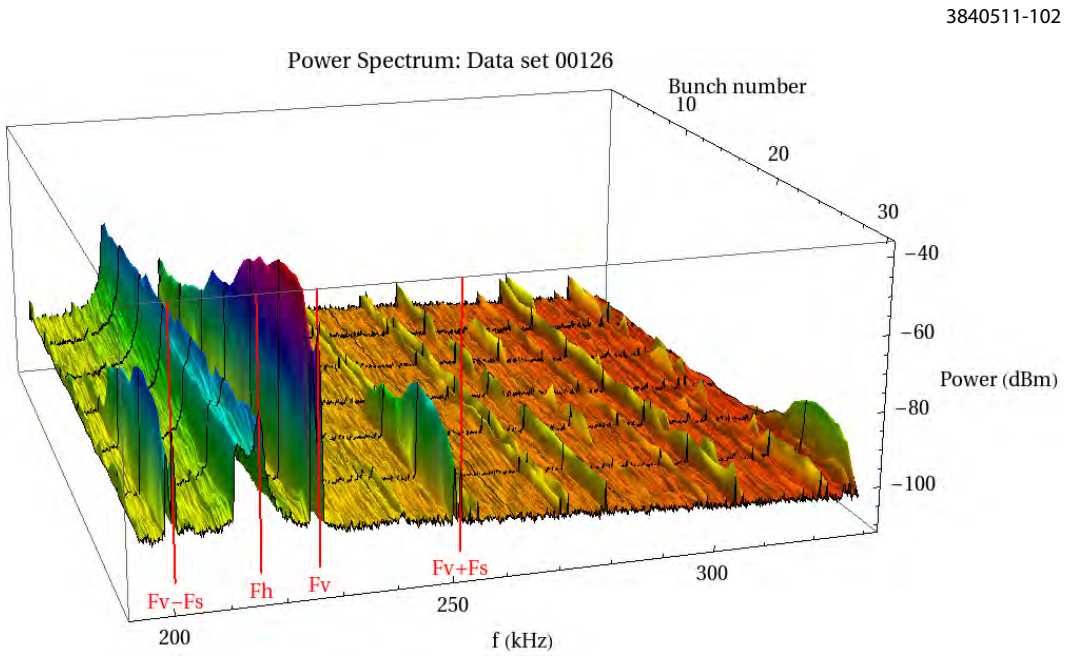

Figure 6.9: Self-excited beam power spectra for bunches 1 through 30 in a 30 bunch-long positron train at 2.1 GeV beam energy. The horizontal axis is the frequency, the vertical axis is the spectral power in dB and the axis into the page is the bunch number with bunch 30 being in the foreground. Red vertical lines in the foreground denote in ascending order the location of the $m = -1$ vertical head-tail line, the horizontal tune, the vertical tune and the $m = +1$ vertical head tail line.

coming from the processing electronics was tested by switching a 6 dB attenuator into the signal path upstream of the peak detector and observing the change in both horizontal and vertical spectral peaks. If the head-tail lines were actually inter-modulation cross-products from the non-linearity of the electronic processing, then they would have decreased by 12 dB, and they only decreased by 6 ± 2 dB.

Although this method for detecting the frequency spectra of the bunches is fairly sensitive, the measurements must be made separately for each individual bunch. The measurement time is about 1 minute per bunch for the selected frequency range. This means that the data represents a time-average of any unstable motion over this period. In addition, due to the finite beam lifetime, the beam must be refilled a number of times during data-taking for one set of conditions. In our case, we choose typically to refill after measuring spectra for five bunches. When these spectra are plotted, the beam intensity decay over five bunches gives the amplitude for the peaks within the spectrum a slightly scalloped shape. This refilling cycle coordinates fairly well with the cycle to measure and readout the bunch-by-bunch and turn-by-turn xBSM data.

We have tried to read out the turn-by-turn and bunch-by-bunch positions from a number of BPMs via the CBPM system (which has a much faster data acquisition time). Unfortunately the head-tail lines are not visible above the noise floor in the CBPM data. Our explanation is that the relay BPM system peak rectifies the position signal and, if there is a temporal variation due to head-tail motion, the arrival time of the signal varies correspondingly. This gives a frequency modulation to the position signal when viewed by the spectrum analyzer. The CBPM processing is different: the signal is sampled at a fixed time corresponding to the positive peak of the button BPM pulse. Any variation in the arrival time produces only a second order variation in amplitude and, even if one moved the sampling time significantly off of the peak, it does not produce any observable signal at the head-tail line frequencies.

6.1.2.2 Bunch-by-Bunch Beam Size

At CesrTA, bunch-by-bunch beam sizes are measured using an x-ray monitor (xBSM: see Sec. 2.4.2) built on the D Line of the CHESS light source for viewing positrons, as shown in Figure 6.10. (A similar line for viewing electrons is installed at the C Line.) The detector can read out bunch-by-bunch, turn-by-turn signals at 14 ns or 4 ns spacing. Three sets of x-ray optics can be selected in the optics box: Coded Aperture (CA), Fresnel Zone Plate (FZP) and an adjustable slit. The coded aperture mask permits single-shot, photon-statistic-limited resolutions of $\sim 2-3$ μm at beam sizes of 10-20 μm[145].

During a given set of instability measurements, typically xBSM data were taken using all three sets of optics. This allows the greatest range of sensitivity for measurements of the vertical size and centroid motion of the beam. During the measurement cycle, the beam size data are taken bunch-by-bunch and turn-by-turn generally immediately after the train has been topped off, which usually occurs after taking the frequency spectrum for every fifth bunch.

6.1.3 Mode Growth Rates

A complement to the instability measurements, described in the preceding section, are the damping rate measurements for the coherent transverse modes. The instability measurements easily record the large amplitude coherent signals as the bunches become unstable and ultimately limit due

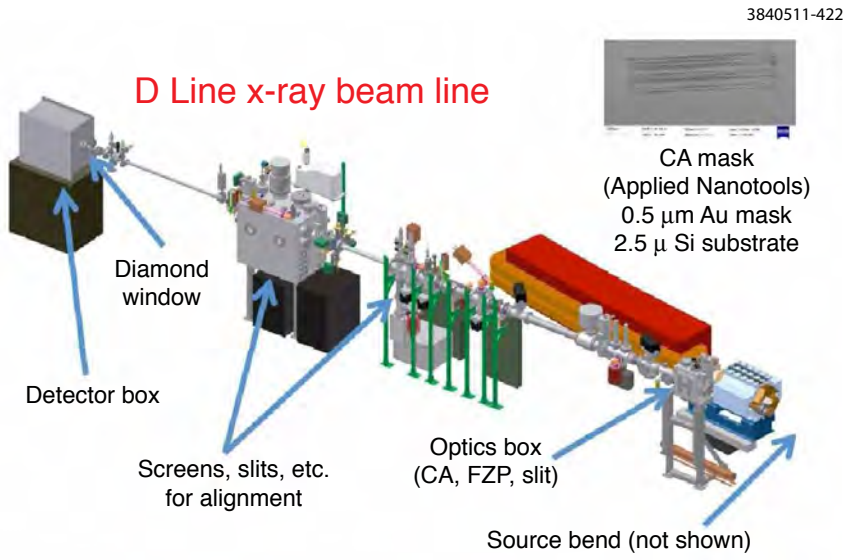

Figure 6.10: Layout of x-ray beam line for viewing positron beams at CesrTA.

to non-linearities in the bunch dynamics. However, the damping measurements give information about the stability of the bunch at small amplitudes before the bunch goes unstable, the regime in which storage rings and damping rings will actually operate. These studies give some insight about how the beam instability begins developing as one looks from earlier to later bunches along the train.

6.1.3.1 Drive-Damp Excitation: Method

The basic idea for these observations is to employ the same relay BPM configuration as is used for the instability measurements. However, the spectrum analyzer's center frequency is adjusted to be at either the vertical betatron dipole-mode frequency or one of the head-tail mode frequencies while the spectrum analyzer is set to be in "Zero Span" mode. In this mode the analyzer functions as a tuned receiver with its display producing signal amplitude vs. time. The spectrum analyzer's tracking generator output is sent to the vertical feedback system's external modulation input. Aside from the spectrum analyzer's control settings, this is quite similar to the hardware configuration shown in Fig. 6.1. By adjusting the digital timing controls for the feedback modulator's external input, it possible to drive only one bunch, as long as the bunch spacing is greater than 6 ns (if the bunch spacing is 4 ns, then the duration of the pulse on the beam stabilizing feedback system stripline kicker is long enough to deflect the bunch under study and also slightly deflect the following bunch). To permit the drive-damp modulation of the beam, there is one additional element added to the block diagram of Fig. 6.1. This element is a modulating gate for the spectrum analyzer's tracking generator signal. The modulator gate is timed with the spectrum analyzer's timing sweep to pass the tracking generator output for 3 ms at the beginning of the sweep and then to gate off its output until the start of the next sweep.

An illustration of the timing and the expected signal response are shown in Fig. 6.11. The red curve shows that the amplitude of the transverse excitation of the bunch vs. time is an impulse. The expected beam response initially grows during the driving impulse, usually reaching a saturated

level, and then decays exponentially after the drive is switched off (shown in the logarithmic plot as a linear decrease vs. time). If the frequency of the spectrum analyzer tracking generator is tuned away from the bunch resonant frequency, the decaying response can have more than one frequency component, resulting in periodic oscillatory beats. So during the measurement it is necessary to make small tuning adjustments to the excitation frequency to produce the most exponential decay possible.

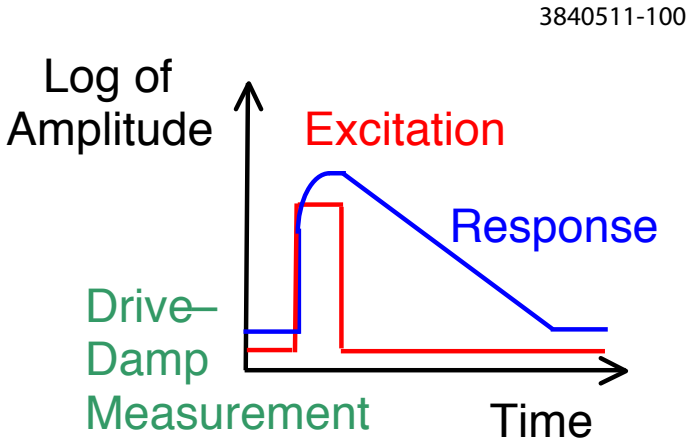

Figure 6.11: Illustration of the drive-damp measurement: The red trace is the amplitude of the excitation driving the bunch. The blue trace is the bunch response.

The excitation of the bunch is accomplished in a somewhat different manner for the betatron dipole mode and the head-tail modes. In both cases the frequency of the spectrum analyzer is set to drive the coherent mode frequency being measured. However, for the head-tail modes it is necessary to also continuously drive the external modulation input for RF cavity phase at the synchrotron oscillation frequency. This imposes a longitudinal energy oscillation on all of the bunches within the train, causing them to uniformly shift their arrival times and displace the train centroid horizontally proportional to the local dispersion. The typical amplitude of this oscillation is relatively large, with the peak fractional energy varying as much as $\pm 7.6 \times 10^{-3}$ for all of the bunches within the train. Due to the RF systems non-linearities, there may be some increase in the energy spread (and bunch length) of the bunches. In the presence of the large energy variation, the transverse field from the stripline kicker deflects the lower energy particles in the bunch (displaced toward the head of the bunch) more than the higher energy particles (displaced toward the tail of the bunch.) Although this is a fairly small differential effect, the bunch is being driven on the head-tail resonance, allowing the oscillation amplitude to build up.

6.1.3.2 Drive-Damp Excitation: Examples

Two examples of actual drive-damp measurements are found in Figs. 6.12 and 6.13. In Fig. 6.12 the betatron dipole mode amplitude ramps up for the first 3 ms and then decays exponentially thereafter. Fig. 6.13 shows one of the head-tail modes being excited. The initial 7 dB drop in the amplitude of the signal represents the off-resonance excitation of the dipole mode, which

immediately switches to oscillating at its resonant frequency (outside of the bandwidth of the receiver) when the drive turns off; the roughly exponential shape thereafter is the head-tail mode decay. As a test, the longitudinal drive to the phase of the RF cavity was turned off, and the head-tail mode exponentially damped signal was observed to vanish.

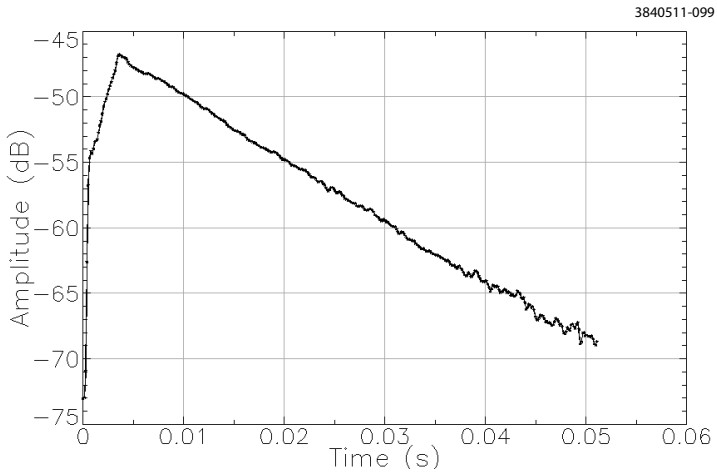

Figure 6.12: Drive-damp measurement: The trace is the response for the bunch being driven at the vertical betatron frequency. The vertical and horizontal scales are 5 dB and 10 ms per division, respectively.

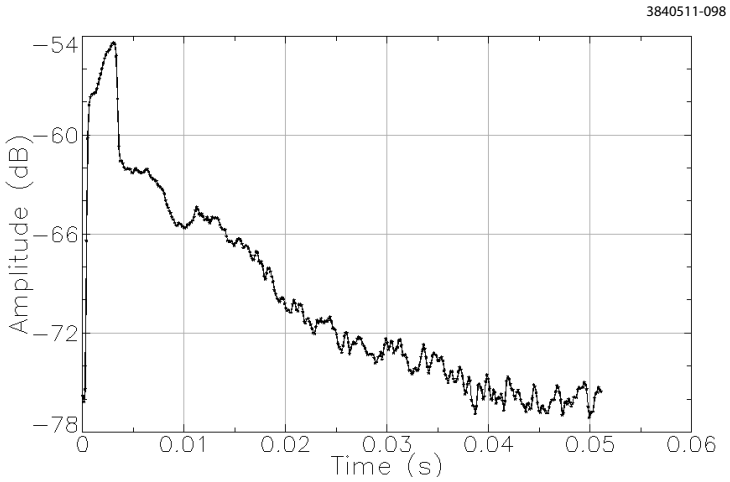

Figure 6.13: Drive-damp measurement: The trace is the response when one of the head-tail modes is excited. The vertical and horizontal scales are 6 dB and 10 ms per division, respectively.

This type of measurement may be very useful for understanding the behavior of bunches within the train before their motion becomes unstable. However, even though much of the data acquisition is automated, there are a few steps which must be completed manually. In particular the fine adjustment of the spectrum analyzer frequency (centering it on the coherent mode frequency) is necessary to optimize the exponential damping curve. The manual adjustment of the frequency makes this type of measurement fairly time-consuming. Routinely, after data is taken for several bunches, the beam is topped off. Beam size measurements are typically taken immediately after

topping off.

6.2 Simulation Tools

6.2.1 Bunch-by-Bunch Tunes

6.2.1.1 General Methodology for Computing Tune Shifts due to the Electron Cloud

In this section, we discuss in a simplified form the methodology used to compute the tune shifts due to the electron cloud. We discuss only vertical motion, in a constant-β lattice. The extension to a real lattice is treated below. The generalization to the horizontal plane is straightforward.

For a constant-β lattice, and in the absence of any perturbing effects, the equation of vertical coherent motion of the beam centroid y_b, relative to the closed orbit, is

$$\frac{d^2 y_b}{dt^2} + \omega_\beta^2 y_b = 0. \tag{6.2}$$

The betatron frequency is

$$\omega_\beta = (N + \delta_\beta)\omega_0, \tag{6.3}$$

in which N is the integral part of the tune and ω_0 is the revolution frequency.

In the presence of an electron cloud whose centroid position is y_c, which generates an electric field $E_y(y, y_c)$, the equation of motion is modified to

$$\frac{d^2 y_b}{dt^2} + \omega_\beta^2 y_b = \frac{e\langle E_y(y_b, y_c)\rangle}{m_0 \gamma}. \tag{6.4}$$

The brackets indicate an average over the beam transverse distribution, which is required to describe the coherent tune shift of the whole beam. In principle, this equation also applies for each longitudinal slice of the beam; for simplicity, we suppress that dependence here, but will include it in the final result.

For small oscillations of the beam, the presence of the cloud introduces a betatron frequency shift, which is proportional to the coefficient of y_b in a Taylor expansion of the right-hand side of this equation about $y_b = 0$.

6.2.1.2 Static Cloud Model

If the position of the cloud centroid y_c is fixed, independent of y_b, then a Taylor expansion of the field about $y_b = 0$ is

$$\langle E_y(y_b, y_c)\rangle = \langle E_y(0, y_c)\rangle + y_b \frac{\partial \langle E_y(0, y_c)\rangle}{\partial y}. \tag{6.5}$$

In this case, the tune shift is proportional to the average field gradient

$$\frac{\partial \langle E_y(0, y_c)\rangle}{\partial y}$$

evaluated at the beam centroid.

In general, however, this "static cloud model" is a poor one. The electron cloud is a dynamic system, which is both generated by the beam, and also driven and focused by the beam.

6.2.1.3 Dynamic Cloud Model

To lowest order, the dynamic motion of the cloud can be treated in this simple model by recognizing that the position of the cloud, y_c, is in fact not independent of the position of the beam. The field depends on the beam position y_b not only directly, but also because the location and shape of the cloud depends on the beam position. This latter dependence comes about because of correlations between the given bunch and the position of previous bunches which generated the cloud, and also because the cloud can be driven and focused as the beam passes through it. The linear part of this additional dependence of the electric field on y_b will be a term in the equations of motion of the bunch which will contribute to the tune shift.

Thus, in this case the Taylor expansion should be written

$$\langle E_y(y_b, y_c(y_b))\rangle = \langle E_y(0, y_c(0))\rangle + y_b \left.\frac{d\langle E_y(y, y_c(y))\rangle}{dy}\right|_{y=0} \tag{6.6}$$

$$= \langle E_y(0, y_c)\rangle + y_b \left(\frac{\partial\langle E_y(0, y_c(0))\rangle}{\partial y} + \frac{\partial\langle E_y(0, y_c(0))\rangle}{\partial y_c} \left.\frac{dy_c}{dy_b}\right|_{y_b=0} \right). \tag{6.7}$$

The tune shift is proportional to to the term

$$\left(\frac{\partial\langle E_y(0, y_c(0))\rangle}{\partial y} + \frac{\partial\langle E_y(0, y_c(0))\rangle}{\partial y_c} \left.\frac{dy_c}{dy_b}\right|_{y_b=0} \right).$$

Under some general conditions, the second term in parentheses can have a significant effect. It can even cancel most of the first term, leading to a very small tune shift. For example, suppose the beam-averaged electric field $\langle E_y(y, y_c)\rangle$ depends primarily on the difference $y - y_c$ rather than on y and y_c separately,

$$\langle E_y(y, y_c)\rangle \approx f(y - y_c). \tag{6.8}$$

Further suppose that, as is typically true in the horizontal plane in dipoles, the centroid of the cloud is closely aligned with the centroid of the beam. Finally, suppose that a train of bunches is oscillating in the lowest frequency coherent mode, for which the centroids of all the bunches have the same displacement. Then the cloud generated by this train will have $y_c = y_b$, and the expression given above shows that the tune shift due to the electron cloud in the dipoles could be very small in this case. This is precisely what is observed for many of the horizontal tune measurements at CesrTA, when the train is "pinged" (i.e, excited in the lowest frequency coherent mode.)

If each bunch in excited individually, then there is no correlation between the center of the cloud generated by previous bunches, and the bunch position. In this case, $\left.\frac{dy_c}{dy_b}\right|_{y_b=0} = 0$. The total derivative is then determined (if we neglect the"pinch") just from the partial derivative of the field with respect to y, as in the static cloud model.

6.2.1.4 Tune Shift from Electron Cloud Buildup Simulations

Electron cloud buildup simulation programs such as `ECLOUD` [89, 90] and `POSINST` [71, 86] can be used to compute the tune shifts approximately, using the static cloud model described above, or more accurately, using the dynamic cloud model.

Modified Static Cloud Model In the static cloud model, the coherent tune shifts are proportional to the field gradient generated by the electron cloud space charge field, averaged over the beam transverse profile. For a finite length bunch, this quantity must also be averaged over the bunch normalized longitudinal distribution $\rho(z)$:

$$\Delta Q_y \propto \int dz \rho(z) \frac{\partial \langle E_y(0, y_c(z), z) \rangle}{\partial y}, \tag{6.9}$$

in which we have explicitly indicated the longitudinal (z) dependence of the field gradient. This field gradient can be computed from the electron cloud simulation results.

As noted above, the static cloud model is a very poor approximation. It neglects both dynamical motion of the cloud on the time scales of the bunch spacing, and also on the time scale of the bunch duration. A significant improvement to the model can be made by incorporating a dynamical correction $D(z)$ on the bunch time scale in the integral above; this correction is discussed in detail in Ref. [146]. In essence, this correction accounts for dipole motion of the cloud during the bunch traversal; that is, it includes the effect of a simple approximation for the dipole short-range wake field of the cloud on the tune shift.

The tune shift including this correction can be written

$$\Delta Q_y^* \propto \int dz \rho(z) D(z) \frac{\partial \langle E_y(0, y_c(z), z) \rangle}{\partial y}. \tag{6.10}$$

In Ref. [146], a simple model for the electron cloud wake is used to show that, for short bunches, the effect of the correction factor $D(z)$ is that the tune shift is approximately given by

$$\Delta Q_y^* \propto \frac{\partial \langle E_y(0, y_c(-\infty)), -\infty) \rangle}{\partial y} \tag{6.11}$$

in which evaluation at $z = -\infty$ corresponds to the field gradient evaluated just before the bunch enters the cloud.

We have verified[2] the approximate accuracy of Eq. (6.11) by evaluating the correction numerically using `POSINST` simulations, and comparing with results computed using the "Dynamic cloud model".

We refer to the use of Eq. (6.11) for the tune shift calculations as the "modified static cloud model". It approximately corrects for dynamic cloud motion on the time scale of the bunch duration, but not on the time scale of the bunch train.

Dynamic Cloud Model An accurate estimate of the tune shift, in which all dynamic cloud effects are included, can be obtained from the electron cloud buildup simulation programs `POSINST` or `ECLOUD`, by using the option which allows the bunches to be offset in the simulations. For example, suppose that one wishes to compute the tune shift of bunch n, which interacts with a cloud generated by the preceding $n-1$ bunches in a train. The method is to perform a buildup simulation for all n bunches, in which bunch n is displaced by a small offset δ. If the train is excited in a coherent mode for which there is a correlation between the offset of the n^{th} bunch and previous bunches, this correlation must be included when the buildup simulation is done.

[2] CesrTA Electron Cloud meeting notes, G. Dugan, 1/7/2009

For example, if the lowest coherent mode of the train is excited, then all bunches should be given the same offset δ. If only bunch n is excited, then the offset of previous bunches is zero. Then, from the simulation, the beam-averaged electric field at longitudinal position z along the length of bunch n is computed numerically: using the terminology of the preceding section (but with z dependence), this is

$$\langle E_y(\delta, y_c(\delta, z), z)\rangle$$

Another simulation is done, with the sign of δ changed. Then, the total derivative which enters into the tune shift calculation is

$$g_y(\delta, z) = \left.\frac{d\langle E_y(y, y_c(y, z), z)\rangle}{dy}\right|_{y=0} \approx \frac{\langle E_y(\delta, y_c(\delta, z), z)\rangle - \langle E_y(-\delta, y_c(-\delta, z), z)\rangle}{2\delta}. \tag{6.12}$$

The coherent tune shift is proportional to the average of this quantity over the bunch normalized longitudinal distribution $\rho(z)$:

$$\Delta Q_y \propto G_y(\delta) = \int dz \rho(z) g_y(\delta, z). \tag{6.13}$$

The integral is to be taken over the length of the bunch. Since the full dynamical evolution of the electron cloud in response to the beam is included in the buildup simulations, including any cloud motion which occurs during the bunch, this method also accounts properly for the "pinching" that occurs during the passage of the bunch.

Ideally, the value chosen for δ is close to the actual displacement given to the beam during the tune measurement. For self-excited tune measurements, $G_y(\delta)$ should be extrapolated close to the limit $\delta \to 0$.

We refer to the use of Eq. (6.13) for the tune shift calculation as the "dynamic cloud model".

Calculation of the Electric Field

`POSINST` The cloud buildup code `POSINST` generates a two-dimensional distribution of macro-electrons within the vacuum chamber, which represent the electron cloud in a given magnetic environment (e.g., drift or dipole) any point in time. For each macro-electron, the beam-averaged electric field components $\langle E_x\rangle$ and $\langle E_y\rangle$ generated by the macro-electron in a vacuum chamber (i.e, including the image charges) are computed analytically, assuming a Gaussian transverse beam distribution. Then, the total electric field of the cloud is obtained by simply summing the contributions from the individual macro-electrons.

`ECLOUD` The `ECLOUD` code computes the electric field sourced by the cloud macro-electrons by first clustering them on a 81×81 Cartesian grid over a 9×5 cm region, then summing the contribution of each grid node, accounting for the boundary conditions of an elliptical vacuum chamber with semi-axes 4.5×2.5 cm by means of 50 image charges. The time-sliced cloud dynamics model includes the 2D electrostatic force from the Gaussian beam (Basseti-Erskine) and the force from any ambient magnetic field. The magnetic field kick is calculated in three dimensions, thus adding longitudinal momentum to any longitudinal components generated when the macro-electrons are produced. For the purpose of the tune shift calculations with displaced beams, the beam-averaged electric field value is calculated via a Gaussian-weighted sum of field values over a 7×7 grid spanning a $3\sigma \times 3\sigma$ region centered on the beam position.

6.2.1.5 Ring Averaging

To compute the total tune shift for a particular ring and lattice, we use

$$\Delta Q_y = \frac{e}{4\pi E} \oint ds\ \beta_y(s) G_y(s). \tag{6.14}$$

in which G_y represents the field difference, computed from a cloud simulation program, as described in the previous section. s is the longitudinal coordinate around the ring. At any point s in the ring, the quantity G depends, in general, on the type of beamline magnetic environment at that location (i.e., drift, dipole, wiggler, quadrupole., etc.), the transverse beam size at that location, and the azimuthal distribution of radiation intensity per unit length (photons per beam particle per meter) at the point s.[3]

Since the transverse size of the cloud is typically much larger than the transverse size of the beam, the dependence of G on the transverse beam size is weak. For simplicity, we neglect part of this dependence, and use the ringwide averaged transverse beam size for each magnetic environment in the cloud simulation used to compute G for that magnetic environment.

Let p be the normalized polar angle which measures a point on the vacuum chamber wall. If we let $N(s,p)$ be the number of photons per beam particle absorbed on the vacuum chamber at the coordinates s and p, then the distribution function of the radiation intensity is

$$D(s,p) = \frac{\partial^2 N(s,p)}{\partial s\, \partial p}. \tag{6.15}$$

Let us designate the type of element by the integer k, which runs from 1 to m, the total number of magnetic environment types. Then, indicating all the dependencies explicitly, we write

$$G_y(k,s) = G_y(k, D_1(s), D_2(s), \ldots, D_P(s)), \tag{6.16}$$

where $D_i(s) = D(s,p_i)$. The quantities $D(s,p_1), D(s,p_2), \ldots, D(s,p_P)$ characterize the photon radiation angular distribution. They may correspond to

- the radiation angular distribution, evaluated at P angular points, or
- the P parameters of a fit to the angular distribution.

We define a reference value $D_{y,i}(k)$ as being equal to the β_y-weighted average of $D_i(s)$ for elements of type k:

$$D_{y,i}(k) = \frac{\int_k ds\ \beta_y(s) D_i(s)}{w_y(k)}, \tag{6.17}$$

in which the weight $w_y(k)$ is

$$w_y(k) = \int_k ds\ \beta_y(s). \tag{6.18}$$

The integral in Eq. (6.18) is taken only over elements of type k. The integral around the ring can be written as

$$\oint ds\ \beta_y(s) G_{y(s)} = \sum_{k=1}^{m} \int_k ds\ \beta_y(s) G_y(k, D_1(s), D_2(s), \ldots, D_P(s)), \tag{6.19}$$

[3] G also depends, of course, on the photoelectron and secondary electron production physics. In principle, this will vary with s: for example, if the vacuum chamber surface properties vary around the ring. But in this analysis, we neglect this s variation, effectively using a ringwide average photoelectron and secondary electron model.

in which we separated the ring integral into sums over integrals of the different magnetic element types.

The general dependence of G on $D_i(s)$ can be approximated as a power series. Expanding in a Taylor series about the reference values $D_{y,i}(k)$, we have, to second order,

$$\begin{aligned} & G_y(k, D_1(s), D_2(s), \ldots, D_P(s))) \approx G_y(k, D_{y,1}(k), D_{y,2}(k), \ldots, D_{y,P}(k)) \\ + & \sum_{i=1}^{P} \left.\frac{\partial G_y}{\partial D_i}\right|_{D_i = D_{y,i}(k)} (D_i(s) - D_{y,i}(k)) \\ + & \frac{1}{2} \sum_{i=1}^{P} \sum_{j=1}^{P} \left.\frac{\partial^2 G_y}{\partial D_i \, \partial D_j}\right|_{D_i = D_{y,i}(k), D_j = D_{y,j}(k)} (D_i(s) - D_{y,i}(k))(D_j(s) - D_{y,j}(k)) \end{aligned} \tag{6.20}$$

Integrating around the ring, and ignoring the second oder terms, we find,

$$\oint ds \; \beta_y G_y \;\; = \;\; \sum_{k=1}^{m} T_y(k) \tag{6.21}$$

where

$$\begin{aligned} T_y(k) \;\; &= \;\; G_y(k, D_{y,1}(k), D_{y,2}(k), \ldots, D_{y,P}(k)) \int_k ds \; \beta_y(s) \\ &+ \;\; \sum_{i=1}^{P} \frac{\partial G_y}{\partial D_i} \int_k ds \; \beta_y(s)(D_i(s) - D_{y,i}(k) \qquad (6.22) \\ &= \;\; G_y(k, D_{y,1}(k), D_{y,2}(k), \ldots, D_{y,P}(k)) w_y(k) \qquad (6.23) \end{aligned}$$

The second term has vanished because of the way that the reference value $D_{y,i}(k)$ is defined.

The tune shift, in this approximation, is then

$$\Delta Q_y = \frac{e}{4\pi E} \sum_{k=1}^{m} T_y(k). \tag{6.24}$$

Since we have ignored the second order terms $\frac{\partial^2 G_y}{\partial D_i \, \partial D_j}$ in the Taylor expansion, this result assumes that the field differences are strictly linear in the radiation intensities. In general, at high cloud densities for which space charge effects are important, nonlinear terms may be present. It is possible to check the accuracy of the linearity assumption, and, if necessary, include also the second order terms. We have not yet done this, but it is planned for future work.

6.2.2 Analytical Formulae for Coherent Instability Thresholds (Adapted from [147])

When the positron beam passes through the electron cloud, the electrons near the beam oscillate in the electric potential of the positron bunch. In the analytic treatment, we describe the system as a dynamic interaction between the beam and the electron cloud, each with a transverse Gaussian distribution, and consider only the linear term of the interaction.

The motions of the beam and the electron cloud centroids are characterized by $y_b(s,z)$ and $y_e(s,t)$ at location s, longitudinal coordinate z, and time t, respectively. Note that $z<0$ for the backward direction. The equations of motion for the beam and cloud are expressed as [148]

$$\frac{d^2y_b(s,z)}{ds^2}+\frac{\omega_{\beta,y}^2}{c^2}y_b(s,z)=-\frac{\omega_{b,y}^2}{c^2}\left(y_b(s,z)-y_e(s,\frac{s-z}{c})\right), \tag{6.25}$$

$$\frac{d^2y_e(s,t)}{dt^2}=-\omega_{e,y}^2\left(y_e(s,t)-y_b(s,s-ct)\right), \tag{6.26}$$

where $\omega_{\beta,y}$ denotes the angular betatron frequency without the electron cloud interaction. The two coefficients $\omega_{b,y}$ and $\omega_{e,y}$ characterize the linearized force between beam and cloud, and are given by

$$\omega_{b,y}=\sqrt{\frac{\lambda_e r_e c^2}{\gamma\sigma_y(\sigma_x+\sigma_y)}},\quad \omega_{e,y}=\sqrt{\frac{\lambda_b r_e c^2}{\sigma_y(\sigma_x+\sigma_y)}}, \tag{6.27}$$

where λ_e and λ_b are the line densities of the cloud and the beam, r_e is the classical electron radius, c is the speed of light, γ is the beam Lorentz factor, and σ_x and σ_y are the horizontal and vertical beam sizes.

From Eq. (6.25) and Eq. (6.26), the equation of beam motion is obtained as

$$\frac{d^2y_b(s,z)}{ds^2}+\frac{\tilde{\omega}_\beta^2}{c^2}y_b(s,z)=\frac{\omega_{b,y}^2\omega_{e,y}}{c^3}\int_z^\infty dz' y_b(s,z')\sin\frac{\omega_{e,y}}{c}(z-z'), \tag{6.28}$$

where $\tilde{\omega}_\beta^2=\omega_{\beta,y}^2+\omega_{b,y}^2$ is the angular betatron frequency including the frequency shift due to the electron cloud. The right-hand side of Eq. (6.28) can be represented by a wake function, which depends only on the longitudinal distance. Integrated over the ring circumference L, the wake field $W_1(z)$ can be written as

$$W_1(z)=c\frac{R_S}{Q}\sin(\frac{\omega_{e,y}}{c}z), \tag{6.29}$$

where

$$c\frac{R_S}{Q}=\frac{\lambda_e}{\lambda_b}\frac{L}{\sigma_y(\sigma_x+\sigma_y)}\frac{\omega_{e,y}}{c}. \tag{6.30}$$

This wake field does not damp in z in this model. Actually the electron frequency $\omega_{e,y}$ has a finite spread, since the frequency of each electron depends on its oscillation amplitude and the horizontal position of the electron. This nonlinear effect causes the oscillation of the electrons to damp. If we add a damping term $2\alpha y_e$ in the left-hand side of Eq. (6.26), the wake field $W_1(z)$ is expressed by

$$W_1(z)=c\frac{R_S}{Q}\frac{\omega_{e,y}}{\tilde{\omega}}\exp(\frac{\alpha}{c}z)\sin(\frac{\tilde{\omega}}{c}z), \tag{6.31}$$

where the damping factor $\alpha=\omega_{e,y}/2Q$ is related to the frequency spread of $\omega_{e,y}$ and $\tilde{\omega}=\sqrt{\omega_{e,y}^2-\alpha^2}$. In a nonlinear resonator model, the wake field due to the electrons has a finite quality factor $Q=Q_{nl}$. From comparisons with numerical simulations [148], the nonlinear resonator quality factor is estimated to be $Q_{nl}\sim 7$.

The single-bunch instability is caused by the wake effect of electron motion with the frequency $\omega_{e,y}$. The phase angle of the electron oscillation during the passage of the bunch is characterized by

$$\chi=\frac{\omega_{e,y}\sigma_z}{c}, \tag{6.32}$$

where σ_z is the bunch length. The nature of the instability depends on the phase factor, χ.

The corresponding effective transverse impedance is given by a Fourier transformation of the wake function,

$$Z_\perp(\omega) = i\int_{-\infty}^{\infty}\frac{dz}{c}\exp(-\frac{i\omega z}{c})W_1(z). \tag{6.33}$$

From Eq. (6.31) and Eq. (6.33), the resonator impedance is expressed by

$$\begin{aligned} Z_\perp(\omega) &= \frac{c}{\omega}\frac{R_S}{1+iQ(\frac{\omega_{e,y}}{\omega}-\frac{\omega}{\omega_{e,y}})} \\ &= \frac{\lambda_e}{\lambda_b}\frac{L}{\sigma_y(\sigma_x+\sigma_y)}\frac{\omega_{e,y}}{\omega}\frac{Z_0}{4\pi}\frac{Q}{1+iQ(\frac{\omega_{e,y}}{\omega}-\frac{\omega}{\omega_{e,y}})}, \end{aligned} \tag{6.34}$$

where $Z_0 \simeq 377\ \Omega$ is the vacuum impedance .

We can estimate the stability requirement for a positron beam which experiences this effective impedance. For $\chi > 1$, the coasting beam model is available to study the fast head-tail instability. For zero chromaticity, the stability criterion is given by the dispersion relation as [149]

$$\begin{aligned} U &= \frac{\sqrt{3}\lambda_b r_e\beta_y}{\gamma\nu_s\omega_{e,y}\sigma_z/c}\frac{|Z_\perp(\omega_{e,y})|}{Z_0} \\ &= \frac{\sqrt{3}\lambda_b r_e\beta_y}{\gamma\nu_s\chi}\frac{Q}{4\pi}\frac{\lambda_e}{\lambda_b}\frac{L}{\sigma_y(\sigma_x+\sigma_y)} = 1, \end{aligned} \tag{6.35}$$

where ν_s is the synchrotron tune, and β_y is average vertical beta function. For $U > 1$, the beam becomes unstable.

The number of electrons in the beam cross-section area, λ_e, is $2\pi\rho_e\sigma_x\sigma_y K$ [150], where ρ_e is the density of the electron cloud. The electrons are gathered around the positron beam path by the electric force produced by the circulating positrons. Due to the pinch effect, the number of electrons, which contributes to the instability, is enhanced by a factor K, where K should depend on χ. This stability condition gives the threshold of the electron density for the instability as

$$\rho_{e,th} = \frac{2\gamma\nu_s\chi}{\sqrt{3}KQr_e\beta_y L}. \tag{6.36}$$

For a finite bunch length, the quality factor should not be larger than χ. Thus $Q = \mathrm{Min}(Q_{nl}, \chi)$ is used. And $K = \chi$ is chosen as a simple model. With these assumptions, the threshold of the electron density for the instability is

$$\rho_{e,th} = \frac{2\gamma\nu_s}{\sqrt{3}\mathrm{Min}(Q_{nl},\chi)r_e\beta_y L}. \tag{6.37}$$

The synchrotron tune can be related [149] to the momentum-compaction factor α by

$$\frac{\nu_s\omega_{e,y}\sigma_z}{c} = \frac{\alpha\sigma_\delta\omega_{e,y}}{\omega_0}, \tag{6.38}$$

in which σ_δ is the rms relative momentum spread, and ω_0 is the revolution frequency. From Eq. (6.36) and Eq. (6.38), we can get the relationship between the threshold density and momentum-compaction factor as

$$\rho_{e,th} = \frac{2\gamma\alpha\sigma_\delta\omega_{e,y}}{\sqrt{3}KQr_e\beta_y\omega_0 L}. \tag{6.39}$$

A high momentum-compaction factor suppresses the fast head-tail instability.

The sum of the tune shifts induced by the electric focusing force for a certain electron cloud density is given approximately by [146]

$$\Delta\nu_{x+y} = \Delta\nu_x + \Delta\nu_y = \frac{r_e}{\gamma}\rho_e\beta L, \tag{6.40}$$

where ν_x and ν_y are the horizontal and vertical betatron tunes and ρ_e is the electron cloud density.[4] The averaged beta function in the horizontal and vertical is assumed the same and denoted as β in the above equation.

This simplified analytical model of the electron cloud impedance neglects many of the important dynamical features of the electron cloud-beam interaction. Macroparticle simulations, which incorporate a fuller model of the physics, provide a better tool for comparison with measurements. These are described in Sec. 6.3.5.2 and Sec. 6.2.3.

6.2.3 Simulation of Beam Response to the Electron Cloud using CMAD

CMAD is a many-particle systems program to simulate the transport of charge particle beams in an accelerator lattice in the presence of electron cloud interaction [144]. The program tracks the beam across the full lattice of the accelerator, while computing the beam-electron cloud interactions within every element of the lattice. The lattice representation may be imported from any standard accelerator program such as MAD [151] in the form of transfer maps. The interaction between the beam and electron cloud is modeled using the particle-in-cell (PIC) algorithm. CMAD runs on multiple processors and is optimized for speed in computation. CMAD has been validated against two other programs that perform similar calculations [152], namely HEADTAIL [90] and WARP [132].

6.2.3.1 Representation of the Lattice for the Purpose of Tracking

While computing the beam electron cloud interactions, it is important to correctly model the effect of the variation of the Twiss function around the ring. The beta function as well as the dispersion influences the distribution of the particles comprising the beam. This determines how the electron cloud distribution evolves during a bunch passage, described by the so called pinching process. This pinching process in turn influences the beam response to the cloud. Thus, it is important to take into account these details rather than use a constant focusing model, although the latter would greatly simplify the simulation process. Before starting the computation, the beam distribution needs to be matched to the twiss functions at the point where the tracking begins. The macro-particles comprising the beam are then propagated across each element based on transfer functions obtained from the lattice description. Coupled with the tracking through the lattice elements the beam particles would undergo an "electron cloud kick", which is described later in this subsection.

The longitudinal phase space coordinates are defined by δ, the relative energy offset and z, the position along the bunch. To match the distribution in this degree of freedom, the coordinates are assigned to each particle as follows.

$$\begin{vmatrix} z \\ \delta \end{vmatrix} = \begin{vmatrix} \frac{c|\eta|\sigma_\delta}{\omega_s} & 0 \\ 0 & \sigma_\delta \end{vmatrix} \begin{vmatrix} z_G \\ \delta_G \end{vmatrix} \tag{6.41}$$

[4] This is the same as Eq. (6.59).

where c is the speed of light, ω_s is the angular synchrotron frequency and η is the slippage, σ_δ is the equilibrium relative energy spread. The quantities z_G and δ_G are assigned to each particle using a Gaussian distribution random generator with a standard deviation of unity over all the particles. We have assumed that the relativistic parameter $\beta_0 = v_0/c \approx 1$. The transverse phase space coordinates are defined by x the horizontal position, x' the horizontal angle, y the vertical position and y', the vertical angle. For a matched distribution the particles are chosen in order to satisfy the following relationship,

$$\begin{vmatrix} x \\ x' \end{vmatrix} = \sqrt{\frac{\epsilon_x}{\beta_x}} \begin{vmatrix} \beta_x & 0 \\ -\alpha_x & 1 \end{vmatrix} \begin{vmatrix} x_G \\ x'_G \end{vmatrix} + \delta \begin{vmatrix} D_x \\ D_{x'} \end{vmatrix} \tag{6.42}$$

$$\begin{vmatrix} y \\ y' \end{vmatrix} = \sqrt{\frac{\epsilon_y}{\beta_y}} \begin{vmatrix} \beta_y & 0 \\ -\alpha_y & 1 \end{vmatrix} \begin{vmatrix} y_G \\ y'_G \end{vmatrix} + \delta \begin{vmatrix} D_y \\ D_{y'} \end{vmatrix} \tag{6.43}$$

where $\beta_{x/y}$, $\alpha_{x/y}$, $D_{x/y}$, $D_{x'/y'}$ are the horizontal/vertical values of the beta function, the alpha function, the dispersion and dispersion gradient respectively at the given position in the lattice the distribution is matched to. Also, $\epsilon_{x/y}$ is the horizontal/vertical beam emittance. The quantities x_G/y_G and x'_G/y'_G are assigned to each particle using a Gaussian distribution random generator with a standard deviation of unity over all the particles. The particle distribution is truncated along each axis at a pre-specified value given by an integer multiple of the root mean square (rms) extent of the full distribution.

The tracking across the lattice elements is done with the help of transfer functions as specified in Ref [153]. These include first order transfer matrices and higher order phase space tensors. The transfer across each element may be expressed as

$$v_i^{(2)} = \sum_{j=1}^{6} R_{ij} v_j^{(1)} + \sum_{j=1}^{6} \sum_{k=1}^{6} T_{ijk} v_j^{(1)} v_k^{(1)} \tag{6.44}$$

where v_i is the set of components of the phase space vectors in six dimensions, R_{ij} are the components of the matrix elements representing linear transport and T_{ijk} are the components of the third order tensor representing nonlinear transport. The set of components in R_{ij} for the all the lattice elements provide all the effects of the linear beam optics, which include the influence of Twiss functions on the size of the distribution, the betatron tune and the slippage undergone by the off energy particle. Based on a pre-specified synchrotron tune, the particles undergo a kick in energy at every turn, which is analogous to an RF cavity. This provides for longitudinal confinement and the synchrotron oscillations executed by the particles. The formulation of this kick is given by

$$\delta^{(2)} = \frac{(2\pi Q_s)^2}{\eta C} z + \delta^{(1)} \tag{6.45}$$

where Q_s is the synchrotron tune, and C the circumference of the ring.

The combined effect of the T_{ijk} tensors from all the elements provide for higher order effects in the beam optics. These include the natural chromaticity and correction of the same due to sextupoles. Other less important features provided by the terms T_{ijk} include higher order dispersion and momentum compaction. Yet another effect would be the quadrupole component arising from a sextupole for an off centered orbit. It may be noted that the T_{ijk} tensors break symplecticity in the beam transport. Loss in symplecticity would lead to violation of conservation of phase space area, leading to artificial damping and particle excursion especially when tracking the beam over

several thousands of turns. However, chromaticity is a key higher order effect that needs to be retained in any computation of electron cloud effects on the dynamics of beams in storage rings. Chromaticity is defined by gradient of betatron tune with respect to energy offset, which is given by $Q' = dQ/(dp/p)$, where Q' is the chromaticity, Q the betatron tune and p the momentum of the synchronous particle. These higher order effects vanish in the absence of the T_{ijk} tensors acting on the particles. In order to circumvent this problem, one can retain only the first order terms in the tracking scheme, that is the R_{ij}, thus retaining the symplectic structure of the beam transport, and yet model the chromaticity with the help of a single transfer matrix applied once per turn. If we define the transverse space variables (x, x', y, y') as t_i and the corresponding momentum dispersion component as D_i, then we may express the chromaticity transformation as

$$t_i^{(2)} = \sum_{j=1}^{4} C_{ij} t_j^{(1)} - \sum_{j=1}^{4} (C_{ij} + I_{ij}) D_j \delta \tag{6.46}$$

where I_{ij} is the respective component of the identity matrix $\mathbf{I}$ and C_{ij} that of a matrix given by

$$\mathbf{C} = \begin{vmatrix} \mathbf{Cx} & \mathbf{I} \\ \mathbf{I} & \mathbf{C_y} \end{vmatrix} \tag{6.47}$$

with

$$\mathbf{C_x} = \begin{vmatrix} \cos(Q'_x\delta) + \alpha_x \sin(Q'_x\delta) & \beta_x \sin(Q'_x\delta) \\ \frac{1+\alpha_x^2}{\beta_x} \sin(Q'_x\delta) & \cos(Q'_x\delta) - \alpha_x \sin(Q'_x\delta) \end{vmatrix} \tag{6.48}$$

and

$$\mathbf{C_y} = \begin{vmatrix} \cos(Q'_y\delta) + \alpha_y \sin(Q'_y\delta) & \beta_x \sin(Q'_y\delta) \\ \frac{1+\alpha_y^2}{\beta_y} \sin(Q'_y\delta) & \cos(Q'_y\delta) - \alpha_y \sin(Q'_y\delta) \end{vmatrix} \tag{6.49}$$

Simulations performed so far with `CMAD` have used first order tracking along with chromaticity modeled according the transformation described above.

6.2.3.2 Modeling the Beam - Electron Cloud Interaction

The general method of modeling the beam transport through the ring with electron cloud effects involves tracking a certain number of beam particles around the ring with the help of transfer maps as already described above, coupled with several discrete "beam-electron cloud interacting points" (IPs) in the ring. `CMAD` allows one to have an IP within each element with a pre-specified electron density. These IPs provide the kick, or deviation in momentum of the beam due to the electron cloud.

The beam is divided into a certain number of slices along the length of the bunch. The charge from each particle is deposited on to adjacent slices, represented by two-dimensional grids extending transversely. The electron cloud at the IP is represented by a single slice, which translates to charge deposited onto a single two dimensional grid. Since each IP represents a certain length along the transport channel, this would be equivalent to a situation where all the electrons along this length are collapsed on to a single two dimensional grid. After such a decomposition, one is left with computing the interaction between a set of two dimensional charge distributions (the sliced beam) and a single two dimensional charge distribution, (the electron cloud). This is done with the help of a field solver and particle pusher method prescribed by the two dimensional particle-in-cell (PIC) algorithm described later in this subsection. All the forces and motion of particles are now purely

transverse to the beam propagation. It is easy to justify such an approximation because the beam is ultra-relativistic. As a result the electrons would experience, for all practical purposes, only a transverse field component. On the other hand, the electrons, which extend over a finite length will not have a significant longitudinal field component to perturb the motion of an ultra relativistic beam. Thus, longitudinal field components may be disregarded altogether. The self field forces of each species acting upon themselves are also disregarded. Given the beam is ultra-relativistic, we know that the beam space charge force acting upon the beam particles is insignificant. One can determine this by transforming the fields to the rest frame of the beam, or by calculating the combined effect of the electric and magnetic fields in the rest frame of the laboratory, where the forces due to the electric and magnetic fields almost cancel each other. The space charge forces due to the electrons acting upon the electrons may also be disregarded. This is because electron densities are of the order of $10^{11}-10^{12}$ m^{-3}, while the beam consists of about 10^{10} particles confined within micron sized dimensions transversely and about a centimeter longitudinally. Thus, within the vicinity of the beam, the forces exerted by the beam space charge on the electrons is many orders of magnitude higher than the forces of the electrons acting upon each other.

In this scheme, the transverse fields produced in each of the beam slices are computed first. These slices are made to pass through the two dimensional electron distribution in succession, and the electrons are made to move accordingly with every slice passage. With a positively charged beam, the electrons would converge toward the center as the beam slices pass through and in some cases even overshoot and cross the center. This process is often referred to as "pinching". Figure 6.14 shows the electron cloud pinch caused by the different beam slices and Fig 6.15 shows the presence of a slice of electron cloud within each element, with the beam being transported across the elements. The field produced by the electrons is computed and recorded after every interaction with a beam slice or, in other words after every pinch introduced by the respective slice. Finally, these computed fields due to the electrons are acted upon the beam particles of the corresponding slice. This provides focusing to the beam particles in addition to focusing arising from the quadrupoles. The focusing caused by the electrons is not uniform, leading to an amplitude dependent tune shift, in addition to a coherent tune shift. Since the beam is not rigid in this model, *i.e.*, it consists of discrete particles, one can study effects such as emittance growth caused by the electron cloud, distortions in beam shape and orientation due to head-tail interaction, the spread in tune amongst the particles, and other such effects that cannot be seen by a rigid beam model.

6.2.3.3 Particle-in-Cell (PIC) Algorithm

The (PIC) method has been widely used in simulating many particle systems. The general method involves solving for the force fields over a mesh, and moving particles in the system based on the field calculation, a process repeated at every time step. In our case the force fields are computed by solving a two dimensional Poisson's equation over a mesh using Fourier transforms. As explained earlier, the fields need be solved over a two dimensional grid. Poisson's equation in two dimensions is

$$\frac{\partial^2\phi}{\partial x^2}+\frac{\partial^2\phi}{\partial y^2}=-\frac{\rho}{\epsilon_0}. \tag{6.50}$$

In general, the above equation may be solved in Fourier space, where it reduces to a simple equation rather than a differential one, and then taking the inverse Fourier transforms to determine ϕ. In the present case, since all values are given over a mesh, we use the discrete Fourier transform (DFT). The DFTs and their inverses are computed using the package `FFTW` [154]. The area used in the field

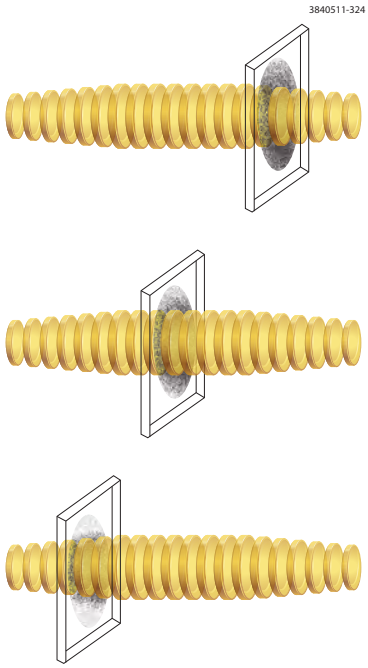

Figure 6.14: Figure describing the pinching of the cloud as the slices of the beam pass through the two dimensional cloud

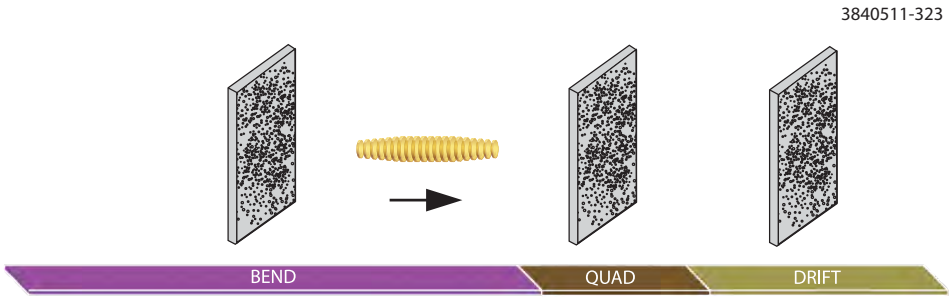

Figure 6.15: Figure describing the distribution of the two dimensional cloud slices across each element, which represents an IP

computation spans about 10-20 times the beam size, which is much smaller than the vacuum chamber cross section. In order for the field computation to be unaffected by these artificial boundaries, the boundary conditions are set so that it creates the effect of "open boundaries". This is done by first computing the field on the boundary nodes using Green's function for open boundaries due to the charge present in the computational domain. Using these values as boundary conditions, Poisson's equation is solved for all grid points within these boundaries using fast Fourier transforms (FFT). The charge distribution is represented by a set of macro-particles, which are computational particles carrying the weight of a finite number of physical particles. At a given time a macro-particle can be located anywhere within the computational domain. In order to solve Poisson's equation using DFTs, one needs to assign the charge of these macro-particles onto the grid nodes. Additionally, once the fields are computed, their values need to be interpolated onto the position of the particles. The schemes used for evaluating the fields from the potential by discretizing the

gradient operator (the Laplacian operator) to express Poisson's equation, interpolation of charge onto the nodes, and interpolation of the field from the node to the particle position, are all similar to that described in Ref [155]. They are briefly summarized here.

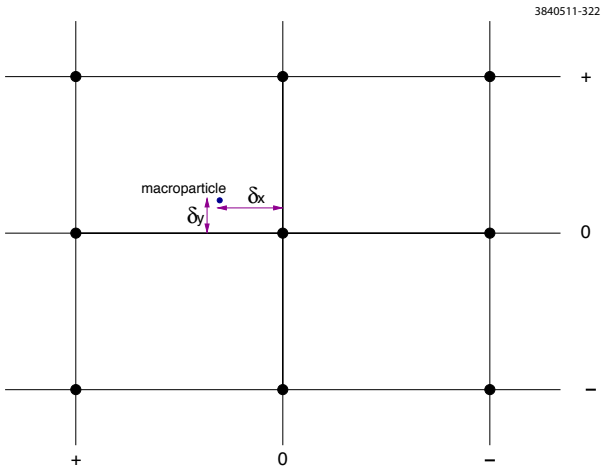

Figure 6.16: Figure illustrating the 9 point charge interpolation scheme

The assignment of the charge onto the grid nodes is done over a set of nine nearest neighboring points representing the nodes as shown in Fig 6.16. We use 0 to denote the first, + as the second, and − as the third nearest lines. Following the notation of Ref. [155], we define H_x as the horizontal dimension of the grid and H_y as the vertical dimension. Also δx and δy are defined as the perpendicular distance from the nearest horizontal and vertical grid line respectively. The weights assigned to these nine nodes are quadratic polynomials of the ratios $r_x = \delta_x/H_x$ and $r_y = \delta_y/H_y$. The coefficients of the weights along the x axis are given by

$$\begin{aligned} w_x^0 &= \frac{3}{4} - r_x^2 \\ w_x^+ &= \frac{1}{2}(\frac{1}{4} + r_x + r_x^2) \\ w_x^- &= \frac{1}{2}(\frac{1}{4} - r_x + r_x^2) \end{aligned} \tag{6.51}$$

It may be noted that $w_x^0 + w_x^+ + w_x^- = 1$, which is required for satisfying charge conservation. The formulae for weighing the charges along the y axis is identical, and are denoted as w_y^0, w_y^+ and w_y^- respectively. Finally, the weight to be assigned at a node will be a product of the two one-dimensional weights based on the position of the node along the two axis. For example $w^{00} = w_x^0 w_y^0$ and $w^{+-} = w_x^+ w_y^-$, *etc.*

The two dimensional Laplacian operator is approximated by a five point difference scheme, and Poisson's equation is discretized as follows,

$$\frac{\phi_{i-1,j} + \phi_{i+1,j} - 2\phi_{i,j}}{H_x^2} + \frac{\phi_{i,j-1} + \phi_{i,j+1} - 2\phi i, j}{H_y^2} = -\frac{\rho_{i,j}}{\epsilon_0} \tag{6.52}$$

where i and j are the horizontal and vertical indices that label the nodes over the mesh. The field is computed from the potential using the gradient operator which is approximated by a six point

difference scheme. This is given by

$$E_{xi,j} = -\frac{1}{12H_x}[(\phi_{i+1,j+1} - \phi_{i-1,j+1} + 4(\phi_{i+1,j} - \phi_{i-1,j}) + (\phi_{i+1,j-1} - \phi_{i-1,j-1})]$$
$$E_{yi,j} = -\frac{1}{12H_y}[(\phi_{i+1,j+1} - \phi_{i+1,j-1} + 4(\phi_{i,j+1} - \phi_{i,j-1}) + (\phi_{i-1,j+1} - \phi_{i-1,j-1})]. \quad (6.53)$$

Once the force on each of the particles is computed, their positions and velocities are advanced in time according to the values of the time step and the force exerted. In order to do this, we use the leap frog scheme when the effect of an external magnetic field is not included and the Boris [156] integrator when the particles are influenced by an external magnetic field. The particle's equations of motion to be integrated are

$$\begin{aligned} m\frac{d\mathbf{v}}{dt} &= q(\mathbf{E} + \mathbf{v} \times \mathbf{B}) \\ \frac{d\mathbf{r}}{dt} &= \mathbf{v}. \end{aligned} \quad (6.54)$$

The only situation in which the magnetic field $\mathbf{B}$ is taken into account is when cloud electrons move in the presence of an external magnetic field. For $\mathbf{B} = 0$, the discretized integration is given as follows,

$$\begin{aligned} \mathbf{v}_{t+\Delta t/2} &= \mathbf{v}_{t-\Delta t/2} + \frac{q}{m}\mathbf{E}_t \Delta t \\ \mathbf{r}_{t+\Delta t} &= \mathbf{r}_t + \mathbf{v}_{t+\Delta t/2}\Delta t \end{aligned} \quad (6.55)$$

Thus, we see that in this scheme, the position and velocity coordinates are always half a time step apart. In the presence of an external magnetic field, we need to solve

$$\frac{\mathbf{v}_{t+\Delta t/2} - \mathbf{v}_{t-\Delta t/2}}{\Delta t} = \frac{q}{m}\left[\mathbf{E}_t + \frac{\mathbf{v}_{t+\Delta t/2} + \mathbf{v}_{t-\Delta t/2}}{2} \times \mathbf{B}\right] \quad (6.56)$$

To do this, we follow the method of Boris [156] which involves the following expressions,

$$\begin{aligned} \mathbf{v}_{t-\Delta t/2} &= \mathbf{v}^- - \frac{q\mathbf{E}_t}{m}\frac{\Delta t}{2} \\ \mathbf{v}_{t+\Delta t/2} &= \mathbf{v}^+ + \frac{q\mathbf{E}_t}{m}\frac{\Delta t}{2} \end{aligned} \quad (6.57)$$

If we substitute the above expressions into Eq. (6.56), we get

$$\frac{\mathbf{v}^+ - \mathbf{v}^-}{\Delta t} = \frac{q}{2m}(\mathbf{v}^+ + \mathbf{v}^-) \times \mathbf{B} \quad (6.58)$$

Thus, in order to advance the velocity in time, we need to carry out the following procedure; first compute $\mathbf{v}^-$ according to Eq ((6.57)) using the value of $\mathbf{E}_t$, then solve for $\mathbf{v}^+$ using Eq ((6.58)), and then solve for $\mathbf{v}_{t+\Delta t/2}$ once again using $\mathbf{E}_t$ and Eq ((6.57)). The position vector $\mathbf{r}$ is advanced in the same manner as in the zero magnetic field case.

6.2.3.4 Parallel Implementation

As mentioned previously, `CMAD` has been optimized for high speed computation and runs on multiple processors. In this algorithm, one or more beam slices are assigned to a processor. Figure 6.17 shows

a schematic describing this algorithm with each processor containing three slices. Each processor moves or pinches its cloud electrons according to the fields produced by the beam particles of the slice. When the processor is done with all its slices, it passes the resulting electron distribution to the processor containing the adjacent slices for further processing. After passing the electron distribution on, the processor continues to calculate the field resulting from the electron distribution and uses it to calculate the "electron cloud kick" to the beam particles. Then each beam particle is propogated to the next element by applying the transfer map described earlier in this subsection. It may be noted that the process of providing the "electron cloud kick" and transportation to the next element in the lattice can be done by each processor independently, which results in considerable saving in overall computation time when several processors are used. It is clear that optimal speed in computation is achieved when the number of processors used equals the number of slices the beam is divided into. Calculations for CesrTA are regularly carried out with 100 slices using 100 processors at the National Energy Research Scientific Computation Center (NERSC).

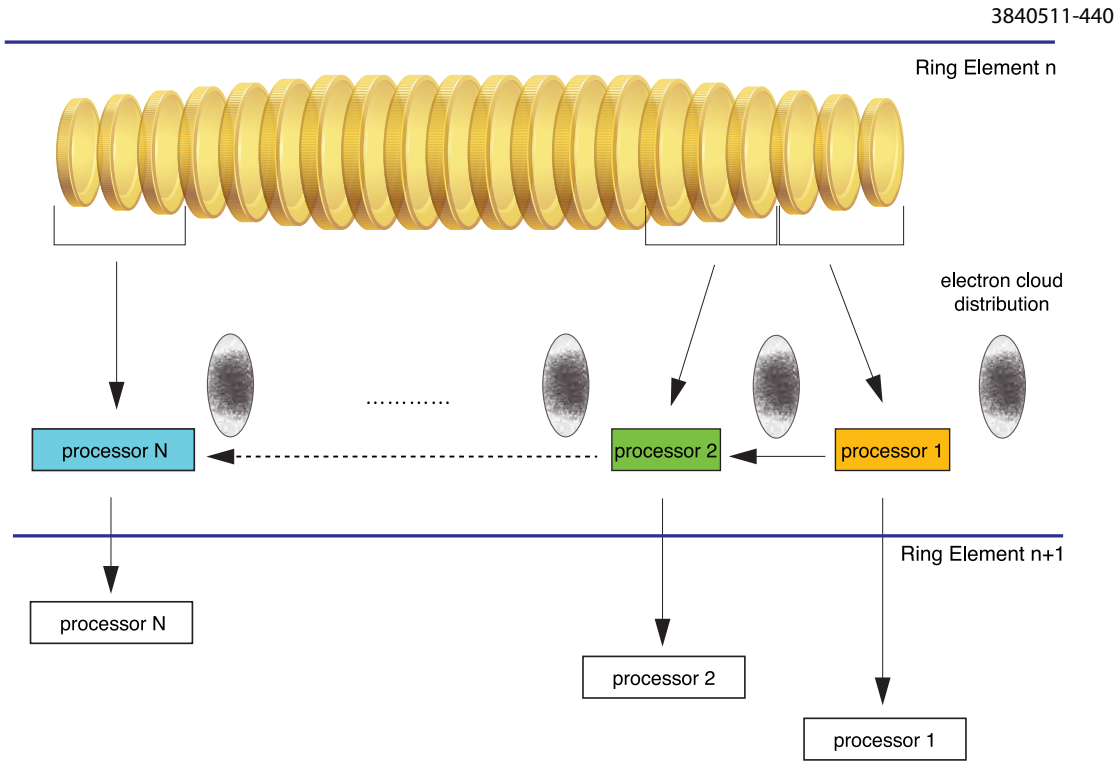

Figure 6.17: Figure illustrating the flow of information for parallel computation implemented in `CMAD`

6.3 Experimental Observations and Comparison With Simulation

6.3.1 Bunch-by-Bunch Tunes

The CesrTA program has included extensive measurements of bunch-by-bunch coherent betatron tune shifts for a variety of electron and positron beam energies, emittances, bunch population levels, and bunch train configurations [135, 136, 157]. The tune shift measurement methods are described in Section 6.1.1.

Comparisons to two advanced electron cloud simulation codes (`ECLOUD` [89, 90] and `POSINST` [71, 86]), using the methods described in Section 6.2.1, have shown that the bunch-by-bunch tune shifts result primarily from the interaction of the beam with the space-charge field of the photoelectron-seeded electron cloud in the vacuum chamber. These comparisons have allowed the accuracy of the codes to be checked, and constraints to be placed (for the conditions of the CesrTA vacuum chamber) on the codes' physical model parameters. Together with local direct measurements of the electron cloud using retarding field analyzers, shielded buttons and TE-waves, described in Chapter 5, the tune shift measurements will help to develop a robust electron cloud model, well tested experimentally, which can be used to predict with confidence the features of the electron cloud effect in future linear collider damping rings.

6.3.1.1 General Remarks on Bunch-by-Bunch Tune Shifts

The basic tools required for simulations of the bunch-by-bunch coherent tune shifts are

1. knowledge of the beam parameters, element layout and lattice, vacuum chamber characteristics, and radiation distribution (including scattered radiation) around the ring.

   We have detailed optics models for each CesrTA lattice configuration. For our tune shift simulations in 2008 through 2011, the radiation intensity for a given beam current was provided by a program called `Synrad`, which computes the radiation intensity striking the vacuum chamber wall (approximately a 4.5 cm $\times$ 2.5 cm elliptical Al beampipe) in the bend plane from the magnetic lattice and the beam parameters. An empirically determined "photon reflectivity" parameter is used in the electron cloud codes to describe the scattered radiation (assumed to be uniformly distributed) striking the vacuum chamber out of the bend plane.

   As discussed in Section 4.1.4.1, we have developed a three-dimensional radiation propagation code called `Synrad3D` which computes the radiation intensity per unit beam current in a given lattice, including specular and diffuse photon scattering in a realistic 3D model of the CesrTA vacuum chamber. This code gives the complete photon radiation distribution around the perimeter of the vacuum chamber cross section, at any longitudinal position. We will use the results of this code to improve the tune shift simulations in future studies. Some preliminary tune shift simulations based on `Synrad3D` are presented below in Section 6.3.1.7.

2. a program which uses primary photoelectron and secondary electron models to simulate the buildup of the cloud.

   We have used the 2D codes `POSINST` and `ECLOUD` to model the cloud buildup along a bunch train, and decay after the end of the train. A description of recent benchmarking comparisons between `ECLOUD` and `POSINST` can be found in Ref. [158]. For the tune shift calculations, the

electron cloud has been modeled in drifts and dipoles only, since electron cloud effects in these elements dominate the bunch-by-bunch tune shifts in the CesrTA ring.

The 3D codes `WARP/POSINST` [84, 93] and `CLOUDLAND` [91, 92, 111] have been employed to study tune shifts in quadrupoles and wigglers. The contributions to the bunch-by-bunch tune shift differences along the train from these elements is generally quite small; however, because of the presence of trapped cloud in these devices, there may be observable effects on the tune shifts of the leading bunch in a train, and on other features of the beam dynamics (see below, Section 6.3.2.14). This is an area to be studied in the future.

Further details concerning the modeling of photoelectron production are discussed in Section 5.1.3.3, and also below in Section 6.3.1.7. Additional information, as well as the detailed assumptions in the secondary electron yield model, can be found in Refs. [135, 159].

The cloud buildup depends on the secondary electron emission characteristics of the vacuum chamber surface, which in principle will change with time as the surface is conditioned by photon and electron bombardment. However, the tune shifts are sensitive to the ringwide average surface condition, and CESR has been operating in a high current environment for many years. The ringwide average vacuum chamber surface is thus essentially fully conditioned, and no significant time dependence in its secondary emission characteristics is expected.

3. a method of calculating the coherent tune shifts from the (dynamic) electron cloud charge densities provided by the simulation codes. This is described above in Section 6.2.1.

6.3.1.2 Initial Tune Shift Studies to Determine the Reference Simulation Parameter Values

To determine the approximate values of the electron cloud simulation parameters which reproduced measured tune shift data, a data set from 2007 was studied intensively. The radiation intensities in drifts and dipoles were fixed as computed from the lattice and the beam current. Starting with a parameter set suggested by recent direct measurements of the SEY properties of technical Al surfaces at SLAC, the internal simulation parameters in the `POSINST` code were varied. A reference parameter set, which did the best job of reproducing the 2007 data set, was determined by trial-and-error comparisons. The numerical parameters of the `POSINST` simulation (such as time step size, space charge grid size, and number of beam slices) were chosen such that variations in these numerical parameters did not change the results of the simulation significantly.

The reference values for six key parameters for the simulations are shown in Table 6.1. Fig. 6.18 shows a comparison between the 2007 data set and a `POSINST` simulation with the reference values, and two simulations with the total secondary yield parameter varied by $\pm 10\%$ away from the reference.

6.3.1.3 Tune Shift Data Summary, and Comparison with `POSINST` Simulations

A large variety of coherent tune shift data have been taken, covering a wide range of machine conditions such as beam energy, beam size, lattice configuration, particle species, bunch current, bunch train configuration, and mode of oscillation of the bunches.

Table 6.1: `POSINST` initial reference parameter values (aluminum chamber). The same values are used for drifts and dipoles.

`POSINST` Parameter	Description	Unit	Value
`queffp`	Quantum efficiency	%	12
`refleff`	Photon reflectivity	%	15
`ek0phel`	Peak photoelectron energy	eV	5
`eksigphel`	RMS photoelectron energy	eV	5
`E0tspk`	Energy of peak true secondary yield	eV	310
`dtotpk`	Peak total secondary yield		2.0
`P1epk`	Elastic yield at zero energy		0.5
`P1rinf`	Rediffused yield at high energy		0.19

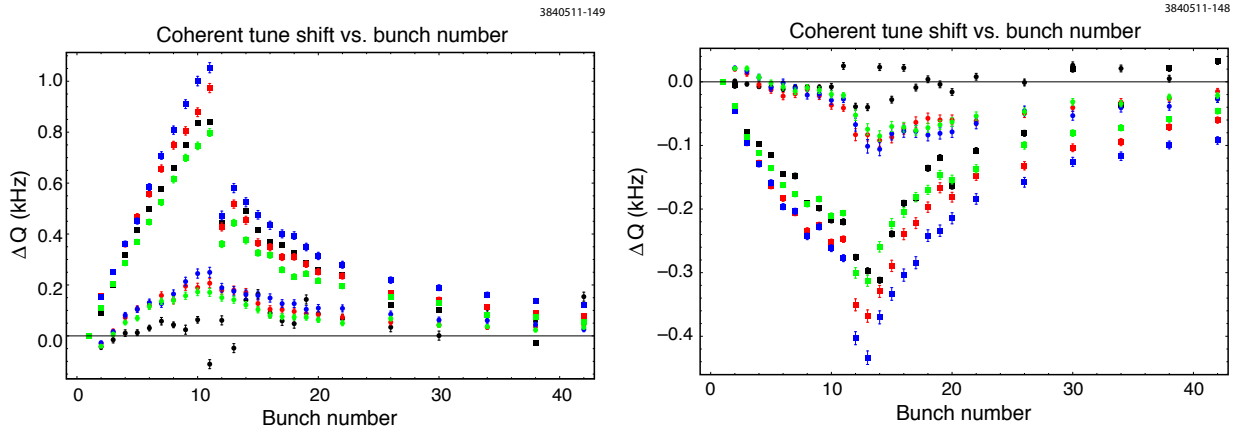

Figure 6.18: Coherent tune shifts, 2007 data and `POSINST` simulations compared. Left: positron beam. Right: electron beam. The data and simulations are for a 10 bunch train with a bunch current of 0.75 mA, followed by witness bunches, all with 14 ns spacing, and 1.9 GeV beam energy. Squares: Vertical tune shift. Disks: Horizontal tune shift. Black: data. Red: `POSINST` simulation using parameters given in Table 6.1. Blue: `POSINST` simulation with Table 6.1, except peak total secondary yield = 2.2. Green: `POSINST` simulation with Table 6.1, except peak total secondary yield = 1.8.

The tune shift data can be grouped into four types based on the measurement technique employed:

a. "Pinged" beam measurements, for which all the bunches in the train are oscillating in phase. This measurement type is described in Section 6.1.1.1. For this mode of excitation, the horizontal tune shifts are suppressed, as discussed above in Section 6.2.1.3.

b. Measurements in which a single bunch in the train is excited with a fast kicker. This measurement type is described in Section 6.1.1.2.

c. Measurements in which the Dimtel feedback system response is used to measure the tune. In this case, the mode of oscillation of the train is unknown. This measurement type is described in Section 6.1.1.3.

d. Measurements in which the bunches in the train are self-excited; in this case also, the mode

of oscillation of the train is unknown. This measurement type is described in Section 6.1.1.4.

For each of these measurement types, there are also two possible kinds of bunch patterns:

- Measurements involving witness bunches, which are single bunches placed at a variable distance after the end of a train, to probe the time evolution of the cloud. For these studies, the train lengths were typically short (no more than 20 bunches).
- Measurements with long trains of bunches (up to 45 bunches), with no witnesses.

As discussed above in Section 6.2.1.3, the tune shifts depend in general on the mode of oscillation of the train, and this dependence can be taken into account by using the "Dynamic cloud model." For type *a* data, all the bunches in the train are oscillating in phase, and the cloud buildup simulations done for comparisons with type *a* data were done by offsetting all the bunches in the train by the same amount. The offset used in the simulations was 2 mm.

For data type *b*, only a single bunch in the train is oscillating. The corresponding simulation should be done using the "Dynamic cloud model" with a single bunch offset. Simulation studies have shown, however, that when only a single bunch in the train is offset by a small displacement ($\lesssim$ 0.5 mm), tune shifts computed using the "Modified static cloud model" (Section 6.2.1.4) are close to those computed using the "Dynamic cloud model". For the simulations reported here for this data type, we have used the "Modified static cloud model" (Eq. (6.11)). In the future, we will use the "Dynamic cloud model" (with a single bunch offset equal to the displacement used for the measurement) for data type *b* as well as data type *a*.

For data types *c* and *d*, the excitation of the beam is spontaneous, and the mode of oscillation is not directly measured. However, we believe that the dependence of the tune shift on the mode of oscillation of the train is relatively weak[5], except for the special case of the horizontal tune shift in dipoles being very small for the lowest frequency multibunch mode. This belief is supported by horizontal tune spectra measurements for type *d* data, such as shown in Fig. 6.38 below. The spectrum exhibits two peaks: one smaller peak at very small tune shifts, associated with the lowest frequency multibunch mode, and another larger peak with a large tune shift, associated with all the other modes. Thus, by focusing on the frequency of the largest amplitude spectral peak, we are measuring the tune shift associated with the higher frequency multibunch modes. To compute the tune shift for the these modes, we use the "Modified static cloud model".

The major tune measurement data sets, grouped by measurement type, are the following:

type *a*:

1a. A large series of data sets taken in 2007 and 2008, with witness bunches and short trains. These are listed in Table 6.2. Examples of data-simulation comparisons from this set are shown in Fig. 6.18, Fig. 6.19, and Fig. 6.20.

2a. A series of data sets taken in 2009 with 45 bunch trains, with a range of bunch currents. Examples are shown in Fig. 6.21, Fig. 6.29 and Fig. 6.30.

3a. A series of data sets taken in 2010 to explore special lattice or beam conditions. Examples are shown Fig. 6.22. Studies of special lattice conditions are discussed below in Section 6.3.1.6.

Inspection of the data and simulation comparisons for the type *a* groups shows that the reference parameter set given in Table 6.1 does a fairly good job of representing the data, with the following exceptions:

[5] This supposition should be confirmed by simulations.

Table 6.2: Short train and witness data sets from 2007-2008 (Group *1a*). The train and witness bunches are spaced at 14 ns. The data sets were taken with different values of the bunch current, train length, and witness configuration. The ranges for these values are given in the table.

Energy (GeV)	Species	Bunch current (mA)	Train length (no. of bunches)	No. of witness bunches following the train	Number of data sets
1.9, 2.1	Positrons	0.25, 0.5, 0.75, 1.0, 1.25, 3.0	3, 10, 11, 19, 20, 21	5-15	23
1.9, 2.1	Electrons	0.25 ,0.5, 0.75, 1.0, 1.25, 3.0	10, 11, 19, 20, 21	5-15	10
5.3	Positrons	0.75, 1.5, 5.0	3, 10	5-10	3
5.3	Electrons	1.5	10	10	1

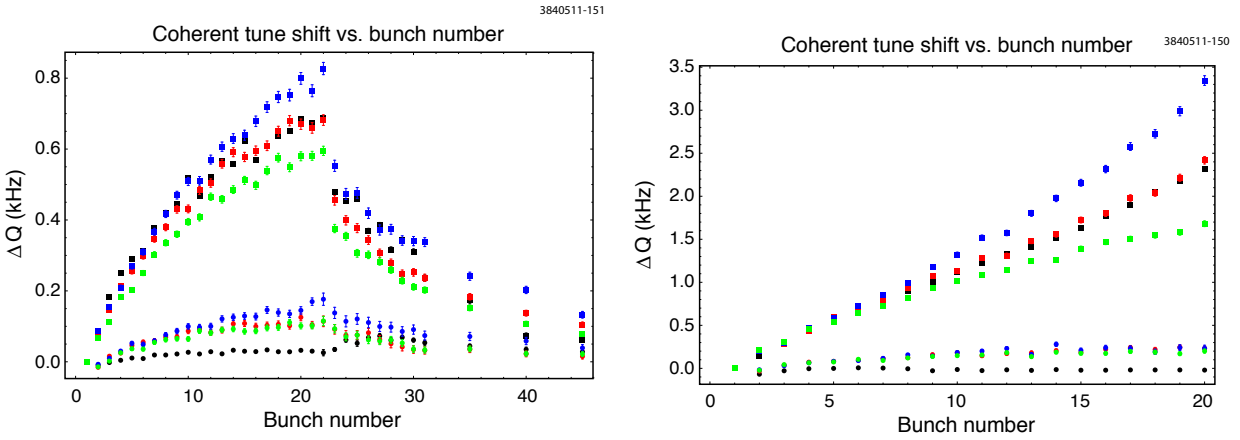

Figure 6.19: Coherent tune shifts, 2008 data and `POSINST` simulations compared. Left: 21 bunch train followed by witnesses, 0.5 mA bunch current. Right: 20 bunch train, 1 mA bunch current. Beam for all cases: positron, 2.1 GeV energy, 14 ns bunch spacing. Squares: Vertical tune shift. Disks: Horizontal tune shift. Black: data. Red: `POSINST` simulation using parameters given in Table 6.1. Blue: `POSINST` simulation with Table 6.1, except peak total secondary yield = 2.2. Green: `POSINST` simulation with Table 6.1, except peak total secondary yield = 1.8.

- Generally, the horizontal simulated tune shifts, while small, are still larger than the data.
- The vertical tune shifts at 5.3 GeV are overestimated.
- The high bunch current (2 mA) witness bunch vertical tune shifts at 4 GeV may be underestimated.

The first two exceptions are discussed further in Section 6.3.1.7 below.

type *b*: Tune measurements with a single bunch drive excitation with 1-2 mm amplitude. An example is shown in Fig. 6.23. Since there is no coherent oscillation of the entire train, the horizontal tune shifts are not suppressed. It is evident that the simulations overestimate the data, for the bunches near the end of the train. This disagreement may be related to the fact that the simulations were done using the "Modified static cloud model", which may not be a good approximation for this data type. More measurements of this type, in which both the mode of oscillation of the bunches and the oscillation amplitude are well-specified, are planned in

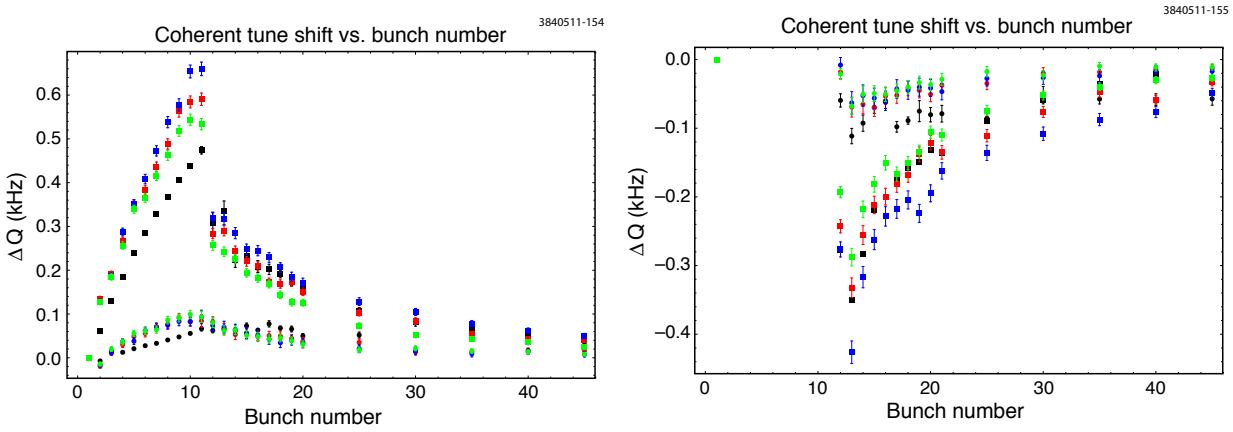

Figure 6.20: Coherent tune shifts, 2008 data and POSINST simulations compared. Left: 10 bunch positron train followed by witnesses, 0.75 mA bunch current. Right: 10 bunch electron train, 1.5 mA bunch current, followed by witnesses, 0.5 mA bunch current; only the witness bunches are shown. For all cases: 14 ns bunch spacing, 5.3 GeV beam energy. Squares: Vertical tune shift. Disks: Horizontal tune shift. Black: data. Red: POSINST simulation using parameters given in Table 6.1. Blue: POSINST simulation with Table 6.1, except peak total secondary yield = 2.2. Green: POSINST simulation with Table 6.1, except peak total secondary yield = 1.8.

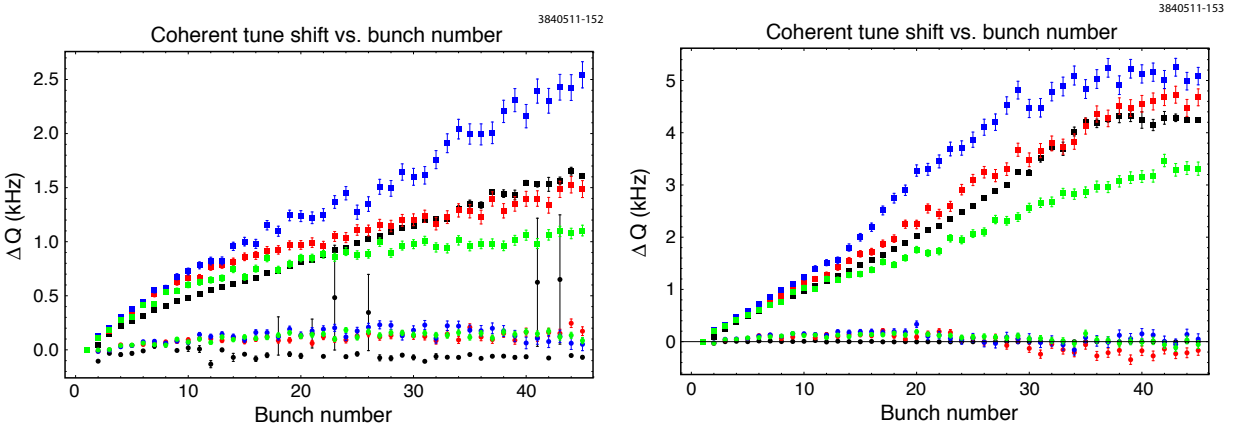

Figure 6.21: Coherent tune shifts, 2009 data and POSINST simulations compared. Left: 45 bunch train, 0.6 mA bunch current. Right: 45 bunch train, 1 mA bunch current. All for positrons with 14 ns spacing, and 2.1 GeV beam energy. Squares: Vertical tune shift. Disks: Horizontal tune shift. Black: data. Red: POSINST simulation using parameters given in Table 6.1. Blue: POSINST simulation with Table 6.1, except peak total secondary yield = 2.2. Green: POSINST simulation with Table 6.1, except peak total secondary yield = 1.8.

the future.

type *c*: Tune measurements taken using the Dimtel feedback system. An example is shown in Fig. 6.24 and described in Ref. [159]. This is one of the few data sets taken to date with a bunch spacing of 4 ns. This data set, for which the horizontal tune shifts are quite large, clearly favors a higher value of the total peak secondary yield parameter than the reference parameter set. More data sets with this spacing are planned for future experiments.

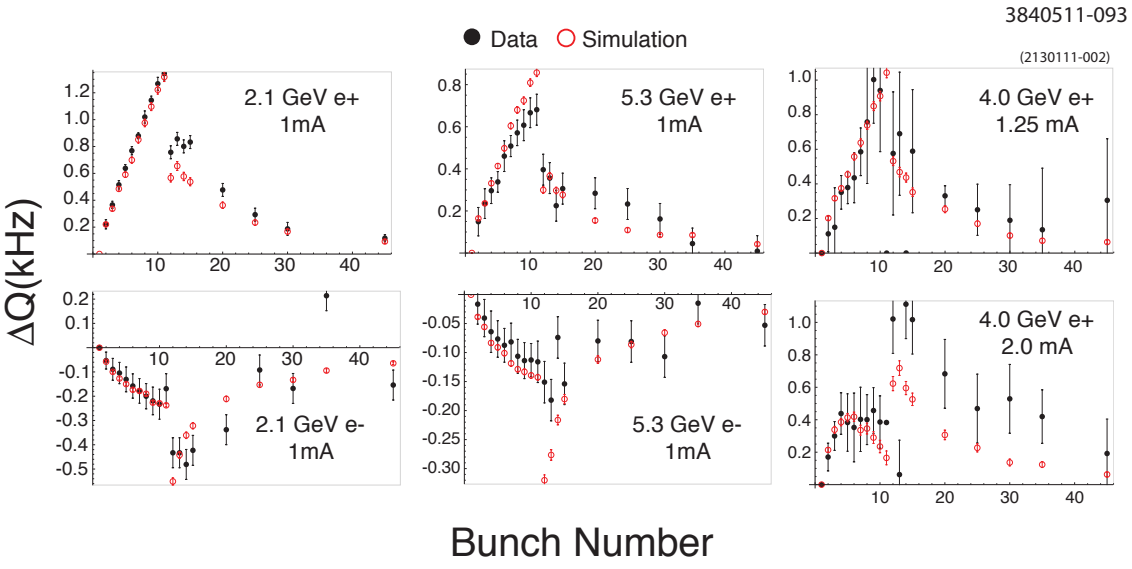

Figure 6.22: Vertical coherent tune shifts, 2010 data and POSINST simulations compared, using the parameters in Table 6.1.

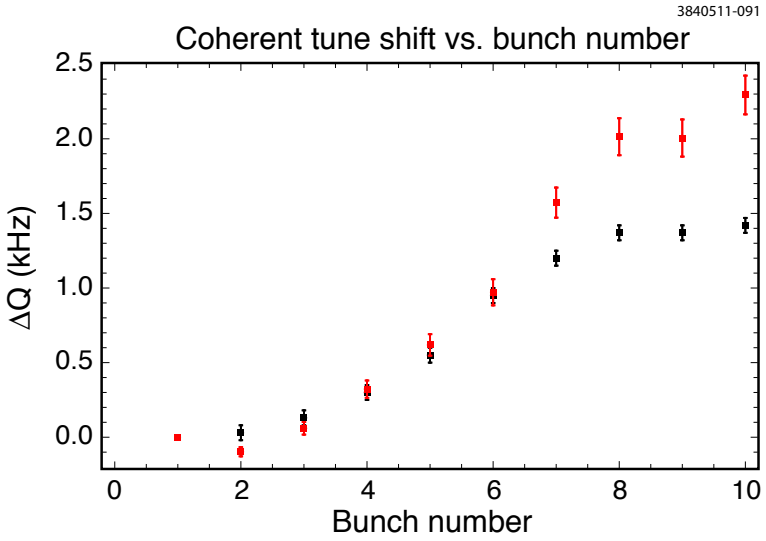

Figure 6.23: Horizontal coherent tune shifts, single-bunch-excitation data (black) and POSINST simulations (red) ("Modified static cloud model") compared. 10 bunch train, 4 mA bunch current 2.1 GeV beam energy. POSINST simulation using parameters given in Table 6.1.

type *d*: Tune measurements without a drive excitation, obtained from the analysis of BPM frequency spectra taken in conjunction with instability measurements, as discussed in Section 6.1.2. Examples are shown in Fig. 6.41 in the next section.

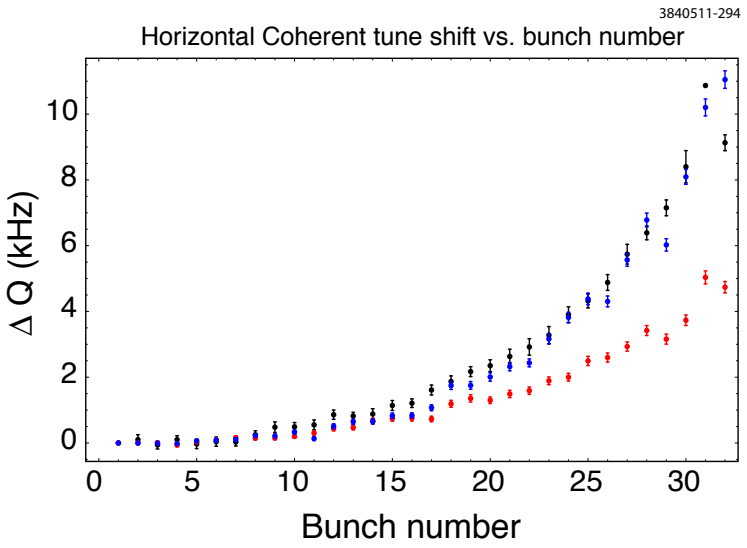

Figure 6.24: Horizontal coherent tune shifts, Dimel data (black) and POSINST simulations (red, blue) ("Modified static cloud model") compared. 32 bunch train, 0.8 mA bunch current, 2.1 GeV beam energy, 4 ns bunch spacing. Red: POSINST simulation using parameters given in Table 6.1. Blue: same simulation parameters except total peak secondary yield = 2.3

6.3.1.4 Systematic Study of Electron Cloud Model Parameters from POSINST Simulations

To gain confidence in the ability of the POSINST simulation to predict the performance of future storage rings and to tune the POSINST parameters, a systematic effort was made to compare the simulations with measurements under a wide variety of conditions. Comparisons of measurements with simulations were made for 54 data runs with electron and positron beams at 1.9, 2.1, 4.0, and 5.3 GeV energy, in trains of 3 to 45 bunches, with bunch charges of 0.5 to 4.2 nC (0.2 to 1.6 mA bunch current, respectively) representing the data in groups *1a* (2007-2008) and *2a* (2009).

For each data set, all six of the critical parameters shown in Table 6.1 were varied $\approx \pm 10\%$ relative to the reference parameter set. This was done independently for the horizontal and vertical tune shifts, and for the train and witness bunches, in order to monitor the consistency of the values obtained. A χ^2 was computed from the differences between the data and simulations, and a parabola was fit to the three χ^2 values to determine a best parameter value for each of the data sets.

Fig. 6.25 (left) shows the resulting values for the determination of the total secondary emission yield (SEY), for each data type, for the group *1a* and group *2a* data sets. Within the errors, the best-fit values for the total SEY parameter determined from the various data sets and data types are approximately the same.

It became quite clear during the evaluation process that the six POSINST parameters are correlated. To try to assess the correlations, we examined the secondary emission yield paired with each of the other five parameters. The fit χ^2 was evaluated at nine points for each pair, $\pm 10\%$ and zero offset from the reference value, and a two-dimensional parabolic fit was attempted at each data set. Often there was either no minimum, or a false minimum at a physically absurd value was found. In general, fits for the horizontal tunes failed, possibly because the POSINST model is inadequate,

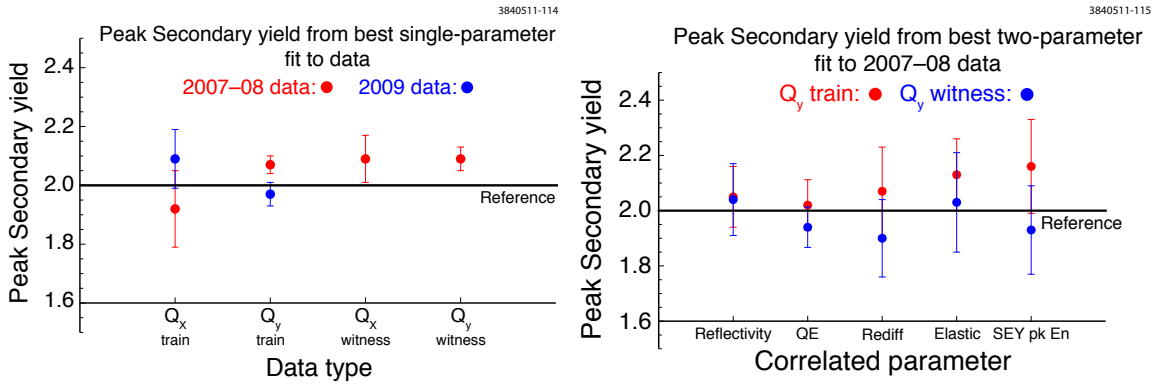

Figure 6.25: The best fit peak secondary emission yield parameter, as determined from a single-parameter fit, vs. data type (left); The best fit peak secondary emission yield parameter, as determined from a two-parameter fit, vs. the other parameter in the fit (right).

as noted above.

The results of this procedure are shown in Fig. 6.25 (right). Here we display the best-fit total SEY parameter obtained from a two-parameter fit, as a function of the other parameter, for the vertical tune data types. Although the results are consistent, the error bars are larger than for the single-parameter fits, reflecting the additional uncertainty caused by correlations between the total SEY parameter and the other parameters.

In Fig. 6.26, Fig. 6.27, and Fig. 6.28, we show the results of varying the other five critical parameters about the reference values given in Table 6.1. The plots show the best fit values obtained from single-parameter fits using the group *1a* and group *2a* data sets separately, and the best-fit values obtained from the two-parameter fits, in which the other parameter was the peak SEY. Table 6.3 summarizes numerically the values that could be extracted from the fits that succeeded, and gives the correlations extracted from the two-parameter fits.

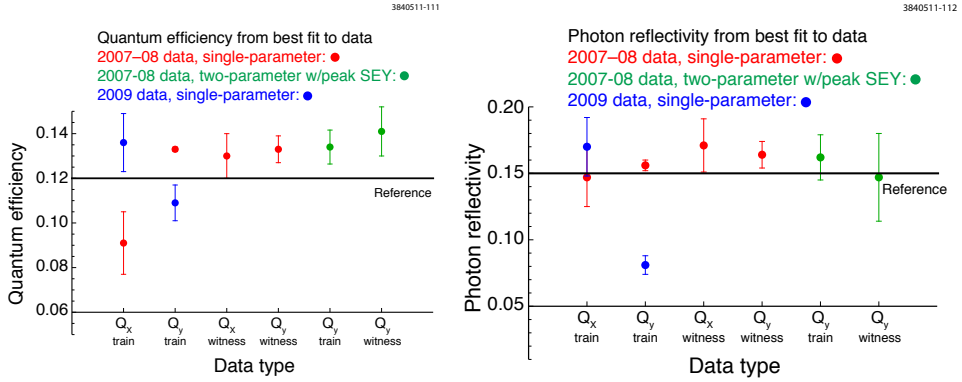

Figure 6.26: The best fit QE parameter Y (left) and photon reflectivity (right), as determined from single-parameter fits and two-parameter fits with the total SEY, vs. data type. While some of the single-parameter fit results appear inconsistent, the error bars obtained from the two-parameter fits are the best estimate of the true uncertainties.

It is clear that the effort of fitting has not yielded a dramatic improvement in the determination

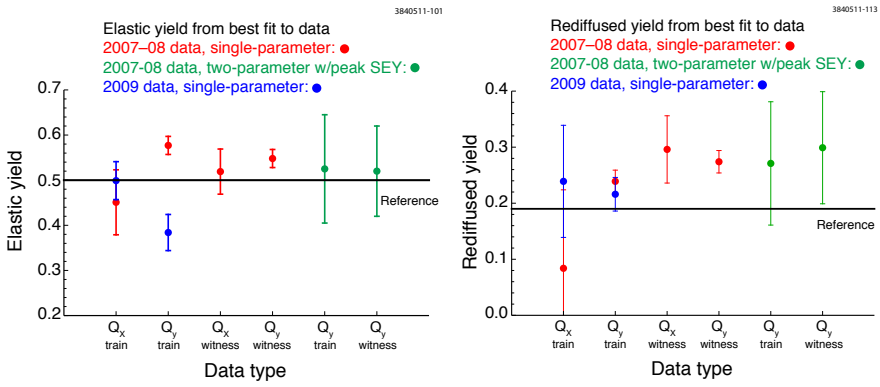

Figure 6.27: The best fit elastic SEY parameter (left) and rediffused SEY parameter (right), as determined from single-parameter fits and two-parameter fits with the total SEY, vs. data type. While some of the single-parameter fit results appear inconsistent, the error bars obtained from the two-parameter fits are the best estimate of the true uncertainties.

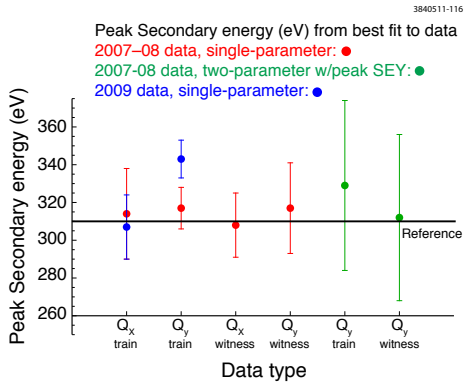

Figure 6.28: The best fit SEY peak energy parameter as determined from single-parameter fits and two-parameter fits with the total SEY, vs. data type.

of the POSINST parameters. In an effort to improve this technique we are using more sophisticated statistical techniques to help weed out poor measurements, which lead to misleading values of χ^2. Additional data have been taken at different bunch spacings in the hopes of better distinguishing primary from secondary electron emission.

Finally, it is possible that the simulation improvements noted in Section 6.3.1.7 may resolve some of the issues.

6.3.1.5 Comparisons Between Data and ECLOUD Simulations

Comparisons between CesrTA tune shift data and ECLOUD simulations have been previously reported in Refs. [135] and [136]. An example is shown in Figure 6.29, which corresponds to measurements from group *2a* for 45 positron bunches at a beam energy of 2.1 GeV with 14 ns-spacing and a bunch current of 0.4 mA. The magnitude and time dependence of the vertical tune shifts are well described by the ECLOUD and POSINST simulations.

The relative contributions of the field-free and dipole regions of the ring to the vertical tune shift

Table 6.3: Evaluating `POSINST` parameters. The reference SEY peak value is 2.0. Reference values for the other parameters are in the first column, and their best-fit values using train and witness tune shifts are in the next two columns.

Ref	Q_yTrain	Q_yWitness
	SEY peak $= 2.05 \pm 0.11$	SEY peak $= 2.04 \pm 0.13$
0.15	Reflectivity $= 0.162 \pm 0.017$	Reflectivity $= 0.147 \pm 0.033$
	Correlation $= -0.83 \pm 0.12$	Correlation $= -0.89 \pm 0.08$
	SEY peak $= 2.02 \pm 0.09$	SEY peak $= 1.94 \pm 0.07$
0.12	Quantum Efficiency $= 0.134 \pm 0.008$	Quantum Efficiency $= 0.141 \pm 0.011$
	Correlation $= -0.83 \pm 0.08$	Correlation $= -0.74 \pm 0.21$
	SEY peak $= 2.07 \pm 0.16$	SEY peak $= 1.90 \pm 0.14$
0.19	Rediffused at infinity $= 0.27 \pm 0.11$	rediffused at infinity $= 0.30 \pm 0.10$
	Correlation $= -0.84 \pm 0.12$	Correlation $= -0.89 \pm 0.04$
	SEY peak $= 2.02 \pm 0.09$	SEY peak $= 1.94 \pm 0.07$
0.50	Elastic SEY peak $= 0.53 \pm 0.12$	Elastic SEY peak $= 0.52 \pm 0.10$
	Correlation $= -0.72 \pm 0.21$	Correlation $= -0.89 \pm 0.10$
	SEY peak $= 2.02 \pm 0.09$	SEY peak $= 1.94 \pm 0.07$
310 eV	True Secondary $E_{\text{peak}} = 329 \pm 45$ eV	True Secondary $E_{\text{peak}} = 312 \pm 44$ eV
	Correlation $= 0.5 \pm 0.4$	Correlation $= 0.48 \pm 0.23$

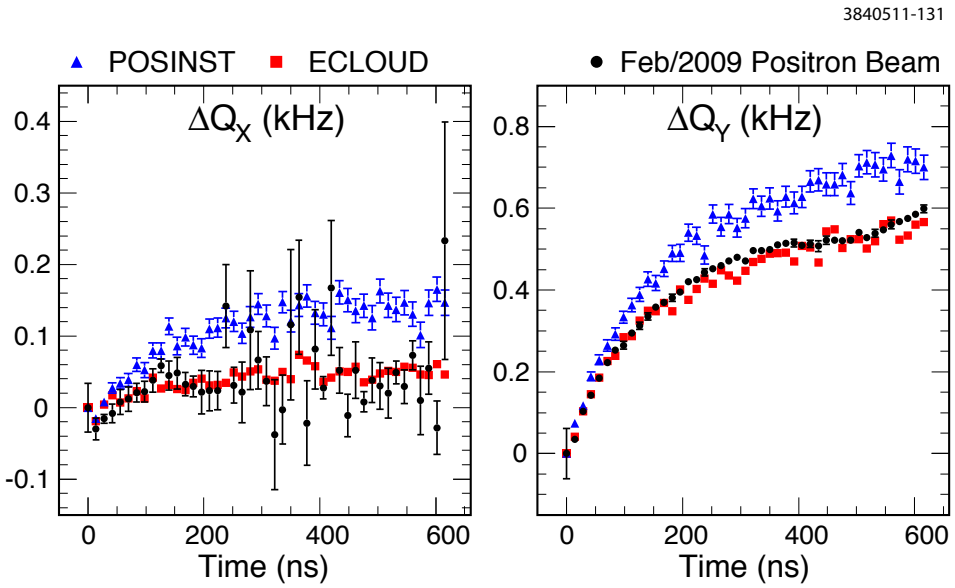

Figure 6.29: Comparison of the measured and simulated horizontal and vertical tune shifts along a 45-bunch train of 2.1 GeV positrons spaced by 14 ns. The bunch current is 0.4 mA. `POSINST` simulations using parameters given in Table 6.1. The `ECLOUD` and `POSINST` simulations show that, for this bunch current, the contribution to the vertical tune shift from the the dipole regions is only about 40% of the total tune shift, even though the ratio of dipole region length to drift region length is about 3:1.

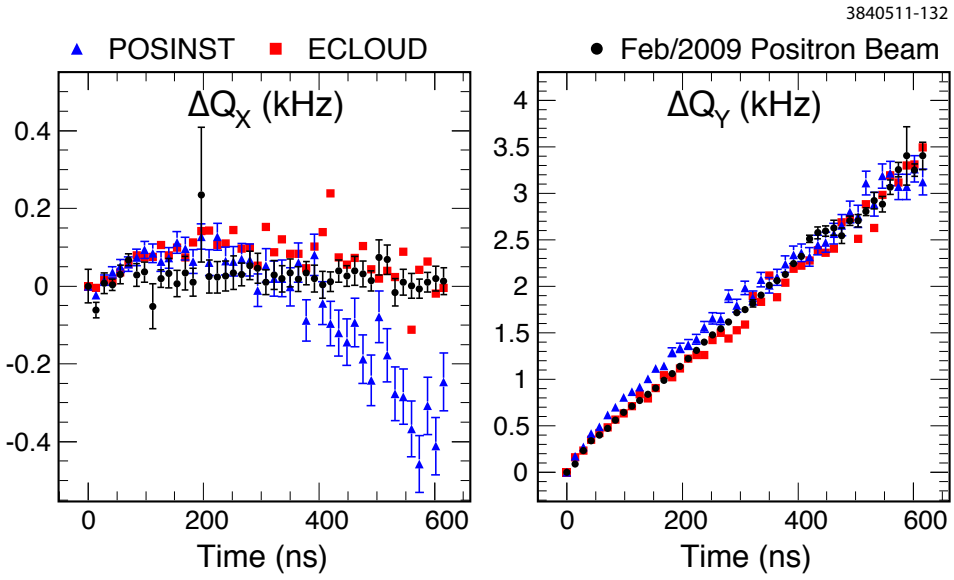

Figure 6.30: Measured and simulated tune shifts under the same conditions as for Fig. 6.29, but with double the bunch population. Under these conditions, the beam kicks are strong enough that the cloud buildup is dominated by the secondary yield on the top and bottom of the dipole vacuum chambers in the vertical plane containing the beam.

depend strongly on the bunch population, as can be seen by comparing Fig. 6.29 with Fig. 6.30, where the measurements were taken under identical conditions, but for a bunch population of 0.8 mA. Here the dipole contribution dominates after about 15 bunches in the train, resulting in the characteristic linear rise of the vertical tune shift. The beam kicks on the cloud electrons are strong enough for this bunch population that the secondary yield on the top and bottom of the vacuum chamber in the vertical plane containing the beam now dominate the vertical space-charge field gradients.

These measurement conditions are very similar to those described in Ref. [135]. However, the discrepancy (see Fig. 3 in [135]) between the data and the `ECLOUD` simulations reported in [135] has been resolved. Numerical approximations in the `ECLOUD` calculation have been improved, and, more importantly, the re-diffused component in the secondary yield model has been introduced. The re-diffused secondaries carry a substantial fraction of the kinetic energy of the incident cloud electrons [86]. If this contribution from re-diffused cloud electrons is omitted, the simulated dipole contribution to the vertical tune shift reaches a level about half of the measured tune shift of the 45^{th} bunch. Figure 6.31 illustrates the effect of the re-diffused component, distinguishing the contributions to the vertical tune shift from the drift and dipole regions. The dipole contribution at the higher bunch current is responsible for the continuing increase of the vertical tune shift along the bunch train, and the slope of the increase is largely due to the re-diffused secondary yield component. We also verified that the `POSINST` model shows a discrepancy with the measurement similar to that of `ECLOUD` when its re-diffused secondary yield component is removed.

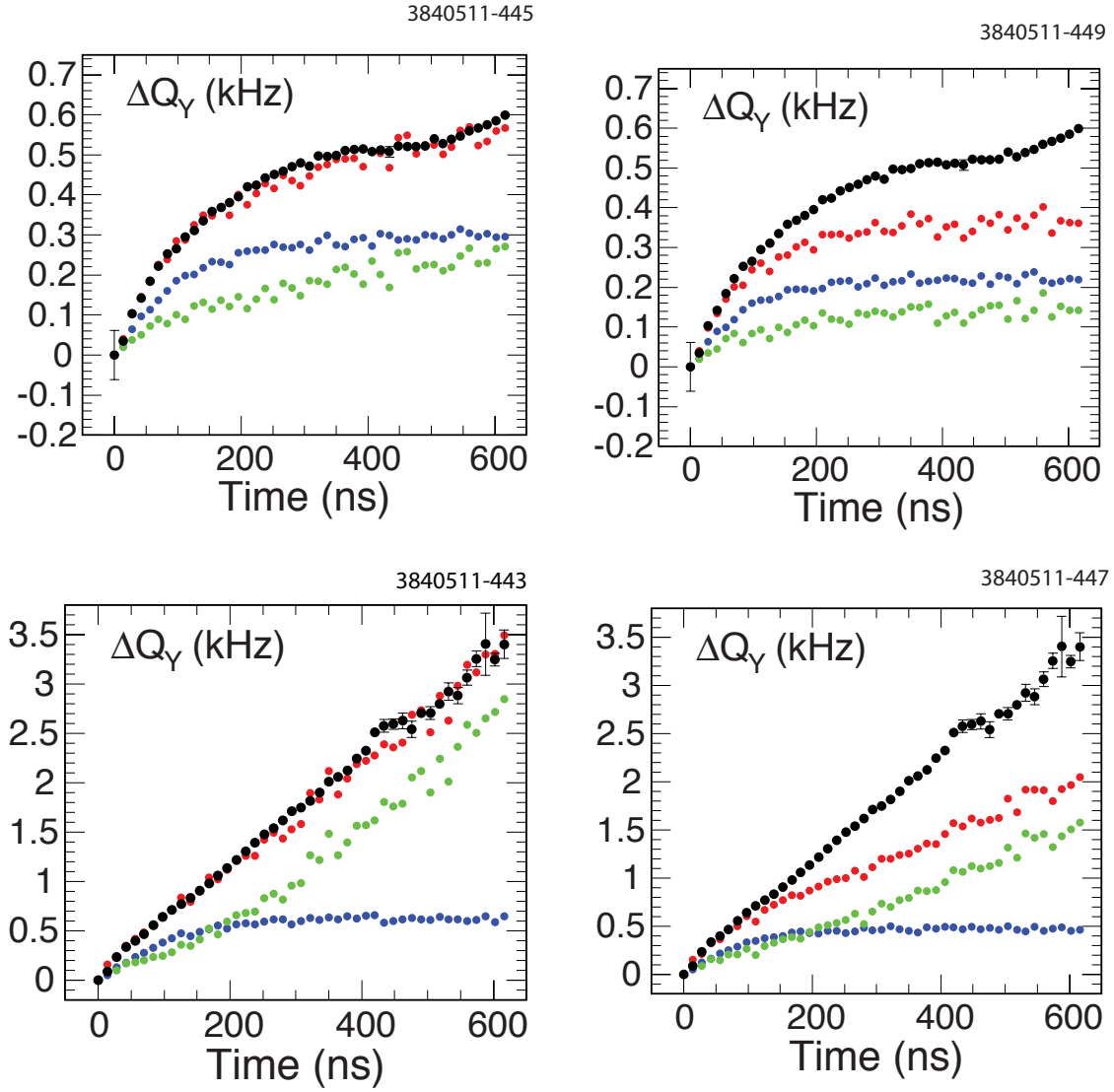

Figure 6.31: Measured and ECLOUD-simulated vertical tune shifts under the same conditions as for Figs. 6.29 and 6.30, showing the effect of the re-diffused SEY component on the contributions from the drift and dipole regions. The green points show the dipole contribution, the blue points show the drift contribution, and the red points show their sum. The measurements are shown as black points. The upper (lower) row shows the results for a bunch current of 0.4 mA (0.8 mA). The re-diffused secondary yield was set to 0.19 (0.00) while maintaining the peak secondary yield at 2.0 to obtain the results in the left (right) row.

6.3.1.6 Study of the Effects of Solenoids in the CesrTA Drifts

The tune shifts observed in CesrTA are due to electron cloud present in both the drift regions of the ring (about 179 m) and the dipole regions (about 475 m). Attempts have been made to separate the tune effects in the dipoles as opposed to the drift regions by introducing a 40 G solenoidal field in the most of the drift regions. By keeping photoelectrons accelerated by the beam from hitting the walls, the effects of secondary emission should be reduced in the regions with solenoids. Data sets (group *3a*) comparing solenoids on and off are shown in Fig. 6.32. Data are shown for 2.1 GeV positrons (top left) and electrons (bottom left) and 5.3 GeV positrons (top right) and electrons (bottom right). The solid curve is the `POSINST` simulation including both dipoles and drifts, and the dotted curve includes only dipoles. The reference values for the parameters, shown in Table 6.1, were used for the simulations.

It is clear from Fig. 6.32 that the `POSINST` simulations underestimate the solenoid-on tune shifts, particularly for the case of 2.1 GeV positrons. Additional simulation work is needed here to understand this.

6.3.1.7 Improvements to Electron Cloud Modeling for Tune Shifts at CesrTA

Use of the Photon Transport Code `Synrad3D` The simulations described above use the photon intensities corresponding to the synchrotron-radiated photons striking the vacuum chamber in the bend plane, together with a single empirically determined "photon reflectivity" parameter to describe the reflected photons. However, since the source of the synchrotron radiation is well known, and the reflection of the radiation from the walls can be modeled, it is possible to make reliable estimates of both the in-bend-plane and scattered radiation. These estimates allow a full characterization of the radiation absorbed on the walls to be made, without the need for an empirically determined reflectivity parameter. Since the radiation characterization can be made for any beam energy, ring lattice, and vacuum chamber profile, this greatly facilitates the extrapolation of electron cloud buildup calculations to future positron rings.

As described in Section 4.1.4.1, we have developed a three-dimensional photon production, transport and scattering simulation code, `Synrad3D`, which can predict the distribution of photon absorption sites on the vacuum chamber wall at any longitudinal position. The predictions from `Synrad3D` are supplied as inputs to `POSINST` or `ECLOUD` to provide a fully characterized description of the incident radiation. The description is limited by the accuracy of the vacuum chamber model, and by the approximations used in the scattering model. Initially, the radiation calculations were done with a simple, longitudinally uniform, vacuum chamber model, and with a scattering model based on purely specular reflection from an aluminum surface. More recently, as discussed above in Sec. 5.1.3.2, we have used the code to model the actual complex vacuum chamber shape of the CesrTA chamber, and to include diffuse scattering.

In Fig. 6.33 and Fig. 6.34, we compare (in red) the tune shifts calculated using the `Synrad` photon intensities for the bend plane radiation, together with an empirical reflectivity parameter describing a uniform distribution over the rest of the chamber, with (in blue) a calculation based on the `Synrad3D` photon distributions, computed using the actual CesrTA vacuum chamber, and including diffuse scattering, as described in Sec. 5.1.3.2, Example 4. Both calculations use the reference simulation parameters presented in Table 6.1 for the SEY model parameters. For the results derived from the `Synrad3D` photon distributions, we have used lower values for the empirical quantum

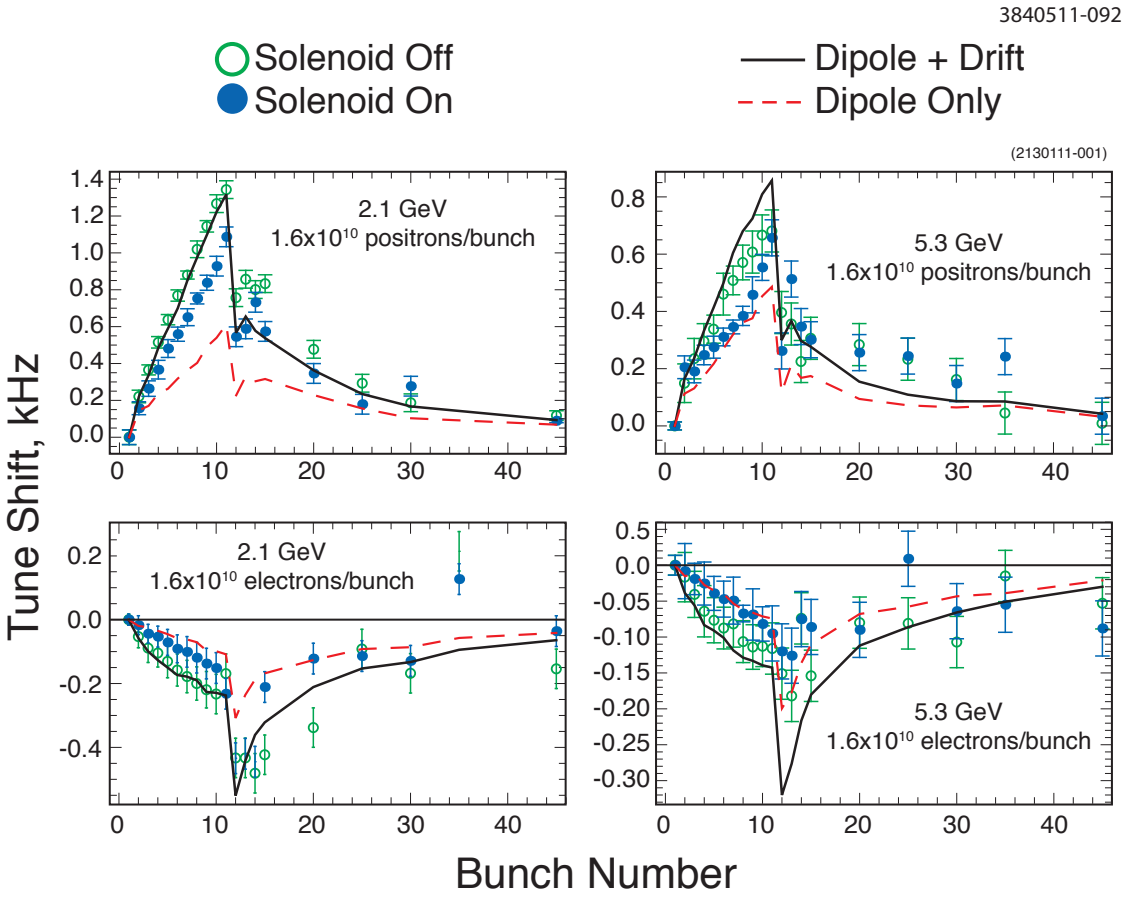

Figure 6.32: Dependence of vertical tune shifts on solenoids in drift regions. Positron (top) and electron (bottom) tune shifts vs. bunch number, for 2.1 (left) and 5.3 GeV (right) beams. The green circles and blue dots represent data taken with solenoids off and on, respectively. The solid curve is the `POSINST` simulation including both dipoles and drifts, and the dotted curve includes only dipoles, using the parameters in Table 6.1.

efficiency (10.8% for dipoles, 9.7% for drifts) to optimize agreement with the vertical tune shifts for the 2.1 GeV data, and, in addition, a more realistic Lorentzian photoelectron energy distribution (see next subsection).

Examination of Fig. 6.33 and Fig. 6.34 shows a modest improvement in the agreement between the horizontal tune shift data and the simulations (especially for 5.3 GeV), when using the `Synrad3D` photon distributions. Most of this improvement results from the use of a highly nonuniform photon distribution on the vacuum chamber out of the bend plane (see, for example, Fig. 5.8), as predicted by `Synrad3D`, in contrast to the simpler uniform distribution used in simulations based on `Synrad`.

The decay of the horizontal tune shift after the passage of the 10 bunch train depicted in the left plot of Fig. 6.34 is not well modeled. It should be noted that the horizontal tune shifts are very small in this type of pinged beam measurement, and the simulation depends on the delicate cancellation described in Sec. 6.2.1.3, so a substantial disagreement need not be a cause for concern.

Fig. 6.34 also shows an improvement in the agreement between the vertical tune shift data and the simulations. Although a discrepancy remains, we note that the quantum efficiency should be different (and lower) at 5.3 GeV than at 2.1 GeV, since the photon spectrum at 5.3 GeV is harder, and the quantum efficiency decreases at higher photon energies. Using the methodology outlined in Section 5.1.3.3 above, and the photon energy spectra from `Synrad3D` simulations, the relative reduction in quantum efficiency from 2.1 GeV to 5.3 GeV should be about 20%.

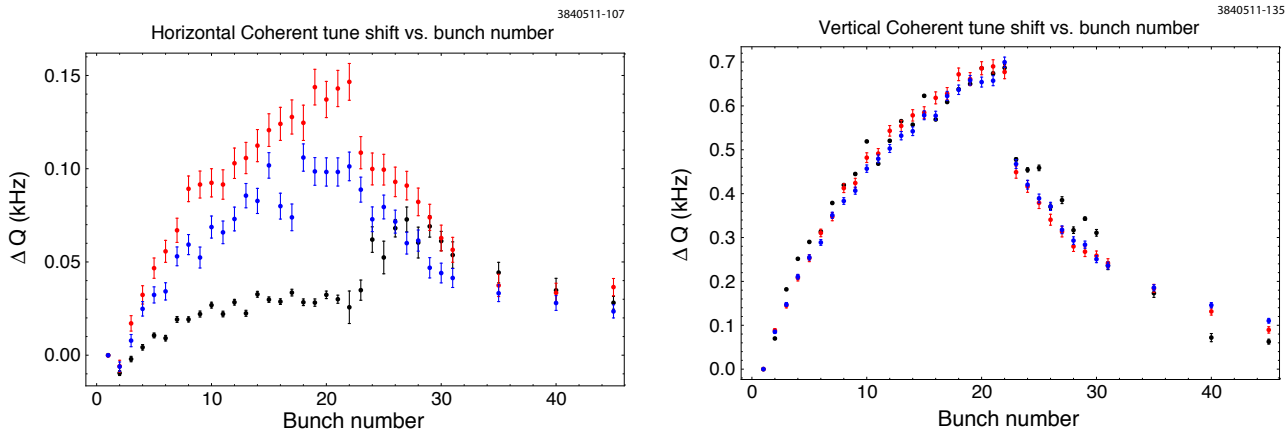

Figure 6.33: Tune shifts vs. bunch number, for 2.1 GeV data set corresponding to Fig. 6.19, left, computed (using `POSINST`) from `Synrad` (red points) and `Synrad3D` (blue) photon simulations, compared with data (black).

Photoelectron Modeling (see also Section 5.1.3.3) In connection with studies of electron cloud effects for the LHC, direct measurements [102] have been made of the photoelectron energy spectrum produced by soft VUV photons. The measurements indicate that the photoelectron energy spectrum can be well represented by a Lorentzian with a peak and width of a few eV. Studies of the shielded button data (see Section 5.2.2) demonstrate that, although a simple Lorentzian distribution is adequate for the photons generated by a 2 GeV CesrTA beam, for the harder photon spectrum generated by a 5 GeV beam, a high energy tail, with a power law falloff slower than that of a Lorentzian, is required. Consequently, a new parameterization, using a Lorentzian

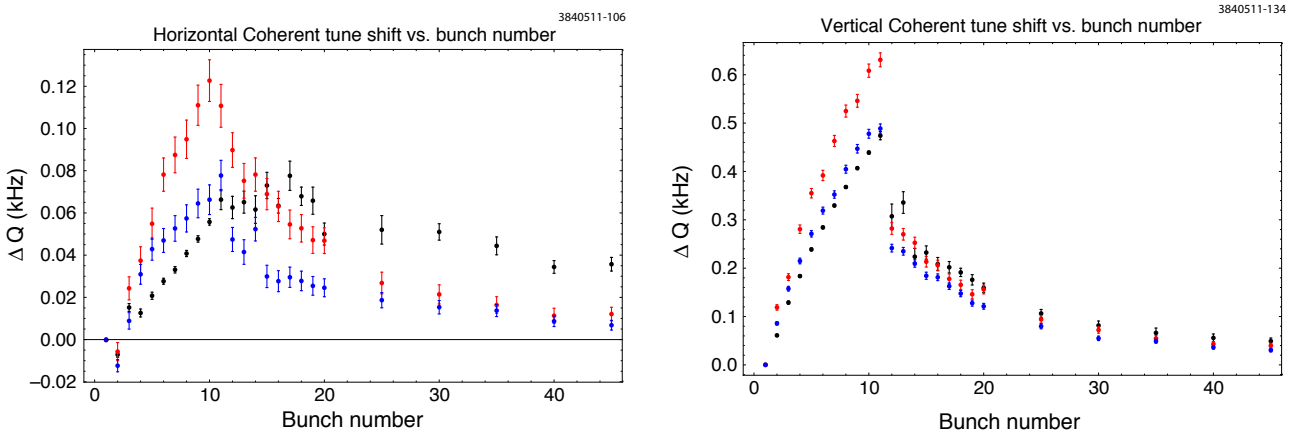

Figure 6.34: Tune shifts vs. bunch number, for 5.3 GeV data set corresponding to Fig. 6.20, left, computed (using `POSINST`) from `Synrad` (red points) and `Synrad3D` (blue) photon simulations, compared with data (black).

spliced to a power law distribution with an adjustable exponent at high photoelectron energies, has been installed in `POSINST`. Preliminary re-evaluation of the tune shift simulations for both positron and electron beams at 5 GeV indicate that the presence of a high energy tail in the photoelectron energy spectrum makes only a small difference in the simulated tune shifts.

6.3.1.8 Future Work

Measurements at bunch spacings of 4 ns and 8 ns, similar to the proposed ILC damping ring bunch spacing of 6 ns are planned. Also, considerably more data will be taken for data type *b* (single-bunch excitation), for which the oscillation mode is well controlled and the comparison with simulation is cleaner.

6.3.2 Instability Thresholds: Experimental Measurements

As described in Sec. 6.1.2, we have developed the capability to make automated measurements of frequency spectra of individual bunches, to look for signals of single-bunch instabilities. During such measurements, for each bunch in a train, several frequency spectra are acquired, covering a range which spans the lowest betatron sidebands. Machine conditions, such as bunch current, magnet settings, feedback system parameters, etc. are automatically recorded and stored before and after each single-bunch spectrum is taken.

Using this system, during the July-August, 2010, and September runs, a number of observations were made which illuminate the dynamics of the electron-cloud/beam interaction at CesrTA. Some of the results from these experiments are described below.

General Remarks Unless otherwise noted, all experiments discussed in this section were done at 2.085 GeV in a low emittance lattice. The machine parameters for these experiments are shown in Table 6.4.

Table 6.4: Nominal machine parameters at 2 GeV. The emittances and tunes are those of a single bunch in the machine.

Parameter	Unit	Value
Energy	GeV	2.085
Lattice		2085mev_20090516
Horizontal emittance	nm	2.6
Vertical emittance	pm	~ 20
Bunch length	mm	10.8
Horizontal tune		14.55
Vertical tune		9.58
Synchrotron tune		0.065
Momentum compaction		6.8×10^{-3}
Revolution frequency	kHz	390.13

Trains having bunches numbering from $30 - 45$, with a bunch spacing of 14 ns, and bunch currents in the range of $0.5 - 1.25$ mA ($0.8 - 2.0 \times 10^{10}$ particles) per bunch were studied. In all cases, except where specifically noted, the beam particles were positrons.

Several systematic checks were undertaken:

- Checks were made to rule out intermodulation distortion in the BPM electronics and in the BPM itself.
- The betatron and synchro-betatron (head-tail) lines moved as expected when the vertical, horizontal, and synchrotron tunes were varied.

The longitudinal feedback was off for these measurements. The vertical and horizontal feedback were turned down to 20% of full power. Some experiments explored the effect of turning the vertical feedback fully off.

More details on the experimental technique can be found in Section 6.1.2.

General Observations The basic observation is that, under a variety of conditions, the frequency spectra exhibit the vertical $m = \pm 1$ synchro-betatron (head-tail) lines, separated from the vertical betatron line by the synchrotron frequency, for many of the bunches along the train. The amplitude of these lines typically (but not always) grows along the train.

Typically, for the bunch at which the vertical synchro-betatron lines first appear above the noise floor (which is about 40 dB below the vertical betatron line), we observe (on a bunch-by-bunch x-ray beam size monitor) growth in the beam size, which continues to increase along the train (see Section 6.3.4).

Under some conditions, the first bunch in the train also exhibits a synchrobetatron line ($m = -1$ only). The presence of a "precursor" bunch, placed about 180 ns before the train, eliminates the $m = -1$ signal in the first bunch.

Subsequent sections will present the details of these observations, together with their dependence on machine and beam parameters such as bunch current, number of bunches, chromaticity, synchrotron

tune, beam emittance, vertical feedback, beam energy, and particle species. In Sec. 6.3.3, some preliminary observations on measurements of bunch-by-bunch damping rates are presented.

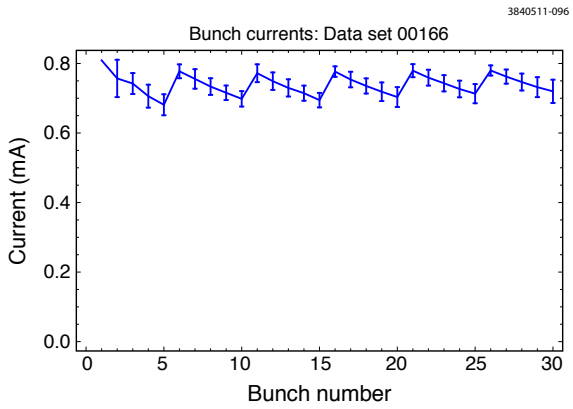

Figure 6.35: Data set 166: Bunch-by-bunch currents

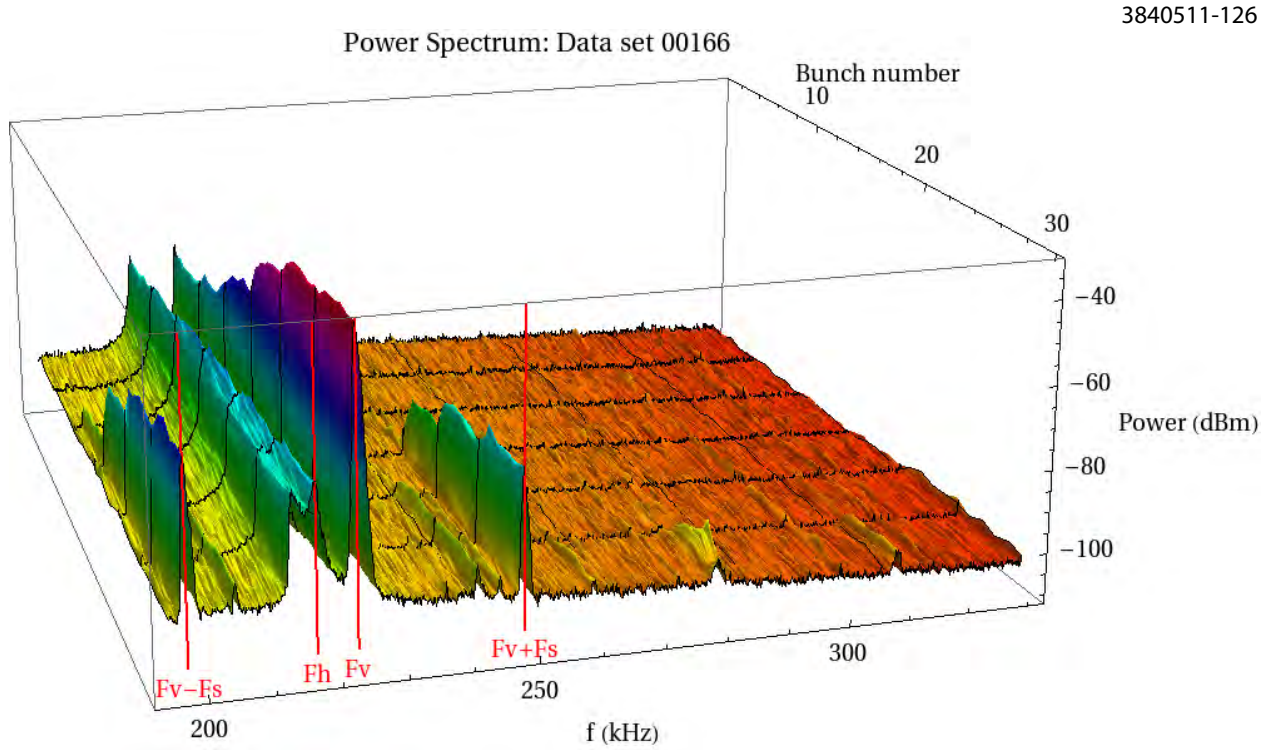

Figure 6.36: Data set 166: Bunch-by-bunch power spectrum

6.3.2.1 Bunch-by-Bunch Power Spectrum

To measure a bunch-by-bunch power spectrum, the machine is loaded with a bunch train with a uniform current per bunch, and software is run to automatically collect frequency spectra from a button BPM gated on the first bunch. The data acquisition takes a few minutes, and the gate is

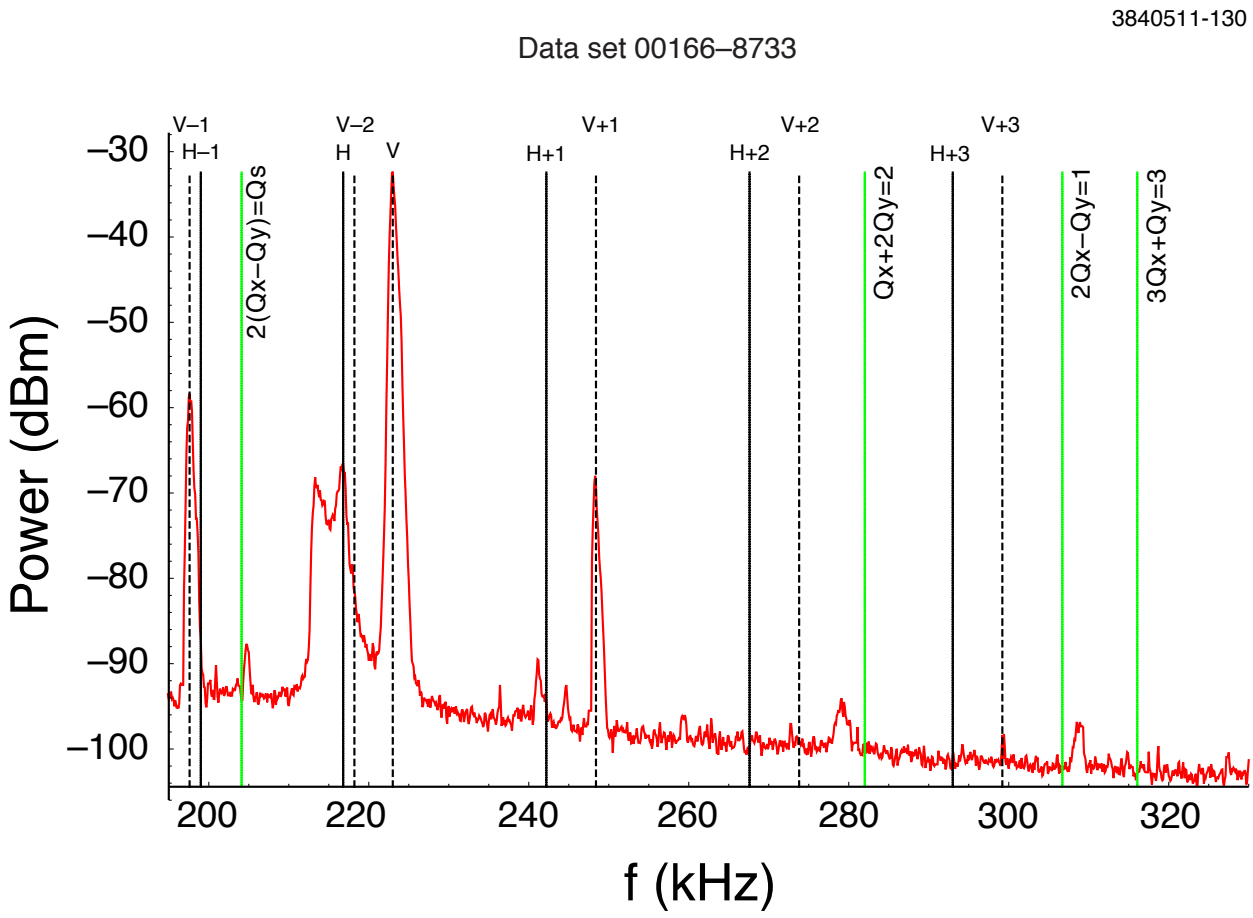

Figure 6.37: Data set 166: Power spectrum for bunch 30. The lines labelled, for example,"V+1" and "V-1" are shown at frequencies of $\pm$ f_s from the vertical betatron line ("V"), in which f_s is the synchrotron frequency. The locations of several machine resonances are also indicated.

then moved to the second bunch, and so on through the train. For bunch spacings greater than about 6 ns, the gate width is smaller than the bunch spacing, so only the motion of the gated bunch is observed. The frequency spectra are 10 s averages, acquired in 4 measurements, each with a 40 kHz span, covering the range from 170 to 330 kHz.

Since the beam has a relatively short lifetime, it is necessary to periodically pause the measurements and "top off" the bunch train. Typically, this is done after data acquisition is completed for a group of 5 bunches. Fig. 6.35 shows the beam current as a function of bunch number for a 30 bunch train (data set 166). In this figure, the current per bunch plotted for bunch n corresponds to the average value of the bunch current for all bunches earlier than bunch n; the error bar represents the rms variation in this number, principally due to irregularities in the fill. The dips at bunches 5, 10, ..., and peaks at 6, 11, ..., correspond to when the train is "topped off."

The bunch-by-bunch power spectrum observed in data set 166 is shown in Fig. 6.36. The figure plots the power spectrum for each bunch, as measured at the button BPM, vs. frequency. The four prominent peaks seen correspond, from lower to higher frequency, to the $m = -1$ vertical synchrobetatron line, the horizontal betatron line, the vertical betatron line, and the $m = +1$ vertical synchrobetatron line. Fig. 6.37 shows the spectrum of the last bunch, bunch 30, in greater

detail. For this data set, the vertical chromaticity (defined as $dQ/d\delta$, where δ is the relative momentum and Q is the tune) was 1.16, and the horizontal chromaticity was 1.33.

The principal features exhibited in Fig. 6.36 and Fig. 6.37 are discussed in more detail in the next subsections.

6.3.2.2 Power Spectrum Features near the Betatron Lines

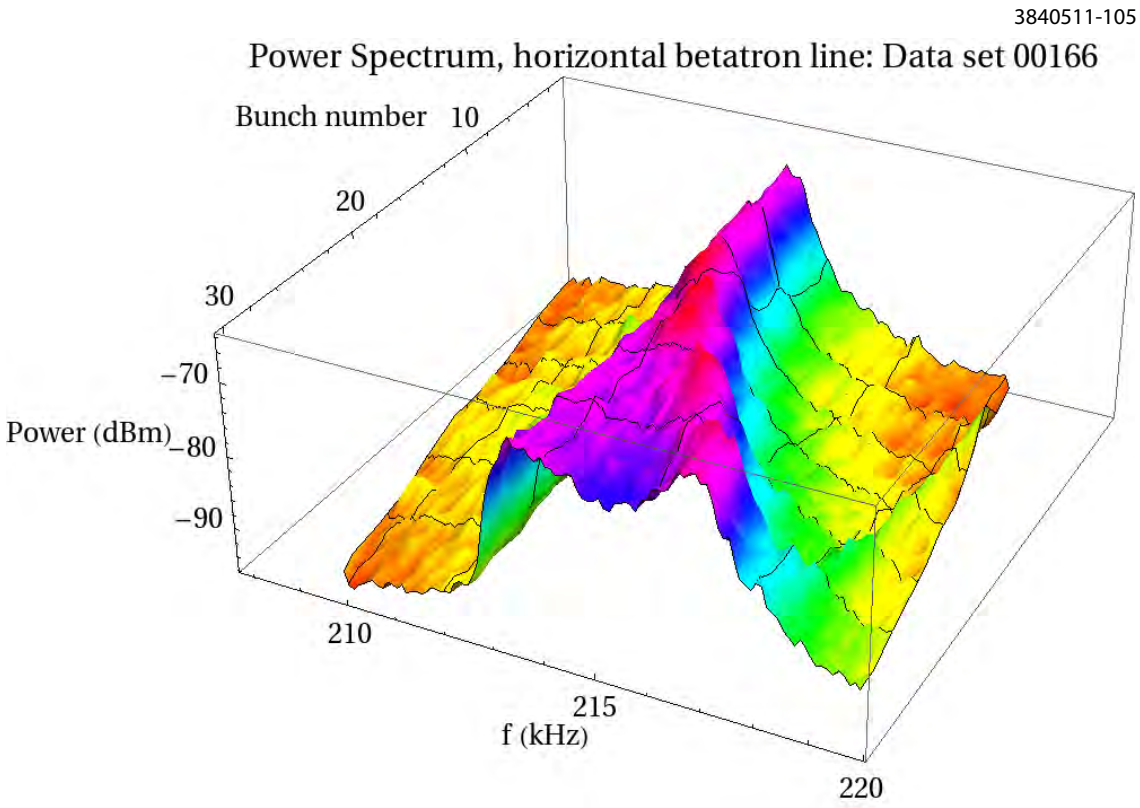

Figure 6.38: Data set 166: Bunch-by-bunch power spectrum: detail at horizontal betatron line. Chromaticity: (H,V) = (1.33, 1.16). Bunch current = 0.74 mA.

Horizontal Betatron Lineshape Fig. 6.38 shows the bunch-by-bunch power spectrum near the horizontal betatron line. There is a major peak which shifts up in frequency by about 4 kHz during the bunch train. This shift is attributable to the electron cloud. A quantitative comparison with simulations is presented below. In addition, there is a lower amplitude "shoulder", which appears to be roughly constant in frequency during the bunch train (i.e., there is no tune shift). A plausible explanation for this shoulder is the following: tune shift measurements and simulations (see Section 6.2.1.3) have shown that, when the all the bunches in the train are oscillating in-phase, the horizontal tune shift due to the electron cloud in a dipole-dominated ring such as CesrTA is very small. However, for the data set shown in Fig. 6.38, the bunches in the train are spontaneously excited, so a mixture of multibunch modes will be present. This mixture of multibunch modes will exhibit a spectrum of electron-cloud-induced tune shifts, ranging from nearly zero tune shift for the

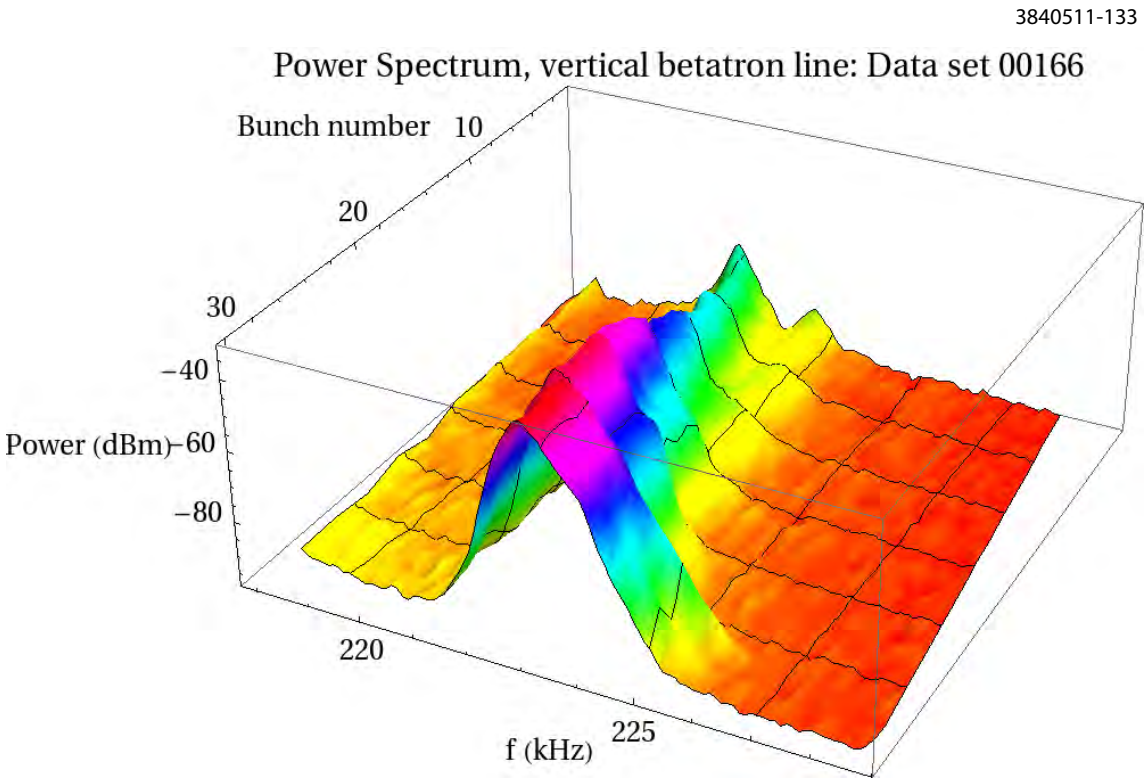

Figure 6.39: Data set 166: Bunch-by-bunch power spectrum: detail at vertical betatron line. Chromaticity: (H,V) = (1.33, 1.16). Bunch current = 0.74 mA.

mode in which the bunches are oscillating in phase, to large tune shifts for modes in which bunches are oscillating with different phases. Qualitatively, this should produce a spectrum similar to that shown in Fig. 6.38.

Vertical Betatron Lineshape Fig. 6.39 shows the bunch-by-bunch power spectrum near the vertical betatron line. In this case, there is a shift up in frequency of the major peak by about 2 kHz during the bunch train, which is again attributable to the electron cloud. In addition, there is a smaller peak at a higher frequency, present even on the first bunch, which appears to grow in amplitude and merge with the main peak near the end of the bunch train. Since this peak is present even for the first bunch, it is unlikely that it is due to a multibunch mode dependence of the vertical electron cloud tune shifts. Also, measurements and simulations (see Section 6.2.1) have shown that the dependence of the *vertical* tune shifts on the multibunch mode is much smaller than for the horizontal tune shifts. This suggests that the structure in the vertical plane may be a single-bunch effect, but we have no good explanation for it.

Horizontal and Vertical Betatron Lines: Peak Power and Frequency On the right side of Fig. 6.40, the peak power point[6] for each of the horizontal and vertical betatron lines is shown, as a

[6]For all the relative power plots shown in this paper, the plotted points were obtained as follows: A frequency region is selected, 10 kHz wide, centered approximately on the frequency of interest. The average background power

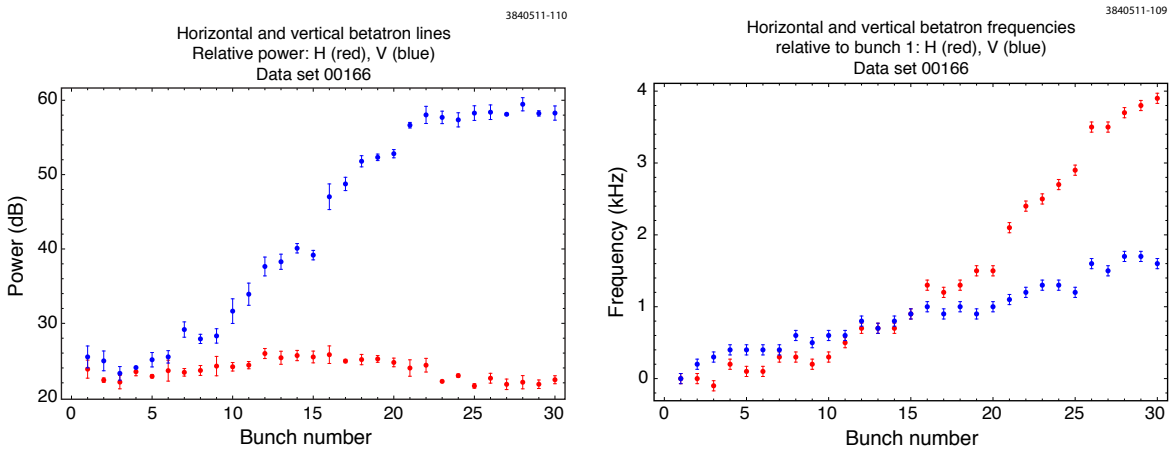

Figure 6.40: Data set 166: Left, Horizontal and vertical peak power vs. bunch number; right, Horizontal and vertical tune shifts vs. bunch number. Chromaticity: (H,V) = (1.33, 1.16). Bunch current = 0.74 mA.

function of bunch number. The strong excitation of vertical dipole motion is evident in the increase in vertical betatron line power along the train. There is minimal if any additional excitation in the horizontal plane.

In Fig. 6.40, the frequency of the peak power point is given, relative to the frequency of the first bunch. Thus, Fig. 6.40 illustrates the tune shift along the train, which is primarily due to the electron cloud effect.

Comparison with Electron Cloud Buildup Simulations The cloud buildup program `POSINST` can be used to compute the cloud density corresponding to a set of beam and vacuum chamber properties at CesrTA, and from this density the tune shifts can be computed (in this case, we have used the "Modified static cloud model": see Section 6.2.1.4). These calculations can be compared with the measured tune shifts shown in Fig. 6.40. Comparisons between simulations and measurements are shown in Fig. 6.41. The key parameters used in the `POSINST` simulation are given[7] in Table 6.1 (in Section 6.3.1).

The error bars on the simulated points are due to macro-particle statistics; for the vertical tune shifts, the comparison would benefit from an increased number of macro-particles, which was not feasible due to computer run time limitations. Nevertheless, inspection of Fig. 6.41 indicates that the simulation compares well with the data.

6.3.2.3 Estimates of the Electron Cloud Density at the Instability Threshold

level in this region is determined. Then, the maximum value of the power in this region is found, and subtracted from the background power level, to obtain the relative power.

Because of this background subtraction, if the relative power is close to zero (as in the plots of head-tail line power later in the paper), this signifies the absence of any significant peak.

The frequency plots show the frequency at which the power spectrum peaks.

The errors shown in the frequency plots correspond to the bin widths of the frequency spectra (100 Hz). The errors shown in the relative power plots are estimated from the variation in the power over a spectral bin width.

[7]Except for the total secondary yield, which was 2.05.

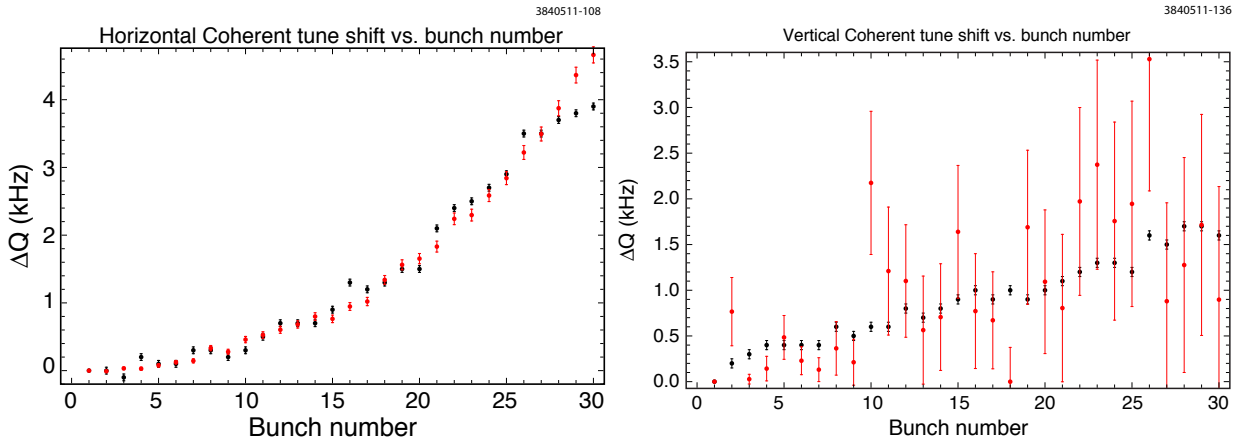

Figure 6.41: Data set 166 tune shifts: comparison between data (black) and simulation (red) from `POSINST` with parameters given in Table 6.1. Left: Horizontal tune shift vs. bunch number; right: Vertical tune shift vs. bunch number.

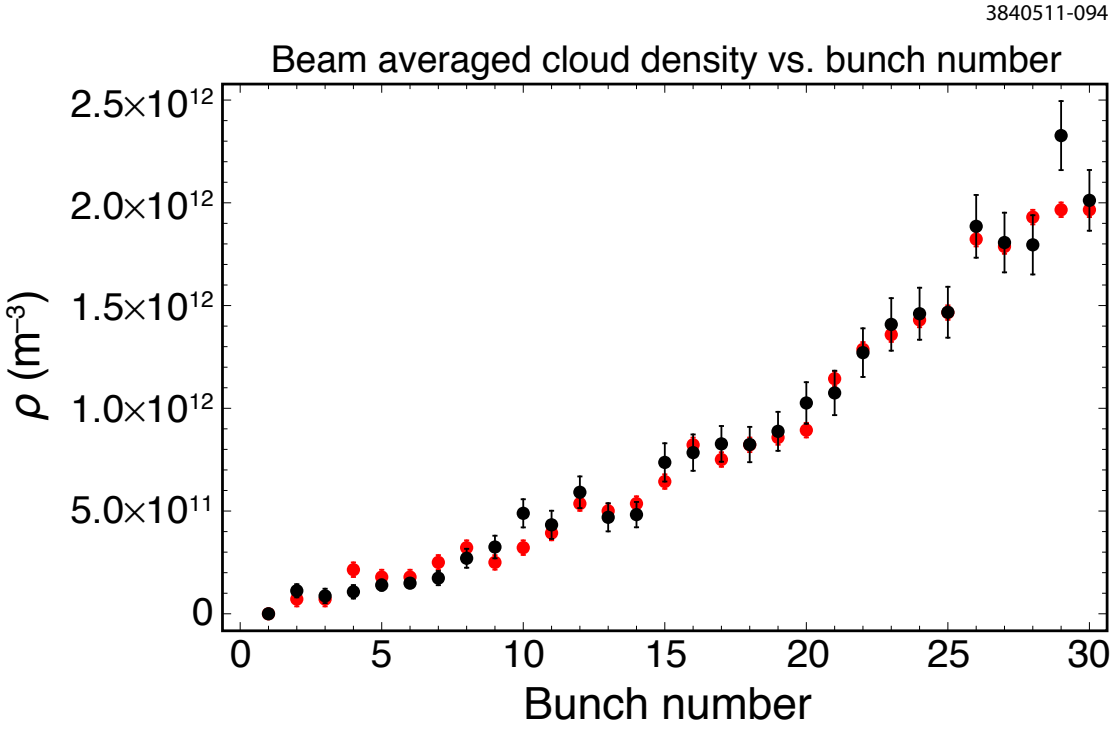

Figure 6.42: Data set 166: Average initial (i.e., before the "pinch") electron cloud density vs. bunch number, comparison between estimate from measured tune shifts (red), and simulation (black) from `POSINST` with parameters given in Table 6.1.

Cloud Density from Measured Betatron Tune Shifts In this section, the measured tune shifts are used to estimate the average electron cloud density. For a lattice in which the beta functions are equal in both planes, the electron-cloud-induced tune shifts δQ_x and δQ_y may be

directly related to the average electron cloud density $\langle \rho_c \rangle$ via the relation

$$\langle \rho_c \rangle = \gamma \frac{\delta Q_x + \delta Q_y}{r_e \langle \beta \rangle C}, \tag{6.59}$$

in which $\langle \beta \rangle$ is the average beta function, C is the ring circumference, γ is the beam Lorentz factor, and r_e is the classical electron radius. This relation may be used to obtain an estimate of the cloud density along the train. For CesrTA we use $C = 649$ m (sum of all drift and dipole lengths) and $\langle \beta \rangle = 16$ m. The cloud densities for each bunch resulting from this calculation are shown as the red points in Fig. 6.42.

Comparison with Electron Cloud Buildup Simulations We can compare the cloud density, obtained from the measured tune shifts, with the density obtained from the `POSINST` simulations discussed in the previous section. This comparison is shown in Fig. 6.42. For the simulation result, shown as black dots in the figure, the cloud density is evaluated at the time corresponding to the leading edge of the bunch (i.e., before the "pinch"), and is averaged over the transverse profile of the beam. The density shown is the weighted average over drifts (total length 175 m) and dipoles (total length 474 m). It is clear from Fig. 6.42 that the cloud density computed directly from the tune shifts is quite close to the simulation result.

6.3.2.4 Vertical Head-tail Lines

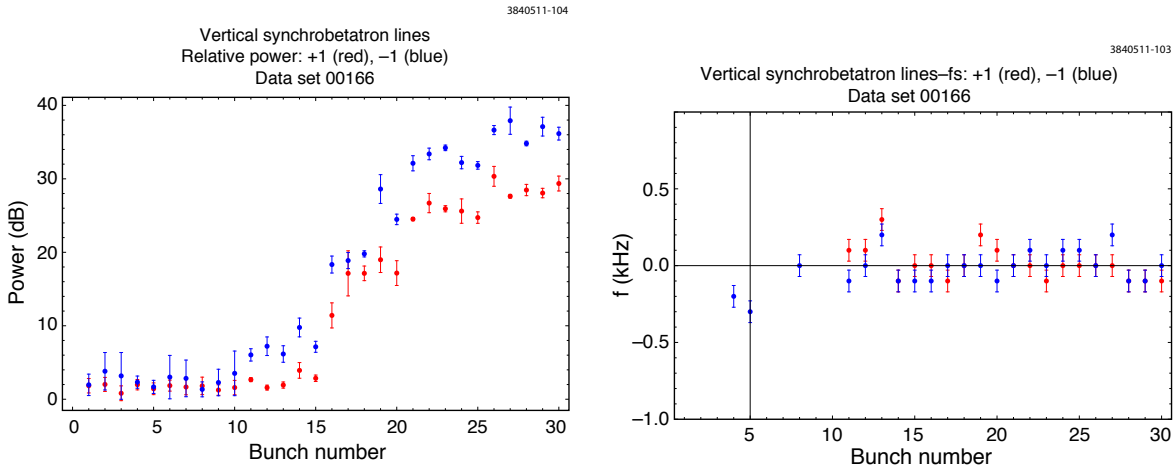

Figure 6.43: Data set 166: Vertical head tail lines: left, peak power vs. bunch number; right, frequency difference from vertical betatron line vs. bunch number, with the synchrotron frequency removed from the offset. Chromaticity: (H,V) = (1.33, 1.16). Bunch current = 0.74 mA.

Head-tail Line Power and Frequency Characteristics As shown in Fig. 6.36 and Fig. 6.37, there are two lines which appear in the bunch-by-bunch power spectrum, starting part way along the train, which have frequencies which are close to the betatron frequency plus and minus the synchrotron frequency. In Fig. 6.43, we plot the power (relative to the vertical betatron line) and the frequency (± the synchrotron frequency) of these lines. We associate the lower frequency line with the $m = -1$ head-tail line, which arises as a result of head-tail bunch motion driven by the broadband impedance of the electron cloud. Similarly, we associate the higher frequency line with

the $m = +1$ head-tail line. From Fig. 6.43, we see that these lines appear above the noise level around bunch 15 or 16. The $m = -1$ line is somewhat more strongly excited than the $m = +1$ line.

Observations of beam size growth under similar beam conditions (see Section 6.3.4) show rapid emittance growth starting at about the same point in the train.

Fig. 6.43 shows that, for bunch numbers greater than about 15, where the head-tail lines appear above the background, the frequency difference between these head-tail lines and the vertical betatron line is equal to the synchrotron frequency (within the errors).

Head-tail Lines: Correlation with Cloud Density Comparing Fig. 6.42 and Fig. 6.43, the average electron cloud density at which the head-tail lines are first observed can be established. For the conditions of data set 166, the head-tail lines emerge at an initial (i.e., before the "pinch") beam-averaged cloud density around 8×10^{11} m^{-3}.

6.3.2.5 Reproducibility

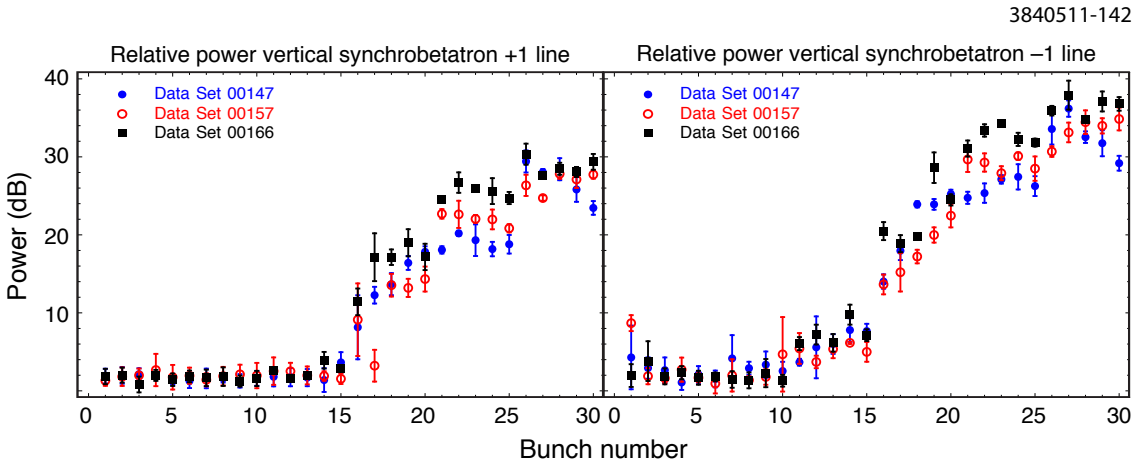

Figure 6.44: Data sets 147, 157 and 166: vertical head-tail lines compared. All sets have the same nominal bunch current and chromaticity.

The reproducibility of the observations of the head-tail lines is illustrated in Fig. 6.44. This plot shows the power in the vertical head-tail lines for three data sets taken on different dates (data set 147 on September 25, 2010, data set 157 on September 26, 2010, and data set 166 on September 28, 2010) but under the same nominal machine and beam conditions. Fig. 6.44 shows that the head-tail line observations are reasonably reproducible when the machine is set to the same nominal conditions.

6.3.2.6 Chromaticity Dependence

The chromaticity dependence of the head-tail lines is illustrated in Fig. 6.45. For all data sets, the nominal bunch current was abut 0.74 mA. We see that for data set 142, with a higher value of the

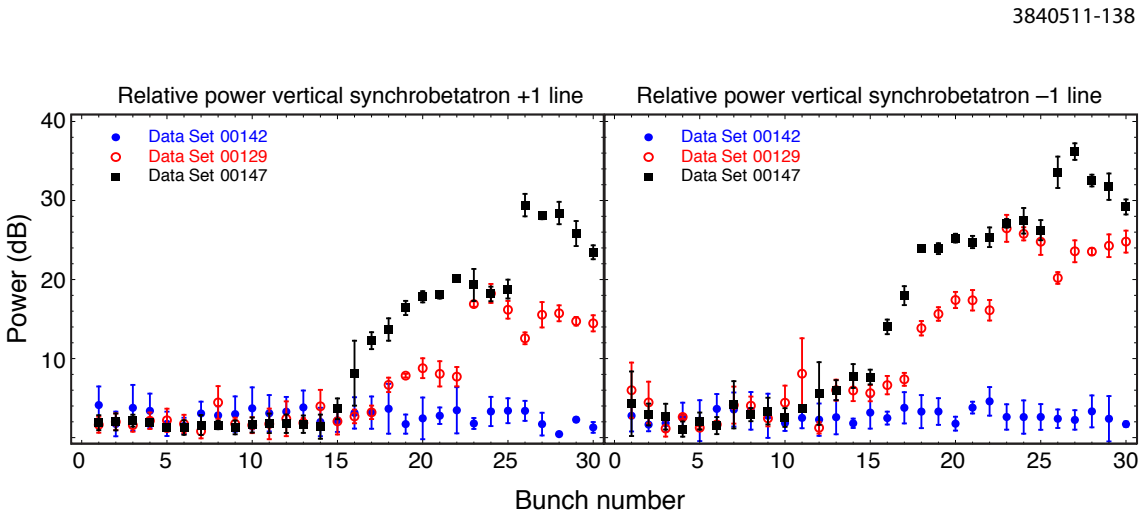

Figure 6.45: Data sets 142, 129 and 147: vertical head-tail lines compared. All sets have the same nominal bunch current (about 0.75 mA) but different chromaticities, as follows: 142: (H,V) = (1.34, 1.99); 129: (H,V) = (1.07, 1.78); 147: (H,V) = (1.33, 1.16)

vertical chromaticity than data set 147, there are no head-tail lines observed. For data set 129, with lower values of both chromaticities than data set 142, head-tail lines are observed, but their excitation levels are lower than in data set 147, which has the lowest vertical chromaticity.

6.3.2.7 Current Dependence

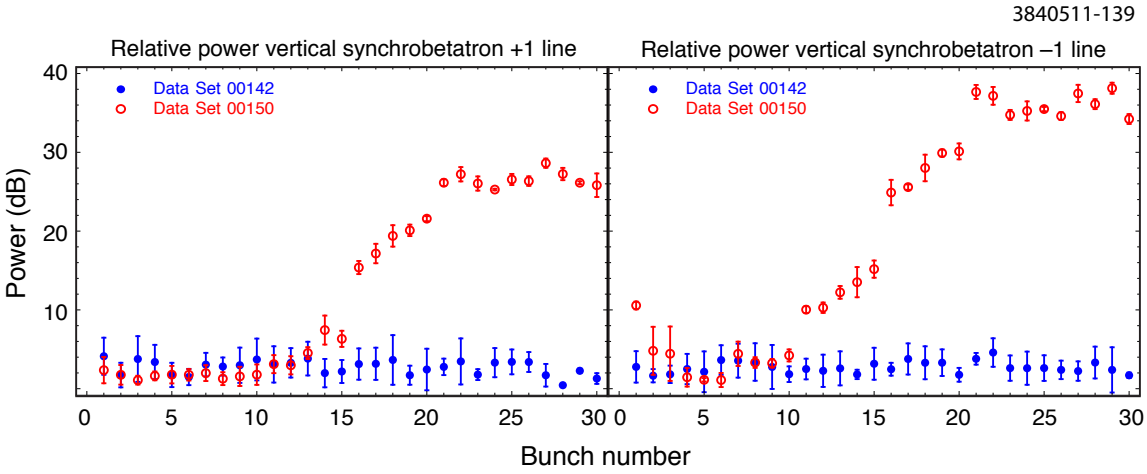

Figure 6.46: Data sets 142 and 150: vertical head-tail lines compared. Both sets have the same chromaticity [(H,V) = (1.34, 1.99)] but different bunch currents as follows: 142: 0.74 mA; 150: 0.95 mA

The current dependence of the head-tail lines is illustrated in Fig. 6.46 and Fig. 6.47. In Fig. 6.46, both data sets have the same chromaticity, but the data set with the lower bunch current (data set

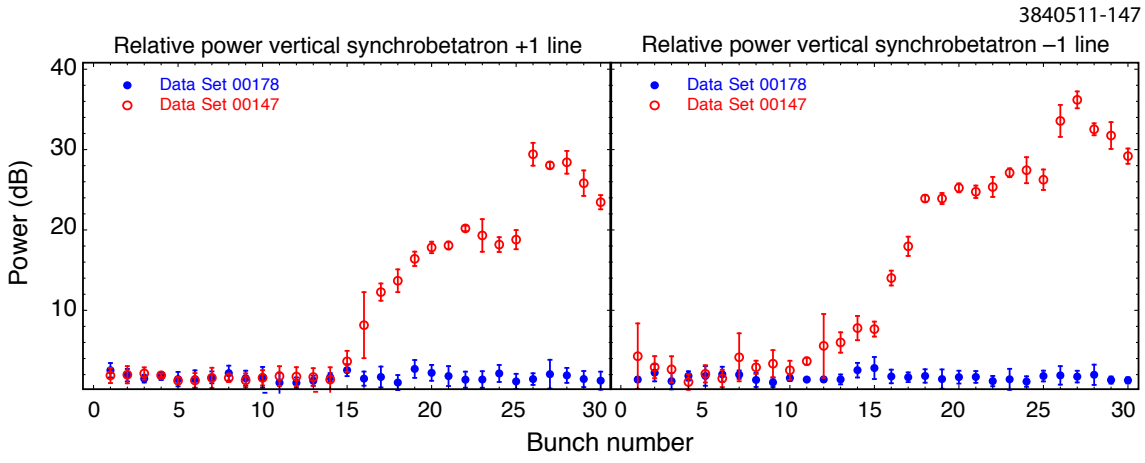

Figure 6.47: Data sets 147 and 178: vertical head-tail lines compared. Both sets have the same chromaticity [(H,V) = (1.33, 1.16)] but different bunch currents as follows: 147: 0.74 mA; 178: 0.5 mA

142) shows no head-tail lines, while the higher current data set (data set 150) shows head-tail lines starting to emerge around bunch 12. Similarly, in Fig. 6.47, both data sets have the same (lower) chromaticity, but the data set with the lower bunch current (data set 178) shows no head-tail lines, while the higher current data set (data set 147) shows head-tail lines staring to emerge around bunch 13.

6.3.2.8 Bunch Number Dependence

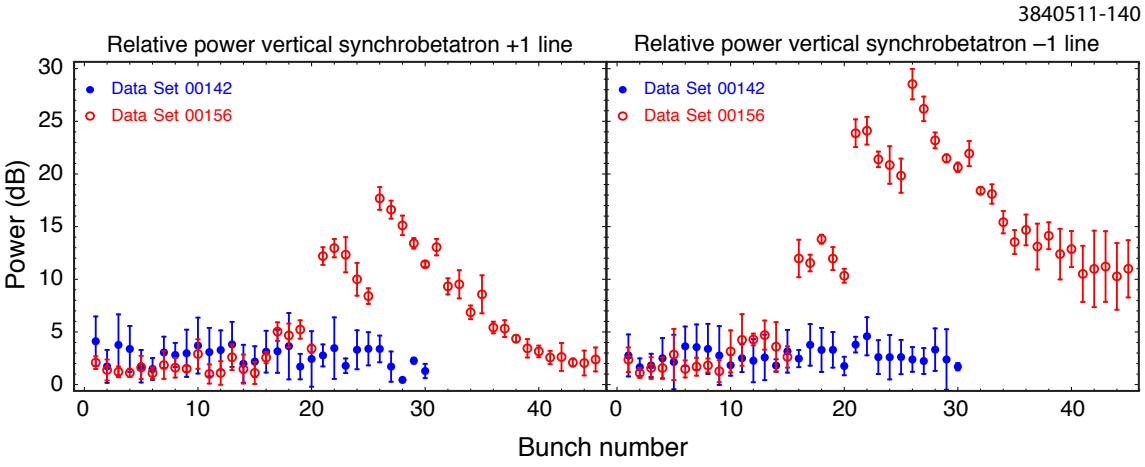

Figure 6.48: Data sets 142 and 156: vertical head-tail lines compared. Both sets have the same chromaticity [(H,V) = (1.34, 1.99)] and bunch current (0.74 mA), but different numbers of bunches, as shown in the figure. The increased amplitude in data set 156 at bunches 21 and 26 is an artifact due to refilling of the train at these bunch numbers.

The bunch number dependence of the head-tail lines is illustrated in Fig. 6.48. Both data sets have the same chromaticity and bunch current, but data set 156 contains 45 bunches in the train. The

vertical tunes of the first bunch were slightly different for the two runs: for run 142, it was about 227 kHz, while for run 156 the tune was about 221 kHz. No head-tail lines are observed in data set 142 out to the end of the train, bunch 30. But with 45 bunches, head-tail lines are observed starting around bunch 18, then growing to a peak around bunch 25, and falling off at the end of the train. The fact that the head-tail lines are seen with a 45 bunch train with the same bunch current as a 30 bunch train for which no lines are seen, is suggestive that there is a residual cloud density which lasts more than one turn, and which depends on the total current.

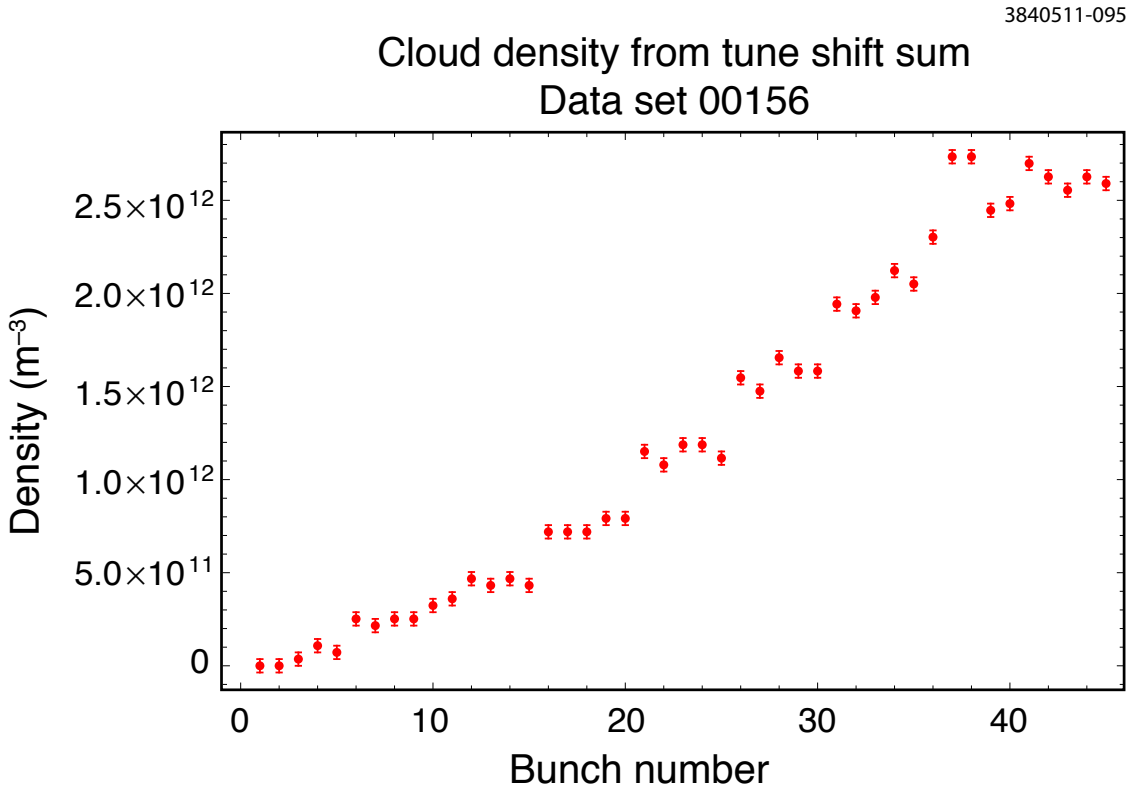

Figure 6.49: Data set 156: Average initial electron cloud density vs. bunch number, estimate from measured tune shifts

45 Bunch Train: Correlation with Cloud Density In Fig. 6.49, we show the cloud density as a function of bunch number, computed from the measured tune shifts, as discussed above. Comparison with Fig. 6.48 shows that the head-tail lines emerge from the background at a cloud density of about 8×10^{11} m^{-3}, which is the same as the threshold density found for data set 166, even though the vertical chromaticity was higher for data set 156. The fall-off of the head-tail lines after bunch 25 suggests that the instability is saturating. Yet the cloud density continues to increase after bunch 25 (at least until around bunch 35) as Fig. 6.49 shows. The head-tail instability threshold is expected to be sensitive to the vertical beam size, so what may be happening is that the instability is driving vertical beam size growth along the train, and the increase in the threshold as the beam size increases provides a mechanism for the instability to saturate.

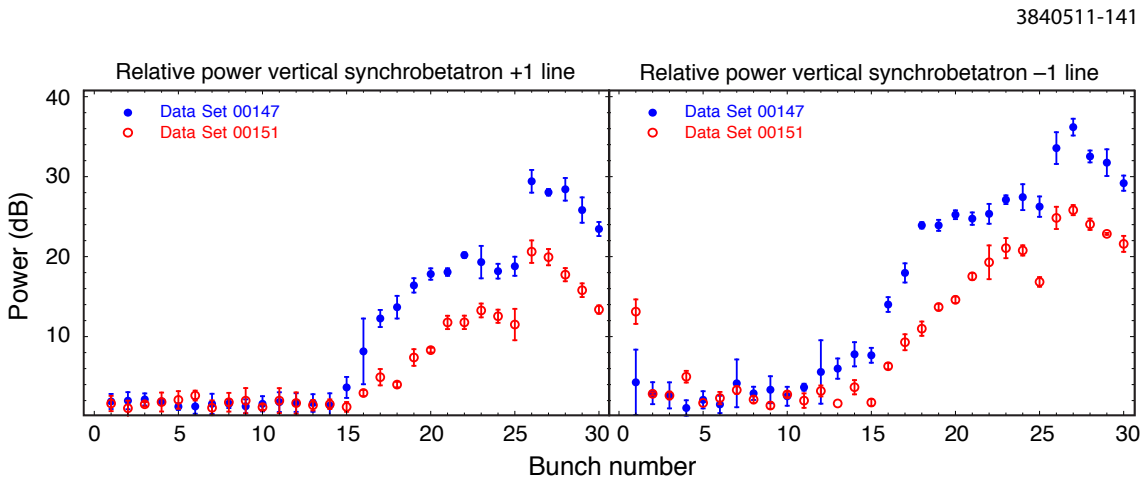

Figure 6.50: Data sets 147 and 151: vertical head-tail lines compared. Both sets have the same chromaticity [(H,V) = (1.33, 1.16)] and bunch current (0.74 mA), but different values of the bunch length and synchrotron frequency, as follows: 147, $f_s = 25.4$ kHz and $\sigma_z = 10.8$ mm; 151, $f_s = 20.7$ kHz and $\sigma_z = 12.8$ mm.

6.3.2.9 Synchrotron Tune Dependence

The synchrotron tune dependence of the head-tail lines is illustrated in Fig. 6.50. Both data sets have the same chromaticity and bunch current, but data set 151 has a reduced synchrotron frequency of 20.7 kHz, and an increased bunch length of 12.8 mm. The nominal frequency and bunch length, for data set 147, are 25.4 kHz and 10.8 mm.

For both data sets, the separation between the vertical betatron lines and the head-tail lines equals the synchrotron frequency. Fig. 6.50 shows that the head-tail line threshold is about the same in both cases, but the power in the lines grows more slowly with bunch number for the data set with a reduced synchrotron frequency, and longer bunch length.

6.3.2.10 Single-bunch Vertical Emittance Dependence

The vertical emittance dependence of the head-tail lines is illustrated in Fig. 6.51. Both data sets have the same chromaticity and bunch current, but data set 158 has an increased single-bunch vertical emittance of ~ 300 pm.[8] The nominal single-bunch vertical emittance, for data set 147, is ~ 20 pm.

Fig. 6.51 shows that the head-tail line growth is very similar for the two different vertical emittances. The power in the lines seems to plateau at a lower level for the data set with smaller vertical emittance. However, there is not a great deal of difference. Another observation which explores the vertical emittance dependence of the head-tail lines is shown in Fig. 6.52. Both data sets have 45 bunches and have the same chromaticity and bunch current, but data set 159 has an increased single-bunch vertical emittance of ~ 300 pm. The single-bunch vertical emittance, for data set 156 is ~ 20 pm.

[8]This number was estimated from a lattice model, not directly measured.

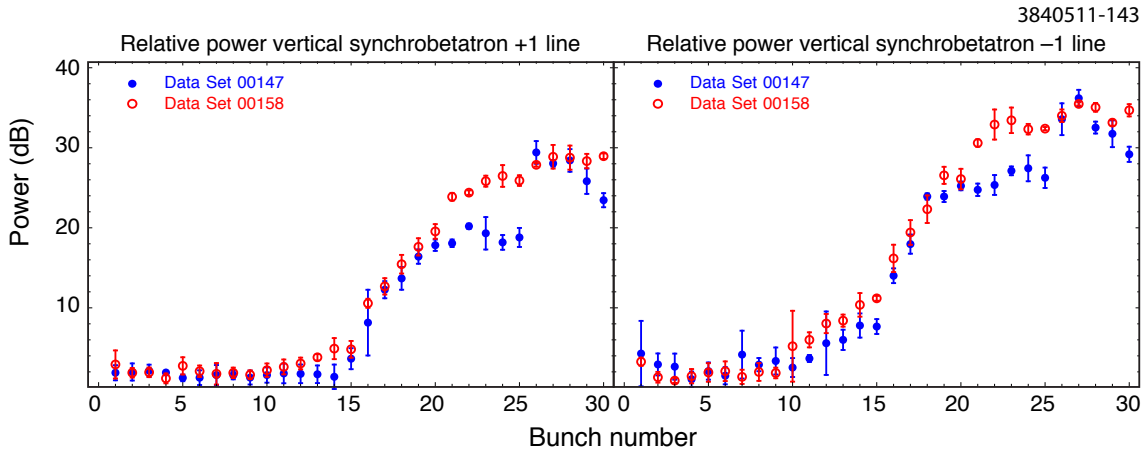

Figure 6.51: Data sets 147 and 158: vertical head-tail lines compared. Both sets have the same chromaticity [(H,V) = (1.33, 1.16)] and bunch current (0.74AmA), but different values of the single-bunch vertical emittance, as follows: 147, Vertical emittance $\sim$ 20 pm; 158, Vertical emittance $\sim$ 300 pm

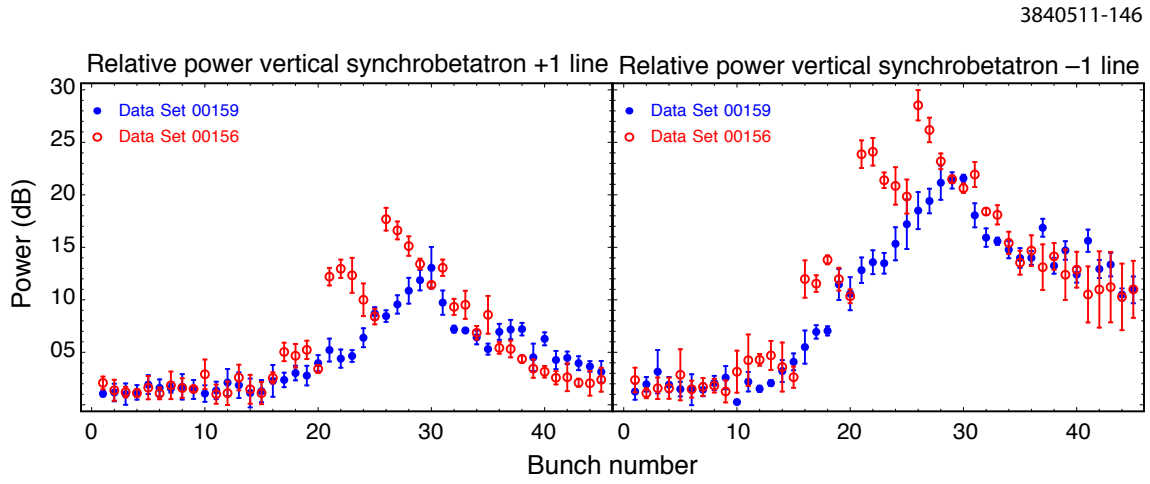

Figure 6.52: Data sets 156 and 159: vertical head-tail lines compared. Both sets have 45 bunches, the same chromaticity [(H,V) = (1.34, 1.99)] and bunch current (0.74 mA), but different values of the single-bunch vertical emittance, as follows: 156, Vertical emittance $\sim$ 20 pm; 159, Vertical emittance $\sim$ 300 pm

Inspecting Fig. 6.52, we see that, in this case, the power in the lines peaks at a lower level, and at a later bunch, for the data set with larger vertical emittance. This would suggest that the instability is slightly stronger for the case of smaller vertical emittance.

6.3.2.11 Vertical Feedback Dependence

The vertical feedback dependence of the head-tail lines is illustrated in Fig. 6.53. Both data sets have the same chromaticity and bunch current, but data set 126 has the vertical (dipole) feedback

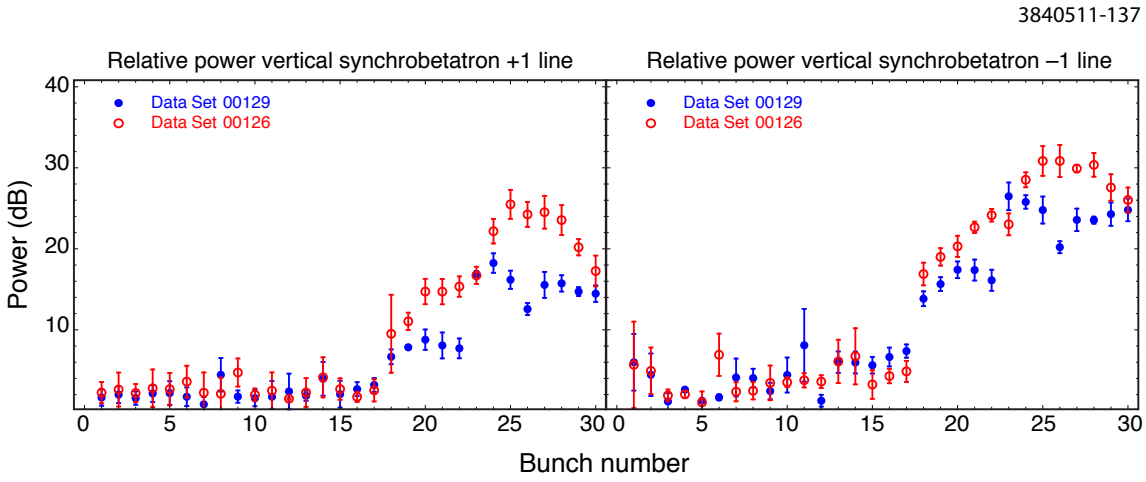

Figure 6.53: Data sets 126 and 129: vertical head-tail lines compared. Both sets have the same chromaticity and bunch current, but different values of the vertical feedback, as follows: 126, Vertical feedback off; 129, Vertical feedback at 20% of full gain.

off. For data set 129, as for all the other data sets discussed here (except 126), the vertical feedback is set to 20% of full gain.

Fig. 6.53 shows that the head-tail line threshold is about in the same place for these two data sets. But for data set 126 (feedback off), the power peaks a few dB higher than for data set 126, and then falls off.

6.3.2.12 Beam Energy Dependence

In data set 265, the structure of the frequency spectrum was studied for a beam energy of 4 GeV. Fig. 6.54 shows the beam current as a function of bunch number for this data set. The bunch current was about 1.1 mA/bunch. The machine parameters for this measurement are presented in Table 6.5

Power Spectrum Fig. 6.55 shows the power spectrum as a function of bunch number. Clearly visible are the horizontal and vertical betatron lines, the head-tail line above the vertical, and another line around 285 kHz. The line at 285 kHz corresponds to excitation of the $Q_x + 2Q_y = 2$ resonance.

Betatron Lineshapes Fig. 6.56 shows the bunch-by-bunch power spectrum near the horizontal betatron line. As at 2 GeV, there is a major peak which shifts up in frequency by about 4 kHz during the bunch train. This shift is attributable to the electron cloud. Fig. 6.57 shows the bunch-by-bunch power spectrum near the vertical betatron line. There is considerably more structure in this line than at 2 GeV, including a splitting of the main peak which persists throughout the train, and some smaller satellite peaks which seem to develop after bunch 20.

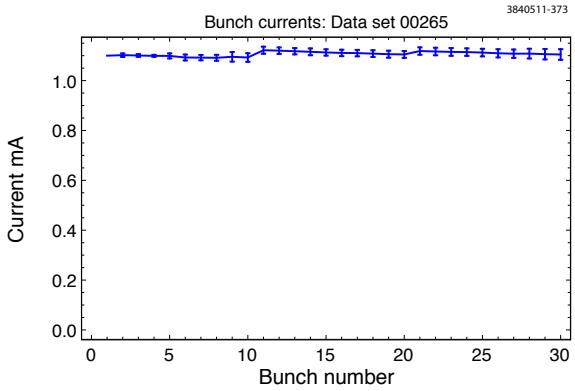

Figure 6.54: Data set 265: Bunch-by-bunch currents, 4 GeV beam energy

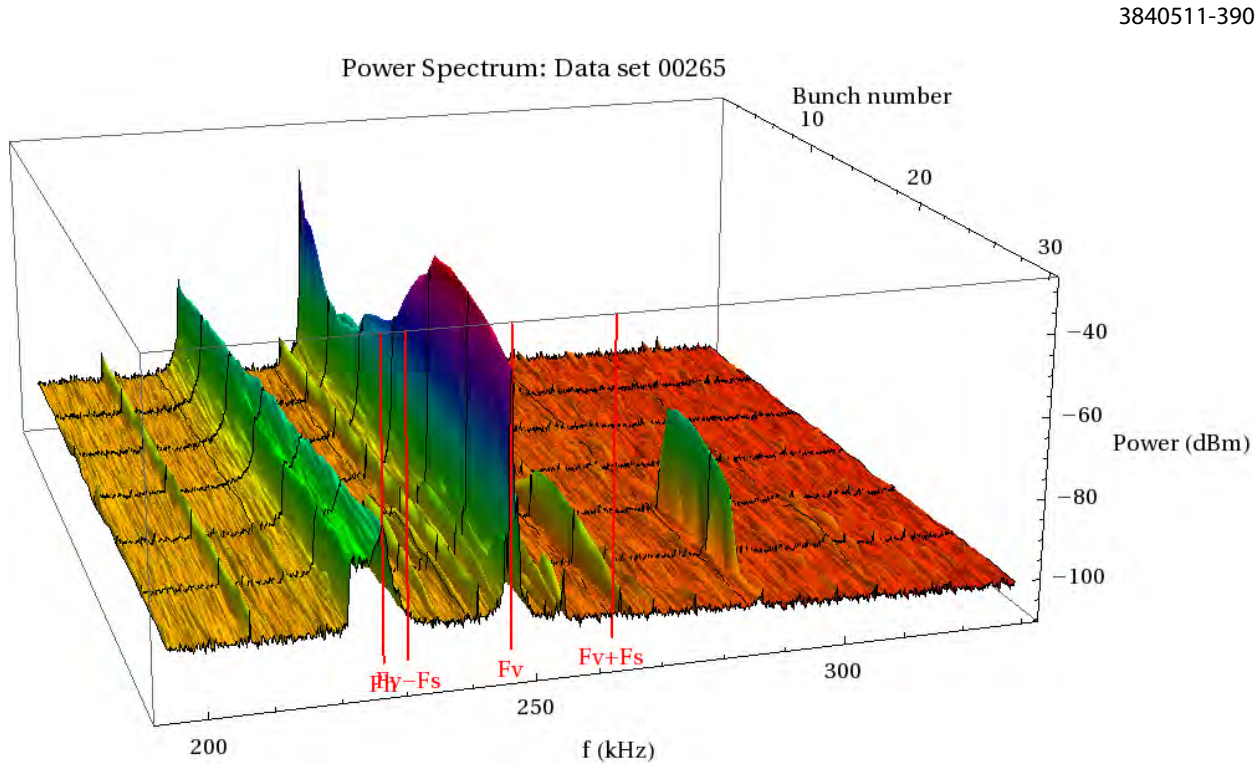

Figure 6.55: Data set 265: Bunch-by-bunch power spectrum, 4 GeV. Chromaticity: (H,V) = (1.3, 1.4). Bunch current = 1.1 mA.

Vertical Head-tail Lines In Fig. 6.58, we plot the power (relative to the vertical betatron line) and the frequency (± the synchrotron frequency) of the head-tail lines. We see that these lines appear above the noise level around bunch 18. The lower frequency line ($m = -1$ head-tail line) is close to the horizontal line, and is weakly excited, so its power is not well determined, and it is omitted from the frequency plot. The frequency plot shows that, for the ($m = +1$ head-tail line), the head-tail line frequency minus the vertical betatron line frequency differs from the synchrotron frequency by about 1 kHz. This is in contrast to the observations made at 2 GeV, for which this

Table 6.5: Nominal machine parameters at 4 GeV. The emittances and tunes are those of a single bunch in the machine.

Parameter	Unit	Value
Energy	GeV	4.00
Lattice		4000 mev_23 nm_20090816
Horizontal emittance	nm	23
Vertical emittance	pm	~ 180
Bunch length	mm	17.2
Horizontal tune		14.55
Vertical tune		9.58
Synchrotron tune		0.041
Momentum compaction		6.3×10^{-3}
Revolution frequency	kHz	390.13

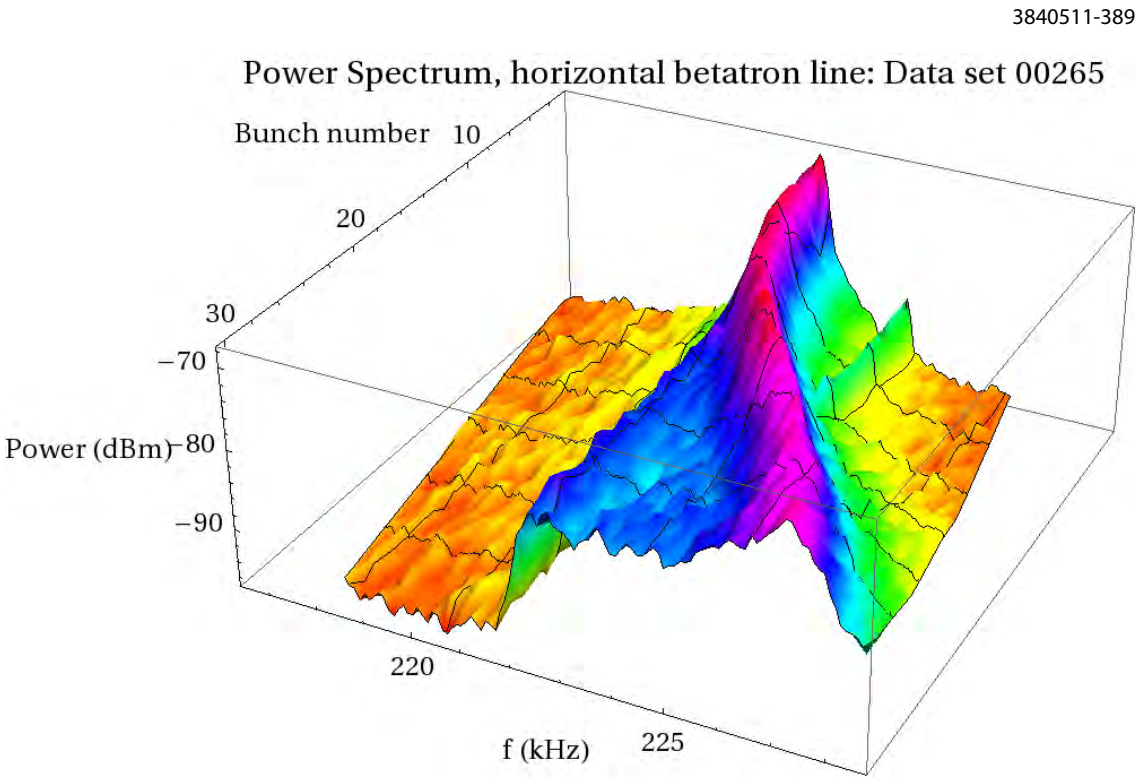

Figure 6.56: Data set 265: Bunch-by-bunch power spectrum: detail at horizontal betatron line, 4 GeV. Chromaticity: (H,V) = (1.3, 1.4). Bunch current = 1.1 mA.

difference is essentially zero.

Instability Threshold Estimate In Fig. 6.59, we show the cloud density as a function of bunch number, computed from the measured tune shifts, as discussed above. Comparison with Fig. 6.58 shows that the head-tail lines emerge from the background at a cloud density of about

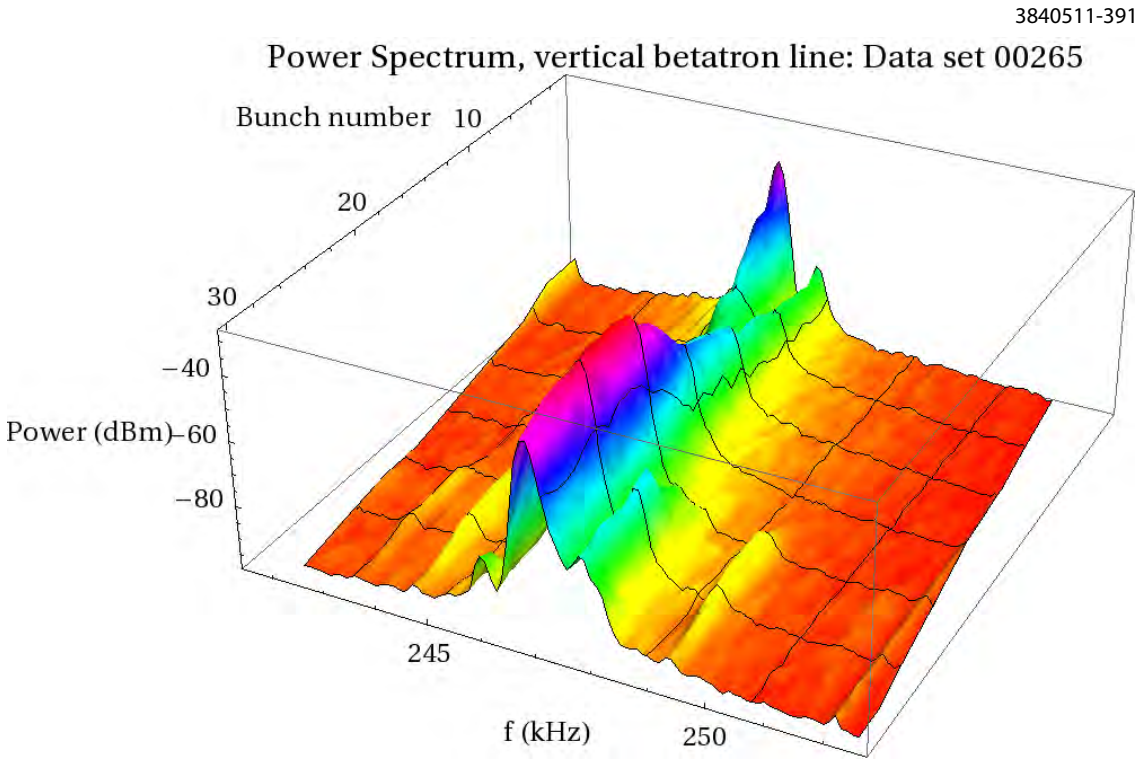

Figure 6.57: Data set 265: Bunch-by-bunch power spectrum: detail at vertical betatron line, 4 GeV. Chromaticity: (H,V) = (1.3, 1.4). Bunch current = 1.1 mA.

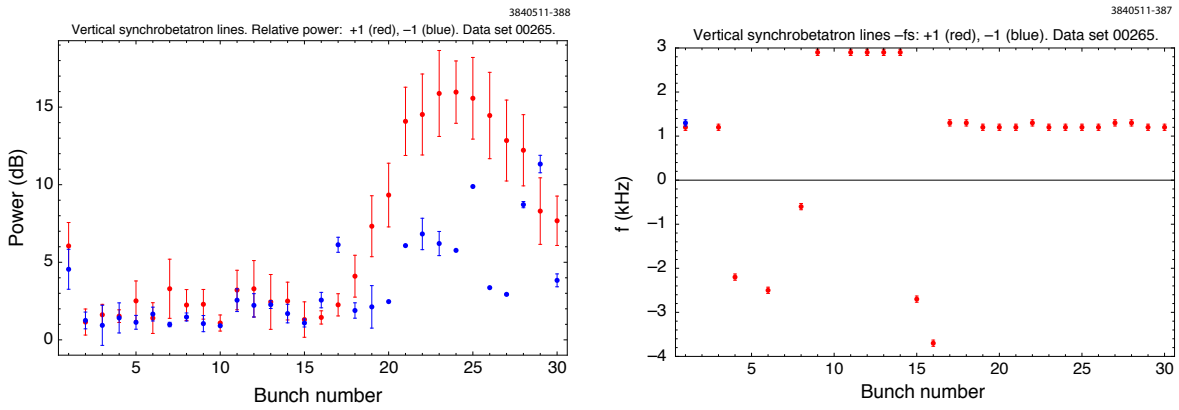

Figure 6.58: Data set 265: Vertical head tail lines: left, peak power vs. bunch number; right, frequency difference from vertical betatron line vs. bunch number, with the synchrotron frequency removed from the offset. Beam energy 4 GeV. Chromaticity: (H,V) = (1.3, 1.4). Bunch current = 1.1 mA.

2×10^{12} m^{-3}.

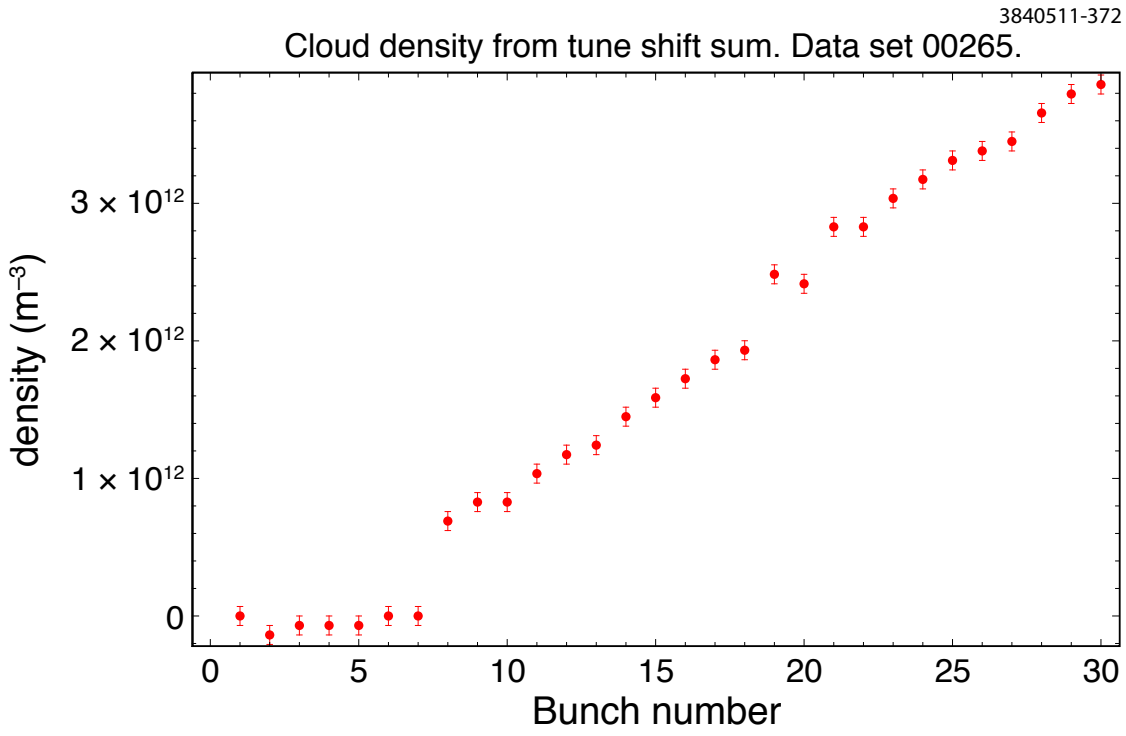

Figure 6.59: Data set 265: Average initial electron cloud density vs. bunch number, estimate from measured tune shifts. 4 GeV beam energy.

6.3.2.13 Beam Particle Species Dependence

The beam species (e^+ or e^-) dependence of the bunch-by-bunch power spectrum is illustrated by comparing data set 166 (Fig. 6.36) and data set 154 (Fig. 6.60). Both data sets have the same chromaticity and bunch current, but data set 154 is for an electron beam. In this latter case we see less vertical excitation along the train, and smaller head-tail line excitation, than for a positron beam. The large tune shifts observed with the positron beam are also absent. The details of the different structures of the head-tail lines for electrons and positrons can be seen in Fig. 6.61. For electrons, the head-tail lines start later in the train, grow more slowly, and at their maxima are 20 dB lower than the positron head-tail lines.

The positron-beam head-tail excitation is presumably due to electron cloud effects. The physical mechanism responsible for the head-tail excitation in the electron case is not likely to be either electron cloud or positive ions.

6.3.2.14 Precursor Bunch Dependence

In Fig. 6.62, the power spectrum of bunch 1 for data set 151 is shown (red trace). Note the presence of a prominent $m = -1$ head-tail line. This line disappears for the second bunch, and does not re-appear until much later in the train, as shown in Fig. 6.63. Moreover, beam size measurements (see Section 6.3.4) indicate that the first bunch in the train is frequently larger in size than the next few bunches.

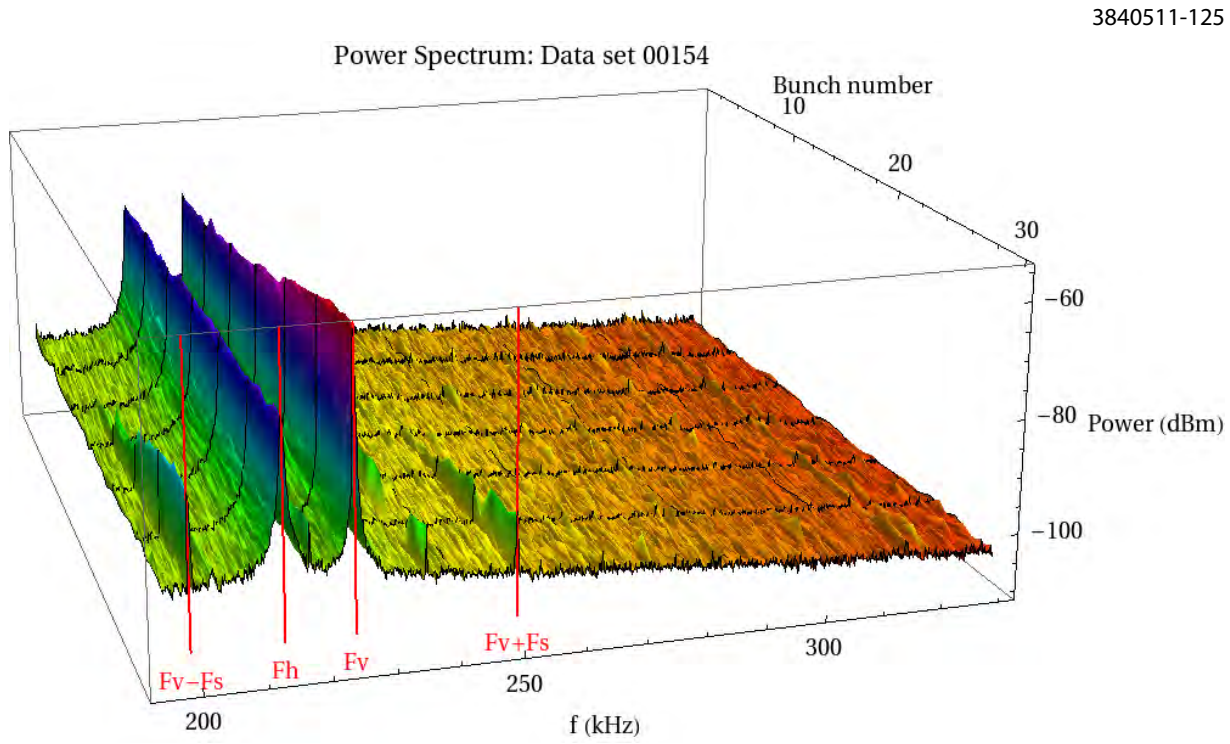

Figure 6.60: Data set 154: Bunch-by-bunch power spectrum. This data set is for an electron beam, but has the same chromaticity and bunch current parameters as data set 166 (Fig. 6.36).

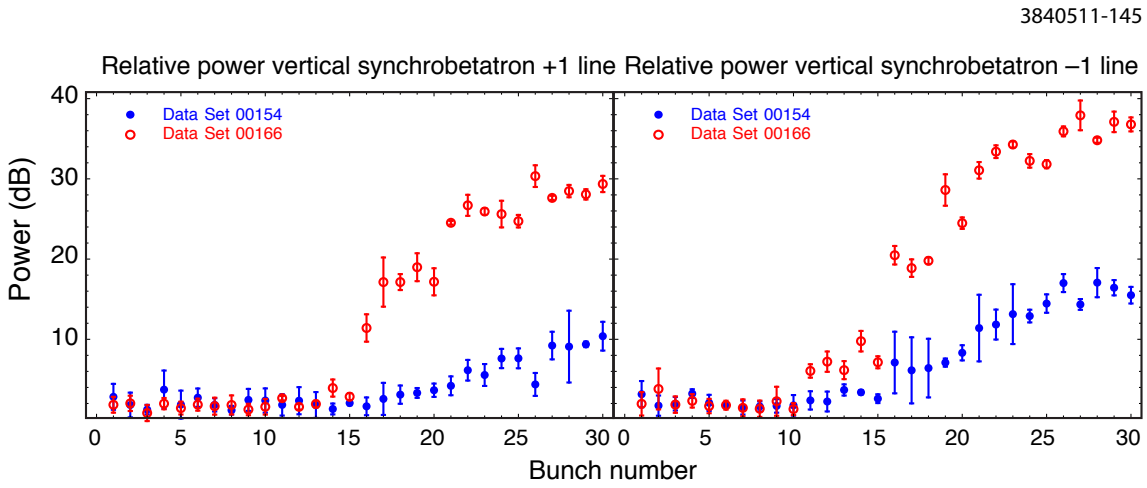

Figure 6.61: Data sets 166 and 154: vertical head-tail lines compared. Both sets have the same chromaticity and bunch current, but data set 166 was taken with a positron beam while data set 154 was taken with an electron beam.

This suggests that the trapped cloud density near the beam, which persists after the train ends, may be sufficiently high, even for the first bunch in the train, that spontaneous head-tail motion occurs. However, the interaction of the first bunch with this trapped cloud evidently destabilizes it, causing it to disperse, so that bunch 2 does not suffer from spontaneous head-tail motion.

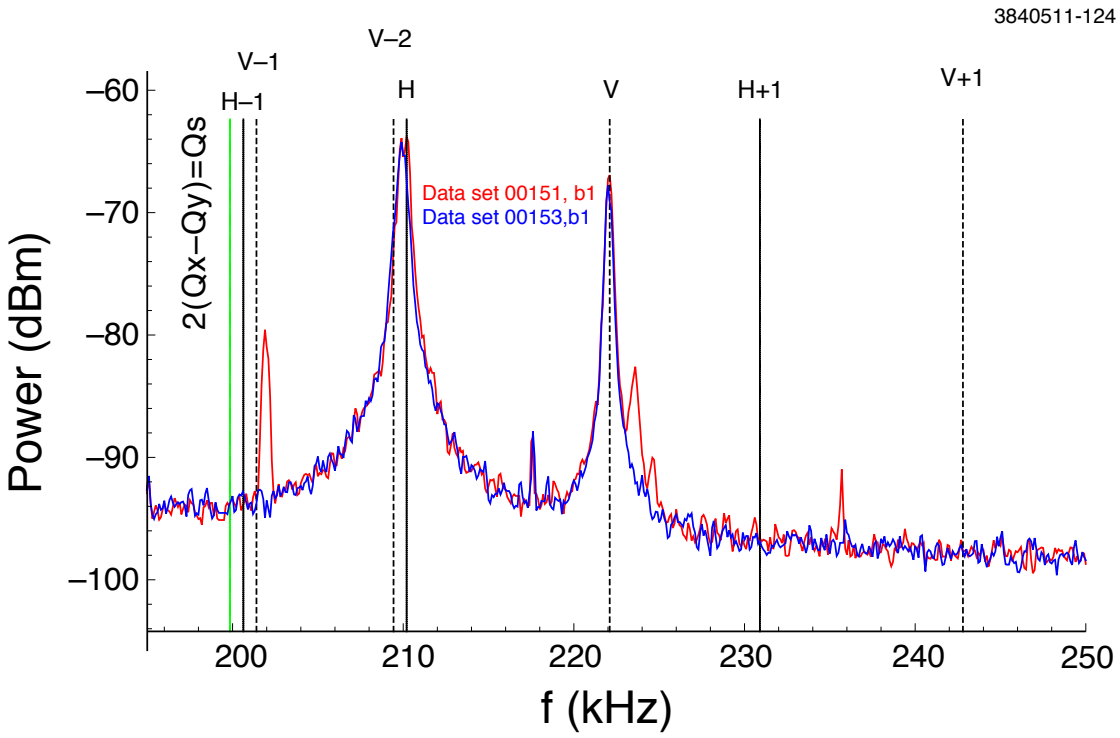

Figure 6.62: Data set 151 and 153 : Power spectrum, bunch 1, compared. Both sets have the same chromaticity and bunch current, but there is a precursor bunch present for data set 153, as described in the text. The lines labelled, for example,"V+1" and "V-1" are shown at frequencies of $\pm f_s$ from the vertical betatron line ("V"), in which f_s is the synchrotron frequency. For these data sets, f_s = 20.7 kHz. The location of a machine resonance is also indicated.

Simulations and witness bunch measurements indicate that the electron cloud lifetime in dipoles and drifts is much shorter than one turn in CesrTA. Cloud density which persists for many turns may be due to trapped cloud in quadrupoles and wigglers. Simulations and RFA measurements in quadrupoles have both indicated that trapped cloud may be present.

To test this hypothesis, in data set 153, a 0.75 mA "precursor" bunch was placed 182 ns before bunch 1. Otherwise, conditions were the same as for data set 151. The spectrum of the first bunch for data set 153 is shown (blue trace) in Fig. 6.62. Note that the lower head-tail line is now absent. In addition, the structure seen on the upper edge of the vertical betatron line in Fig. 6.62 is disappears. Finally, there is a small line at 235.7 kHz (13.6 kHz above the vertical betatron line) which also disappears when the precursor bunch is introduced.

It is quite interesting to note that the frequency difference between the head-tail line of the first bunch for data set 151 (shown in Fig. 6.62) and the vertical betatron line is 20.2 $\pm$0.1 kHz, which is significantly different from the synchrotron frequency, 20.7 kHz. The head-tail lines which develop later in the train, both above and below the vertical betatron line, always have a separation equal to the synchrotron frequency, within the measurement errors (see Fig. 6.40).

We have observed a prominent $m = -1$ head-tail line for the first bunch in the train in two other data sets: data set 150 (see Fig. 6.46) and data set 157 (see Fig. 6.44). In both of these cases, the $m = -1$ line is separated from the vertical betatron line by significantly less (typically 0.6 to

0.7 kHz) than the synchrotron frequency, and there is a doublet structure to the vertical betatron line, as shown in Fig. 6.62 for data set 151. In Fig. 6.63, the power in the vertical head-tail lines is

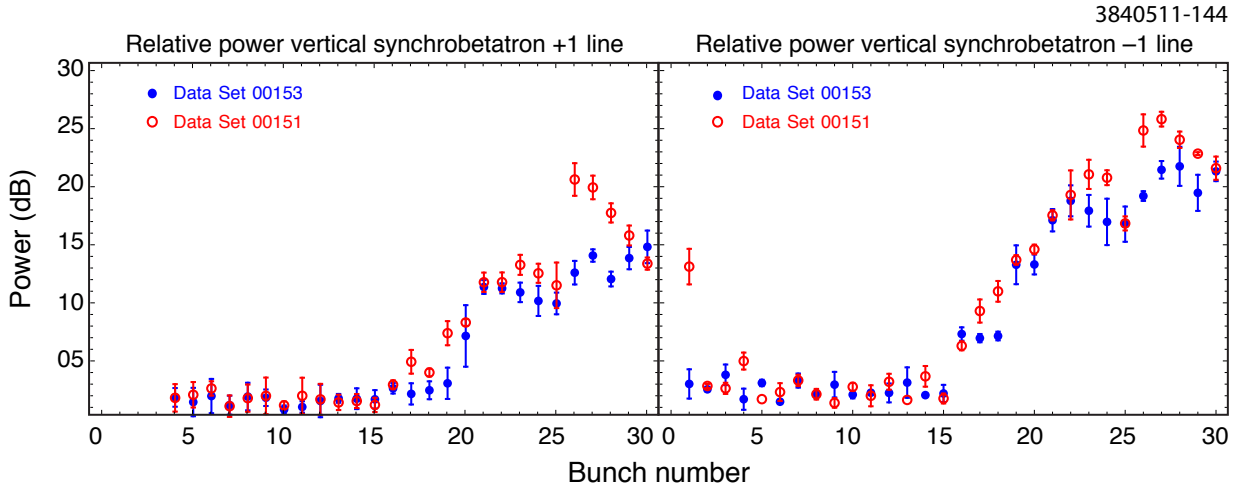

Figure 6.63: Data sets 151 and 153: vertical head-tail lines compared. Both sets have the same chromaticity and bunch current, but there is a precursor bunch present for data set 153, as described in the text.

shown as a function of bunch number, for data sets 151 and 153. The figure shows little difference between the head-tail line growth for the two data sets. The data set without the precursor bunch has a slightly higher line power near the end of the train.

6.3.2.15 Single Bunch Current Variation Experiment

To explore further the dynamics of the interaction of the last bunch in the train with the cloud, a series of power spectral measurements were made, in which the current in the first 29 bunches in a 30 bunch train was fixed, but the current in the last bunch was varied. The power spectrum with the last bunch at 0.25 mA (data set 167) is compared with the power spectrum with the last bunch at 1.25 mA (data set 171) in Fig. 6.64.

The vertical excitation of the bunch, both at the vertical betatron line and at the head-tail lines, is much larger for the higher current bunch. The $m = +1$ head-tail line appears to acquire a low-frequency shoulder at the higher current.

In addition, the frequency of the vertical betatron line is almost independent of the current in the bunch. The shift from 0.25 mA to 1.25 mA is less than 0.2 kHz. Note that this behavior is very different from what would be expected for a conventional machine impedance, for which one would expect a strong current dependence for the tune.

6.3.2.16 Summary

The basic observation is that, under a variety of conditions, single-bunch frequency spectra in multi-bunch positron trains exhibit the $m = \pm 1$ head-tail (HT) lines, separated from the vertical

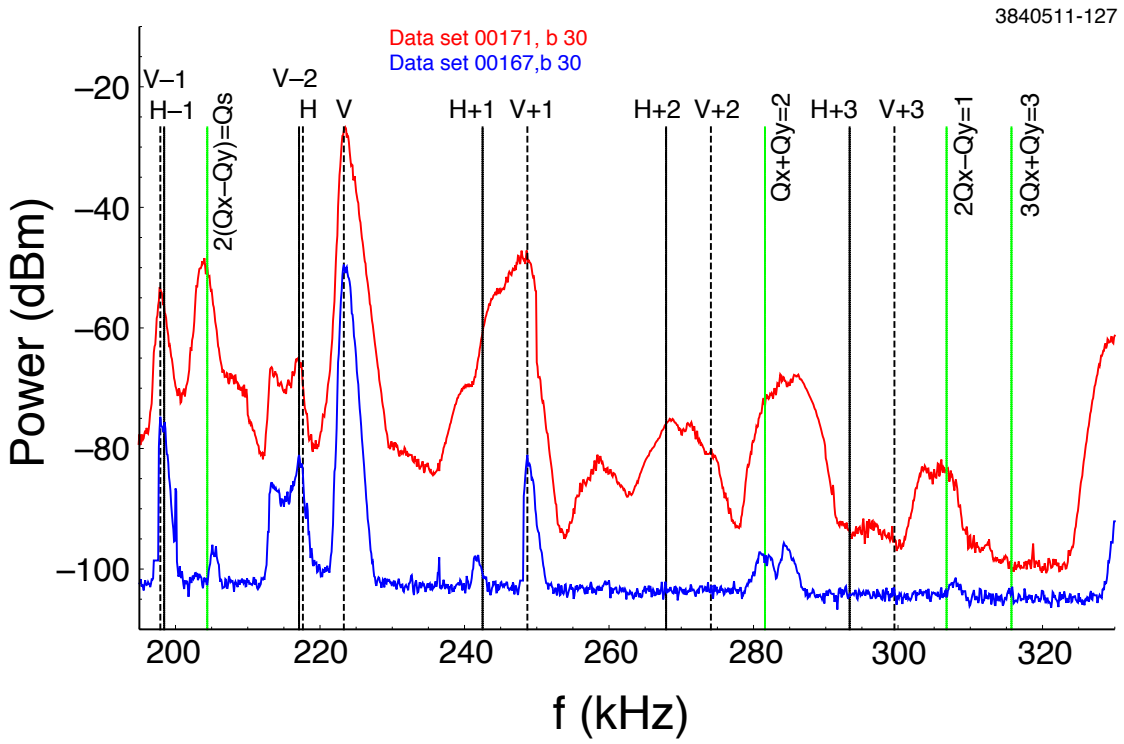

Figure 6.64: Data set 167 and data set 171: Power spectrum, bunch 30 compared. The lines labelled, for example,"V+1" and "V-1" are shown at frequencies of $\pm f_s$ from the vertical betatron line ("V"), in which f_s is the synchrotron frequency. The locations of several machine resonances are also indicated.The first 29 bunches had a nominal current of 0.75 mA/bunch. Chromaticity: (H,V) = (1.33, 1.16). For data set 167, bunch 30 had a current of 0.25 mA. For data set 171, bunch 30 had a current of 1.25 mA.

line by the synchrotron frequency, for some of the bunches during the train. A summary of more detailed observations is presented in the following list.

- For a 30 bunch train with 0.75 mA/bunch at 2.1 GeV beam energy, the onset of the HT lines occurs at a ringwide initial (i.e., before the "pinch") beam-averaged cloud density of around 8×10^{11} m^{-3} (assuming no cloud density at the start of the train).
- For a 30 bunch train with 1.1 mA/bunch at 4 GeV beam energy, the onset of the HT lines occurs at a ringwide initial (i.e., before the "pinch") beam-averaged cloud density of around 2×10^{12} m^{-3} (assuming no cloud density at the start of the train).
- The betatron lines exhibit structure which varies along the train. The vertical line power grows along the train and has a fine structure that is not understood.
- The amplitude of the HT lines depends strongly on the vertical chromaticity, the beam current and the number of bunches.
- For a 45 bunch train, the HT lines have a maximum power around bunch 30; the line power is reduced for later bunches.
- There is a weak dependence of the onset of the HT lines on the synchrotron tune, the single-

bunch vertical emittance, and the vertical feedback.

- Under identical conditions, HT lines also appear in electron-beam trains, but the onset is later in the train, develops more slowly, and is much weaker, than for positron beam trains.
- Under some conditions, the first bunch in the train also exhibits a head-tail line ($m = -1$ only). The presence of a "precursor" bunch can eliminate the $m = -1$ signal in the first bunch. The implication is that there may be a significant "trapped" cloud density near the beam which lasts long after the bunch train has ended, and which is dispersed by the precursor bunch. Indications from RFA measurements and simulations indicate this "trapped" cloud may be in the quadrupoles and wigglers.
- There is a strong dependence of the HT line structure observed on last bunch in a 30 bunch train, as a function of the current in that bunch. But the frequency of the vertical betatron line of this bunch is only very weakly dependent on the current in the bunch.
- Future work will include more checks for systematics (looking at different BPM's, for example), as well as measurements at different bunch spacings and beam energies.

6.3.3 Mode Growth Rates

In addition to the power spectrum measurements described in the previous section, in which spontaneous excitations of single bunches are passively monitored, we have also made measurements in which we actively excite a single bunch in a train, and measure the rate at which the bunch damps after the excitation is turned off. These bunch-by-bunch damping rate measurements come in two varieties:

- $m = 0$ *(dipole mode).* In this case, we drive a single bunch by delivering a narrow pulse to the transverse feedback system's kicker. We observe the $m = 0$ motion (betatron line) on a button BPM, gated on the same bunch. Using a spectrum analyzer in zero span mode, tuned to the betatron line, we measure the damping rate of the $m = 0$ line's power after the drive is turned off.
- $m = \pm 1$ *(head tail modes).* In this case, we apply a CW drive to the RF cavity phase, to provide a large amplitude longitudinal excitation. We then perform a transverse drive-damp measurement, as in the previous case, but with the spectrum analyzer tuned to the head-tail line's frequency.

A number of measurements were made to investigate the systematics of this technique. More details can be found in Section 6.1.3.

6.3.3.1 Quantitative Analysis of Drive-Damp Measurements

The analysis of the data for these drive-damp measurements utilized two different fitting methods. The first and most obvious is to fit the amplitude of the mode spectrum to an exponential decay (or more properly, since the mode amplitude is measured in the dBm, a linear fit to the amplitude in dBm vs. time.) The second fitting method, which has been employed for all of the measurements presented here, was inspired by the observation that a number of the damping waveforms exhibit a more complicated decay than a simple exponential. Examples of the most common of these non-exponential decays are shown in Fig. 6.65.

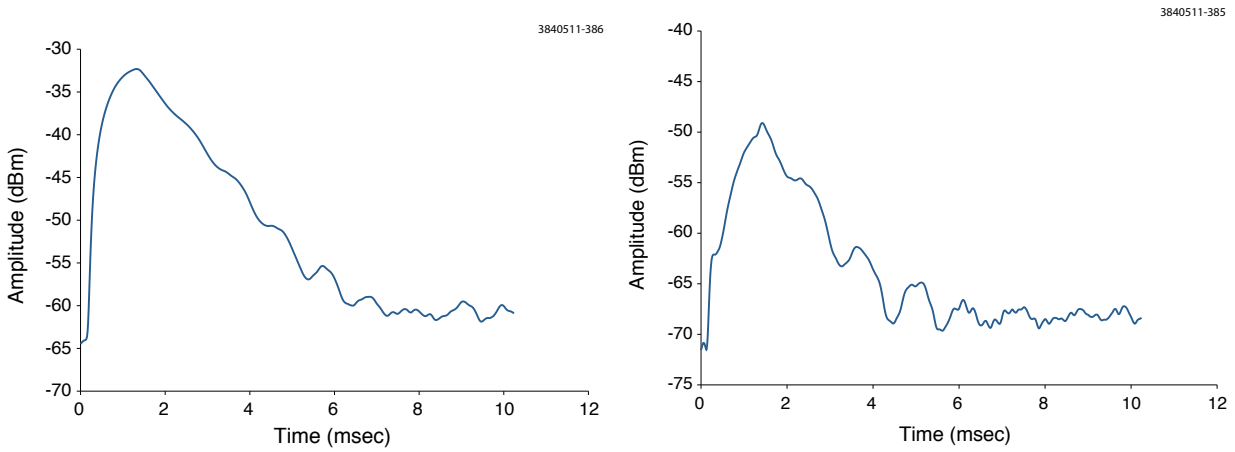

Figure 6.65: Plot of the amplitude vs. time for a drive-damp measurements. Left: $m = 0$ mode. Right: $m = -1$ mode.

The characteristic feature in these two plots is an exponential decay of what appear to be two modes of slightly different frequency, generating a damped interfering decay of their combined amplitudes. There is an explanation for this effect in some cases. In the case when there is a simple exponential damped oscillation and the center frequency of spectrum analyzer is mistuned away from the actual frequency of the mode, an exponential decay with a beat frequency becomes visible with the amplitude of the beats increasing as the center frequency detuning is increased. As a result during the drive-damp measurements care is taken to manually adjust the spectrum analyzer center frequency to minimize the observed oscillation amplitude.

However, even if this is done, in a number of cases there is still a significant damped oscillatory signal present in the damping plot and this may be due to a damped oscillation of two independent coupled modes. Taking a broader view of drive-damp measurements, since the real interest is in determining the longest characteristic decay time for the mode of oscillation, one is actually interested in the amplitude envelope that fully contains the beam displacement vs. time. As a result, our analysis of the damped decay of the beam's vertical oscillation utilizes a fit to two modes of nearly the same frequency, each having their own damping rate. We then write the time evolution of the vertical position of a bunch as

$$y(t) = \mathrm{Re}\left\{Y(t)\right\} = \mathrm{Re}\left\{a_1 \exp(j\omega_1 t - \alpha_1 t) + a_2 \exp(j\omega_2 t - \alpha_2 t)\right\} \tag{6.60}$$

where a_1 and a_2 are the mode position amplitudes, α_1 and α_2 the mode damping rates, and ω_1 and ω_2 the mode angular frequencies. Since the spectrum analyzer displays the amplitude as the power in the spectral line at the center frequency vs. time, we must write the power as

$$\text{Power in } y(t) \propto |Y(t)|^2 = a_1^2 \exp(-2\alpha_1 t) + a_2^2 \exp(-2\alpha_2 t) + 2a_1 a_2 \exp\left\{-(\alpha_1 + \alpha_2)t\right\} \cos(\Delta\omega\, t) \tag{6.61}$$

where $\Delta\omega = \omega_1 - \omega_2$. Since we are interested particularly in the longest-lived oscillation, we generally focus on the mode that has the longer damping time, *i.e.* the lower damping rate. Thus we fit the drive-damp data to this two-damped-oscillator model, and by convention assign $\alpha_1 < \alpha_2$ (unless the oscillation amplitude of the longer-lived mode is a very small contribution to the bunch

vertical displacement). Plots of the damping rate display results from the second fitting method, *i.e.* the value determined to be α_1.

6.3.3.2 Observations

We have made drive-damp measurements of positron beams under different conditions. They will be described here in two parts:

- **Single Bunch Damping Rates**: Measurements of single bunches for the study of CESR's "baseline" stability; and
- **Damping Rates for Trains of Bunches**: Measurements of trains of bunches to characterize the electron cloud effects.

Single Bunch Damping Rates To characterize the overall stability of CesrTA we have measured the single bunch positron damping rates for a variety of different settings of the vertical feedback gain and the vertical chromaticity. These were studied in same optics at 2.08 GeV as were used for the 30 bunch train drive-damp measurements described below. Only a single operating parameter is varied as a part of each set of observations. All of the single bunch measurements were made at 0.75 mA.

Single bunch damping rates were measured for the vertical dipole mode and both vertical head-tail modes. Figure 6.66 displays these damping rates as a function of the vertical chromaticity ($Q' = dQ/d\delta$, where δ is the fractional energy deviation). The vertical feedback was turned off for these measurements. The figures also have a plot of the best linear fit to the measured data points. The results of the linear fits may generally be written as

$$\alpha_v = \frac{\partial \alpha_v}{\partial I} \times \left(\frac{I_b}{1 \text{ mA}} \right) \times Q'_v + \alpha_{v0} \tag{6.62}$$

where the chromaticity contribution is expected to scale with current and the constant term is expected to be the radiation damping contribution. The linear fits for the three plots are

$$\alpha_v \left[\text{sec}^{-1}\right] = \begin{cases} (-3 \pm 20) \times \left(\frac{I_b}{1 \text{ mA}} \right) \times Q'_v + 110 \pm 60 & \text{for the } m = 0 \text{ mode} \\ (21 \pm 18) \times \left(\frac{I_b}{1 \text{ mA}} \right) \times Q'_v + 4 \pm 46 & \text{for the } m = 1 \text{ mode} \\ (17 \pm 6.6) \times \left(\frac{I_b}{1 \text{ mA}} \right) \times Q'_v + 33 \pm 14 & \text{for the } m = -1 \text{ mode} \end{cases} \tag{6.63}$$

where there are uncertainties included for the fits with over-constrained data, and where I_b is the current in the bunch. Within uncertainties, the head-tail modes display a fairly similar dependence on the vertical chromaticity. Although it is not determined accurately, the zero chromaticity damping rate is consistent with the vertical radiation damping rate of 18 s^{-1}. In this first measurement for the dipole ($m = 0$) mode, the result is much less damping than is expected. This dependence will need to be re-measured at the next convenient time.

Measurements of the damping rates were made as a function of the 14 ns vertical dipole feedback system setting. Figure 6.67 plots the vertical damping rates for the vertical dipole mode and both vertical head-tail modes. These measurements were undertaken with the vertical and horizontal chromaticities set to 2.13 and 0.58, respectively. The damping rates of the head-tail modes are a

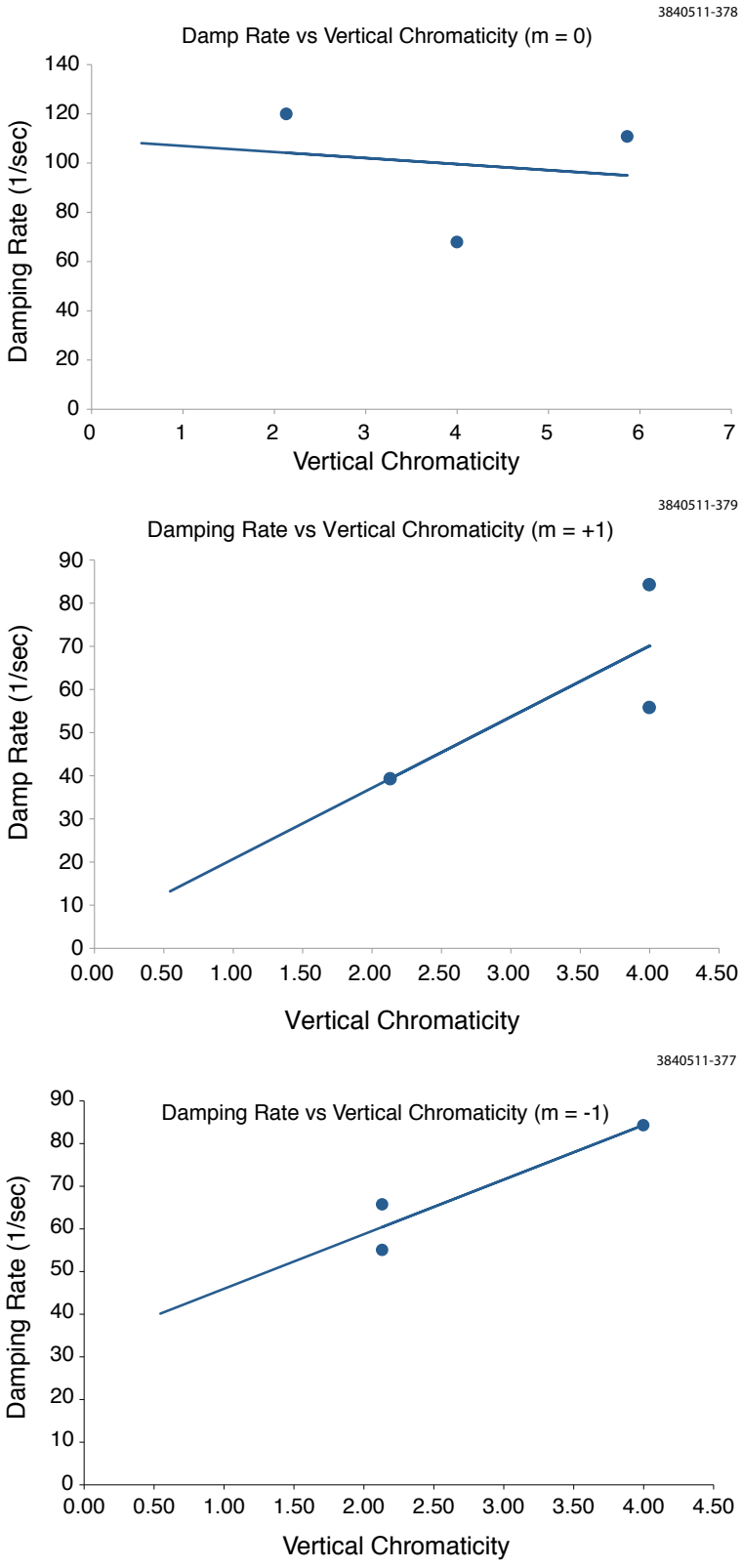

Figure 6.66: Single bunch damping rate vs. vertical chromaticity. Top: vertical dipole mode. Center: vertical $m = +1$ head-tail mode. Bottom: vertical $m = -1$ head-tail mode.

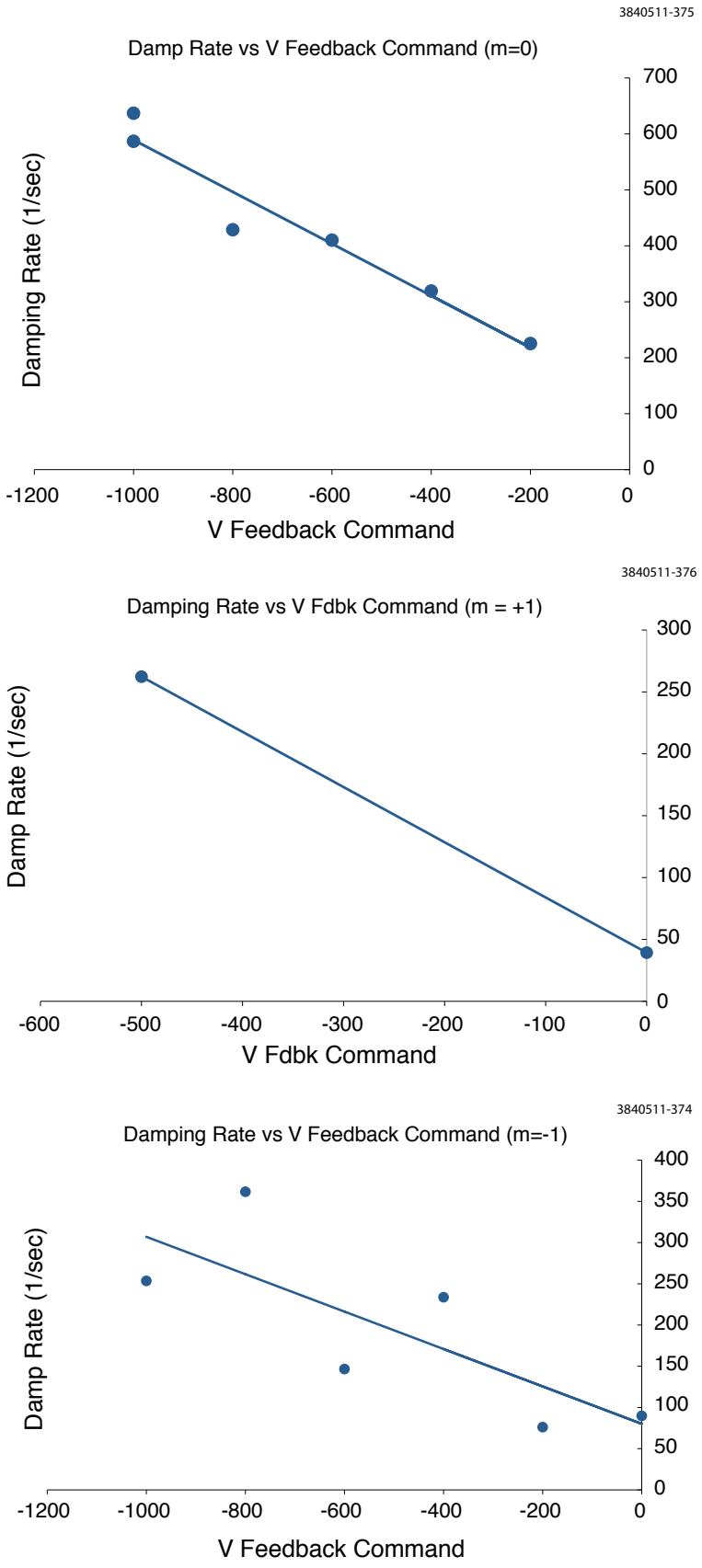

Figure 6.67: Single bunch damping rate vs. vertical dipole feedback. Top: vertical $m = 0$ mode. Center: vertical $m = +1$ head-tail mode. Bottom: vertical $m = -1$ head-tail mode.

surprisingly stronger function of the vertical feedback than would be anticipated, while, as expected, the vertical dipole mode is a function of the feedback and all will be proportional to the current per bunch. The figures also contain the best linear fit to the observed data. The best linear fits for the three plots may be written as

$$\alpha_v \left[\text{sec}^{-1}\right] = \begin{cases} (-620 \pm 80) \times \left(\frac{I_b}{1 \text{ mA}}\right) \times Q'_v \times \left(\frac{\text{Fdbk Cmd}}{1000}\right) + 130 \pm 42 & \text{for the } m = 0 \text{ mode} \\ -590 \times \left(\frac{I_b}{1 \text{ mA}}\right) \times Q'_v \times \left(\frac{\text{Fdbk Cmd}}{1000}\right) + 39 & \text{for the } m = 1 \text{ mode} \\ (-300 \pm 130) \times \left(\frac{I_b}{1 \text{ mA}}\right) \times Q'_v \times \left(\frac{\text{Fdbk Cmd}}{1000}\right) + 80 \pm 57 & \text{for the } m = -1 \text{ mode} \end{cases} \tag{6.64}$$

where uncertainties for the fit values are given when the fits are over-constrained. The feedback off values for the damping rates are remarkably consistent with those calculated from the preceding fits for chromatic and radiation damping, with the values for the $m = 0$, $+1$, and -1 modes being 105, 38 and 60 s^{-1}, respectively. The damping rates due to feedback for the two head-tail modes are also reasonably consistent with being the same. These sets of results for the chromatic and feedback damping are necessary calibrations for the damping rates for trains of bunches presented next.

Damping Rates for Trains of Bunches A series of drive-damp measurements were taken with 30 bunch trains in September and December of 2010 and June of 2011. We present here the data analyzed from the September 2010 and June 2011 runs. (The December 2010 run has an orphaned set of data, which is still being analyzed.) All of the data sets were taken at 2.08 GeV with 30 bunch trains of positrons. The earlier data sets (177 and 182) were taken with approximately 0.75 mA, while the later data sets (697, 699 and 700) had approximately 0.35 mA stored bunches. The lower current runs were undertaken to allow the electron cloud to build up more slowly through the train. The damped amplitudes for each bunch in these data sets have been fit to the two damped oscillator model.

In some cases the fitting algorithm had difficulty converging on reasonable values. This can occur when 1) the bunch's oscillation signal level is too low, 2) the bunch's motion exhibits large oscillations after the initial motion has damped out, confusing the fitter, 3) the bunch's motion is unstable and the algorithm is attempting to fit undamped motion or 4) the fitter algorithm is not able to converge on a reasonable solution. The damping rates for these bunches are not plotted in the figures below, which display the damping rate vs. bunch number within the train.

For the first two of the data sets, we show the line power as a function of time, and bunch number. For data set 182 (Fig. 6.68), the $m = 0$ mode was excited and monitored. For data set 177 (Fig. 6.69), the $m = -1$ mode was excited and monitored. The damped amplitudes for each bunch in these data sets are displayed in Fig. 6.70 for $m = 0$ mode (top) and the $m = -1$ mode (bottom).

In data set 182 (Fig. 6.68), we can see that the first bunch is more easily excited than the next few bunches, but the damping rates are similar. But further along the train, the excitation level increases and the damping time gets very long near the end of the train. In the damping rate plot (and Fig. 6.70, top) we observe that the beam stability is relatively constant through the train (with some reduction in stability in the neighborhood of bunches 8 through 12) and then generally decreases (damping rate decreases) as we proceed from bunch 21 onward. The fastest rates observed for the first bunches are consistent with what is expected from the feedback system, chromatic

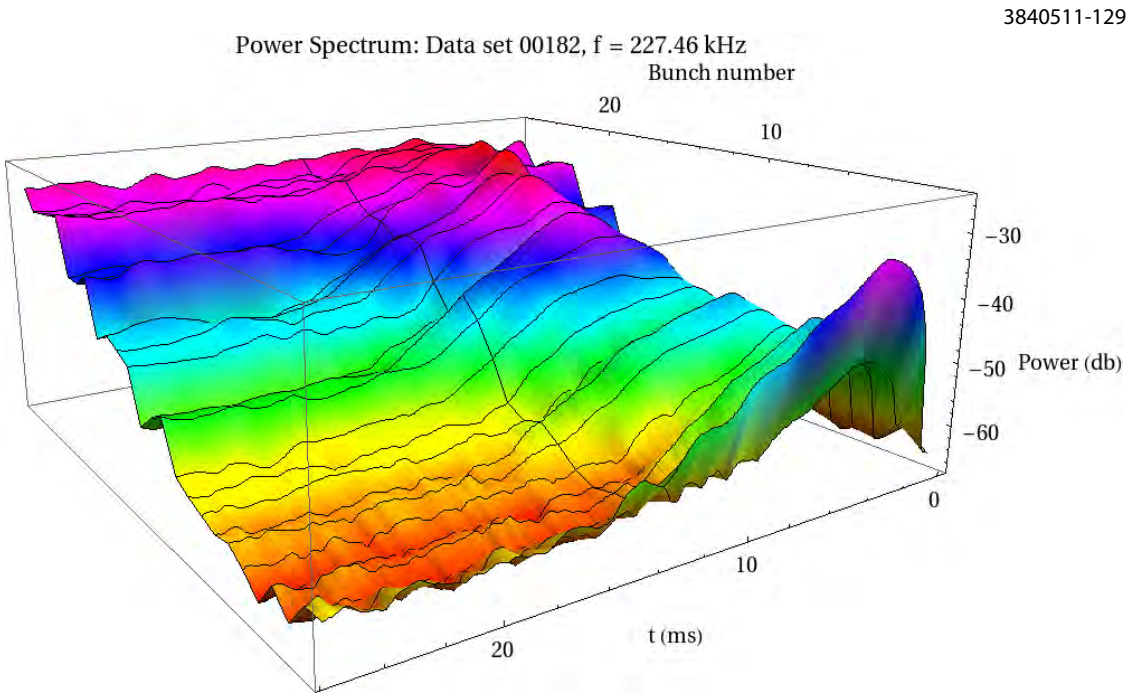

Figure 6.68: Data set 182: Grow-damp measurements for $m = 0$ mode. Chromaticity: (H,V) =(1.28, 2.39). Bunch current = 0.72 mA

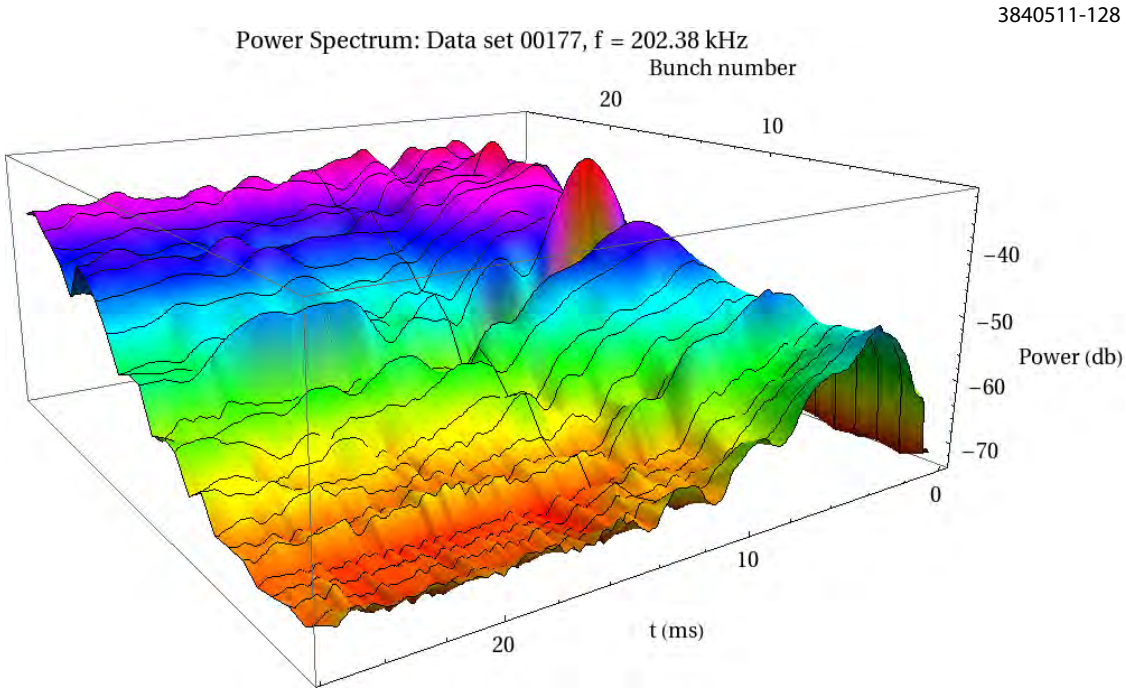

Figure 6.69: Data set 177: Grow-damp measurements for $m = -1$ mode. Chromaticity: (H,V) =(1.28, 2.39). Bunch current = 0.75 mA

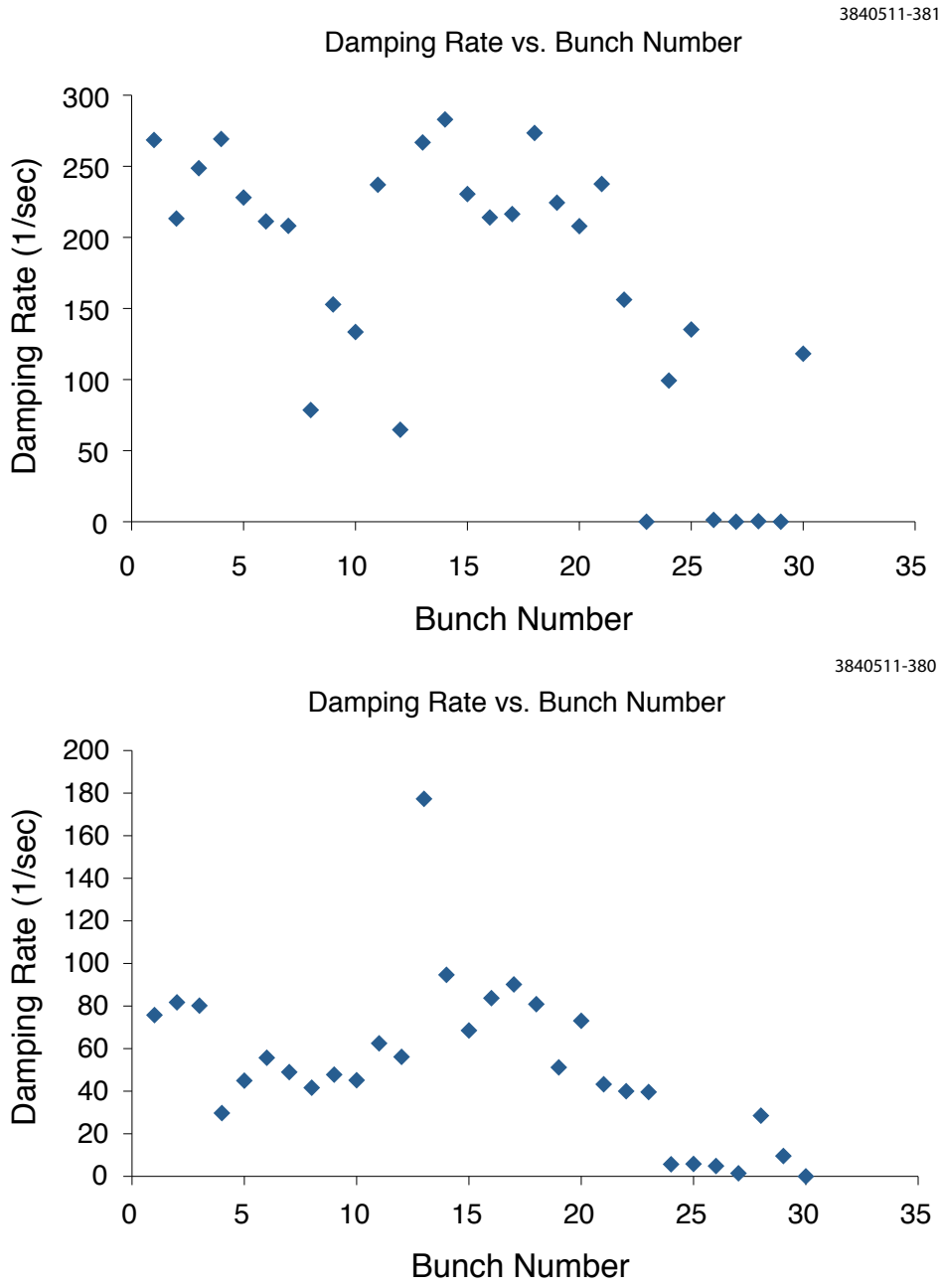

Figure 6.70: Vertical damping rate vs. the bunch number of a 30-bunch-long train of positrons. Chromaticity: (H, V) =(0.58, 2.13) and the vertical feedback setting is 20% of full scale. Top: Data set 182. $m = 0$ mode. Bunch current = 0.72 mA; estimated single bunch damping rate of 200 s^{-1}. Bottom: Data set 177. $m = -1$ head-tail mode. Bunch current = 0.75 mA; estimated single bunch damping rate of 110 s^{-1}.

and radiation damping (approximately 200 s^{-1}). Bunches after number 26 have amplitudes and damping rates consistent with unstable motion.

In data set 177, we see a similar trend, except that the first 20 bunches all appear to have similar

damping times and excitation levels (with the notable exception of bunch 13, which does appear to have a much higher damping rate.) Again, further along the train, the excitation level increases and after bunch number 20 the damping time gets very long as we approach the end of the train. The fastest damping rates observed for the first 20 bunches are consistent with being somewhat less than what is expected from the feedback system, chromatic and radiation damping (approximately 110 s^{-1}).

The next three data sets were also taken at 2.08 GeV with single 30-bunch trains of positrons, but in these cases the current per bunch was lowered to 0.35 mA to allow the instability to develop over a larger number of bunches in the train. The $m = 0$ (dipole) mode was excited for data set 700, while the $m = -1$ and $+1$ (head-tail) modes were driven for data sets 697 and 699, respectively. For the data set 697, the vertical and horizontal chromaticities were -0.20 and 0.73, respectively, while for data sets 699 and 700 the vertical and horizontal chromaticities were changed to -2.07 and 0.79, respectively. The vertical chromaticity in particular needed to be at these low values in order to produce unstable head-tail motion within the train. For these sets we operated with the Dimtel feedback system, and the data-taking software gated off the vertical feedback for the bunch being measured.

The damping rate vs. bunch number plot (Fig. 6.71, top) for data set 700 indicates a slight increase in the damping rate for the first bunch; after the first bunch the next 17 or so bunches have damping rates that are similar. There are a few exceptional bunches (e.g. bunches 11 and 19) that appear to be less stable and even a bunch (number 8) that seems to have a much great damping rate than its neighbors. (There is some suspicion that the data acquisition software's communications pathway, needed to gate off the feedback for bunch 8, may have failed during this bunch's measurement.) The damping rate seems to fluctuate toward less stability as we approach the end of the train beginning at bunch 19. The damping rates observed for the first 18 bunches (approximately 20 s^{-1}) are much less than what is expected from the feedback system, chromatic and radiation damping (approximately 110 s^{-1}.)

As is typical for the observations of head-tail damping for the $m = +1$ mode (Fig. 6.71, center) and the $m = -1$ mode (Fig. 6.71, bottom) there tend to be larger fluctuations in the measured damping rates. The estimate of the combination of the chromatic and radiation damping rate for the $m = +1$ mode is approximately 20 s^{-1}. A similar estimate for the $m = -1$ mode is approximately 3 s^{-1} (consistent with zero.) In both cases we see a decrease of stability occurring in the range of bunches 16 to 25 within the accuracy of the present measurements. This is also the range of bunches, for which the dipole ($m = 0$) mode indicates larger fluctuations in stability from bunch to bunch. For the $m = +1$ mode the damping rate for the first third of the train is consistent with or slightly less than chromatic and radiation damping, while for the $m = -1$ mode the damping rate for the first third is also in neighborhood of the magnitude of chromatic and radiation damping, although the measured damping rates appear to be consistently slightly higher. The large fluctuations in damping, beginning around bunch 20 of the train, represent the fact that the fitting routine is becoming somewhat confused by the growth of a single unstable oscillation. This instability begins about 20 ms after the drive signal is turned off and the head-tail motion has damped, grows to a peak amplitude about 30 ms later and then damps in another 20 ms. For the last bunches in the train the peak amplitude in this unstable "pulse" can exceed the initial head-tail motion by a factor of three.

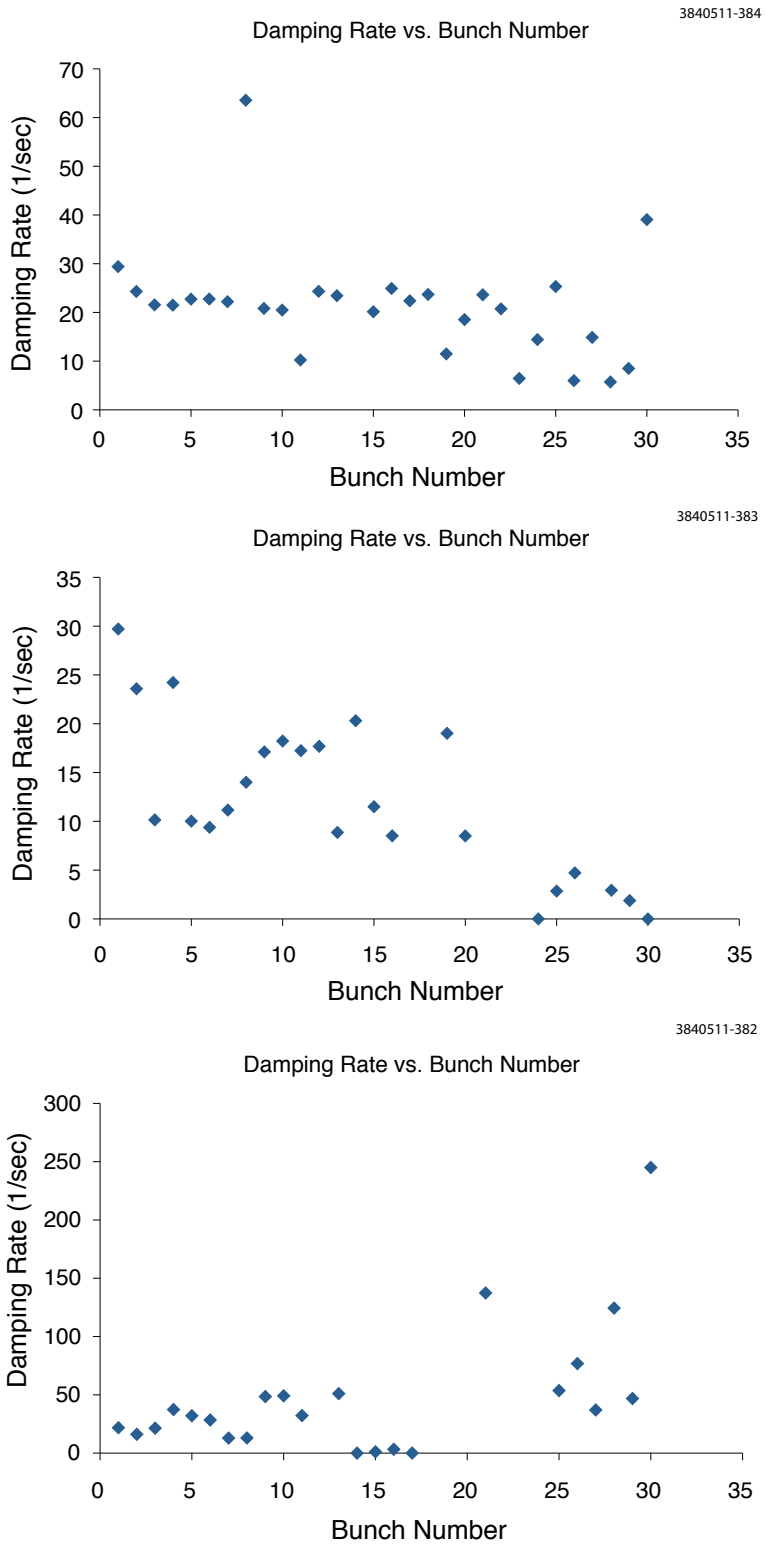

Figure 6.71: Veritcal damping rates vs. bunch number of a 30-bunch-long train of positrons. Bunch current = 0.35 mA. The vertical Dimtel feedback is in operation, but is gated OFF for the bunch being measured. Top: Data set 700. $m = 0$ mode. Chromaticity: (H, V) =(-2.07, 0.79). Estimated single bunch damping rate of 110 s^{-1}. Center: Data set 699. $m = +1$ head-tail mode. Chromaticity: (H, V) =(-2.07, 0.79). Estimated single bunch damping rate of 20 s^{-1}. Bottom: Data set 697. $m = -1$ head-tail mode. Chromaticity: (H, V) =(-0.20, 0.73). Estimated single bunch damping rate of 3 s^{-1}.

Conclusions from Drive-damp Measurements This technique is useful for studying stability of bunches within trains before the motion becomes unstable. In the conditions that we have studied, the damping rate for motion of bunches in the train lessens as the electron cloud builds up. The vertical dipole and head-tail modes become unstable at approximately the same bunch within the train, although the data is suggestive of the head-tail modes becoming unstable at a slightly earlier bunch than when the dipole mode destabilizes. The quality of the present data is not sufficient to specify whether the head-tail and dipole motion initially becomes unstable for the same bunch or not. However, what is clear is that motion of the bunches remain stable with essentially the same damping rates until it becomes unstable with a transition over relatively few bunches later in the train.

What can be said is that the effects of the electron cloud on the bunches within a train have both similarities to and differences from the dynamics typically observed for conventional accelerator impedances. For a transverse cavity mode excited resonantly by a train of bunches, if the Q of this mode is low enough that the cavity field decays before the train returns, one would expect the energy contained in the interaction between the cavity mode and the beam is only carried forward from one turn to the next by the beam itself.

The part of the coherent interaction between the bunch and the electron cloud which is similar to that of an RF cavity mode is as follows. If all of the bunches within the train have transverse feedback applied except for the one which is being observed, then the motion of this particular bunch will become unstable when the deflection from that the cavity mode grows (more rapidly than the mechanisms that damp the beam) as the amplitude of the bunch's displacement increases. This is true both for dipole and head-tail modes. Now for a conventional low-Q RF cavity transverse mode, the peak deflection is 90° out of RF phase with the energy loss from the bunch that excites the mode. Thus for this transverse mode to deflect the bunch either 1) it must have a very large transverse impedance or 2) the time for its field to vary must be comparable to the temporal length of the bunch. A similar conclusion can be drawn for the effect of the electron cloud that has accumulated partway through the train. At this location there must be a rapid temporal variation in the cloud's field in order to drive a bunch to become unstable, i.e. this must be a fairly high frequency phenomena.

However, the electron cloud has a characteristic which is unlike a cavity deflecting mode's interaction with the beam. If all bunches within the train are stabilized except one, then this bunch can feel a constant deflection from the accumulated RF fields from earlier bunches. This will cause a constant perturbation of the orbit, but will not inherently drive this bunch unstable. This implies that the strength of the instability will grow proportional to the current in this bunch, but will not matter where the bunch is within the train; all positions will be nearly equivalent. Since the electron cloud builds up along the train, the strength of the electron cloud-beam interaction grows along the train. This will cause unstable motion, which is not present for earlier bunches, to develop in later bunches in the train. These drive-damp measurements presented here support this view. Also, since the bunch, at which head-tail motion becomes unstable, is essentially the same bunch, at which dipole motion becomes unstable, this implies that the electron cloud's interaction occurs over longitudinal distances less than the bunch length. This would allow the center and tail of the bunch to feel the transverse kick.

6.3.3.3 Future Work

Future measurements are planned to repeat the single bunch damping rates vs. changes in the chromatic damping.

6.3.4 Vertical Emittance Growth Along Bunch Trains: Experimental Studies

This section will discuss measurements made using the x-ray beam size monitor (xBSM) described in Sec. 6.1.2.2. All measurements were made in the 2 GeV low-emittance lattice, unless otherwise noted. Comparisons are made with similar observations at KEKB[160, 161] when appropriate.

6.3.4.1 Bunch Current Dependence

Initial data were taken with the bunches at 14 ns spacing, using 45-bunch trains. For each bunch, the turn-by-turn vertical sizes and positions were fitted, and then the sizes were averaged over all turns. For each bunch, the rms of the positions were calculated to represent the motion of the bunch. Fig. 6.72 shows the bunch-by-bunch sizes and rms motions along the train at bunch currents of 0.5 mA (top), 1.0 mA (center) and 1.3 mA (bottom). For the 1.0 and 1.3 mA/bunch cases, a slow growth can be seen starting at the beginning of the train, with the bunch size growing more rapidly after around bunch 25 for 1.0 mA, and around bunch 20 for 1.3 mA. This is consistent with the cloud density increasing more rapidly along the train as bunch currents increase. As discussed above in Sec. 6.3.2.4, a synchrotron-betatron sideband signal is present from all bunches from the fast blow-up threshold to the end of the train. The beam size growth seen in Fig. 6.72 (top), and in Fig. 6.72 (center, bottom) before the fast blow-up threshold (around bunches 10-15), may be due to incoherent emittance growth. The growth seen after the fast blow-up threshold may be due to both incoherent effects and the coherent instability.

The head of the train was also seen to be somewhat enlarged. The cause of this is under investigation, but is believed to be possibly due to long-lived trapped electrons in the CesrTA ring which is dipole-dominated (unlike KEKB, where no such effect was evident), and/or possibly due to feedback tuning issues. The tail of the train is also seen to fall off gradually in size, an effect which was not observed at KEKB, where the beam size simply saturated going to the back of the train. The reason for this difference is not yet understood. It is worth mentioning that the bunch lifetimes followed roughly the measured beam sizes, with longer lifetimes for bunches with larger measured sizes, as might be expected from Touschek effect, which provides backing evidence that the sizes really do vary in the manner reported by the x-ray monitor.

Finally, Figure 6.73 shows the bunch-by-bunch position spectrum as measured by the x-ray monitor. The vertical tune line can be seen at the upper part of the plot, shifting downward in frequency (upward in tune units), due presumably to the electron cloud density increasing along the train.

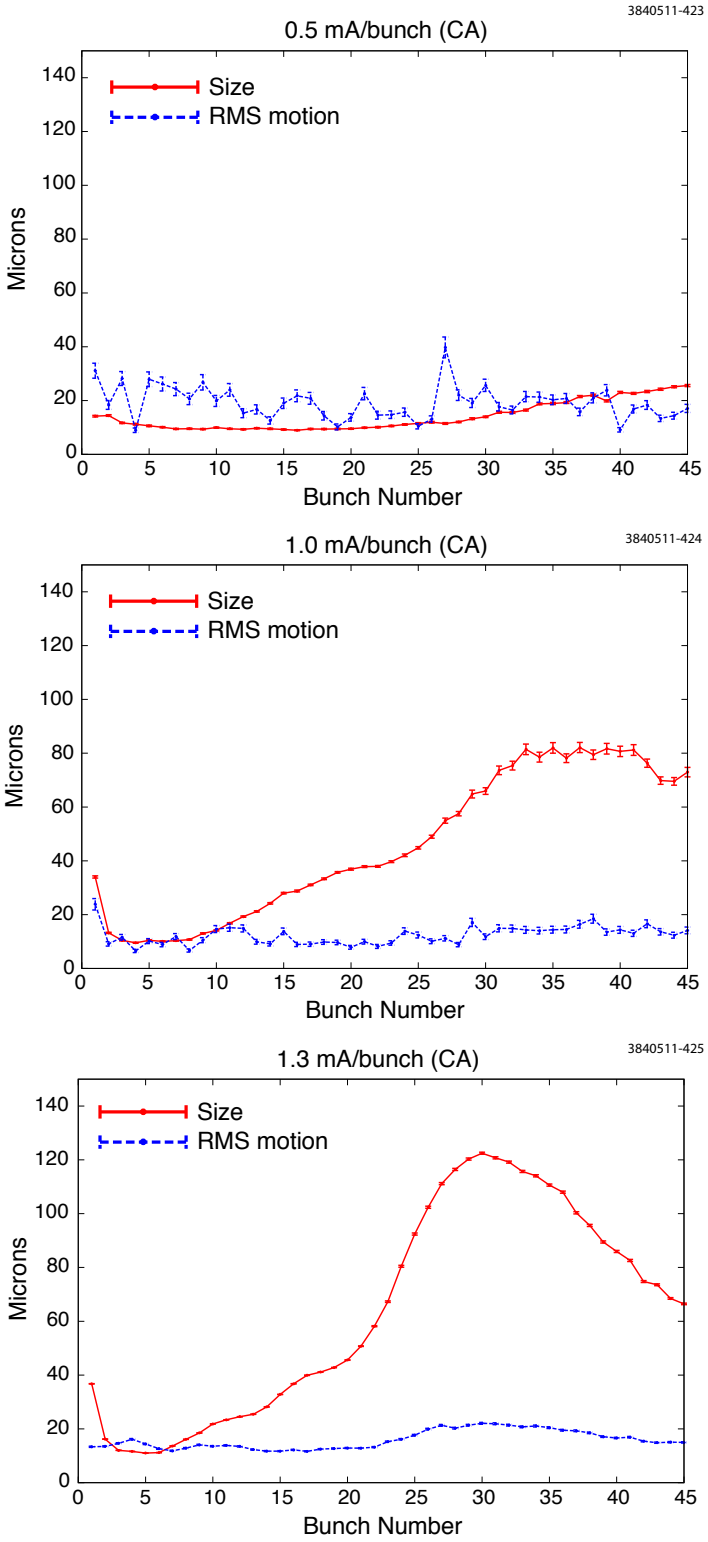

Figure 6.72: Bunch-by-bunch beam size and rms motion at 14 ns spacing. Top: bunch current 0.5 mA/bunch (128 turns). Center: bunch current 1 mA/bunch (4096 turns). Bottom: Bunch current 1.3 mA/bunch (4096 turns). The beam profile data are taken using the coded aperture (CA) X-ray optics. The beam size growth seen in the top plot, and in the center and bottom plots before the fast blow-up threshold (around bunches 10-15), may be due to incoherent emittance growth. The growth seen after the fast blow-up threshold may be due to both incoherent effects and the coherent instability.

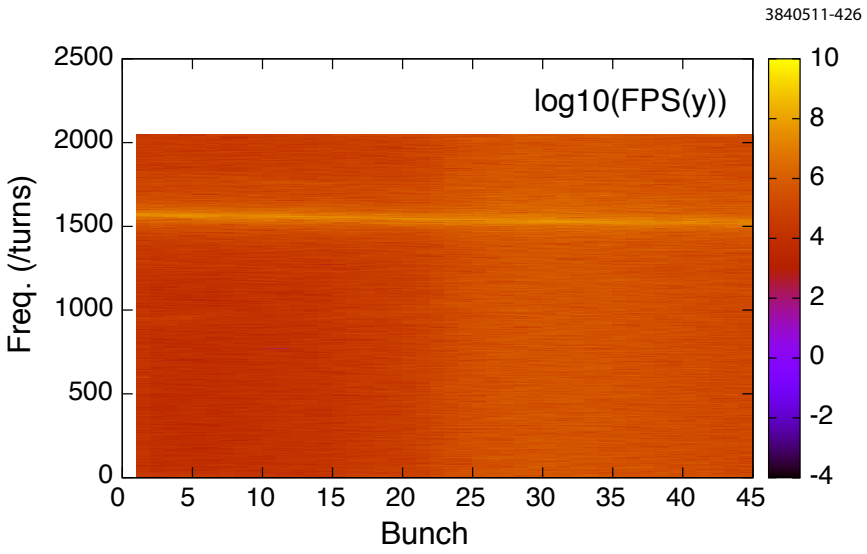

Figure 6.73: Fourier power spectrum of beam position measured by x-ray monitor at 14 ns spacing with 1.3 mA/bunch (4096 turns).

6.3.4.2 Chromaticity and Bunch Spacing Dependence

At KEKB, the coherent instability threshold was found to change with the chromaticity, with higher chromaticities pushing the onset of the instability back along the train. At CesrTA, two sets of measurements were taken varying the chromaticity, one at 14 ns spacing and one at 4 ns spacing. Figure 6.74 shows the bunch-by-bunch size and rms motion for a vertical chromaticity of 1.2 (left), and 2.2 (right). Here the transverse feedback gains were set very low (20% in vertical and horizontal directions, with longitudinal off). Greater dipole oscillations can be seen in the blue rms motion plot at chromaticity 1.2 towards the end of the train, while the rms motions in Fig. 6.72 of the previous section (where all feedbacks were at full normal gain settings) show no such increase in motion. The right side of Fig. 6.74 shows that raising the chromaticity to 2.2 suppresses the dipole oscillations to some extent, but the beam sizes do not change and the blow-up threshold does not change appreciably.

Figure 6.75 shows the results at 4 ns spacing, for vertical chromaticities of ~ -0.8 and ~ -0.4, respectively. Again, the blow-up threshold is not seen to change noticeably, although the beam size blowup is larger when the chromaticity is smaller. (The reason for the sudden drop off in bunch size at the end of the train is not clear, but may relate to the dipole oscillation becoming so large that much of the beam image is no longer contained on the detector, resulting in bad fits.)

It is also seen that the blow-up threshold does not change appreciably when changing from 14 ns spacing to 4 ns spacing. This may be due to the cloud lifetime being very long compared to be bunch spacing in the dipole-dominated CesrTA, and so the cloud does not decay appreciably over the space of 14 ns, making the cloud density a function of the number of preceding bunches. This is different from KEKB, where the instability threshold depends on the bunch spacing as well as the bunch currents.

The reason for the insensitivity to chromaticity change, in contrast to the case at KEKB, is not known, though it may be noted that the total chromaticity changes tried so far at CesrTA are

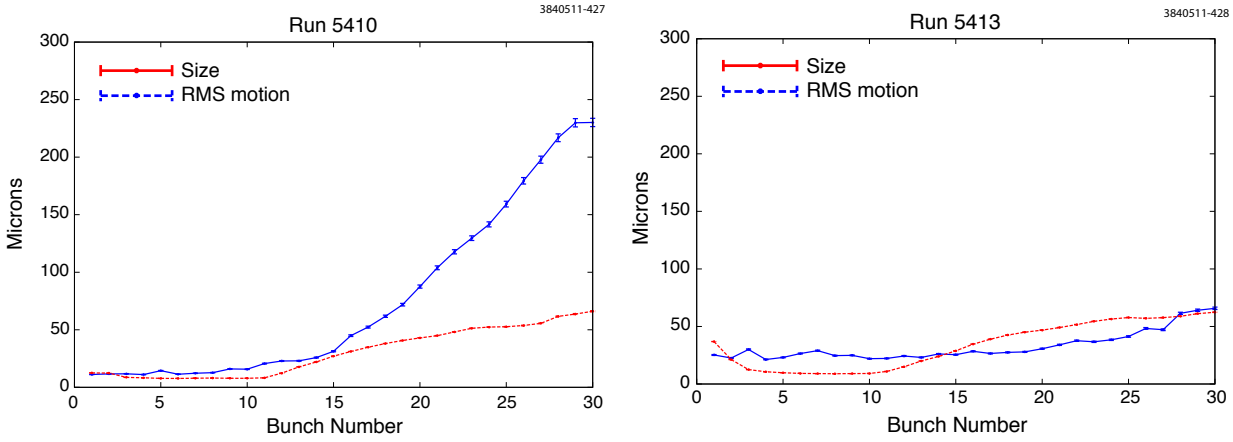

Figure 6.74: Bunch-by-bunch beam size and rms motion at 14 ns spacing, 0.75 mA/bunch. Left: vertical chromaticity ~ 1.2. Right: vertical chromaticity ~ 2.2.

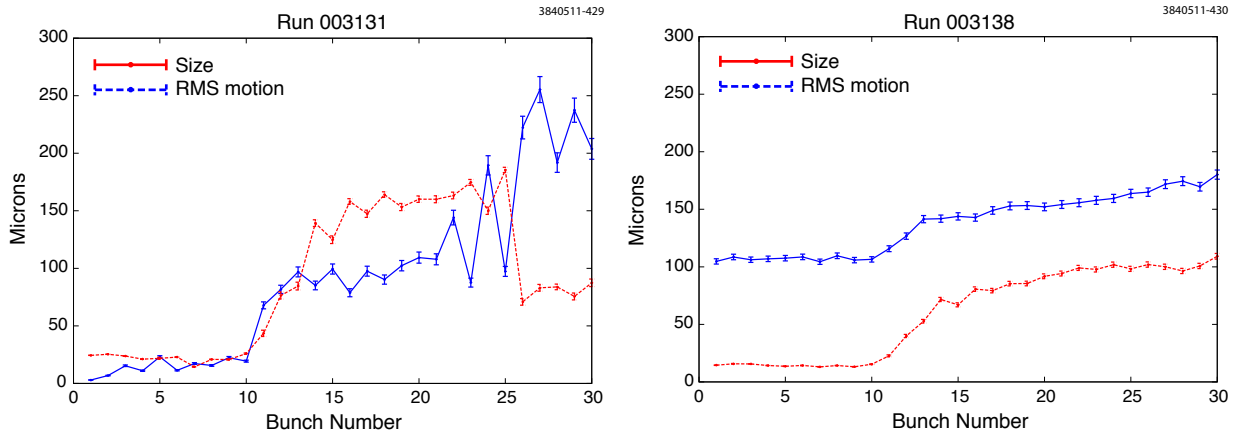

Figure 6.75: Bunch-by-bunch beam size and rms motion at 4 ns spacing, 0.75 mA/bunch. Left: vertical chromaticity ~ -0.8. Right: vertical chromaticity ~ -0.4.

smaller than those tried at KEKB (several units). It should be mentioned that the sideband amplitude was observed to change with chromaticity, as shown above in Sec. 6.3.2.6.

6.3.4.3 Emittance Dependence

At KEKB, it was found that changing the initial beam size did not change the blow-up instability threshold. The initial beam size at CesrTA was also varied, using dispersion bumps through two wiggler sections in the L1 and L5 regions of the ring. The data for the enlarged-emittance beam, with an estimated smearing function of ~ 30 μm (to be taken in quadrature with the natural beam size) are shown in Figure 6.76 (right). This should be compared with the un-enlarged beam data (Figure 6.76 (left)). It can be seen that the initial beam size is enlarged, and there is still emittance growth along the train to about the same level as for the small emittance data, indicating that the threshold is similar. These data shown were taken at 4 ns spacing; similar results were found at 14 ns spacing.

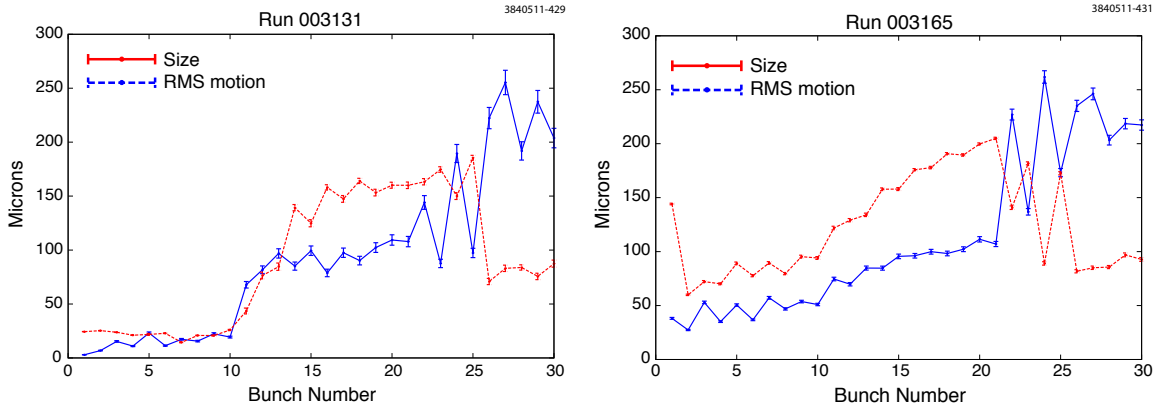

Figure 6.76: Bunch-by-bunch beam size and rms motion at 4 ns spacing with 0.75 mA/bunch. Left: nominal emittance. Right: increased initial emittance.

The reason for the lack of dependence of the threshold on the beam size can be seen from Eq. (6.37). The phase factor χ is 9.5 for CesrTA at 2.1 GeV (see Tab. 6.6), which is larger than the numerically estimated natural $Q_{nl} \sim 7$ for a coasting beam [148]. In this case, the threshold is independent of vertical beam size (for small changes in the beam size).

Eq. (6.40) only applies at zero chromaticity. At non-zero chromaticity, there is an additional dependence of the threshold on the beam size. Typically for these measurements, CesrTA was operated with a relatively small vertical chromaticity. However, it is possible that measurements at much larger vertical chromaticities would show a dependence of the blow-up threshold on initial beam size.

6.3.4.4 Feedback Gain Dependence

Finally, it was observed that the transverse bunch-by-bunch feedback had no effect on the coherent instability signal at KEKB [160]. Figure 6.77 shows two different settings of the transverse feedback gain at CesrTA : 20% and 40% gain settings, for both vertical and horizontal feedback. While the dipole motion behavior changes somewhat with the change in gains, the blow-up behavior is not

changed at all, consistent with results seen at KEKB. This is also what would be expected if the beam size blowup was due to a single-bunch instability.

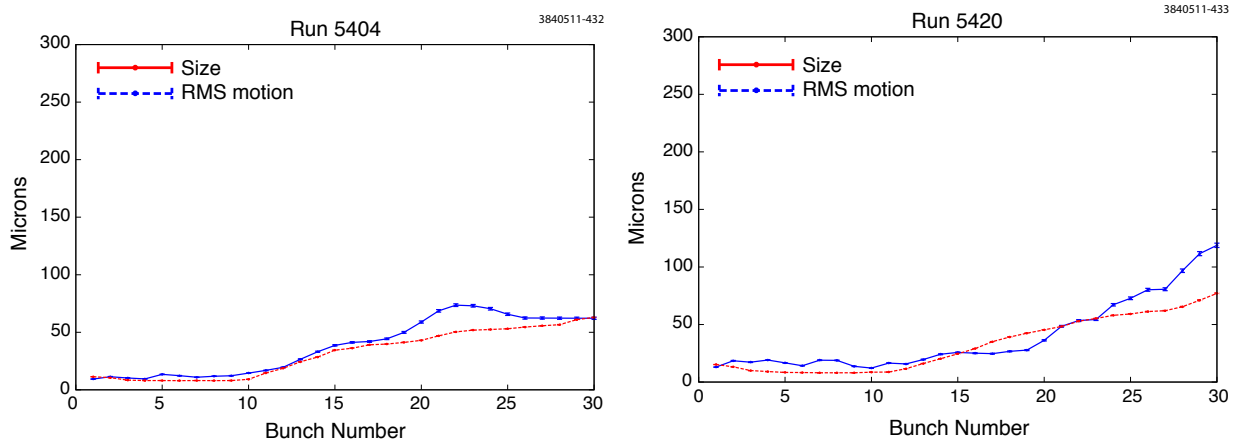

Figure 6.77: Bunch-by-bunch beam size and rms motion at 14 ns spacing with 0.75 mA/bunch. Left: LOW feedback gain. Right: HIGH feedback gain.

6.3.4.5 Comparison with Bunch-by-Bunch Frequency Spectra

In Fig. 6.78, the bunch-by-bunch beam size and rms motion are shown for a measurement with a 14 ns train, at 4 GeV, with 1.1 mA/bunch. The conditions for this measurement are exactly the same as those for the bunch-by-bunch frequency measurement described in Sec. 6.3.2.12. For that measurement, the growth of the vertical head-tail lines are shown in Fig. 6.58. The $m = 1$ vertical head-tail line starts growing at bunch 18 and peaks around bunch 22. Comparing with Fig. 6.78, the vertical emittance growth starts at bunch 17 and reaches a plateau around bunch 22. Thus the onset and development along the train of the vertical head-tail lines is very similar to the onset and development along the train of vertical emittance growth.

6.3.5 Instability Threshold and Vertical Emittance Growth: Comparison with Simulations

6.3.5.1 Analytical Estimates

Using the formulae presented in Sec. 6.2.2, Table 6.6 gives the key instability parameters for CesrTA at 2.1 and 4 GeV, based on the parameters given in Tables 6.4 and 6.4. At 2.1 GeV, the analytical estimate of the threshold density of 1.3×10^{12} m^{-3} is about 60% higher than the measured threshold of 8×10^{11} m^{-3} presented in Sec. 6.3.2.4. At 4 GeV, the analytical estimate of the threshold density is 2.65×10^{12} m^{-3}, about 30% higher than the measured threshold of 2×10^{12} m^{-3} presented in Sec. 6.3.2.12.

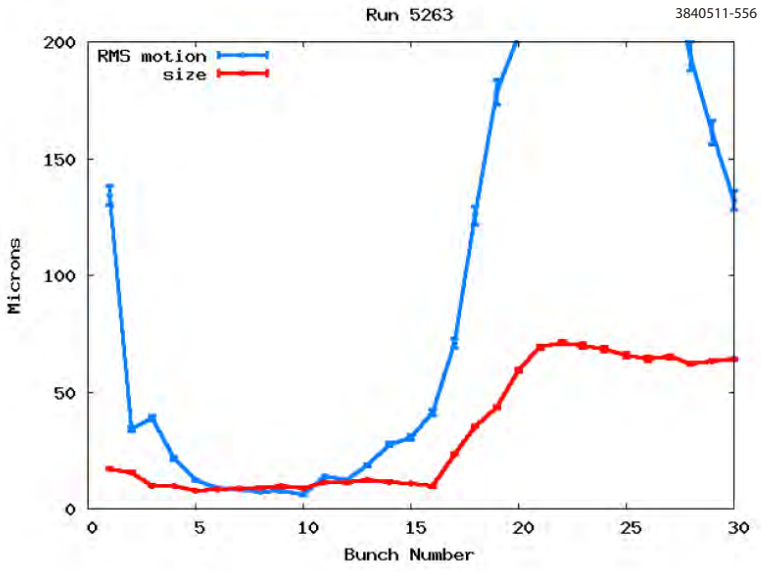

Figure 6.78: Bunch-by-bunch beam size and rms motion at 14 ns, 4 GeV, with 1.1 mA/bunch.

Table 6.6: Analytical estimates of CesrTA EC instability thresholds

	CesrTA: 2.1 GeV	CesrTA: 4 GeV
Circumference L (m)	768	768
Energy E (GeV)	2.1	4.0
Bunch population N_+ ($\times 10^{10}$)	2	2
Horizontal emittance ε_x (nm)	2.6	23
Vertical emittance ε_y (pm)	20	177
Momentum compaction α ($\times 10^{-4}$)	68.0	63.0
Rms bunch length σ_z (mm)	10.5	17.2
Rms energy spread σ_E/E ($\times 10^{-3}$)	0.81	0.93
Horizontal betatron tune ν_x	14.57	14.57
Vertical betatron tune ν_y	9.62	9.62
Synchrotron tune ν_s	0.065	0.041
Damping time $\tau_{x,y}$ (ms)	56.4	19.5
Average vertical beta function β_y (m)	16	16
Electron frequency $\omega_e/2\pi$ (GHz)	43	11.3
Phase angle χ	9.5	4.1
Threshold density $\rho_{e,th}$ ($\times 10^{12}$ m^{-3})	1.3	2.65
Tune shift at threshold $\Delta\nu_{x+y}$ ($\times 10^{-3}$)	10.7	11.6

6.3.5.2 PEHTS Simulations (Adapted from [147])

Particle-in-cell simulations for the beam-electron-cloud interaction, using the PEHTS code [94], were executed to evaluate the threshold of the single-bunch instability. The machine parameters were taken to be those in Table 6.7.

In these simulations, a bunch and the electron cloud are represented by 400,000 and 100,000 macro-particles, respectively. The bunch is sliced into 40 pieces along the rms bunch length σ_z, each slice

Table 6.7: Parameters of CesrTA used for PEHTS simulations

	CesrTA/2	CesrTA/5
Circumference L (m)	768	768
Energy E (GeV)	2.1	5.0
Bunch population N_+ ($\times 10^{10}$)	2	2
Horizontal emittance ε_x (nm)	2.6	40
Vertical emittance ε_y (pm)	20	308
Momentum compaction α ($\times 10^{-4}$)	67.6	62.0
Rms bunch length σ_z (mm)	12.2	15.7
Rms energy spread σ_E/E ($\times 10^{-3}$)	0.80	0.94
Horizontal betatron tune ν_x	14.57	14.57
Vertical betatron tune ν_y	9.62	9.62
Synchrotron tune ν_s	0.055	0.0454
Damping time $\tau_{x,y}$ (ms)	56.4	19.5
Average vertical beta function β_y (m)	20	20
Electron frequency $\omega_e/2\pi$ (GHz)	35	11
Phase angle χ	8.9	3.7
Threshold density $\rho_{e,th}$ ($\times 10^{12}$ m^{-3})	0.8	3.2

containing approximately 10,000 macro-particles. The bunch interacts with the cloud electrons slice by slice on the two-dimensional $x - y$ plane.

One interaction between the bunch and electron cloud is treated as 40 interactions between slices and the electron cloud. The choice of the number of bunch slices can be important for a low emittance beam. The number of slices should be larger than $\omega_{e,y}\sigma_z/c$ to faithfully represent the oscillation of electrons in the simulation of single-bunch instability. The chosen number of slices, 40, is enough by this criterion, but we checked by using 100 slices and the same number of macro-particles in each slice. The results did not change significantly.

The simulation divides the circumference of the ring into n_{step} sections, each of which contains a 2-dimensional cloud. This cloud, consisting of 100,000 macro-particles, is initialized at every interaction with the bunch just before the first slice passes. We can characterize the transverse extent of the simulation in units of the beam sizes (σ_x, σ_y). Usually, we choose (10,20), but have compared results with larger cloud sizes and find the results to be consistent.

The fast head-tail instability should be independent of the integration step size if the number of steps in a synchrotron period is sufficient. A rule of thumb is to choose the number of integration steps to be 8 per revolution; that is, 160 steps for one synchrotron period in CesrTA, for which $\nu_s = 0.05$. When the tune shift and tune spread of the beam are large in a single interaction, an artificial incoherent emittance growth may arise. To avoid this emittance growth, the number of steps needs to be properly chosen. A incorrect choice of step number may also induce structure resonance peaks in the frequency spectrum. Therefore, simulations with different numbers of steps should be done. We also tried an integration step number of 10, as a comparison.

The simulation calculates the transverse distribution of every bunch slice and electron interacting with them. Figure 6.79 shows a typical result of vertical position and the size of every bunch slice and the vertical position of electrons interacting with the slices above the threshold. Figures 6.79 (a) and 6.79 (b) are given for 2 and 5 GeV beam energies for CesrTA. Coherent motions of the beam

and cloud are seen. The beam size increases due to the smear of the coherent motion. The longitudinal structure of the bunch for CesrTA/2 is more complex than that of CesrTA/5 due to the high phase factor χ.

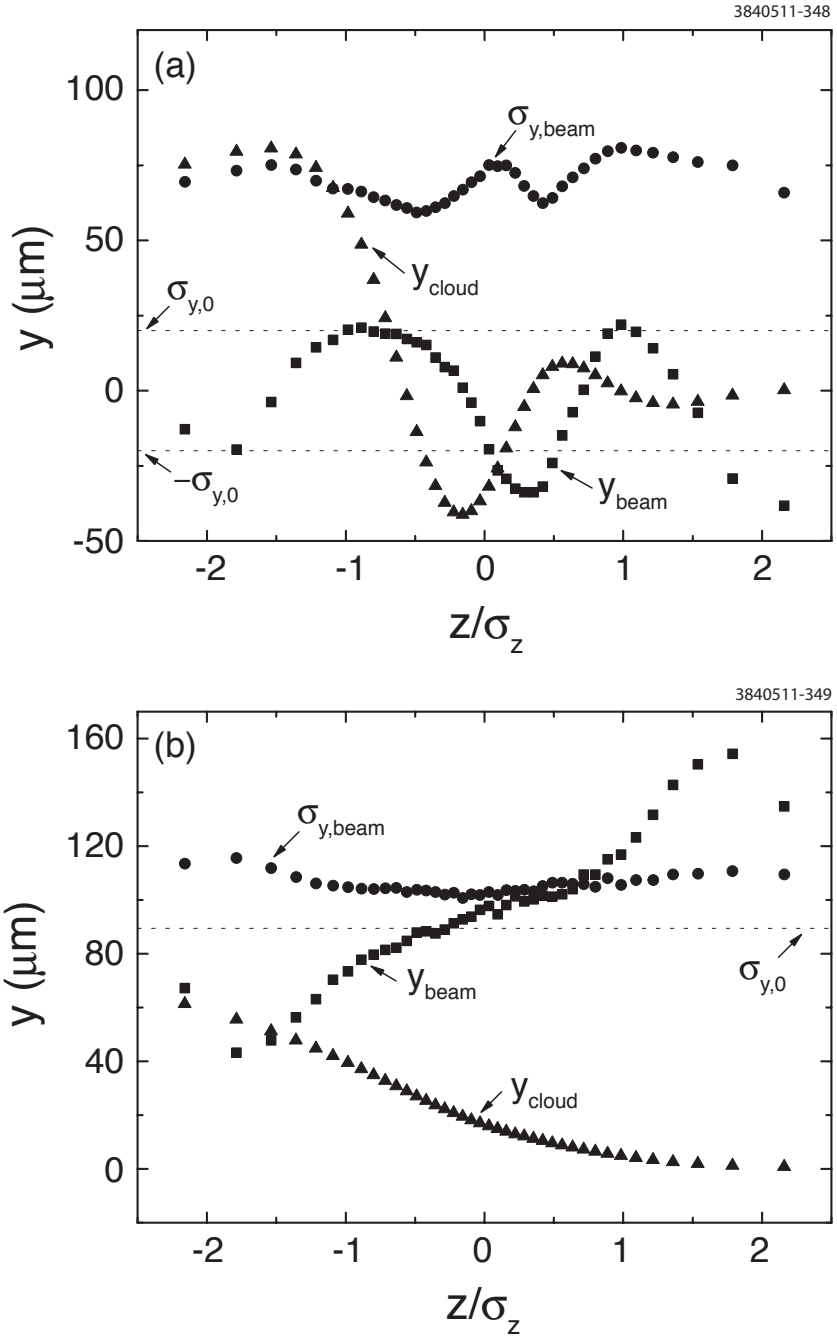

Figure 6.79: The vertical position and size of the bunch slices and the vertical position of the electron cloud interacting with the slices above the threshold are depicted for (a) 2 and (b) 5 GeV beam energies. The dotted lines indicate the initial vertical beam sizes. The head of the bunch is at $z > 0$.

The simulation is done for several cloud densities to estimate the threshold of instability. Fig. 6.80

shows the evolution with turn number of the beam size as given by the projected particle distribution of all slices in a bunch. The instability threshold is declared to be crossed when a rapid increase of beam size, as shown in Fig. 6.80, is accompanied by coherent motion as shown in Fig. 6.79.

The instability threshold cloud densities are about 0.6×10^{12} and 4.0×10^{12} m^{-3} for beam energies of 2 and 5 GeV, respectively. Compared with the analytical estimates shown in Table 6.7, the numerical simulations indicate thresholds which are 25% lower at 2 GeV and 25% higher at 5 GeV.

Above the threshold densities, the coherent motion shown in Fig. 6.79 is seen clearly. Simulations using the smaller cloud size of (10,10) predict very different thresholds of 1.2×10^{12} and 3.0×10^{12} m^{-3}. But the thresholds are consistent with the value of (10,20) for larger cloud sizes (20,40) and (40,80).

A slow growth of the beam size is seen below the threshold for both beam energies. During the slow growth, any coherent motions as shown in Fig. 6.79 are not seen. The slow growth is caused by an artificial incoherent effect, which is due to the integration with 8 steps for one revolution. Unphysical structure resonances related to $a\nu_x + b\nu_y = 8n$ are induced. Precise estimation of the incoherent emittance growth is discussed later.

Above a threshold cloud density, the coherent head-tail motion causes emittance growth. Direct evidence for the instability has been given by the observation of the synchrobetatron mode of a bunch, both in simulations and in measurements (using a bunch-by-bunch position monitor) at KEKB [162].

The synchrobetatron signal is obtained from the simulation by taking the Fourier transformation of the dipole position turn-by-turn. Figure 6.81 shows the Fourier spectra for the dipole moment of the beam above and below the threshold. The spectra for 2 and 5 GeV beam energies are very different. Clear dipole mode and lower synchrotron sideband are seen at 2 GeV. The lower synchrotron sideband also appears in the experimental observations discussed in Sec. 6.3.2. Both mode signals are enhanced above the threshold at 2 GeV. At 5 GeV, several additional modes appear, and the dipole mode splits into two modes above the threshold. And a sideband appears at around $\nu_\beta + 0.07$ (above the dipole mode) above the threshold. The appearance of this higher frequency sideband above threshold is similar to the synchrobetatron sideband observed at the KEKB LER [160, 163].

Mode coupling may be considered as a mechanism for generating the instability and the resulting emittance growth. Figure 6.82 shows the visible modes as a function of the cloud density for different cloud sizes (10,10) and (10,20) in 2 and 5 GeV beam energies. The mode spectra for a different integration step number, 10, are depicted to distinguish the unphysical structure resonances. The mode frequencies are almost the same for both integration steps. At 2 GeV, a sideband at lower frequency is seen for both cloud sizes. The tune shift evaluated by Eq. (6.40) is not seen when the electron-cloud density increases at 2 GeV, but the vertical betatron tune shift is coincident with the tune shift evaluated by Eq. (6.40) for 5 GeV. But, at 2 GeV, the tune shift is more complex because of the high phase factor, χ.

At 5 GeV, the vertical betatron peak splits into two frequencies above the threshold, and the sideband at a higher frequency is induced for both (10,10) and (10,20). A similar spectrum appears at a larger cloud size (20,40). For cloud sizes larger than (10,20), the threshold density of the electron cloud saturates, but the mode frequencies do not differ greatly from the cloud sizes (10,10) and (10,20) at 2 and 5 GeV. It is difficult to conclude which modes are merged at the threshold

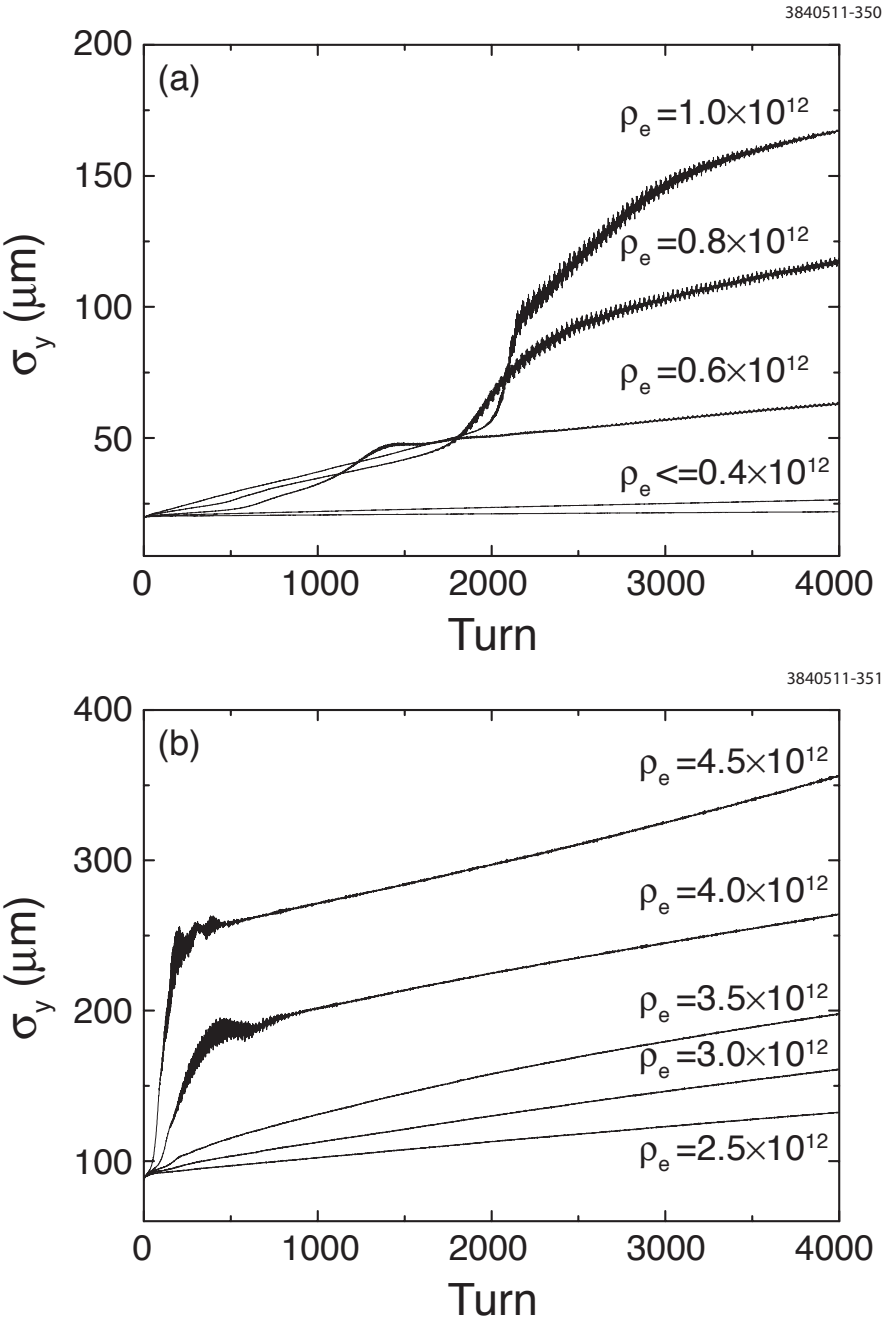

Figure 6.80: Evolution of vertical beam size growth for various cloud densities in CesrTA (a) 2 and (b) 5 GeV beam energies. The electron cloud density ρ_e is in units of m^{-3}.

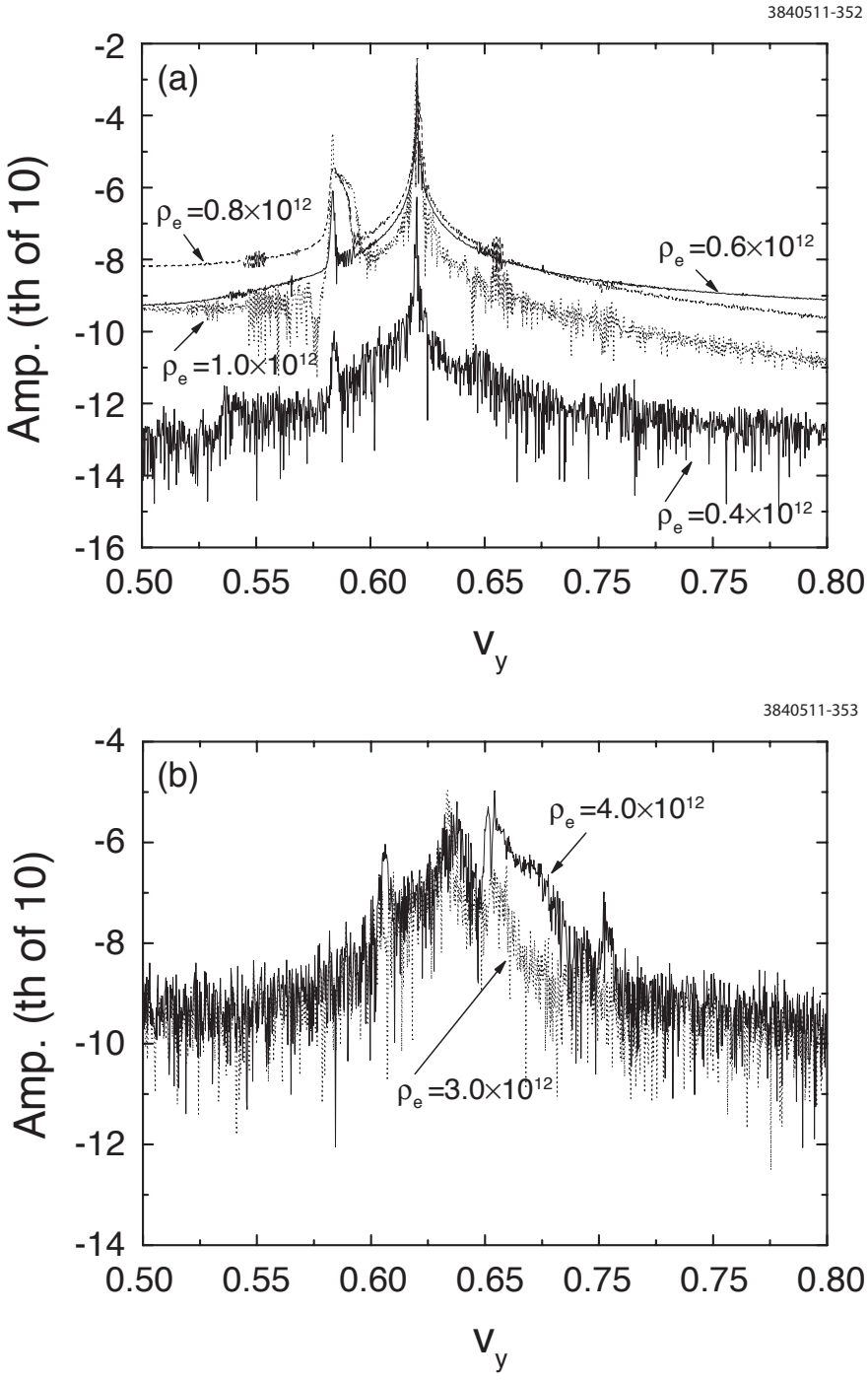

Figure 6.81: Frequency spectra for the dipole moments of (a) 2 and (b) 5 GeV beam energies. Vertical axis indicates the amplitude of frequency spectra and the index corresponds to the power of 10. The electron cloud density ρ_e is in units of m^{-3}.

density from the figures.

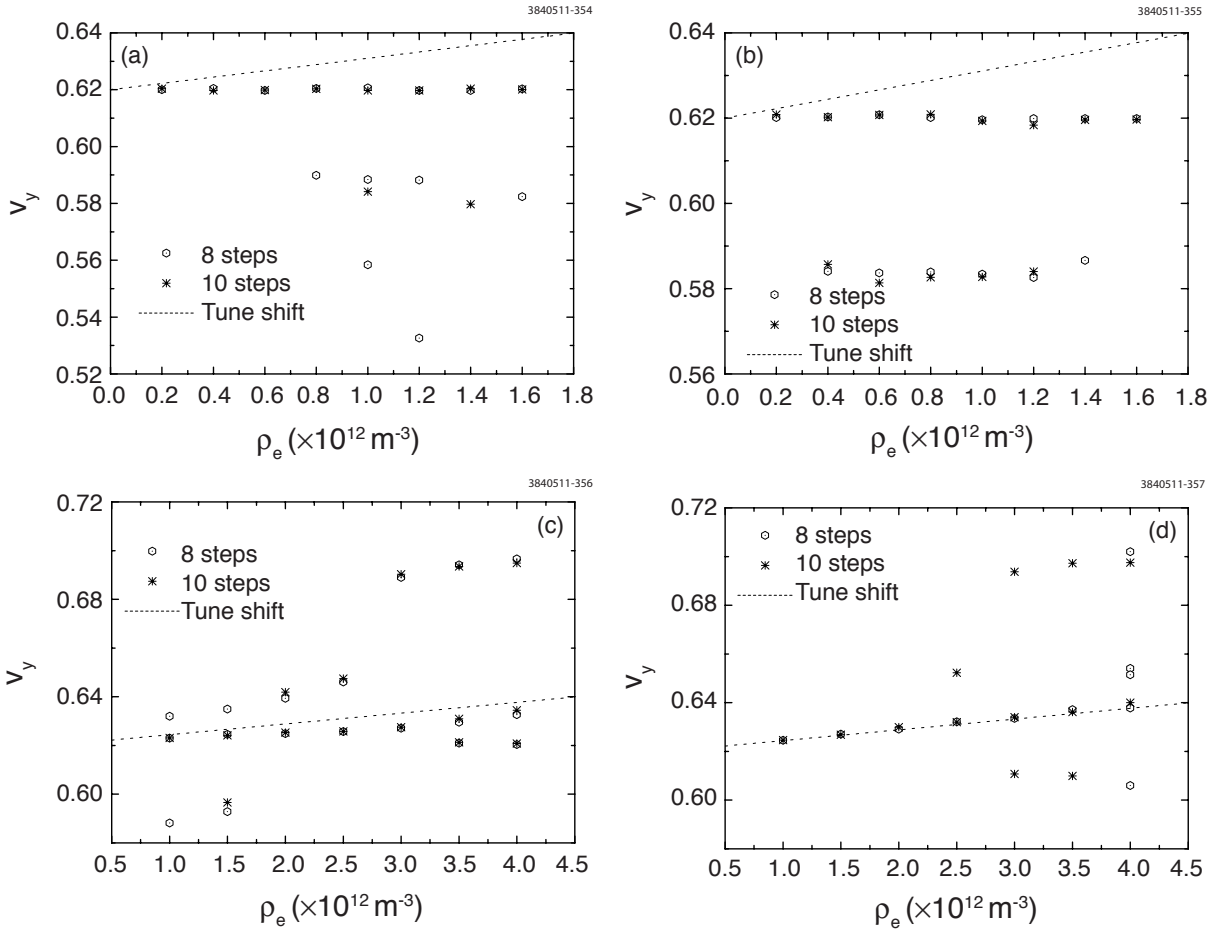

Figure 6.82: Mode frequencies for various cloud densities at different cloud sizes (10,10) and (10,20): (a) cloud size (10,10) for 2 GeV, (b) (10,20) for 2 GeV, (c) (10,10) for 5 GeV, and (d) (10,20) for 5 GeV beam energies, respectively. The dotted line indicates the tune shift evaluated by Eq. (6.40).

Feedback Effect For a single-bunch instability, dipole motion is usually dominant above the threshold density. Therefore, we investigate the effect of a dipole feedback system on the electron-cloud instability. Figure 6.83 shows the amplitude of vertical dipole motion with and without the feedback, and the growth of beam size with the feedback on, at 2 GeV. The feedback-damping time is 50 turns. Dipole motion is dominant as shown in Fig. 6.83(a). The bunch-by-bunch feedback system kicks the beam based on an observation of the amplitude of dipole motion. The transverse kick received by the feedback can be expressed by

$$\mathbf{y}_{n,+} = \mathbf{y}_{n,-} - k\mathbf{M}\left\langle \mathbf{y}_{n-1,+} \right\rangle , \tag{6.65}$$

where $\mathbf{y}$ is the vector consisting of the vertical coordinate of each macro-particle in the bunch and its derivative in time, (y, y'), n means the n-th turn, $+$ $(-)$ means the time after (before) the feedback kick, k is the feedback-damping factor, $\mathbf{M}$ is the revolution matrix, and $\langle \mathbf{y}_{n-1,+} \rangle$ is the averaged value of $\mathbf{y}_{n-1,+}$ measured by using two position monitors. The system feeds back the vertical oscillation with a one turn delay. Fig. 6.83(b) shows that the amplitude of dipole motion

decreases significantly with the feedback system. The threshold density increases to 0.8×10^{12} m^{-3} as shown in Fig. 6.83(c). The feedback reduces the amplitude of dipole motion, and the threshold density increases to some extent. However the threshold is not improved with a stronger feedback-damping factor. Therefore the feedback system does not entirely suppress emittance growth at 2 GeV.

Figure 6.84 shows the Fourier spectrum with the feedback on at 2 GeV. The feedback system is not effective in reducing the lower sideband peak. Several small sideband peaks appear at frequencies above that of the dipole mode. The spectrum is similar to that at 5 GeV, as shown in Fig. 6.81(b).

Figure 6.85(a) shows the evolution of the beam size with the feedback at 5 GeV. The feedback damping time is 50 turns. The amplitude of the beam size and the threshold density do not change significantly with the feedback system on. Figure 6.85(b) shows the dipole motion without and with the feedback system at the threshold density, 4.0×10^{12} m^{-3}. The lower order head-tail instability which does not couple to the dipole mode is dominant because of lower $\omega_{e,y}\sigma_z/c$, but the dipole instability is not serious at the threshold density for 5 GeV beam energy. The amplitude of dipole motion does not change significantly with the feedback system. For a stronger feedback-damping factor, the threshold density does not change as at 2 GeV. Therefore, the feedback system does not suppress emittance growth at 5 GeV.

Dispersion Effect Dispersion affects the electron-cloud instability because the electrons in the horizontal plane oscillate with different frequencies depending on their horizontal coordinate[164]. Figure 6.86 shows the beam size evolution in the presence of dispersion. The dispersion is assumed to be 0.8 and 0.7 m, which are averaged values for the realistic lattices of CesrTA at 2 and 5 GeV. The threshold is clearly degraded at 2 GeV: $\rho_{e,th} = 0.2 \times 10^{12}$ m^{-3} from 0.6×10^{12} m^{-3}. The degradation is also visible at 5 GeV, though it is smaller than at 2 GeV: the threshold decreases from 4.0×10^{12} to 3.0×10^{12} m^{-3}. The difference between the 2 and 5 GeV beam energies seems to be due to the difference in the phase factor.

Realistic Lattices Realistic lattices were used to investigate the effects of lattice variations on the electron cloud in CesrTA. The Twiss parameters of the realistic lattices are obtained from the MAD program [151]. The lattice functions used are shown in Fig. 6.87.

There are 83 bending magnets, and we consider those as the interaction points between the bunch and the cloud. The magnetic field of the bending magnets is set to be 0.076 T and 0.19 T, for 2 and 5 GeV lattices, respectively. Figure 6.88 shows the evolution of vertical beam size for various cloud densities in the 2 and 5 GeV beam energies, respectively. The thresholds of cloud densities are about 1.2×10^{12} and 5.0×10^{12} m^{-3}, for the 2 and 5 GeV beam energies, respectively. These values are about 50% higher than the analytical estimates.

Summary of Threshold Density Simulations and Comparison with Experiment. The threshold densities obtained with various simulation assumptions, for the parameters given in Table 6.7, are presented in Table 6.8. Also shown are the experimental measurements for the threshold densities at 2 and 4 GeV, presented in Sec. 6.3.2.4 and Sec. 6.3.2.12.

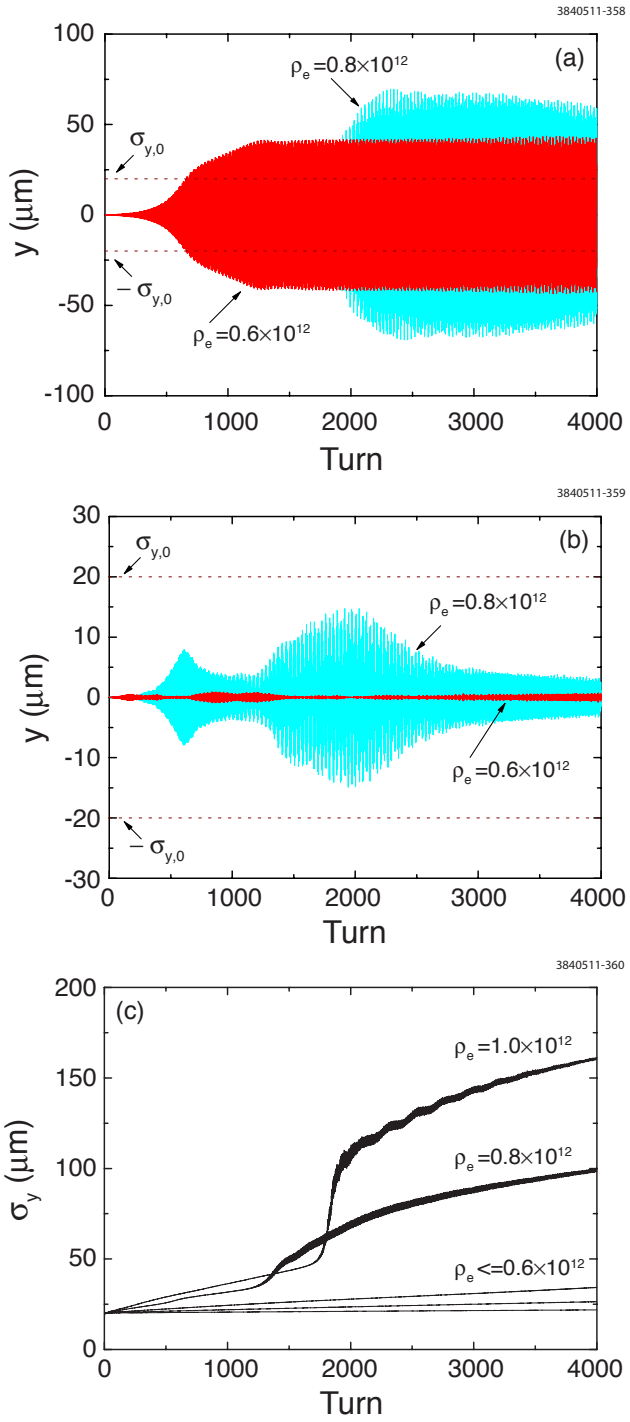

Figure 6.83: Evolution of the dipole motion (a) without and (b) with feedback at 2 GeV. (c) Vertical beam size growth with feedback at 2 GeV. The electron cloud density ρ_e is in units of m^{-3}.

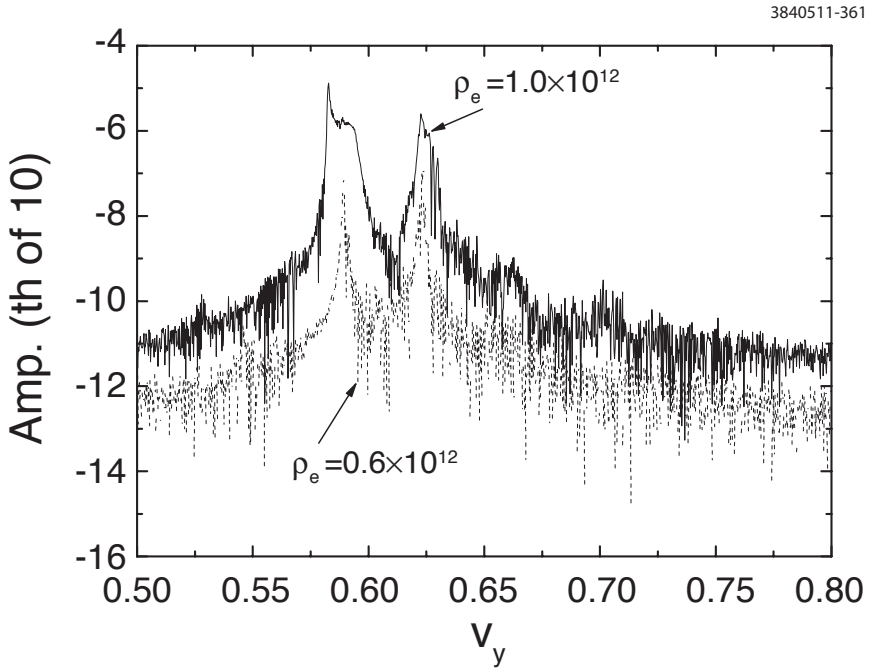

Figure 6.84: Frequency spectrum with feedback at 2 GeV. The electron cloud density ρ_e is in units of m^{-3}.

Table 6.8: Instability threshold estimates for the ecloud density (in units of 10^{12} m^{-3}) for CesrTA. The simple model consists of the eight integration steps and uniform beta function at each interaction point. The lattice parameters for the realistic model are obtained from the MAD program. The experimental results correspond to the beam parameters in Table 6.6, which are slightly different than the ones used for the simulations (Table 6.7).

Condition	2 GeV	4 GeV	5 GeV
Analytical estimate, using equations given in Sec. 6.2.2	0.82		3.2
Simple model (zero η_x, without feedback)	0.6		4.0
Simple model (zero η_x, with feedback)	0.8		4.0
Simple model (non-zero η_x, without feedback)	0.2		3.0
Realistic model	1.2		5.0
Experimental results	0.8	2.0	

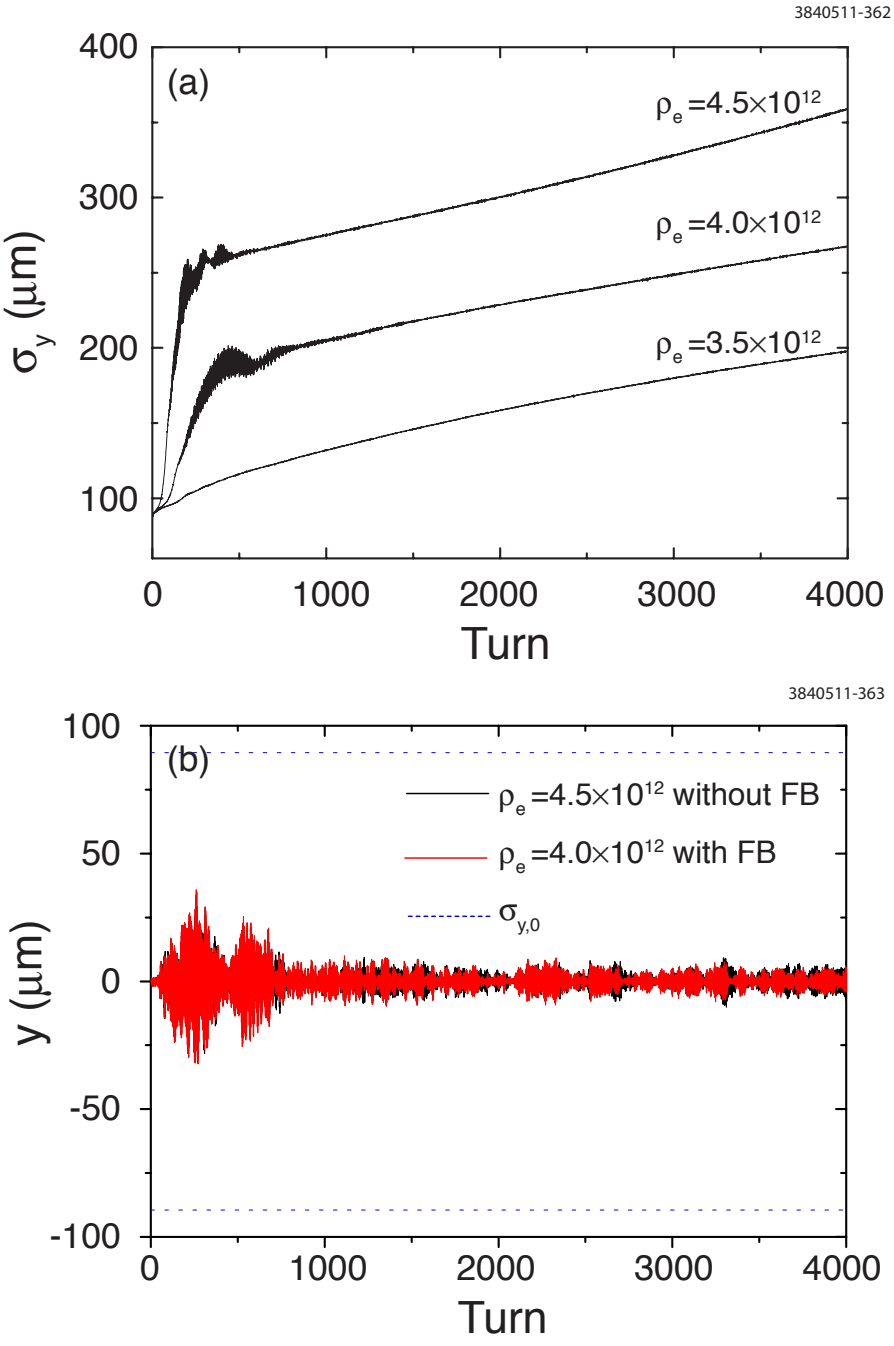

Figure 6.85: (a) Evolution of the beam size with feedback and (b) dipole moment with and without feedback at 5 GeV. The electron cloud density ρ_e is in units of m^{-3}.

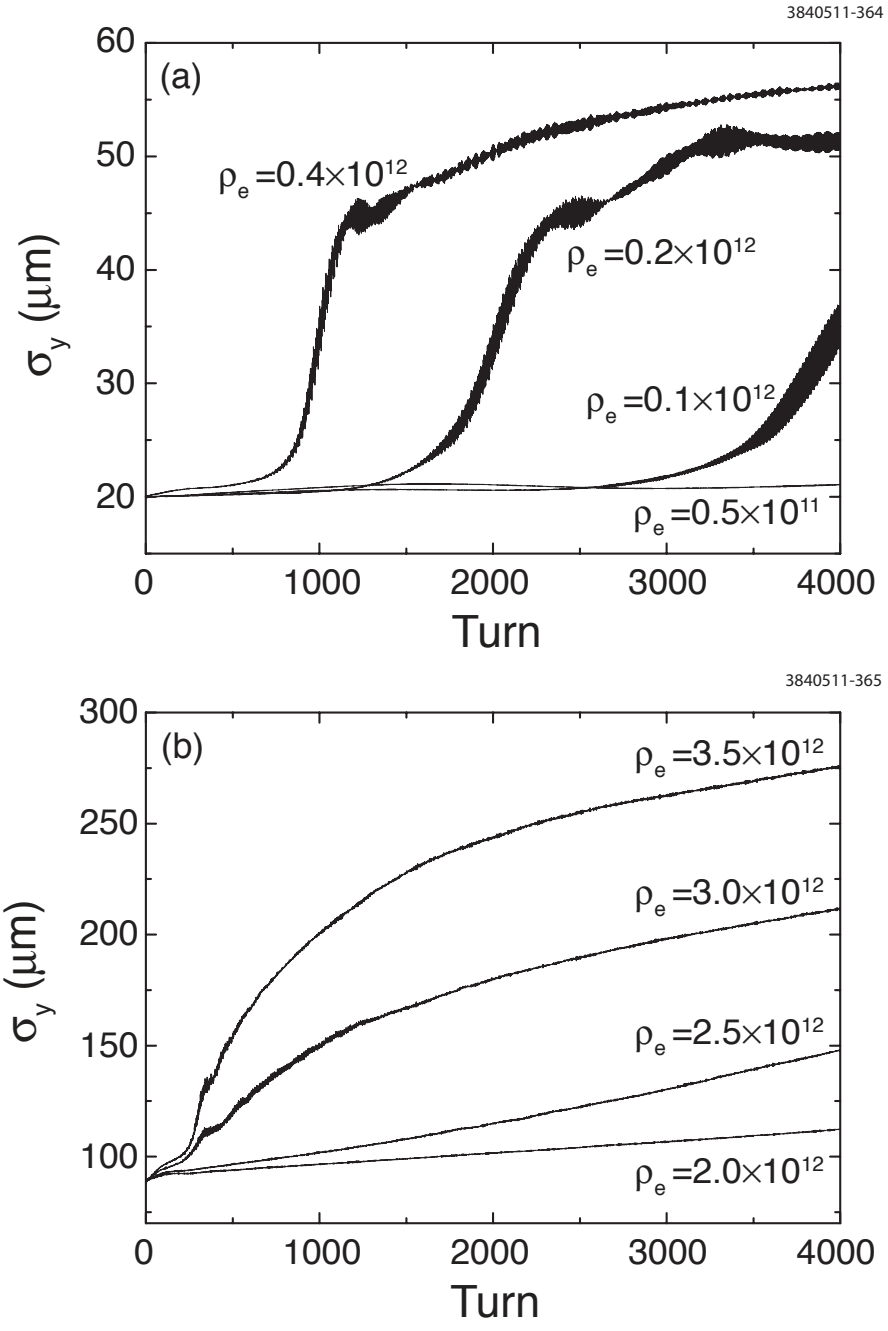

Figure 6.86: Evolution of the beam size with dispersion in (a) 2 and (b) 5 GeV beam energies. The ecloud density ρ_e is in units of m^{-3}.

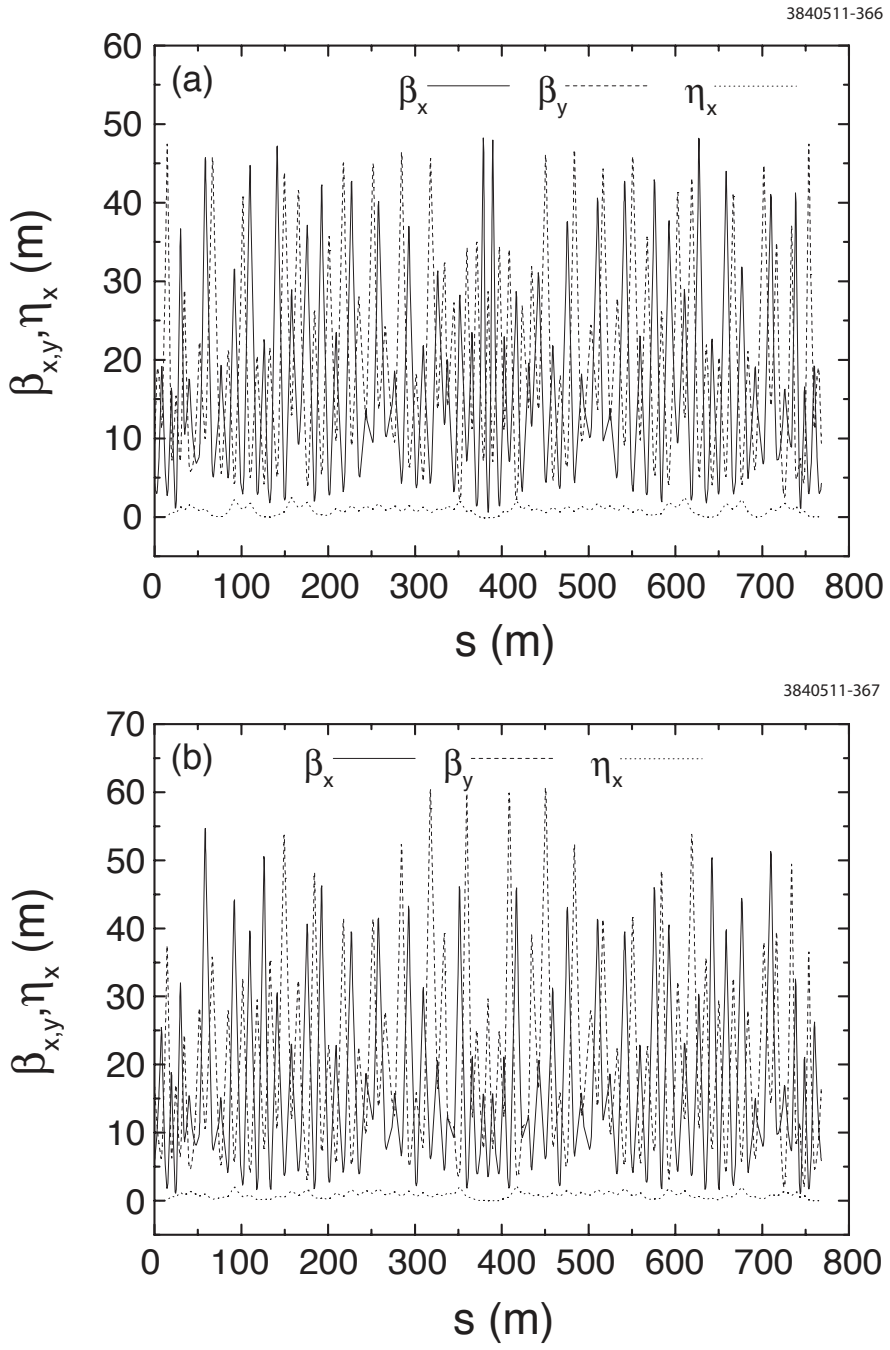

Figure 6.87: Lattice functions used for `PEHTS` simulations for (a) 2 and (b) 5 GeV beam energies in CesrTA. The super-periodicity is one for both beam energies. The horizontal, vertical beta functions ($\beta_{x,y}$) and the dispersion (η_x) are depicted. The average β_x (β_y) is about 15 (20) m in 2 GeV and 16 (20) m in 5 GeV beam energies. The average η_x is about 0.8 and 0.7 m in 2 and 5 GeV beam energies, respectively.

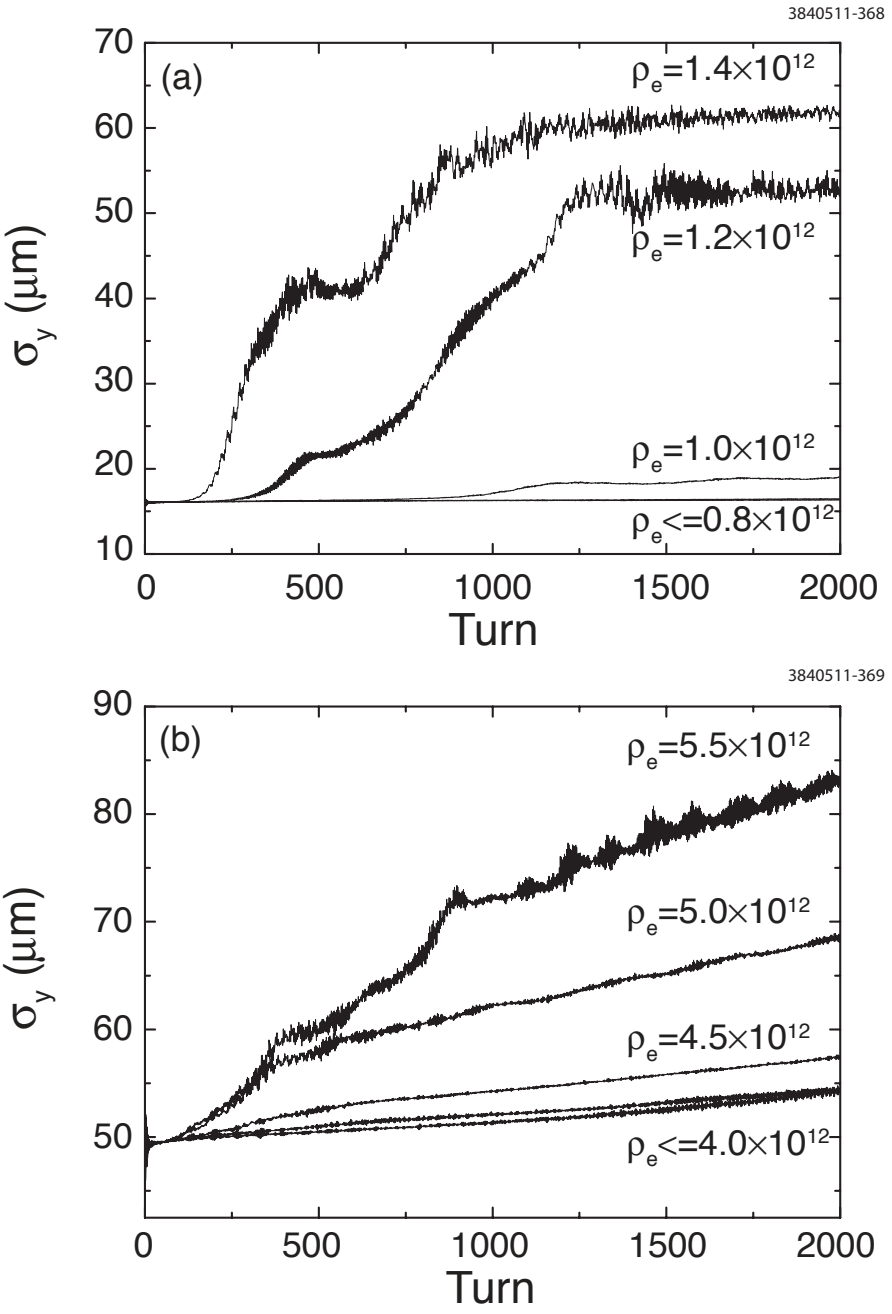

Figure 6.88: Evolution of the beam size in (a) 2 and (b) 5 GeV beam energies using the realistic lattices. The electron cloud density ρ_e is in units of m^{-3}.

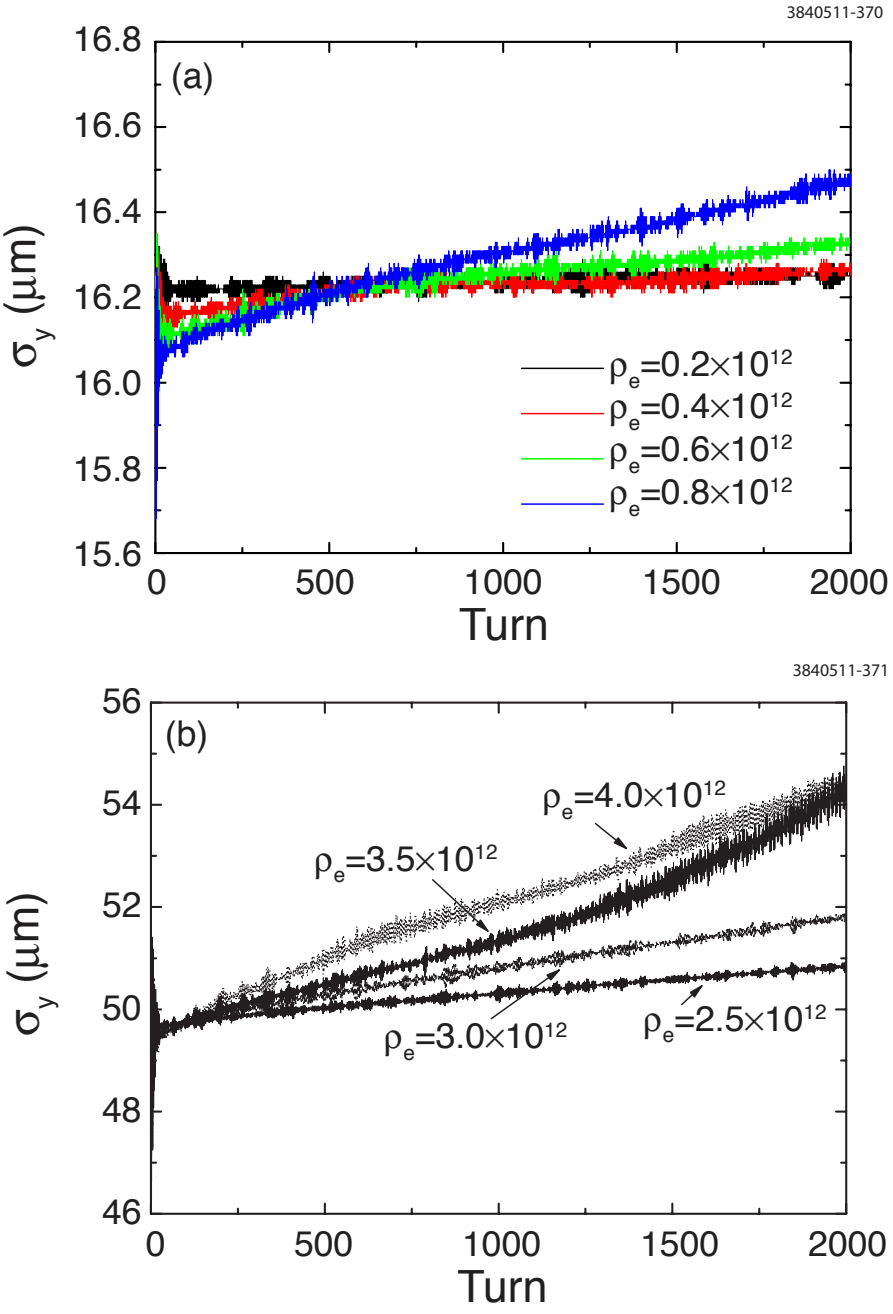

Figure 6.89: Evolution of the beam size below the threshold in (a) 2 and (b) 5 GeV beam energies. The electron cloud density ρ_e is in units of m^{-3}.

Incoherent Emittance Growth Below the Instability Threshold Electrons in the cloud are pinched by the beam force when the beam passes through the electron cloud. This pinching of the electrons produces a nonlinear force distribution which results in an enhancement of the beam tune spread and the enlargement of the vertical emittance. This type of emittance growth is caused by a diffusion due to the nonlinear force [165].

We used the realistic lattices to investigate the incoherent effects of the electron cloud in CesrTA. Figure 6.89 shows the evolution of vertical beam size for various cloud densities below the threshold. The coherent motion of cloud and bunch shown in Fig. 6.79 does not appear. The growth rate increases for larger cloud densities.

For 2 GeV beam energy, at the electron-cloud density 0.8×10^{12} m^{-3}, from Figure 6.89, the growth rate is about 1.9×10^{-4} μm/turn. This is smaller than the radiation damping rate of CesrTA at 2 GeV, $4.6 \times 10^{-5}\sigma_y$/turn. (Typically $\sigma_y \sim 20$ μm). Assuming the electron cloud growth rate is independent of beam size, the equilibrium vertical emittance will increase by a factor of ~ 1.25 due to sub-threshold incoherent emittance growth. Beam size increases of this magnitude are significant, and should be observable at CesrTA. For example, the slow growth along the train seen in Fig. 6.72 (top), at a bunch current below the coherent instability threshold, may be due to incoherent emittance growth.

Similarly, at 5 GeV for an electron-cloud density 4.0×10^{12} m^{-3}, the growth rate is about 2.25×10^{-3} μm/turn. This is smaller than the radiation damping rate of CesrTA at 5 GeV, $1.4 \times 10^{-4}\sigma_y$/turn. Assuming the electron cloud growth rate is independent of beam size, the equilibrium vertical emittance will increase by a factor of ~ 1.32 due to sub-threshold incoherent emittance growth.

6.3.5.3 `CMAD` Simulations

This subsection provides a comprehensive set of results obtained using the simulation program `CMAD`. Details of the computation methods employed by `CMAD` have been discussed in Section 6.2.3. In particular, we take a closer look at electron cloud induced effects on positron beams, including head-tail motion, emittance growth and motion of single particles for parameters specific to ongoing experimental studies at CesrTA. The correspondence between simulation and experimental results will also be discussed.

The parameters used here represent conditions of CesrTA during experiments being carried out to study the influence of electron clouds on the dynamics of positron beams. Several features such as head tail motion and beam emittance calculations show similar features as to what has already been observed [166, 167]. In these experiments, we have typically used trains varying from 30 to 45 bunches in length. Depending upon properties such as the bunch current, bunch spacing, surface properties of the vacuum chamber, etc, each bunch creates a certain amount of cloud and, as a result trailing bunches experience a higher cloud density than leading bunches. CesrTA instrumentation has the ability to observe the turn-by-turn position and the beam size of each of the bunches. `CMAD` tracks a single bunch and so in order to simulate the effect of different bunches along the train, we perform a set of independent calculations with varying pre-specified cloud densities. The cloud densities seen by the different bunches can be estimated from cloud build up simulations or from experimentally observed tune shifts. The tune shifts calculated from build up simulations have agreed well with observed tune shifts [157, 168]. `CMAD` presently assumes a uniform distribution of electrons. Work is underway to have the program be able to use any

distribution as an initial condition. In the results presented here, we used a 2.08 GeV beam, which is the energy at which most of the experiments have been performed. In these simulations, particles are tracked through the full lattice, where each element of non-zero length in the lattice consists of a cloud-beam "interaction point". Thus, the simulation takes into account the variation of the beam size based upon the beta function and dispersion all around the ring. The calculations model the bunch in 96 slices, and the charge from each slice is distributed over a 128×128 grid, with 300,000 macro particles (positrons) and 100,000 macro electrons. The beam parameters used for the simulations are given in Table 6.9.

Table 6.9: Beam parameters used in CMAD simulations

Parameter	**Unit**	**Value**
Energy	GeV	2.08
Bunch Current	mA	1
Bunch Length	mm	12.2
Vertical emittance	pm	20
Horizontal emittance	nm	2.6
Energy spread		8.12×10^{-4}
Horizontal tune		14.57
Vertical tune		9.62
Synchrotron tune		0.055
Horizontal chromaticity	$dQ/(dp/p)$	0.6
Vertical chromaticity	$dQ/(dp/p)$	2.3

Motion of Bunch Centroid In this section, we discuss the behavior of the centroid motion for varying cloud densities. The bunch initially has no offset. Nevertheless, a small inaccuracy in the centroid position introduced by the finite number of macro particles is sufficient to trigger a self excitation of the centroid motion that increases with cloud density. A very similar trend in the self excitation has been seen in actual CesrTA measurements. Of course, in real life, the initial beam perturbation is not numerical; it is due to nonlinear coupling between the two transverse degrees of freedom. In addition, the effect of longitudinal motion will also play a role due to the presence of dispersive coupling between the longitudinal and horizontal motion.

Figure 6.90 shows the vertical bunch displacement versus turn, normalized to the initial beam size, for varying cloud densities. The extent of self excitation clearly grows with cloud density. In some cases, we also see stages of damping induced by the electron clouds. The oscillation clearly becomes more chaotic as the cloud density increases. The horizontal motion, not shown here, is far more stable than the vertical simply because the horizontal size of the beam is larger by about a factor of 100.

Figure 6.91a shows the spectrum of centroid motion of all the bunches simulated, with the electron density progressively increasing as it would along a train. The primary peak corresponds to the vertical betatron tune and the secondary peaks on either side of the betatron peak are first and second order syncho-betatron sidebands. We see the tunes, along with the sidebands, gradually shifting as we go further along the "train". The second order sidebands become clearly visible, somewhere midway in the "train". The first order sidebands have been observed in experiments conducted at CesrTA [166, 167] under similar conditions. Certain details such as the nature of the splitting of the betatron tune peak look different in simulations than in experimental observations.

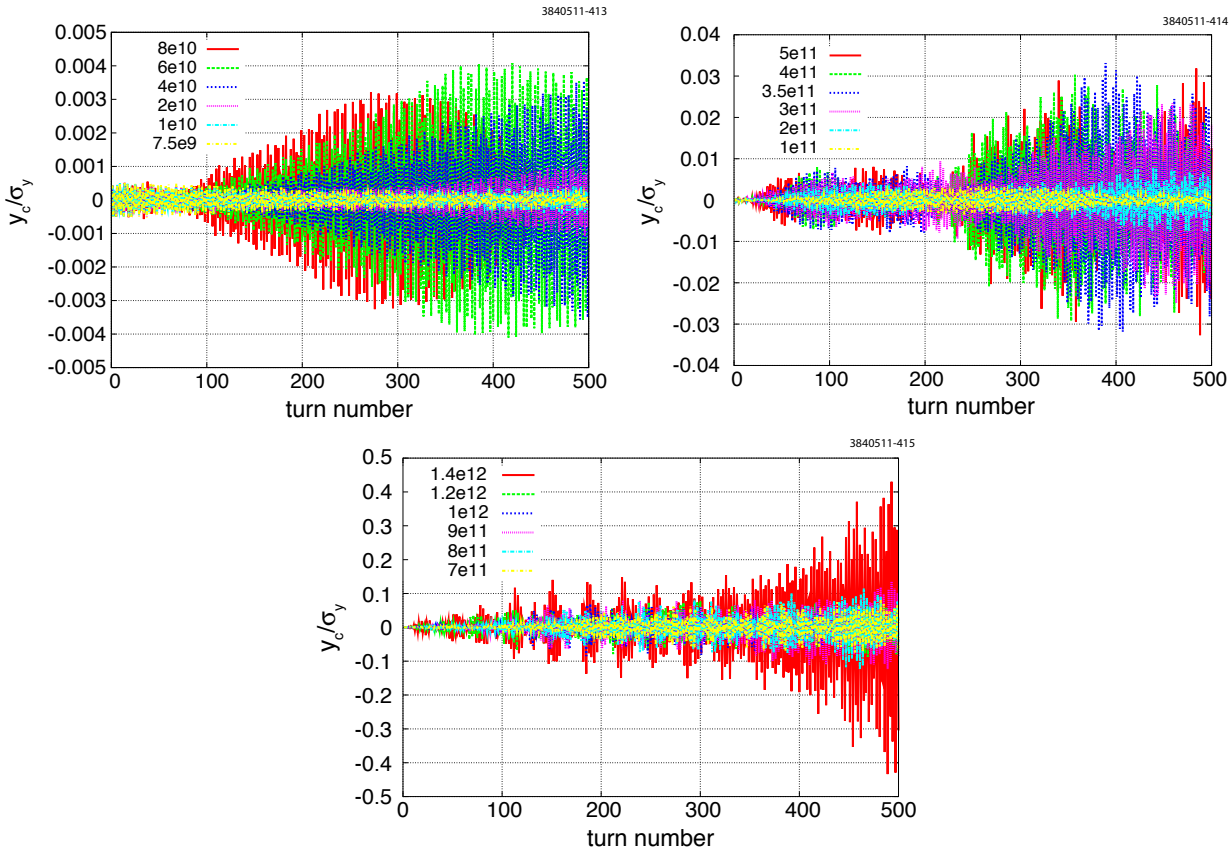

Figure 6.90: Motion of vertical bunch centroid for varying cloud densities, in units of m^{-3}.

Figure 6.91b shows a summary of the heights of the left and right first order sidebands along with vertical betatron peaks for the same set of cloud densities as shown in Figure 6.91a. We see that a transition in the relative height of at least one of the sideband peaks occurs at cloud densities of 3.5×10^{11} m^{-3} and 4×10^{11} m^{-3}. For cloud densities beyond these values, we see that both the sideband heights remain relatively close in height to the betatron peaks. Figure 6.91c shows the position of the betatron and both the sideband peaks in tune space. We see a gradual shift in the betatron tune which the sideband peaks follow, keeping consistently spaced from the betatron peak by the value of the synchrotron frequency. There is no evidence of the first and second order sidebands approaching each other as has been seen at KEK [160]. This phenomenon occurs due to coupling between the different order modes. On the other hand, our simulation results are consistent with what has been observed at CesrTA under the same conditions. It is possible that such a mode coupling would become observable at higher bunch currents and cloud densities. The conditions at CesrTA necessary to observe such a mode coupling have yet to be established.

Calculation of Emittance Growth Rate Figure 6.92 shows the vertical emittance growth versus turn. The vertical emittance undergoes a higher growth rate due to its smaller initial value compared to the horizontal emittance, not shown here. In PIC simulations, one needs to worry about numerical noise contributing to emittance growth. Numerical noise can contribute to particles artificially straying away from a stable region to an unstable one. This can be minimized by optimally choosing certain computational parameters such as grid spacing, macro particles and

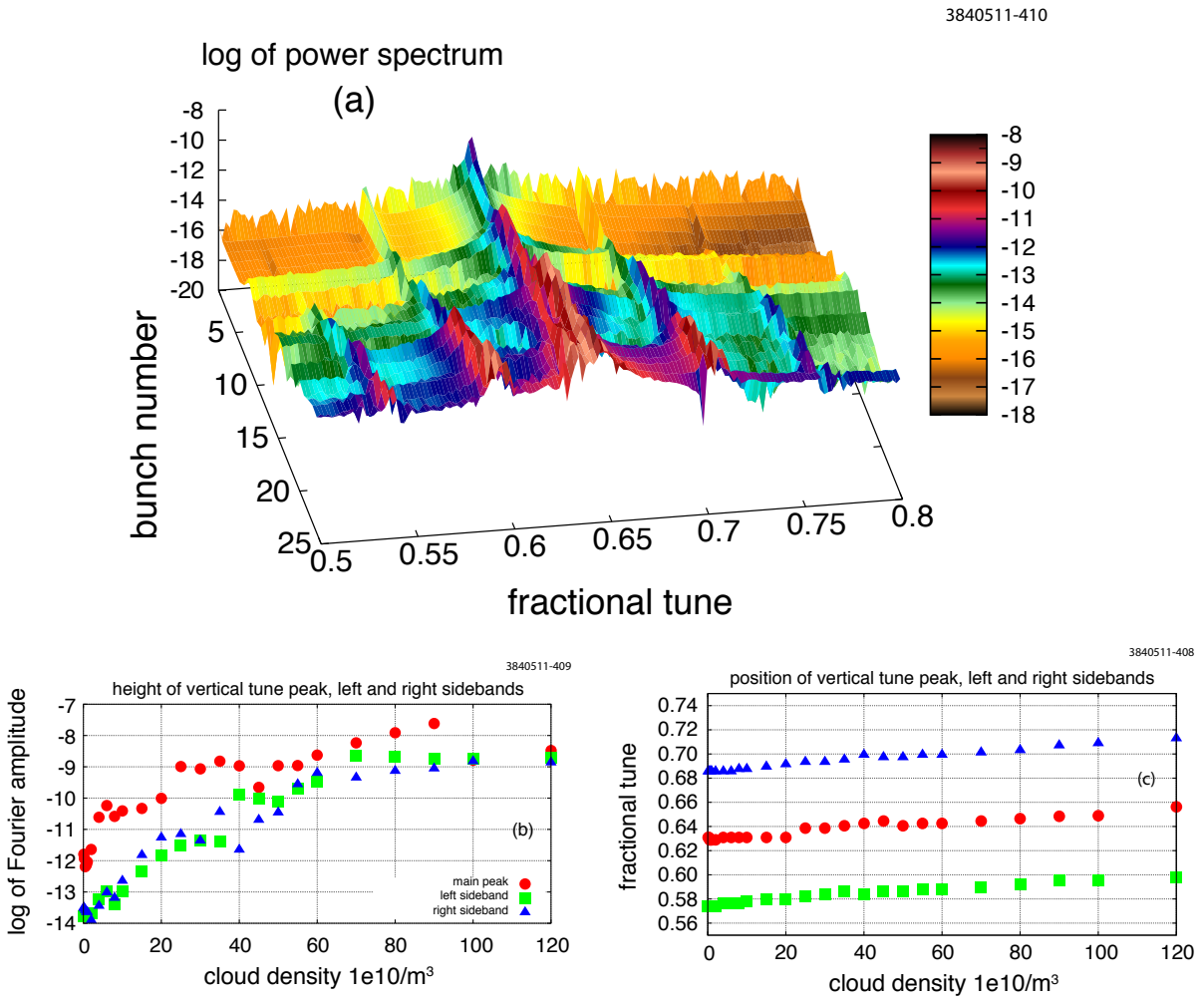

Figure 6.91: Plots showing the combined spectra of all bunches simulated and the relative heights and positions of betatron and sideband peaks.

extent of the cloud. A study was conducted over a range of these parameters before deciding upon the current set used in these simulations.

Despite the uncertainty in estimating the emittance growth rate, we see a definite increase in this quantity in correspondence with the height of the sidebands which is consistent with observations from the X-ray beam size monitor (xBSM) at CesrTA. However, it must be noted that the xBSM measures the beam size after the beam has reached a quasi-equilibrium state, while in simulations we are, in the first 500 turns, still looking at a transient state, with the emittance still growing linearly. We also see a transition from a linear to an exponential emittance growth when the cloud density increases from 1.4×10^{12} to 1.6×10^{12} m^{-3}. In order to make a closer comparison between experiments and simulations, one needs to calculate the quasi equilibrium emittance. This would require including the effect of radiation damping and quantum excitations and tracking the beam for several damping times. The beam size damping time of the CesrTA 2 GeV configuration is about 21,000 turns, which is computationally unfeasible.

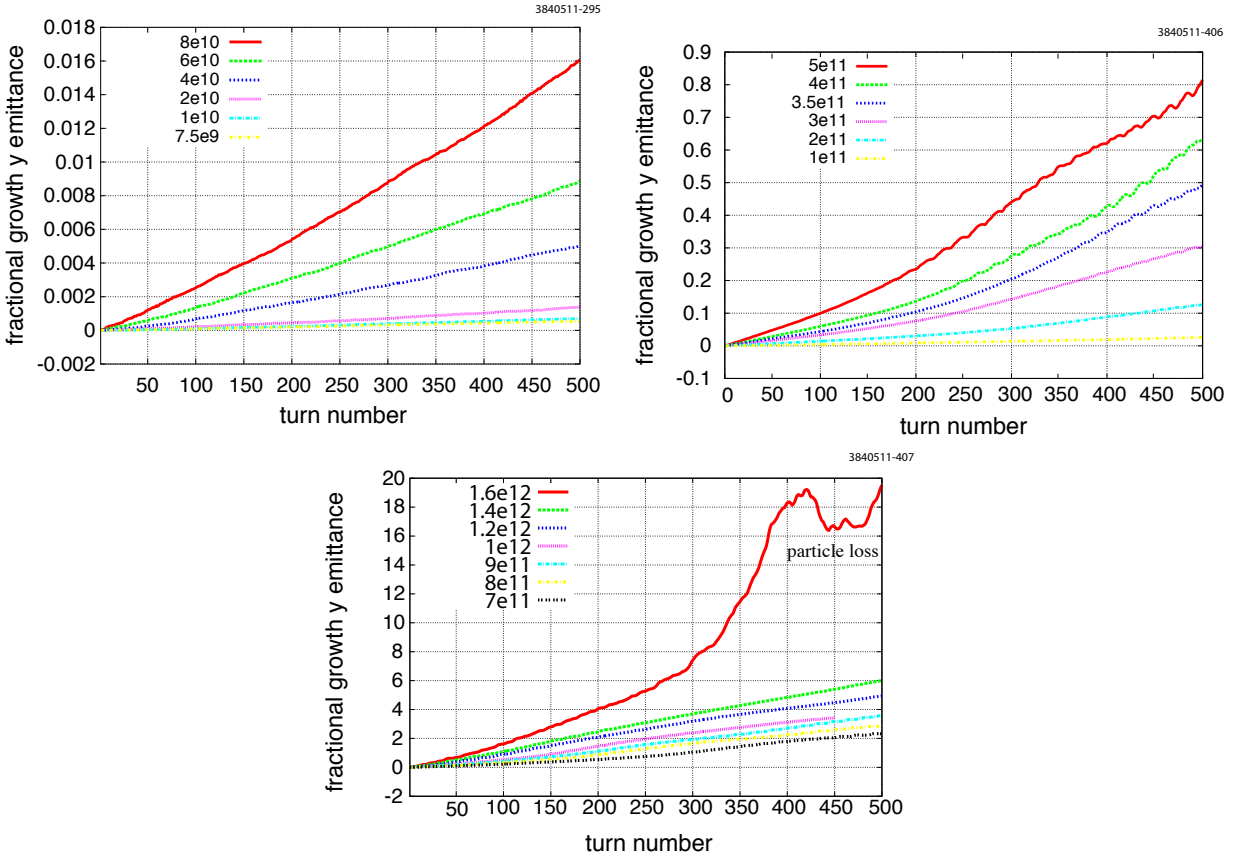

Figure 6.92: Vertical emittance growth rate for varying cloud densities, in units of m^{-3}.

Motion of Individual Particles We have followed the motion of individual simulated test particles in order to study their confinement properties for varying cloud densities and also how their oscillation frequency varies with change in oscillation amplitude. Although it would be difficult to determine these quantities experimentally, probing into such details with the help of simulations can provide significant insight into the underlying physical processes and the mechanisms that drive the beams unstable in the presence of electron clouds.

In Figure 6.93, we show the vertical phase space trajectories of particles initially at $x = 0.1 \times \sigma_x$, $y = 0.1 \times \sigma_y$ and $z = 0.1 \times \sigma_z$. Initially offsetting all three degrees of freedom ensures that any coupling among them will be reflected in the dynamics of the particle motion. We clearly see that the particles stray away from the ellipse as the electron density increases. The variation of the tune with oscillation amplitude for various cloud densities can in principle be estimated with the help of such single particle trajectories. We plan to extend the analysis of single particle trajectories beyond just phase space traces to computing tune footprints for different cloud densities.

In conclusion, we note that `CMAD` has been able to reproduce several features of the dynamics of positron beams observed in experiments. This study was performed for a parameter set corresponding to one set of observations at CesrTA. We intend to extend this study to other conditions at which observations have been made and will be made in future. At the same time, there is an ongoing effort to include more features into `CMAD` to enable more detailed quantitative comparisons with measurements.

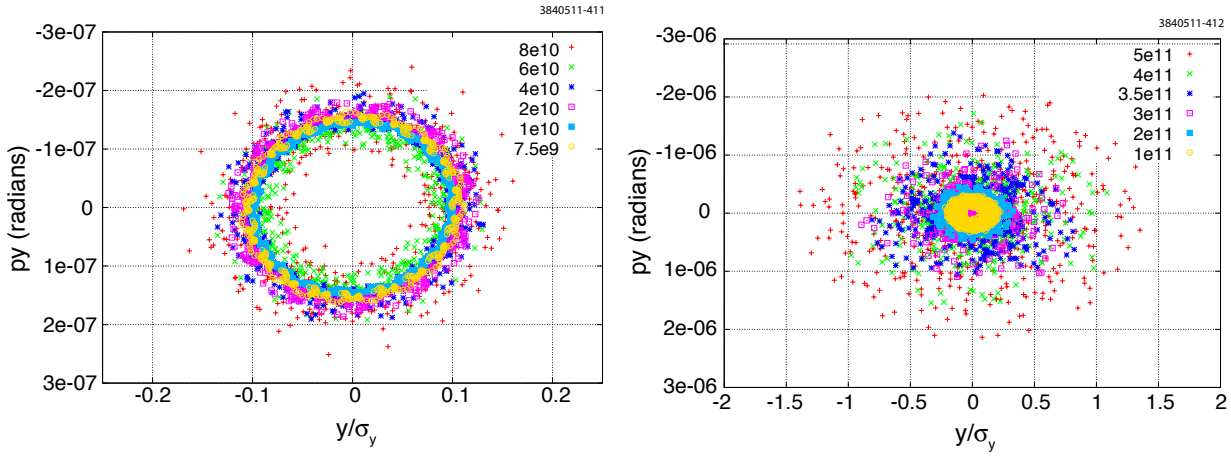

Figure 6.93: Vertical phase space for varying cloud densities, in units of m^{-3}.

6.3.5.4 Comparisons Between PEHTS and CMAD Simulations

It is interesting to compare the PEHTS simulation results with those of the CMAD simulation for the 2.1 GeV CesrTA parameters.

Growth Above the Coherent Instability Threshold The PEHTS results for a realistic lattice, shown in Fig. 6.88(a), may be compared with the CMAD results shown in Fig. 6.92. For example, for a cloud density of 1.4×10^{12}, PEHTS shows a growth in beam size from about 16 μm to 42 μm over the first 500 turns, corresponding to a fractional emittance growth of $\Delta\epsilon/\epsilon = 2(\Delta\sigma/\sigma) = 2 \times 1.6 = 3.2$. CMAD simulations show a fractional emittance growth of 6 over 500 turns for the same cloud density.

Growth Below the Coherent Instability Threshold In this case, we refer to the PEHTS results shown in Fig. 6.89(a), and again compared with the CMAD results shown in Fig. 6.92. For example, for a cloud density of 0.8×10^{12} m^{-3}, PEHTS shows a growth in beam size from about 16.1 μm to 16.5 μm over the first 500 turns, corresponding to a fractional emittance growth of $\Delta\epsilon/\epsilon = 2(\Delta\sigma/\sigma) = 2 \times 0.025 = 0.05$. CMAD simulations show a fractional emittance growth of 3 over 500 turns for the same cloud density. The much larger growth shown by CMAD may be a numerical problem, related to issues with the Poisson solver in CMAD for beams with very small vertical size. This problem will be resolved in future versions of CMAD.

6.4 Summary and Further Investigations

In this Chapter, we have described the experimental measurements performed at CesrTA, and the supporting simulations, which probe the interaction of the electron cloud with the stored beam. These experiments have been done over a wide range of beam energies, emittances, bunch currents, and fill patterns, to gather sufficient information to be able to fully characterize the beam-electron-cloud interaction and validate the simulation programs. The beam conditions are chosen to be as close as possible to the those of the ILC damping rings, with enough variation in the

conditions that the extrapolation to the ILC damping ring can be trusted. This will validate the simulation programs so they can be used to predict with confidence the cloud-related behavior of these rings.

6.4.1 Experimental Hardware and Techniques

6.4.1.1 Summary

The principal experimental methods used to study the dynamics of the beam in the presence of the electron cloud are:

- bunch-by-bunch tune measurements using one or more gated BPM's, in which a whole train of bunches is coherently excited, or in which individual bunches are excited;
- bunch-by-bunch frequency spectral measurements of self-excited bunch trains, using a high-sensitivity, filtered and gated BPM, and a spectrum analyzer;
- bunch-by-bunch, turn-by-turn beam size measurements of self-excited bunch trains, using an x-ray beam size monitor; and
- bunch-by-bunch frequency damping time measurements of drive-damp excited bunch trains in dipole and head-tail modes, using a high-sensitivity, filtered and gated BPM, a spectrum analyzer, a transverse kicker and an RF-cavity phase modulator.

6.4.2 Simulation Tools

6.4.2.1 Summary

This section discusses:

- the methods used to compute the bunch-by-bunch tune shifts for specific beamline elements, from the electric fields of the charge distributions generated by the electron cloud buildup simulation codes;
- the methods used to average over all beamline elements to produce a ringwide tune shift;
- the analytic theory used to estimate the head-tail instability threshold in the coasting beam approximation; and
- the methodology used in the `CMAD` simulation program, which directly simulates the beam-cloud interaction using a realistic storage ring model in a multi-particle simulation.

6.4.3 Coherent Tune Measurements

6.4.3.1 Summary

A large variety of coherent tune shift data have been taken, covering a wide range of machine conditions such as beam energy, beam size, lattice configuration, particle species, bunch current, bunch train configuration, and mode of oscillation of the bunches.

Generally, quite good agreement has been found between the measurements and the tune shifts computed from cloud buildup simulations, using either of the buildup codes `POSINST` (See, for example, Fig. 6.18, Fig. 6.21, Fig. 6.22, Fig. 6.23, Fig. 6.24, Fig. 6.41, and Fig. 6.32) or `ECLOUD` (see Figure 6.29, Fig. 6.30).

This agreement, which is found for the same set of simulation parameters applied across a wide variety of machine conditions, both constrains many of the model parameters (see Table 6.3) and gives confidence that the models do in fact predict accurately the density of the electron cloud generated in CesrTA.

To better define the photoelectron distributions which seed the cloud in CesrTA, and to allow accurate extrapolation to other radiation environments, a new simulation program, `Synrad3D`, has been developed, which predicts the distribution and energy of absorbed synchrotron radiation photons around the ring. The output from this program is used by the cloud buildup codes, thereby eliminating the need for any ad-hoc assumptions in the buildup codes about the photon distributions. Tune shifts computed from buildup simulations with input from `Synrad3D` agree well with measurements (see Fig. 6.33 and Fig. 6.34).

6.4.3.2 Further investigations

Simulations based on `Synrad3D` will be compared systematically with data, to attempt to improve the constraints on the cloud buildup code models. The photoelectron model in the buildup codes will also be improved, based on observations made with RFA's and shielded pickups. An improved method has been developed for computing the tune shifts when only a single bunch in the train is excited. Tune shifts computed with this method will be compared with existing data.

Additional data will be taken with bunch spacings of 4 ns and 8 ns, to expand the breadth of the data sets in the bunch spacing regime closer to that planned for the ILC damping ring (6 ns).

6.4.4 Instability Threshold Measurements

6.4.4.1 Summary

Under conditions in which the beam is self-excited via the electron cloud, bunch-by-bunch frequency spectra exhibit the vertical $m = \pm 1$ head-tail (HT) lines, separated from the vertical betatron line by the synchrotron frequency, for many of the bunches along the train. The amplitude of these lines typically (but not always) grows along the train. Some detailed conclusions from these observations are:

- For a 30 bunch train with 0.75 mA/bunch at 2.1 GeV beam energy, the onset of the HT lines occurs at a ringwide initial (i.e., before the "pinch") beam-averaged cloud density of around 8×10^{11} m^{-3} (assuming no cloud density at the start of the train) (see Fig. 6.42 and Fig. 6.43).
- For a 30 bunch train with 1.1 mA/bunch at 4 GeV beam energy, the onset of the HT lines occurs at a ringwide initial (i.e., before the "pinch") beam-averaged cloud density of around 2×10^{12} m^{-3} (assuming no cloud density at the start of the train) (see Fig. 6.59 and Fig. 6.58).

- The betatron lines exhibit structure which varies along the train. The vertical line power grows along the train and has a fine structure that is not understood. (See Fig. 6.38, Fig. 6.39, Fig. 6.56, and Fig. 6.57)
- The amplitude of the HT lines depends strongly on the vertical chromaticity, the beam current and the number of bunches (See Fig. 6.45, Fig. 6.46, Fig. 6.47, and Fig. 6.48).
- For a 45 bunch train, the HT lines have a maximum power around bunch 30; the line power is reduced for later bunches (see Fig. 6.48).
- There is a weak dependence of the onset of the HT lines on the synchrotron tune, the single-bunch vertical emittance, and the vertical feedback (see Fig. 6.50, Fig. 6.51, and Fig. 6.53).
- Under identical conditions, HT lines also appear in electron trains, but the onset is later in the train, develops more slowly, and is much weaker, than for positrons (see Fig. 6.61).
- Under some conditions, the first bunch in the train also exhibits a head-tail line ($m = -1$ only). The presence of a "precursor" bunch can eliminate the $m = -1$ signal in the first bunch (see Fig. 6.62). The implication is that there may be a significant "trapped" cloud density near the beam which lasts long after the bunch train has ended, and which is dispersed by the precursor bunch. Indications from RFA measurements and simulations indicate this "trapped" cloud may be in the quadrupoles and wigglers.
- There is a strong dependence of the HT line structure observed on last bunch in a 30 bunch train, as a function of the current in that bunch. But the frequency of the vertical betatron line of this bunch is only very weakly dependent on the current in the bunch (see Fig. 6.64).

6.4.4.2 Further investigations

Future work will include:

- Studies with 4, 8, 10 and 12 ns spacing.
- More studies with very high currents, long trains, high chromaticity and strong feedback (at 2 GeV, 14 ns, at 4 ns, and at 4 GeV).
- Studies exploring the dependence of the "precursor bunch" effect on timing, and attempts to observe the effect at 4 ns and at 4 GeV.

6.4.5 Mode Growth Rate Measurements

6.4.5.1 Summary

To measure the damping or anti-damping effects attributable to the electron cloud, we have made measurements in which we actively excite a single bunch in a train, and measure the rate at which the bunch damps after the excitation is turned off. These bunch-by-bunch damping rate measurements can be made for the $m = 0$ (dipole mode) of motion, and for the $m = \pm 1$ (head tail modes).

To interpret the measurements of bunch-by-bunch damping rates along a train of bunches properly, it is necessary to first understand single-bunch damping rates. Consequently, measurements of

single-bunch damping rates, as a function of chromaticity, were made for the $m = 0$ and $m = \pm 1$ modes (see Figure 6.66 and Figure 6.67)

Measurements of bunch-by-bunch damping rates have only been made to date for a two sets of conditions. In the conditions that we have studied, the damping rate for motion of bunches in the train decreases as the electron cloud builds up. The vertical dipole and head-tail modes become unstable at approximately the same bunch within the train. The data are suggestive of the head-tail modes becoming unstable at a slightly earlier bunch than when the dipole modes destabilizes (see Fig. 6.70 and Fig. 6.71), but the quality of the present data is insufficient to establish this with certainty. However, what is clear is that motion of the bunches remain stable with essentially the same damping rates until it becomes unstable with a transition over relatively few bunches later in the train.

6.4.5.2 Further investigations

Damping rate measurements will be made over a wider range of conditions, to study the dependence of the rates on machine and beam parameters such as bunch current, chromaticity, synchrotron tune, and beam emittance.

6.4.6 Measurements of Vertical Emittance Growth Along Bunch Trains

6.4.6.1 Summary

Using an x-ray monitor, bunch-by-bunch beam position and size measurements have been made on a turn-by-turn basis. From the beam size measurements, the evolution of the beam emittance along trains of bunches has been measured.

Beam centroid motion and the vertical emittance is observed to grow along the train. The growth pattern is a strong function of the bunch current (see Fig. 6.72). Often, the first bunch in the train has an anomalously large size, which correlates with of the observation of a vertical head-tail line in the spectrum of this bunch, as discussed in Sec. 6.3.2.14.

Beam size growth along the train is not very sensitive to the chromaticity or the bunch spacing (see Fig. 6.74 and Fig. 6.75).

Beam size growth along the train is also not very sensitive to the initial beam size or the feedback gain (see Figure 6.76 and Figure 6.77).

The onset and development along the train of the vertical head-tail lines is very similar to the onset and development along the train of vertical emittance growth (compare Fig. 6.58 and Fig. 6.78).

6.4.6.2 Further investigations

Additional studies with the x-ray beam size monitor are planned to measure emittance growth along bunch trains with electrons, and to further study the dependence of the beam size growth on beam and machine parameters.

6.4.7 Instability Threshold and Vertical Emittance Growth: Comparisons with Simulations

6.4.7.1 Summary

The analytic theory presented in Sec. 6.2.2 was used to estimate the head-tail instability threshold in the coasting beam approximation. At 2.1 GeV, the analytical estimate of the threshold density of 1.3×10^{12} m^{-3} is about 60% higher than the measured threshold of 8×10^{11} m^{-3} presented in Sec. 6.3.2.4. At 4 GeV, the analytical estimate of the threshold density is 2.65×10^{12} m^{-3}, about 30% higher than the measured threshold of 2×10^{12} m^{-3} presented in Sec. 6.3.2.12.

Numerical simulations using `PEHTS` have been done to refine the estimates of the threshold density at both 2 and 5 GeV. These simulations show both vertical emittance growth, and the presence of head-tail lines in the beam's dipole motion spectrum, above the threshold density. The simulations show that dipole feedback is not able to suppress the emittance growth. The effects of dispersion, and a realistic lattice with 83 beam-cloud interaction points, were also studied. The threshold densities found for the realistic lattice were about 50% higher than the analytical estimates.

Using the realistic lattice, `PEHTS` was also used to estimate incoherent emittance growth below the head-tail threshold. At the electron-cloud density, 0.8×10^{12} m^{-3} in the 2 GeV case, the growth rate is about 7.4×10^{-6} σ_y/turn.

Numerical simulations using `CMAD` were also done for 2 GeV beam energy. These simulations use a realistic lattice, with beam-cloud interaction points at every lattice element. As with `PEHTS`, they show both vertical emittance growth, and the presence of head-tail lines in the beam's dipole motion spectrum. For the same cloud density above the head-tail threshold, `CMAD` and `PEHTS` predict the same level of vertical emittance growth after 500 turns, within a factor of 2. But for a cloud density below the head-tail threshold, `CMAD` predicts a much larger sub-threshold emittance growth than does `PEHTS`.

6.4.7.2 Further investigations

It is planned to explore the dependence of the `CMAD` simulation results on beam parameters such as energy, emittance, and chromaticity. The origin of the "precursor" effect will also be studied. In addition, the capability of using a non-uniform initial cloud distribution will be provided.

Chapter 7

Status of Our Understanding of a General Electron Cloud Model

7.1 Preface

In the interest of conciseness, and to afford a broad perspective of the ecloud effect particularly within the CesrTA R&D program, this chapter is written in a more or less self-contained, if superficial, fashion. References to previous chapters for detailed information are given as appropriate.

7.2 Recap of the model, and assumptions made

The research reported in this document focuses on the physical model that underlies the electron-cloud formation and dissipation. The "electron-cloud model" was defined in Sec. 4.1.2. We now provide a brief recap followed by more details on the various components of the model, in order to better explain our understanding.

As in all high-energy positron storage rings, the electron cloud in CesrTA forms when the beam is injected into an empty vacuum chamber. Copious synchrotron radiation is emitted when the beam traverses magnetic elements of the ring, primarily dipole bending magnets. Photoelectrons are emitted when the synchrotron radiation photons strike the vacuum chamber walls. These electrons are "rattled around" by successive bunch passages, striking the walls and emitting secondary electrons, which are added to the electron cloud. Depending upon a combination of beam and chamber surface parameters, the number of electrons can grow quickly to significant levels. For typical operating parameters in CesrTA and for most other existing or planned high-energy storage rings, including the ILC Damping Rings, the average electron density typically reaches a level in the range $10^{10} - 10^{12}$ m^{-3}, in tens of nanoseconds following injection. While this electron density is many orders of magnitude below typical plasma physics applications, it is high enough to lead to a variety of serious detrimental effects in high-energy storage rings. Furthermore, owing to the lightness of the electron, and to the intensity of the beam bunches, the electron cloud density has strong spatial (on the scale of centimeters or smaller) and temporal (on the scale of nanoseconds or smaller) dependencies. The simulation programs used to describe the electron-cloud build-up and decay aim

to quantify as completely as possible these details of the electron density distribution.

In addition to photoemission it should be pointed out that, in general, there are other "primary" mechanisms that seed the electron-cloud formation. In typical hadron storage rings, where synchrotron radiation and hence photoemission are historically negligible, ionization of residual gas yields the electrons that seed the electron cloud growth. Another mechanism that may contribute to electron generation is lost beam particles striking the walls of the chamber. Among all hadron machines, the LHC is a notable exception, being the first hadron storage ring ever built in which synchrotron radiation is significant, hence its electron cloud seeding mechanism is analogous to that in typical positron storage rings. In general, all of the three above-mentioned seed mechanisms coexist; in the case of CesrTA, and in essentially all other positron storage rings, photoemission dominates by far. In this report, therefore, we only consider photoemission as the seed mechanism. In any case, it is usually the compounding effect of secondary electron emission that dominates the formation of the electron cloud; this secondary mechanism is similar in lepton and hadron machines.

Beam parameters are typically well known or well determined in any given experiment. Beam energy, of course, is rather precisely controlled. Parameters that may vary from bunch to bunch, (and that therefore may vary on the ns-to-μs scale) such as emittances, intensity, bunch length, closed orbit, bunch spacings and fill pattern are also reliably determined. Essentially all such beam parameters are therefore used as fixed inputs to our simulations. The vacuum chamber geometry at the centimeter level is precisely known and is therefore a given fixed input to the simulations. But its geometry at the micron level (surface roughness) is typically not well-known and effectively becomes an indirect component of the model because it affects the photon reflectivity, hence the geometrical distribution of photons striking the chamber surface. Electronic properties of the chamber surface (see below) are also a priori not well known, hence become important components of the model.

Certain components used to describe the dynamics of the electron cloud (Sec. 4.1.3) are fairly well established. Such components are: (1) the electron motion in an EM field, which is based on mature tracking methods such as the Runge-Kutta integrator, the Boris pusher [85, 169], or analytic formulas whenever applicable; (2) computation of space-charge forces, based on PIC methods; and (3) computational parameters such as integration time step, space-charge grid size, and number of macroparticles. Rules of thumb exist for these computational parameter values that yield sensible trade-offs between accuracy and CPU time. These parameters may require a bit of adjusting in the beginning stages of most simulation studies in order to establish adequate numerical convergence.

We have extensively benchmarked the build-up codes `POSINST` and `ECLOUD` against each other. We are satisfied that they yield similar results when the simulation conditions are similar.[1] Consequently, this report focuses on the details of the physical model rather than on the codes themselves.

7.2.1 Code components

Setting aside the well known components described above, the fundamental ingredients of the physical model upon which we focus our attention in this report are:

[1] We recall that the codes are not identical, especially the implementation of the physical model, hence the results cannot be identical even for nominally identical simulation conditions.

1. photon emission by beam particles
2. photon reflectivity off the chamber walls
3. quantum efficiency (photoelectric emission yield) and emission spectrum
4. secondary emission yield and emission spectrum

These components are implemented via simulation programs that track individual particles. These programs include analytic expressions for the emission spectra; a sufficiently large number of individual simulated photons or electrons are generated via the Monte-Carlo process from these spectra, in order to resolve the features of the cloud distribution to the desired level of precision.

At the present stage of development, photon tracking, electron tracking, and the response of the beam to the electron cloud, are done separately, using different codes. Presumably, given enough time and investing enough effort, these three aspects of the electron-cloud will be integrated into a single comprehensive computer tool. At present, photon tracking is done with the code `Synrad3D`; its main output, namely the distribution of absorbed photons around the chamber, is fed as input to the electron cloud build-up codes `POSINST`, `ECLOUD` or `CLOUDLAND`. These codes are used to track the electrons under the action of a prescribed (non-dynamical) beam. The main output from such codes, namely the electron cloud intensity and distribution, is then fed as input to the beam dynamics codes such as `CMAD`, `HEADTAIL` or `PEHTS`, and the effects on the beam are computed.[2]

The energy-angle emission spectrum of the synchrotron-emitted photons is well known [170]; in our photon tracking simulations with the code `Synrad3D`, we take this spectrum as given. Prior to the availability of `Synrad3D`, the electron-cloud simulation codes involved a rather simplified description of the photon impact distribution along the chamber. In addition to the ability to calculate the point of first impact of any given photon on the chamber surface for realistic chamber geometries, the code `Synrad3D` is able to take into account multiple specular photon reflections around the chamber, as well as diffuse photon scattering owing to surface roughness. The photon reflectivity for a given surface roughness is obtained from a published database [95]. The spectrum of diffused-scattered photons is computed using existing formalisms [96, 97].

7.2.2 What is not well-known, and why

The last three items in the list in Sec. 7.2.1 are, in practice, not well known. While there exists a substantial body of published data for photon reflectivity, quantum efficiency and secondary electron yield, most of this data pertains to surfaces that are pure and/or monocrystalline, and is typically inapplicable to "technical" surfaces of which the vacuum chamber is fabricated. The technical materials with which we are concerned are amorphous, have rough and/or striated surfaces, and contain impurities near the surface that significantly affect their electronic properties.

Data for technical materials does exist from bench and in situ measurements at several accelerator laboratories around the world. We have taken such data as starting points in our simulations. However, even if such data is reliably measured at a given storage ring, it should be kept in mind that some of the relevant quantities, particularly the SEY, gradually decrease in time owing to electron bombardment from the very EC effect to which the SEY contributes. Such "conditioning effect" has been consistently observed in all operating accelerators in which it has been measured;

[2] Actually, there already is a fair amount of integration of electron cloud build-up codes and beam dynamics codes. Examples of such codes we have employed are `WARP-POSINST` and `CLOUDLAND`.

it is attributed to the migration of impurities from the surface into the bulk of the metal as a result of the electron bombardment. The ECE, therefore, is a self-conditioning effect. However, as it should be clear from this explanation, self-conditioning decreases exponentially in time because the more the SEY decreases, the weaker the electron bombardment, which in turn means slower conditioning. In effect, therefore, there is a practical limit to the benefit from beam conditioning. Recent experience at the LHC [64] shows that conditioning occurs comfortably rapidly (typically with a time scale of several hours or a few days of beam running), but it does not go far enough to sufficiently lower the SEY for the cases of high beam intensity. The search for new low-emission coatings, therefore, is an active area of R&D at CERN and other labs.

Photon Reflectivity When a photon strikes the wall of the chamber, it may be absorbed, possibly leading to photoemission, or it can scatter and strike the wall downstream. Depending on the photon wavelength and the details of the surface roughness, the scattering may be approximately specular or diffuse. The code `Synrad3D` [88] incorporates a well-developed formalism to determine the magnitude and emission distribution of the scattered photons. Owing to the lack of detailed knowledge of the surface geometry at the sub-micron scale in CesrTA we have assumed typical parameter values that are found in other measurements pertinent to accelerator vacuum chambers. Specifically, we have assumed a roughness RMS height $\sigma = 0.1$ μm, and exponential roughness autocorrelation along the surface with an autocorrelation coefficient $T = 5$ μm. We believe these assumptions to be reasonable, but validation awaits detailed measurements. More details are provided in Sec. 4.1.4.1.

Quantum efficiency and emission spectrum Concerning the QE parameter Y, we looked at one set of direct measurements made at the LHC (see Section 4.1.4.2). The measurements for aluminum, shown in Fig. 4.12, were made with a VUV photon energy spectrum, and were found to be quite sensitive to the surface material and conditioning. Consequently, in comparing simulation and data, we have treated Y as an unknown parameter to be fit, under the simplifying assumption that it does not depend on the incident photon energy or incident angle. As such, the fitted value the QE parameter Y is an effective quantum efficiency, i.e., it represents an average over the incident photon spectrum.

For the photoelectron emission energy spectrum, we have generally assumed a simple shifted Gaussian formula, with peak and width of 5 eV photoelectron kinetic energy. While this assumption can give good agreement between simulation and data for a number of electron-cloud-related observables, we have found that, for 5 GeV high-current electron beams, the RFA measurements (see Section 5.1.4.2) and the shielded pickup measurements (see Section 5.2.2.2) require the introduction of a substantial high-energy tail into the photoelectron energy distribution.

Secondary electron yield and emission spectrum The SEY is, typically, the single most important ingredient that contributes to the intensity of the ECE. Many measurements have been carried out at accelerator labs in the US, Europe and Japan for technical materials such as copper, stainless steel and aluminum. Measurements also exist when some of these materials are coated with low-emission substances such as TiN, TiZrV, amorphous carbon and crystalline carbon. Besides the modification of the electronic properties of the chamber surface achieved with low-SEY coatings, the geometrical properties can also be modified to reduce the SEY. One such possibility, that has been tested at CesrTA (see Section 5.1.4.1), consists in etching narrow longitudinal grooves along

the chamber, of mm-scale size. Such grooves trap the emitted electrons, thus effectively reducing the SEY. In addition, the grooved surface may be coated with a low-SEY material.

The SEY is characterized by the function $\delta(E_0)$, where E_0 is the incident electron kinetic energy. In our simulations and fits to the data we have paid special attention to the peak value $\delta_{\max}$, and to the energy $E_0 = E_{\max}$ at which $\delta(E_0) = \delta_{\max}$. These two quantities, particularly $\delta_{\max}$, determine the exponential growth rate of the EC density when the conditions imply such a behavior. Another quantity that we have closely examined in our simulations is the value of $\delta(E_0)$ for very low values of E_0, below ~ 20 eV, characterized by the limiting value $\delta(0)$. Such a parameter determines the dissipation rate of the EC: the higher $\delta(0)$, the longer the electrons survive between successive bunch passages, or from one turn of the beam to the next. Consequently, $\delta(0)$ directly influences the longer-term accumulation or dissipation of electrons.

The function δ also depends on the incident electron angle θ_0. For technical surfaces, $\delta(\theta_0)$ grows monotonically with θ_0 at fixed E_0 such that $\delta(\theta_0 = \pi/2)$ (grazing incidence) is roughly 70% larger that $\delta(\theta_0 = 0)$.[3] More refined fits to the θ_0-dependence to prior data are found in Ref. [87], which we have adopted for our simulations without further examination. In any case, simulations typically show that the values of θ_0 relevant to CesrTA and to the ILCDR is close to 0 (normal incidence): a reasonable rule of thumb is that $\langle \cos\theta_0 \rangle \gtrsim 0.8$ for essentially any region of the ring we have simulated. Therefore, the details of the θ_0 dependence far from normal incidence are not very relevant to our studies.

The SEY is made up of three primary components: true secondaries ($\delta_{\rm ts}(E_0)$), rediffused ($\delta_r(E_0)$) and elastically backscattered electrons ($\delta_e(E_0)$). Each of these corresponds to three distinct mechanisms by which electrons are emitted from the material, and have distinct emission spectra [87]. In particular, the rediffused electrons are emitted with a broad energy spectrum, spanning roughly the entire allowed energy range, namely $(0, E_0)$, where E_0 is the incident electron energy. The rediffused component $\delta_r(E_0)$ contributes significantly to the persistence of the EC in the vacuum chamber, a somewhat subtle phenomenon involving the interplay of E_0 and the above-mentioned broad emission spectrum [106].

It should be pointed out, however, that, in practice, the distinction between the three above-mentioned SEY components, particularly between $\delta_e(E_0)$ and $\delta_r(E_0)$, becomes unclear as E_0 drops below ~ 50 eV or so. While $\delta_{\rm ts}(E_0) \to 0$ as $E_0 \to 0$, this is not the case for $\delta_e(E_0)$ or $\delta_r(E_0)$, both of which reach a nonzero value at $E_0 = 0$. Electron-cloud energies $\lesssim 50$ eV are typical after several 10's of nanoseconds of beam absence, and hence the EC dissipation mechanism after such a relatively long time cannot be clearly attributed to either $\delta_e(E_0)$ or $\delta_r(E_0)$.

Given the incident electron energy E_0, each of the above-mentioned three components of the yield has a characteristic dependence of the emitted differential electron energy yield spectrum $d\delta/dE$, where E is here the emitted electron energy. Our `POSINST` model represents these components rather faithfully, with parameters obtained from fits to previously published data [87]. Since our simulations are particle-by-particle, knowing $d\delta/dE$, however, is not enough: the simulations require knowledge of the emitted electron momentum spectrum $dN/d^3\mathbf{p}$, where $\mathbf{p}$ is the emitted electron momentum. We have not found data for $dN/d^3\mathbf{p}$, but we have implemented in `POSINST` what we sensibly believe are the simplest formulas that (1) respect energy conservation, and (2) reproduce $d\delta/dE$ separately for each of the three components upon integration over $\mathbf{p}$ at fixed E_0 and E.

[3] We adopt the standard convention that $\theta_0 = 0$ represents normal electron incidence. The θ_0 dependence of δ is qualitatively different, and irrelevant for our purposes, for very smooth or monocrystalline surfaces.

7.3 Which model parameters are sensitive to which measurements

As explained in Chapter 4, photoemission and secondary electron emission depend differently on the beam properties: photoelectron emission behaves linearly in beam intensity, is very sensitive to beam energy, and is independent of the sign of the beam particle charge, while secondary emission behaves nonlinearly in beam intensity, is not very sensitive to beam energy, and is sensitive to the sign of the beam particle charge. These features, in combination with the diverse instrumentation and the operational flexibility of CesrTA allow an unprecedented ability to disentangle the two phenomena and determine several of the corresponding parameters. Table 7.1 summarizes the most important dependencies.

Table 7.1: Dependencies of measurement techniques on model quantities
($\Delta\nu$ = coherent tune shift, I = beam current, I_b = bunch current, $\delta(0)$ = SEY at 0 incident electron energy, $d\delta/dE$ = energy spectrum of the SEY, δ_r = rediffused secondary electron yield, δ_e = backscattered secondary electron yield, $\delta_{\rm ts}$ = true secondary electron yield, $E_{\rm max}$ = incident electron energy at peak SEY, **powts**= shape parameter of the true SEY in the `POSINST` SEY model).

	$\Delta\nu$ at low I train	$\Delta\nu$ at high I train	witness $\Delta\nu$	RFA, time averaged	SPU, time resolved, train	SPU, time resolved, witness
$\delta(0)$	weak at low t_b, strong at high t_b	weak	strong	strong for high I_b and/or high t_b	weak	linear
$d\delta/dE$	weak	U*	U	weak; may be sensitive to t_b	strong (see Fig. 5.86)	strong (see Fig. 5.87)
$\delta_{\rm ts}$	weak	strong	U	strong for high I and/or low t_b	strong; correlated with δ_r	strong; correlated with δ_r
δ_r	weak	strong; can easily distinguish between δ_r and $\delta_{\rm ts}$	U	strong for high I; correlated with $\delta_{\rm ts}$	strong; correlated with $\delta_{\rm ts}$ and $\delta(0)$	strong; correlated with $\delta_{\rm ts}$ and $\delta(0)$
$E_{\rm max}$	U	U	U	weak	weak	some sensitivity
powts	U	U	U	strong for high I; correlated with $\delta_{\rm ts}$	weak	weak
Y	linear	linear	U	strong for low I and/or high t_b	linear	linear
dY/dE	linear	linear	U	strongly nonlinear for e^- beam	strong; more sensitive than RFA	strong; more sensitive than RFA

*The entry "U" indicates that the sensitivity is unclear or unknown at this point.

7.4 How confident are we of the model

As a starting point in our simulations for CesrTA we adopted model parameters for the electronic properties of the chamber surface that had been previously obtained in other contexts, which we were confident would amount to a good first approximation. Early indications of good agreement between simulations and observations were obtained in the measurements of the bunch-by-bunch coherent tune shifts, and the tune shift of a witness bunch placed at various distances following the end of the bunch train (see Sec. 6.3.1). In particular, the decrease of the tune shift after the passage of the bunch train can be readily described by the simulations as due to the "release" of the electron cloud as the train comes to an end.

While the CesrTA R&D effort is quite comprehensive, the complexity of the model is such that the measurements do not provide a unique determination of all of the parameters. However,

some parameters are more relevant than others for any given measurement technique and beam configuration, as discussed in Sec. 7.3. In practice, therefore, we are not optimizing the model one parameter at a time, but rather a few parameters at a time in a simultaneous χ^2-matrix minimization to specific measurements. By carrying out such a process we have improved the overall agreement between simulations and measurements. Diverse fits yield consistent parameter values, which give us confidence in the correctness of the model. In addition, for a set of "good" parameter values for the vacuum chamber surface, the behavior of the ecloud intensity as a function of beam intensity and energy remains in good agreement with measurements. This agreement, which is found for the same set of simulation parameters applied across a wide variety of beam conditions, both constrains many of the model parameters and gives confidence in the correctness of the model.

7.4.1 Caveats and Future Work

While the CesrTA electron-cloud R&D program is arguably the most comprehensive program carried out to date dedicated to the understanding of the ECE, and our confidence in the model is strong, the state of the art in this field still lags, in some ways, the field of instability dynamics produced by conventional impedances. Rules of thumb are emerging that allow one to reasonably forecast the conditions under which the electron cloud will be a serious issue; what is needed however, is one or more rules of thumb that allow one to predict, without major simulations, conditions under which the electron cloud in a given storage ring will be sufficiently weak for safe beam operation. The electron cloud dynamics is more complicated than that in conventional instabilities, on account of the large span of time scales involved and the possibility of space charge domination. The jury is still out on whether a simple set of rules of thumb for safe beam operation vis-à-vis the electron cloud will eventually emerge.

At present, and probably for the foreseeable future, progress in understanding and characterizing the ECE, relies on detailed simulations coupled with detailed measurements. In the effort described in this report, we have constrained the model and determined the main parameters for the CesrTA conditions. We recall, that we have not fitted all parameters; some of them, which we believe to be less important, were fixed a priori based on prior experience. A consequence of the local, rather than global, optimization procedure is that some of the fitted parameters remain correlated with others that are outside the local fit; therefore, it is possible that a better global solution might be found with additional work. Nevertheless, the parameter values we have obtained are quite consistent with those published in the standard literature, hence we are reasonably confident that a more extensive global minimization process will not change our present results significantly.

One of the simplest rules of thumb in the ECE is that if the peak SEY is too large (typically $\delta_{\max} \gtrsim 1.4$ or so), the EC density is high enough to lead to undesirable effects on the beam. For this reason, new low-emission coatings and other mechanisms (grooved surfaces, clearing electrodes and weak solenoidal fields) to reduce secondary emission are being actively studied at many laboratories, with the goal of achieving $\delta_{\max} < 1$. In the CesrTA R&D program described in this report we have tested and analyzed a few such coatings and other low-SEY techniques, and demonstrated their efficacy. It seems clear to us that all future high-intensity storage rings will be equipped with such coatings or devices. Once the "battle of the SEY" is won in this way, photoemission becomes competitive with secondary emission and hence becomes relatively more important. Such a situation is expected to arise in the ILC DRs, and especially in the proposed SUPER-B and SUPER-KEK factories, which will have very intense synchrotron radiation from the beam. The focus of ECE

R&D effort will then surely shift to better describe the photon intensity and distribution in 3D at all locations around the ring. The development and implementation of the code `Synrad3D` within the CesrTA R&D program described here constitutes a major step in this direction. Indeed, we have verified the importance of using a realistic photon distribution around the chamber in order to improve the quantitative agreement of the simulations with the coherent tune shift data. Ingredients that still remain to be improved are measurements (or reliable calculations) of the photon reflectivity, the diffusive component of photon-surface scattering, and details of the QE and photoemission spectrum. We are certain that such areas will increase in importance and receive greater attention in future EC research. The goal will be to improve the photon tracking and photoemission components of the model embodied in the simulation codes to a level at least as detailed and reliable as the present model for secondary emission. With such tools, the antechamber aperture and its detailed geometry will be determined with greater confidence than is now possible for radiation-dominated storage rings.

7.5 Conclusion

Given the good overall agreement between build-up simulations and measurements, the CesrTA R&D program has demonstrated that an ecloud model does exist. Thus, for a given machine, it is possible (though laborious) to constrain or fix the model parameters, and hence to predict the ecloud distribution and density as a function of time and space at any location around the ring for a given beam configuration. With this information, the EC effects on the beam (e.g., instability thresholds) can be computed via beam dynamic codes, and hence help define a reliable machine operation régime.

This Phase I of the CesrTA R&D program has without a doubt pushed the state of the art in the physics of the electron cloud. The program has informed a validation of the model embodied in the simulation codes. The results confirm and quantify the benefit of low secondary emission surfaces, of methodical simulations carried out in tandem with equally methodical measurements, and shifts the attention to the area of photon distribution and photoemission. We expect that this latter area of physics will be a major focus of Phase II.

While much detailed work remains to be carried out to fully describe and quantify the physics of the EC, the results contained here will improve the design of future machines and their operational reliability, both for lepton and hadron storage rings.

Chapter 8

Recommendations for the ILC Positron Damping Ring

8.1 Introduction

The development of the electron cloud in the ILC positron damping ring represents one of the most significant risks to the overall physics performance of the collider. In the original design studies for the damping rings, it was estimated that the peak SEY values for the vacuum chamber surfaces in the positron ring would need to be maintained at values < 1.2 in order to safely remain below the EC-induced instability threshold with the specified baseline operating parameters [171–173].

As described in Chapter 1, the principal deliverables of the CesrTA Phase I R&D program were:

1. To provide technical demonstrations of EC mitigation techniques that can reduce the EC densities in the positron damping ring to sufficiently low levels that stable operation at the ultra low emittance target is possible;

2. To evaluate our understanding of the EC-induced instability thresholds and the potential for sub-threshold emittance growth in an emittance regime approaching that of the ILC damping rings.

Chapters 5 and 6 have described the range of experiments carried out to evaluate each of these issues. The following sections describe the implications of these measurements for the ILC positron DR.

8.2 Inputs to the EC Mitigation Evaluation

Table 8.1 summarizes the range of vacuum chambers that have been tested as part of the CesrTA program to understand the efficacy of various EC mitigations. Each of the listed chambers incorporates one or more RFAs with which to study the beam-induced EC build-up in the chamber. These studies have spanned each of the key magnetic environments where mitigations will be required in the positron DR. In many cases, reference chambers without mitigations were employed to improve

our understanding of the relative performance of the various techniques as well as to provide data to help characterize the models of the EC development.

Table 8.1: Vacuum chambers fabricated for testing during the CesrTA R&D program. Mitigation studies have been conducted in drift, dipole, quadrupole, and wiggler magnetic field regions.

Mitigation	Drift	Quad	Dipole	Wiggler	Contributing Institutions
Al	✓	✓	✓		CU, SLAC
Cu	✓			✓	CU, KEK, LBNL, SLAC
TiN on Al	✓	✓	✓		CU, SLAC
TiN on Cu	✓			✓	CU, KEK, LBNL, SLAC
Amorphous C on Al	✓				CERN, CU
Diamond-like C on Al	✓				CU, KEK
NEG on SS	✓				CU
Solenoid Windings	✓				CU
Fins w/TiN on Al	✓				CU, SLAC
Triangular Grooves:					
On Cu				✓	CU, KEK, LBNL, SLAC
With TiN on Al			✓		CU, SLAC
With TiN on Cu				✓	CU, KEK, LBNL, SLAC
Clearing Electrode				✓	CU, KEK, LBNL, SLAC

Detailed studies of the performance of the vacuum chambers in Table 8.1 have guided the selection of the preferred mitigation methods for the baseline design of the ILC Positron DR. Through the course of the CesrTA studies, several conclusions about the efficacy and viability of the various mitigations have been drawn. Key conclusions in each of the magnetic field environments are described in the following sections.

An important result of the CesrTA experiments has been the clear demonstration of the need to include detailed information about the distribution of photons in the vacuum system, as well as the SEY properties, in order to adequately model the experimental results. Thus the development of the Synrad3D program, as described in Section 4.1.4.1, to model photon production, transport, scattering and absorption within the damping ring is a critical addition to the arsenal of tools for designing the damping ring vacuum system and evaluating its performance.

8.2.1 Drift Region

Three coatings were tested in the Q15E and Q15W EC experimental regions through the course of the program. These were TiN, amorphous carbon (a-C) and diamond-like carbon (DLC). Performance was compared with that of an uncoated Al vacuum chamber. A fourth coating, the non-evaporable getter (NEG) TiZrV, was tested in the L3 EC experimental region.

The CesrTA evaluations indicated good performance of each of these coatings. As was described in Section 2.2.3.1, the vacuum performance, as characterized by the dP/dI of the TiN and a-C were somewhat worse than the Al surface, while the DLC coating showed an extended period of higher dP/dI which was predominantly due to hydrogen evolution. The observed vacuum performance of the NEG coating was quite good, as anticipated. With respect to the SEY performance, good

performance, consistent with peak SEY values near unity, was observed for all of the coatings. Direct comparisons of the SEY performance for the TiN, a-C and DLC coatings can bee seen in Figures 5.22 through 5.24. On this basis, coating-based mitigations for the drift regions of the ILC damping ring should provide the necessary SEY performance. In the electron cloud working group evaluation, the final choice of coating was determined largely by the vacuum performance and known durability of the coating. On this basis, TiN coating was chosen for the primary mitigation. Continued observation of the durability of the other coatings is planned for Phase II of the CesrTA research program.

Time-resolved measurements at the Q15E/W experimental locations have begun to yield even more detailed information about the performance of the various coatings. The comparisons between TiN and a-C coatings discussed in Section 5.2.2 provide direct sensitivity to the photoelectron yield parameters of various surfaces (eg, see Figures 5.94 and 5.95). In a damping ring with vacuum surfaces designed to minimize the SEY and with sections of the ring exposed to dipole or wiggler radiation, photoelectron production can become the performance limiting effect. For the ILC DR, drift sections in these regions will incorporate antechambers to help control photoelectron production in the central part of the vacuum chamber. If alternate coatings, such as a-C, are found to be sufficiently durable for use in an operating ring, then the further suppression of photoelectron production may be of interest in future designs.

8.2.2 Quadrupole Region

A major conclusion of the CesrTA measurements in quadrupoles was that growth of the EC could not be accounted for using single-pass beam simulations. Cloud is trapped in the quadrupoles and builds up over tens of turns as discussed in Section 5.1.3.4. Furthermore, this effect is a likely candidate for beam blow-up of the first bunch in a train where there is time for the cloud to "relax" into the vicinity of the beam axis during a long gap (see Section 6.3.4.1). The CesrTA measurements have shown that the use of a TiN coating strongly suppresses the cloud build-up and this is the baseline EC mitigation which has been specified for the ILC DR. It remains of interest, however, to design quadrupole chambers that incorporate grooves or clearing electrodes which can be tested as part of the ongoing R&D program.

8.2.3 Dipole Region

In dipoles, the implementation of vacuum chambers with TiN coating and triangular grooves on the top and bottom surfaces has proven very effective in suppressing EC build-up in these chambers. Figure 5.27 shows the performance comparisons of an untreated surface, a TiN-coated smooth surface, and a TiN-coated grooved surface obtained in the CesrTA measurements. These results strongly support the choice of the grooved and coated chamber as the baseline mitigation choice for the ILC DR. Antechambers (both radially inside and outside) are required to keep the production of photoelectrons under control. For the ILC DR vacuum chamber design, Synrad3D provides the necessary capability to evaluate the performance of the antechambers and optimize the final vacuum chamber design. Testing of a prototype grooved chamber designed for use in SuperKEKB is planned as part of the Phase II R&D program at CesrTA .

Given the efficacy of clearing electrodes as observed in the wiggler chambers (see Figure 5.42), this is a solution that warrants further exploration for dipole chambers as well, if the ongoing R&D

program permits. Any improvements in EC performance must be carefully balanced against the increase in vacuum feedthroughs and active elements required.

8.2.4 Wiggler Region

In the wiggler regions, which are of particular concern for the DR design, the most efficacious solution for mitigating EC growth has proven to be clearing electrodes (see Figure 5.42). The use of a thin clearing electrode structure applied with thermal spray techniques along with low profile feedthrough connections was extensively tested under a wide range of beam conditions in CESR (see Section 2.2.3.3). Operations with this design were found to be stable and reliable.

Antechambers should be employed on both sides of the vacuum chamber in the DR wiggler straight in order to provide a path to discrete photon stops and to prevent excessive photoelectron production in the central chamber. As in the case of the arc regions, Synrad3D provides the ability to evaluate and optimize the performance of the antechamber and photon stop designs.

8.3 Studies of Beam Instabilities and Emittance Growth

Using the formulae presented in Sec. 6.2.2, Table 8.2 gives the key parameters and instability thresholds for CesrTA and the ILC damping ring, based on the parameters given in Table 8.3. As described in Chapter 6, the observed instability thresholds for the CesrTA experimental conditions are in good agreement with these calculations when one estimates the EC density near the beam by way of tune-shift measurements along the train. This applies both to the appearance of synchrobetatron side-bands in our tune measurements as well as rapid beam size growth as observed with the xBSM. The good agreement between data and experiment in CesrTA gives us confidence in the tools that are being employed to make instability threshold estimates for the ILC DR.

There is some evidence in the beam size data (eg, see Figure 6.72) that there may be emittance growth before the full onset of the head-tail instability. In the CesrTA data, such effects occur at EC densities which are a few times smaller than the calculated instability thresholds. This suggests that some additional margin may be required in our estimates of the safe EC densities for stable operation of a damping ring. In order to explore such effects in detail, more sophisticated simulations of the beam dynamics will be necessary. In particular, the ability to run beam dynamics simulations, which incorporate radiation damping, over a number of turns exceeding a damping time would be very valuable in evaluating these emittance effects in the CesrTA data. For instance, the necessary code extensions and studies are being considered for CMAD. For the time being, however, allowing some additional margin, beyond that calculated for the head-tail instability, in the allowable EC densities in the ILC DR is indicated.

8.4 The ILC Mitigation Recommendations

The ILC Damping Ring EC mitigation recommendations are summarized in Table 8.4 [174]. The recommendations were prepared by a working group with representatives from ANL, CERN, Cornell, INFN-LNF, KEK, LBNL and SLAC. The recommendations drew heavily on the results of the

Table 8.2: Analytic estimate of the fast head-tail instability threshold for CesrTA and the ILC damping ring.

	CesrTA (2 *GeV*)	CesrTA (5 *GeV*)	ILC DR
Bunch Population N_+ ($\times 10^{10}$)	2	2	2
Bunch Spacing ℓ_{sp} (ns)	4	4	6
Average Vertical Beta Function β_y (m)	16	16	24
Electron Frequency $\omega_e/2\pi$ (GHz)	35	11	111
Phase Angle χ	8.9	3.7	14.0
Threshold Density $\rho_{e,th}$ ($\times 10^{12}$ m^{-3})	0.82	3.22	0.23
Tune Shift at Threshold $\Delta\nu_{x+y}$ ($\times 10^{-3}$)	9	14	5

Table 8.3: Parameters of CesrTA and the ILC damping ring used for instability threshold estimates.

	CesrTA (2 *GeV*)	CesrTA (5 *GeV*)	ILC DR
Circumference L (m)	768	768	3245
Energy E (GeV)	2.1	5.0	5.0
Bunch Population N_+ ($\times 10^{10}$)	2	2	2
Emittance ε_x (nm)	2.6	40	0.45
Momentum Compaction α ($\times 10^{-4}$)	67.6	62.0	3.3
RMS Bunch Length σ_z (mm)	12.2	15.7	6
RMS Energy Spread σ_E/E ($\times 10^{-3}$)	0.80	0.94	1.09
Horizontal Betatron Tune ν_x	14.57	14.57	47.37
Vertical Betatron Tune ν_y	9.62	9.62	28.18
Synchrotron Tune ν_s	0.055	0.0454	0.031
Damping Time $\tau_{x,y}$ (ms)	56.4	19.5	24

CesrTA program and also incorporated input from research carried out at the other participating laboratories. The evaluations used to arrive at these recommendations included:

- The efficacy of the mitigation method;
- The expected cost of the mitigation method;
- The risks associated with the mitigation (including: manufacturing challenges, technical uncertainty, incomplete information about the mitigation method, as well as the reliability and durability of the technique);
- The impact on other aspects of machine performance (eg, vacuum, impedance, optics design, operational issues)

Overall, a strong emphasis was placed on specifying the most effective and reliable mitigation scheme for each region, as long as the assessed risks and secondary impacts on machine operation were not felt to be significant.

In Table 8.2, the ILC DR instability thresholds are calculated for the baseline low power operating mode. The luminosity upgrade path for the ILC envisions roughly doubling the number of bunches in the main linac bunch train. Although the baseline plan is to add a second positron DR to support this upgrade, it is hoped that the upgrade can be achieved by doubling the number of bunches in a single positron DR. This makes it imperative to deploy the most effective EC mitigation scheme possible. Thus, in most regions, primary and secondary mitigation methods have been specified as

part of an aggressive plan to defeat the build-up of the EC.

Finally, it should be noted that the choices of mitigation methods in Table 8.4 are nearly identical to the choices that have been made for the construction of the SuperKEKB [175] vacuum system. Thus operation of the SuperKEKB positron ring will serve as a crucial performance test that will further improve our understanding of the anticipated performance of the ILC DR.

Table 8.4: Summary of the *Electron Cloud Mitigation Recommendations* for the ILC positron damping ring. These recommendations were agreed upon at a satellite meeting of the ***ECLOUD 2010*** workshop, held at Cornell University on October 13, 2010. The meeting included members of the working group as well as a number of experts who were in attendance at the workshop.

Field Region	**Baseline Mitigation Recommendation**		**Alternatives for Further Investigation**
	Primary	***Secondary***	
Drift*	TiN Coating	Solenoid Windings	NEG Coating
Dipole	Triangular Grooves with TiN Coating	Antechambers for synchrotron radiation power loads and photoelectron control	R&D into the use of clearing electrodes
Quadrupole*	TiN Coating		R&D into the use of clearing electrodes or grooves with TiN coating
Wiggler	Clearing Electrodes	Antechambers for synchrotron radiation power loads and photoelectron control	Grooves with TiN coating

* Where drift and quadrupole chambers are in arc or wiggler straight regions of the machine, the chambers will incorporate features of those sections, ie, antechambers for power loads and photoelectron control.

Chapter 9

Conclusions and Future Plans

The CesrTA Phase I research program represents an integrated effort to understand the critical physics issues of ultra low emittance damping rings. Thus the experimental program has encompassed:

- Reconfiguration of CESR into a damping ring;
- Development of a range of diagnostics to characterize the growth of the electron cloud in vacuum chambers;
- Implementation of the most promising electron cloud mitigation methods in a variety of vacuum chambers and magnetic field environments;
- Development of optics correction techniques to prepare low emittance beams;
- Development of beam diagnostics for characterizing low emittance beams;
- Implementation of instrumentation capable of characterizing beam dynamics effects in bunch trains, which are induced by the electron cloud (and other sources).

By utilizing the inherent flexibility of ring operations with CesrTA, the research program was able to launch a systematic exploration of the fundamental physics of damping rings with a primary focus on electron cloud effects. This research effort supported a rich range of developments in beam instrumentation, beam tuning and low emittance correction, electron cloud measurement techniques, electron cloud analysis and modeling, electron cloud mitigation techniques, and engineering for damping ring design. The sensitivity achieved with key studies has demonstrated the potential to obtain detailed surface physics information in a working accelerator environment. The level of detail of the studies has enabled application of the results to other machines. The ability to conduct detailed systematic studies has provided confidence in the extrapolation and application of the results to other machines. Thus the program has provided both the required technical inputs as well as the confidence required to develop the ILC damping ring design. More broadly, results have been obtained which are applicable to damping rings, electron-positron colliders, proton machines sensitive to the electron cloud, and light sources.

A Phase II research program has now begun which will expand on the research thrusts of the Phase I effort. Furthermore, the accelerator capabilities implemented for Phase I now provide a robust foundation for extending research into new areas such as intra-beam scattering and fast ion effects during Phase II.

9.1 CesrTA Instrumentation and Infrastructure

The goals of the initial phase of the CesrTA R&D program required new instrumentation for tuning and measuring emittance, measuring density, growth and decay of the electron cloud and the effectiveness of various mitigation techniques, determining secondary emission yields of various vacuum chamber surfaces and coatings, and characterizing beam dynamics effects due to the cloud.

The new BPM electronics and the x-ray beam size monitor enabled emittance tuning and measurement of the size of the low emittance beams. Retarding field analyzers in drift, dipole, quadrupole and wiggler fields provided measurements of the time averaged dependence of the electron cloud density and energy spectrum on beam structure and magnetic field. Time resolved measurements of the electron cloud with shielded button electrode pickups were used to extract information about growth and decay of the cloud. The high bandwidth of the BPM system, and a feedback system with 4 ns bunch-to-bunch capability were exploited to measure electron cloud induced tune shifts and instabilities. The bunch-by-bunch bandwidth of the beam size monitor was essential to quantifying the sub-threshold emittance growth due to the cloud and quantify the onset of full-blown beam instabilities.

9.2 Findings

The principal findings of the CesrTA research program are the electron cloud related design criteria of a low emittance, high intensity positron damping ring. RFAs have been used to characterize the effectiveness of more than a dozen mitigation techniques. Effects of beam processing for various chamber types have been quantified with in-situ measurement of secondary emission yield. Measurements of cloud induced tune shift are in good agreement with the elaborate model that includes everything from the distribution, scatter, and absorbtion of primary synchrotron radiated photons on the walls of a realistic vacuum chamber to the dynamics the cloud electrons kicked by the circulating bunches within the static B-field of the storage ring guide field magnets, producing secondaries on collision with that same vacuum chamber. Local measurements of the electron cloud growth and decay with RFAs and SPUs have been used to further constrain the model parameters. Additional information about local cloud build-up has been obtained with a variety of techniques utilizing microwave transmission through short sections of the CESR vacuum system. With the beam instrumentation We have measured threshold densities for electron cloud induced instabilities and emittance growth.

The findings with respect to mitigations and emittance diluting cloud density thresholds are the basis of the recommendations for the ILC damping ring design.

We have developed techniques and instrumentation for emittance tuning and consistently achieve less than 10 pm-rad vertical emittance in a variety of lattice configurations. The measurements of residual coupling and vertical dispersion are based on resonant excitation of normal modes. We have succeeded in reducing the typical time for a single iteration of measurements and their corrections to a few minutes. The beam based measurements depend on the precision of the turn-by-turn beam position monitors. We have implemented procedures for their routine calibration to minimize systematic measurement errors. The x-ray beam size monitor provides continuous monitoring of vertical emittance.

9.3 Future Plans

During the next phase of the program we will add tools for measuring horizontal beam size (a visible light interferometer), beam energy spread (horizontal size versus variable dispersion), and bunch length (streak camera). The simultaneous measurement of vertical, horizontal and longitudinal phase space will be essential to the study of intra-beam scattering emittance dilution. As a complement to the x-ray beam size camera, we will explore an alternative technique for measuring vertical beam size that depends on the angular distribution and polarization of visible synchrotron radiation. We will be developing an x-ray beam size monitor with response times that allow resolution of variation of the size along the length of the bunch.

We will also be installing more sophisticated detectors for making time resolved measurements of the growth and decay of the electron cloud in dipole and quadrupole, as well as drift fields.

9.3.1 Emittance Tuning

The low emittance tuning procedure is at present limited by systematics associated with measurements of vertical dispersion. We plan to better understand those limitations with the help of modeling and simulation. We are developing a beam based technique for measuring the physical tilt of the beam position monitors. We are also building machinery for analysis of the AC-dispersion data using singular value decomposition rather than simple Fourier techniques. As the required coupling measurements depend on the beam position monitors, we will continue to investigate effects of timing jitter and drifts. Our goal is to improve the resolution of the dispersion measurement from 15 mm to as few as 3 mm.

9.3.2 Intra-Beam Scattering

Measurement and analysis of intra-beam scattering is an important component of the next phase of the CesrTA program. The instrumentation described above will provide a complete set of measurements of the equilibrium charge density. As that equilibrium has a strong beam energy dependence, measurements over a range of energies will help us to distinguish IBS from other emittance diluting effects. Measurements with electron as well as positron beams will disentangle the contributions from ions and electron cloud.

9.3.3 Ion Effects

CesrTA is an excellent laboratory for investigating ion effects in electron beams, and in particular the fast ion instability in bunch trains in the ultra-low vertical emittance regime. The turn-by-turn spectra gathered with the high bandwidth beam position and vertical beam size monitors for each bunch in a train can provide signatures of ion-beam coupling and emittance dilution. Measurement of instability thresholds as a function of vacuum pressure, and for positrons as well as electrons will be used to isolate ion effects from other collective phenomena. Simulations will be developed to support the study.

9.3.4 Electron Cloud

Electron cloud R&D conducted at CesrTA has made important contributions to our understanding of electron cloud growth and its mitigation, and to electron cloud induced beam dynamics.

We have developed models for calculating the buildup of the cloud, including the dependence on beam parameters and vacuum chamber surface characteristics, and made extensive comparison with measurements. The calculations are in reasonable agreement with both global (tune shift) and local (RFA, SPU and TE wave) measurements in CesrTA. With the help of coatings and geometries that mitigate the production of secondary electrons, the contribution from primaries becomes increasingly important. Our research will extend to the physics of quantum efficiency and modeling of primary electron distributions, in addition to further refining our understanding of secondary processes.

There will be ongoing monitoring of RFA and SPU data to characterize the durability of mitigations and the effects of beam processing. We are extending the capability of the device for in-situ measurement of SEY to cover an expanded angular and energy range.

RFA detectors that share both time averaging and time resolving capability have been installed along with various mitigations in the dipole chicane. The same chambers are within a region accessible to TE wave measurements. Comparison of the complementary measurements will help us to better understand model parameters.

While both global measurements of cloud lifetime with tune shift data, and local measurements with SPUs suggest that the lifetime of the cloud is of order hundreds of nanoseconds, there is some evidence of a long lived cloud with lifetime of many CESR revolutions $\tau_{\rm rev} = 2.56$ μs. Such a long-lived cloud could have important implications for the performance of damping rings and other low emittance machines.

There remain a number of outstanding questions regarding electron cloud beam dynamics phenomena in the positron storage ring environment. We have observed electron-cloud-induced emittance growth and head tail instability, the former by direct measurement of beam size and the latter from the turn-by-turn bunch position spectra. But we have yet to determine to what extent the emittance growth and instability are related. Is the emittance growth simply a manifestation of the head-tail motion, or is there a sub-threshold incoherent growth in beam size? While the signature of the instability appears in the BPM data, we have yet to reproducibly identify that signature in the turn-by-turn bunch size data.

We are developing both analytic and computational tools for analysis of instabilities and emittance dilution. CMAD, the code that is used to model interaction of the bunch with the cloud and that predicts the onset of instabilities, is being extended with new algorithms for greater efficiency and realism. Analysis of BPM response to head tail motion will help us to make the connection between the amplitude of lines in the position spectrum and bunch size. We are also developing new instrumentation for characterizing intra-bunch motion, including an extension of the xBSM to measure longitudinal dependence of bunch vertical cross section and offset.

Appendix A

Glossary of Acronyms Used in the Report

BnnE Bending magnet number nn in the East half of CESR.

BnnW Bending magnet number nn in the West half of CESR.

BPM Beam position monitor.

CBPM CESR beam position monitor data acquisition system.

CCG Cold cathode gauge.

CESR Cornell Electron/Positron Storage Ring.

CESR-c CESR collider, configured as a charm factory.

CesrTA CESR Test Accelerator.

CHESS Cornell High Energy Synchrotron Source, synchrotron light source.

CLOUDLAND A storage ring beam dynamics simulation code.

CMAD A storage ring beam dynamics simulation code.

CMM Coordinate measuring machine.

DIP Distributed sputter-ion pump in the CESR bending magnets.

DSP Digital signal processor.

EB-weld Electron beam weld.

EC Electron cloud.

ECE Electron cloud effect.

ECLOUD An electron-cloud build-up simulation code.

EMI Electro-magnetic interference.

EPICS Experimental Physics and Industrial Control System controls architecture.

FFT Fast Fourier transform.

FPGA Field programmable gate array, electronic digital processing.

HEP High energy physics.

HOML Higher order mode loss: energy loss by scattering of the beams electro-magnetic field from discontinuities of the vacuum chamber walls.

IHT Head-tail, refers to front-to-back beam shape oscillation of the bunch.

IOC EPICS Input-Output Controller.

IR Interaction region, which held the CLEO-c detector for HEP research.

L0 Southern long straight section in CESR.

L3 Northern long straight section in CESR.

LET Low emittance tuning.

NEG Non-evaporable getter vacuum pump.

PEHTS A storage ring beam dynamics simulation code.

PEP-II Positron-Electron Project B-factory.

PEP-II LER PEP-II low energy ring.

POSINST A positron/electron electron-cloud build-up simulation code.

QA/QC Quality assurance / quality control.

QCM Quartz Crystal Micro-balance.

QE Quantum efficiency (same as photoemission yield).

QnnE Quadrupole magnet number nn in the East half of CESR.

QnnE Quadrupole magnet number nn in the West half of CESR.

RFA Retarding field analyzer.

RGA Residual gas analyzer.

SCW Superconducting wiggler.

SEY Secondary emission yield.

SIP Sputter ion pump.

SPU Shielded pickup, instrument for measuring the time development of the electron cloud.

SR Synchrotron radiation.

Synrad A two-dimensional simulation code for synchrotron radiation.

Synrad3D A three-dimensional simulation code for synchrotron radiation.

TE-Wave Transverse electric waveguide mode, used as a diagnostic to determine the average electron cloud density.

TiSP Titanium sublimation (vacuum) pump.

TDR Time domain reflectometer for measuring transmission line matching.

UHV Ultra-high vacuum.

xBSM X-ray beam size monitor.

Appendix B

Acknowledgments

The authors would like to acknowledge the many contributions that have helped make the CesrTA research program a success. It would not have occurred without the support of the International Linear Collider Global Design Effort led by Barry Barish. Furthermore, our colleagues in the electron cloud research community have provided countless hours of useful discussion and have been uniformly supportive of our research goals.

We would also like to thank the technical and research staff at Cornell's Laboratory for Accelerator ScienceS and Education (CLASSE) for their efforts in maintaining and upgrading CESR for Test Accelerator operations. Along the way, we have lost two of our colleagues, each of whom provided invaluable support for the research program. They are Mike Comfort who contributed critical electronics and controls support as the research program began and Valeri Medjidzade who tirelessly designed, monitored fabrication, and oversaw installation of the EC experimental regions and wiggler straight for CesrTA experimental operations. They are both sorely missed.

Finally, we would like to acknowledge the funding agencies that helped support the program. The U.S. National Science Foundation and Department of Energy implemented a joint agreement to fund the CesrTA effort under contracts PHY-0724867 and DE-FC02-08ER41538, respectively. Further program support was provided by the Japan/US Cooperation Program. Finally, the beam dynamics simulations utilized the resources off the National Energy Research Scientific Computing Center (NERSC) which is supported by the Office of Science in the U.S. Department of Energy under contract DE-AC02-05CH11231.

Bibliography

[1] M. A. Palmer *et al.*, "The Conversion and Operation of the Cornell Electron Storage Ring as a Test Accelerator (CesrTA) for Damping Rings Research and Development," in *Proceedings of the 2009 Particle Accelerator Conference, Vancouver, BC* (2009), p. 4200–4204.

[2] M. A. Palmer *et al.*, "Electron Cloud at Low Emittance in CesrTA," in *Proceedings of the 2010 International Particle Accelerator Conference, Kyoto, Japan* (2010), p. 1251–1255.

[3] R. Kersevan, Y. Li & N. B. Mistry, "Operational Experience of Novel Vacuum Chambers Incorporating Massive Titanium-Sublimation Pumping in the Cornell Electron-Positron Storage Ring Interaction Region," *J. Vac. Sci. Technol. A* **15**, p. 716–722 (May 1997).

[4] Y. Li, Y. He & M. A. Palmer, "Vacuum Modifications for the Installation of a New CESR-c Fast Luminosity Monitor," in *Proceedings of the 2005 Particle Accelerator Conference, Knoxville, TN*, C. Horak, Ed. (2005), p. 2836–2838.

[5] G. Stupakov & M. Pivi, "Suppression of the Effective Secondary Emission Yield for a Grooved Metal Surface," in *Proceedings of ECLOUD 2004: 31st ICFA Advanced Beam Dynamics Workshop on Electron-Cloud Effects, Napa, CA*, M. Furman, S. Henderson & F. Zimmerman, Eds. (2004), CERN-2005-001, p. 139–141.

[6] M. Pivi *et al.*, "Sharp Reduction of the Secondary Electron Emission Yield from Grooved Surfaces," *J. Appl. Phys.* **104**, 104904 (Nov. 2008).

[7] A. A. Krasnov, "Molecular Pumping Properties of the LHC Arc Beam Pipe and Effective Secondary Electron Emission from Cu Surface with Artificial Roughness," *Vacuum* **73**, p. 195–199 (Mar. 2004).

[8] L. Wang, T. O. Raubenheimer & G. Stupakov, "Suppression of Secondary Emission in a Magnetic Field Using Triangular and Rectangular Surfaces," *Nucl. Instrum. Methods Phys. Res.* **A571**, p. 588–598 (Feb. 2007).

[9] Y. Suetsugu *et al.*, "First Experimental and Simulation Study on the Secondary Electron and Photoelectron Yield of NEG Materials (Ti-Zr-V) Coating Under Intense Photon Irradiation," *Nucl. Instrum. Methods Phys. Res.* **A554**, p. 92–113 (Dec. 2005).

[10] P. Costa Pinto *et al.*, "Thin Film Coatings for Suppressing Electron Multipacting in Particle Accelerators," in *Proceedings of the 2011 Particle Accelerator Conference, New York, NY* (2011), p. 2096–2098.

[11] Y. He *et al.*, "Design and Operation of the Cryostat for the CESR-c Superconducting Wiggler Magnets," in *Proceedings of the 2003 Particle Accelerator Conference, Portland, OR*, J. Chew, P. Lucas & S. Webber, Eds. (2003), p. 2399–2401.

[12] L. Wang & F. Zimmermann, "Electron Cloud in the Wigglers of the Positron Damping Ring of the International Linear Collider," in *Proceedings of the 2007 Particle Accelerator Conference, Albuquerque, NM*, C. Petit-Jean-Genaz, Ed. (2007), p. 1808–1810.

[13] L. Wang, private communication.

[14] Y. Suetsugu *et al.*, "Demonstration of Electron Clearing Effect by Means of a Clearing Electrode in High-Intensity Positron Ring," *Nucl. Instrum. Methods Phys. Res.* **A598**, p. 372–378 (Jan. 2009).

[15] Y. Li *et al.*, "Design and Implementation of CesrTA Superconducting Wiggler Beampipes with Thin Retarding Field Analyzers," in *Proceedings of the 2009 Particle Accelerator Conference, Vancouver, BC* (2009), p. 3507–3509.

[16] R. A. Rosenberg & K. C. Harkay, "A Rudimentary Electron Energy Analyzer for Accelerator Diagnostics," *Nucl. Instrum. Methods Phys. Res.* **A453**, p. 507–513 (Oct. 2000).

[17] Y. Li *et al.*, "CesrTA Vacuum System Modifications," in *Proceedings of the 2009 Particle Accelerator Conference, Vancouver, BC* (2009), p. 357–359.

[18] J. Calvey *et al.*, "Simulations of Electron-Cloud Current Density Measurements in Dipoles, Drifts and Wigglers at CesrTA," in *Proceedings of the 2009 Particle Accelerator Conference, Vancouver, BC* (2009), p. 4628–4630.

[19] S. De Santis *et al.*, "Measurement of Electron Clouds in Large Accelerators by Microwave Dispersion," *Phys. Rev. Lett.* **100**, 094801 (Mar. 2008).

[20] N. Eddy *et al.*, "Measurement of Electron Cloud Development in the Fermilab Main Injector Using Microwave Transmission," in *Proceedings of the 2009 Particle Accelerator Conference, Vancouver, BC* (2009), p. 1967–1969.

[21] S. De Santis *et al.*, "Characterization of Electron Clouds in the Cornell Electron Storage Ring Test Accelerator using TE-Wave Transmission," *Phys. Rev. ST Accel. Beams* **13**, 071002 (Jul. 2010).

[22] S. Federmann, F. Caspers & E. Mahner, "Measurements of Electron Cloud Density in the CERN Super Proton Synchrotron with the Microwave Transmission Method," *Phys. Rev. ST Accel. Beams* **14**, 012802 (Jan. 2011).

[23] M. A. Heald & C. B. Wharton, *Plasma Diagnostics with Microwaves*, John Wiley & Sons, New York (1965).

[24] J. P. Sikora, S. De Santis & K. Hammond, "TE Wave measurements at CesrTA," in *Proceedings of ECLOUD 2010: 49th ICFA Advanced Beam Dynamics Workshop on Electron Cloud Physics, Ithaca, NY*, K. Smolenski, Ed. (in press), Paper PST04.

[25] S. De Santis *et al.*, "TE Wave Measurements of the Electron Cloud in a Dipole Magnetic Field," in *Proceedings of the 2011 Particle Accelerator Conference, New York, NY* (2011), p. 531–533.

[26] E. Mahner, T. Kroyer & F. Caspers, "Electron Cloud Detection and Characterization in the CERN Proton Synchrotron," *Phys. Rev. ST Accel. Beams* **11**, 094401 (Sep. 2008).

[27] J. Sikora *et al.*, "A Shielded Pick-Up Detector for Electron Cloud Measurements in the CesrTA Ring," in *Proceedings of BIW 2010: Fourteenth Beam Instrumentation Workshop, Santa Fe, NM*, C. Dillingham & J. Chew, Eds. (2010), p. 345–349.

[28] L. F. Wang *et al.*, "Mechanism of Electron Cloud Clearing in the Accumulator Ring of the Spallation Neutron Source," *Phys. Rev. ST Accel. Beams* **7**, 034401 (Mar. 2004).

[29] J. Kim *et al.*, "In Situ SEY Measurements at CesrTA," in *Proceedings of ECLOUD 2010: 49th ICFA Advanced Beam Dynamics Workshop on Electron Cloud Physics, Ithaca, NY*, K. Smolenski, Ed. (in press), Paper PST12.

[30] J. Kim *et al.*, "In-Situ Secondary Electron Yield Measurement System at CesrTA," in *Proceedings of the 2011 Particle Accelerator Conference, New York, NY* (2011), p. 1253–1255.

[31] F. Le Pimpec *et al.*, "Secondary Electron Yield Measurements of TiN Coating and TiZrV Getter Film," Tech. Rep. LCC-0128/SLAC-TN-03-052, Linear Collider Collaboration/SLAC, Stanford, CA (Aug. 2004), revised from original version of Oct 2003.

[32] D. Sagan *et al.*, "Betatron Phase and Coupling Measurements at the Cornell Electron/Positron Storage Ring," *Phys. Rev. ST Accel. Beams* **3**, 092801 (Sep. 2000).

[33] R. E. Meller & M. A. Palmer, "Digital Tune Tracker for CESR," in *Proceedings of the 2011 Particle Accelerator Conference, New York, NY* (2011), p. 504–506.

[34] M. A. Palmer *et al.*, "CESR Beam Position Monitor System Upgrade for CesrTA and CHESS Operations," in *Proceedings of the 2010 International Particle Accelerator Conference, Kyoto, Japan* (2010), p. 1191–1193.

[35] J. T. Rogers *et al.*, "Operation of a Fast Digital Transverse Feedback System in CESR," in *Proceedings of the 1995 Particle Accelerator Conference, Dallas, TX* (1995), p. 2426–2428.

[36] M. Billing *et al.*, "Performance of the Beam Stabilizing Feedback Systems at CESR," in *Proceedings of the 2001 Particle Accelerator Conference, Chicago, IL*, P. Lucas & S. Webber, Eds. (2001), p. 1243–1245.

[37] D. Teytelman, "iGp-1281F Signal Processor: Technical User Manual, Revision 1.7," Tech. rep., Dimtel, Inc., San Jose, CA (May 2009).

[38] D. Rice, "CESR-c: A Wiggler-Dominated Collider," in *Proceedings of the 2007 Particle Accelerator Conference, Albuquerque, NM*, C. Petit-Jean-Genaz, Ed. (2007), p. 48–52.

[39] Y. Cai, M. Pivi & M. A. Furman, "Buildup of Electron Cloud in the PEP-II Particle Accelerator in the Presence of a Solenoid Field and with Different Bunch Pattern," *Phys. Rev. ST Accel. Beams* **7**, 024402 (Feb. 2004).

[40] H. Fukuma, "Electron Cloud Instability in KEKB and SuperKEKB," in *ICFA Beam Dynamics Newsletter*, M. E. Biagini, Ed., International Committee on Future Accelerators, No. 48, p. 112–118 (Apr. 2009).

[41] S. M. Liuzzo *et al.*, "Tests of Low Emittance Tuning Techniques at SLS and DAΦNE," in *Proceedings of the 2012 International Particle Accelerator Conference, New Orleans, LA* (2012), p. 1065–1067.

[42] R. Dowd *et al.*, "Achievement of Ultralow Emittance Coupling in the Australian Synchrotron Storage Ring," *Phys. Rev. ST Accel. Beams* **14**, 012804 (Jan. 2011).

[43] T. O. Raubenheimer, *The Generation and Acceleration of Low Emittance Flat Beams for Future Linear Colliders*, Ph.D. thesis, Stanford University, Stanford, California (Nov. 1991).

[44] D. Sagan, "Bmad: A Relativistic Charged Particle Simulation Library," *Nucl. Instrum. Methods Phys. Res.* **A558**, p. 356–359 (Mar. 2006).

[45] D. Sagan *et al.*, "A Magnetic Field Model for Wigglers and Undulators," in *Proceedings of the 2003 Particle Accelerator Conference, Portland, OR*, J. Chew, P. Lucas & S. Webber, Eds. (2003), p. 1023–1025.

[46] R. W. Helms & G. H. Hoffstaetter, "Orbit and Optics Improvement by Evaluating the Nonlinear Beam Position Monitor Response in the Cornell Electron Storage Ring," *Phys. Rev. ST Accel. Beams* **8**, 062802 (Jun. 2005).

[47] D. Sagan & D. Rubin, "Linear Analysis of Coupled Lattices," *Phys. Rev. ST Accel. Beams* **2**, 074001 (Jul. 1999).

[48] M. D. Woodley *et al.*, "Beam Based Alignment at the KEK-ATF Damping Ring," in *Proceedings of the 2004 European Particle Accelerator Conference, Lucerne, Switzerland* (2004), p. 36–38.

[49] D. L. Rubin *et al.*, "Beam Based Measurement of Beam Position Monitor Electrode Gains," *Phys. Rev. ST Accel. Beams* **13**, 092802 (Sep. 2010).

[50] M. Izawa, Y. Sato & T. Toyomasu, "The Vertical Instability in a Positron Bunched Beam," *Phys. Rev. Lett.* **74**, p. 5044–5047 (Jun. 1995).

[51] K. Ohmi, "Beam-Photoelectron Interactions in Positron Storage Rings," *Phys. Rev. Lett.* **75**, p. 1526–1529 (Aug. 1995).

[52] S. A. Heifets, "Study of an Instability of the PEP-II Positron Beam (Ohmi Effect and Multipactoring)," in *Proceedings of the International Workshop on Collective Effects and Impedance for B-Factories: CEIBA95, Tsukuba, Japan*, Y. H. Chin, Ed. (1995), KEK Proceedings 96-6.

[53] P. Cruikshank *et al.*, "Mechanical Design Aspects of the LHC Beam Screen," in *Proceedings of the 1997 Particle Accelerator Conference, Vancouver, BC, Canada* (1997), p. 3586–3588.

[54] F. Zimmermann, "A Simulation Study of Electron-Cloud Instability and Beam-Induced Multipacting in the LHC," Tech. Rep. SLAC-PUB-7425/CERN LHC Project Report 95, SLAC/CERN, Stanford, CA/Geneva, Switzerland (Feb. 1997).

[55] M. A. Furman, "The Electron-Cloud Effect in the Arcs of the LHC," Tech. Rep. LHC Project Report 180/LBNL-41482/CBP Note 247, CERN, Geneva, Switzerland (May 1998).

[56] F. Ruggiero, "Electron Cloud in the LHC," in *Beam Dynamics Issues for e+ e- Factories: Proceedings: 14th Advanced ICFA Beam Dynamics Workshop, Frascati, Italy, 1997*, L. Palumbo & G. Vignola, Eds. (1997), Fascati Physics Series, Vol. 10, p. 437–444.

[57] J. M. Jimenez *et al.*, "Vacuum and Cryogenic Observations for Different Bunch Spacing," in *Proceedings of the 2011 LHC Performance Workshop, Chamonix*, C. Carli, Ed. (2011), CERN-ATS-2011-005, p. 56–62.

[58] O. Gröbner, "Bunch Induced Multipactoring," in *Proceedings of the X International Conference on High Energy Accelerators, Protvino, USSR, 1977*, Y. M. Ado *et al.*, Eds. (1977), p. 277–282.

[59] R. J. Macek *et al.*, "Status of Experimental Studies of Electron Cloud Effects at the Los Alamos Proton Storage Ring," in *Proceedings of ECLOUD 2004: 31st ICFA Advanced Beam Dynamics Workshop on Electron-Cloud Effects, Napa, CA*, M. Furman, S. Henderson & F. Zimmerman, Eds. (2004), CERN-2005-001, p. 63–75.

[60] V. Dudnikov, "Some Features of Transverse Instability of Partly Compensated Proton Beams," in *Proceedings of the 2001 Particle Accelerator Conference, Chicago, IL*, P. Lucas & S. Webber, Eds. (2001), p. 1892–1894.

[61] T. Holmquist & J. T. Rogers, "A Trapped Photoelectron Instability in Electron and Positron Storage Rings," *Phys. Rev. Lett.* **79**, p. 3186–3189 (Oct. 1997).

[62] T. S. Wand & A. J. Jason, Eds., *Workshop on Electron Effects in High-Current Proton Rings, Santa Fe, NM, 1997*, LA-UR-98-1601, Los Alamos National Laboratory, Los Alamos, NM (1997).

[63] Y. H. Chin, Ed., *Proceedings of MBI97: International Workshop on Multibunch Instabilities in Future Electron and Positron Accelerators, Tsukuba, Japan, 1997*, KEK Proceedings 97-17 (1997).

[64] *Proceedings of ECLOUD 2012: 5th International Workshop on Electron-Cloud Effects, La Biodola, Elba, Italy* (in preparation).

[65] K. C. Harkay & R. A. Rosenberg, "Properties of the Electron Cloud in a High-Energy Positron and Electron Storage Ring," *Phys. Rev. ST Accel. Beams* **6**, 034402 (Mar. 2003).

[66] Z. Y. Guo *et al.*, "The Experimental Study on Beam-Photoelectron Instability in BEPC," in *Proceedings of the 1997 Particle Accelerator Conference, Vancouver, BC, Canada* (1997), p. 1566–1568.

[67] J. A. Holmes *et al.*, "Computational Beam Dynamics Studies of Collective Instabilities Observed in SNS," in *Proceedings of the 2008 European Particle Accelerator Conference, Genoa, Italy* (2008), p. 1640–1642.

[68] W. Fischer *et al.*, "Electron Cloud Observations and Cures in the Relativistic Heavy Ion Collider," *Phys. Rev. ST Accel. Beams* **11**, 041002 (Apr. 2008).

[69] R. J. Macek *et al.*, "Electron Cloud Diagnostics in Use at the Los Alamos PSR," in *Proceedings of the 2003 Particle Accelerator Conference, Portland, OR*, J. Chew, P. Lucas & S. Webber, Eds. (2003), p. 508–510.

[70] R. Cimino *et al.*, "Electron Cloud Build-Up Study for DAΦNE," in *Proceedings of the 2005 Particle Accelerator Conference, Knoxville, TN*, C. Horak, Ed. (2005), p. 779–781.

[71] M. A. Furman & G. R. Lambertson, "The Electron-Cloud Instability in the Arcs of the PEP-II Positron Ring," in *Proceedings of MBI97: International Workshop on Multibunch Instabilities in Future Electron and Positron Accelerators, Tsukuba, Japan, 1997*, Y. H. Chin, Ed. (1997), KEK Proceedings 97-17, p. 170.

[72] A. Kulikov *et al.*, "The Electron Cloud Instability at PEP-II," in *Proceedings of the 2001 Particle Accelerator Conference, Chicago, IL*, P. Lucas & S. Webber, Eds. (2001), p. 1903–1905.

[73] X. Zhang *et al.*, "Electron Cloud Studies at Tevatron and Main Injector," in *Proceedings of*

the 2007 Particle Accelerator Conference, Albuquerque, NM, C. Petit-Jean-Genaz, Ed. (2007), p. 3501–3503.

[74] R. Cappi *et al.*, "Electron Cloud Buildup and Related Instability in the CERN Proton Synchrotron," *Phys. Rev. ST Accel. Beams* **5**, 094401 (Sep. 2002).

[75] G. Rumolo *et al.*, "Experimental Studies on the SPS Electron Cloud," in *Proceedings of BEAM 2007: CARE-HHH-APD Workshop on Finalizing the Roadmap for the Upgrade of the CERN & GSI Accelerator Complex, Geneva, Switzerland*, W. Scandale & F. Zimmermann, Eds. (2007), CERN-2008-005/CARE-Conf-08-004-HHH, p. 202–208.

[76] K. Akai, "High Intensity Issues for Super B-Factories," in *Proceedings of the 2003 Particle Accelerator Conference, Portland, OR*, J. Chew, P. Lucas & S. Webber, Eds. (2003), p. 356–360.

[77] G. Rumolo, W. Bruns & Y. Papaphilippou, "Electron Cloud Build Up and Instability in the CLIC Damping Rings," in *Proceedings of the 2008 European Particle Accelerator Conference, Genoa, Italy* (2008), p. 661–663.

[78] M. Pivi *et al.*, "Suppressing Electron Cloud in Future Linear Colliders," in *Proceedings of the 2005 Particle Accelerator Conference, Knoxville, TN*, C. Horak, Ed. (2005), p. 24–28.

[79] F. Le Pimpec *et al.*, "Properties of TiN and TiZrV Thin Film as a Remedy Against Electron Cloud," *Nucl. Instrum. Methods Phys. Res.* **A551**, p. 187–199 (Jul. 2005).

[80] Y. Funakoshi *et al.*, "KEKB Performance," in *Proceedings of the 2001 Particle Accelerator Conference, Chicago, IL*, P. Lucas & S. Webber, Eds. (2001), p. 3546–3548.

[81] D. P. Grote *et al.*, "The WARP Code: Modeling High Intensity Ion Beams," in *Proceedings of ECRIS 2004: Electron Cyclotron Resonance Ion Sources: 16th International Workshop on ECR Ion Sources, Berkeley, CA*, M. Leitner, Ed., American Institute of Physics (2004), AIP Conference Proceedings 749, p. 55–58.

[82] R. J. Macek *et al.*, "Recent Observations, Experiments and Simulations of Electron Cloud Buildup in Drift Spaces and Quadrupole Magnets at the Los Alamos PSR," in *Proceedings of the 2009 Particle Accelerator Conference, Vancouver, BC* (2009), p. 4722–4724.

[83] R. Macek *et al.*, "Electron Cloud Generation, Trapping and Ejection from Quadrupoles at the Los Alamos PSR," Presented at ECLOUD 2010: 49th ICFA Advanced Beam Dynamics Workshop on Electron Cloud Physics, Ithaca, NY, October 2010, Talk DIA05.

[84] C. M. Celata, "Electron Cloud Dynamics in the Cornell Electron Storage Ring Test Accelerator Wiggler," *Phys. Rev. ST Accel. Beams* **14**, 041003 (Apr. 2011).

[85] R. W. Hockney & J. W. Eastwood, *Computer Simulation Using Particles*, Hilger, Bristol (1988).

[86] M. A. Furman & M. T. F. Pivi, "Probabilistic Model for the Simulation of Secondary Electron Emission," *Phys. Rev. ST Accel. Beams* **5**, 124404 (Dec. 2002).

[87] M. A. Furman & M. T. F. Pivi, "Simulation of Secondary Electron Emission Based on a Phenomenological Probabilistic Model," Tech. Rep. LBNL-52807/SLAC-PUB-9912, Lawrence Berkeley National Laboratory, University of California, Berkeley, CA (Jun. 2003).

[88] G. Dugan & D. Sagan, "Synrad3D Photon Propagation and Scattering Simulation," in *Proceedings of ECLOUD 2010: 49th ICFA Advanced Beam Dynamics Workshop on Electron Cloud Physics, Ithaca, NY*, K. Smolenski, Ed. (in press), Paper PST08.

[89] D. Schulte & F. Zimmermann, "Electron Cloud Build-Up Simulations using ECLOUD," in *Proceedings of ECLOUD 2004: 31st ICFA Advanced Beam Dynamics Workshop on Electron-Cloud Effects, Napa, CA*, M. Furman, S. Henderson & F. Zimmerman, Eds. (2004), CERN-2005-001, p. 143–152.

[90] G. Rumolo & F. Zimmermann, "Electron Cloud Simulations: Beam Instabilities and Wakefields," *Phys. Rev. ST Accel. Beams* **5**, 121002 (Dec. 2002).

[91] L. F. Wang *et al.*, "Numerical Study of the Photoelectron Cloud in KEKB Low Energy Ring with a Three-Dimensional Particle in Cell Method," *Phys. Rev. ST Accel. Beams* **5**, 124402 (Dec. 2002).

[92] L. F. Wang, "User's Guide for CLOUDLAND," Tech. Rep. KEK Internal 2003-2, KEK, Tsukuba, Japan (2003).

[93] J.-L. Vay *et al.*, "Update on Electron-Cloud Simulations Using the Package WARP-POSINST," in *Proceedings of the 2009 Particle Accelerator Conference, Vancouver, BC* (2009), p. 4719–4721.

[94] K. Ohmi, "Particle-in-Cell Simulation of Beam-Electron Cloud Interactions," in *Proceedings of the 2001 Particle Accelerator Conference, Chicago, IL*, P. Lucas & S. Webber, Eds. (2001), p. 1895–1897.

[95] B. L. Henke, E. M. Gullikson & J. C. Davis, "X-Ray Interactions: Photoabsorption, Scattering, Transmission, and Reflection at $E = 50$–$30{,}000$ eV, $Z = 1$–92," *At. Data Nucl. Data Tables* **54**, p. 181–342 (Jul. 1993).

[96] P. Beckmann & A. Spizzichino, *The Scattering of Electromagnetic Waves from Rough Surfaces*, Pergamon Press, New York (1963).

[97] J. A. Ogilvy, *Theory of Wave Scattering from Random Rough Surfaces*, Hilger, Bristol (1993).

[98] F. Zimmermann, "Synchrotron Radiation in the LHC Arcs — Monte-Carlo Approach," Tech. Rep. LHC Project Note 237, CERN, Geneva, Switzerland (Oct. 2000).

[99] H. Hogrefe & C. Kunz, "Soft X-Ray Scattering from Rough Surfaces: Experimental and Theoretical Analysis," *Appl. Opt.* **26**, p. 2851–2859 (Jul. 1987).

[100] R. J. Noll & P. Glenn, "Mirror Surface Autocovariance Functions and their Associated Visible Scattering," *Appl. Opt.* **21**, p. 1824–1838 (May 1982).

[101] N. Mahne *et al.*, "Experimental Determination of e-Cloud Simulation Input Parameters for DAΦNE," Tech. Rep. EUROTEV-REPORT-2005-013, EUROTeV (2005).

[102] R. Cimino, I. R. Collins & V. Baglin, "VUV Photoemission Studies of Candidate Large Hadron Collider Vacuum Chamber Materials," *Phys. Rev. ST Accel. Beams* **2**, 063201 (Jun. 1999).

[103] B. L. Henke *et al.*, "Low-Energy X-Ray Interaction Coefficients: Photoabsorption, Scattering, and Reflection: $E = 100$–2000 eV $Z = 1$–94," *At. Data Nucl. Data Tables* **27**, p. 1–144 (Jan. 1982).

[104] G. Rumolo, F. Ruggiero & F. Zimmermann, "Simulation of the Electron-Cloud Build Up and Its Consequences on Heat Load, Beam Stability, and Diagnostics," *Phys. Rev. ST Accel. Beams* **4**, 012801 (Erratum: 029901) (Jan. 2001).

[105] G. Rumolo *et al.*, "Dependence of the Electron-Cloud Instability on the Beam Energy," *Phys. Rev. Lett.* **100**, 144801 (Apr. 2008).

[106] M. A. Furman, "Studies of E-Cloud Build Up for the FNAL Main Injector and for the LHC," in *Proceedings of HB2006: 39th Advanced Beam Dynamics Workshop: High Intensity High Brightness Hadron Beams, Tsukuba, Japan* (2006), p. 102–106.

[107] R. Cimino *et al.*, "Can Low-Energy Electrons Affect High-Energy Physics Accelerators?" *Phys. Rev. Lett.* **93**, 014801 (Jul. 2004).

[108] M. A. Furman, "Formation and Dissipation of the Electron Cloud," in *Proceedings of the 2003 Particle Accelerator Conference, Portland, OR*, J. Chew, P. Lucas & S. Webber, Eds. (2003), p. 297–301.

[109] F. Zimmermann, "Electron-Cloud Effects in the LHC," in *Mini Workshop on Electron Cloud Simulations for Proton and Positron Beams—ECLOUD'02, Geneva, Switzerland*, G. Rumolo & F. Zimmermann, Eds. (2002), CERN-2002-001, p. 47–55.

[110] G. Arduini *et al.*, "Electron-cloud Build-Up Simulations and Experiments at CERN," in *Proceedings of the 2004 European Particle Accelerator Conference, Lucerne, Switzerland* (2004), p. 1933–1935.

[111] L. Wang & M. Pivi, "Trapping of Electron Cloud in ILC/CesrTA Quadrupole and Sextupole Magnets," in *Proceedings of ECLOUD 2010: 49th ICFA Advanced Beam Dynamics Workshop on Electron Cloud Physics, Ithaca, NY*, K. Smolenski, Ed. (in press), Paper MOD05.

[112] F. Zimmermann, G. Rumolo & K. Ohmi, "Electron Cloud Build Up in Machines with Short Bunches," in *ICFA Beam Dynamics Newsletter*, K. Ohmi & M. Furman, Eds., International Committee on Future Accelerators, No. 33, p. 14–24 (Apr. 2004).

[113] M. A. Palmer *et al.*, "Design, Implementation and First Results of Retarding Field Analyzers Developed for the CesrTA Program," in *Proceedings of the 2009 Particle Accelerator Conference, Vancouver, BC* (2009), p. 3510–3512.

[114] J. R. Calvey *et al.*, "CesrTA Retarding Field Analyzer Modeling Results," in *Proceedings of the 2010 International Particle Accelerator Conference, Kyoto, Japan* (2010), p. 1970–1972.

[115] M. T. F. Pivi *et al.*, "Observation of Magnetic Resonances in Electron Clouds in a Positron Storage Ring," *Nucl. Instrum. Methods Phys. Res.* **A621**, p. 33–38 (Sep. 2010).

[116] C. M. Celata *et al.*, "Cyclotron Resonances in Electron Cloud Dynamics," in *Proceedings of the 2009 Particle Accelerator Conference, Vancouver, BC* (2009), p. 1807–1811.

[117] C. M. Celata *et al.*, "Electron Cloud Cyclotron Resonances in the Presence of a Short-Bunch-Length Relativistic Beam," *Phys. Rev. ST Accel. Beams* **11**, 091002 (Sep. 2008).

[118] Y. Suetsugu *et al.*, "Experimental Studies on Grooved Surfaces to Suppress Secondary Electron Emission," in *Proceedings of the 2010 International Particle Accelerator Conference, Kyoto, Japan* (2010), p. 2021–2023.

[119] F. Le Pimpec, F. King & R. E. Kirby, "Electron Conditioning of Technical Aluminum Surfaces," Tech. Rep. LCC-0153/SLAC-TN-04-051, Linear Collider Collaboration/SLAC, Stanford, CA (Sep. 2004).

[120] K. G. McKay, "Secondary Electron Emission," in *Advances in Electronics*, L. Marton, Ed., Academic Press, New York, vol. I, p. 65–130 (1948).

[121] T. Kroyer *et al.*, "Unexpected Results on Microwave Waveguide Mode Transmission Measurements in the SPS Beam Pipe," in *Proceedings of ECLOUD 2004: 31st ICFA Advanced Beam Dynamics Workshop on Electron-Cloud Effects, Napa, CA*, M. Furman, S. Henderson & F. Zimmerman, Eds. (2004), CERN-2005-001, p. 89–94.

[122] B. Carlson *et al.*, "Implementation and Comparison of Electron Cloud Measurements at the Cornell Electron Storage Ring," REU Report, LEPP, Cornell University, Ithaca, NY (2009).

[123] K. Hammond *et al.*, "Effects of Reflections on TE-Wave Measurements of Electron Cloud Density," in *Proceedings of ECLOUD 2010: 49th ICFA Advanced Beam Dynamics Workshop on Electron Cloud Physics, Ithaca, NY*, K. Smolenski, Ed. (in press), Paper PST06.

[124] S. J. Buchsbaum & S. C. Brown, "Microwave Measurements of High Electron Densities," *Phys. Rev.* **106**, p. 196–199 (Apr. 1957).

[125] R. G. Carter, "Accuracy of Microwave Cavity Perturbation Measurements," *IEEE Trans. Microwave Theory Tech.* **49**, p. 918–923 (May 2001).

[126] C. Nieter & J. R. Cary, "VORPAL: a Versatile Plasma Simulation Code," *J. Comput. Phys.* **196**, p. 448–473 (May 2004).

[127] K. S. Yee, "Numerical Solution of Initial Boundary Value Problems Involving Maxwell's Equations in Isotropic Media," *IEEE Trans. Antennas Propag.* **14**, p. 302–307 (May 1966).

[128] J.-P. Berenger, "A Perfectly Matched Layer for the Absorption of Electromagnetic Waves," *J. Comput. Phys.* **114**, p. 185–200 (Oct. 1994).

[129] K. Sonnad *et al.*, "Simulation and Analysis of Microwave Transmission through an Electron Cloud, a Comparison of Results," in *Proceedings of the 2007 Particle Accelerator Conference, Albuquerque, NM*, C. Petit-Jean-Genaz, Ed. (2007), p. 3525–3527.

[130] R. J. Goldston & P. H. Rutherford, *Introduction to Plasma Physics*, Institute of Physics, Bristol (1995).

[131] M. T. F. Pivi *et al.*, "Microwave Transmission Measurement of the Electron Cloud Density in the Positron Ring of PEP-II," in *Proceedings of the 2008 European Particle Accelerator Conference, Genoa, Italy* (2008), p. 694–696.

[132] J.-L. Vay, A. Friedman & D. P. Grote, "Self-Consistent Simulations of High-Intensity Beams and E-Clouds with WARP POSINST," in *Proceedings of ICAP 2006: International Computational Accelerator Physics, Chamonix, France* (2006), p. 256–262.

[133] S. De Santis *et al.*, "TE Wave Measurements of the Electron Cloud in the Cesr-TA Ring," in *Proceedings of the 2010 International Particle Accelerator Conference, Kyoto, Japan* (2010), p. 1188–1190.

[134] J. R. Calvey *et al.*, "Methods for Quantitative Interpretation of Retarding Field Analyzer

Data," in *Proceedings of ECLOUD 2010: 49th ICFA Advanced Beam Dynamics Workshop on Electron Cloud Physics, Ithaca, NY*, K. Smolenski, Ed. (in press), Paper PST03.

[135] J. A. Crittenden *et al.*, "Studies of the Effects of Electron Cloud Formation on Beam Dynamics at CesrTA," in *Proceedings of the 2009 Particle Accelerator Conference, Vancouver, BC* (2009), p. 4631–4633.

[136] J. A. Crittenden *et al.*, "Progress in Studies of Electron-cloud-induced Optics Distortions at CesrTA," in *Proceedings of the 2010 International Particle Accelerator Conference, Kyoto, Japan* (2010), p. 1976–1978.

[137] R. P. Badman, "Comparing ECLOUD Simulation Results to 2.1 and 5.3 GeV Positron Shielded Pickup Data," REU Report, LEPP, Cornell University, Ithaca, NY (Aug. 2011).

[138] L. Boon *et al.*, "Application of the SYNRAD3D Photon-Tracking Model to Shielded Pickup Measurements of Electron Cloud Buildup at CesrTA," in *Proceedings of the 2011 International Particle Accelerator Conference, San Sebastián, Spain* (2011), p. 2319–2321.

[139] U. Iriso & G. Rumolo, "Benchmarking Electron Cloud Data with Computer Simulation Codes," in *Proceedings of the 2006 European Particle Accelerator Conference, Edinburgh, Scotland* (2006), p. 363–365.

[140] J. A. Crittenden *et al.*, "Recent Developments in Modeling Time-Resolved Shielded-Pickup Measurements of Electron Cloud Buildup at CESRTA," in *Proceedings of the 2011 International Particle Accelerator Conference, San Sebastián, Spain* (2011), p. 2313–2315.

[141] J. A. Crittenden *et al.*, "Electron Cloud Modeling Results for Time-Resolved Shielded Pickup Measurements at CesrTA," in *Proceedings of ECLOUD 2010: 49th ICFA Advanced Beam Dynamics Workshop on Electron Cloud Physics, Ithaca, NY*, K. Smolenski, Ed. (in press), Paper PST09.

[142] J. A. Crittenden *et al.*, "Electron Cloud Modeling Results for Time-Resolved Shielded Pickup Measurements at CesrTA," in *Proceedings of the 2011 Particle Accelerator Conference, New York, NY* (2011), p. 1752–1754.

[143] J. A. Crittenden *et al.*, "Time-Resolved Shielded-Pickup Measurements and Modeling of Beam Conditioning Effects on Electron Cloud Buildup at CesrTA," in *Proceedings of the 2012 International Particle Accelerator Conference, New Orleans, LA* (2012), p. 1966–1968.

[144] M. T. F. Pivi, "CMAD: A New Self-consistent Parallel Code to Simulate the Electron Cloud Build-up and Instabilities," in *Proceedings of the 2007 Particle Accelerator Conference, Albuquerque, NM*, C. Petit-Jean-Genaz, Ed. (2007), p. 3636–3638.

[145] J. W. Flanagan *et al.*, "Single-Shot Resolution of X-Ray Monitor using Coded Aperture Imaging," in *Proceedings of DIPAC 2011: 10th European Workshop on Beam Diagnostics and Instrumentation for Particle Accelerators, Hamburg, Germany*, M. Marx *et al.*, Eds. (2011), p. 561–563.

[146] K. Ohmi, S. Heifets & F. Zimmermann, "Study of Coherent Tune Shift Caused by Electron Cloud in Positron Storage Rings," in *Proceedings of the Second Asian Particle Accelerator Conference, Beijing, China* (2001), p. 445–447.

[147] H. Jin *et al.*, "Electron Cloud Effects in Cornell Electron Storage Ring Test Accelerator and International Linear Collider Damping Ring," *Jpn. J. Appl. Phys.* **50**, 026401 (Feb. 2011).

[148] K. Ohmi, F. Zimmermann & E. Perevedentsev, "Wake-Field and Fast Head-Tail Instability Caused by an Electron Cloud," *Phys. Rev. E* **65**, 016502 (Dec. 2001).

[149] A. W. Chao, *Physics of Collective Beam Instabilities in High Energy Accelerators*, John Wiley & Sons, New York (1993).

[150] K. Ohmi, "Electron Cloud Instabilities in the Damping Ring of International Linear Collider," in *Proceedings of the 2005 International Linear Collider Physics and Detector Workshop and Second ILC Accelerator Workshop, Snowmass, CO*, N. A. Graf, Ed. (2005), SLAC-R-798/eConf:C0508141, Paper ILCAW0424.

[151] H. Grote & F. C. Iselin, "The MAD Program (Methodical Accelerator Design) Version 8.10 User's Reference Manual," Tech. Rep. CERN-SL-90-13-AP-rev-3, CERN, Geneva, Switzerland (Jan. 1993).

[152] K. G. Sonnad *et al.*, "Progress on Simulation of Beam Dynamics with Electron Cloud Effects: An Update," in *Proceedings of ECLOUD 2010: 49th ICFA Advanced Beam Dynamics Workshop on Electron Cloud Physics, Ithaca, NY*, K. Smolenski, Ed. (in press), Paper PST05.

[153] F. C. Iselin, "Lie Transformations and Transport Equations for Combined-Function Dipoles," *Part. Accel.* **17**, p. 143–155 (Oct. 1985).

[154] M. Frigo & S. G. Johnson, "The Design and Implementation of FFTW3," *Proc. IEEE* **93**, p. 216–231 (Feb. 2005).

[155] Y. Cai *et al.*, "Simulation of the Beam-Beam Effects in e^+e^- Storage Rings with a Method of Reduced Region of Mesh," *Phys. Rev. ST Accel. Beams* **4**, 011001 (Jan. 2001).

[156] J. P. Boris, "Relativistic Plasma Simulation—Optimization of a Hybrid Code," in *Proceedings of the Fourth Conference on the Numerical Simulation of Plasmas, Washington DC*, J. Boris & R. Shanny, Eds., Naval Research Laboratory, Washington DC (1970), p. 3–67.

[157] D. L. Kreinick *et al.*, "Using Coherent Tune Shifts to Evaluate Electron Cloud Effects on Beam Dynamics at CesrTA," in *Proceedings of ECLOUD 2010: 49th ICFA Advanced Beam Dynamics Workshop on Electron Cloud Physics, Ithaca, NY*, K. Smolenski, Ed. (in press), Paper PST10.

[158] J. R. Calvey *et al.*, "Electron Cloud Modeling Considerations at CesrTA," in *Proceedings of the 2009 Particle Accelerator Conference, Vancouver, BC* (2009), p. 3306–3308.

[159] G. F. Dugan, M. A. Palmer & D. L. Rubin, "ILC Damping Rings R&D at CesrTA," in *ICFA Beam Dynamics Newsletter*, J. Urakawa, Ed., International Committee on Future Accelerators, No. 50, p. 11–33 (Dec. 2009).

[160] J. W. Flanagan *et al.*, "Observation of Vertical Betatron Sideband due to Electron Clouds in the KEKB Low Energy Ring," *Phys. Rev. Lett.* **94**, 054801 (Feb. 2005).

[161] J. W. Flanagan *et al.*, "Further Studies on Betatron Sidebands due to Electron Clouds," in *Proceedings of the 2006 European Particle Accelerator Conference, Edinburgh, Scotland* (2006), p. 2898–2900.

[162] K. Ohmi *et al.*, "Simulation Analysis of Head-Tail Motion Caused by Electron Cloud," in *Proceedings of the 2005 Particle Accelerator Conference, Knoxville, TN*, C. Horak, Ed. (2005), p. 907–909.

[163] E. Benedetto *et al.*, "Simulation of the Synchro-Betatron Sideband Instability Caused by Electron Clouds at KEKB," in *Proceedings of the 2007 Particle Accelerator Conference, Albuquerque, NM*, C. Petit-Jean-Genaz, Ed. (2007), p. 4033–4035.

[164] K. Ohmi & H. C. Jin, "Fast Head Tail Instability due to Electron Cloud under the Presence of the Dispersion," in *Proceedings of the 2009 Particle Accelerator Conference, Vancouver, BC* (2009), p. 4686–4688.

[165] E. Benedetto, G. Franchetti & F. Zimmermann, "Incoherent Effects of Electron Clouds in Proton Storage Rings," *Phys. Rev. Lett.* **97**, 034801 (Jul. 2006).

[166] M. Billing *et al.*, "Techniques for Observing Beam Dynamical Effects Caused by the Presence of Electron Clouds," in *Proceedings of ECLOUD 2010: 49th ICFA Advanced Beam Dynamics Workshop on Electron Cloud Physics, Ithaca, NY*, K. Smolenski, Ed. (in press), Paper PST07.

[167] M. G. Billing *et al.*, "Measurement Techniques to Characterize Instabilities Caused by Electron Clouds," in *Proceedings of the 2011 Particle Accelerator Conference, New York, NY* (2011), p. 1852–1854.

[168] D. L. Kreinick *et al.*, "Application of Coherent Tune Shift Measurements to the Characterization of Electron Cloud Growth," in *Proceedings of the 2011 Particle Accelerator Conference, New York, NY* (2011), p. 1680–1682.

[169] C. K. Birdsall & A. B. Langdon, *Plasma Physics Via Computer Simulation*, Taylor & Francis, New York (2005).

[170] J. D. Jackson, *Classical Electrodynamics*, John Wiley & Sons, New York, second ed. (1975).

[171] K. L. Bane *et al.*, "Configuration Studies and Recommendations for the ILC Damping Rings," Tech. Rep. LBNL-59449/Cockroft-06-04, Lawrence Berkeley National Laboratory, University of California, Berkeley, CA (Feb. 2006).

[172] M. Pivi *et al.*, "Simulation of the Electron Cloud for Various Configurations of a Damping Ring for the ILC," in *Proceedings of the 2006 European Particle Accelerator Conference, Edinburgh, Scotland* (2006), p. 2958–2960.

[173] G. Aarons *et al.*, "International Linear Collider Reference Design Report," Tech. Rep. ILC-REPORT-2007-001, International Linear Collider, Batavia, IL/Tsukuba, Japan/Hamburg, Germany (Aug. 2007).

[174] M. T. F. Pivi *et al.*, "Recommendation for Mitigations of the Electron Cloud Instability in the ILC," in *Proceedings of the 2011 International Particle Accelerator Conference, San Sebastián, Spain* (2011), p. 1063–1065.

[175] Y. Suetsugu *et al.*, "Design and Construction of the SuperKEKB Vacuum System," *J. Vac. Sci. Technol. A* **30**, 031602 (May 2012).